UNIVERSIDAD COMPLUTENSE DE MADRID
FACULTAD DE CIENCIAS QUÍMICAS
Departamento de Ingeniería Química y de Materiales

TESIS DOCTORAL

Corrosión atmosférica marina de aceros al carbono

MEMORIA PARA OPTAR AL GRADO DE DOCTOR

PRESENTADA POR

Jenifer Alcántara González

Directores

Manuel Morcillo Linares
Belén Chico González

Madrid
Ed. electrónica 2019

UNIVERSIDAD COMPLUTENSE DE MADRID

FACULTAD DE CIENCIAS QUÍMICAS

Departamento de Ingeniería Química y de Materiales

CORROSIÓN ATMOSFÉRICA MARINA DE ACEROS AL CARBONO

Jenifer Alcántara González

Directores

Prof. Manuel Morcillo Linares (CENIM/CSIC)

Dra. Belén Chico González (CENIM/CSIC)

CONSEJO SUPERIOR DE INVESTIGACIONES CIENTÍFICAS (CSIC)

CENTRO NACIONAL DE INVESTIGACIONES METALÚRGICAS (CENIM)

Departamento de Ingeniería de Superficies, Corrosión y Durabilidad

CENIM
Centro Nacional de Investigaciones Metalúrgicas

CSIC
Consejo Superior de Investigaciones Científicas

TESIS DOCTORAL 2018

UNIVERSIDAD COMPLUTENSE DE MADRID

FACULTAD DE CIENCIAS QUÍMICAS

Departamento de Ingeniería Química y de Materiales

TESIS DOCTORAL

CORROSIÓN ATMOSFÉRICA MARINA DE ACEROS AL CARBONO

MEMORIA para optar al grado de Doctor presentada por:

Jenifer Alcántara González

Licenciada en Ingeniería de Materiales

Directores

Prof. Manuel Morcillo Linares (CENIM/CSIC)

Dra. Belén Chico González (CENIM/CSIC)

Tutora

Dra. Endzhe Matykina (UCM)

CONSEJO SUPERIOR DE INVESTIGACIONES CIENTÍFICAS (CSIC)

CENTRO NACIONAL DE INVESTIGACIONES METALÚRGICAS (CENIM)

Departamento de Ingeniería de Superficies, Corrosión y Durabilidad

MADRID, 2018

“El hombre nunca sabe de lo que es capaz de hacer hasta que lo intenta.”

Charles Dikens

AGRADECIMIENTOS

Después de un largo y tedioso, pero a la vez fascinante camino para culminar este trabajo, te das cuenta de la gran cantidad de personas que, directa o indirectamente, han participado apoyándome incondicionalmente, dando ánimo, teniendo paciencia, acompañando en los momentos de crisis y en los momentos de felicidad además de prestándome ayuda, colaborando y compartiendo su experiencia para llevar a término este trabajo. A todos ellos deseo expresar mi agradecimiento en este apartado.

En primer lugar me gustaría agradecer a mis dos directores de tesis. Al Prof. Manuel Morcillo por haberme aceptado a formar parte de su grupo de trabajo, dirigiendo esta tesis doctoral, al que le he hecho dudar hasta el último momento, si la presente tesis doctoral vería la luz debido a mis grandes altibajos. Lo que nunca ha dudado es en apoyarme y darme ánimo a continuar hasta al final, además de estar encantado de enseñarme su conocimiento, facilitándome el trabajo y ayudándome en todo lo necesario. Debo agradecer también a mi segunda directora, la Dra. Belén Chico, por sus valiosas aportaciones al conocimiento, además de apoyarme y animarme para finalizar este trabajo.

A la Dra. Endzhe Matykina, por querer formar parte de esta tesis y ejercer de tutora de la misma facilitándome el poder realizarla fuera de la universidad.

Agradecer también al resto de integrantes del grupo CAPA donde he desarrollado este trabajo. Al Dr. Iván Díaz por su disponibilidad para ayudarme, aconsejarme y facilitarme el trabajo durante mi estancia en el CENIM. Al Dr. Joaquín Simancas por la gran amabilidad con la que siempre me ha atendido. Al Dr. Daniel de la Fuente, al que hoy en día puedo hablar de mi amigo Daniel, que me ha aconsejado, ayudado y apoyado a pesar de mi testarudez a lo largo de estos años, tanto en el ámbito laboral como personal, siempre con una actitud positiva y optimista, quitando importancia a las cosas para que yo viese la luz al final del camino. A mi amiga y compañera de despacho Cristina Zea que me ha acompañado, ayudado, apoyado, aconsejado, animado en todo momento, etc… no solo en estos años de desarrollo de la tesis doctoral sino desde nuestra etapa universitaria. A Lara, una persona muy especial que compartió con nosotros una estancia de tan solo cuatro meses inolvidables, pero que me trae buenos momentos a la memoria, siempre alegre y dispuesta a ayudarte en lo que hiciera falta con una sonrisa de oreja a oreja.

También agradecer a mis compañeros del departamento de Ingeniería de superficies, corrosión y durabilidad, Emilio, Cristina, Mª Lorenza, Sebas, Juan Carlos, Irene, Santi, Blanca, Marc, Conchi, Fede, etc… en particular a Ana por los consejos y apoyo moral que me ofrecía escuchándome en los momentos bajos.

A lo largo de estos años han sido varias las personas y entidades que han colaborado en la parte técnica de la presente tesis tanto permitiéndome el uso de sus instalaciones como realizando algunas técnicas de caracterización necesarias en la investigación llevada a cabo, a las cuales debo expresar mi agradecimiento:

- A ENEL y Gas Natural por dejarnos usar su Parque Eólico de Cabo Vilano como campo de experimentación de nuestras probetas de ensayo, además de facilitarnos datos acerca del Parque Eólico.
- A la Agencia Estatal de Meteorología (AEMET) y Puertos del Estado por facilitarnos datos para nuestro estudio.
- D. José Antonio Jiménez y de Dña. Irene Llorente por la técnica de XRD, realizada en el Centro Nacional de Investigaciones Metalúrgicas (CENIM/CSIC).
- D. José María González Calbet y su grupo de investigación por la adquisición de las imágenes por TEM y análisis EDS realizados en el ICTS Centro Nacional de Microscopía Electrónica de la UCM.
- D. José F. Marco por la técnica de espectroscopía Mössbauer realizada en el Instituto de Química Física Rocasolano (IQFR/CSIC).
- Dña. Paloma Adeva, D. Alfonso García y D. Antonio Tomás por la adquisición de las imágenes por SEM y análisis EDS (CENIM/CSIC).
- A Hybriscan Technologies (Arnhem, Países Bajos) por permitirnos realizar las medidas SEM/μRaman en sus instalaciones, aunque con un gran coste económico sufragado por el grupo de investigación.

Por último y no menos importante debo agradecer en el plano personal, a mis padres, Norberto y Gloria, por todo lo que han hecho para que pudiese llegar hasta este punto, así como a mi hermano que ha estado presente en todo momento a mi lado, tendiéndome la mano sin dudar tantas veces como he necesitado, a pesar de las continuas ayudas necesitadas. A Jorge por su apoyo incondicional y ánimo pese a tener que aguantar las crisis que se sufren durante este duró trabajo. Agradecerle también por hacer posible cumplir unos de nuestros mayores deseos de formar una familia, Sofía, la gran ilusión de mi vida que ha sido el punto de inflexión para darme fuerza y luz y por fin decidirme a terminar la presente tesis.

ÍNDICE

RESUMEN

El acero al carbono es el material metálico, hoy por hoy, más empleado en las estructuras que operan al aire libre y mantiene una posición predominante en la ingeniería de materiales. Se utiliza, tanto por ser un material relativamente económico como por su notable resistencia mecánica. Una gran parte del acero queda expuesto a la intemperie y, a menudo, en atmósferas fuertemente contaminadas en las que la corrosión se acelera de modo considerable respecto a la corrosión en un medio rural y limpio.

La corrosión atmosférica en regiones costeras es un tema particularmente relevante debido a su gran trascendencia para la sociedad. Aproximadamente la mitad de la población mundial vive en regiones costeras y la industrialización de países desarrollados tiende a concentrar las plantas de producción próximas a la costa.

Desde un inicio nos planteamos clarificar algunas de las incertidumbres existentes en este campo científico:

(a) Estudiar el aerosol marino: su dependencia de parámetros ambientales y su efecto en la corrosión atmosférica del acero al carbono.
(b) Profundizar en el conocimiento de las fases de herrumbre que se forman sobre el acero cuando se expone a atmósferas marinas, como es el caso de la fase akaganeita, fase fundamental en los procesos de corrosión atmosférica marina.
(c) Existe un gran desconocimiento sobre las morfologías que presentan las distintas fases de herrumbre: lepidocrocita, goetita, akaganeita, magnetita, etc. En esta investigación, con la ayuda de una nueva técnica, SEM/μRaman, se ha podido por primera vez caracterizar analíticamente las variadas morfologías que pueden presentar las distintas fases de herrumbre.
(d) La exposición del acero al carbono en atmósferas marinas con altas velocidades de depósito de cloruros conduce a la formación de capas muy gruesas de herrumbre que tienden a exfoliarse (desprenderse) del sustrato de acero, dejándolo desprotegido. La velocidad de corrosión del acero en estas condiciones es elevadísima por lo que resultó especialmente importante caracterizar, con profundidad y rigor científico, la estructura interna de estas capas exfoliadas de herrumbre.

La investigación que se presenta en esta Memoria fue realizada con probetas de acero suave al carbono (0,13 % de C) expuestas a la atmósfera marina pura del Parque Eólico de Cabo Vilano

situado en la Costa de la Muerte, concretamente en el Municipio de Camariñas, en la provincia de La Coruña. Se expusieron probetas de ensayo en estaciones de corrosión que se fijaron a diversos aerogeneradores del Parque Eólico ubicados a distintas distancias de la línea de costa. En este trabajo se muestran los resultados obtenidos a lo largo del periodo abril 2013 a octubre 2015 de exposición. Al tratarse de una atmósfera marina pura, el parámetro más importante desde el punto de vista de la corrosión del acero al carbono expuesto en este ambiente es la velocidad de depósito de cloruros (salinidad atmosférica). Las estaciones de corrosión disponían de un dispositivo (candela húmeda) para la determinación de la salinidad atmosférica en ese determinado lugar.

Para la caracterización de las herrumbres formadas sobre el acero al carbono se acudió a un número importante de técnicas experimentales: microscopía óptica (con y sin luz polarizada), Difracción de Rayos X (XRD), Microscopía Electrónica de Barrido (SEM), Espectroscopía Infrarroja por Transformada de Fourier (FTIR), Microscopía Electrónica de Transmisión (TEM) (en el Centro Nacional de Microscopía Electrónica de la Universidad Complutense de Madrid), Espectroscopía Mössbauer (en el Instituto de Química-Física Rocasolano, CSIC) y SEM/μRaman (en Hybriscan Technologies, Arnhem, Países Bajos).

Los resultados obtenidos evidencian que el campo experimental donde se ha llevado a cabo el estudio presenta una humedad relativa alta (83,2% HR), temperatura suave (13,5°C) y alta precipitación ($>$ 155 días/año), lo que da lugar a altos tiempos de humectación de la superficie metálica que favorecen los procesos de corrosión atmosférica. Además, la zona está sometida a fuertes vientos marinos con un considerable arrastre del aerosol marino (predominante en la dirección NE), que ha potenciado enormemente la velocidad de corrosión del acero al carbono.

Las herrumbres formadas sobre el acero suave están constituidas por diferentes oxihidróxidos y óxidos de hierro. En todas las herrumbres se observa la presencia de lepidocrocita, goetita, magnetita/maghemita y akaganeita como fases principales. La lepidocrocita y la goetita son los productos mayoritarios, en tanto que la magnetita/maghemita y la akaganeita se suelen encontrar en las herrumbres en menores concentraciones.

Como se verá a lo largo de esta Memoria, la akaganeita, fase que únicamente se forma en las atmósferas marinas, tiene un papel fundamental en el proceso de corrosión atmosférica marina del acero al carbono. Las condiciones ambientales de la atmósfera que conducen a la formación de esta fase son: una humedad relativa media anual $\geq$ 80%, y simultáneamente una velocidad media anual de depósito de ion cloruro $\geq$ 60 mg $Cl^-/m^2 \cdot$día.

La akaganeita se localiza preferentemente en la herrumbre existente en la intercara herrumbre/ sustrato metálico, lo que dificulta su identificación. Además, debido a su pequeño tamaño, se requiere operar a altos aumentos en las observaciones microscópicas. Mediante microscopía electrónica de barrido de alta resolución se han logrado detectar los agregados “tipo esponja” de akaganeita en la capa más interna de la herrumbre, constituidos por un entramado de finos cristales alargados con la morfología tipo varilla de esta fase.

La lepidocrocita presenta morfologías muy variadas, globulares y laminares de diferentes tipos: en forma de barras, nidos de gusanos, nidos de pájaros, plumas, etc. La goetita tiende a formar morfologías aciculares y tubulares. La magnetita básicamente presenta dos tipos de morfologías: en forma de manchas negras planas y formaciones toroidales negras en forma de anillos circulares.

La estructura de las capas de productos de corrosión formadas sobre la superficie de acero presenta dos situaciones extremas, que van desde la formación de una "capa de herrumbre consolidada" (a salinidades atmosféricas relativamente bajas) hasta la formación de gruesas capas altamente imperfectas y agrietadas (a muy altas salinidades), "capas de herrumbre exfoliadas", que se desprenden fácilmente del acero base.

Los mecanismos de corrosión atmosférica en estas dos situaciones son completamente diferentes. En el caso de una "capa de herrumbre consolidada", el mecanismo de corrosión está controlado por procesos de difusión, por los que las especies agresivas de la atmósfera (oxígeno, agua y cloruro) pasan a través de la capa de óxido para interactuar con el acero subyacente. La reacción catódica predominante es la reducción de oxígeno disuelto en la película acuosa. La velocidad de corrosión depende de la concentración de iones cloruro en la atmósfera. Estos iones se incorporan a las películas de humedad condensada o películas acuosas depositadas sobre la superficie del acero y aceleran el proceso de corrosión atmosférica. Los productos de corrosión formados están compuestos principalmente de lepidocrocita y goetita, y en menor medida magnetita y akaganeita.

En el caso de una "capa de herrumbre exfoliada", la alta concentración de cloruro en la capa acuosa depositada sobre la superficie del acero da lugar a la formación de cloruro ferroso, que hidroliza el agua, elevando notablemente la acidez del electrolito. En esta situación, la reacción catódica de evolución de hidrógeno es importante, acelerando notablemente el proceso de corrosión atmosférica. La alta concentración de cloruro, las condiciones ácidas y el agotamiento de oxígeno en la intercara acero/ herrumbre conducen a la formación de altos contenidos de akaganeita y magnetita en la capa de herrumbre.

Al final de esta Memoria se anexan las seis publicaciones que consideramos más representativas del estudio realizado. Como se observa en estos artículos la investigación llevada a cabo es más amplia que la descrita en esta Memoria, decidiéndose así para facilitar la lectura de la misma, destacando únicamente lo más relevante. Además de las publicaciones anexadas, hay otras publicaciones en revistas de alto impacto realizadas por el grupo de investigación, en las que la doctoranda ha sido también coautora, que amplían el trabajo expuesto en esta Memoria.

SUMMARY

Carbon steel is the most widely used metallic material in outdoor structures and holds a predominant position in materials engineering today. Its popularity is due to both its relative low cost and its good mechanical strength. A large amount of steel is exposed to open air conditions, often in highly polluted atmospheres where corrosion is considerably accelerated in comparison to clean and rural environments.

Atmospheric corrosion in coastal regions is a particularly relevant matter with a considerable impact on modern society. About half of the world's population lives in coastal regions and industrialisation in developing countries tends to be concentrated in areas close to the sea.

From the outset, our aim has been to shed light on some of the grey areas in this scientific field:

(a) Studying marine aerosol: its dependence on environmental parameters and its effect on the atmospheric corrosion of carbon steel.
(b) Furthering knowledge of the rust phases that form on steel exposed to marine environments; such as the akaganeite phase, which plays a fundamental role in marine atmospheric corrosion processes.
(c) There are large gaps in knowledge about the morphologies with which the various rust phases (lepidocrocite, goethite, akaganeite, magnetite, etc.) can appear. In this research, with the assistance of a new SEM/µRaman technique, it has been possible for the first time to analytically characterise different morphologies of each rust phase.
(d) The exposure of carbon steel in marine atmospheres with high chloride deposition rates leads to the formation of very thick rust layers that tend to exfoliate (become detached) from the steel substrate, leaving it unprotected. The steel corrosion rate in these conditions is extremely high. It is especially important to characterise the internal structure of these exfoliated rust layers in depth and with full scientific rigor, with the aim to know the corrosion mechanisms involved.

The research presented in this doctoral thesis was carried out with mild steel specimens (0,13 wt% C) exposed to the pure marine atmosphere of Cabo Vilano Wind Farm in the municipal district of Camariñas, located on the Atlantic coast of Corunna province in north-western Spain. Test specimens were exposed in testing stations that were affixed to several wind turbine towers situated at different distances from the shoreline. This work focuses on

exposure results obtained for the period from April 2013 to October 2015. As this is a pure marine atmosphere, the most important parameter from the viewpoint of carbon steel corrosion resulting from exposure to this environment is the chloride deposition rate (atmospheric salinity). The testing stations incorporated a wet candle device to determine the atmospheric salinity level at that particular point.

A large number of experimental techniques were used in the characterisation of the rusts formed on carbon steel: optical microscopy (with and without polarised light), X-ray diffraction (XRD), scanning electron microscopy (SEM), Fourier transform infrared spectroscopy (FTIR), transmission electron microscopy (TEM) (at the National Centre for Electron Microscopy at the Univesity Complutense of Madrid), Mössbauer spectroscopy (at the Rocasolano Institute of Physical Chemistry (IQFR-CSIC)), and SEM/μRaman (at Hybriscan Technologies, Arnhem, Netherlands).

The results obtained reveal that the test site where the study was carried out presents a high relative humidity (83,2% RH), mild temperature (13,5°C) and high rainfall (>155 days/year), giving rise to prolonged times of wetness of the metallic surface and thus favouring atmospheric corrosion processes. Moreover, the area is subject to strong marine winds (predominantly north-easterly) with considerable entrainment of marine aerosol, which greatly boosts the carbon steel corrosion rate.

The rusts formed on the mild steel are composed of different iron oxides and oxyhydroxides. Lepidocrocite, goethite, magnetite/maghemite and akaganeite are seen to be the main phases present in all the rusts. Lepidocrocite and goethite are the major products while magnetite/maghemite and akaganeite are usually found in smaller concentrations.

As will be seen throughout this dissertation, akaganeite (a phase that only forms in marine atmospheres) plays a fundamental role in the marine atmospheric corrosion process of carbon steel. It was found that the atmospheric environment conditions that lead to the formation of this phase are a mean annual relative humidity of ≥80% and simultaneously a mean annual chloride ion deposition rate of ≥ 60 mg $Cl^-/m^2 \cdot day$.

Akaganeite is preferentially located in rust at the rust/metallic substrate interface and is therefore difficult to identify. Furthermore, its small size means that microscopic observations need to be carried out at high magnification levels. Using high resolution scanning electron microscopy it has been possible to detect “sponge-type” akaganeite aggregates in the

innermost rust layer, constituted by a framework of long thin crystals with the rod-type morphology of this phase.

Lepidocrocite presents highly varied morphologies, with globular and laminar morphologies of different types: bar-shaped, worm's nest, bird's nest, feathers, etc. Goethite tends to form acicular and tubular morphologies. Magnetite basically presents two types of morphologies: flat black patches and toroidal black formations in the form of circular rings.

The structure of the corrosion product layers formed on the steel surface presents two extreme situations, going from the formation of a "consolidated rust layer" at relatively low atmospheric salinities to the formation of highly imperfect and cracked thick layers at very high salinities, "exfoliated rust layers", which easily become detached from the base steel. The atmospheric corrosion mechanisms in these two situations are entirely different.

In the case of a "consolidated rust layer" the corrosion mechanism is controlled by diffusion processes, in which aggressive species from the atmosphere (oxygen, water and chloride) pass through the oxide layer to interact with the underlying steel. The predominant cathodic reaction is the reduction of oxygen dissolved in the aqueous film. The corrosion rate depends on the chloride ion concentration in the aqueous layer. These ions are incorporated in the condensed moisture films or aqueous films deposited on the steel surface and accelerate the atmospheric corrosion process. The corrosion products formed are composed mainly of lepidocrocite and goethite and to a lesser extent magnetite and akaganeite.

In the case of an "exfoliated rust layer" the high chloride concentration in the aqueous layer deposited on the steel surface gives rise to the formation of ferrous chloride which hydrolyses the water, notably raising the acidity of the electrolyte. In this situation the cathodic reaction of hydrogen evolution is important, accelerating even more the atmospheric corrosion process. The high chloride concentration, acid conditions and oxygen depletion at the steel/rust interface lead to the formation of high akaganeite and magnetite contents in the rust layer.

The six publications considered to be most representative of the study performed are attached as annexes to this document. As can be seen in these papers, the research that has been carried out has a broader scope than that which has been described in this dissertation, the intention here being to facilitate its reading and to highlight only the most relevant aspects. In addition to the annexed publications, the research group has produced other publications in

high impact journals in which the doctoral candidate has also participated as joint author, complementing the work undertaken during this time.

LISTADO DE PUBLICACIONES

Publicación 1 (Anexo I)

Airborne chloride deposit and its effect on marine atmospheric corrosion of mild steel.
J. Alcántara, B. Chico, I. Díaz, D. de la Fuente and M. Morcillo
Corrosion Science 97 (2015) 74-88

Publicación 2 (Anexo II)

An attempt to classify the morphologies presented by different rust phases formed during the exposure of carbon steel to marine atmospheres.
J. Alcántara, B. Chico, J. Simancas, I. Díaz, D. de la Fuente and M. Morcillo
Materials Characterization 118 (2016) 65-78

Publicación 3 (Anexo III)

Environmental conditions for akaganeite formation in marine atmosphere mild steel corrosion products and its characterization.
M. Morcillo, J.M. González-Calbet, J.A. Jiménez, I. Díaz, J. Alcántara, B. Chico, A. Mazarío-Fernández, A. Gómez-Herrero, I. Llorente, and D. de la Fuente
Corrosion 71 (7) (2015) 872-886

Publicación 4 (Anexo IV)

Rust exfoliation on carbon steels in chloride-rich atmospheres.
B. Chico, J. Alcántara, E. Pino, I. Díaz, J. Simancas, A. Torres-Pardo, D. de la Fuente, J. A. Jiménez, J. F. Marco, J. M. González-Calbet and M. Morcillo
Corrosion Review 33 (5) (2015) 263-282

Publication 5 (Anexo V)

Corrosion mechanisms of mild steel in chloride-rich atmospheres.
D. de la Fuente, I. Díaz, J. Alcántara, B. Chico, J. Simancas, I. Llorente, A. García-Delgado, J. A. Jiménez, P. Adeva and M. Morcillo
Materials and Corrosion 67 (2015) 227-238

Publicación 6 (Anexo VI)

Marine atmospheric corrosion of carbon steel: a review.
J. Alcántara, D. de la Fuente, B. Chico, J. Simancas, I. Díaz and M. Morcillo
Materials 10 (4) (2017) 406

DECLARACIÓN DE AUTORÍAS

Bajo la supervisión de mis directores, he realizado la mayor parte del trabajo experimental que incluye esta Memoria: preparación de muestras para su exposición a la atmósfera, exposición y retirada con una periodicidad de tres meses de las muestras metálicas y de los captadores medidores de parámetros ambientales, análisis de los parámetros ambientales del campo de experimentación, determinaciones de granulometría y espesor de herrumbre, pérdidas de masa (gravimetría), etc.

Para la caracterización de las capas de herrumbre formadas, he realizado la preparación de las todas las muestras y estudios por microscopía óptica, SEM/EDS y FTIR. Para aquellas otras técnicas cuyos equipos son manejados por técnicos especializados (XRD, TEM/EDS, espectroscopía Mössbauer, SEM/μRaman, etc.) he colaborado con las siguientes personas:

- D. José Antonio Jiménez y de Dña. Irene Llorente, para la adquisición de los difractogramas por XRD y ajustes de los patrones por Rietveld, medidas de XRD en área seleccionada y GIXRD, en el Centro Nacional de Investigaciones Metalúrgicas (CENIM/CSIC).
- D. José María González Calbet, D. Adrián Gómez Herrero, Dña. Almudena Torres Pardo y D. Ángel Mazarío Fernández, para la adquisición de las imágenes por TEM y análisis EDS, en el ICTS Centro Nacional de Microscopía Electrónica de la UCM.
- D. José F. Marco, para la adquisición e interpretación de los espectros Mössbauer, en el Instituto de Química Física Rocasolano (IQFR/CSIC).
- Dña. Paloma Adeva, D. Alfonso García y D. Antonio Tomás, para la utilización del SEM y análisis EDS (CENIM/CSIC).
- Las medidas de SEM/μRaman fueron realizadas en Hybriscan Technologies (Arnhem, Países Bajos) aunque un primer intento de adquisición de las medidas SEM/μRaman fue llevado a cabo en el laboratorio LASPEA de la Universidad del País Vasco.

La interpretación y análisis de los datos obtenidos se realizó en colaboración con mis directores de tesis e integrantes del grupo de investigación en el que he desarrollado este trabajo (D. Daniel de la Fuente, D. Iván Díaz y D. Joaquín Simancas).

Mi contribución en los artículos anexados a esta Memoria ha sido la siguiente: como se ha comentado anteriormente he realizado la mayor parte del procedimiento experimental.

La interpretación de datos ha sido discutida por los integrantes del grupo de investigación en el que he realizado el presente trabajo, con una gran ayuda de mi director de tesis Manuel Morcillo debido a su gran conocimiento adquirido en esta temática. Por último, en cuanto a los manuscritos, he redactado con gran ayuda de mis directores de tesis aquellos en los que soy primera autora, mientras que en los restantes, he contribuido en la redacción de los mismos.

1. INTRODUCCIÓN

1.1 Trascendencia de la corrosión atmosférica marina del acero al carbono

El acero al carbono es el material metálico, hoy por hoy, más empleado en las estructuras que operan al aire libre. Se utiliza en la fabricación de gran variedad de equipos y grandes estructuras metálicas, tanto por ser un material relativamente económico como por su notable resistencia mecánica. Una gran parte del acero queda expuesto a la intemperie y, a menudo, en atmósferas fuertemente contaminadas en las que la corrosión se acelera de modo considerable respecto a la corrosión en un medio rural y limpio.

Evaluaciones llevadas a cabo por comités de expertos en corrosión y protección contra la corrosión, fijan las pérdidas anuales causadas por la corrosión (costos directos) en torno al 3,5% del producto nacional bruto (PNB) de un país [1, 2]. El sector "marino" participa en un 21% de dicho índice, lo que indica la importancia económica del medio marino en el alcance de la corrosión metálica.

La corrosión atmosférica es la causa más frecuente de la destrucción de metales y aleaciones. La contaminación atmosférica, bien sea de origen natural (p. ej. el aerosol marino) o antropogénico (p. ej. el SO_2) acelera el proceso de corrosión atmosférica.

Desde los primeros compases del siglo XX se ha dedicado un esfuerzo investigador muy notorio al estudio de la corrosión de metales en atmósferas naturales. Como consecuencia de ello, la importancia de las diversas variables meteorológicas (temperatura, humedad relativa, lluvia, etc.) y de contaminación atmosférica en la corrosión atmosférica es bien conocida. Sin embargo, así como el efecto del anhídrido sulfuroso (SO_2) en la corrosión atmosférica del acero al carbono ha sido muy estudiado, no deja de extrañar que la acción de los cloruros marinos haya recibido hasta hace relativamente poco tiempo escasa atención por parte de los investigadores, teniendo en cuanta del enorme incremento de la velocidad de corrosión del acero en las regiones marinas con relación a una atmósfera libre de contaminación.

La corrosión atmosférica en regiones costeras es un tema particularmente relevante debido a su gran trascendencia para la sociedad. Aproximadamente la mitad de la población mundial vive en regiones costeras y la industrialización de países desarrollados tiende a concentrar las plantas de producción próximas a la costa.

El primer estudio riguroso sobre la salinidad de las atmósferas marinas y su efecto en la corrosión metálica se debe a Ambler y Bain [3] en Nigeria y data de 1955. Durante mucho

tiempo la doctrina existente se limitaba a exponer que los cloruros marinos se disolvían en la película de humedad existente sobre la superficie metálica aumentando la conductividad del electrolito y destruyendo eventuales películas pasivantes. En 1973, Barton [4] ya apuntaba que el mecanismo que gobierna el efecto de los iones cloruro en la corrosión atmosférica no estaba completamente dilucidado, y que las altas velocidades de corrosión del acero al carbono en las atmósferas marinas podía deberse también a otras causas: (a) las especies cloruradas (NaCl, $CaCl_2$, $MgCl_2$, etc.), al ser higroscópicas, promueven el proceso de corrosión electroquímica al favorecer la formación del electrolito a relativamente bajos valores de humedad relativa (HR), y (b) la solubilidad de los productos de corrosión formados también puede desempeñar un papel importante. Así, en el caso del hierro, que no forma cloruros básicos estables, la acción de los cloruros es más pronunciada que en otros metales (zinc, cobre, etc.) cuyas sales básicas son tan sólo ligeramente solubles.

A finales del siglo XX, Nishimura et al. también comentan que, a excepción de unos pocos estudios, la investigación sobre los mecanismos fundamentales de la formación de herrumbre en atmósferas marinas ricas en iones cloruros había sido muy escasa. Estos investigadores realizan en esos años una importante investigación de laboratorio [5, 6], que constituye un punto de inflexión en el conocimiento científico de la corrosión atmosférica del acero al carbono en atmósferas marinas. Desde entonces, se han realizado grandes progresos en este campo científico.

1.2. Conceptos básicos sobre corrosión atmosférica marina

1.2.1. El proceso de corrosión atmosférica

La corrosión, en términos generales, es la destrucción o deterioro de un material a causa de su combinación o reacción con el medio ambiente.

La corrosión metálica se puede clasificar de diversos modos obedeciendo a criterios muy variados: en función del medio en contacto con la superficie metálica, en función de la morfología de ataque, etc. En esencia, cabe distinguir dos procesos de corrosión marcadamente distintos, tanto en lo que concierne a los mecanismos de ataque como a las condiciones experimentales en que se desarrollan:

a) corrosión a alta temperatura, y

b) corrosión electroquímica.

En la corrosión a alta temperatura el metal reacciona directamente con el agente agresivo (O_2, SO_2, etc.), afectando el ataque de manera similar a toda la superficie metálica. En cambio, la corrosión electroquímica, que recibe también la denominación de corrosión acuosa o húmeda, se produce cuando el metal se halla en contacto con electrolitos (agua, soluciones salinas, ácidos, bases, etc.). En este caso, el ataque ocurre solamente en las zonas anódicas del metal y no afecta por igual a toda la superficie.

Si nos centramos en la corrosión metálica húmeda, que es la que se presenta con mayor frecuencia, el fenómeno corrosivo resulta del funcionamiento de pilas eléctricas microscópicas que se constituyen entre diversas partes no idénticas de un metal, lo que implica la existencia de un proceso redox, siendo por tanto la superficie metálica sede de dos reacciones de electrodo:

- la reacción anódica de oxidación (disolución metálica)

$$M \rightarrow Mz^+ + ze^- \qquad (1)$$

- y la reacción catódica de reducción

$$Ox^+ + e^- \rightarrow Red \qquad (2)$$

siendo M el metal, z su valencia y Ox^+ una especie química contenida en el medio ambiente (electrolito) y susceptible de reducirse (Red). La corriente eléctrica en el sentido real fluye de los ánodos a los cátodos.

En principio, cualquier proceso de reducción puede suministrar la reacción catódica de la pila de corrosión. Sin embargo, de las innumerables reacciones catódicas posibles, sólo a dos son imputables la mayoría de los procesos habituales de corrosión electroquímica. Nos estamos refiriendo a la reacción de descarga de iones hidrógeno, propia de las soluciones ácidas:

$$2H^+ + 2e^- \rightarrow H_2 \qquad (3)$$

y a la reacción de reducción del oxígeno disuelto en la solución, típica de los medios prácticamente neutros (agua, atmósfera, suelo, etc.):

$$½O_2 + H_2O + 2e^- \rightarrow 2OH^- \qquad (4)$$

¿A qué se debe la aparición sobre la superficie metálica de esas pilas electroquímicas microscópicas? Las pilas de corrosión pueden ser debidas a múltiples causas o

heterogeneidades que presenta la superficie metálica. Incluso considerando un monocristal (cristal metálico simple que exhibe una estructura perfecta), los átomos de las esquinas o bordes tienen mayor tendencia a pasar a la solución (disolverse) que los átomos del interior del cristal.

En la práctica, los metales son materiales policristalinos constituidos por innumerables pequeños granos, en los que la distribución de los átomos está bastante lejos de la perfección exhibida por el monocristal. Hay numerosas imperfecciones o heterogeneidades que son causa de diferencias de potencial electroquímico y que motivan la aparición sobre la superficie metálica de micropilas de corrosión: (a) heterogeneidades debidas al metal (fases dispersas en la matriz metálica, bordes de grano, segregaciones, dislocaciones, regiones de metal deformado en frío, uniones bimetálicas, etc.), y (b) heterogeneidades del medio corrosivo (diferencias de temperatura, de concentración salina, de concentración de oxígeno, de composición, de pH, etc.).

El proceso de corrosión atmosférica es suma de los procesos parciales (individuales) de corrosión que tienen lugar cada vez que se forma la capa de electrolito sobre el metal. Las precipitaciones acuosas (lluvia, nieve, o niebla) y la condensación de humedad por cambios de temperatura (rocío) son, sin duda, los principales promotores de la corrosión en la atmósfera. Aun a HR inferiores al 100 % la superficie metálica puede recubrirse de una película de humedad. Son factores importantes al respecto, la condensación por adsorción, la condensación capilar y la condensación química. La suma de los tiempos parciales de humectación constituye el llamado tiempo de humectación (TDH), durante el cual es posible la corrosión metálica. Se ha encontrado una buena correlación entre el TDH y el tiempo en que la HR supera un determinado nivel de humedad, por lo general, superior al 80 % [7]. A Cole et al. [8] y Schindelholz y Kelly [9] se deben estudios recientes sobre la humectación de las superficies metálicas.

Entre los factores externos que determinan primariamente la intensidad del fenómeno están: a) la vida de la película de electrolito sobre la superficie del metal, b) la composición química de la atmósfera (contaminación del aire con gases, vapores ácidos y aerosoles de agua de mar), y c) la temperatura ambiente. La participación de gran número de otros factores es generalmente secundaria.

La velocidad de las reacciones de corrosión aumenta con la concentración de sustancias capaces de ionizarse en la película de humedad. Bajo esta película, el metal se corroe por medio del proceso catódico de reducción de oxígeno procedente del aire (ec. (4)). Únicamente

en el caso de un alto grado de contaminación por productos ácidos adquiere importancia la reacción de descarga de iones hidrógeno (ec. (3)).

El proceso anódico de corrosión del acero al carbono, y los mencionados procesos catódicos pueden expresarse de modo simplificado por las reacciones:

- proceso anódico

  $Fe \rightarrow Fe^{2+} + 2e^-$ (5)

- proceso catódico en medios neutros

  $½O_2 + H_2O + 2e^- \rightarrow 2OH^-$ (4)

  Los iones OH^- migran a las áreas anódicas formando $Fe(OH)_2$ como producto inicial de corrosión.

- proceso catódico por productos ácidos

  $2H^+ + 2e^- \rightarrow H_2$ (3)

1.2.2. El efecto del aerosol marino

Está perfectamente establecido el importante efecto del aerosol marino en la corrosión metálica, sin embargo la información cuantitativa disponible es menos abundante que en el caso del SO_2. El origen de los cloruros atmosféricos corresponde principalmente al agua de mar, que puede arrastrar el ion cloruro disuelto, o como sal sódica tras la evaporación. Ambas formas alcanzan en la atmósfera concentraciones comprendidas entre 0,5 y 5 $\mu g/m^3$ [10].

El depósito de partículas salinas sobre la superficie metálica acelera su corrosión. Para que el ion cloruro acelere la corrosión es necesario que la superficie metálica esté humedecida. El valor de la HR a partir de la cual la sal comienza a absorber agua de la atmósfera (higroscopicidad) es crítico desde el punto de vista de la corrosión. Ambler y Bain [3] comprobaron que la humedad del 78%, que es la de equilibrio con una solución saturada de NaCl, coincidía con una fuerte aceleración de la corrosión del acero al carbono.

La salinidad de las atmósferas marinas varía dentro de muy amplios límites, desde valores extremos en áreas de aguas muy agitadas (rompientes) a valores bajos en zonas de agua de mar en calma. Entre las variables con influencia en la salinidad atmosférica destacan: régimen

de vientos dominantes (dirección y velocidad), distancia a la costa, topografía de la zona, altitud, etc.

La alta concentración de cloruros en la capa acuosa depositada sobre el acero y la alta retención de humedad debajo de las capas de herrumbre dan lugar a la formación de cloruro ferroso ($FeCl_2$), que hidroliza el agua:

$$FeCl_2 + H_2O \rightarrow FeO + 2HCl \qquad (6)$$

aumentando notablemente la acidez del electrolito. En esta situación la reacción catódica (3) puede ser predominante acelerando de modo importante el proceso de corrosión.

2. OBJETIVOS PERSEGUIDOS EN LA INVESTIGACIÓN

Como se ha comentado en la Introducción la corrosión atmosférica marina del acero al carbono es un campo científico relativamente joven y es escasa la investigación realizada sobre los mecanismos fundamentales de formación de herrumbre en atmósferas marinas ricas en iones cloruro.

La investigación realizada, que se expone en esta Memoria, ha tratado de clarificar algunas de las incertidumbres existentes en este campo científico, concretamente:

1. El aerosol marino: su dependencia de parámetros ambientales y su efecto en la corrosión atmosférica del acero al carbono. Con relación al primero, aspectos tales como el efecto de la altura espectral de las olas y las características del viento en la producción y transporte del aerosol marino, así como su variación con la distancia a la línea de costa, son cuestiones importantes a considerar. En cuanto al segundo, hay abundante información bibliográfica, sin embargo ésta es escasa para altas salinidades atmosféricas como las que se consideran en esta investigación.

2. Es conocido que entre las fases de herrumbre (productos de corrosión) que se forman sobre el acero al carbono cuando se expone a atmósferas marinas, la akaganeita es una fase fundamental en los procesos de corrosión atmosférica que tienen lugar. Sin embargo, hay un desconocimiento notable de esta fase sobre aspectos tales como:
    a) condiciones ambientales que conducen a su formación entre los productos de corrosión. ¿Existe un umbral crítico de salinidad atmosférica para su formación?
    b) su localización preferente en la capa de herrumbre, y
    c) técnicas de caracterización más adecuadas para su identificación,

3. Existe un gran desconocimiento sobre las morfologías que presentan las distintas fases de herrumbre: lepidocrocita, goetita, akaganeita, magnetita, etc. En esta investigación, se pretende caracterizar analíticamente las variadas morfologías que pueden presentar las distintas fases de herrumbre.

4. La exposición del acero al carbono en atmósferas marinas con altas velocidades de depósito de cloruros conduce a la formación de capas muy gruesas de herrumbre que tienden a exfoliarse (desprenderse) del sustrato de acero, dejándolo desprotegido. La velocidad de corrosión del acero en estas condiciones es elevadísima. Conviene caracterizar, con profundidad y rigor científico, la estructura interna de estas capas exfoliadas de herrumbre.

5. Las capas de herrumbre formadas sobre el acero al carbono en atmósferas marinas presentan dos situaciones extremas: capas de herrumbre consolidadas y adherentes (a bajas salinidades atmosféricas), de relativamente bajo espesor, y capas de herrumbre de baja consistencia y fácilmente exfoliables (a altas salinidades atmosféricas), de muy alto espesor. Los mecanismos de corrosión en ambas situaciones extremas son muy distintos y la investigación realizada trata de descifrarlos.

3. METODOLOGÍA EXPERIMENTAL

3.1 El acero al carbono utilizado

La investigación que se presenta en esta Memoria se ha llevado a cabo con un acero suave al carbono, cuya composición se presenta en la Tabla 1.

Tabla 1. Composición química (% en peso) del acero utilizado.

Tipo de acero	Composición química (% en peso)							
	C	Si	Mn	P	S	Cr	Ni	Cu
Suave	0,13	0,09	0,55	< 0,020	0,018	0,02	0,02	0,02

En la Figura 1 puede observarse la microestructura característica del tipo ferrita- perlita que exhibe este acero.

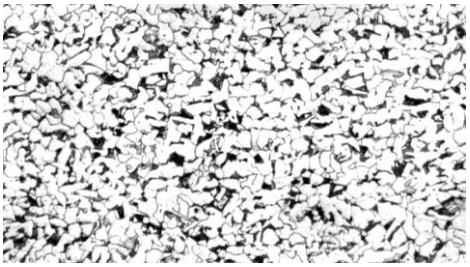

Figura 1. Microestructura a 200 aumentos, obtenida por microscopia óptica, del acero al carbono utilizado en la investigación.

3.2 Preparación de probetas de ensayo

Las probetas utilizadas fueron de 1 mm y 2,5 mm de espesor y se han preparado con unas dimensiones de 50 x 100 mm. La exposición de los aceros a la atmósfera marina se realizó en dos fases. En la primera fase se emplearon probetas de 1 mm de espesor, sin embargo debido al fuerte ataque que presentaban en las atmósferas marinas más agresivas se optó por utilizar probetas de mayor espesor (2,5 mm) en la siguiente fase del estudio.

En primer lugar se llevó a cabo la preparación de las probetas de ensayo mediante corte en taller de la chapa de acero, obteniéndose probetas de las dimensiones anteriormente especificadas. A continuación se procedió a la matriculación de todas las probetas por estampación de un código alfanumérico y posteriormente a su limpieza con etanol. Una vez realizada la matriculación y la limpieza superficial de las probetas, éstas fueron pesadas en una balanza analítica de precisión 0,0001g y almacenadas en desecador hasta su utilización.

3.3 Ensayos de corrosión atmosférica

3.3.1 Características meteorológicas y oceanográficas del campo de experimentación.

El lugar seleccionado para llevar a cabo el estudio ha sido el Parque Eólico de Cabo Vilano, situado en la Costa de la Muerte, concretamente en el Municipio de Camariñas, en la provincia de La Coruña. Puesto que existe una práctica ausencia de otros contaminantes en la atmósfera (por ejemplo, el contenido de SO_2 puede considerarse despreciable a efectos prácticos ya que se encuentra en el rango 0,7 – 0,9 mg SO_2/m^2·día) la atmósfera cabe clasificarla como marina pura. Por tanto, el parámetro más importante desde el punto de vista de la corrosión del acero en esta atmósfera es la salinidad atmosférica.

En la Figura 2 se muestra la situación geográfica del Parque Eólico de Cabo Vilano. Se trata de una zona bien caracterizada desde el punto de vista meteorológico debido a la ubicación, en el mismo parque, de una estación meteorológica de la Agencia Estatal de Meteorología (AEMET), Estación Cabo Vilán 1393, la cual nos ha suministrado datos de temperatura, humedad relativa y velocidad y dirección de vientos.

Figura 2. Situación geográfica del campo experimental dónde se ha realizado el estudio.

En esta misma figura también puede observarse la cercanía al campo experimental de la boya Villano - Sisargas de Puertos del Estado. Este organismo tiene a lo largo de toda la costa española un complejo sistema de boyas dotadas de varios tipos de sensores que suministran, entre otros, parámetros del oleaje (altura de las olas). La boya Villano - Sisargas está fondeada lejos de la línea de costa, a gran profundidad (386 m), por lo que las medidas de oleaje no están perturbadas por efectos locales.

En la Tabla 2 se exponen los parámetros meteorológicos que caracterizan el entorno donde se ha llevado a cabo el estudio, obtenidos a partir de los registros de AEMET en la estación "Cabo Vilan", situada a unos pocos metros de nuestra estación 2 (Viravento), durante el primer

año de estudio (abril 2013 - marzo 2014). La Tabla 2 también muestra las alturas espectrales significativas de las olas en ese año de estudio, información suministrada por la boya Villano - Sisargas.

Tabla 2. Características meteorológicas del campo experimental situado en el Parque Eólico de Cabo Vilano.

	T (°C)	HR (%)	Precipitación total (l/m^2)	Días de precipitación	Velocidad media del viento (Km/h)	Alturas espectrales significativas de las olas (m)	Nº de días con ráfagas máximas ≥ 70 Km/h	Dirección del viento con frecuencias ≥ 20%
Abril 2013	11,7	78,0	87,4	15	35	3,38	10[a]	NE, NNE
Mayo 2013	12,4	78,8	91,7	14	30	2,46	2[a]	NE
Junio 2013	14,3	85,8	46,4	13	29	2,28	9[a]	NE
Julio 2013	16,8	86,8	13,8[a]	>6	b	1,61	2[a]	b
Agosto 2013	17,6	85,0	20,2	9	29	1,52	9[a]	NE
Septiembre 2013	b	b	7,4[a]	>7	21	1,84	2[a]	NE, NNE
Octubre 2013	14,9	85,8	63,4[a]	>4	29	2,42	18[a]	SSO, S
Noviembre 2013	12,2	77,8	98,14	17	32	3,24	13[a]	NE
Diciembre 2013	b	b	114,0[a]	>9	b	4,14	7[a]	b
Enero 2014	9,7	88,0	163,6[a]	>22	26	5,08[a]	8[a]	OSO
Febrero 2014	9,5	84,5	224,2[a]	>20	36	4,97[a]	14[a]	OSO, SSO
Marzo 2014	10,9	84,0	60,6[a]	>14	25	3,22	8[a]	$OSO_{(15-20)}$, $N_{(15-20)}$
Media anual	**13,0[a]**	**83,5[a]**	**990.8[a]**	**>150**	**29,2[a]**	**3,01[a]**	**97[a]**	

[a] *Valores obtenidos con los datos disponibles.*
[b] *Datos no disponibles.*

Como se puede observar la zona donde se ha llevado a cabo el estudio presenta una humedad relativa alta (HR_{media} 83,5%), temperatura suave ($T_{promedio}$ 13°C) y alta precipitación (>900 l/m^2·año y > 150 días de precipitación/año). Estos valores indican altos tiempos de humectación de la superficie metálica que favorecen los procesos de corrosión atmosférica. También se observa que el campo experimental está sometido a fuertes vientos, principalmente del nordeste, y la velocidad media del viento es alta (> 29,2 km/h), así como el número de días al año con ráfagas ≥ 70 km/h (97 días). La dirección N, a la cual fueron orientadas las estaciones de ensayo y la proximidad de las estaciones a la línea de costa indican que éstas han estado sometidas a fuertes vientos marinos con un considerable arrastre de aerosol marino (salinidad atmosférica), que ha potenciado en gran medida el proceso de corrosión metálica.

3.3.2 Estaciones de corrosión

En la Figura 3 se observa la situación de las 12 estaciones de corrosión consideradas en la investigación, ubicadas a diferentes distancias de la línea de costa. Cada estación se ha fijado mediante potentes imanes de neodimio al mástil del aerogenerador, orientándose hacia la dirección norte. La altura a la cual se ubicaron las estaciones de ensayo fue de 3 metros desde la base del aerogenerador, altura suficiente para salvar la altura mínima que indica la norma ISO 8565 [11] y suficiente para impedir el alcance de la misma y así evitar posibles actos vandálicos.

Figura 3. Ubicación de la red de estaciones de ensayo en el Parque Eólico de Cabo Vilano.

La peculiaridad del punto de experimentación exigió un diseño específico de la estación de ensayos. Esta consistió en un bastidor en cuyo interior se ubicó el dispositivo de medida de la salinidad atmosférica (candela húmeda) y en la parte superior del mismo se fijaron las regletas donde se situaron las probetas de ensayo. En la Figura 4 se muestra una fotografía de la

estación de corrosión y su situación en el aerogenerador y en la Figura 5 un esquema de la estación con mayor detalle.

Figura 4. Estación de ensayo de corrosión atmosférica y su ubicación en el aerogenerador.

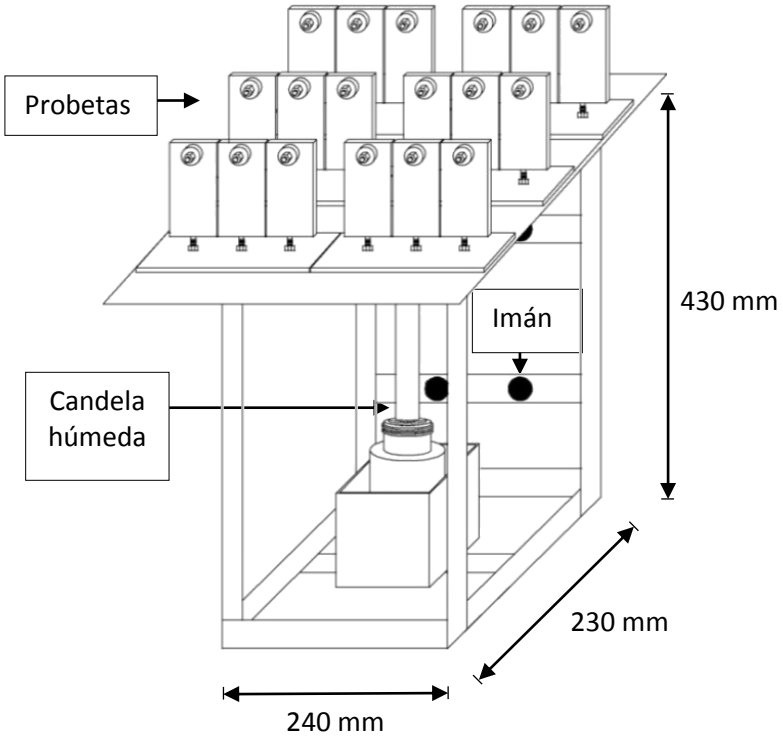

Figura 5. Esquema de la estación de ensayo de corrosión atmosférica.

El estudio ha comprendido dos fases de experimentación. La primera fase, de abril de 2013 a octubre de 2014, y la segunda fase de abril de 2014 a octubre de 2015. En la Tabla 3 se detallan las estaciones de corrosión consideradas en cada fase del estudio.

Tabla 3. Fases del estudio: periodo de exposición y estaciones de corrosión involucradas.

Fases	Periodo de exposición	**Estaciones de corrosión donde se llevó a cabo el estudio (Aerogenerador del Parque Eólico)**
I	Abril 2013 a octubre 2014	1 (A-6), 2 (Viravento), 3 (A-10), 4 (A-16), 7 (AE-3), 9 (AE-5), 10 (AE-6), 11 (AE-12)
II	Abril 2014 a octubre 2015	2 (Viravento), 5 (AE-1), 6 (AE-2), 7 (AE-3), 8 (AE-4), 9 (AE-5), 12 (AE-13)

La salinidad se ha determinado mediante el método de la candela húmeda, de acuerdo a la norma ISO 9225 [12]. Esta técnica consiste en exponer, protegido de la lluvia y durante un tiempo especificado, un material textil de superficie conocida. La cantidad de cloruro depositada se determina mediante análisis químico, calculándose la velocidad de depósito de ion cloruro expresada en mg Cl^-/m^2·día La superficie a exponer se consigue enrollando alrededor de un tubo de vidrio una gasa humedecida, quedando expuesta a la atmósfera una superficie de 110 cm^2. Antes de iniciar el ensayo, la gasa se hierve dos veces en agua destilada para eliminar posibles restos de cloruros. El tubo se inserta en un tapón de goma el cual lleva unos rebajes a través de los cuales pasan los extremos libres de la gasa. El tapón con la candela se ajusta posteriormente en el cuello de una botella de polietileno, de volumen 500 ml, que contiene una disolución de agua destilada y glicerina al 20% y en la que se sumergen los extremos de la gasa. A esta disolución se añaden asimismo 10 gotas de ácido octanoico para evitar la formación de hongos.

Durante los años de estudio se han retirado y expuesto trimestralmente dispositivos de medida de salinidad (realizándose, por tanto, 4 mediciones de esta variable por año y estación), determinada posteriormente en el laboratorio mediante un electrodo selectivo de ion cloruro. A pesar de la fuerte sujeción de las estaciones de ensayo a los bastidores con potentes imanes de neodimio, debido a los fuertes vientos se ha producido en alguna ocasión el desprendimiento de la estación del aerogenerador, impidiendo así obtener algunos datos trimestrales.

En la Tabla 4 se presenta la salinidad media anual en cada una de las estaciones de ensayo en los diferentes periodos anuales de estudio.

Tabla 4. Salinidad media anual de la atmósfera correspondiente a las distintas estaciones de ensayo en diferentes periodos del estudio.

Estación	Aerogenerador	Distancia a la costa en dirección N (m)	**Media anual de velocidad de depósito de ion Cl^- (mg Cl^-/m^2·día)**		
			Abril 2013 a abril 2014	Abril 2014 a abril 2015	Abril 2015 a abril 2016
1	A-6	270	824[a]		
2	Viravento	332	1905[a]	886[a]	1497
3	A-10	420	665		
4	A-16	590	266		
5	AE-1	710		130[a]	428
6	AE-2	820		153	230
7	AE-3	945	206	98[a]	122
8	AE-4	1130		105	109
9	AE-5	1250	109	73	124
10	AE-6	1580	92[b]		
11	AE-12	2400	69		
12	AE-13	2580		68[a]	

[a] *Valores correspondientes únicamente a los primeros 6 meses de exposición (por caída de la estación).*
[b] *Valores correspondientes únicamente a los primeros 9 meses de exposición (por caída de la estación).*

3.3.3. Cronograma de exposiciones y retiradas de las probetas de ensayo.

En la Tabla 5 se expone el cronograma de exposiciones y retiradas de las probetas de ensayo a lo largo del estudio.

Tabla 5. Cronograma de exposiciones y retiradas de las probetas de ensayo.

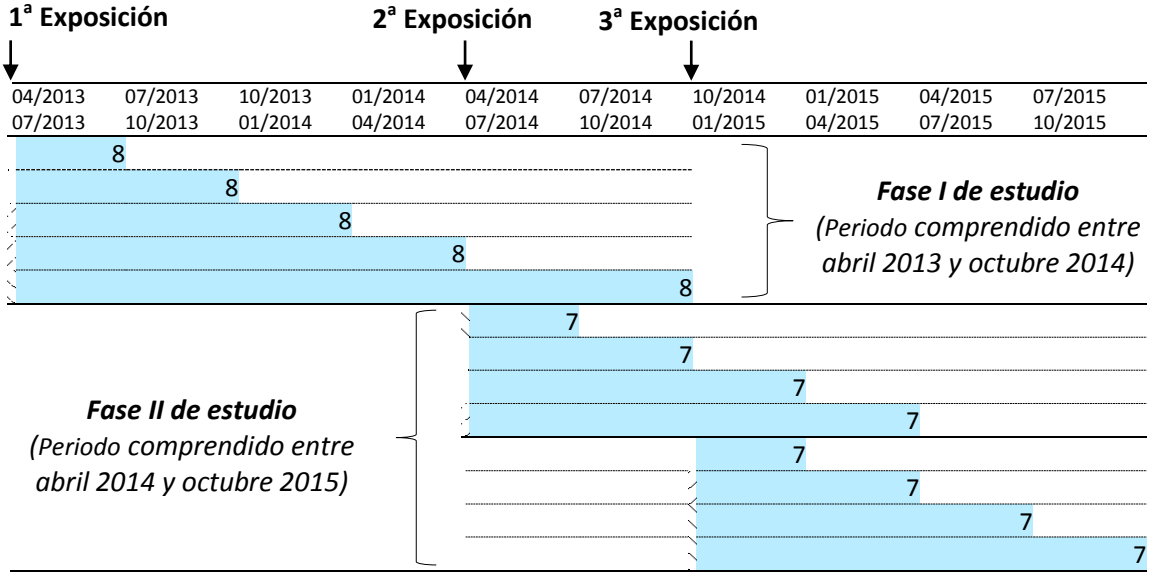

**El número en el interior de cada una de las barras indica el número de estaciones consideradas.*

3.4 Determinación del dato de corrosión

Para la determinación del ataque que experimenta el acero como consecuencia de su exposición a la atmósfera se ha seguido la técnica de pérdida de masa. El procedimiento seguido se describe en la norma ISO 9226 [7]. Éste consiste en sumergir las probetas (previamente pesadas antes de su exposición en la atmósfera) en una disolución específica durante un tiempo determinado, para posteriormente extraerlas y lavarlas en agua destilada y etanol. Una vez secas se procede a su pesada en una balanza analítica de precisión 0,0001 g. Se realizan tantos ciclos de limpieza como sean necesarios hasta eliminar completamente los productos de corrosión. Estos se deben eliminar sin atacar al acero base y por ello se utiliza una disolución específica de decapado consistente en: 500 ml de HCl, 3,5 g de hexametilentetramina y agua destilada hasta 1 litro.

La velocidad de corrosión expresada en µm/año viene dada por la ecuación:

$$\mathrm{Vcorr} = \frac{\Delta \mathrm{m}}{\mathrm{A} \cdot \rho \cdot \mathrm{t}}$$

donde (Δm) es la pérdida de masa, expresada en gramos; (A) es el área de la superficie, expresada en m^2; (ρ) la densidad del metal, que en el caso del hierro es 7,86 g/cm^3, y (t) el tiempo de exposición, expresado en años.

3.5 Técnicas experimentales utilizadas

Como consecuencia del proceso de corrosión atmosférica, sobre la superficie del acero se forman capas de herrumbre integradas por productos de corrosión. Tras los diferentes tiempos de exposición de las probetas de acero en las diferentes estaciones de ensayo, se ha llevado a cabo una exhaustiva caracterización de las capas de herrumbre formadas. Además del estudio sobre la naturaleza de los productos de corrosión formados, también se han analizado características de las capas de herrumbres, tanto en superficie como en sección transversal.

3.5.1 Naturaleza de los productos de corrosión

Los productos de corrosión del hierro y sus aleaciones, conocidos como herrumbre, comprenden varios tipos de óxidos, óxidos hidratados, oxihidróxidos y otras sustancias

cristalinas y amorfas que se forman como resultado de la reacción entre el hierro y el medio atmosférico.

De entre los productos de corrosión atmosférica del hierro más comúnmente encontrados (Tabla 6), las fases más abundantes son lepidocrocita, goetita, akaganeita y magnetita/maghemita

Tabla 6. Productos de corrosión del hierro más comúnmente encontrados en la corrosión atmosférica del acero.

Oxihidróxidos	Fórmula
Lepidocrocita	ɣ-FeOOH
Akaganeita	β-FeOOH
Goetita	α-FeOOH
Feroxihita	δ'-FeOOH
Ferrihidrita	$Fe_5HO_8 \cdot 4H_2O$

Óxidos	Fórmula
Magnetita	Fe_3O_4
Maghemita	ɣ-Fe_2O_3
Hematita	α-Fe_2O_3

La proporción de cada uno de estos productos (fases) depende de la composición del acero, del tipo de ambiente de exposición (rural, urbano, industrial o marino) e intensidad de los distintos factores meteorológicos tales como el viento, temperatura, humedad relativa, volumen y pH del agua de lluvia, etc. El tiempo de exposición también influye enormemente.

La naturaleza de los productos de corrosión formados sobre el acero tras los diferentes períodos de exposición ha sido analizada mediante diferentes técnicas de caracterización. Los estudios se llevaron a cabo en áreas representativas de las superficies de las probetas. A continuación se presenta la metodología empleada para cada una de ellas.

3.5.1.1 Difracción de Rayos X (XRD)

La difracción de rayos X constituye una herramienta básica para la caracterización de los productos cristalinos de corrosión atmosférica. El fundamento de esta técnica reside en hacer incidir un haz de rayos X monocromático sobre el material cristalino produciendo rayos X difractados a varios ángulos, de acuerdo con la Ley de Bragg. Esta ley relaciona la longitud de onda del haz primario (λ), el ángulo de difracción (θ) y la distancia entre planos en muestras cristalinas (d):

$$n \cdot \lambda = 2 \cdot d \cdot \text{sen}\theta \qquad (7)$$

y es condición necesaria que se debe satisfacer para que la interferencia de los rayos dispersados sea constructiva.

La identificación de productos de corrosión cristalinos de tamaño de partícula inferior a 15 nm es muy complicada debido al ensanchamiento de los picos, quedando enmascarados en la línea base del espectro de identificación de los mismos [13, 14]. En cambio, para tamaños de partícula superiores a 15 nm, la identificación de los óxidos es relativamente sencilla y no necesariamente requiere un análisis completo de los patrones de difracción o el cálculo de los parámetros de red. La posición y la intensidad de los picos de difracción son característicos para cada material cristalino, por lo tanto, una comparación de los difractogramas de XRD de los productos de corrosión con aquellos correspondientes a los óxidos patrones es suficiente para identificar las fases presentes en la herrumbre.

La Tabla 7 presenta una lista con los parámetros de XRD de los picos más intensos que se utilizan para la identificación de los óxidos de hierro (fases) que forman parte de la herrumbre. Estos datos corresponden a la radiación Kα del cobalto.

Tabla 7. Parámetros de XRD de los picos más intensos que se utilizan para la identificación de fases en una herrumbre.

Óxido	2θ(°)	d(Å)	I/I_o	Índice Miller
γ-FeOOH (Lepidocrocita)	16,443	6,1688	100	(020)
α-FeOOH (Goetita)	24,695	4,1695	100	(110)
β-FeOOH (Akaganeita)	13,760	7,4540	40	(110)
	65,952	1,6434	35	(521)
γ-Fe_2O_3 (Maghemita)	35,265	2,9530	35	(220)
Fe_3O_4 (Magnetita)	35,093	2,9670	30	(220)

I/I_0 es la relación de intensidad de la señal respecto al pico más intenso del espectro.

Para la identificación completa de los productos de corrosión se usa un rango de 20° a 120°, siendo generalmente suficiente la región de 10° a 60°.

La maghemita y la magnetita tienen estructuras cristalinas (tipo espinela) y parámetros de red prácticamente idénticos, por lo que no es posible la identificación por separado de ambas, pero sí la identificación conjunta mediante el pico (220) cuyo ángulo de difracción 2θ aparece entre 35,093° y 35,265°. Esta limitación es posible solventarla usando espectroscopía Mössbauer y espectroscopía Raman, ya que sus parámetros hiperfinos y frecuencia Raman difieren entre sí.

El análisis por XRD se llevó a cabo generalmente en muestras de herrumbre en polvo obtenidas por molienda en un mortero de ágata y posterior cribado para obtener un tamaño de partícula inferior a 125 µm. El polvo de herrumbre fue obtenido mediante un vigoroso cepillado con un cepillo de cerdas de nylon. Se analizaron así las herrumbres formadas en la cara A (orientadas al cielo) de las probetas de ensayo. En aquellas probetas en las que no era posible realizar una toma de muestra destructiva, se realizó el análisis por XRD directamente sobre la probeta de acero herrumbrada.

Las medidas de XRD se realizaron usando un difractómetro Bruker AXS D8 (modelo D8 Advance) equipado con un tubo de rayos X de cobalto, óptica de espejo Goebel y una posición lineal del detector sensible LYNXEYE para las mediciones de difracción de rayos X ultrarrápidos. Este tipo de radiación es especialmente adecuado para muestras ricas en hierro (se evita así la fuerte fluorescencia resultante de la radiación del cobre) y para producir datos de alta resolución. Se aplicó una corriente de 30 mA y una tensión de 40 kV. Se seleccionaron condiciones de operación para obtener difractogramas de XRD de calidad suficiente, estadísticas de conteo óptimas, picos estrechos, y detección de pequeños picos de difracción de las fases de menor importancia. Los datos de difracción de rayos X se recogieron en un rango 2θ de 10 a 80° con una anchura de paso de 0.02°. La identificación cualitativa de las fases cristalinas presentes en la herrumbre formada sobre los aceros se realizó a partir de los patrones de difracción de rayos X utilizando la base de datos JCPDS y software DIFFRACplus EVA de Bruker AXS.

En el transcurso de la investigación, en el caso de probetas exfoliadas se realizaron medidas de XRD en áreas seleccionadas, con fin de conocer la composición de la herrumbre a lo largo del espesor de la capa exfoliada. Las mediciones de XRD fueron obtenidas con el mismo difractómetro anterior, equipado con un tubo de rayos X de cobalto, un colimador de haz primario, un láser que se centró en el punto de la superficie a analizar (500 micras de diámetro), y un detector lineal (LYNXEYE). Los ajustes del generador fueron 40 kV y 30 mA. Los datos de difracción de rayos X se recogieron en un rango 2θ de 10 a 100° con un anchura de paso de 0,03° y un tiempo de adquisición de 3s / paso.

En algunos casos también se han realizado análisis por XRD de ángulo rasante (GIXRD). Esta técnica utiliza pequeños ángulos de incidencia de los rayos X entrantes, que aumentan significativamente la trayectoria recorrida por los rayos X. El ángulo de incidencia pequeño hace la superficie de difracción sensible, y se obtiene información principalmente de películas delgadas o de la superficie de las capas de herrumbre, a diferencia de XRD convencional, que

por lo general contiene información de toda la capa de herrumbre. Las mediciones GIXRD se llevaron a cabo con el mismo difractómetro. En la configuración utilizada, el tubo de rayos X de cobalto está equipado con óptica de espejo Goebel para obtener un haz de rayos X paralelos y monocromático. La configuración del tubo utilizada correspondió a una corriente de 30 mA y una tensión de 40 kV. Los datos de difracción de rayos X se recogieron con un ángulo de incidencia del haz de 1° en un rango 2θ (entre 15 y 75°), con un anchura de paso de 0,03° y un tiempo de adquisición de 5s /paso. Tanto en ángulo rasante como convencional θ-2θ, se realizó la identificación utilizando el software AbsorbDX de Bruker AXS.

Los métodos de análisis cuantitativo por XRD se clasifican en dos grupos, los métodos que emplean picos seleccionados y los métodos que utilizan todo el difractograma. La forma más rápida para llevar a cabo el análisis de difracción de rayos X es el método RIR (relación de intensidad de referencia). El análisis semi-cuantitativo por RIR se realizó con el programa Match 2 y con una relación de I/Ic de la tarjeta de archivos de difracción de polvo [15]. Este análisis semi-cuantitativo se basa en la semi-cuantificación del pico más intenso de cada una de las fases usando la relación I/Ic para cada fase, donde I es la intensidad del pico mayor de la fase y Ic es la intensidad de la reflexión mayor del corindón en un 50/50 en peso de la mezcla procedente del polvo de difracción [15]. Sin embargo, éste método que emplea picos seleccionados, está sujeto a una gran inexactitud debido al solapamiento de picos de las diferentes fases presentes, sobre todo de las fases minoritarias. Así, por ejemplo, en los productos de corrosión que contienen las fases akaganeita, magnetita, lepidocrocita y goetita, los picos más intensos de la magnetita y de la lepidocrocita se solapan con varias reflexiones de las otras fases, produciendo un importante error relativo en la determinación de fracciones de fase. Además, no incluyen ninguna corrección para el efecto de textura, teniendo en cuenta que las fases presentes en la película de herrumbre pueden presentar formas anisotrópicas causando efectos de orientación preferente en las mediciones de XRD. Es por ello que se aconseja utilizar el método de cuantificación Rietveld.

El método Rietveld se adapta a la totalidad del patrón de difracción. Todas las reflexiones, se solapen o no, se utilizan en el proceso de ajuste. El método Rietveld ha sido ampliamente reportado como una de las técnicas más adecuadas para la cuantificación en el patrón de XRD de las fases cristalinas presentes en sistemas multifásicos [16, 17]. El método Rietveld considera el difractograma total como la suma de los patrones individuales de cada fase y se extrae la información sin separar en componentes, minimizando la diferencia entre el difractograma experimental y el calculado. En este método las constantes de calibración se calculan a partir de datos estructurales fiables en lugar de por ajustes laboriosos. Además, las

reflexiones múltiples para cada fase se incluyen de forma explícita y las correcciones de orientación preferencial se pueden introducir en el análisis cuantitativo.

La aplicación del método de Rietveld a los patrones GIXRD da lugar a desviaciones significativas de las intensidades registradas en la geometría Bragg-Brentano. Con el fin de tener en cuenta este hecho, en el refinamiento por Rietveld, las funciones del instrumento se parametrizan empíricamente a partir del análisis del perfil de forma de una muestra de corindón medido en ángulo rasante en las mismas condiciones. En este estudio, para el refinamiento de datos de XRD hemos utilizado la versión 4.0 del programa de análisis Rietveld TOPAS (Bruker AXS). Los refinamientos se realizaron usando el grupo espacial y la información cristalográfica de la lepidocrocita, goetita, akaganeita y magnetita o maghemita obtenidos de la base de datos "Pearson's Crystal Structure" [18].

3.5.1.2 Espectroscopía Infrarroja por Transformada de Fourier (FTIR)

La espectroscopía de infrarrojo por transformada de Fourier se fundamenta en la absorción de la radiación IR por las moléculas en vibración. Una molécula absorberá la energía de un haz de luz infrarroja cuando dicha energía incidente sea igual a la necesaria para que se dé una transición vibracional de la molécula. Es decir, la molécula comienza a vibrar de una determinada manera gracias a la energía que se le suministra mediante luz infrarroja. En principio, cada molécula presenta un espectro IR característico, debido a que todas las moléculas (excepto las especies diatómicas homonucleares como O_2 y Br_2) tienen algunas vibraciones que, al activarse, provocan la absorción de una determinada longitud de onda en la zona del espectro electromagnético correspondiente al infrarrojo. De esta forma, analizando cuales son las longitudes de onda que absorbe una sustancia en la zona del infrarrojo, podemos obtener información acerca de las moléculas que componen dicha sustancia.

En el presente estudio, la técnica de FTIR se ha utilizado como técnica complementaria a otras técnicas para la confirmación de las fases presentes en las herrumbres formadas sobre el acero. Con esta técnica se han podido observar también otras fases no cristalinas presentes en las herrumbres. El espectrómetro infrarrojo por transformada de Fourier utilizado es un Magna-IR^{TM} Spectrometer 550 Nicolet, utilizando el software Omnic driver disc versión 7.4.

La capa de herrumbre de las probetas se debe pulverizar para que el tamaño de sus partículas sea menor que la longitud de onda de la radiación y así evitar efectos de dispersión. Una vez pulverizada la muestra se elaboran unas pastillas compuestas por aproximadamente 1mg de la

herrumbre en polvo y 100 mg de polvo de yoduro de cesio desecado. Se mezclan ambos compuestos en un pequeño mortero de ágata. Posteriormente se presiona la mezcla en un troquel especial, entre 700 y 1000 kg/cm^2, hasta obtener un disco transparente. El disco resultante se coloca en la trayectoria del haz del instrumento para su examen espectroscópico.

El espectro infrarrojo se divide en tres regiones denominadas infrarrojo cercano, medio y lejano, lo que corresponde a las longitudes de onda entre 1mm y 700 nm. La región del espectro de estudio es la comprendida entre 3600 cm^{-1} y 400 cm^{-1} aunque la región de especial interés se sitúa entre 1200 cm^{-1} y 600 cm^{-1}, denominada "huella dactilar", ya que es donde pequeñas diferencias en la estructura de una molécula provocan cambios en esta región del espectro. La identificación de compuestos mediante esta técnica se lleva a cabo identificando grupos funcionales presentes en el espectro de estudio, y después, por comparación del espectro obtenido con espectros de compuestos puros, se identifican las fases presentes en la muestra de estudio.

Los espectros son, a menudo, complicados y resulta difícil asignar cada una de las bandas que aparecen en ellos a movimientos atómicos específicos. Tanto es así que existe en la literatura una gran dispersión en las longitudes de ondas correspondientes a las frecuencias de vibración de los enlaces de las diferentes fases presentes en los productos de corrosión. Tras una exhaustiva revisión bibliográfica, hemos unificado todos los datos, presentando en la Tabla 8 las longitudes de onda en los que aparecen las principales frecuencias vibracionales de los enlaces característicos de las fases presentes en la herrumbre.

Tabla 8. Frecuencias vibracionales más características de las distintas fases de herrumbre.

Compuesto	**Fórmula**	**Refs.**	**Longitud de onda (cm^{-1})**
Lepidocrocita	(γ-FeOOH)	[19-22]	1625-1615*,1150, 1020*,<u>750</u>, 490
Goetita	(α-FeOOH)	[19-29]	890*, 795*
Akaganeita	(β-FeOOH	[19, 23, 30]	1630-1615*, 858-840*,390-420*
Feroxihita	(δ'-FeOOH)	[19, 20, 22, 28]	1110*,470
Magnetita	(Fe_3O_4)	[19, 22-24, 26, 27, 31]	580*
Maghemita	(γ-Fe_2O_3)	[19, 23, 27]	700-690,630-620,570*
Hematita	(α- Fe_2O_3)	[19, 23, 27]	574-530*

* *Pico más intenso.*
<u>Subrayado</u>: El siguiente pico más intenso.

3.5.1.3 Espectroscopía Mössbauer

La espectroscopía Mössbauer está basada en el efecto Mössbauer, es decir, en la emisión o absorción resonante de rayos gamma por núcleos sin pérdida de energía debida al retroceso nuclear. El proceso es relativamente simple. Un núcleo que se encuentra en estado excitado de energía (Ee) regresa al estado fundamental de energía (Ef) mediante la emisión de un fotón (o radiación γ), que a su vez puede ser nuevamente absorbido por otro núcleo idéntico en estado fundamental. Para que esto ocurra, la energía del fotón (γ) emitido debe ser exactamente igual a la energía de la transición (Ee–Ef) del núcleo absorbente. Este fenómeno se denomina absorción resonante. Sin embargo, pueden producirse pérdidas de energía por retroceso durante la emisión del fotón.

Mediante espectroscopía Mössbauer se realizó la caracterización de la herrumbre compacta existente en el interior de las capas exfoliadas de herrumbre. Es importante discernir su composición y saber si se componen de magnetita, maghemita, o ambas. Con el objetivo de identificar la composición de esas herrumbres compactas, con la ayuda de un utensilio punzante y un cúter, se pudieron aislar dos láminas de herrumbre compacta, un trabajo bastante laborioso debido a la fragilidad que presentan las capas exfoliadas de herrumbre. A continuación, cada lámina se molió en un mortero de ágata y se cribó para obtener un tamaño de partícula inferior a 125 μm. Ambas muestras fueron analizadas por espectroscopía Mössbauer, una técnica que permite la diferenciación de estas dos fases, magnetita y maghemita.

Los espectros Mössbauer realizados en la presente investigación han sido efectuados en el Instituto de Química-Física Rocasolano (IQFR/CSIC) en la modalidad de transmisión. El espectrómetro Mössbauer consta de una fuente radiactiva acoplada a un transductor electromecánico que le impulsa un movimiento sincronizado con el barrido de una unidad de registro. Los datos Mössbauer se registraron a temperatura ambiente y a 16 K utilizando un espectrómetro convencional de aceleración constante, criogenerador de He de ciclo cerrado, y una fuente de ^{57}Co (Rh). El límite de detección en la espectroscopía Mössbauer en condiciones favorables es de aproximadamente 0,5% en peso, aunque, en función de la complejidad de los espectros, como en el caso de múltiples solapamientos de diferentes sextetes, fases que aparecen a mayores concentraciones de 0,5% en peso podrían no ser detectadas. La escala de velocidad se calibró usando una lámina de hierro natural de 6 μm de espesor. Todos los espectros fueron ajustados por ordenador y los desplazamientos isómericos fueron referenciados a temperatura ambiente con respecto al centroide del Fe-α.

3.5.1.4 Microscopía Electrónica de Transmisión/Difracción de Electrones en Área Seleccionada (TEM/SAED)

La microscopía electrónica de transmisión (TEM) es una técnica que aprovecha los fenómenos físico-atómicos que se producen cuando un haz de electrones suficientemente acelerado colisiona con una muestra delgada convenientemente preparada. Cuando los electrones colisionan con la muestra, en función de su grosor y del tipo de átomos que la forman, parte de ellos son dispersados selectivamente, es decir, hay una gradación entre los electrones que la atraviesan directamente y los que son totalmente desviados. Todos ellos son conducidos y modulados por unas lentes para formar una imagen final. La información que se obtiene es una imagen con distintas intensidades de gris que se corresponden con el grado de dispersión de los electrones incidentes.

La imagen del TEM, tal como se ha descrito, ofrece información sobre la estructura de la muestra, tanto si ésta es amorfa o cristalina. Si la muestra es cristalina, es decir, hay una estructura de planos periódica, puede ocurrir que varias familias de esos planos cumplan la condición de Bragg y difracten de forma coherente con la onda electrónica incidente. Esto da lugar a un diagrama de difracción, que es una imagen de distintos puntos ordenados respecto a un punto central (electrones transmitidos no desviados), que nos aportan información sobre la orientación y estructura de los cristales presentes.

Para la caracterización de la herrumbre compacta de la capa exfoliada formada en las probetas de acero tras su exposición en una atmósfera marina muy agresiva se utilizó un microscopio electrónico de transmisión (TEM) de alta resolución bajo la técnica de difracción de electrones en área seleccionada (SAED),perteneciente a la Facultad de Ciencias Químicas de la UCM. La principal finalidad era poder confirmar la presencia de la fase akaganeita entre los productos de corrosión. Para ello se utilizó la herrumbre en polvo (molida), donde anteriormente, mediante la técnica de XRD, se había detectado, aunque con muy baja señal la presencia de esta fase. Las mediciones se realizaron en un microscopio electrónico JEOL 300 FEG. La composición química de los cristales akaganeita se determinó por EDS con el sistema analizador Inca Oxford. Las muestras se dispersaron por ultrasonidos en n-butanol y después se transfirieron a rejillas de cobre recubiertas de carbono.

3.5.1.5 Análisis de cloruros solubles en la herrumbre

Es posible encontrar compuestos salinos solubles, en este caso cloruros, entre los productos de corrosión del acero expuesto a atmósferas marinas. Sus efectos son nocivos y afectan al proceso de corrosión atmosférica por diferentes causas: absorbiendo humedad del aire, aumentando la conductividad de la película acuosa que se forma sobre el metal, estableciendo sobre la superficie pilas de concentración diferencial, disminuyendo el pH de la solución en contacto con la superficie metálica, etc.

El procedimiento seguido para la identificación y cuantificación de contaminantes salinos existentes entre los productos de corrosión atmosférica del acero, ha consistido en la extracción de 100 mg de herrumbre en 20 ml de agua destilada en un baño de ultrasonidos durante dos horas y a temperatura ambiente. Posteriormente se filtró la solución, se llevó a volumen constante y se analizaron los cloruros en solución mediante un electrodo selectivo de este ion. El cloruro obtenido así se define como cloruro soluble.

3.5.2 Morfologías de las fases de herrumbre

En los últimos años los equipos de investigación que trabajan en corrosión atmosférica, incluyendo el grupo de investigación en el que he desarrollado el presente trabajo [26, 32-35], generalmente han atribuido fases de herrumbre a las morfologías obtenidas por SEM simplemente sobre la base de referencias bibliográficas, sin llevar a cabo una caracterización analítica rigurosa de los compuestos formados. A menudo, esto ha dado lugar a especulaciones e interpretaciones poco fiables. Términos tales como "granos de arena", "bolas de algodón", "estructuras de nido", etc., acuñados previamente por Raman et al., [36-39] se han utilizado para describir y tipificar las fases de herrumbre encontradas.

Únicamente Raman et al. [36-39] han intentado indirectamente identificar morfologías observadas por SEM comparándolas con morfologías estándares de fases de herrumbre sintetizadas en laboratorio e identificadas por XRD e IR. Es por ello que en el presente estudio nos planteamos abordar la posibilidad de identificar analíticamente esas distintas morfologías que presentan las fases de herrumbre obtenidas en campo. Esto fue posible al uso conjunto de las técnicas de SEM y μRaman, usando la técnica SEM para observar las morfologías que exhiben las fases de herrumbre y la espectroscopía Raman para su caracterización analítica.

La combinación de una técnica de imagen, como el SEM, integrada con una técnica de análisis, como es la espectroscopía Raman, resulta muy útil para la identificación de las diferentes fases presentes en la herrumbre, suponiendo un avance muy importante para el establecimiento de correspondencias entre morfologías y fases. No se conoce en la bibliografía sobre corrosión la utilización de esta nueva técnica combinada.

3.5.2.1 SEM

El microscopio electrónico de barrido es un microscopio capaz de ampliar las imágenes de objetos utilizando un haz de electrones para crear la imagen. La imagen se obtiene rastreando la superficie de la muestra con un haz de electrones. Este haz de electrones incide sobre la muestra e interactúa con los átomos de dicha muestra, generando electrones secundarios o retrodispersados del haz inicial.

El sistema que capta e interpreta la imagen depende de la muestra y del tipo de análisis que se quiera realizar. Para el estudio de nuestras probetas se utilizaron los siguientes detectores:

a) Detector de electrones secundarios (SEI: Secundary Electron Image), para la obtención de imágenes de alta resolución.
b) Detector de electrones retrodispersados (BEI: Backscattered Electron Image), para obtener imágenes de composición y topografía de la superficie.
c) Detector de energía dispersiva (EDS: Energy Dispersive Spectrometer). Este detector captura los rayos X generados por la muestra, lo que permite obtener mediante un software la composición elemental de las herrumbres formadas en las probetas, así como mapas de distribución elemental.

Como la imagen se hace con electrones es necesario que la muestra sea conductora, en caso contrario se acumula carga y la superficie a observar repele a los electrones que llegan posteriormente deteriorando la imagen. Por lo tanto, para asegurar una capa conductora homogénea sobre la superficie de las probetas, estas se metalizaron previamente depositando un fina capa de grafito.

Se ha empleado un microscopio electrónico de barrido de alta resolución (3 nm en el modo de alto vacío), modelo Hitachi S4800, equipado con detectores de electrones secundarios y electrones retrodispersados, así como un sistema de microanálisis composicional por dispersión de energía de rayos X, modelo Oxford Inca (EDS).

3.5.2.2 Espectroscopía Raman

La espectroscopía Raman es una técnica fotónica de alta resolución. Es de las técnicas más rápidas y no destructivas, que proporciona información química y estructural prácticamente de cualquier matriz en cualquier estado de la materia, permitiendo así su identificación. El análisis se basa en el examen de la luz dispersada por un material al incidir sobre él un haz de luz monocromático. Una pequeña porción de luz es dispersada inelásticamente experimentando ligeros cambios de frecuencia, que son característicos del material a analizar e independiente de la frecuencia de la luz incidente.

Con la espectroscopía Raman se obtiene un espectro vibracional, similar al de la espectroscopía infrarroja, sin embargo con diferentes mecanismos y reglas de selección. El efecto Raman, una forma de dispersión inelástica, puede ser interpretado del siguiente modo: las moléculas son excitadas desde su estado fundamental a un estado virtual de energía, por la incidencia de un fotón con una energía significativamente mayor a la transición vibracional, el cual abandona rápidamente este estado virtual emitiendo un fotón para pasar a uno de los niveles de energía permitido. La frecuencia a la cual es liberado este fotón dependerá del salto energético realizado por la molécula. Por consiguiente, pueden ocurrir tres tipos de fenómenos de dispersión:

1. Dispersión Rayleigh: los fotones son dispersados elásticamente, es decir, con la misma frecuencia de incidencia, lo que produce la misma energía que los fotones incidentes.
2. Dispersion Raman Stoke: la energía del fotón dispersado es inferior a la del fotón incidente. El fotón pierde la energía necesaria en generar la vibración molecular y su frecuencia queda reducida.
3. Dispersión Raman anti-Stoke: la energía del fotón dispersado es superior a la del fotón incidente. El estado vibracional final de la molécula es de menor energía que el del estado inicial.

Esta técnica de análisis se realiza directamente sobre la probeta a analizar sin necesidad de ninguna preparación especial y no conlleva ninguna alteración de la superficie sobre la que se realiza el análisis.

En la bibliografía existe una gran dispersión de las frecuencias a las que aparecen los picos característicos de las fases presentes en las herrumbres formadas. Tras una exhaustiva revisión bibliográfica, hemos unificado todos los datos, presentando en la siguiente Tabla 9 las longitudes de onda a las que aparecen los principales picos Raman de las fases de herrumbre.

Tabla 9. Rangos de longitud de onda (cm^{-1}) a los que frecuentemente aparecen los principales picos Raman de las fases de herrumbre, según diferentes fuentes bibliográficas.

Compuesto	Fórmula	Referencia	Longitud de onda (cm^{-1})
Lepidocrocita	γ-FeOOH	[40-53]	(248-252)*, (<u>378-380</u>), (528-530), (650-655), (1300-1310)
Goetita	α-FeOOH	[40, 42, 43, 45-48, 50-56]	(241-250), (<u>298-301</u>), (385-390)*, (478-483), (549-552), (680-685), (1000-1120)M
Akaganeita	β-FeOOH	[40, 41, 44, 46, 48, 50-52, 57]	(310-314)*, (385-390)*, (497-499), (538-541), (720-723)
Feroxihita	δ'-FeOOH	[44, 46-49, 52, 55]	(385-392), <u>400</u>, (655-680)*
Magnetita	Fe_3O_4	[40-43, 45-48, 50-52, 54, 55]	(298-302), (540-550), (663-670)*
Maghemita	γ-Fe_2O_3	[40, 43, 44, 46-52, 54]	(342-350), (500-506)a, (700-720)*, (1400-1440)M
Hematita	α- Fe_2O_3	[42, 43, 46-48, 50-52, 54, 55]	(220-228)*, (240-247), (289-299)*, (400-415)*, (497-502), (609-615), (1320-1330)M
Ferrihidrita	$Fe_5HO_8{\cdot}4H_2O$	[23, 40, 49, 51, 52]	370,510,710*, (1380-1600)

* *Pico más intenso.*
<u>Subrayado</u>: El siguiente pico más intenso.
M *Pico magnum.*

3.5.2.3 SEM/μRaman

Los espectros Raman se midieron con el módulo Raman Hybriscan Tecnologies HSCMM-21, montado en un SEM modelo JEOL JSM-6610LV equipado con un espectrómetro de energía dispersiva de rayos X (EDS) y detector de retrodispersión. El módulo Raman es un módulo de microscopía confocal Raman completamente integrado que incluye un microscopio óptico de vídeo y una plataforma XY de alta resolución situada en la parte superior del SEM. La ubicación del módulo Raman está aproximadamente a 40 mm a un lado de la ubicación SEM. El módulo se integra completamente con el SEM de tal manera que la trayectoria óptica y la trayectoria del haz de electrones no interfieren entre sí. La fuente de excitación es un láser de 785 nm con una potencia regulable sobre la muestra. Tras las pruebas preliminares, las medidas de espectroscopía Raman se ajustaron a las condiciones siguientes: potencia del láser de 75 mW y un tiempo de acumulación total (adquisición) de 60 s. Estas condiciones tuvieron éxito en la mayoría de los casos. El sistema de cámara digital del microscopio óptico permitía simultáneamente la obtención de imágenes ópticas durante las mediciones Raman.

Las imágenes Raman se obtuvieron mediante el análisis de la muestra punto por punto con la plataforma XY de alta resolución montada en la parte superior del SEM. La correlación entre las imágenes de SEM y las imágenes Raman se logró por una superposición del video de la cámara digital y la imagen SEM de la propia muestra. Una vez que se obtuvo tal superposición, la región de interés para la adquisición del espectro Raman se pudo seleccionar basándose en la imagen SEM.

La observación microscópica se realizó tanto en la superficie de la herrumbre, para la observación de la morfología de los distintos productos de corrosión que conforman la herrumbre, como en sección transversal, observando la estructuración de la capa de herrumbre, formación de picaduras en el acero base y distribución de Cl^- en la herrumbre.

3.5.3 Capas de herrumbre: superficie externa

Como consecuencia del proceso de corrosión atmosférica, sobre la superficie del acero se forman capas de herrumbre integradas por productos de corrosión. Es fundamental caracterizar las capas de herrumbre que se forman sobre el acero al estar expuesto en la atmósfera marina para poder así esclarecer los mecanismos de corrosión y el comportamiento del acero suave cuando se expone a este tipo de atmósferas.

Tras los diferentes tiempos de exposición de las probetas de acero ubicadas en diferentes estaciones de ensayo, se ha llevado a cabo una exhaustiva caracterización de las capas de herrumbre formadas en ambas caras de las probetas. Han sido caracterizadas tanto las superficies como las secciones transversales de las capas de herrumbre formadas tras diferentes periodos de exposición. En cuanto a la caracterización de la superficie de las capas de herrumbre se determinó su coloración y textura (granulometría) que pasamos ahora a comentar.

3.5.3.1 Apariencia (coloración)

El color de la herrumbre varía con la corrosividad de la atmósfera, tipo de acero, tiempo de exposición, orientación y posición de la probeta, etc. Las coloraciones más claras de las herrumbres se presentan en las atmósferas de mayor agresividad (mayor corrosión) y conforme va disminuyendo la agresividad de la atmósfera (menor corrosión) las herrumbres exhiben coloraciones más oscuras. Las coloraciones de las herrumbre se vuelven más oscuras

conforme progresa el tiempo de exposición. También existe una diferencia en las tonalidades que exhiben las dos caras de las probetas, observándose una coloración más homogénea y oscura en la herrumbre de la cara que mira al cielo mientras que la cara opuesta (que mira al suelo) presenta coloraciones de herrumbre más claras y heterogéneas.

3.5.3.2 Textura (granulometría)

Para la determinación de la granulometría (textura) de las herrumbres, se ha utilizado el denominado "método de la cinta", consistente en adherir un trozo de cinta adhesiva, de dimensiones 2 x 2 cm^2, sobre la capa de herrumbre formada, presionando fuertemente y de manera uniforme sobre la superficie. Una vez despegada, se examinan tanto la densidad como el tamaño de las partículas de herrumbre [58].

Estas texturas de herrumbre se han clasificado de la siguiente forma: herrumbre en forma de granos o partículas (G), aglomerados de granos (A), escamas de herrumbre (F) y herrumbre multicapa (ML), en parte siguiendo los términos acuñados por Raman et al. [20, 59]. En la herrumbre en forma de granos se aíslan finas partículas de herrumbre (polvo de herrumbre), mientras que los aglomerados de herrumbre son de mayor tamaño y consisten en una aglomeración de granos o partículas. Las escamas de herrumbre y la herrumbre multicapa son fragmentos de la capa de herrumbre y presentan una superficie mayor y mayor compacidad que las otras dos texturas. La herrumbre multicapa presenta estratificación, con la existencia de subcapas de herrumbre compacta en su interior. En la Figura 6 se presentan las distintas texturas que puede presentar la herrumbre.

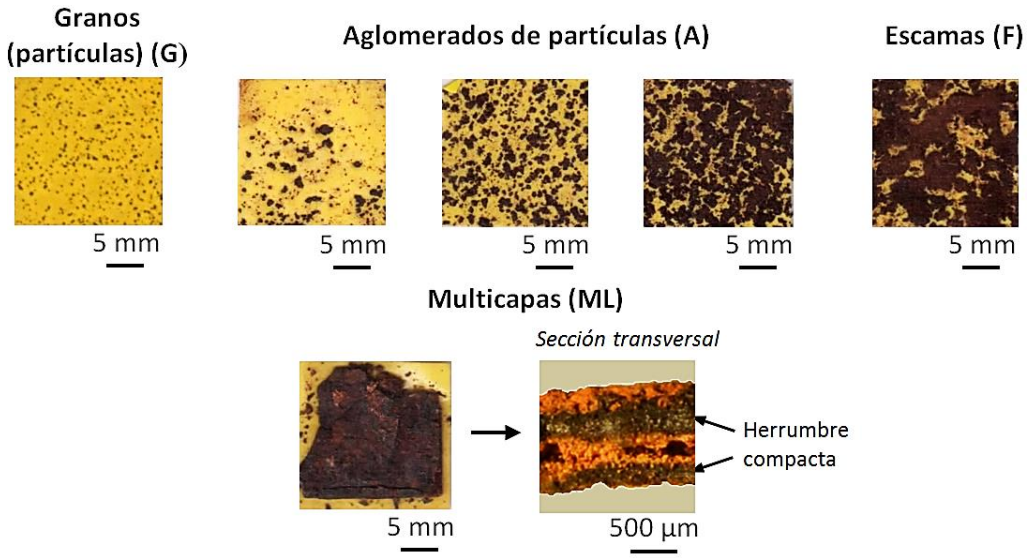

Figura 6. Tipos de texturas de herrumbre formadas sobre acero al carbono expuesto en atmósferas marinas.

La textura que exhibe la superficie más externa de la capa de herrumbre varía con el grado de agresividad de la atmósfera, función a su vez de la salinidad registrada en cada estación. Así, se observan herrumbres más heterogéneas y agrietadas en las atmósferas más agresivas, es decir en aquellas estaciones donde se registran los valores más altos de salinidad, y herrumbres más homogéneas en las atmósferas de menor salinidad.

3.5.4 Capas de herrumbre: sección transversal

3.5.4.1 Espesor de la capa de herrumbre

Se ha determinado el espesor de las capas de herrumbre formadas. Para ello se ha utilizado un medidor de espesores electromagnético, marca Elcometer modelo 355. Las medidas se han realizado en un área de 10 cm^2, tomando 9 puntos y obteniendo un valor promedio.

3.5.4.2 Estructura de la capa de herrumbre

La microscopía óptica nos ha permitido observar de forma rápida y sencilla la estratificación de la herrumbre, su compactación, etc., así como también el espesor de la capa de productos de corrosión formada sobre el acero.

Para la preparación de las muestras se procedió al corte de las probetas, de dimensiones 1 x 1 cm^2, mediante una cortadora de precisión Buehler Isomet con disco de diamante. Posteriormente fueron embutidas en frío con una resina epoxi para evitar posibles transformaciones de fase de los productos de corrosión.

Se ha utilizado un microscopio óptico con luz polarizada de la marca Nikon, modelo EPIPHOT 300, obteniéndose las imágenes mediante una cámara Infinity 2 acoplada al microscopio.

También se observaron las muestras con luz polarizada. Para ello, se realizaron secciones transversales de las capas de herrumbre y se obtuvieron las micrografías más representativas de algunas de las muestras. Algunas zonas de la herrumbre son activas frente a la luz polarizada, manifestándose de color anaranjado, mientras que otras zonas no son activas a la luz polarizada, no coloreándose al verlas al microscopio.

4. RESULTADOS

4.1 Características meteorológicas del campo de experimentación

En la Tabla 10 se exponen los parámetros meteorológicos que caracterizan el entorno donde se ha llevado a cabo el estudio. Fueron obtenidos a partir de los registros de AEMET en la estación "Cabo Vilan", situada a unos pocos metros de nuestra estación 2 (Viravento), durante el periodo de estudio, de Abril 2013 a Marzo 2016.

Tabla 10. Información meteorológica de la estación de Cabo Vilan durante el desarrollo del estudio. Valores obtenidos con los datos AEMET disponibles.

Periodo	Temperatura media anual (°C)	Humedad relativa media anual (%)	Precipitación anual (l/m^2)	Días al año de precipitación	Velocidad media anual del viento (Km/h)	Dirección del viento con frecuencias ≥20%
Abril 2013 a marzo 2014	13	83,5	990,8	>150	29,2	NE
Abril 2014 a marzo 2015	14	83,8	822,6	>163	24,2	NE
Abril 2015 a marzo 2016	14	82,4	1110,9	>151	27,7	NE

Asimismo, también procedente de AEMET, se ha dispuesto de las rosas de viento anuales correspondientes a esa misma estación meteorológica y que se exponen en la Figura 7.

Frecuencias anuales de viento

Abril 2013 a marzo 2014 | Abril 2014 a marzo 2015 | Abril 2015 a marzo 2016

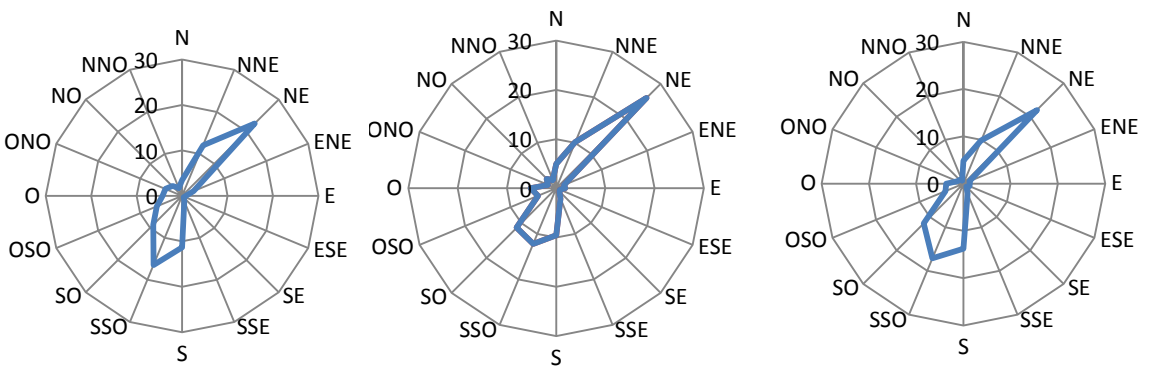

Figura 7. Rosas de vientos correspondientes a la estación "Cabo Vilan" de AEMET durante los años en que se realizó el estudio.

Como se puede observar la zona donde se ha llevado a cabo el estudio presenta una humedad relativa alta, temperatura suave y alta precipitación. Estos valores indican altos tiempos de humectación de la superficie metálica que favorecen los procesos de corrosión atmosférica. También se observa que el campo experimental está sometido a fuertes vientos, principalmente del nordeste, y la velocidad media del viento es alta. La dirección N a la que fueron orientadas las estaciones de ensayo y la proximidad de éstas a la línea de costa indican que las estaciones de ensayo han estado sometidas a fuertes vientos marinos con un considerable arrastre del aerosol marino (salinidad atmosférica), que ha potenciado en gran medida el proceso de corrosión metálica.

4.2 Velocidades de depósito de cloruros (salinidad atmosférica)

En la Tabla 11 se exponen los datos trimestrales de salinidad atmosférica obtenidos en las distintas estaciones del ensayo durante los años de estudio. Como se puede observar faltan algunos datos trimestrales de algunas estaciones de ensayo, debido al desprendimiento de los captadores por los fuertes vientos.

Esta información refleja el fuerte carácter marino que exhibe el campo experimental donde se ha llevado a cabo el estudio, ya que se han registrado valores altos de velocidad de depósito de ion cloruro incluso en aquellas estaciones que estaban ubicadas a cientos de metros tierra adentro, alejadas de la línea de costa.

Se observan las fluctuaciones que experimenta la salinidad atmosférica en una misma estación a lo largo de todo el estudio. Esto es debido a la fuerte dependencia de esta variable con la dirección, velocidad y frecuencia de los vientos marinos en un determinado periodo.

Tabla 11. Datos trimestrales de salinidad atmosférica obtenidos en las distintas estaciones de ensayo durante los años de estudio.

Velocidad de depósito del ion cloruro (mg Cl^-/m^2·día)					
ESTACIÓN (aerogenerador)	***Periodo de abril 2013 a abril 2014***				Media anual
	Abril 2013 Julio 2013	Julio 2013 Octubre 2013	Octubre 2013 Enero 2014	Enero 2014 Abril 2014	
1 (A-6)	1136	511	-	-	824[a]
2 (Viravento)	2177	1634	-	-	1905[a]
3 (A-10)	889	524	584	664	665
4 (A-16)	245	160	200	460	266
7 (AE-3)	173	137	178	337	206
9(AE-5)	102	52	59	222	109
10 (AE-6)	110	71	94	-	92[b]
11(AE-12)	44	33	40	161	69
	Periodo de abril 2014 a abril 2015				Media anual
	Abril 2014 Julio 2014	Julio 2014 Octubre 2014	Octubre 2014 Enero 2015	Enero 2015 Abril 2015	
2 (Viravento)	881	891	-	-	886[a]
5 (AE-1)	160	100	-	-	130[a]
6 (AE-2)	110	70	170	262	153
7 (AE-3)	122	75	-	-	98[a]
8 (AE-4)	75	31	141	174	105
9 (AE-5)	54	27	156	56	73
12 (AE-13)	67	70	-	-	886[a]
	Periodo de abril 2015 a abril 2016				Media anual
	Abril 2015 Julio 2015	Julio 2015 Octubre 2015	Octubre 2015 Enero 2016	Enero 2016 Abril 2016	
2 (Viravento)	2073	644	1776	-	1497[b]
5 (AE-1)	438	126	858	290	428
6 (AE-2)	106	89	316	410	230
7 (AE-3)	101	90	183	115	122
8 (AE-4)	77	59	110	189	109
9 (AE-5)	64	65	250	118	124

(-) Valor no disponible por desprendimiento del captador de ion cloruro.
(a) Valores correspondientes a los primeros 6 meses de exposición (por caída de la estación de ensayo).
(b) Valores correspondientes a los primeros 9 meses de exposición (por caída de la estación de ensayo).

4.3 Velocidades de corrosión del acero

En este apartado se exponen los resultados obtenidos sobre velocidades de corrosión del acero suave correspondientes a las dos fases del estudio: fase I comprendida entre los meses de abril 2013 a octubre 2014 y fase II comprendida entre los meses de abril 2014 a octubre 2015. En las Tablas 12 y 13 se indican las velocidades de corrosión que experimenta el acero durante las dos fases de estudio y las correspondientes velocidades de depósito de cloruros.

Tabla 12. Velocidades de corrosión del acero suave en las diferentes estaciones de ensayo durante la fase I de estudio y las correspondientes velocidades de depósito de cloruros.

Fase I de estudio (Periodo comprendido entre abril 2013 y octubre 2014)						
Estación	Tiempo de exposición					
	6 meses		12 meses		18 meses	
	Corrosión (µm)	**Salinidad (mg/m²·día)**	Corrosión (µm)	**Salinidad (mg/m²·día)**	Corrosión (µm)	**Salinidad (mg/m²·día)**
1	210	**824**	[a]	[a]	[a]	[a]
2	177	**1905**	[a]	[a]	[a]	[a]
3	145	**706**	240	**665**	[b]	[b]
4	101	**203**	123	**266**	[b]	[b]
7	74	**155**	78	**206**	171	**170**
9	60	**77**	66	**109**	80	**86**
10	55	**91**	[a]	**92[x]**	[a]	[a]
11	57	**38**	50	**69**	[b]	[b]

[a] ***Valor no disponible por desprendimiento de la estación de ensayo de su ubicación.***
[b] ***Valor no disponible por cambio de ubicación del molino donde estaba ubicada la estación de ensayo.***
[x] ***Valores correspondientes a los primeros 9 meses de exposición.***

Tabla 13. Velocidades de corrosión del acero suave en las diferentes estaciones de ensayo durante la fase II de estudio y las correspondientes velocidades de depósito de cloruros.

Fase II de estudio (Periodo comprendido entre abril 2014 y octubre 2015)								
Estación	***Periodo de exposición (abril 2014 a abril 2015)***							
	3 meses		**6 meses**		**9 meses**		**12 meses**	
	Corrosión (µm)	**Salinidad (mg/m²·d)**	Corrosión (µm)	**Salinidad (mg/m²·d)**	Corrosión (µm)	**Salinidad (mg/m²·d)**	Corrosión (µm)	**Salinidad (mg/m²·d)**
2	66	**881**	137	**886**	[a]	[a]	[a]	[a]
5	38	**160**	69	**130**	[a]	[a]	[a]	[a]
6	29	**110**	47	**90**	52	**117**	60	**153**
7	28	**122**	55	**98**	[a]	[a]	[a]	[a]
8	23	**75**	47	**53**	39	**82**	51	**105**
9	21	**54**	40	**41**	38	**79**	47	**73**
12	21	**67**	38	**68**	[a]	[a]	[a]	[a]
Estación	***Periodo de exposición (octubre 2014 a octubre 2015)***							
	3 meses		**6 meses**		**9 meses**		**12 meses**	
2	[a]	[a]	[a]	[a]	[a]	[a]	[a]	[a]
5	[a]	[a]	[a]	[a]	[a]	[a]	[a]	[a]
6	31	**170**	49	**216**	69	**179**	78	**157**
7	[a]	[a]	[a]	[a]	[a]	[a]	[a]	[a]
8	25	**141**	39	**157**	49	**130**	64	**113**
9	22	**156**	36	**106**	48	**92**	53	**85**
12	[a]	[a]	[a]	[a]	[a]	[a]	[a]	[a]

[a] ***Valor no disponible por desprendimiento de la estación de ensayo de su ubicación.***

4.4 Información obtenida de las herrumbres formadas

4.4.1 Naturaleza de los productos de corrosión

A continuación se expone la caracterización realizada de las fases de herrumbre presentes en las capas de productos de corrosión formadas sobre el acero suave expuesto en las diferentes estaciones de ensayo durante las dos fases de estudio.

El gran número de probetas ensayadas hizo necesario acotar el número de probetas a estudiar, sobre todo a la hora de aplicar técnicas de caracterización económicamente costosas a probetas similares desde el punto de vista de la corrosión. Es por ello que de ambas fases de estudio fueron seleccionadas algunas de las probetas de ensayo para aplicar las técnicas de caracterización oportunas.

4.4.1.1 XRD (RIR y Rietveld)

Mediante la técnica de difracción de rayos X fueron analizadas las probetas expuestas en cada una de las estaciones de ensayo transcurridos los 3 primeros meses de exposición en ambas fases de estudio. Para los siguientes periodos de exposición fueron seleccionadas aquellas estaciones de mayor relevancia y de las cuales se dispusiera de continuidad a lo largo del tiempo de exposición.

Como ya se comentó en el apartado de metodología experimental, uno de los métodos sencillo, rápido y económico de semicuantificar los productos de corrosión que componen la herrumbre de las probetas es mediante el método RIR (Reference Intensity Ratio), método normalmente utilizado para cuantificar las fases presentes en las herrumbres. Sin embargo, es un método poco preciso y con el fin de obtener una cuantificación más exacta de los productos de corrosión se utilizó el método Rietveld en algunas de las probetas.

En la primera fase de estudio los análisis de XRD fueron realizados con una muestra en polvo de herrumbre raspada de la superficie de la probeta a estudiar (Tabla 14), sin embargo en la segunda fase del estudio, como se detalla en la Tabla 15, se realizaron análisis directamente sobre probeta herrumbrada en aquellas probetas donde no se quería realizar un ensayo destructivo, como ocurre en el raspado de la herrumbre.

Se expone en las Tablas 14 y 15 un resumen de los análisis de difracción de rayos X que han sido llevados a cabo a lo largo del estudio en cada una de sus fases.

Tabla 14. Análisis de XRD realizados en las probetas de la fase I de estudio.

Fase I de estudio (periodo de abril 2013 a octubre 2014)						
Tiempo de exposición	Métodos de cuantificación		Salinidad			Cara de la probeta
	RIR	Rietveld	Muy alta	Alta	Moderada	
3 meses	X		1, 2, 3	4, 7, 9	10, 11	A y B
		X	2		11	A
6 meses	X		2	4	11	A
		X	2		11	A
9 meses	X		2	4	11	A
		X	2		11	A
12 meses	X		3	4	11	A
		X	3		11	A

Los números indican la estación de ensayo.
Cara A (cara de la probeta que mira al cielo); Cara B (cara de la probeta que mira al suelo).

Tabla 15. Análisis de XRD realizados en las probetas de la fase II de estudio.

Fase II de estudio (periodo de abril 2014 a octubre 2015)								
Tiempo de exposición	Método de cuantificación		Muestra		Salinidad			Cara de la probeta
	RIR	Rietveld	En polvo	Sobre chapa	Muy alta	Alta	Moderada	
3 meses	X		X		2, 5, 6, 7, 8, 9		12	A y B
		X		X		8		A
6 meses	X		X		2, 5, 7, 9			A
		X		X		8		A
9 meses		X		X		8		A
12 meses		X		X		8		A

Los números indican la estación de ensayo.
Cara A (cara de la probeta que mira al cielo); Cara B (cara de la probeta que mira al suelo).

Las herrumbres formadas sobre el acero suave están constituidas por diferentes oxihidróxidos y óxidos de hierro. En todas las herrumbres se observa la presencia de lepidocrocita, goetita, magnetita/maghemita y akaganeita como fases principales.

La lepidocrocita y la goetita son los productos mayoritarios, la magnetita/maghemita son otros óxidos comúnmente encontrados en las herrumbres, en menores concentraciones, y son mencionados en este apartado en conjunto, ya que no es posible discernir mediante XRD ambas fases por separado. Además, en las atmósferas marinas con concentraciones elevadas de cloruros, también se forma akaganeita como producto de corrosión.

La presencia de akaganeita no solo depende de la concentración de cloruros en la atmósfera sino también de otros factores como el tipo de acero, tiempo de exposición, tiempo de humectación de la superficie metálica, régimen de penetración de los cloruros en la capa de herrumbre durante la exposición atmosférica, etc. En apartados posteriores se explicará más detalladamente cuales son las condiciones ambientales necesarias para que tenga lugar la formación de este producto de corrosión.

En la Figura 8 se muestra el difractograma típico encontrado en las muestras de herrumbre. Se ponen de relevancia los picos que exhiben cada una de las fases presentes en las herrumbres.

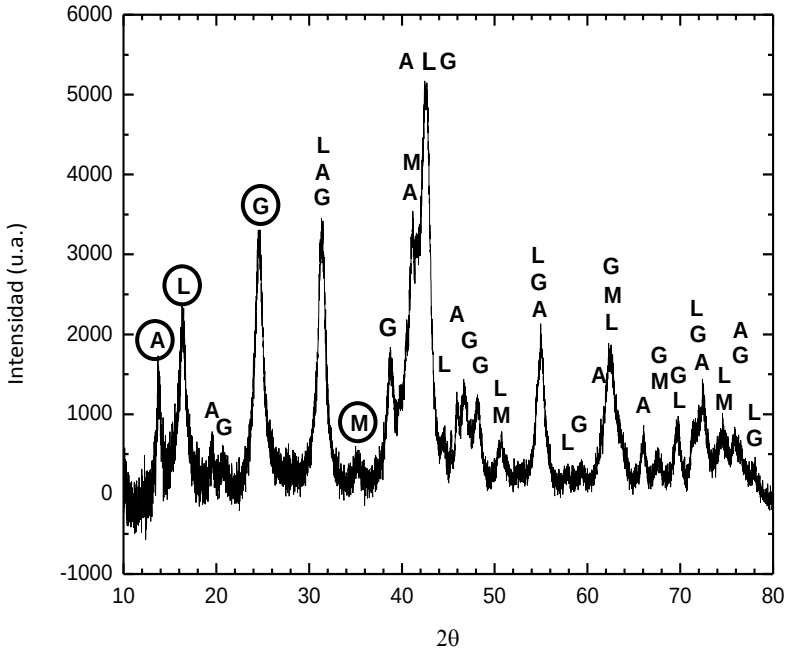

Figura 8. Difractograma de rayos X típico de las herrumbres formadas sobre el acero de estudio, mostrando la presencia de las fases lepidocrocita (L), goetita (G), akaganeita (A) y magnetita/maghemita (M). La letra redondeada indica el pico de difracción más intenso de cada una de las fases.

En la Figura 9 se expone un análisis semi-cuantitativo mediante RIR, de las fases de herrumbre, (a) lepidocrocita, (b) goetita, (c) magnetita/maghemita, (d) akaganeita, presentes en los productos de corrosión de las probetas de acero suave expuestas durante 3, 6, 9 y 12 meses.

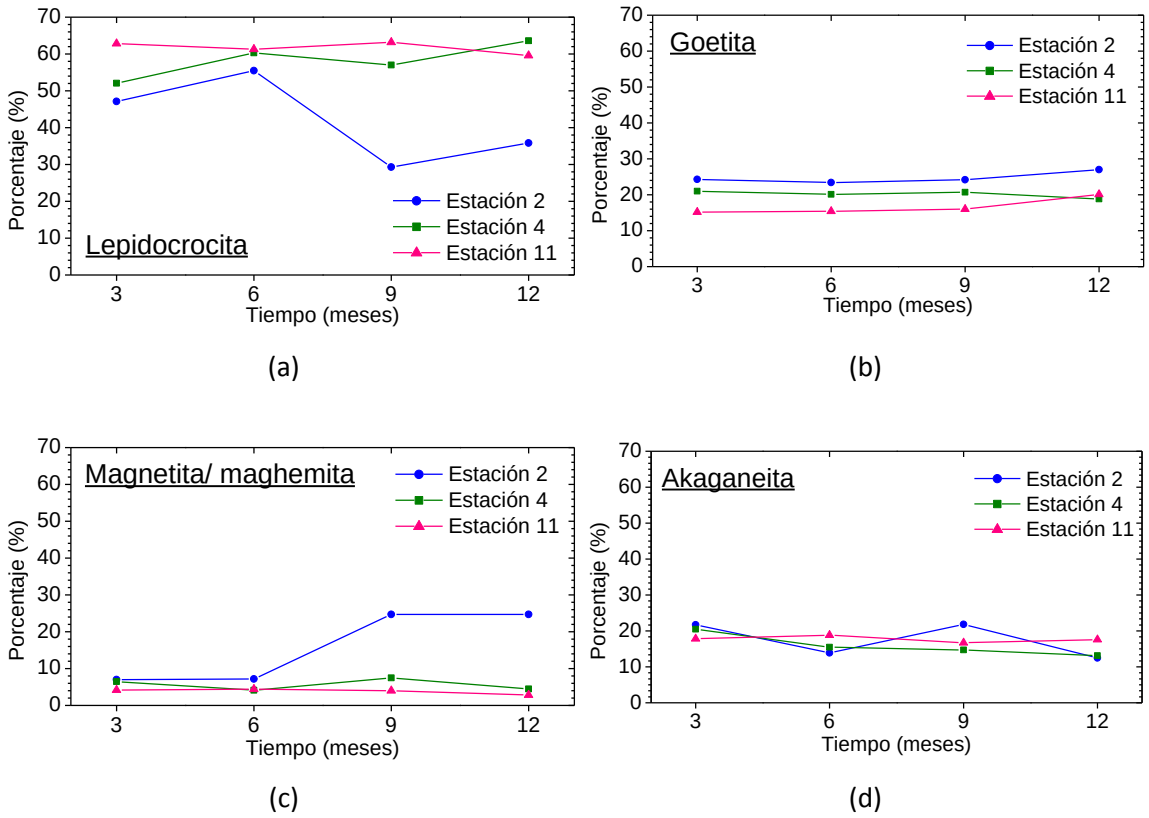

Figura 9. Análisis semi-cuantitativo mediante XRD de las fases de herrumbre (a) lepidocrocita, (b) goetita, (c) magnetita/maghemita y (d) akaganeita, identificadas en la herrumbre formada sobre el acero suave expuesto en las estaciones 2, 4 y 11, después de 3, 6, 9 y 12 meses de exposición.

Se observa para la estación 2 que a tiempos superiores a 6 meses de exposición aumenta el contenido en magnetita/maghemita, a expensas de una disminución importante en el contenido en lepidocrocita.

Con el fin de una cuantificación más exacta de los productos de corrosión se realizó un análisis cuantitativo mediante el método Rietveld. En la Tabla 16 se presentan los resultados de los productos de corrosión encontrados en la herrumbre correspondiente a dos estaciones, estación 2, de muy alta salinidad, y estación 11, de salinidad moderada.

Tabla 16. Resultados de la cuantificación mediante XRD (ajuste Rietveld) de las fases encontradas en la herrumbre formada sobre la cara A (cara que mira al cielo) del acero suave expuesto en dos estaciones de diferente salinidad, estación 2 (de muy alta salinidad) y estación 11 (de salinidad moderada), durante 3, 6, 9 y 12 meses.

Estación	Tiempo de exposición (meses)	**Fases de herrumbre (%)**			
		Lepidocrocita	Magnetita/maghemita (espinela)	Goetita	Akaganeita
2	3	26,0	11,3	53,5	9,2
	6	31,7	12,9	41,9	6,3
	9	8,6	42,4	42,5	6,5
	12	13,1	42,0	44,4	0,5
11	3	47,4	4,8	40,6	7,2
	6	43,8	8,6	36,8	10,9
	9	48,0	10,0	36,4	5,6
	12	51,6	8,2	35,9	4,3

A fines de comparación entre una primera semicuantificación de los productos de corrosión por RIR y una cuantificación más rigurosa por Rietveld, en la Figura 10 se exponen los resultados obtenidos por XRD mediante RIR y Rietveld de los productos de corrosión formados en una misma estación (estación 2) durante 3, 6, 9 y 12 meses de exposición.

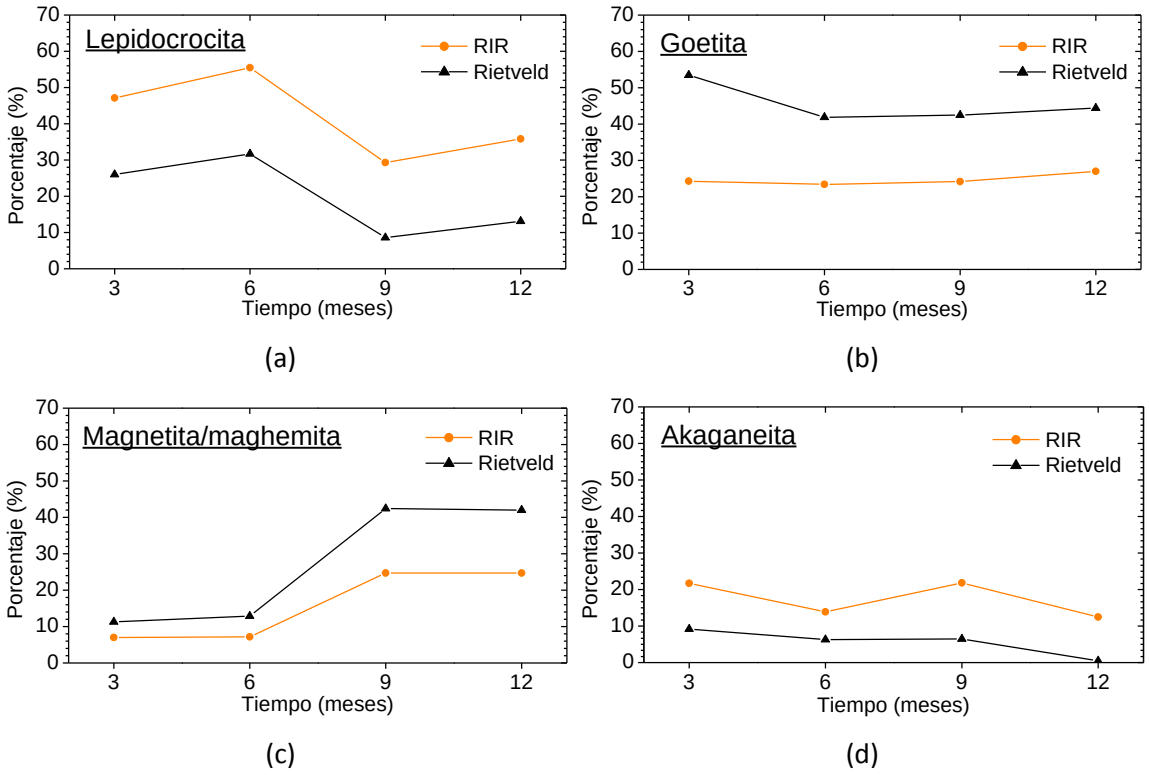

Figura 10. Cuantificación, mediante RIR y Rietveld, de las fases de herrumbre, (a) lepidocrocita, (b) goetita, (c) magnetita/maghemita y (d) akaganeita, formadas sobre el acero correspondiente a la estación 2 después de 3, 6, 9 y 12 meses de exposición.

Con esta técnica se ha podido comprobar, una vez más, que se trata de un ambiente marino muy severo ya que incluso en aquellas estaciones ubicadas a cientos de metros de la línea de costa se observan los picos de difracción característicos de la akaganeita, producto de corrosión común en atmósferas marinas.

La semicuantificación mediante RIR de las fases de herrumbre no tiene en cuenta el solapamiento de los picos de difracción de las distintas fases, lo que provoca una sobrecuantificación de algunas fases (lepidocrocita y akaganeita) y una cuantificación por defecto de otras (goetita y magnetita/maghemita). En el capítulo de discusión se llevará a cabo un estudio en mayor profundidad de los resultados obtenidos.

4.4.1.2 FTIR

Como ya se comentó en el apartado de metodología experimental, la espectroscopía infrarroja por transformada de Fourier se ha utilizado como una técnica complementaria a otras técnicas para la confirmación de las fases principales presentes en las herrumbres formadas sobre el acero suave.

En la Figura 11 se exponen los espectros infrarrojo de muestras de herrumbre en 3 estaciones de diferente salinidad: muy alta (estación 2), alta (estación 5) y moderada (estación 9) al cabo de 3 y 6 meses de exposición

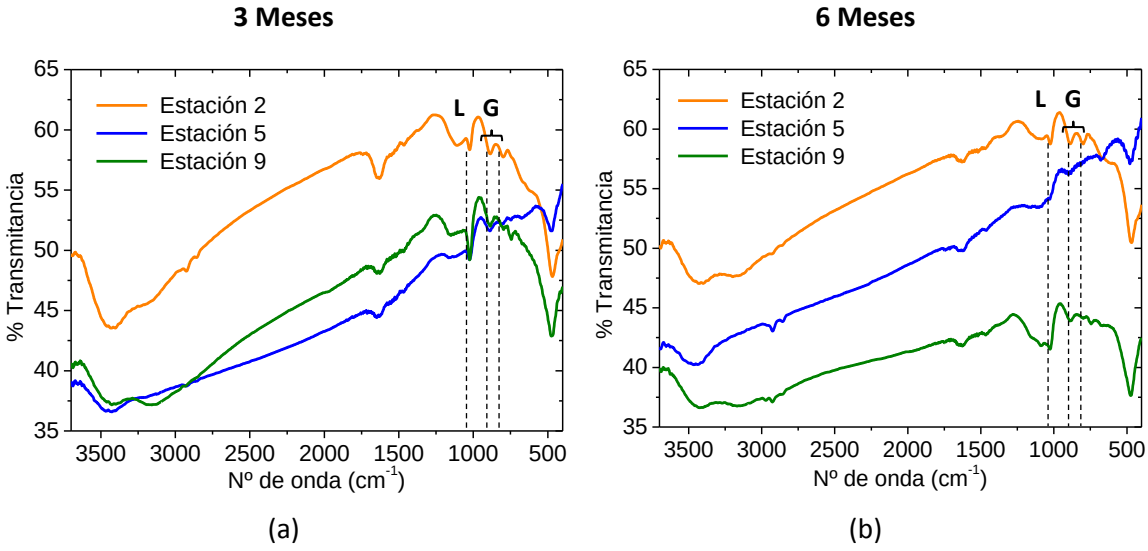

Figura 11. Espectros infrarrojos por transformada de Fourier de las herrumbres formadas en tres estaciones de distinta salinidad tras 3 meses (a) y 6 meses de exposición del acero (b).

Se observan con claridad los picos característicos de los dos oxihidróxidos mayoritarios de la herrumbre, lepidocrocita (1020 y 750 cm^{-1}) y goetita (889 y 795 cm^{-1}). Sin embargo el resto de picos del espectro no se puede atribuir a una sola fase.

En una primera aproximación, el pico a 470 cm^{-1} se le podría asignar a la fase feroxihita, fase no cristalina presente en la herrumbre, sin embargo también la fase lepidocrocita exhibe este pico en su espectro [60].

No se han podido identificar las fases, akaganeita y magnetita, fases presentes en las herrumbres en cantidades minoritarias, debido a que ambas fases de herrumbre se localizan generalmente en la parte interna de la capa de herrumbre en una zona muy próxima a la intercara acero/herrumbre, donde es complicado tomar una muestra de herrumbre por estar muy adherida al sustrato de acero.

Los picos que se producen en la región alrededor de 1500, 2920 y 2850 cm^{-1} surgen del estiramiento de los enlaces C = O y O-H de compuestos presentes en la atmósfera y la banda ancha en la región 3000 - 3500 cm^{-1} se debe a la hidratación de la herrumbre [60, 61].

Mediante esta técnica apenas se aprecian diferencias en la evolución de los productos de corrosión con el tiempo, por lo que se decidió realizar el ensayo únicamente en los dos periodos mencionados (3 y 6 meses de exposición).

4.4.1.3 Espectroscopía Mössbauer

En la exposición del acero al carbono en atmósferas marinas muy agresivas, se puede producir la formación de gruesas capas de herrumbre (que contienen en su interior láminas de herrumbre compacta) que se separan (exfolian) fácilmente del sustrato metálico.

Es importante analizar en profundidad la composición y estructura de esta gruesa capa exfoliada. En la discusión se explicará con más detalle el mecanismo de formación y estructura de esta gruesa capa, pero se puede anticipar que la capa exfoliada está compuesta de varios estratos de herrumbre (herrumbre multicapa), como puede observarse en la sección transversal mostrada en la Figura 12. Estos estratos los denominamos como: herrumbre más externa, herrumbre compacta, herrumbre inconsistente y herrumbre más interna [62].

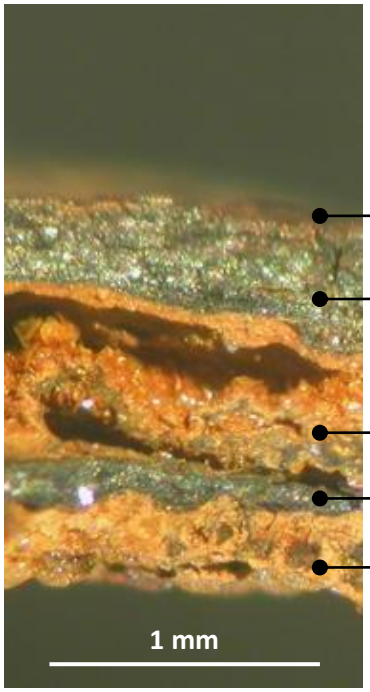

SUBCAPA	CARACTERÍSTICAS
Herrumbre más externa	Color marrón-rojizo. Su apariencia superficial, textura y composición química son típicas de la capa de herrumbre más externa formada sobre acero suave en atmósferas marinas.
Herrumbre compacta	Capa de herrumbre frágil y compacta de color grisáceo-negruzco y brillo metálico Su estructura interna es altamente porosa con abundantes huecos dispuestos linealmente
Herrumbre inconsistente	Color rojizo-anaranjado. Capa de herrumbre inconsistente y altamente porosa
Herrumbre compacta	
Herrumbre más interna	Capa heterogénea con zonas anaranjadas y zonas marrones.

(a) (b)

Figura 12. (a) Micrografía óptica de una capa exfoliada de herrumbre formada sobre acero al carbono expuesto durante un año en una atmósfera marina muy agresiva (665 mg Cl^-/m^2·día). (b) Denominación y características de las diferentes subcapas que integran la capa exfoliada.

La estructura interna de la herrumbre exfoliada contiene una o más capas de herrumbre compacta que están por lo general bien adheridas aunque pueden con mayor o menor dificultad separarse con la ayuda de un cuchillo de hoja muy fina. Es importante discernir la composición del interior de estas láminas compactas de herrumbre y saber si está compuesta de magnetita, maghemita o ambas. Para este propósito la espectroscopía Mössbauer es una técnica capaz de diferenciar ambas fases.

En la Figura 13 se exponen los espectros Mössbauer registrados a partir del polvo obtenido al moler las láminas de herrumbre compacta externa (O) e interna (I). Los espectros se obtuvieron a temperatura ambiente y 16 K. El análisis e interpretación de los resultados fue realizado en el Instituto de Química-Física “Rocasolano” del CSIC (Prof. Marco).

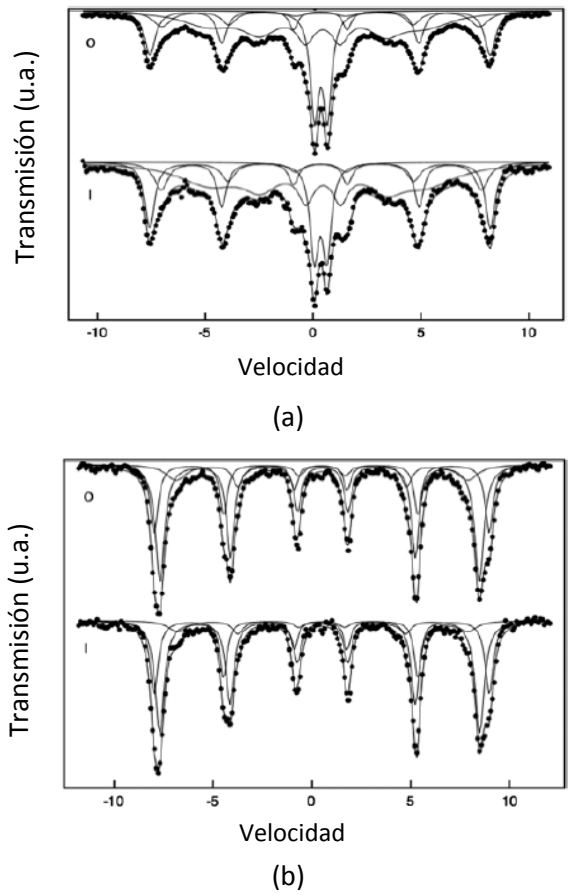

Figura 13. Espectros Mössbauer obtenidos a partir del polvo correspondiente a la lámina externa (O) y el polvo correspondiente a la lámina interna (I) a temperatura ambiente (a) y 16 K (b).

Los espectros registrados a temperatura ambiente para las dos láminas (Figura 13(a)) se ajustaron usando el mismo número de componentes: tres sextetes y un doblete paramagnético. Los parámetros de Mössbauer obtenidos del ajuste y de las correspondientes áreas espectrales se presentan en la Tabla 17. El sextete M1 tiene parámetros característicos de la maghemita [63]. El sextete M2 tiene un desplazamiento isomérico, δ, que es típico del Fe^{3+}, un bajo desplazamiento de cuadrupolo, 2ε, que no es muy diferente de la del sextete M1, y un campo magnético hiperfino, H, inferior al mostrado por el sextete M1. El sextete M2 está asociado con una fracción de maghemita de un tamaño de partícula más pequeño que el que da lugar al sextete M1, cuyos parámetros Mössbauer son similares a los mostrados por la maghemita en bulk. De hecho, el ajuste a dos sextetes es una simplificación de la evidente distribución del campo magnético originado por la presencia de una distribución del tamaño de partícula de la maghemita. **La presencia de magnetita puede ser descartada** porque el sextete correspondiente al $Fe^{2.5+}$, componente octaédrico de este óxido que se caracteriza por un gran desplazamiento del isómero δ = 0,6 - 0,7 mm/s [63], está ausente. El ancho del componente magnético M3 tiene parámetros Mössbauer que se pueden asociar con toda

seguridad con la presencia de goetita [63]. Finalmente, los parámetros Mössbauer del doblete paramagnético no permiten una asignación inequívoca, ya que puede ser debido a goetita superparamagnética, lepidocrocita, o ambas [63]. Para cerciorarse de la naturaleza de este doblete, los espectros se registraron a 16 K.

Tabla 17. Parámetros Mössbauer y áreas espectrales relativas obtenidas del ajuste del espectro realizado a temperatura ambiente.

	Sextete M1	Sextete M2	Sextete M3	Doblete
δ (mm/s)	0.35	0.36	0.35	0.36
2ε, Δ^a (mm/s)	-0.01	-0.03	-0.23	0.60
H (T)	48.9	45.8	30.9	-
Lámina externa	22	14	44	20
Lámina interna	24	14	48	15
Asignación	Maghemita	Maghemita	Goetita	Lepidocrocita/ Goetita superparamagnética

δ, desplazamiento isomérico.
2ε, desplazamiento del cuadrupolo.
Δ, desdoblamiento cuadrupolar.
H, campo magnético hiperfino.

Una inspección de los datos a temperatura ambiente indica que la fracción de componentes paramagnéticos/ superparamagnéticos aumenta en el orden "lámina exterior (O) <lámina interior (I)".

Los espectros registrados a 16 K para las dos láminas se muestran en la Figura 13(b). Todos eran muy similares y se ajustaron a tres componentes magnéticos diferentes (Tabla 18), cuyos parámetros Mössbauer son característicos de maghemita, goetita y lepidocrocita [63]. La goetita es el componente más intenso en todos los casos. La contribución de la maghemita aumenta en el siguiente orden " lámina exterior (O) <lámina interior (I)", mientras que la contribución de la lepidocrocita disminuye en el mismo orden. Una comparación de los datos recogidos en las Tablas 17 y 18 indica que el doblete contiene contribuciones tanto de la goetita como de la lepidocrocita. Las diferencias encontradas en la cantidad de maghemita entre temperatura ambiente y los datos de baja temperatura pueden explicarse en términos de diferencias en las fracciones libres de retroceso de las diversas fases a las dos temperaturas fijadas. Ya que las diferencias en las fracciones libres de retroceso a 16 K de las tres contribuciones son mínimas, la composición más fiable de las diferentes láminas es la obtenida del espectro realizado a 16 K. Así pues, a tenor de los resultados obtenidos por espectroscopía Mössbauer las subcapas de herrumbre compacta muestran la presencia de maghemita y se descarta la presencia de magnetita.

Tabla 18. Parámetros Mössbauer y áreas espectrales relativas obtenidas del ajuste del espectro realizado a 16K.

	Maghemita	Goetita	Lepidocrocita
δ (mm/s)	0.47	0.48	0.51
2ε, Δ^a (mm/s)	0.05	-0.17	0.03
H (T)	52.5	50.0	45.5
Lámina externa	28	55	17
Lámina interna	33	55	11

δ, desplazamiento isomérico.
2ε, desplazamiento del cuadrupolo.
Δ, desdoblamiento cuadrupolar.
H, campo magnético hiperfino.

4.4.1.4 TEM/SAED

Hemos visto que en las atmósferas marinas suele formarse akaganeita entre los productos de corrosión del acero. Sin embargo, es muy frecuente que en los estudios de corrosión atmosférica marina no llegue a detectarse por XRD y cuando se detecta los investigadores no llegan a identificar los cristales de este compuesto.

Por ello, en nuestro estudio [64] hemos tratado de aislar nanocristales de akaganeita utilizando la técnica TEM/SAED. En este caso, nos centramos en la zona más interna de la capa de herrumbre (intercara acero/ herrumbre), accesible cuando se produce la exfoliación de la gruesa capa de herrumbre formada sobre el acero expuesto en atmósfera marinas con elevadas velocidades de depósito de cloruros (Estación 2, Viravento). La akaganeita se localiza preferentemente en las zonas anaranjadas de la herrumbre existentes en la intercara (Figura 14). El estudio fue realizado en el Centro Nacional de Microscopía Electrónica de la Facultad de Ciencias Químicas de la UCM (Prof. González Calbet).

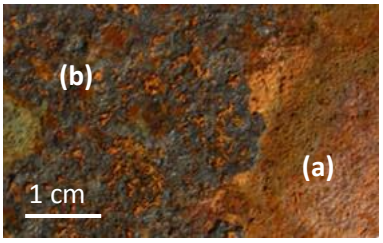

Figura 14. Apariencia heterogénea de la región más interna de la capa de herrumbre cuando se produce su exfoliación en atmósferas marinas con elevadas velocidades de depósito de cloruros. Se observan dos zonas de distinta tonalidad, (a) anaranjada y (b) marrón oscuro.

La Figura 15 muestra una micrografía obtenida por SEM/EDS de un agregado de nanocristales de akaganeita presente en esas zonas anaranjadas y la Figura 16(b) una micrografía obtenida por TEM de un nanocristal alargado, típico de akaganeita, perteneciente al mencionado agregado.

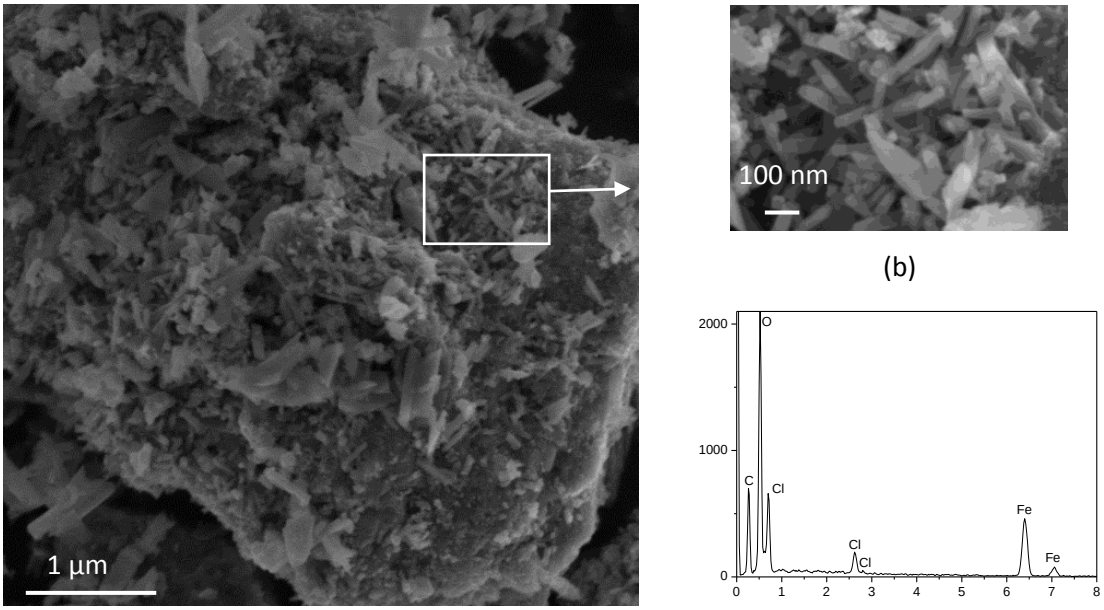

(a) (b) (c)

Figura 15. (a) Micrografía SEM de uno de los agregados de partículas existentes en las zonas anaranjadas de la Figura 14; (b) ampliación de la micrografía anterior; (c) espectro EDS correspondiente a (b).

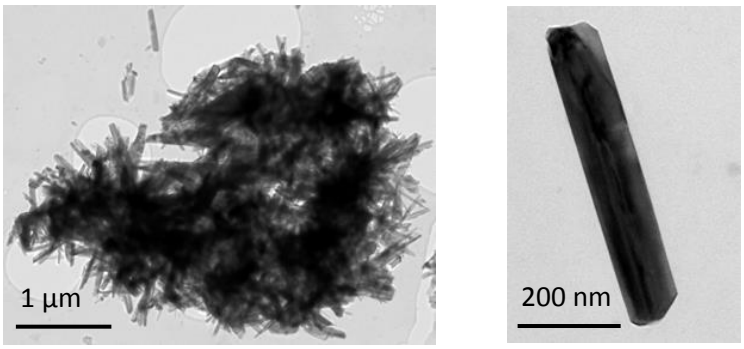

(a) (b)

Figura 16. (a) Micrografía TEM mostrando un agregado de cristales alargados; (b) micrografía TEM de una de las nanopartículas que constituyen el agregado mostrado en (a).

Con el fin de identificar con rigurosidad la naturaleza de esos nanocristales se acudió a la técnica SAED, obteniéndose el patrón de difracción que se expone en la Figura 17. El patrón se corresponde con una celda unitaria monoclínica de parámetros de red de 1.06, 0.303, 1.05 nm y β=90,24° a lo largo del eje de zona [-1-11], característico del tipo estructural hollandita correspondiente a la akaganeita.

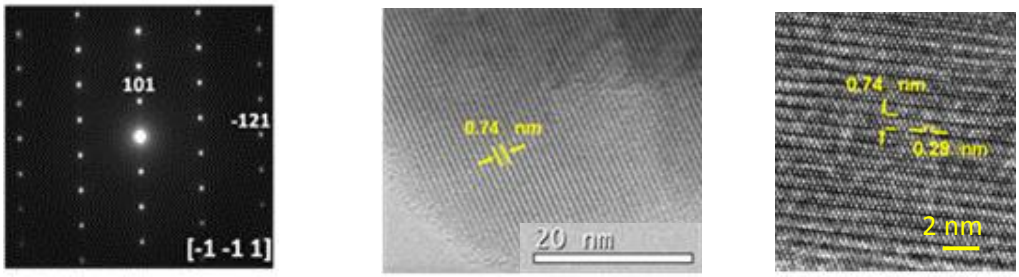

(a) (b) (c)

Figura 17. (a) Patrón SAED a lo largo del eje de zona [-1-11]; (b) imagen TEM a lo largo de esta proyección; (c) imagen TEM de alta resolución mostrando espaciados d de 0,74 nm (d_{101}) y 0,28 nm (d_{-121}) correspondientes a la estructura de la akaganeita a lo largo de [-1-11].

La transformada de Fourier y el patrón SAED a lo largo de esta proyección (Figura 18) demuestran claramente que esos nanocristales presentan unas características estructurales correspondientes a la akaganeita.

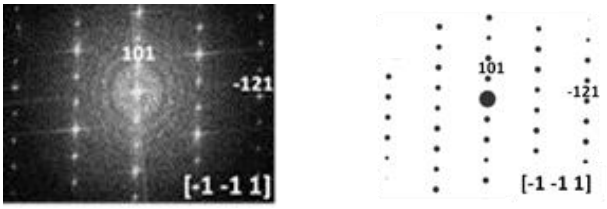

(a) (b)

Figura 18. Transformada de Fourier (a) y patrón SAED (b) a lo largo de la proyección [-1-11].

4.4.1.5 Contenido en cloruros solubles de la herrumbre

Se analizó el contenido en cloruros solubles de las herrumbres formadas sobre el acero a los 3 y 12 meses de exposición en la fase I de estudio. Debido al gran número de probetas se decidió acotar el ensayo, estudiando únicamente las probetas de 2 estaciones de diferente salinidad: alta (estación 4) y moderada (estación 11). En la Tabla 19 se muestra el contenido en sales solubles de las herrumbres formadas sobre el acero después de 3 y 12 meses de exposición.

Tabla 19. Contenido en cloruros solubles de las herrumbres formadas sobre el acero a los 3 y 12 meses de exposición en dos estaciones de ensayo de diferente salinidad.

	3 Meses		12 Meses
	Cara A	Cara B	Cara A
Estación 4	1,993%	2,015%	0,194%
Estación 11	0,463%	1,509%	0,132%

Se observa un mayor contenido en cloruros solubles en la herrumbre formada en la estación de mayor salinidad. Así mismo se observa un mayor contenido en cloruros solubles en la cara B de la probeta (menor lavado de los cloruros solubles de la herrumbre al estar esta cara menos expuesta a la acción de la lluvia) y decaimiento del contenido en cloruros solubles a altos tiempos de exposición, por la mayor dificultad que ofrece la capa de herrumbre al ingreso de nuevos iones cloruro a su interior.

4.4.2 Morfologías de las fases de herrumbre

Para una caracterización analítica rigurosa de las distintas morfologías que presentan las diferentes fases de herrumbre se ha acudido a la técnica SEM/μRaman. El estudio se ha realizado preferentemente en la superficie más externa de la capa de herrumbre. A continuación presentamos una síntesis de los principales resultados obtenidos [65-69].

La lepidocrocita puede presentar un abanico muy amplio de morfologías. En la Figura 19 se exponen algunas de ellas: morfología globular (Figura 19(a-b)); laminar, tipo barra (Figura 19(c)), laminar, tipo nido de gusanos (Figura 19(d-e)); laminar, tipo nido de pájaro (Figura 19(f-g)) y laminar, tipo pluma de ave (Figura 19 (h-i)). La morfología laminar es la forma más frecuente de esta fase.

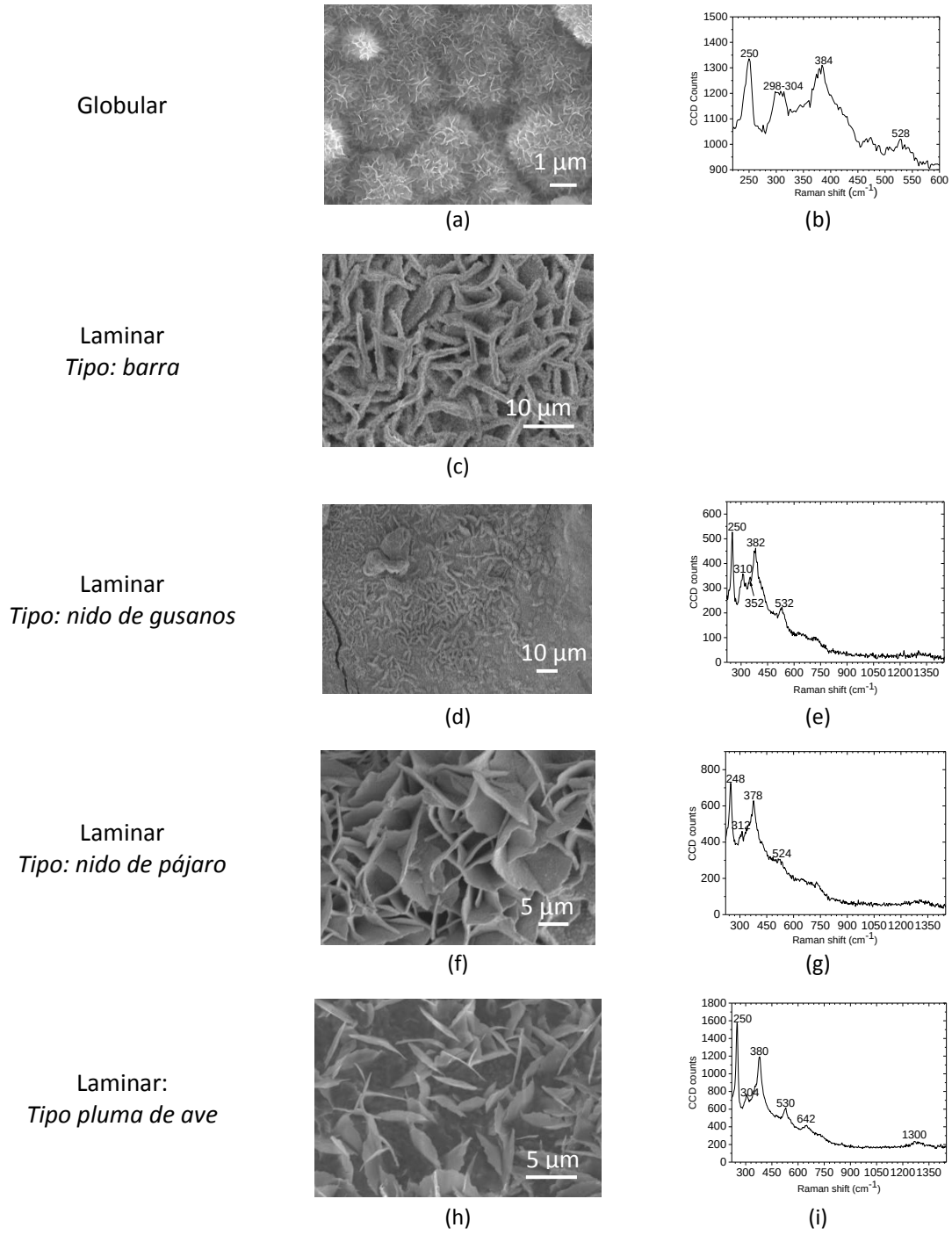

Figura 19. Distintas morfologías que puede presentar la fase lepidocrocita y sus correspondientes espectros Raman.

La goetita suele presentar dos tipos de morfologías (Figura 20): tubular (prismática) y acicular (estrella o aguja). Esta última suele formarse en la periferia de los glóbulos de lepidocrocita (Figura 20(c)), por lo que el espectro Raman resultante es una mezcla de ambas fases, lepidocrocita y goetita.

Tubular
Tipo: prismático

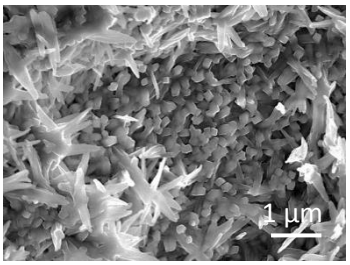

(a)

Acicular
Tipo: estrella

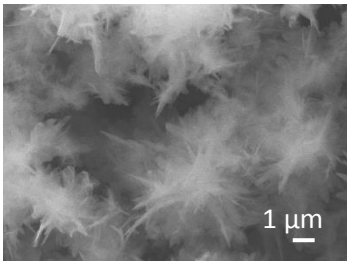

(b)

Acicular
Tipo: aguja

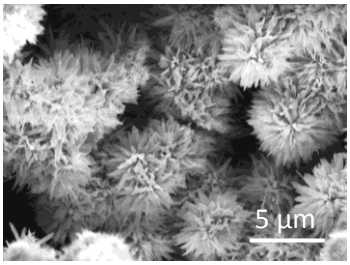

(c)

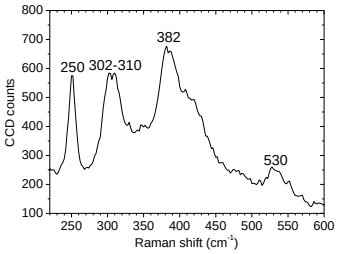

(d)

Figura 20. Distintas morfologías que puede presentar la fase goetita. Suele formarse en la periferia de los glóbulos de lepidocrocita (Figura 2 c-d)

La akaganeita suele presentar una morfología tubular, (Figura 21), ya descrita anteriormente (ver apartado 4.4.1.4).

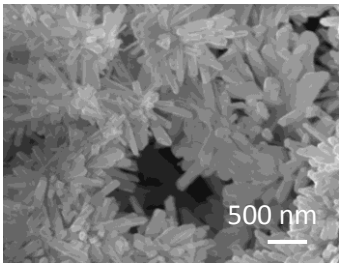

(a)

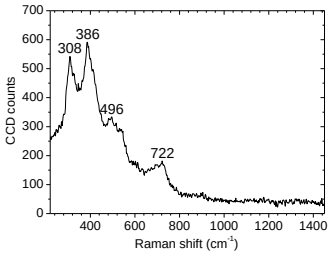

(b)

Figura 21. Morfología tubular que suele presentar la akaganeita (a) y su correspondiente espectro Raman (b).

Finalmente, la magnetita suele presentar dos tipos de morfologías: toroidal (Figura 22(a-b)) y en forma de manchas negras (Figura 22(b-c)) que se forman muy próximas al sustrato del acero.

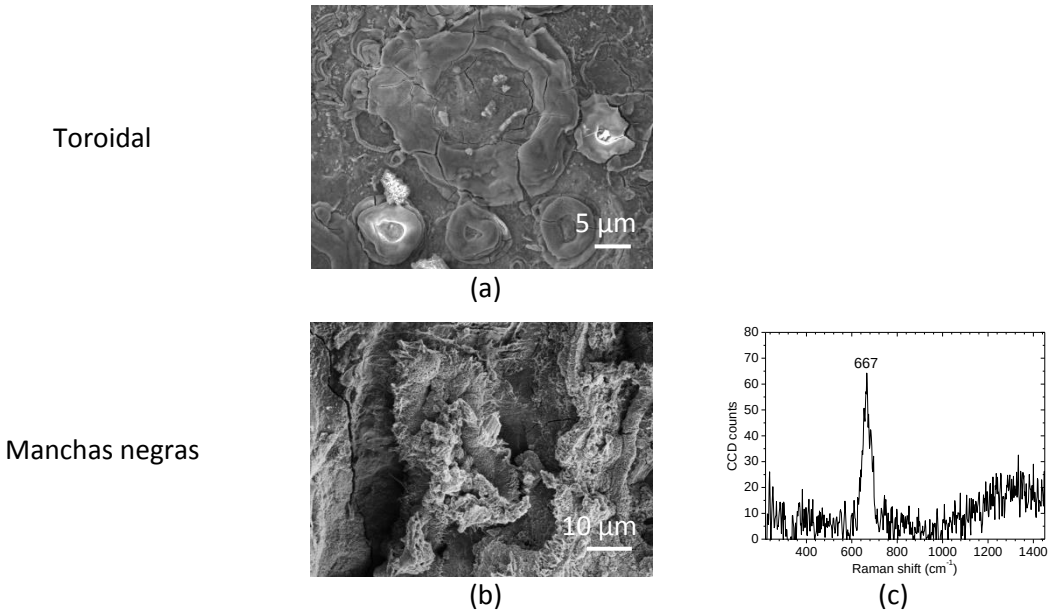

Figura 22. Morfologías que suele presentar la magnetita.

También mediante la técnica SEM /µRaman se ha obtenido información del interior de la capa de herrumbre. Este es el caso de la herrumbre existente en el interior de la picaduras formadas sobre el acero cuando este se expone en atmósferas marinas de alta salinidad (Figura 23(a)). Prácticamente la totalidad de la herrumbre correspondía a la fase akaganeita (Figura 23(b)).

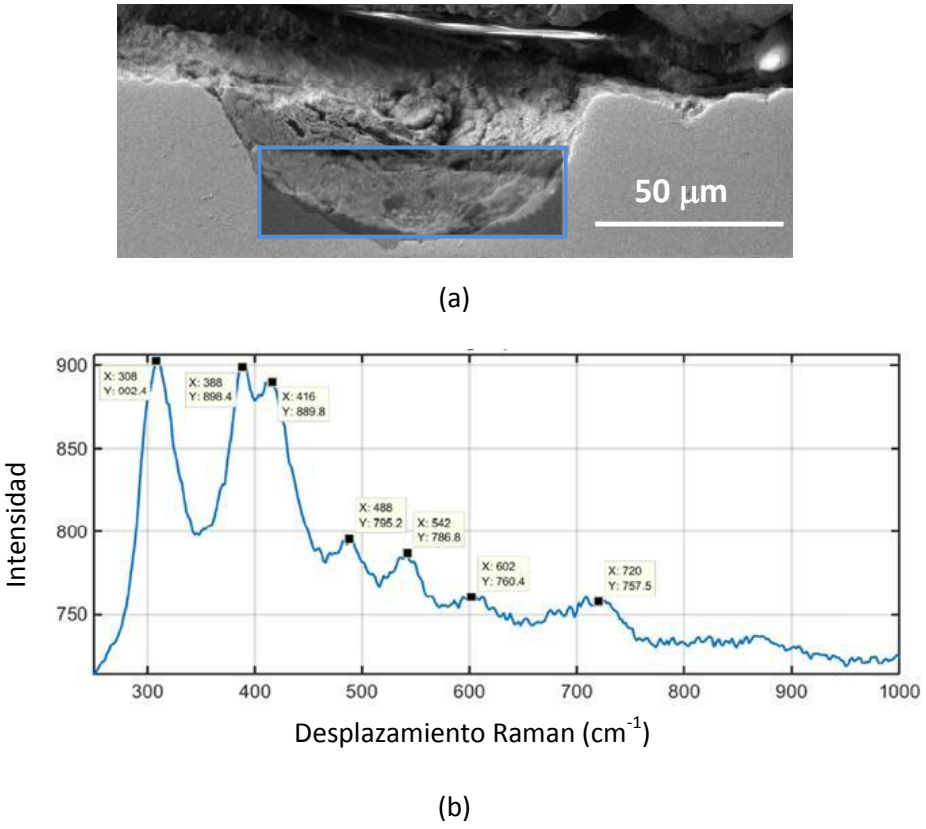

Figura 23. (a) Sección transversal del sustrato de acero en una zona de picado profundo. (b) Identificación por µRaman de akaganeita en el interior de la picadura.

4.4.3 Capas de herrumbre: superficie externa

4.3.3.1 Apariencia (coloración)

Las Figuras 24 y 25 muestran el aspecto que presentaban las herrumbres formadas sobre el acero suave al cabo de distintos periodos de exposición en la fase I de estudio. Distinguimos la apariencia de la herrumbre formada en la probeta en su cara que mira al cielo (cara A) (Figura 24) de la que se forma en su cara que mira al suelo (cara B) (Figura 25). No se dispone de la información correspondiente a los 12 y 18 meses de alguna de las estaciones por caída de la estación debido a los fuertes vientos en la zona.

Con respecto a la apariencia de las herrumbres formadas en el periodo de exposición de la fase II de estudio, no se exponen los resultados ya que no se observan apenas diferencias con el aspecto que presentaban las herrumbres formadas en la fase I de estudio.

En las fotografías de la Figuras 24 y 25 se observa que el color de la pátina formada sobre la superficie varía con el grado de agresividad de la atmósfera, función a su vez de la salinidad registrada en cada estación. Así, se observan colores de herrumbre más vivos en las estaciones que sufren una mayor corrosión, es decir en aquellas estaciones donde se registran los valores más altos de salinidad, y herrumbres más oscuras en las estaciones con menor salinidad.

También se aprecia una diferencia de apariencia entre las dos caras de exposición de las probetas de ensayo (caras A y B), con herrumbres menos protectoras en la cara B, lo que se refleja en su aspecto superficial.

Estación	Cara A "*Mirando al cielo*"				
	3 Meses	6 Meses	9 Meses	12 Meses	18 Meses
1					
2					
3		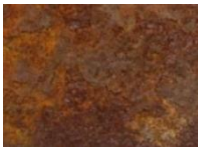			
4		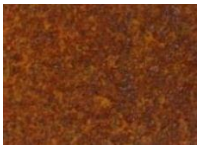			
7		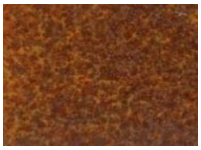		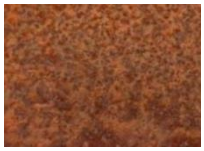	
9		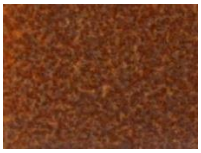	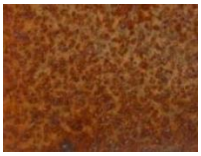	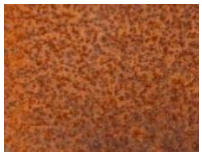	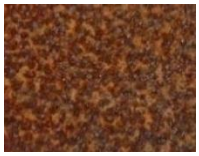
10		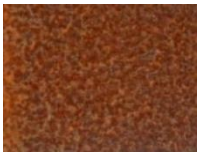			
11	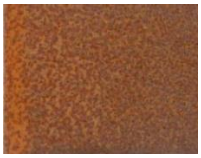	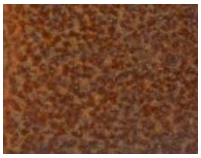	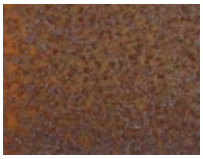		

Figura 24. Aspecto que presentaban las probetas de ensayo de acero suave al cabo de los distintos periodos de exposición en la fase I de estudio (Cara A: mirando al cielo); (Escala 1:2).

Estación	Cara B "*Mirando al suelo*"				
	3 Meses	6 Meses	9 Meses	12 Meses	18 Meses
1					
2					
3					
4			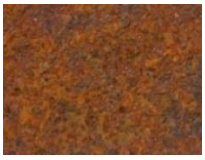		
7		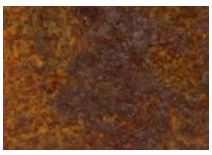			
9			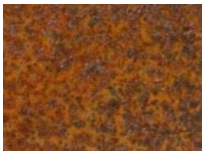		
10		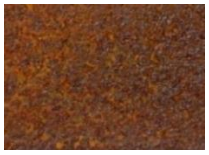			
11					

Figura 25. Aspecto que presentaban las probetas de ensayo de acero suave al cabo de los distintos periodos de exposición en la fase I de estudio (Cara B: mirando al suelo); (Escala 1:2).

4.4.3.2 Textura (granulometría)

Respecto a la textura (granulometría) de la herrumbre formada sobre la superficie del acero, en la Figura 26 se exponen los resultados del ensayo de la cinta [58] llevado a cabo con las herrumbres formadas sobre el acero expuesto a la atmósfera en las 8 estaciones de ensayo correspondientes a la fase I de estudio.

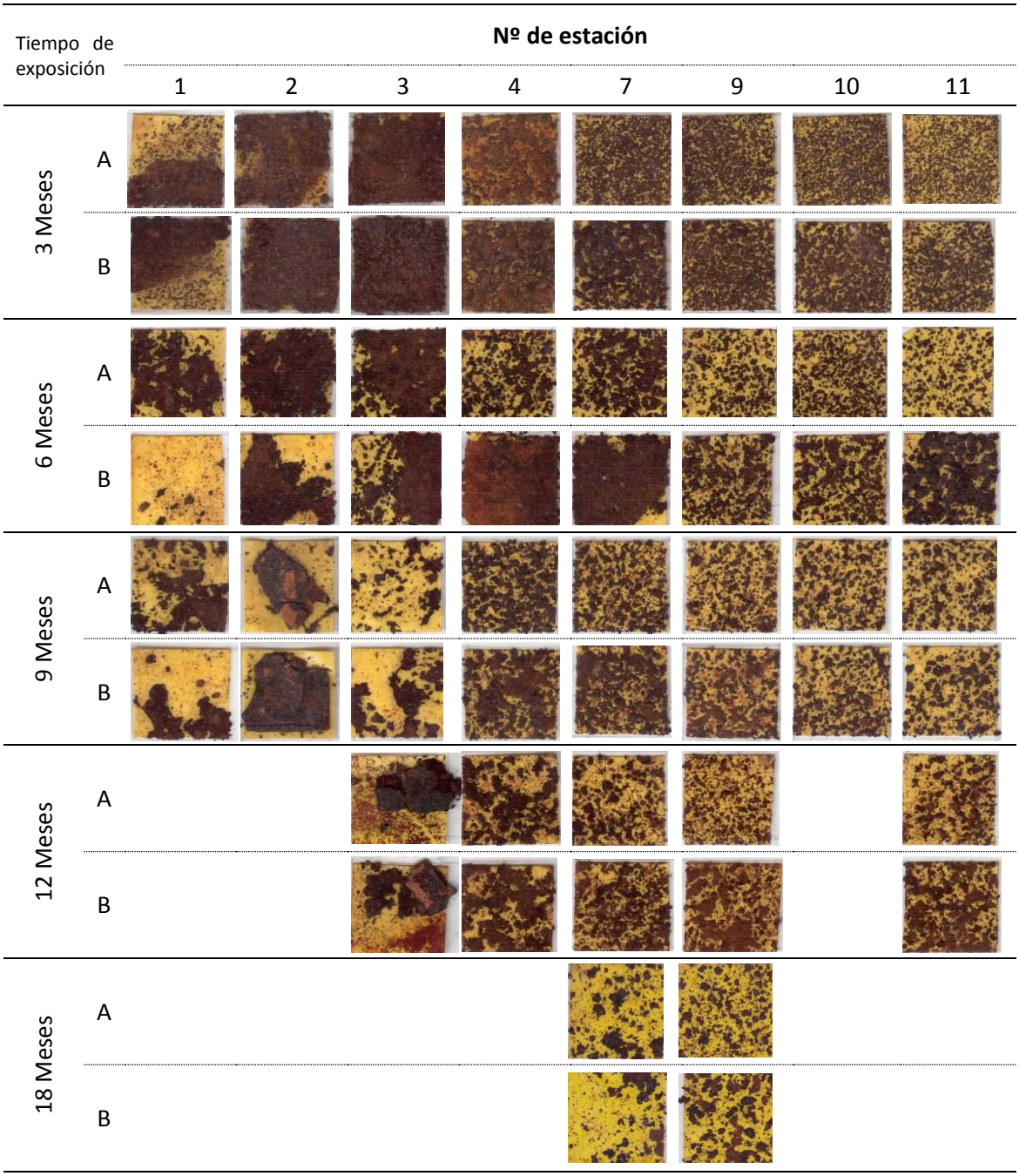

A (cara de la probeta que mira al cielo).
B (cara de la probeta que mira al suelo).

Figura 26. Granulometrías de las herrumbres formadas sobre el acero en las distintas estaciones de ensayo en la fase I de estudio; (Escala 3:4).

Únicamente se exponen los resultados obtenidos de las herrumbres formadas en la fase I de estudio (Figura 26), ya que de nuevo apenas existen diferencias entre las herrumbres formadas en ambas fases de estudio.

Se aprecian también diferencias en la textura de la herrumbre entre las diferentes estaciones de ensayo. En rasgos generales se observa un aspecto superficial más heterogéneo y granulometrías más groseras en aquellas estaciones más agresivas (estaciones de muy alta salinidad, como son las estaciones 1, 2 y 3), de mayor entidad conforme mayor es el tiempo de exposición. Se observan, en cambio, pátinas más homogéneas y granulometrías más finas en las estaciones que registran valores más bajos de salinidad, es decir las estaciones 9, 10 y 11. Las estaciones 4 y 7, intermedias en salinidad, presentan un aspecto intermedio entre los dos anteriores.

Por las razones apuntadas en los apartados anteriores, no se dispone de la información a los 12 meses de exposición de las estaciones 1, 2 y 10, y únicamente se tiene información de las estaciones 7 y 9 a los 18 meses de exposición.

Al realizar el ensayo de la cinta para evaluar la granulometría de la herrumbre formada en las estaciones 1 a 3, no se consiguió desprender partículas de herrumbre en todas ellas, debido a que las probetas se encontraban fuertemente exfoliadas y la cinta no tenía la suficiente fuerza como para levantar toda la capa exfoliada de herrumbre. Es por ello que en algunas de las imágenes simplemente se ven restos de la capa de exfoliación. Este fenómeno de exfoliación se ha observado en aquellas estaciones de ensayo más agresivas (más cercanas a la línea de costa), ya desde los primeros meses de exposición de las probetas.

4.4.4 Capas de herrumbre: sección transversal

4.4.4.1 Espesor de la capa de herrumbre

En las Tablas 20 y 21 se exponen los espesores de las herrumbres formadas sobre la superficie del acero en la fase I de estudio tras 3, 6 y 9 meses de exposición. Únicamente se exponen los resultados obtenidos de las herrumbres formadas en la fase I de estudio, ya que de nuevo apenas existen diferencias entre las herrumbres formadas en ambas fases de estudio.

Se observa con claridad un aumento del espesor de la capa de herrumbre con el tiempo de exposición y conforme mayor es la salinidad de la atmósfera (menor numeración de la estación de ensayo) donde se expuso el acero.

Tabla 20. Espesores (en μm) de las capas de herrumbre formadas sobre el acero en las distintas estaciones de ensayo en la fase I de estudio a los 3, 6 y 9 meses de exposición (Cara A: mirando al cielo).

Nº de estación	**Cara A "*Mirando al cielo*"**		
	Tiempo de exposición		
	3 Meses	6 Meses	9 Meses
1	179	422	661
2	96	337	770
3	112	238	297
4	81	117	89
7	77	107	89
9	66	90	72
10	54	90	92
11	57	82	113

Tabla 21. Espesores (en μm) de las capas herrumbre formadas sobre el acero en las distintas estaciones de ensayo en la fase I de estudio a los 3, 6 y 9 meses de exposición (Cara B: mirando al suelo).

Nº de estación	**Cara B "*Mirando al cielo*"**		
	Tiempo de exposición		
	3 Meses	6 Meses	9 Meses
1	221	440	672
2	232	441	781
3	195	435	575
4	115	261	186
7	121	166	112
9	90	152	114
10	109	104	130
11	68	94	88

4.4.4.2 Estructura de la capa de herrumbre

Se realizaron micrografías por microscopía óptica con luz polarizada de las capas de herrumbre formadas en las probetas de acero suave expuestas en tres estaciones de diferente salinidad (estaciones 2, 4 y 11) durante 3 y 12 meses de exposición.

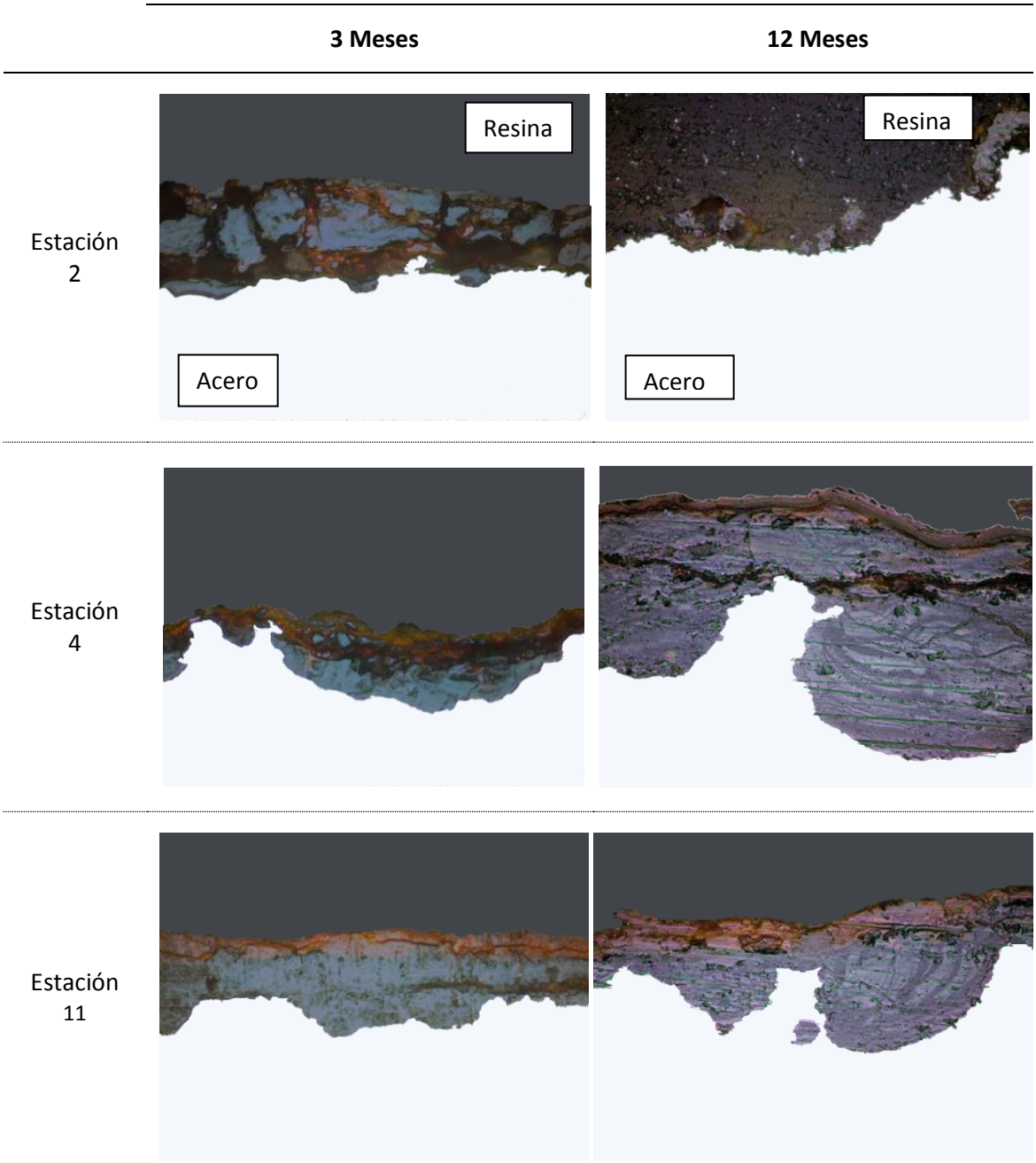

Figura 27. Micrografías ópticas con luz polarizada de las capas de herrumbre formadas sobre el acero suave expuesto durante 3 y 12 meses en las estaciones de ensayo 2, 4 y 11; (x 500 aumentos).

En las atmósferas más agresivas (estación 2 ubicada muy cerca de la línea de costa) la capa de productos de corrosión que se forma apenas transcurridos tres meses de exposición es muy heterogénea y agrietada, pudiendo incluso llegar a desprenderse del acero base, observándose éste prácticamente desnudo. En las atmósferas de menor agresividad (estaciones 4 y 11), las capas de herrumbre formadas están menos agrietadas (son más compactas), observándose con mayor claridad la estructura dual de dos subcapas, una subcapa externa, zona de la

herrumbre activa a la luz polarizada, principalmente formada por lepidocrocita, y una subcapa interna menos activa y formada principalmente por goetita.

Se realizaron observaciones SEM de las secciones transversales de las capas de herrumbre formadas sobre el acero suave, analizándose asimismo por EDS la composición elemental en diferentes zonas de la capa. En las Figuras 28 y 29 se exponen algunas de las micrografías obtenidas más representativas, y en la Tabla 22 los resultados correspondientes a los espectros EDS.

Las capas de herrumbre formadas en las estaciones de muy alta salinidad se presentaban fuertemente agrietadas, desprendiéndose en algunas zonas dejando el acero al descubierto (Figura 28).

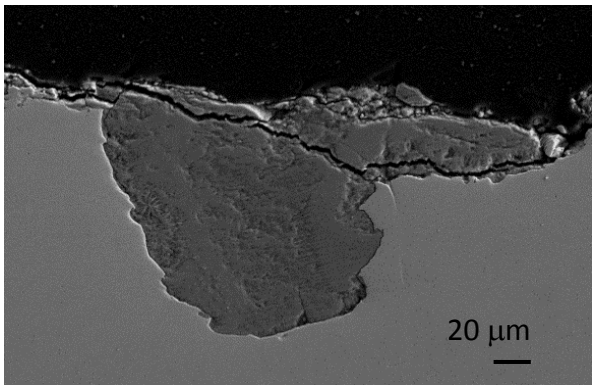

Figura 28. Observación mediante SEM de una zona donde se había desprendido (exfoliado) la capa de herrumbre dejando el acero al descubierto. Se observa asimismo una picadura profunda. Probeta de acero suave (Cara B) expuesta durante 3 meses en la estación 1.

Otras zonas, en cambio, presentaban algún resto de la capa de herrumbre (Figura 29(a)), o bien presentaban toda la capa de herrumbre aunque notablemente agrietada (Figura 29(b)). Puede observarse en los espectros EDS (Tabla 22) un alto contenido en Cl, principalmente en las picaduras del acero base, espectro de la Figura 29(a) y espectro de la Figura 29(b).

La herrumbre formada en estaciones de salinidad moderada no se exfoliaba y se presentaba menos agrietada y las picaduras del acero base eran menos profundas (Figura 29(c)). Los espectros EDS muestran también la presencia de Cl en el fondo de las picaduras, si bien en menor proporción (Tabla 22).

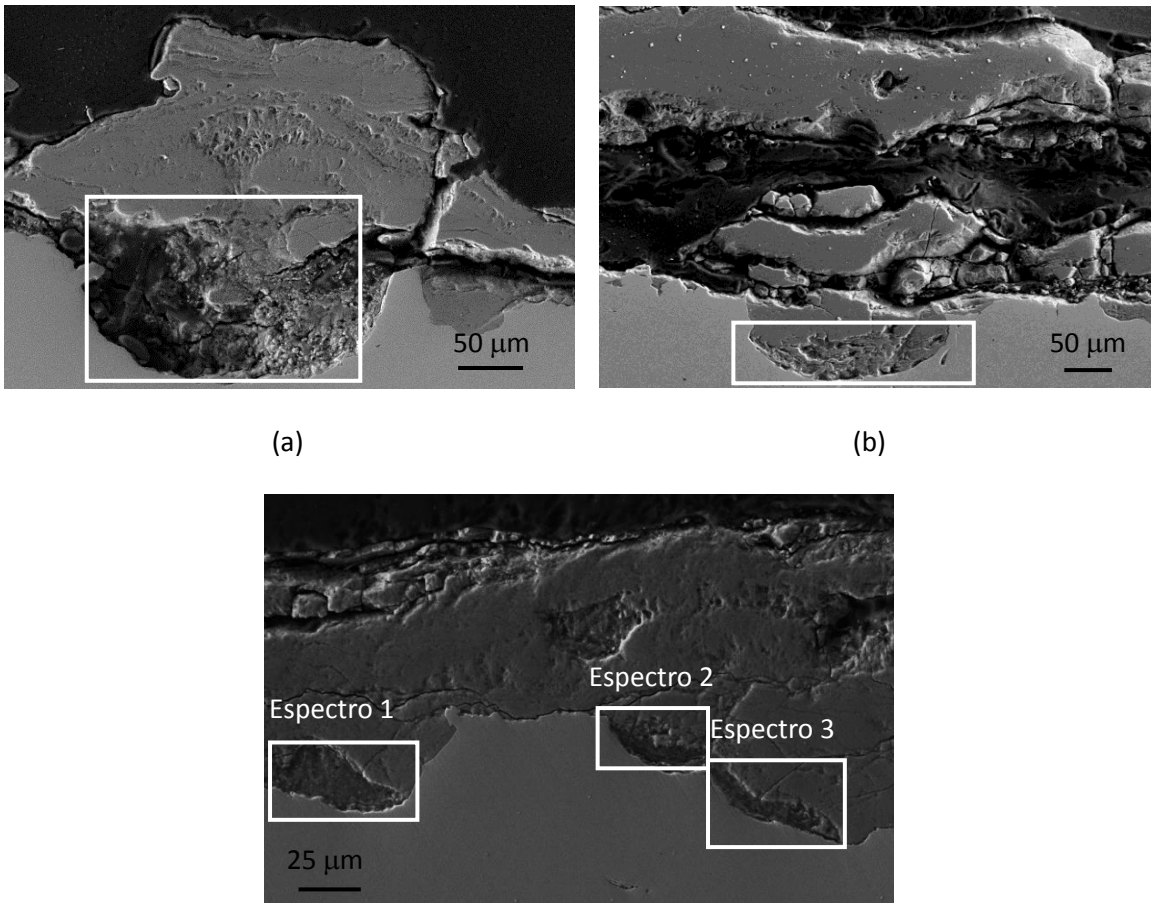

Figura 29. Observación mediante SEM de la sección transversal de las probetas de acero suave expuestas durante tres meses en diferentes estaciones de corrosión.
(a) Probeta (Cara A) expuesta en la estación 1.
(b) Probeta (Cara B) expuesta en la estación 1.
(c) Probeta (Cara A) expuesta en la estación 9.

Los resultados de los espectros EDS se muestran en la Tabla 22.

Tabla 22. Resultados de los espectros EDS correspondientes a diferentes zonas de las capas herrumbre mostradas en la Figura 29.

Zona Fig. 29	**Elemento (% atómico)**			
	Fe	O	C	Cl
Fig. 29(a)	16.11	33.00	49.93	0.96
Fig. 29(b)	23.11	47.79	27.06	2.04
Fig. 29(c) (espectro 1)	30.74	39.23	29.02	0.43
Fig. 29(c) (espectro 2)	26.34	39.20	33.95	0.51
Fig. 29(c) (espectro 3)	29.27	43.42	26.22	0.38

Como ya se ha comentado anteriormente, la corrosión es diferente en las dos caras que presenta la probeta. En la imagen de la Figura 30, correspondiente a una zona de la probeta donde prácticamente ha desaparecido el metal, se puede observar el perfil más irregular de la superficie del acero (existencia de picaduras más profundas) de la cara B, que mira al suelo.

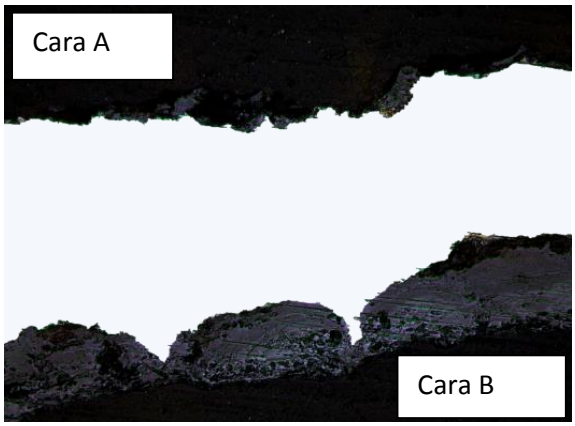

Figura 30. Micrografía óptica con luz polarizada del acero suave expuesto 12 meses en la estación 11; (x 200 aumentos).

5. DISCUSIÓN

En la sección 2 de esta Memoria señalábamos los objetivos perseguidos en la investigación. Se trata ahora de profundizar en ellos, dando a conocer los avances obtenidos a lo largo del estudio. En cada uno de los subapartados que comprende esta sección se indican las principales publicaciones realizadas, que se exponen en los Anexos de esta Memoria.

5.1 El aerosol marino presente en la atmósfera: su dependencia de parámetros diversos (meteorológicos, oceanográficos, geográficos, topográficos, etc.) y su efecto en la corrosión atmosférica del acero al carbono. (Anexo I)

5.1.1 El aerosol marino

La atmósfera marina se caracteriza por la presencia en ella del aerosol marino. La salinidad atmosférica es un parámetro relacionado con la cantidad de aerosol marino presente en la atmósfera en un momento dado. El aerosol marino se genera debido a la turbulencia que produce la rotura de las olas, formándose burbujas de aire en el agua que colapsan a medida que éstas alcanzan la superficie del mar (alrededor de 300.000 burbujas/$m^2 \cdot s$ pueden romper en la superficie del agua de mar en una ola [70]). Parte de la energía libre superficial de la burbuja se convierte en energía cinética proyectando a la atmósfera un chorro de agua a alta velocidad desde el fondo de las cavidades de las burbujas. Este chorro de agua proyectado, inestable, da lugar a gotas proyectadas (“jet drops”), y gotas peliculares (“film drops”). Finalmente, el agua de las gotas se evapora dejando partículas salinas sólidas a disposición del viento.

Las partículas más gruesas del aerosol marino (diámetro > 10 μm) permanecen durante escaso tiempo en la atmósfera; conforme mayor es su tamaño más corto es su tiempo de permanencia. Ambler y Bain demostraron experimentalmente, hace ya tiempo, que se produce un rápido descenso de la contaminación por cloruros de la atmósfera al pasar de estaciones situadas en la misma línea de la costa, donde rompen las olas, a tierra adentro [3]. Por el contrario, las partículas de diámetro inferior a 10 μm pueden viajar considerables distancias en el aire sin sedimentar [3, 71]. Por ello, el carácter fuertemente marino de la atmósfera se pierde en el interior a unos cuantos cientos de metros de la costa.

En ocasiones se registran valores anormales de salinidad, excesivamente altos, debido a fuertes tormentas que a pesar de su corta duración (unas pocas horas) depositan grandes cantidades de sal, mayores incluso que las depositadas durante todo un mes en un régimen de vientos normal en la zona.

5.1.1.1 Producción del aerosol marino

El viento, agitando el mar y transportando el aerosol marino, es la fuerza responsable de la salinidad presente en las atmósferas marinas. En el mar lejano, la rotura de las olas depende de la velocidad del viento soplando sobre él, en cambio, en las zonas surf costeras, las olas pueden romper sin la necesidad de una acción simultánea del viento.

Los niveles de aerosol en la línea de la costa comprenden el aerosol generado en el mar, que es transportado hacia la costa por los vientos marinos, y el que es generado en la zona surf próxima a la línea de costa [72-74]. Este último es el que más contribuye a los niveles de salinidad presentes en las capas más bajas de la atmósfera en las zonas costeras [73, 75].

Las olas se producen por la transferencia de energía del viento al mar. Esas olas, cuya rotura conduce a la formación del aerosol marino, se originan en las denominadas “zonas de generación” que están generalmente asociadas a fuertes vientos o tormentas locales [76, 77]. La altura de las olas depende de diversos factores: velocidad del viento, tamaño de la zona de generación, tiempo en que el viento está soplando (persistencia del viento) y estado inicial del mar. Por lo tanto, las olas producidas en el mar lejano por una tormenta pueden aparecer a miles de kilómetros de la zona de generación en donde no sopla el viento. Finalmente, cuando alcanzan la costa las olas son inestables y rompen. En las zonas surf costeras las olas son producidas por el surf, aún en ausencia de viento, y la cantidad del aerosol generado depende del tipo de fondo marino (uniformidad, pendiente, etc.) y de la amplitud de la zona surf [78, 79].

En nuestro estudio [80], a pesar de tener una notable dispersión en los datos obtenidos, se observa una clara relación entra la salinidad atmosférica y la altura espectral media de las olas (Figura 31). Como se observa de la Figura 31, una altura espectral media de 1,5-2,0 m puede ser ya suficiente para promover altos valores medios de salinidad (100-200 mg Cl^-/m^2·día).

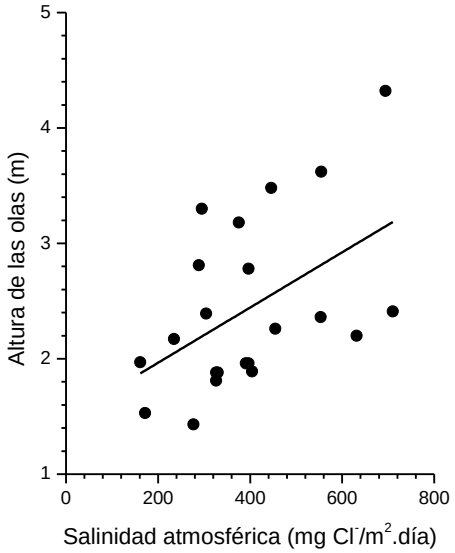

Figura 31. Variación de la salinidad media mensual con la media mensual de la altura espectral de las olas. La línea muestra la tendencia general. Datos de salinidad obtenidos en la estación 2 (Viravento) durante el periodo abril 2010 – febrero 2012. Las alturas espectrales de las olas fueron suministradas por la boya de Villano- Sisargas de Puertos del Estado.

5.1.1.2 Arrastre del aerosol marino

Las partículas que constituyen el aerosol marino son arrastradas hacia el interior por los vientos marinos, sedimentándose después de viajar una cierta distancia. El régimen de vientos de la zona influye enormemente en su transporte [81, 82]. Una reducción en el tamaño y masa de las partículas de aerosol, promovido, por ejemplo, por su secado, aumenta considerablemente la distancia de arrastre. El conocer la influencia del régimen de vientos en la zona en la magnitud de la salinidad atmosférica es, por tanto, un asunto de enorme interés.

En principio sería razonable pensar que los vientos marinos (vientos procedentes del mar), en función de su velocidad, dirección y duración, fueran los que gobernasen la presencia de las masas de aerosol marino en las regiones costeras. En este sentido, es importante conocer cómo varía la salinidad atmosférica en una determinada zona costera con el recorrido de los vientos marinos, es decir, con el sumatorio de la velocidad de cada viento marino multiplicado por su persistencia o tiempo en el que el viento está soplando en una determinada dirección. La figura 32, obtenida en nuestro estudio, explica claramente cómo el aumento en el recorrido de los vientos marinos influye enormemente en los valores de salinidad encontrados. Se observó, asimismo, que la dirección NE del viento en esa zona era la que promovía mayor aporte salino [80].

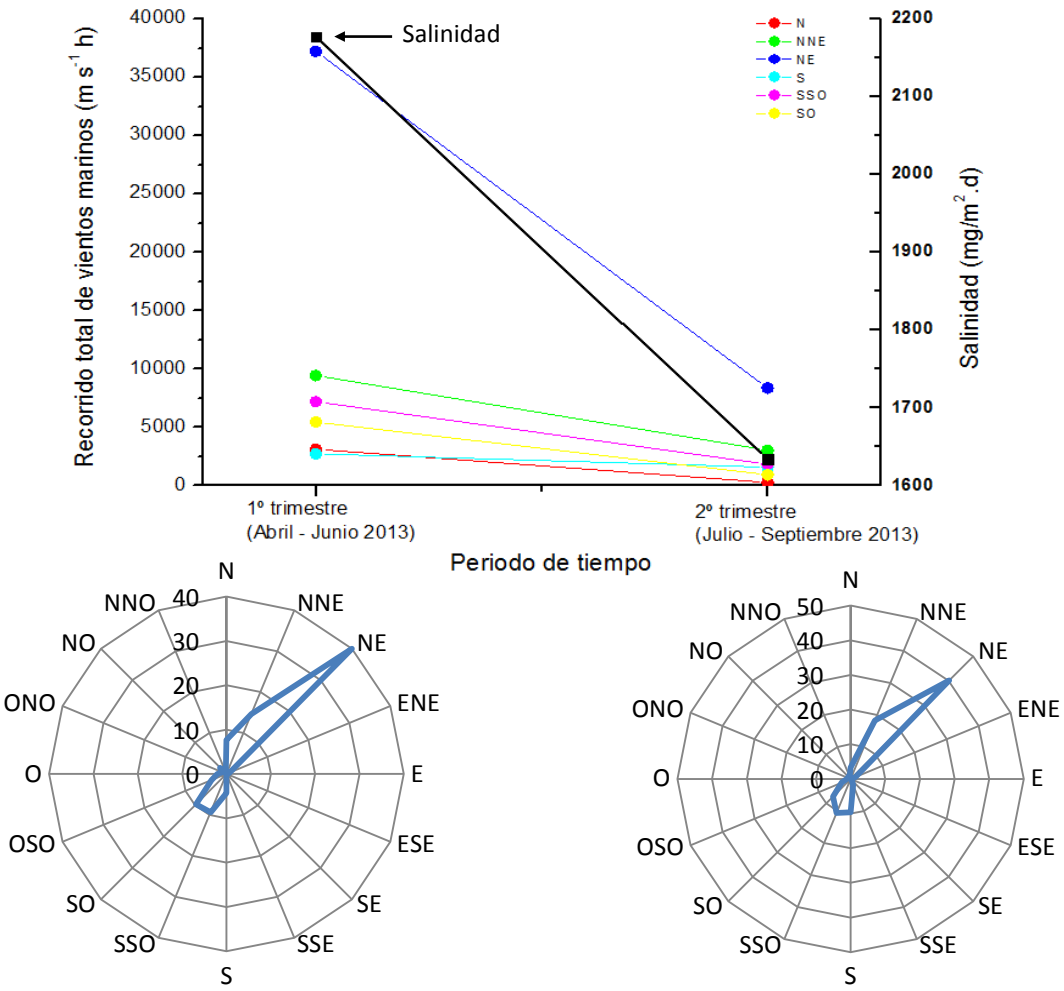

Figura 32. Influencia del recorrido de los vientos marinos en la salinidad atmosférica. Se muestran asimismo las rosas de viento en los dos períodos de tiempo considerados. Datos de salinidad obtenidos en la estación 2 (Viravento). La información sobre vientos fue suministrada por la estación "Cabo Vilan" de AEMET, muy próxima a la estación 2.

La salinidad atmosférica dependerá, por tanto, de la ubicación del sitio de exposición con relación al mar y de la dirección y tipos de vientos que soplan en ese lugar en un momento determinado. No obstante, hay que tener presente que un aumento en la velocidad general del viento, incluso en la misma zona costera, no siempre va a promover un incremento en la salinidad. Podría suceder que un aumento en la velocidad del viento no procedente del mar (viento no marino), llegase incluso a reducir el nivel de salinidad de la atmósfera eliminando (limpiando) de ella el aerosol marino.

Por lo general, la salinidad atmosférica adquiere valores importantes hasta unos pocos cientos de metros de la línea de costa, disminuyendo abruptamente conforme avanzamos hacia el interior [3]. Este decrecimiento en la concentración de partículas de aerosol marino se debe principalmente a procesos de depósito seco. Esencialmente, dos mecanismos son los

responsables de este depósito seco: (a) la sedimentación debido al efecto de la gravedad, y (b) la remoción por el contacto de las masas turbulentas de aire con la tierra. Este último efecto depende de la rugosidad y el tipo de terreno (terreno abierto, presencia de vegetación, etc.). Por lo tanto, la posibilidad de que las partículas de aerosol alcancen puntos más o menos cercanos a la línea de costa, dependerá del balance entre el arrastre hacia el interior por la acción de los vientos marinos y el depósito sobre el terreno por los mecanismos comentados anteriormente [83].

La variación de la salinidad atmosférica con la distancia a la costa suele mostrar un decaimiento exponencial [72, 84]. La figura 33, obtenida con los resultados de nuestro estudio, lo confirma.

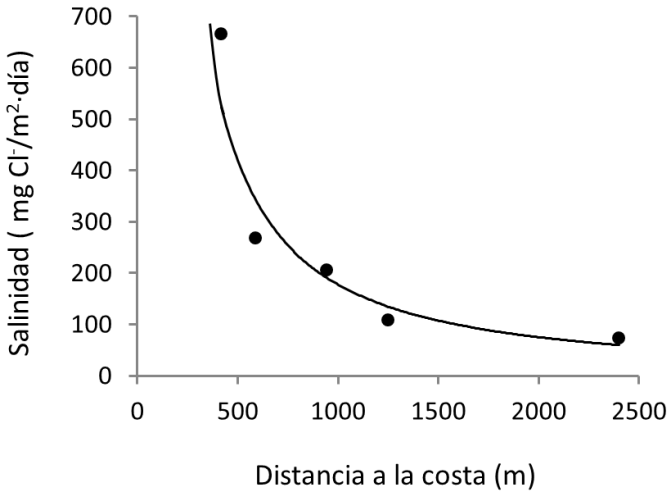

Figura 33. Variación de la salinidad atmosférica con la distancia a la costa. Datos correspondientes al periodo abril 2013 a abril 2014.

La orografía y topografía del terreno pueden jugar también un papel importante en la magnitud de la salinidad atmosférica resultante en un determinado lugar. Este es el caso ocurrido en nuestro estudio [69], donde una estación de ensayo más cercana a la línea de costa (270 m) registraba menor salinidad atmosférica que otra estación algo más alejada de la costa (332 m) (Figura 34). En la figura 35, donde se exponen las vistas al mar en la dirección N desde ambas estaciones, se observa en la estación más cercana a la línea de costa que la presencia de una pequeña colina, en cuya cima está situado el faro de Cabo Vilano, impide parcialmente la llegada del aerosol marino (Figura 35(a)), lo que no ocurre en la estación más lejana a la línea de costa, pero libremente expuesta al aerosol marino (Figura 35(b)).

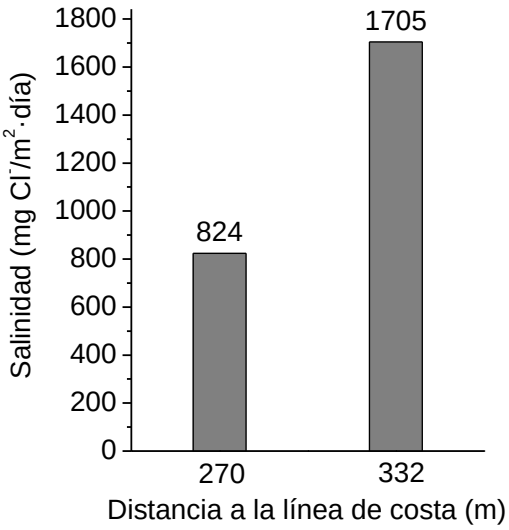

Figura 34. Valores medios de salinidad durante el periodo abril-septiembre 2013 en dos estaciones de ensayo próximas a la costa.

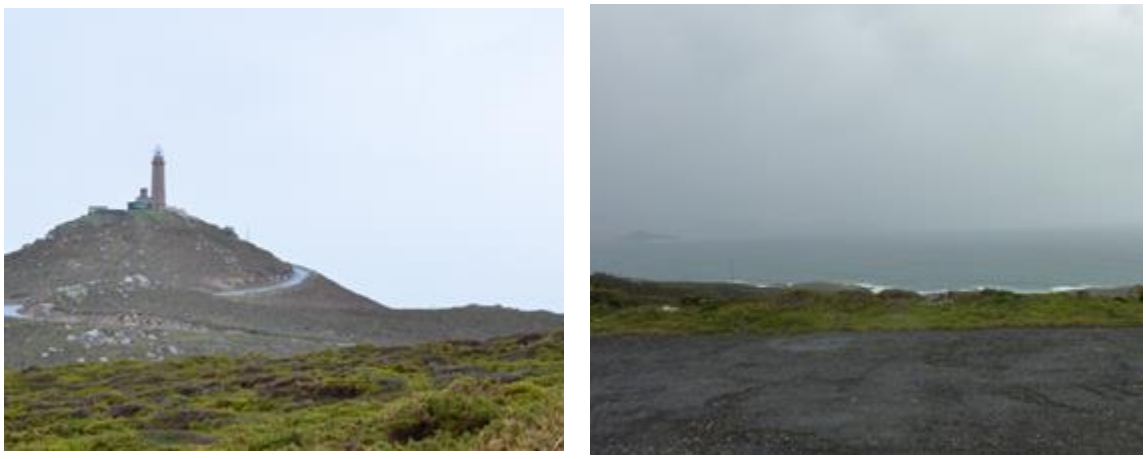

(a) (b)

Figura 35. Vistas del mar en la dirección N desde las dos estaciones referidas en la Figura 3, (a) desde la estación 1 y (b) desde la estación 2.

5.1.1.3 Efecto de la salinidad atmosférica en la corrosión del acero al carbono

El depósito de partículas salinas sobre la superficie metálica acelera su corrosión, sobre todo si, como en el caso de los cloruros, pueden dar lugar a productos de corrosión solubles (cloruros de hierro) en lugar de los escasamente solubles (hidróxidos de hierro) que se forman en agua pura. Los cloruros marinos disueltos en la capa acuosa formada sobre el metal elevan considerablemente la conductividad del electrolito y favorecen los procesos de corrosión.

Obviamente, para que la sal acelere la corrosión es necesario que la superficie metálica esté humedecida.

La figura 36 muestra la variación de la corrosión del acero al carbono con la salinidad atmosférica en un amplio espectro de velocidades de depósito de ion cloruro. La gráfica ha sido obtenida después de realizar una exhaustiva recopilación de información bibliográfica [80]. A pesar de existir una notable dispersión en los datos, la figura 36 ofrece una visión importante de la relación existente entre ambas variables. Para salinidades atmosféricas inferiores a 600 mg Cl^-/m^2·día se observa una tendencia hacia una relación de tipo lineal, donde la corrosión del acero aumenta considerablemente con la salinidad atmosférica. Este hecho se confirma con los datos obtenidos en nuestro estudio para salinidades hasta 300 mg Cl^-/m^2·día (raya continua en la Figura 37).

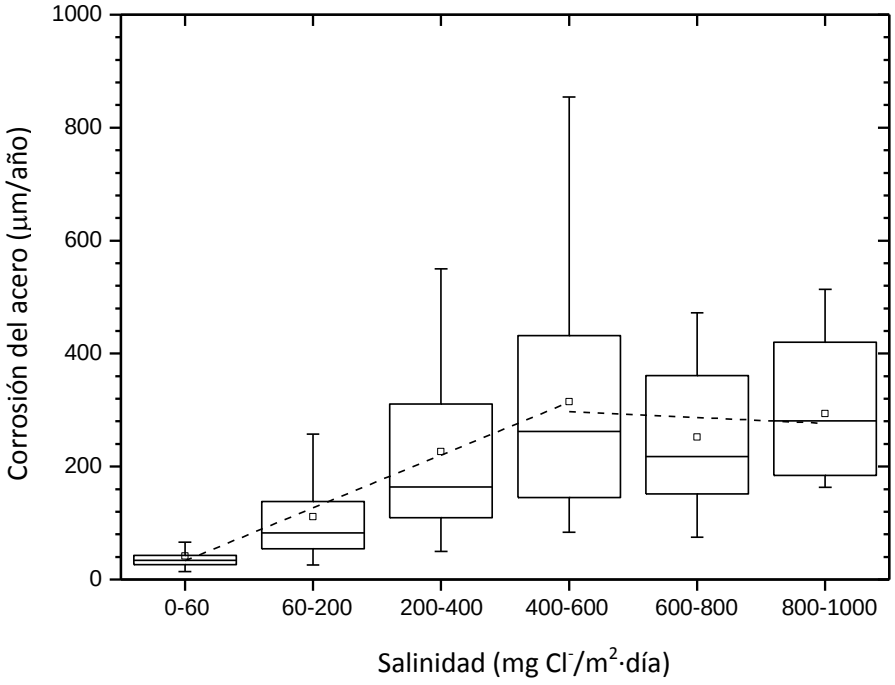

Figura 36. Variación de la velocidad de corrosión del acero al carbono con la salinidad en un amplio espectro de salinidades atmosféricas [80].

En la Figura 36 se observa que para salinidades superiores a ese nivel (600 mg Cl^-/m^2·día), la velocidad de corrosión del acero al carbono parece estabilizarse, sin embargo, son muy escasos los datos disponibles en la literatura para salinidades superiores a 600 mg Cl^-/m^2·día para realizar esa conjetura. En nuestro estudio, por el contrario, para salinidades superiores a 600 mg Cl^-/m^2·día (raya discontinua en la Figura 37) podemos observar que la corrosión del acero se acelera enormemente al pasar de una salinidad de 300 mg Cl^-/m^2·día a otra del orden

de 1000 mg Cl^-/m^2·día, para posteriormente disminuir ligeramente para una salinidad elevadísima, del orden de 2000 mg Cl^-/m^2·día.

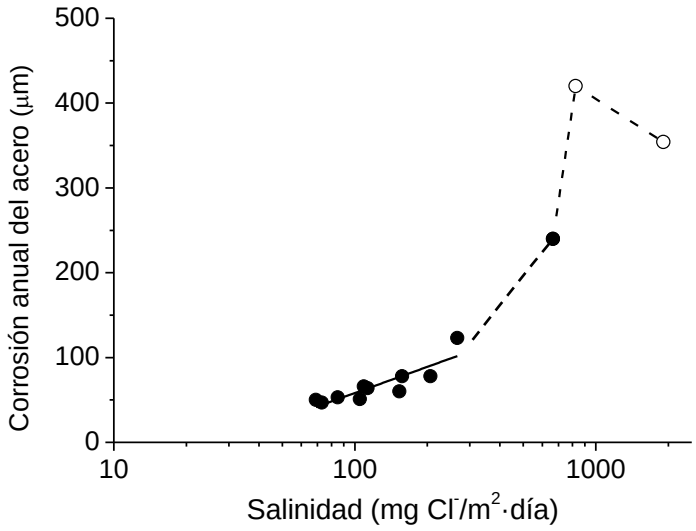

Figura 37. Variación de la corrosión anual del acero al carbono con la salinidad atmosférica.

Esta disminución no es un hecho aislado, Espada et al. [85] también lo observan en el laboratorio con nieblas salinas procedentes de soluciones con muy altas concentraciones de NaCl. Según Riley y Chester [70], la explicación de este hecho podría residir en la menor solubilidad del oxígeno, elemento fundamental para el desarrollo del proceso catódico de corrosión metálica, en la capa acuosa existente sobre la superficie metálica, muy concentrada en NaCl. El descenso de la solubilidad de oxígeno disuelto en agua como consecuencia del incremento de la salinidad, se debería a la débil interacción entre la molécula de agua y la de oxígeno. La molécula de agua, al ser un dipolo permanente, induce un dipolo en la molécula de oxígeno, lo que permite su disolución. Sin embargo, cuando en el agua se encuentran disueltos compuestos inorgánicos salinos, como el NaCl, éstos se disocian completamente en sus iones, solvatándose o rodeándose de moléculas de agua mediante interacciones ion-dipolo permanente, de mayor fortaleza que la interacción dipolo-dipolo inducido en la molécula de oxígeno por el agua. Por tanto, el aumento de la concentración salina en el agua disminuiría o debilitaría la interacción de las moléculas de oxígeno con el agua, disminuyendo la solubilidad del oxígeno.

Sería importante, no obstante, disponer de mayor información en este tipo de atmósferas costeras, con altísimas velocidades de depósito de cloruros, con el fin de confirmar rigurosamente esta hipótesis.

5.1.1.4 Variación de la corrosión del acero con la distancia a la costa

La influencia de la distancia a la costa en la corrosión atmosférica es uno de los aspectos más importantes de la corrosión del acero en áreas costeras. Empíricamente, es conocido que el efecto de la atmósfera marina se extiende principalmente a unos cuantos cientos de metros de la línea de costa y decae rápidamente conforme nos adentramos en el interior. Ambler y Bain en Nigeria fueron los primeros en observar este efecto [3].

En la mayoría de las zonas costeras, para las áreas más cercanas a la línea de costa (~ 400-600 m), el decrecimiento de la velocidad de corrosión del acero con la distancia a la costa se representa bastante bien mediante una simple relación exponencial [72]:

$$C = Co \exp(-Bx) + A \quad (8)$$

donde C es la velocidad de corrosión, Co es una constante (que coincide prácticamente con el valor de la velocidad de corrosión en la línea de costa cuando Co >> A), B es otra constante, x es la distancia a la línea de costa y A es la velocidad de corrosión del acero en ausencia de salinidad.

Como muestra la Figura 38, elaborada con los datos obtenidos en nuestro estudio, se confirma el decrecimiento exponencial de la corrosión del acero con el aumento de la distancia a la costa.

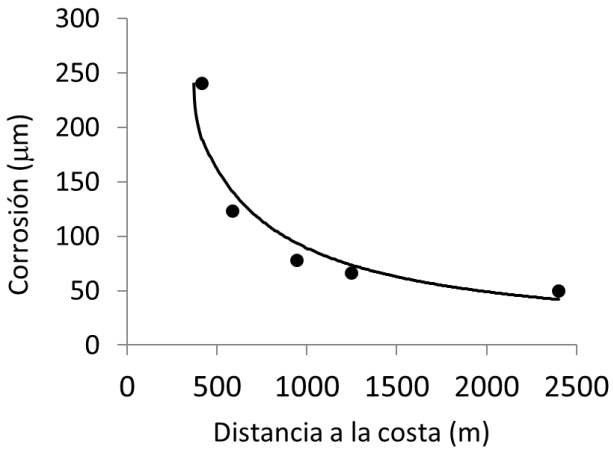

Figura 38. Variación de la corrosión anual del acero suave con la distancia a la costa. Datos correspondientes al periodo abril 2013 a abril 2014.

5.2 Los productos de corrosión formados sobre el acero al carbono expuesto a atmósferas marinas: naturaleza, morfología, localización en la capa de herrumbre, etc. (Anexos II y III)

5.2.1 Formación de los productos de corrosión

Los productos de la corrosión atmosférica del hierro, referidos comúnmente como herrumbre, comprenden diversos tipos de óxidos, hidróxidos, oxihidróxidos y otras sustancias cristalinas o amorfas que se forman como resultado de la interacción del hierro con la atmósfera. En la Tabla 23 se ofrece un listado de algunos de estos productos de corrosión, según Cornell y Schwertmann [23].

Tabla 23. Productos de corrosión atmosférica del hierro, según Cornell y Schwertmann [23].

Tipo	Denominación	Fórmula
Óxidos	Magnetita	Fe_3O_4
	Maghemita	γ-Fe_2O_3
	Hematita	α-Fe_2O_3
Hidróxidos	-	$Fe(OH)_2$
	Bernalita	$Fe(OH)_3$
	Herrumbres verdes	$Fe_x^{III}Fe_y^{II}(OH)_{3x+2y-z}(A^-)_z$ donde $A^- = Cl^-$, $½SO_4^{2-}$
	Ferrihidrita	$Fe_5O_8H.H_2O$
Oxihidróxidos	Goetita	α-FeOOH
	Lepidocrocita	γ-FeOOH
	Akaganeita	β-FeOOH
	Feroxihita	δ'-FeOOH
	Schwertmannita	$Fe_{16}O_{16}(OH)_y(SO_4)_2.nH_2O$

La composición de la herrumbre depende de las características de la capa de electrolito depositada sobre la superficie del acero como consecuencia de su exposición a la atmósfera (agua de lluvia, humedad condensada, cloruros disueltos, etc.) y por tanto varía según el tipo de ambiente. Las condiciones de la reacción en los procesos de humectación/secado, (acidez, temperatura, naturaleza de los aniones, etc.) tienen una fuerte influencia en los cambios de naturaleza estructurales y morfológicos de los productos de corrosión formados durante el proceso de corrosión.

La Figura 39 muestra una representación esquemática de la formación de los productos de corrosión sobre la superficie del hierro expuesta a la atmósfera [86]. Como consecuencia del proceso electroquímico de corrosión se forman inicialmente cationes ferrosos (Fe^{2+}) que están coordinados por seis moléculas de agua $[Fe(H_2O)_6]^{2+}$. En una solución neutra los cationes

metálicos reaccionan con OH^-, O_2 y H_2O para dar lugar a hidroxicationes, tales como $[Fe(OH)_x(H_2O)_{6-x}]^{(3-x)+}$. Su polimerización conduce a la formación de finas partículas de óxidos, hidróxidos y oxihidróxidos, que posteriormente crecen formando granos o capas durante un largo período de envejecimiento y repetición de ciclos de humectación/secado.

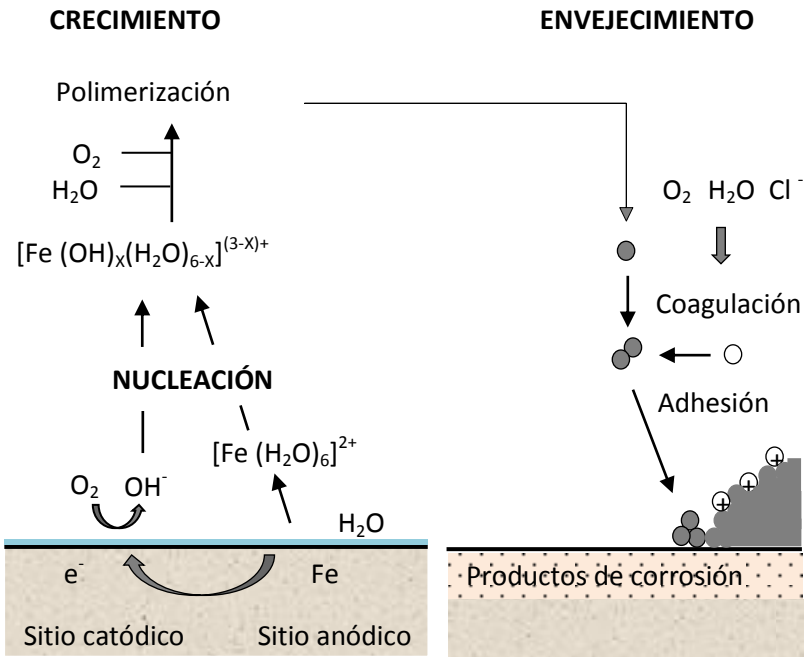

Figura 39.Esquema general de formación de los productos de corrosión atmosférica del hierro [86].

Como se observa en la Figura 39, el proceso de formación de las partículas sólidas de herrumbre puede ser visualizado en tres etapas: nucleación, crecimiento y envejecimiento [87]. La nucleación corresponde a la primera etapa precursora de la condensación y formación del sólido. Durante la segunda etapa (crecimiento) las unidades catiónicas o núcleos de pequeño tamaño condensan formando, básicamente por difusión, partículas de mayor tamaño. Los procesos de coagulación y adhesión durante el envejecimiento generan productos de corrosión que conducen finalmente a la estabilidad del sistema. Durante la etapa de envejecimiento pueden ocurrir fenómenos tales como: aumento del tamaño de partícula, cambios de morfología, etc. [88].

Como se ha comentado en el apartado 3.5.3.2, las morfologías que presenta la herrumbre pueden clasificarse del siguiente modo: herrumbre en forma de granos o partículas (G), aglomerados de granos (A), escamas de herrumbre (F) y herrumbre multicapa (ML), Figura 6. En la herrumbre en forma de granos se aíslan partículas de herrumbre (polvo de herrumbre), mientras que los aglomerados de herrumbre son de mayor tamaño y consisten en una

aglomeración de partículas. Las escamas de herrumbre y herrumbre multicapa son fragmentos de la capa de herrumbre y presentan una mayor superficie y compacidad que las anteriores. La herrumbre multicapa presenta estratificación, con la existencia de distintas subcapas de herrumbre en su interior que más adelante comentaremos.

De acuerdo con Ishikawa et al. [89] la herrumbre puede considerarse como un aglomerado de nanopartículas coloidales de oxihidróxidos férricos (α-, β-, γ-), espinelas (Fe_3O_4/γ-Fe_2O_3) y óxidos de hierro amorfos. Entre las partículas se encuentran huecos (vacíos) de diferentes tamaños.

La textura de las herrumbres varía con la agresividad de la atmósfera donde se ha expuesto el acero. Por lo general, las herrumbres con morfología más grosera se forman en las atmósferas más agresivas (atmósferas industriales y marinas), en tanto que las atmósferas menos agresivas (atmósferas rurales y urbanas) dan lugar a herrumbres con granulometría más fina [90].

En las atmósferas marinas la granulometría de la herrumbre es gruesa, aumentando su tamaño con el tiempo de exposición (Figura 40) [80]. Cuando la salinidad atmosférica es muy elevada, por ejemplo 665 mg Cl^-/m^2·día), la morfología de la herrumbre formada es del tipo “escama” o “multicapa”

Tiempo de exposición	Salinidad media anual (mg Cl^-/m^2·día)				
	70	109	206	272	665
6 meses	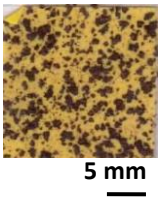	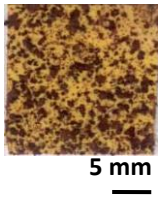	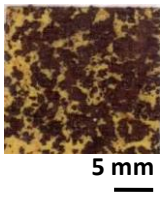	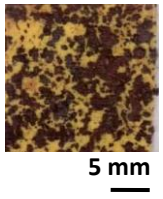	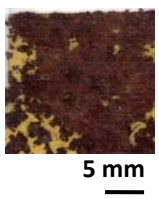
12 meses	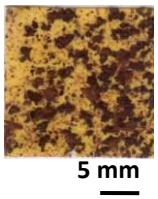	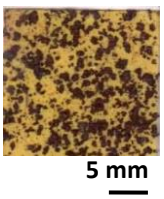	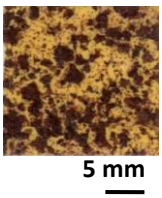	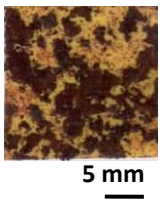	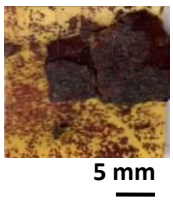

Figura 40. Granulometría de la herrumbre más externa formada sobre el acero al carbono expuesto durante 6 y 12 meses a atmósferas marinas de diferente agresividad.

Estas observaciones confirman los resultados obtenidos por Ishikawa et al [91] sobre el grado de compactación de las capas de herrumbre formadas en distintos tipos de atmósferas. Las herrumbres son aglomerados de finas partículas y cuando se forman en atmósferas marinas su

agregación es mayor que cuando la herrumbre se forma en atmósferas menos agresivas, como por ejemplo en una atmósfera rural. De acuerdo con estos investigadores el tamaño de las partículas de herrumbre influye enormemente en la resistencia a la corrosión atmosférica de los aceros.

5.2.2 Principales productos de corrosión del acero expuesto a atmósferas marinas.

Si bien en los primeros estadios del proceso de corrosión atmosférica los productos de corrosión pueden ser de naturaleza muy variada: hidróxidos, compuestos intermedios, etc., después de un cierto tiempo el sistema se estabiliza y el volumen de productos de corrosión está integrado principalmente por materia cristalina (lepidocrocita, goetita, akaganeita (atmósferas marinas), magnetita/maghemita) y materia amorfa.

5.2.2.1 Lepidocrocita (ɣ-FeOOH) y goetita (α-FeOOH)

Inicialmente se forma lepidocrocita:

$$Fe \xrightarrow{\text{disolución}} Fe^{+2} \xrightarrow{\text{hidrólisis}} FeOH^{+} \xrightarrow{\text{oxidación y precipitación}} \gamma\text{-FeOOH} \qquad (9)$$

Conforme aumenta el tiempo de exposición del acero en la atmósfera, la lepidocrocita se va transformando parcialmente en goetita y magnetita. Según Misawa et al. [22] la transformación discurre vía la formación de un oxihidróxido férrico amorfo, $FeO_x(OH)_{3-2X}$, que se transforma posteriormente en goetita por desprotonación con la ayuda de los iones oxidrilo que suministra el agua de lluvia:

$$\gamma\text{-FeOOH} \xrightarrow{\text{disolución y precipitación}} FeO_x(OH)_{3-2X} \xrightarrow{\text{transformación en estado sólido}} \alpha\text{-FeOOH} \qquad (10)$$

En este momento ya es posible por microscopía óptica mediante luz polarizada, (Figura 41), distinguir en la capa de herrumbre la zona más activa (exterior y anaranjada), integrada principalmente por lepidocrocita, de la zona menos activa (interior y grisácea) de goetita [92].

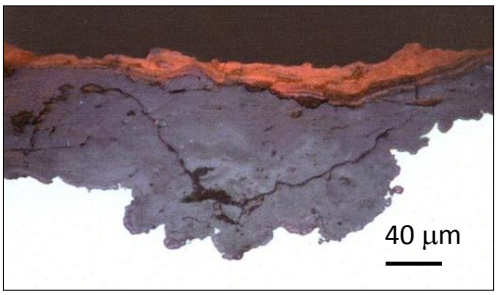

Figura 41. Micrografía típica obtenida por microscopía óptica con luz polarizada de la sección transversal de una capa de herrumbre. Se observa su estructura dual.

Después de un cierto tiempo se consolida esta estructura dual de la capa de herrumbre, integrada por una subcapa externa porosa de lepidocrocita y una subcapa interna más compacta de goetita, a la que la herrumbre debe su capacidad protectora.

5.2.2.2 Akaganeita (β-FeOOH)

Por su gran importancia en el proceso de corrosión atmosférica del acero al carbono en las atmósferas marinas, a esta fase de herrumbre le dedicaremos mayor extensión que a las restantes. Como se ha mencionado anteriormente, a diferencia de los otros oxihidróxidos, la akaganeita únicamente se forma en las atmósferas marinas, donde la capa acuosa depositada sobre el acero contiene iones cloruro.

Su estructura química se expone en la figura 42, consistente en una celda unitaria que contiene cuatro moléculas de FeOOH [23]. Su estructura cristalográfica es isoestructural con la hollandita ($BaMn_8O_{16}$), caracterizada por la presencia de túneles paralelos al eje C de la red.

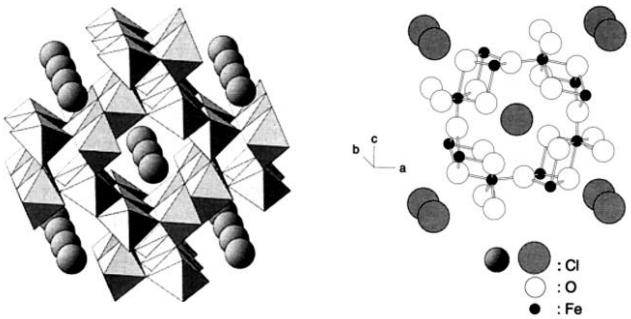

Figura 42. Estructura de la akaganeita, según distintos modelos de representación, formando túneles con iones cloruro en su interior [23].

Los túneles en la estructura de la akaganeita tienen un diámetro de 0,21 a 0,24 nm y están estabilizados por iones cloruro, en un rango de 2 a 7 moles por ciento. Una cantidad mínima de cloruros, de 0,25 a 0,50 mmoles/mol, parece esencial para estabilizar la estructura cristalina de la akaganeita [23]. Ha habido gran controversia sobre si los iones Cl^- están en los túneles o en

la propia estructura cristalina de la akaganeita [93]. Se ha asumido que los túneles están ocupados a temperatura ambiente por agua e iones cloruro, si bien un alto porcentaje de los iones Cl^- están sustituyendo a los iones OH^- en la estructura del oxihidróxido [94].

La morfología de los finos cristales de akaganeita debería en principio observarse fácilmente mediante SEM, sin embargo por lo general están fuertemente aglomerados, por lo que en ocasiones resulta difícil su observación [89].

La akaganeita puede localizarse en la zona más externa de la capa de herrumbre, pero generalmente es más frecuente encontrarla en la región más interna de ella. En nuestra investigación, a pesar de los esfuerzos realizados, solamente en una ocasión se pudo identificar mediante espectroscopía Raman un agregado de akaganeita en la región más externa de la capa de herrumbre (Figura 43(a-b)). Sin embargo, mediante microscopía electrónica de barrido de alta resolución y operando a altos aumentos se han logrado fácilmente detectar los agregados "tipo esponja" de akaganeita en la capa más interna de la herrumbre, constituidos por un entramado de finos cristales alargados con la morfología tipo varilla de este oxihidróxido (Figura 43(c-d)). Por SEM/µRaman [67, 80] y TEM/SAED [64] se realizó una caracterización analítica de esta fase.

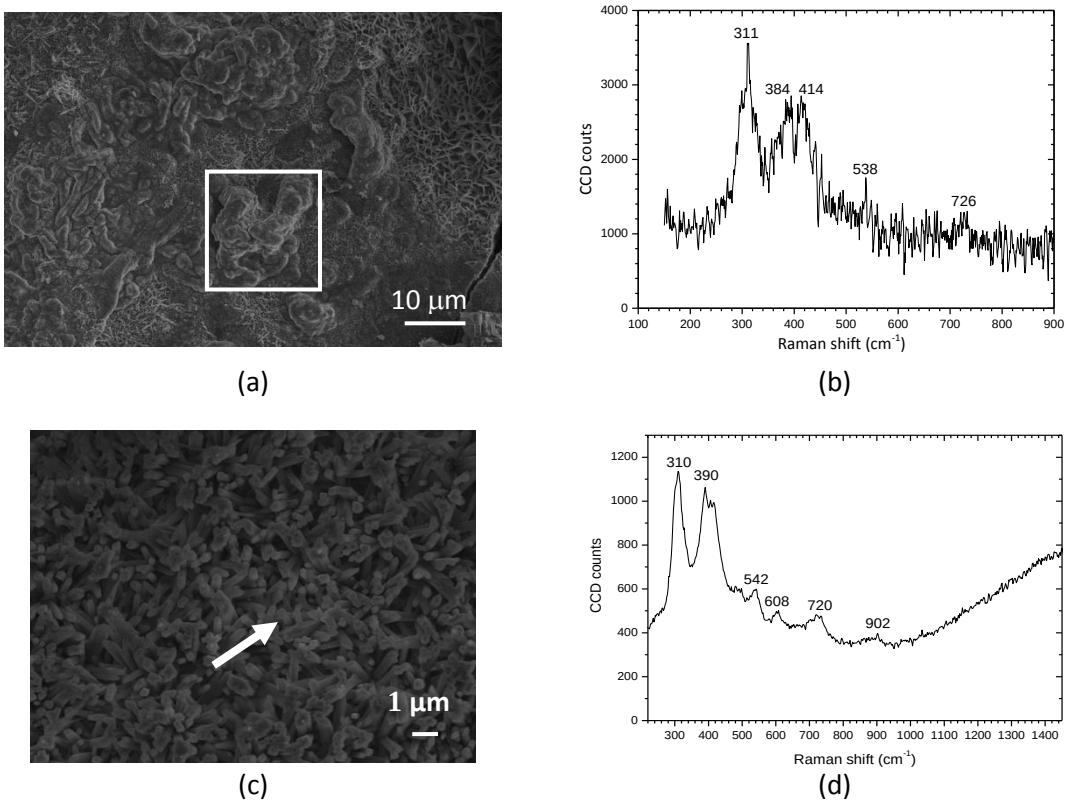

Figura 43. Formaciones de agregados de akaganeita en la región más externa de la capa de herrumbre (a, b) y en la región más interna (c, d). Caracterización analítica realizada mediante espectroscopía Raman.

La formación de la akaganeita está precedida por la acumulación de iones cloruro en la capa acuosa existente sobre el metal, dando lugar a la formación de cloruro ferroso ($FeCl_2$), que hidroliza el agua según la reacción [95]:

$$FeCl_2 + 2\ H_2O \rightarrow Fe\ (OH)_2 + 2\ HCl \qquad (11)$$

aumentando notablemente la acidez del electrolito. Los cationes requieren neutralización, lo que promueve la entrada de nuevos iones cloruro que aumentan su concentración [96].

A Refait et al. [97-101] se deben importantes estudios de laboratorio sobre los mecanismos de formación de la akaganeita. En la intecara acero/ productos de corrosión, donde los iones Cl^- se acumulan, altas concentraciones de cloruro y condiciones ácidas (hemos medido valores de pH entre 4 y 6) conducen a la formación de hidroxicloruro ferroso (β-$Fe_2(OH)_3Cl$), un proceso muy lento que requiere la transformación de precursores metaestables [97, 98]. Rémazeilles y Refait afirman que altas concentraciones de Fe^{2+} y Cl^- son necesarias para la formación de akaganeita [99]. El proceso de oxidación del hidroxicloruro ferroso que conduce a la formación de akaganeita pasa por diferentes etapas vía la formación de un compuesto intermedio de herrumbre verde ($Fe_3^{II}\ Fe^{III}\ (OH)_8Cl{\cdot}nH_2O$) que se suele representar como GR1 o GR(Cl^-) [97, 100, 101]:

$$2\ Fe_2(OH)_3Cl + 2\ H_2O \rightarrow Fe_4(OH)_8Cl + e^- + 2\ H^+ + 2Cl^- \qquad (12)$$

La alta concentración en cloruros de la solución transforma el GR(Cl) en un compuesto sobreclorado GR(Cl)*. Finalmente, el proceso de oxidación de ese compuesto lleva a la formación de akaganeita.

En síntesis, el proceso total de oxidación que conduce a la formación de akaganeita puede resumirse del siguiente modo [97-101]:

$$FeCl_2 \rightarrow \beta\text{-}Fe_2(OH)_3Cl \rightarrow GR1(Cl) \rightarrow GR(Cl^*) \rightarrow \beta\text{-}FeOOH \qquad (13)$$

Es pues un proceso relativamente lento. El tiempo dependerá de las condiciones ambientales: temperatura, concentración de Cl^- y OH^-, flujo de oxígeno, etc. [97-101].

En la literatura científica diversas investigaciones han apuntado la hipótesis de que pudiese existir una concentración crítica de iones cloruro en la atmósfera para que pudiera formarse akaganeita entre los productos de corrosión [102, 103]. Nuestra investigación [64] ha suministrado información sobre las condiciones ambientales de la atmósfera que conducen a la formación de akaganeita: una HR media anual $\geq$ 80%, y simultáneamente una velocidad

media anual de depósito de ion cloruro ≥ 60 mg Cl^-/m^2·día (Figura 44). A partir de un estudio bibliográfico exhaustivo [64] hemos encontrado que, por ejemplo, en la atmósfera marina de Hakhal (Arabia Saudita) (Tabla 24) las bajas HR impiden la formación de akaganeita a pesar de existir muy altas velocidades de depósito de cloruros. Altas humedades relativas pero con relativamente bajas velocidades de depósito (Estación 11, 2400 m de la costa) tampoco dan lugar a la formación de akaganeita. En cambio, a menor distancia a la costa (Estación 2, 332 m) ya se dan las condiciones en cuanto a HR y velocidad de depósito para que tenga lugar la formación de akaganeita.

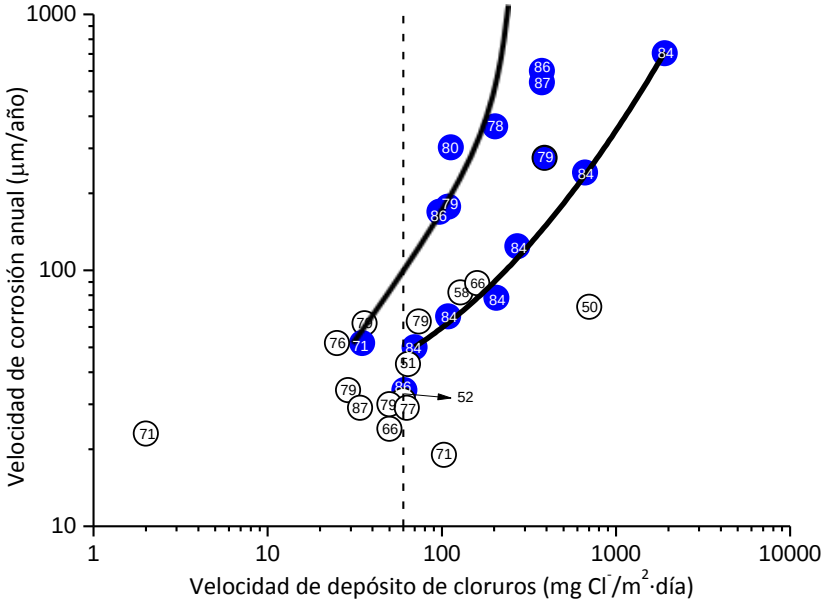

Figura 44. Condiciones ambientales de la atmósfera marina necesarias para la formación de akaganeita. Velocidad de corrosión del acero al carbono durante el primer año de exposición en función del depósito de cloruros de la atmósfera. Los puntos de la gráfica, representados por círculos, incluyen la HR media anual del punto de experimentación. Los círculos azules representan las condiciones donde se identifica por XRD akaganeita, y los puntos en blanco donde no se puede identificar [64].

Tabla 24. Resultados de corrosión del acero al carbono en diferentes estaciones de ensayo situadas en atmósferas marinas indicando la identificación de akaganeita en la herrumbre formada [64].

Estación de ensayo (distancia a la costa)	HR, (%)	Cl^- (mg Cl^-/m^2·día)	Velocidad de corrosión del acero (1^{er} año) (µm/año)	Identificación por XRD de la akaganeita
Hakhal, Arabia Saudita	50	704	72	NO
Estación 11, (2400 m)	79	29	39	NO
Estación 2, (332 m)	79	390	> 550 (perforada)	SI

Estas condiciones críticas en cuanto a HR y salinidad atmosférica confirman los experimentos de laboratorio llevados a cabo por Rémazeilles y Refait [97-101] que indicaban que una alta concentración de cloruros no es suficiente para la formación de akaganeita, sino que el medio debe contener también un alto contenido en Fe^{2+}, lo que ocurre en las atmósferas marinas con altas HR y tiempos de humectación de la superficie metálica que favorecen la presencia de altos contenidos de Fe^{2+} en la capa acuosa.

En la Figura 44 se observa claramente la aceleración del proceso de corrosión del acero por la existencia de akaganeita entre los productos de corrosión.

5.2.2.3 Magnetita (Fe_3O_4)/Maghemita (γ-Fe_2O_3)

Estos dos óxidos de hierro se diferencian en su composición: la magnetita contiene iones Fe^{2+} y Fe^{3+}, en tanto que en la maghemita todos son iones trivalentes [23]. Ambos presentan una estructura con defectos no estequiométrica [104, 105].

Se trata de dos óxidos de hierro con una estructura cristalina cúbica del tipo espinela inversa, en la que los iones O^{2-} forman una red cubica centrada en las caras. A lo largo de esta discusión nos referiremos frecuentemente a las dos como fase espinela.

La magnetita se forma por oxidación del $Fe(OH)_2$ o especies ferroso-férricas tales como la herrumbre verde (GR) [106]. La magnetita también puede formarse por reducción de la lepidocrocita en presencia de una baja concentración de oxígeno [107-109]:

$$2\ \gamma\text{-FeOOH} + Fe^{2+} \rightarrow Fe_3O_4 + 2\ H^+ \qquad (14)$$

Por ello no es de extrañar que la magnetita suela encontrarse en la zona interior de la capa de herrumbre, muy próxima al acero subyacente, donde la concentración de oxígeno está muy limitada.

De acuerdo con Evans [110, 111] y Stratmann [112, 113] la formación de magnetita puede representarse por la siguiente reacción catódica:

$$Fe^{2+} + 8\ FeOOH + 2\ e^- \rightarrow 3\ Fe_3O_4 + 4\ H_2O \qquad (15)$$

De un modo más general, Ishikawa et al. [108] y Tanaka et al. [109] establecen que la formación de las partículas de magnetita ocurre por la reacción de las especies férricas procedentes de la disolución de los oxihidróxidos (-FeOOH) con las especies ferrosas en solución de acuerdo con la ecuación anterior.

La formación de maghemita puede tener lugar por oxidación de la magnetita en estado sólido [23]. Cuando en la espinela las posiciones octaédricas de los iones Fe^{2+} se quedan vacantes como consecuencia de la oxidación de la magnetita, se obtiene un mineral conocido como maghemita (γ-Fe_2O_3):

$$4\ Fe_3O_4 + O_2 \rightarrow 6\ Fe_2O_3 \qquad (16)$$

En las atmósferas marinas con altas velocidades de depósito de cloruros, puntos cercanos a la línea de costa o en carreteras, puentes, etc. donde se utilizan productos de deshielo de la nieve depositada, es frecuente que la herrumbre formada sobre el acero presente altos contenidos de magnetita, superiores a los contenidos en lepidocrocita. Como apuntó Hiller [114], en estos ambientes los contenidos de la herrumbre en magnetita son superiores a los exhibidos por la herrumbre en atmósferas libres de cloruros. En la Figura 45, elaborada con los datos obtenidos en nuestro estudio [62], puede observarse como aumenta el contenido en espinela conforme aumenta la salinidad atmosférica, descendiendo simultáneamente el contenido en lepidocrocita [107](ec. 15). En la bibliografía se encuentran también referencias [115, 116] donde la magnetita puede llegar a ser en este tipo de ambientes la fase principal en la capa de productos de corrosión formada.

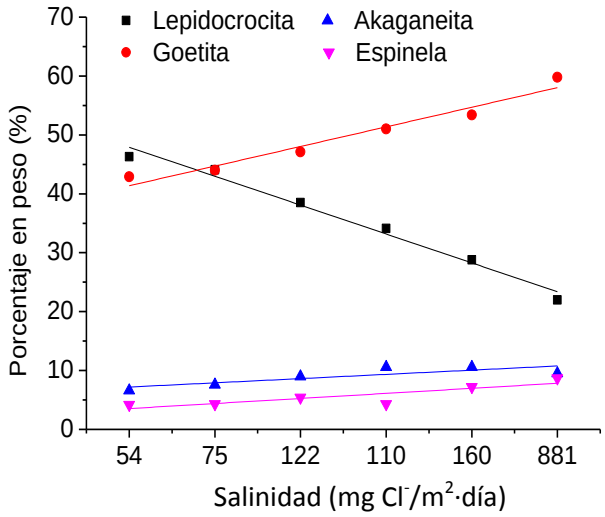

Figura 45. Variación del contenido en diferentes fases de la herrumbre formada en atmósferas marinas con diferentes niveles de salinidad. Tiempo de exposición: 3 meses.

5.3. La capa de herrumbre. El fenómeno de exfoliación de las capas de herrumbre formadas sobre el acero al carbono cuando se expone a atmósferas marinas con altas velocidades de depósito de cloruros. (Anexo IV)

5.3.1 La capa de herrumbre

Como hemos visto anteriormente, como consecuencia del proceso de corrosión atmosférica se forman inicialmente los primeros núcleos de herrumbre, que posteriormente van engrosando llegando a cubrir la superficie del metal. A estos precipitados se les denomina generalmente "productos de corrosión" [117].

Una vez que esta delgada capa de productos de corrosión cubre toda la superficie metálica, su posterior crecimiento requiere que las especies reactivas de la capa acuosa precipitada sean transportadas hacia el metal base, mientras los iones metálicos formados como consecuencia del proceso son transportados hacia el exterior. En capas delgadas o porosas el transporte iónico no está impedido y los productos de corrosión son de baja capacidad protectora. No así, en el caso de capas más gruesas y densas (compactas), de mayor resistencia a la corrosión, donde el transporte de los iones puede estar cada vez más restringido.

El transporte del oxígeno desde la atmósfera a las zonas catódicas de la superficie metálica tampoco suele ser el factor controlante, teniendo en cuenta la solubilidad de este gas en las delgadas películas de humedad condensada o precipitada sobre el metal. Ahora bien, si esta capa acuosa excede un determinado espesor (varias decenas de micrómetros), el transporte de oxígeno puede llegar a ser el factor controlante del proceso de corrosión atmosférica.

A lo largo de esta sección abordaremos distintas propiedades físicas y químicas de las capas de herrumbre. En un primer apartado consideraremos las propiedades organolépticas, su color y textura, para en un segundo apartado considerar aquellas otras propiedades más relacionadas con su capacidad protectora: estratificación, estabilización, espesor y porosidad.

5.3.2 Propiedades organolépticas

5.3.2.1 Apariencia (coloración)

El acero al carbono expuesto a la atmósfera desarrolla inicialmente una herrumbre de color ocre que evoluciona a una coloración marrón-oscura con el tiempo de exposición.

En los ambientes marinos la coloración de la herrumbre varía con la corrosividad de la atmósfera (función a su vez de la velocidad de depósito de cloruros), el tipo de acero, condiciones de exposición, etc. Así, en nuestro estudio [80], en las atmósferas más agresivas, de mayor salinidad, la herrumbre adquiere tonalidades más claras, en tanto que en las atmósferas menos agresivas, de menor salinidad, la herrumbre adquiere tonos más oscuros.

La coloración de la herrumbre torna a tonalidades más oscuras conforme avanza el tiempo de exposición (Figura 46). Se observan, asimismo, diferencias en la apariencia de la herrumbre en las dos caras de la probeta de ensayo: tonalidades más oscuras en la cara que mira al cielo y tonalidades más claras en la cara que mira al suelo [80].

Tiempo de exposición		
3 Meses	9 Meses	18 Meses
		

Figura 46. Variación de la coloración de la herrumbre conforme avanza el tiempo de exposición de una probeta de acero suave en la estación 7 durante 3, 9 y 18 meses de exposición (cara A, que mira al cielo); (Escala 1:2).

5.3.2.2 Textura (granulometría)

En el apartado 4.4.3.2 se hizo referencia a la granulometría de los productos de corrosión. En cierto modo esta propiedad está muy relacionada con la textura que muestra la superficie externa de la capa de herrumbre, propiedad que es captada a través del sentido del tacto. La suavidad, la aspereza y la rugosidad son sensaciones que trasmite la textura.

En trabajos anteriores del grupo de investigación [13, 118] en los que el acero al carbono se expuso durante 3 años en distintos tipos de atmósferas, se observaron diferencias en la textura de las capas de herrumbre formadas. Se observaron pátinas con texturas más lisas (aspecto más homogéneo y granulometrías más finas) en las atmósferas rural y urbana, mientras que en las atmósferas industrial y marina se observaron texturas más rugosas, con aspecto más heterogéneo y granulometrías más groseras (Figura 47), mayor conforme aumentaba el grado de corrosividad del ambiente y mayor era el tiempo de exposición.

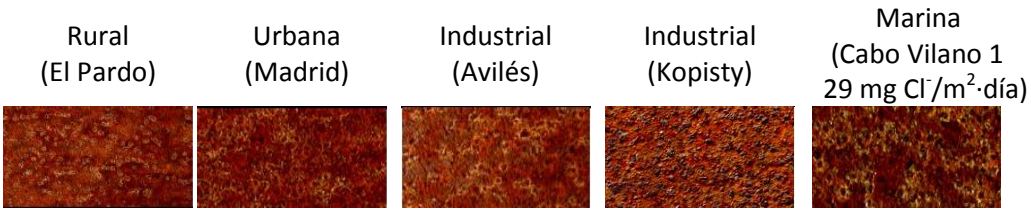

Figura 47. Coloración y textura de las pátinas formadas sobre el acero al carbono expuesto durante tres años en distintos tipos de atmósferas [13, 118].

5.3.3 Propiedades más relacionadas con la capacidad protectora de la capa de herrumbre.

5.3.3.1 Estratificación

Existe gran controversia acerca de la estratificación en diferentes subcapas de las capas de herrumbre formadas sobre el acero al carbono expuesto a la atmósfera, como ocurre en el caso de los aceros patinables [119]. Según estudios recientes de nuestro grupo de investigación [92] la capa de herrumbre está siempre estratificada, independientemente de la composición del acero, sea acero suave o acero aleado (patinable). En estos estudios se ha observado siempre la presencia de dos subcapas: una subcapa interna de color grisáceo y una subcapa externa de coloración marrón anaranjado (Figura 41). Así pues, la naturaleza dual de la capa de herrumbre no es una característica exclusiva de los aceros patinables, a la que según algunos investigadores estos aceros deben su mayor protección y resistencia a la corrosión atmosférica [120, 121], sino que el acero al carbono sin alear, con menor resistencia a la corrosión atmosférica, también genera una capa de herrumbre estratificada durante su exposición atmosférica. De acuerdo con Suzuki la capa externa es menos compacta pero está más cristalizada que la capa interna [122].

5.3.3.2 Estabilización

El desarrollo gradual de la capa de herrumbre toma varios años antes de alcanzar condiciones de estado estacionario en el que la velocidad de corrosión del acero es prácticamente constante. Se considera que se ha alcanzado el estado estacionario (tiempo de estabilización) cuando el decrecimiento de la velocidad de corrosión entre dos años sucesivos es inferior al 10% [123]. La velocidad de corrosión en estado estacionario es la correspondiente al año a partir del cual su decrecimiento es $\leq$ 10 % (Figura 48).

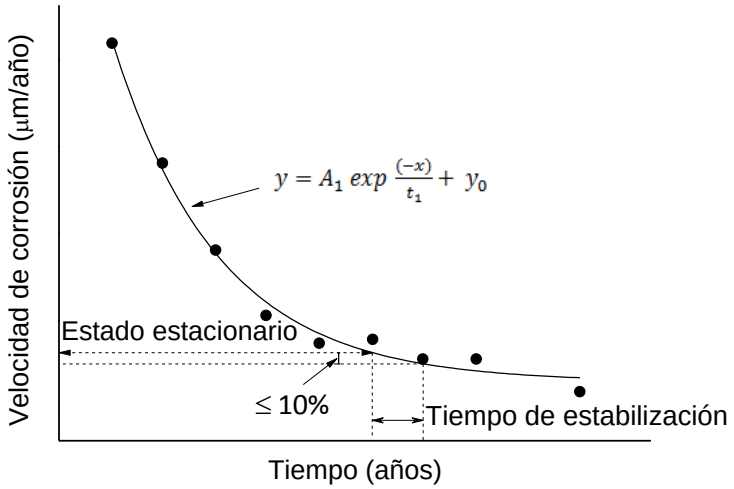

Figura 48. Esquema para la determinación del tiempo de estabilización y velocidad de corrosión en estado estacionario a partir de una función de decrecimiento exponencial obtenida con datos reales de velocidades de corrosión de un acero al carbono a distintos tiempos de exposición [123].

En estudios anteriores [80] se ha observado que el tiempo de estabilización depende fundamentalmente del grado de corrosividad de la atmósfera, es decir del volumen de productos de corrosión formados. En las atmósferas marinas, más corrosivas para el acero al carbono, la estabilización de la capa de herrumbre ocurre más rápidamente, debido a su gran corrosividad y gran volumen de los productos de corrosión formados, si bien su valor protector es inferior al de las capas de herrumbre formadas en atmósferas menos agresivas (rurales, urbanas, industriales) en donde los tiempos de estabilización de las capas son más elevados.

5.3.3.3 Porosidad

Las capas de herrumbre presentan abundante porosidad, así como grietas longitudinales y transversales [35]. La existencia de grietas permite a las especies del medio (H_2O, O_2, iones) penetrar hacia el interior de la capa de herrumbre y entrar en contacto con el sustrato de acero facilitando los procesos corrosivos. Por el contrario, las capas de herrumbre más densas (compactas) son más impenetrables y presentan características más protectoras.

Conforme avanza el tiempo de exposición, el número y tamaño de los defectos (poros, grietas, etc.) suele disminuir debido a procesos de compactación, aglomeración, etc., aumentando la capacidad protectora de las capas de herrumbre [35, 124]. Entre las partículas de herrumbre que integran la capa de productos de corrosión se forman vacíos de diferentes tamaños.

La compacidad de las capas depende del tamaño de las partículas de herrumbre. Las partículas más finas forman capas compactas y menos permeables, al contrario que las partículas más gruesas que dan lugar a capas más permeables y ofrecen al acero menor protección.

Como vimos anteriormente, las herrumbres son aglomerados de partículas. Las partículas de herrumbre están muy aglomeradas, especialmente las formadas en la atmósferas marinas. De este modo, las capas de herrumbre formadas en zonas costeras son aglomerados de gruesas partículas que conforman poros abiertos de gran tamaño [91]. Por el contrario, en atmósferas suaves las finas partículas de herrumbre dan lugar a capas de herrumbre más densas y compactas y con poros más cerrados (Figura 49) [125].

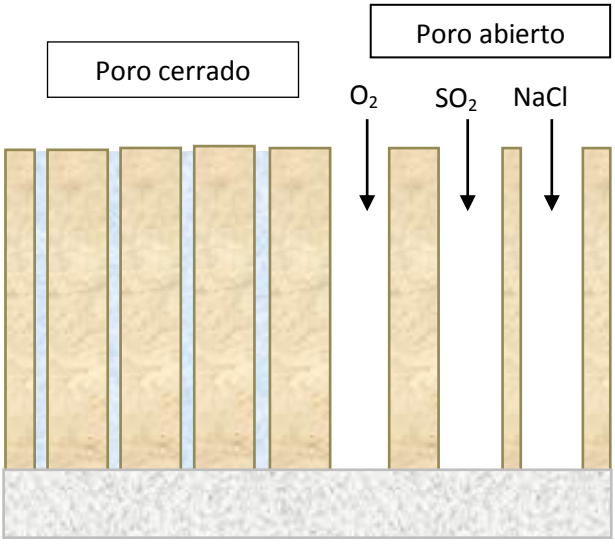

Figura 49. Representación esquemática de las posibilidades de colmatación (sellado) de los poros en las capas de herrumbre por la condensación de agua en su interior. Según Ishikawa et al. [125].

En la Figura 50 puede observarse la variación de la estructura interna de la capa de herrumbre conforme aumenta la velocidad de depósito de cloruros de la atmósfera marina. Mientras a relativamente bajas salinidades atmosféricas (44 y 110 mg Cl^-/m^2·día) las capas de herrumbre son relativamente compactas, a más altas salinidades atmosféricas (173 y 245 mg Cl^-/m^2·día) las capas de herrumbre presentan abundante agrietamiento. A salinidades todavía mayores (889 y 1136 mg Cl^-/m^2·día) las capas de herrumbre se desprenden (exfolian) dejando el acero base prácticamente desnudo. El acero base en esta situación presenta un notable picado, como puede verse en la figura [62].

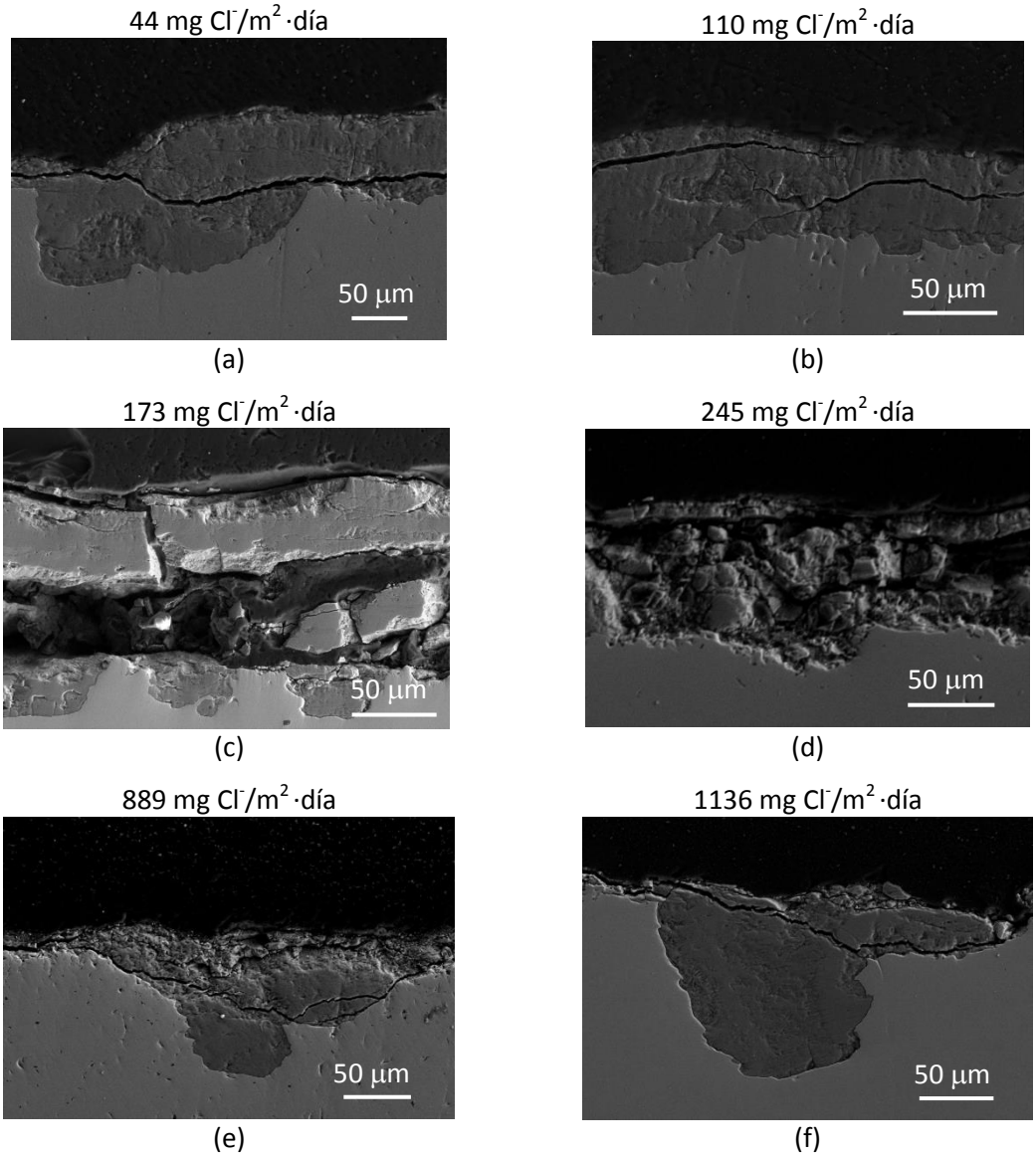

Figura 50. Variación de la estructura interna de la capa de herrumbre con la salinidad atmosférica. Las probetas de acero al carbono se expusieron durante tres meses en diferentes atmósferas marinas.

5.3.3.4 Espesor

El espesor de la capa de herrumbre crece con el tiempo de exposición del acero a la atmósfera. Alcanzado el tiempo de estabilización de la capa de herrumbre, es decir, unas condiciones de estado estacionario en las que la variación de la velocidad de corrosión con el tiempo permanece prácticamente constante, el espesor de la capa de herrumbre crece en menor entidad. El espesor de la capa de herrumbre es función de la agresividad de la atmósfera, encontrándose una relación lineal con la velocidad de corrosión (Figura 51) [118].

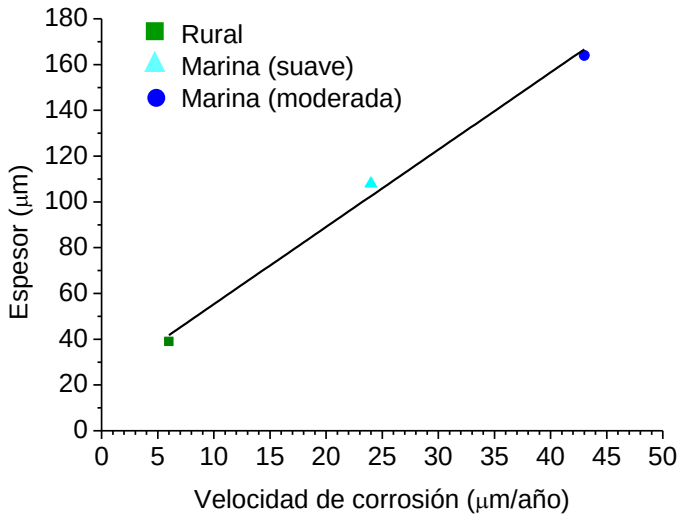

Figura 51. Espesor de la herrumbre vs velocidad de corrosión del acero al carbono expuesto durante dos años en atmósferas de diferentes agresividad [126].

Como hemos visto anteriormente (véase Figura 41), la capa de productos de corrosión presenta una organización en dos subcapas. Esta organización ocurre en los distintos tipos de atmósfera (Figura 52). Mientras la capa externa presenta un espesor reducido, prácticamente independiente del ambiente de exposición, el espesor de la capa interna varía considerablemente en función de la agresividad del medio [13].

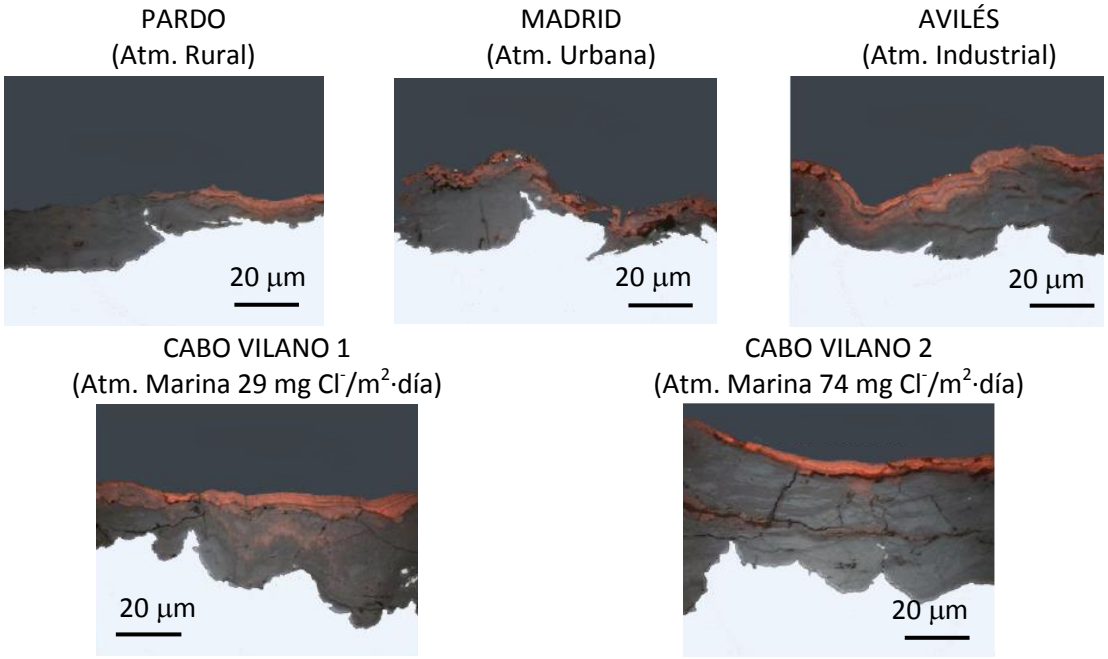

Figura 52. Espesor de la capa de herrumbre en función de la agresividad de la atmósfera [13].Acero al carbono expuesto durante un año en distinto tipo de atmósferas. Orden de agresividad creciente:

Pardo < Madrid < Avilés < Cabo Vilano 1 < Cabo Vilano 2

Tratándose de las atmósferas marinas se presentan dos singularidades que conviene resaltar: el espesor no uniforme de la capa de herrumbre y la formación de capas muy gruesas de herrumbre en atmósferas marinas con elevadas velocidades de depósito de cloruros. El espesor de la capa de herrumbre formado en atmósferas marinas no suele ser uniforme, siendo mayor en unas zonas que en otras. Lo mismo sucede con el perfil de ataque del acero subyacente, que suele mostrar abundante formación de picaduras de profundidad variable.

La Figura 23 (del apartado de resultados), mostró la existencia (prácticamente en su totalidad) de akaganeita en el interior de las picaduras formadas después de la exposición del acero al carbono durante 3 meses en una atmósfera marina con alta velocidad de depósito de cloruros. La identificación de la akaganeita se realizó mediante SEM/μRaman [68, 80] (Figura 23 (b)).

La exposición del acero al carbono en atmósferas marinas muy agresivas (velocidades de depósito de cloruros $\geq$ 300 mg Cl^-/m^2·día) conduce a la formación de capas de herrumbre muy gruesas. Estas gruesas capas de herrumbre tienden a desprenderse (exfoliarse) del sustrato de acero, dejándolo descubierto y sin la protección debida a la propia capa de herrumbre, por lo que su corrosión se acelera enormemente. En el siguiente apartado se aborda con mayor extensión este fenómeno de exfoliación.

5.3.4 El fenómeno de exfoliación

En la estación 2 del Parque Eólico de Cabo Vilano se llegaron a medir espesores de hasta 4 mm de las capas exfoliadas y pérdidas de espesor del sustrato de acero de 550 μm en tan solo un año de exposición atmosférica; el volumen de productos de corrosión formados era unas 8 veces el espesor de metal corroído. La formación de estas gruesas capas de herrumbre tenía lugar a partir de salinidades atmosféricas en el entorno de 300 mg Cl^-/m^2·día (Figura 53) [127]. Las capas exfoliadas estaban compuestas de varios estratos de herrumbre (herrumbre multicapa), como puede observarse en la sección transversal mostrada en la Figura 54, que las denominamos como: herrumbre más externa, herrumbre compacta, herrumbre inconsistente y herrumbre más interna [128]. Llaman la atención, en particular, las capas de herrumbre compacta.

La constitución y naturaleza de los distintos estratos de herrumbre formada (Figura 54) se abordará más adelante.

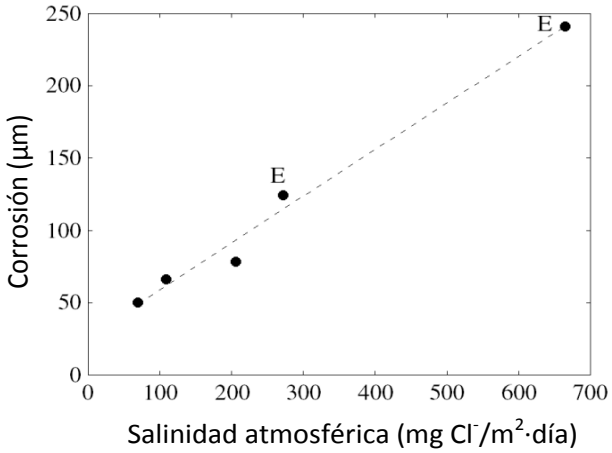

Figura 53. Corrosión del acero suave en función de la salinidad atmosférica. Datos correspondientes a un año de exposición. La letra E indica las situaciones donde se observó exfoliación de las capas de herrumbre.

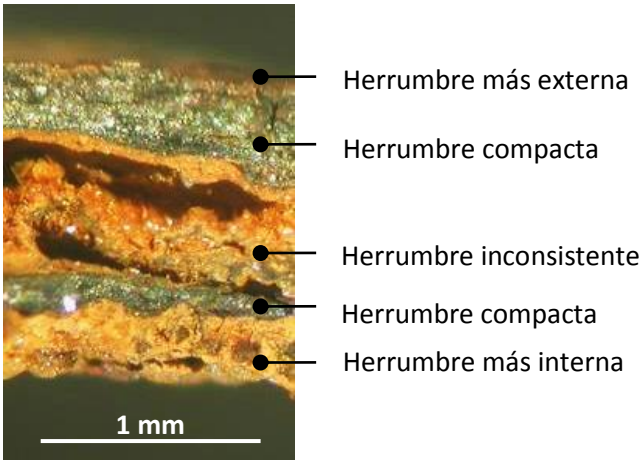

Figura 54. Micrografía óptica de una capa exfoliada de herrumbre formada sobre acero al carbono expuesto durante un año en una atmósfera marina muy agresiva (665 mg Cl^-/m^2·día).

La estructura interna de la herrumbre exfoliada contiene una o más capas de herrumbre compacta que exhiben un color grisáceo-negruzco y brillo metálico. Están por lo general bien adheridas aunque pueden con mayor o menor dificultad separarse con la ayuda de un cuchillo de hoja muy fina. Las capas compactas son frágiles y presentan una estructura interna muy porosa y heterogénea con abundantes huecos de diferente morfología, tanto a nivel macroscópico como microscópico (Figura 55) [127]. Una observación a mayores aumentos nos indica la existencia de abundantes huecos, vacíos lineales longitudinales, grietas transversales y bandas de herrumbre anaranjadas en su interior (Figura 56) [127]. Los mapas de rayos X realizados en uno de esos vacíos nos indican que son realmente huecos y sin herrumbre en su interior por la ausencia de señal del Fe y O (Figura 57) [127].

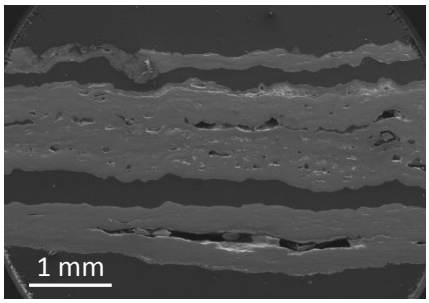

Figura 55. Micrografía SEM que muestra 3 capas de herrumbre compacta. Los espacios entre ellas correspondían a herrumbre inconsistente que fue eliminada durante la preparación metalográfica.

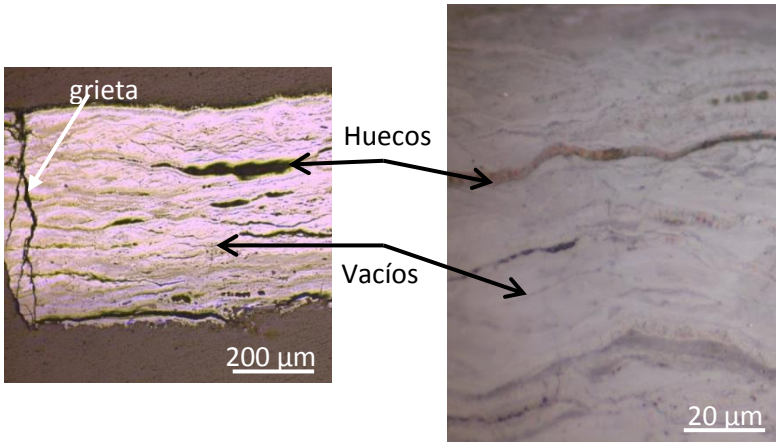

Figura 56. Micrografías ópticas de dos zonas en la sección transversal de una capa de herrumbre compacta en donde se puede observar la existencia de vacíos lineales, grietas transversales y bandas de herrumbre.

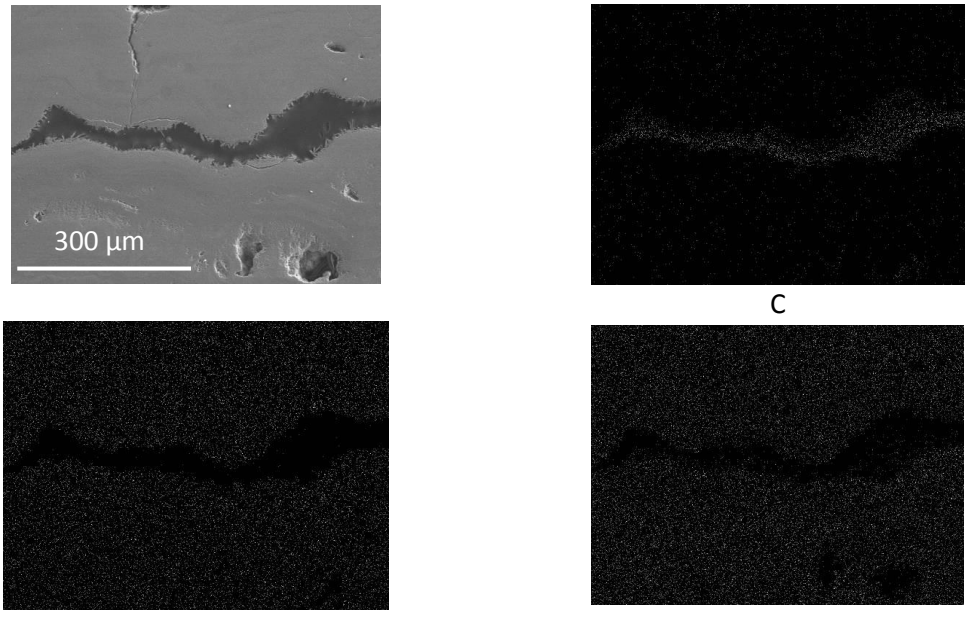

Figura 57. Micrografía SEM de un vacío (hueco) en el interior de una capa de herrumbre compacta y mapas de rayos X correspondientes al C (depositado para la observación microscópica), Fe y O.

5.4 Mecanismos de corrosión atmosférica marina y su dependencia de la velocidad de depósito de cloruros. (Anexo V)

Como se comentó en la introducción de esta Memoria, no deja de extrañar que, a pesar de ser un tema de gran importancia práctica, no haya sido hasta hace relativamente poco tiempo un tema que haya suscitado gran interés por parte de los investigadores. Así pues, estamos ante un campo científico relativamente joven, donde, quedan todavía numerosos pasos que dar y grandes lagunas de conocimiento. Como comentan Nishimura et al. [5, 6], no es hasta la última década del siglo XX cuando se empieza a realizar una mayor investigación sobre los mecanismos fundamentales de formación de herrumbre en atmósferas marinas ricas en iones cloruro.

Barton en 1976 [4] señalaba tres causas que podrían explicar las altas velocidades de corrosión del acero expuesto a atmósferas marinas:

a) el aumento de la conducción iónica por la presencia de sustancias ionizantes (cloruros) en la película acuosa
b) el carácter higroscópico de los productos clorurados formados, y
c) la mayor solubilidad de estos productos, a diferencia de los cloruros básicos estables (más insolubles) que se forman sobre otros metales (Zn, Cu, etc.).

Asimismo Barton señalaba, que el mecanismo que gobierna los efectos de los iones Cl^- en la corrosión atmosférica no estaba todavía completamente clarificado.

En nuestra opinión, al igual que ocurre en el caso del SO_2 atmosférico, dos causas adicionales de enorme importancia explicarían las altas velocidades de corrosión atmosférica del acero en presencia de iones Cl^-:

a) el fuerte carácter despolarizador catódico de los iones Cl^-, formulado anteriormente por Rozenfeld en 1961 [129], y
b) el papel catalítico de los cloruros [96, 130]. Según Burstein [96] la reacción anódica genera cationes por disolución del hierro y H^+ por hidrólisis de los cationes disueltos. Ambos requieren neutralización, que se lleva a cabo mediante el ingreso de nuevo Cl^-, lo que aumenta la concentración local de este anión que favorece aún más la disolución metálica, y así sucesivamente. Estamos pues ante un mecanismo de retroalimentación, también conocido como autocalítico. La migración de los Cl^- al

sustrato de acero está facilitada por la alta permeabilidad a estos iones de la capa de herrumbre. La alta concentración de Cl^- en la intercara acero/herrumbre facilita la formación de akaganeita [131].

5.4.1 El papel fundamental de la akaganeita

Ha quedado bien establecida la existencia de akaganeita entre los productos de corrosión que se forman sobre el acero al carbono cuando se expone a las atmósferas marinas.

Un avance fundamental sobre el papel que desempeña la akaganeita en el proceso de corrosión atmosférica del acero en atmósferas marinas se produce con los estudios de Nishimura et al. [5, 6] en la última década del siglo XX. Nishimura et al. en 1995 [6] evaluaron mediante XRD "in situ" la relación existente entre la resistencia a la corrosión del acero y la concentración en NaCl en un ensayo de laboratorio de humectación/secado. La velocidad de corrosión del acero aumentaba con la concentración de NaCl teniendo lugar un fortísimo aumento de la relación en peso β-FeOOH/γ-FeOOH a partir de una concentración de NaCl del 0,05 % (en peso). La akaganeita se reducía a un óxido intermedio amorfo durante la etapa húmeda del ciclo.

Más adelante, en el año 2000, estos mismos investigadores [5], siguiendo la misma técnica de humectación/secado, observaron mediante impedancia con corriente alterna la transición de GR1 a akaganeita durante la etapa de secado. La cantidad de GR1 dependía de la concentración de Cl^-. Después de depositar una solución de Cl^- (3% en peso) sobre la superficie de acero, se formaba β-FeOOH y la velocidad de corrosión del acero era alta. Sin embargo, para bajas concentraciones de Cl^- (0.03% en peso) se formaba γ-FeOOH a partir de $Fe(OH)_2$, en lugar de β-FeOOH, y la velocidad de corrosión era baja. Estos investigadores realizaron mediante XRD convencional un análisis cuantitativo de las fases de herrumbre formadas durante el ensayo. La fase β-FeOOH era la más abundante y su contenido aumentaba notablemente con la concentración de Cl^- en la solución. La fase α-FeOOH también estaba presente, aunque en menor proporción. Por el contrario, las fases γ-FeOOH y Fe_3O_4 tenían un contenido muy minoritario, independientemente de la concentración de Cl^-. Concluyeron que en un ambiente rico en Cl- es la akaganeita el agente oxidante principal que acelera el proceso de corrosión del acero, a diferencia del papel principal que desempeña la lepidocrocita en ambientes donde no existen Cl^- [113].

5.4.2 La constitución de capas de herrumbre

Las capas de herrumbre presentan una considerable porosidad y agrietamiento dando lugar a huecos de diferentes tamaños entre las partículas de herrumbre. La estructura porosa de las capas de herrumbre influye enormemente en la velocidad de corrosión del acero subyacente, permitiendo la penetración de las especies agresivas del medio (O_2, H_2O, Cl^-, etc.), a su través, hacia el sustrato metálico.

Ishikawa et al. [125, 132], examinando las texturas de las herrumbres, observan, como nosotros, que las herrumbres formadas en regiones costeras son aglomerados de gruesas partículas (de mayor granulometría), que dan lugar a poros de mayores tamaños que los correspondientes a herrumbres formadas en atmósferas rurales y urbanas. El NaCl promueve el crecimiento de las partículas de herrumbre generando en las capas de herrumbre formadas vacíos (huecos) y poros de mayor tamaño, lo que facilita el progreso de ataque del sustrato. El área específica superficial de la herrumbre decrece con la salinidad atmosférica aumentando el diámetro de los poros y dando lugar a capas cada vez menos compactas con bajas propiedades protectoras.

La compacidad de las capas de herrumbre formadas depende de la salinidad atmosférica del lugar. A bajas velocidades de depósito de cloruros de la atmósfera, aunque los tiempos de humectación de la superficie metálica sean altos, se forman capas de herrumbre relativamente consistentes cuyo espesor no suele sobrepasar los 100 µm. Sin embargo, a altas velocidades de depósito de cloruros se forman capas de herrumbre muy porosas con fuerte agrietamiento, que incluso pueden llegar a desprenderse (exfoliarse) del sustrato de acero [127]. En la Figura 50 ya vimos cómo variaba la estructura de la capa de herrumbre conforme aumentaba la salinidad atmosférica. Mientras a relativamente bajas velocidades de depósito de cloruros (44 y 110 mg Cl^-/m^2·día) las capas de herrumbre presentaban bastante compacidad, a mayores salinidades atmosféricas (173 y 245 mg Cl^-/m^2·día) las capas de herrumbre mostraban un notable agrietamiento que facilita su desprendimiento por exfoliación, como puede observarse claramente en las atmósferas con más elevadas velocidades de depósito de cloruros (889 y 1136 mg Cl^-/m^2·día) [62].

En nuestra investigación se ha observado que al cabo de un año de exposición atmosférica las capas de herrumbre formadas a salinidades atmosféricas inferiores a 100 mgCl^-/m^2·día estaban bastante bien consolidadas, eran relativamente compactas y presentaban escaso agrietamiento. Sin embargo, a partir de salinidades atmosféricas en el entorno de 300 mg Cl^-/m^2·día las capas de herrumbre se exfoliaban del sustrato del acero (Figura 53).

Parecen existir, por tanto, dos situaciones extremas donde los mecanismos de corrosión del acero al carbono deben ser notoriamente distintos: (a) establecimiento de una capa consistente (consolidada), continua y adherente (a relativamente bajas velocidades de depósito de cloruros), y (b) formación de muy gruesas capas de herrumbre (a muy altas salinidades atmosféricas) que se desprenden (exfolian) del acero base dejándolo desnudo y sin la protección que le confiere la existencia de la capa de herrumbre [133]. Pasamos a continuación a comentar estas dos situaciones extremas.

5.4.2.1 Capa consolidada de herrumbre

En la situación de existencia de una capa consolidada de herrumbre que permanece adherida al sustrato de acero, se dan las condiciones para que se verifique un mecanismo de corrosión del acero controlado por la difusión de las especies agresivas del medio (O_2, H_2O y Cl^-) a través de la capa de herrumbre para interaccionar con el acero subyacente. El proceso de corrosión tiene lugar mediante las reacciones (17-21):

$$Fe \rightarrow Fe^{2+} \rightarrow \gamma\text{-FeOOH} \quad (17)$$

$$\gamma\text{-FeOOH} \rightarrow \alpha\text{-FeOOH} \quad (18)$$

$$Fe^{2+} + 2\ Cl^- \rightarrow FeCl_2 \quad (19)$$

$$2\ FeCl_2 + 3\ H_2O + \tfrac{1}{2}\ O_2 \rightarrow 2\ FeOOH + 4\ HCl \quad (20)$$

$$FeCl_2 \rightarrow \beta\text{-}Fe_2(OH)_3Cl \rightarrow GR1 \rightarrow \beta\text{-FeOOH} \quad (21)$$

Bajo este mecanismo, la velocidad de corrosión del acero está fuertemente influenciada por la concentración de iones Cl^- presentes en la película de electrolito existente sobre la superficie metálica. Ello explica el notable aumento de la velocidad de corrosión del acero al pasar de la estación de Ponte Do Porto (4 mg Cl^-/m^2·día) a la estación 11 de Cabo Vilano (70 mg Cl^-/m^2·día) (Tabla 25) [133]. La formación de akaganeita acelera el proceso de la corrosión atmosférica del acero y su consumo por reducción electroquímica a espinela justifica el gradual decrecimiento de su contenido en la capa de herrumbre conforme progresa el tiempo de exposición (Tabla 26), así como el crecimiento paralelo del contenido en fase espinela [133].

Tabla 25. Variación del contenido de las diferentes fases de herrumbre formadas sobre el acero expuesto durante un año en estaciones de ensayo con relativamente bajas velocidades de depósito de cloruros.

Estación de ensayo (distacia a la costa)	Velocidad media anual de depósito de cloruros, (mg Cl^-/m^2·día)	% (en peso)				Corrosión (μm)
		Lepidocrocita	Goetita	Akaganeita	Espinela	
Ponte do Porto,700 m [134]	4	100	*	0	0	29
Estación 11, 2400 m (años 2013-2014)	70	59,6	20,0	17,6	2,7	50

*No se descarta una pequeña contribución de esta fase.

Tabla 26. Evolución con el tiempo de exposición del contenido de las diferentes fases de herrumbre formadas sobre el acero en una atmósfera marina con relativamente baja velocidad de depósito de cloruros.

Estación de ensayo (distancia a la costa)	Velocidad de depósito de cloruros, (mg Cl^-/m^2·día)	Tiempo, (meses)	% (en peso)			
			Lepidocrocita	Goetita	Akaganeita	Espinela
Estación 11, 2400 m	70	3	47,4	40,6	7,2	4,8
		6	43,8	36,8	10,9	8,6
		9	48,0	36,4	5,6	10,0
		12	51,6	35,9	4,3	8,2

La formación de akaganeita en esta situación tiene lugar tanto en la superficie de la capa de herrumbre como en la intercara acero/herrumbre [126], ya que el escaso agrietamiento de las capas consolidadas de herrumbre (Figura 50 (a-b)) no facilita una interacción directa de los iones Cl^- con el sustrato metálico.

5.4.2.2 Capa exfoliada de herrumbre

La exposición del acero al carbono a atmósferas marinas muy severas (muy altas velocidades de depósito de iones cloruro) puede conducir a la formación de capas de herrumbre muy gruesas (Figura 50 (c-d)) que tienden a exfoliarse (desprenderse) del sustrato de acero [69, 127]. Este fenómeno ha sido observado también por otros investigadores [135, 136].

Como se ha comentado anteriormente, para que tenga lugar el fenómeno de exfoliación, la velocidad de depósito de cloruros de la atmósfera marina tiene que exceder un umbral crítico cercano a los 300 mg Cl^-/m^2·día (Figura 53) [127]. La velocidad de corrosión anual del acero por encima de ese valor de salinidad se acelera notablemente (Tabla 27) [127], lo que afecta de modo importante a la durabilidad de las infraestructuras de acero al carbono existentes próximas a la línea de costa.

Tabla 27. Variación del contenido de las diferentes fases de herrumbre formadas sobre el acero expuesto en una atmósfera marina con elevada velocidad de depósito de cloruros.

Estación de ensayo (distacia a la costa)	Velocidad media anual de depósito de cloruros (mg Cl^-/m^2·día)	**% (en peso)**				Corrosión (μm)
		Lepidocrocita	Goetita	Akaganeita	Espinela	
Estación 3, 420 m	665	35,8	27,0	12,5	24,7	241

En la Tabla 28 se observa como aumenta notablemente con el tiempo de exposición el contenido en espinela de la herrumbre y paralelamente decrece el contenido en akaganeita por transformación a magnetita.

Tabla 28. Evolución con el tiempo de exposición del contenido de las diferentes fases de herrumbre formadas sobre el acero expuesto en una atmósfera marina con elevada velocidad de depósito de cloruros.

Estación de ensayo (distancia a la costa)	Velocidad de depósito de cloruros (mg Cl^-/m^2·día)	Tiempo (meses)	% (en peso)			
			Lepidocrocita	Goetita	Akaganeita	Espinela
Estación 2, 332m	1906*	3	26.0	53.5	9.2	11.2
		6	31.7	41.9	6.3	12.9
		9	8.6	42.5	6.5	42.4
		12	13.1	44.4	0.5	42.0

En el apartado anterior se expuso con detalle la estructura de estas gruesas capas anómalas de herrumbre (Figura 54), cuya mayor singularidad consiste en la existencia en su interior de subcapas de herrumbre compacta alternadas con subcapas de herrumbre de muy baja consistencia.

El mecanismo global de corrosión que actúa sobre el acero al carbono expuesto a atmósferas marinas muy severas difiere notablemente del que ocurre en el caso de capas consolidadas de herrumbre, comentado anteriormente. La alta concentración de iones Cl^- en la capa acuosa

depositada sobre el metal y los altos tiempos de retención de humedad en las zonas deterioradas de las capas de herrumbre formadas, dan lugar a la formación de $FeCl_2$:

$$Fe^{2+} + 2\ Cl^- \rightarrow FeCl_2 \qquad (19)$$

que hidroliza el agua aumentando notablemente la acidez del electrolito:

$$2\ FeCl_2 + 3\ H_2O + ½\ O_2 \rightarrow 2\ FeOOH + 4\ HCl \qquad (20)$$

Hemos llegado a medir valores de pH = 4 sobre el acero debajo de estas capas [127, 133]. En esta situación la reacción catódica de descarga de hidrógeno puede ser preponderante acelerando notablemente el proceso de corrosión:

$$2\ H^+ + 2\ e^- \rightarrow H_2 \qquad (3)$$

La intercara acero/herrumbre puede llegar a estar saturada con una solución altamente ácida de $FeCl_2$. Los cationes Fe^{2+} y H^+ requieren neutralización, lo que ocurre mediante el ingreso de iones Cl^- que migran hacia el sustrato de acero a través de las grietas existentes en la capa de herrumbre, aumentando la concentración de Cl^- e intensificando el proceso de corrosión, lo que a su vez da lugar a una nueva entrada de iones Cl^- (proceso autocatalítico), como ocurre en el interior de las picaduras durante el fenómeno de picado [96].

En la intercara acero/herrumbre, donde los iones Cl^- se acumulan, la alta concentración de cloruro y las condiciones ácidas dan lugar a la formación de akaganeita previa formación de hidroxicloruro ferroso (Ec. 21). Posteriormente, la reducción electroquímica de la akaganeita daría lugar a magnetita.

Analicemos separadamente cada una de las subcapas que integran la capa de herrumbre exfoliada (Figura 54). A tal fin, puede resultar muy útil acudir a la composición de cada una de ellas, obtenida por diferentes técnicas de caracterización: XRD, XRD en área seleccionada y espectroscopía Mössbauer. La Figura 58 expone algunos de los resultados obtenidos. En general, las cuatro fases, lepidocrocita, goetita, akaganeita y espinela, están presentes en los diferentes estratos de la capa exfoliada, siendo la fase goetita (la más estable de las cuatro) la que presenta un mayor porcentaje. Por ello, a continuación, únicamente nos referiremos a la variación a lo largo de la capa exfoliada de los porcentajes de las otras tres fases.

La subcapa más externa de herrumbre está constituida básicamente por lepidocrocita y goetita. La fracción de espinela es insignificante y el contenido en akaganeita es muy bajo. Esta subcapa es similar a la subcapa más externa de herrumbre en capas consolidadas.

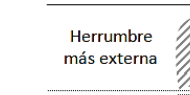

					Lepidocrocita	Goetita	Akaganeita	Espinela	Maghemita
Herrumbre exfoliada	Herrumbre más externa		Promedio	A_m	55	35	9	1	
				B	56	34	9	1	
	Herrumbre compacta		Bulk	A_p	10	48	1	41	
				C	11	55	No detectable	0	33
	Herrumbre inconsistente		Región más interna	B	15	41	34	10	
	Herrumbre compacta		Polvo	C	17	55	No detectable	0	28
	Herrumbre interna		Áreas anaranjadas	B	0	0	77	23	
			Áreas marrones	B	0	30	7	63	
		Deslaminación							
Acero remanente	Herrumbre remanente		Áreas anaranjadas	B	0	0	100	0	
			Áreas marrones	B	9	34	6	51	
	Acero base								

A_m: XRD Convencional (chapa herrumbrada) A_p: XRD Convencional (herrumbre en polvo); B: XRD en área seleccionada; C: Espectroscopía Mössbauer

Figura 58. Cuantificación (% en peso) mediante XRD (Rietveld) y espectroscopía Mössbauer del contenido de las diferentes fases de herrumbre en las distintas zonas de la capa exfoliada.

Las capas de herrumbre compacta tienen un alto contenido en fase espinela. El contenido en lepidocrocita es muy bajo y la presencia de akaganeita es prácticamente insignificante. La espectroscopía Mössbauer nos indica que la fase espinela es maghemita, descartando totalmente la presencia de magnetita [127]. ¿A qué se debe la presencia de maghemita en este estrato de la capa de herrumbre? Cook y van Orden [137] mencionan dos posibles mecanismos para la formación de maghemita: (a) deshidroxilación de la lepidocrocita, y (b) oxidación de la magnetita. En el primer caso, esta transformación no ha sido nunca observada en estudios de campo, solamente en condiciones de laboratorio, mientras que en el segundo caso esa transformación se ha observado en ambas condiciones de exposición. De acuerdo con Cornell y Schwertmann [23] la transformación de lepidocrocita a maghemita tiene lugar en el aire a temperaturas comprendidas entre 200°C y 280°C, lo que excluye su formación en las condiciones normales de exposición atmosférica. Sin embargo, por transformación en estado sólido, la magnetita puede ser rápidamente oxidada a maghemita de acuerdo con la reacción:

$$4\ Fe_3O_4 + 2\ O_2 \rightarrow 6\ Fe_2O_3 \qquad (17)$$

En realidad, si recordamos los comentarios realizados sobre estas dos fases en el apartado 5.2.2.3, el que sea una u otra de estas dos fases tiene que ver con su composición: la maghemita solamente contiene Fe^{3+}, a diferencia de la magnetita que contiene Fe^{2+} y Fe^{3+}. En nuestra opinión la magnetita pura solamente la tendríamos en el mineral. En los productos de corrosión atmosférica, una parte de los iones Fe^{2+} se oxidarían a Fe^{3+}, por lo que estaríamos

ante una magnetita no estequiométrica, con mayor o menor grado de estequiometria, que es lo que suele reseñarse en la bibliografía sobre corrosión atmosférica. En las condiciones fuertemente oxidantes que se verifican en la reducción electroquímica de los oxihidróxidos lepidocrocita y akaganeita en este tipo de capas exfoliadas de herrumbre, no es de extrañar que haya una total oxidación de los iones Fe^{2+} a Fe^{3+}, de tal modo que la espinela resultante fuera maghemita. La alta presencia de fase espinela en la subcapa compacta (Figura 58) se justifica por la reducción electroquímica de las fases lepidocrocita y akaganeita de la subcapa de herrumbre de baja consistencia [128].

En cuanto a la subcapa de herrumbre de baja consistencia (Figura 58), los resultados obtenidos mediante XRD en área seleccionada muestran altos contenidos en akaganeita y bajos contenidos en espinela, lo contrario que ocurría en las subcapas de herrumbre compacta. Todo hace indicar que en los primeros estadios del proceso de corrosión en atmósferas muy contaminadas con iones Cl^- tendría lugar la formación de lepidocrocita y particularmente de akaganeita. Posteriormente, durante las etapas húmedas de los ciclos de humectación/secado tendría lugar la transformación de aquellas dos fases en fase espinela.

Finalmente, resulta de interés conocer las características de la subcapa más interna de herrumbre, aquella en íntimo contacto con el acero subyacente. A tal fin se analizó mediante XRD convencional, XRD de área seleccionada y XRD de ángulo rasante la composición de esta subcapa en sus dos superficies de fractura cuando tiene lugar el fenómeno de exfoliación (Figura 58). Ambas presentaban una estructura muy heterogénea en la que podían observarse zonas de un fuerte color anaranjado, ricas en akaganeita, y zonas de tonalidad gris oscuro ricas en fase espinela (Figura 59). La presencia de ferrita en los difractogramas obtenidos en la primera de ellas nos indicaba su mayor proximidad al acero base, recordándonos la estructura interna de una capa de herrumbre consolidada, con una región más externa rica en lepidocrocita y goetita y una región más interna rica en akaganeita y espinela.

Figura 59. Superficie de fractura de la subcapa más interna de la capa de herrumbre exfoliada mostrando la presencia de zonas anaranjadas (ricas en akaganeita) y zonas de color marrón (ricas en fase espinela).

5.5 Una visión global del proceso de corrosión atmosférica marina del acero al carbono. (Anexo VI)

Basándonos en la información bibliográfica disponible, y en la experiencia adquirida en esta investigación realizada en un amplio espectro de salinidades atmosféricas, a continuación exponemos de un modo simplificado nuestro punto de vista acerca del proceso de corrosión del acero al carbono en atmósferas marinas.

La corrosión atmosférica de metales es un proceso de naturaleza electroquímica, suma de los procesos individuales que tienen lugar cuando una película de electrolito se forma sobre el metal. Esta película de electrolito puede consistir en una delgada película de humedad (solamente unas pocas monocapas) o en una película acuosa de cientos de micrómetros de espesor (cuando el metal está perceptiblemente mojado). Las precipitaciones acuosas (lluvia, niebla, etc.) y la condensación de humedad por cambios de temperatura (rocío), delicuescencia (higroscopicidad), capilaridad, etc., son los principales promotores de la corrosión metálica en la atmósfera.

El acero se corroe de acuerdo con la reacción anódica:

$$Fe \rightarrow Fe^{2+} + 2\ e^{-} \qquad (5)$$

siendo el proceso catódico la reducción del oxígeno disuelto en la película de humedad:

$$½\ O_2 + H_2O + 2\ e^{-} \rightarrow 2\ OH^{-} \qquad (4)$$

Los iones OH^{-} migran hacia las zonas anódicas formando $Fe(OH)_2$ como producto inicial de corrosión:

$$Fe^{2+} + 2\ OH^{-} \rightarrow Fe(OH)_2 \qquad (22)$$

La película acuosa puede adsorber sustancias presentes en la atmósfera, SO_2, NO_x, cloruros marinos, etc., afectando de un modo importante al proceso básico de corrosión atmosférica mencionado anteriormente. Finalmente, la composición de la herrumbre dependerá de las características de la capa de electrolito superficial, variando por tanto con el tipo de atmósfera.

Los productos de corrosión atmosférica del hierro, conocidos como herrumbre (o fases de herrumbre), comprenden varios tipos de óxidos, óxidos hidratados, oxihidróxidos y variadas sustancias cristalinas y amorfas, que se forman como resultado de la interacción del hierro con la atmósfera. Si bien en las etapas iniciales del proceso de corrosión las fases de herrumbre

pueden ser muy variadas (hidróxidos de hierro, ferrihidrita, cloruro ferroso, lepidocrocita, etc.) al cabo de poco tiempo la capa de herrumbre está integrada principalmente por las fases cristalinas, lepidocrocita, goetita, akaganeita (sólo atmósferas marinas) y espinela (magnetita/maghemita), y materia amorfa.

Está bien establecido que la lepidocrocita es el producto cristalino que inicialmente se forma sobre la superficie del acero. Cuando la capa de electrolito superficial es débilmente ácida, la lepidocrocita se transforma en goetita. Schwertmann y Taylor [138] han establecido que esta transformación ocurre en solución a través de diferentes etapas: disolución de la lepidocrocita, formación de núcleos de goetita y crecimiento de esos núcleos.

Conforme aumenta el tiempo de exposición del acero a la atmósfera y va engrosando la capa de herrumbre, la lepidocrocita, electroquímicamente activa, se transforma en goetita y magnetita. En este punto es ya posible distinguir en la capa de herrumbre, mediante microscopía óptica con luz polarizada, la región más externa rica en lepidocrocita (color anaranjado) y la región interna de goetita inactiva (color grisáceo) [13].

La magnetita suele formarse en la región más interna de la capa de herrumbre, adherida al sustrato de acero, donde el acceso del oxígeno está más dificultado [106, 107]. Con una visión más general, Ishikawa et al. [108] y Tanaka et al. [109] demuestran que la formación de magnetita tiene lugar por la reacción de las especies férricas, disueltas a partir de los oxihidróxidos, con las especies ferrosas existentes en la solución:

$$Fe^{2+} + 8\ FeOOH + 2\ e^- \rightarrow 3\ Fe_3O_4 + 4\ H_2O \qquad (15)$$

La cantidad de magnetita formada a partir de los diferentes oxihidróxidos sigue el siguiente orden:

$$\text{akaganeita} > \text{lepidocrocita} \gg \text{goetita (estable)}$$

Cuando el acero se expone a las atmósferas marinas, la capa de electrolito superficial contiene cloruros y tiene lugar la formación de akaganeita.

¿Cuál es el mecanismo de formación de la akaganeita? La alta concentración de cloruros en la capa acuosa depositada sobre la superficie del acero da lugar a la formación de cloruro ferroso:

$$Fe^{2+} + 2\ Cl^- \rightarrow FeCl_2 \qquad (19)$$

que hidroliza el agua aumentando notablemente la acidez del electrolito [95]:

$$2\ FeCl_2 + 3\ H_2O + ½\ O_2 \rightarrow 2\ FeOOH + 4\ HCl \quad (20)$$

Así pues, en la intercara acero/herrumbre, donde se acumulan los iones cloruro, altas concentraciones de Cl^- y condiciones ácidas dan lugar a la formación de akaganeita previa precipitación de hidroxicloruro ferroso [β-$Fe_2(OH)_3Cl$], un proceso muy lento que requiere la transformación de precursores metaestables [97, 98]. Como Remazeilles y Refait comentan son necesarias altas concentraciones de Cl^- e iones Fe^{2+} para que tenga lugar la formación de akaganeita. El proceso de oxidación del hidroxicloruro ferroso que conduce a la formación de akaganeita pasa por distintas etapas, vía la formación de compuestos intermedios del tipo GR1 [97-101]. El proceso completo de oxidación se puede resumir del siguiente modo:

$$FeCl_2 \rightarrow \beta\text{-}Fe_2(OH)_3Cl \rightarrow GR1 \rightarrow \beta\text{-}FeOOH \quad (21)$$

El proceso es muy lento y su velocidad depende de las condiciones ambientales: temperatura, $[Fe^{2+}]$, $[Cl^-]$, $[OH^-]$, flujo de oxígeno, etc.

¿Qué condiciones ambientales de la atmósfera se requieren para la formación de akaganeita? En esta investigación se han establecido las siguientes: una HR anual media de la atmósfera ≥ 80 % y simultáneamente una velocidad media anual de depósito de cloruros $\geq$ 60 mg Cl^-/m^2·día (Figura 44). Estas condiciones confirman los estudios de laboratorio de Remazeilles y Refait [99] que indican que una alta concentración de Cl^- es una condición necesaria pero no suficiente para la formación de akaganeita. El medio debe contener asimismo altos contenidos en Fe^{2+}, lo que ocurre cuando la superficie metálica está expuesta a atmósferas húmedas que promueven altos tiempos de humectación de la superficie metálica.

El depósito de cloruros en las atmósferas marinas da lugar a un aumento notable de la velocidad de corrosión del acero al carbono con relación a una atmósfera limpia. La velocidad de corrosión es función de la actividad del ion Cl^- en la película de humedad [80] (ver Figura 37).

Con relación a los productos de corrosión que se forman sobre el acero al carbono en este tipo de atmósferas, se han preparado las Tablas 25 y 27 que recogen datos obtenidos por los autores en diferentes investigaciones [80, 92, 133]. De la observación de esta tabla se infieren los siguientes hechos: (a) en las atmósferas marinas con extremadamente bajas velocidades de depósito de cloruros (Ponte do Porto) únicamente se detectan por XRD lepidocrocita y goetita, ésta última en una proporción prácticamente insignificante, (b) por debajo del umbral crítico (60 mg Cl^-/m^2·día), no tiene todavía lugar la formación de akaganeita en cantidades significativas y los contenidos en fase espinela son muy bajos, (c) por encima del umbral crítico

de salinidad atmosférica ya se forma akaganeita; los contenidos en akaganeita y espinela se incrementan notablemente con la salinidad atmosférica. Se observa claramente (ver Figura 45) cómo los contenidos en akaganeita, goetita y espinela aumentan con la salinidad atmosférica del lugar y paralelamente los contenidos en lepidocrocita se reducen ostensiblemente [139].

Hiller [114], desde hace tiempo, ya comentaba que la herrumbre formada en atmósferas marinas contenía más magnetita que cuando se formaba en atmósferas libres de iones Cl^-. Del mismo modo que ocurre con la lepidocrocita [140], la akaganeita se reduce electroquímicamente a magnetita en el proceso de corrosión que tiene lugar en las atmósferas marinas, consumiéndose en la etapa de humectación de los ciclos de humectación/secado [5]. Lair et al. [141] demostraron experimentalmente la mayor capacidad reductora de la akaganeita con relación a los otros dos oxihidróxidos férricos, señalando el siguiente orden:

akaganeita > lepidocrocita ≫ goetita (estable)

Esto explica los altos contenidos en magnetita encontrados en las herrumbres formadas sobre el acero al carbono expuesto a atmósferas muy contaminadas con iones Cl^- (Tabla 27).

La compacidad de las capas de herrumbre formadas depende de la salinidad atmosférica del lugar. A bajas velocidades de depósito de cloruros de la atmósfera, a pesar de que los tiempos de humectación de la superficie metálica sean altos, se forman capas de herrumbre relativamente consistentes cuyo espesor no suele sobrepasar los 100 µm. Sin embargo, a altas velocidades de depósito de cloruros se forman capas de herrumbre muy porosas con fuerte agrietamiento, que incluso pueden llegar a desprenderse (exfoliarse) del sustrato de acero [127].

En la nueva figura 60 también puede observarse cómo varía el contenido en las diferentes fases de herrumbre en las capas de corrosión formadas conforme aumenta la salinidad atmosférica. El contenido en fase lepidocrocita disminuye a expensas de un aumento en el contenido en las fases goetita y akaganeita.

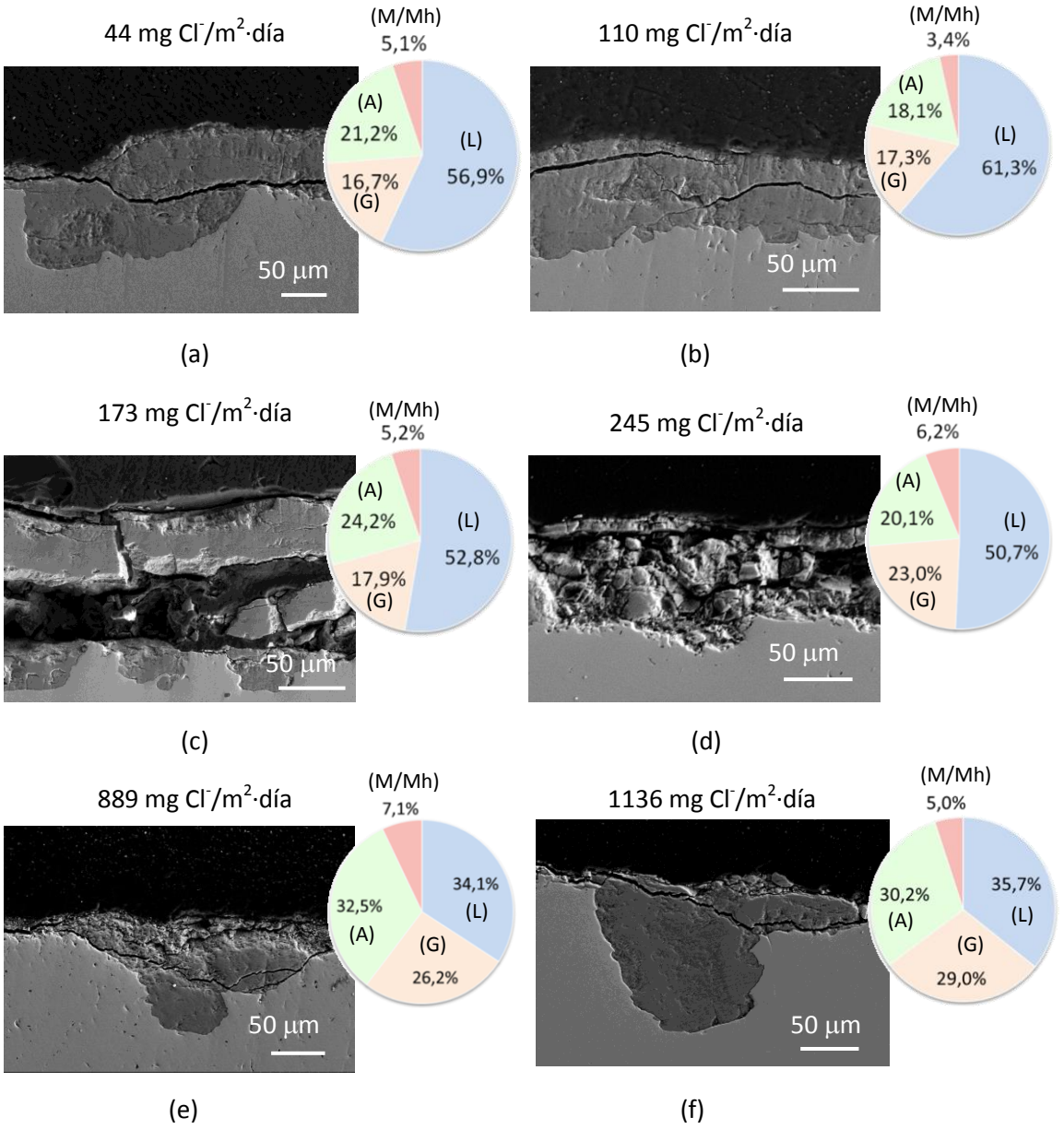

Figura 60. Variación de la estructura de la capa de herrumbre con la salinidad atmosférica. Las probetas de acero estuvieron expuestas durante 3 meses en las distintas atmósferas. Las secciones transversales de la capa de herrumbre corresponden a la cara de las probetas mirando al suelo (cara B). Se exponen asimismo en los círculos el contenido en las diferentes fases de herrumbre, obtenido mediante XRD del polvo de herrumbre (método RIR).

En la investigación realizada se ha observado que al cabo de un año de exposición atmosférica las capas de herrumbre formadas a salinidades atmosféricas inferiores a 100 mg Cl^-/m^2·día estaban bastante bien consolidadas, eran relativamente compactas y presentaban escaso agrietamiento. Sin embargo, a partir de salinidades atmosféricas en el entorno de 300 mg Cl^-/m^2·día las capas de herrumbre se exfoliaban del sustrato del acero (Fig. 53). Parecen existir, por tanto, dos situaciones extremas donde los mecanismos de corrosión del acero al carbono deben ser notoriamente distintos: (a) establecimiento de una capa

consistente (consolidada), continua y adherente, a relativamente bajas velocidades de depósito de cloruros, y (b) formación de muy gruesas capas de herrumbre, a muy altas salinidades atmosféricas, que se desprenden (exfolian) del acero base dejándole desnudo y sin la protección que le confiere la existencia de la capa de herrumbre [133].

Todo ello nos lleva a formular el siguiente mecanismo de formación de gruesas capas de herrumbre con una estructura interna tipo sándwich (multicapa), que se exfolian del sustrato de acero [62, 128]. Este mecanismo comprendería las siguientes etapas (Fig. 61):

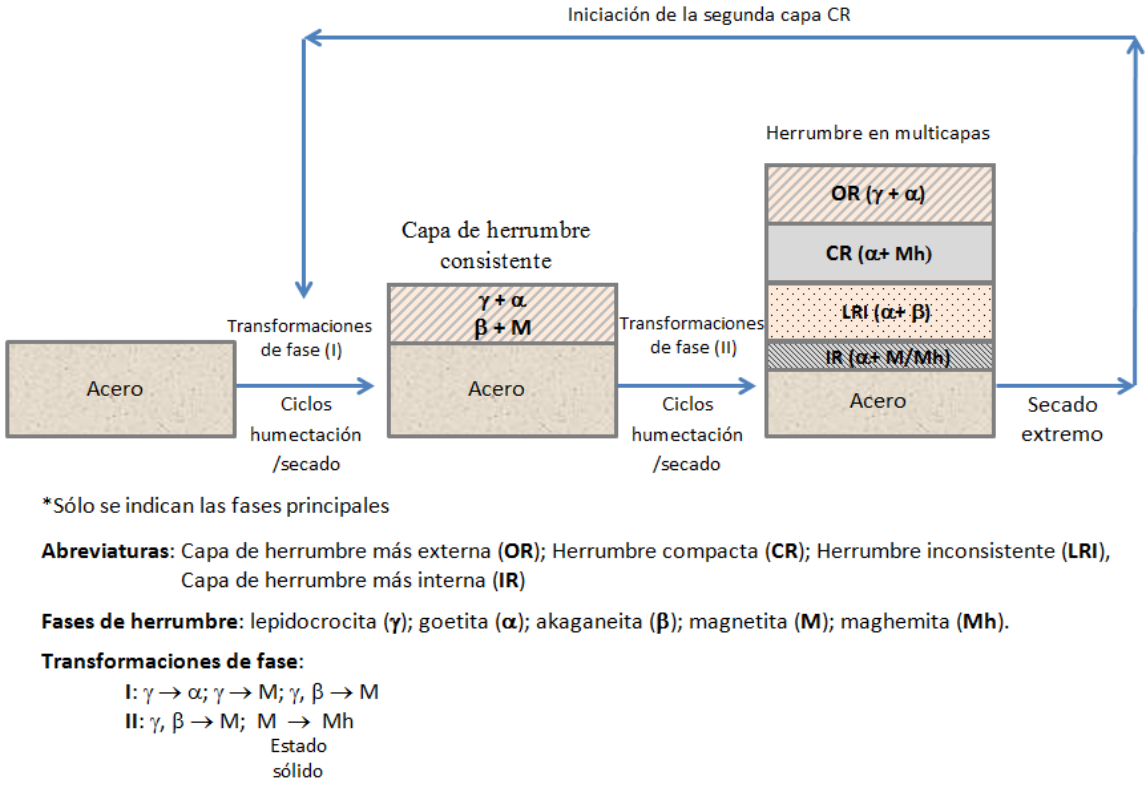

Figura 61. Esquema del mecanismo de formación de multicapas de herrumbre sobre el acero al carbono expuesto a atmósferas marinas severas.

(a) Formación inicial de una capa de herrumbre consolidada.

Cuando el acero al carbono se expone a atmósferas marinas se forma inicialmente la fase lepidocrocita. Posteriormente tiene lugar su transformación a goetita y magnetita.

(b) Formación de akaganeita.

Una vez establecida esa capa inicial de herrumbre, debajo de ella tiene lugar la formación de akaganeita, siempre que se verifiquen las siguientes condiciones ambientales: HR ≥ 80% y velocidad de depósito de cloruros ≥ 60 mg Cl^-/m^2·día. La capa de herrumbre está consolidada e

integrada por una región externa rica en lepidocrocita y goetita (la más externa) y una región más interna, próxima al acero base, constituida por akaganeita y magnetita.

(c) Formación de una subcapa de herrumbre compacta.

Cuando la velocidad de depósito de cloruros es muy elevada tiene lugar la formación de una subcapa de herrumbre compacta muy rica en fase espinela. La estructura de la capa de herrumbre consistiría en: herrumbre más externa (rica en lepidocrocita y goetita), herrumbre compacta (rica en espinela) y herrumbre más interna (heterogénea), con zonas ricas en akaganeita y magnetita.

Durante los periodos húmedos de los ciclos de humectación/secado tendría lugar la transformación de las fases activas de lepidocrocita y akaganeita, de una subcapa previamente formada de herrumbre inconsistente (rica en akaganeita), en magnetita por reducción electroquímica, dando lugar a una subcapa de herrumbre compacta. Posteriormente, tendría lugar una transformación en estado sólido de magnetita a maghemita.

(d) Formación de una estructura tipo sándwich (multicapa).

La sucesión de ciclos de humectación/secado pueden llevar a un consumo total de la subcapa de herrumbre inconsistente. Sin embargo, episodios de extrema sequedad pueden dar lugar al cese del proceso de corrosión, sin haberse agotado totalmente la subcapa de herrumbre inconsistente. Nuevos periodos de humectación de la herrumbre darían lugar a la repetición del ciclo que conduciría a la formación de una nueva subcapa de herrumbre compacta.

La estructura tipo sándwich en las gruesas capas de herrumbre estaría compuesta por distintos estratos: estrato de herrumbre más externa, estratos de herrumbre compacta (uno o varios), estratos de herrumbre inconsistente (uno o varios) y estrato de herrumbre más interna.

(e) Exfoliación (desprendimiento) de la herrumbre multicapa.

Como hemos observado, la formación de estas multicapas es consecuencia de la existencia de diferentes transformaciones entre las diferentes fases de herrumbre: lepidocrocita, goetita, akaganeita y espinela (magnetita/maghemita). Estas transformaciones están facilitadas al estar todas esas fases compuestas por unidades octaédricas FeO_6 [142].

Para conocer en profundidad el fenómeno de exfoliación de las capas de herrumbre sería necesario realizar una investigación dirigida específicamente a esta cuestión. La distinta densidad de las diferentes subcapas involucradas sugiere que la compacidad de estas

subcapas, conjuntamente con sus con propiedades mecánicas, puede desempeñar un papel importante en el fenómeno de exfoliación. Llegado un punto crítico, los cambios en compacidad y las tensiones de compresión/ expansión podrían llegar a ser tan altos como para que la gruesa herrumbre multicapa colapse produciéndose la fractura a lo largo de la subcapa más interna de herrumbre. La existencia de un periodo de sequedad extrema podría asimismo propiciar el desprendimiento de la gruesa capa de herrumbre formada.

6. CONCLUSIONES

El aerosol marino; su dependencia de diversos parámetros y su efecto en la corrosión atmosférica marina del acero al carbono

Se observa una clara relación entre la altura de las olas en el mar cercano, el recorrido de los vientos marinos y la deposición de iones Cl^- en las atmósferas marinas. Por un lado, los valores mensuales promedio de altura de ola espectral (1,5 - 2,0 m) son suficientes para producir altos valores promedios mensuales de salinidad (100 - 200 mg Cl^-/m^2·día). Por otro lado, más que la velocidad promedio del viento en el área de estudio, el recorrido de vientos marinos es el parámetro que tiene la mayor influencia en la salinidad atmosférica del lugar experimental.

La velocidad de deposición de cloruro en el lugar de exposición (salinidad atmosférica) tiene una influencia decisiva en la corrosión atmosférica marina del acero al carbono. Se observa que para las salinidades atmosféricas inferiores a 600 mg Cl^-/m^2·día parece existir una relación lineal entre la velocidad de corrosión del acero al carbono y la velocidad de déposito de iones Cl^-. Para salinidades superiores a este valor, la velocidad de corrosión parece estabilizarse.

Tanto la salinidad atmosférica como la velocidad de corrosión del acero obedecen a una función de decaimiento exponencial con la distancia a la línea de costa.

La orografía y topografía del terreno pueden jugar también un papel importante en la magnitud de la salinidad atmosférica resultante en un determinado lugar.

Productos de corrosión formados sobre el acero expuesto a la atmósfera marina.

i. Naturaleza de los productos de corrosión

Las fases principales encontradas en las herrumbres formadas en el acero al carbono expuesto a la atmósfera marina son lepidocrocita (γ-FeOOH), goetita (α-FeOOH), magnetita (Fe_3O_4)/ maghemita (γ-Fe_2O_3) y akaganeita (β-FeOOH).

Para la caracterización por XRD del contenido en la herrumbre de las diferentes fases, el análisis semicuantitativo realizado por el método RIR, está sujeto a una alta imprecisión debido a las superposiciones en el diagrama de las diferentes fases. Por ello, para una correcta cuantificación de las fases formadas es necesario realizar el ajuste del patrón de difracción utilizando el método de Rietveld.

En los estudios de corrosión atmosférica marina es muy frecuente no llegar a detectar por XRD la fase akaganeita. En nuestro estudio, utilizando el método Rietveld de ajuste, si se ha podido detectar la fase akaganeita, en mayor proporción conforme mayor es la salinidad atmosférica.

Se han establecido las condiciones ambientales atmosféricas necesarias para la formación de akaganeita: una HR promedio anual ≥ 80%, y simultáneamente, una velocidad promedio anual de deposit de ion cloruro ≥ 60 mg Cl^-/m^2·día.

En las atmósferas más ricas en Cl^- hay también una mayor formación de magnetita por transformación de la lepidocrocita.

ii. Morfologías de las fases de herrumbre

Se distinguen principalmente cinco tipos de morfología: globular, acicular, laminar, tubular y toroidal.

La fase lepidocrocita, es la más abundante en la superficie más externa de la capa de herrumbre, mostrando morfologías globulares y morfologías laminares de diferente tipo: en forma de barras, nidos de gusanos, nidos de pájaros, plumas, etc.

La fase goetita presenta dos tipos diferentes de morfología: morfología acicular en forma de agujas y morfología tubular en forma de prismas.

La fase akaganeita presenta principalmente una morfología tubular en forma de finos cristales, tubos o varillas a modo de cigarros, por lo que se requiere para su observación en SEM acudir a altos aumentos (> X 30.000). La técnica TEM/SAED se ha utilizado también con éxito para identificar con precisión la naturaleza y la estructura de esos cristales.

La fase magnetita básicamente presenta dos tipos de morfología: manchas negras planas y formaciones toroidales negras en forma de anillos circulares.

SEM/EDS, XRD en área seleccionada y SEM/µRaman han sido técnicas experimentales muy útiles para caracterizar los productos de corrosión y las capas de herrumbre formadas sobre acero al carbono expuesto a atmósferas ricas en cloruro. La técnica SEM/µRaman ha demostrado ser extremadamente útil para caracterizar las diferentes morfologías que muestran las diversas fases de herrumbre.

La capa de herrumbre

Conforme aumenta la salinidad atmosférica, las herrumbres formadas presentan granulometrías cada vez más groseras (granos y escamas más gruesas). Las capas de herrumbre formadas son menos protectoras y están más agrietadas, pudiéndose desprender

del acero subyacente. El acero base experimenta fuertes picaduras que contienen considerables contenidos de akaganeita en su interior.

Se ha observado el fenómeno de la exfoliación de las capas de herrumbre formadas sobre acero expuesto a la atmósfera. Para que se produzca este fenómeno, la velocidad de deposición de ion cloruro atmosférico debe ser alta y superar un umbral crítico de aproximadamente 300 mg Cl^-/m^2·día. A demás el desprendimiento de las capas de herrumbre del sustrato de acero tiene lugar debido a fluctuaciones de temperatura que exceden las fuerzas de adhesión entre ambos.

Las gruesas capas de herrumbre exfoliadas se componen de múltiples estratos, herrumbre pulverulenta (herrumbre interlaminar) y láminas compactas de herrumbre. Estas láminas son muy imperfectas y presentan grietas, abundantes vacíos y zonas de herrumbre intralaminar. Su grosor aumenta con el tiempo de exposición. Las láminas compactas de óxido están compuestas principalmente por los oxihidróxidos de hierro lepidocrocita (γ-FeOOH) y goetita (α-FeOOH) y maghemita (γ-$Fe_2O·H_2O$ mientras que la herrumbre interlaminar es rica en la fase akaganeita.

Mecanismos de corrosión atmosférica y su dependencia de la salinidad atmosférica

Dependiendo del nivel de salinidad atmosférica, la estructura de las capas de productos de corrosión formadas en la superficie de acero presenta dos situaciones extremas, que van desde la formación de una "capa de herrumbre consolidada" (para salinidades relativamente bajas) hasta la formación de gruesas capas altamente imperfectas y agrietadas "capas de herrumbre exfoliadas" (a muy altas salinidades) que se desprenden fácilmente del acero base.

Los mecanismos de corrosión atmosférica en estas dos situaciones son completamente diferentes. En el caso de una "capa de herrumbre consolidada", se produce un mecanismo de corrosión controlado por difusión, en el que las especies agresivas de la atmósfera (oxígeno, agua y cloruro) pasan a través de la capa de herrumbre para interactuar con el acero subyacente. La reacción catódica predominante es la reducción de oxígeno disuelto en la película acuosa. La velocidad de corrosión depende de la concentración de iones cloruro en la atmósfera. Estos iones se incorporan a las películas de humedad condensadas o películas acuosas depositadas sobre la superficie del acero y aceleran el proceso de corrosión atmosférica. Los productos de corrosión formados están compuestos principalmente de lepidocrocita y goetita, y en menor medida magnetita y akaganeita.

En el caso de una "capa de herrumbre exfoliada", la alta concentración de cloruro en la capa acuosa depositada sobre la superficie del acero da lugar a la formación de cloruro ferroso, que hidroliza el agua, elevando notablemente la acidez del electrolito. En esta situación, la reacción catódica de evolución de hidrógeno es predominante, acelerando el proceso de corrosión. La alta concentración de cloruro, las condiciones ácidas y el agotamiento de oxígeno en la intercara acero/ herrumbre conducen a la formación de altos contenidos de akaganeita y magnetita en la capa de óxido.

La capa de herrumbre exfoliada se compone de diferentes estratos, alternando subcapas de herrumbre altamente consistentes y compactas (láminas) y subcapas de herrumbre muy porosas de poca consistencia (herrumbre interlaminar). El interior de las láminas es altamente rico en maghemita (por transformación en estado sólido de la magnetita), mientras que la herrumbre interlaminar presenta altos contenidos en goetita y akaganeita.

7. PROBLEMÁTICA PENDIENTE

Como en cualquier Tesis Doctoral, a lo largo de la investigación surgen distintos interrogantes científicos que no llegan a esclarecerse totalmente con los medios experimentales disponibles en ese momento. Paso, a continuación, a exponer alguno de ellos.

La velocidad de depósito de cloruros en una atmósfera marina (salinidad atmosférica) y su efecto en la corrosión del acero al carbono

Parece estar bien establecido que para velocidades de depósito hasta 600 mg Cl^-/m^2·día la relación entre ambos parámetros, salinidad y corrosión, es lineal. Para velocidades de depósito superiores a ese valor son muy limitados en la literatura científica los estudios de corrosión atmosférica llevados a cabo. A tenor de los resultados obtenidos en nuestro estudio hay un aumento exponencial de la corrosión del acero en el intervalo 300 – 1000 mg Cl^-/m^2·día para posteriormente disminuir ligeramente para salinidades del orden de 2000 mg Cl^-/m^2·día; sin embargo, es escasa la información obtenida a esta altísimas velocidades de depósito de cloruro. Se presentan, dudas sobre si la corrosión en estas condiciones se estabiliza, sigue aumentando o bien disminuye. Sería importante, por tanto, disponer de mayor información en este tipo de atmósferas costeras.

Sobre los productos de corrosión (fases de herrumbre) formadas sobre el acero al carbono en atmósferas marinas

Hemos visto que las fases de herrumbre encontradas por XRD, técnica de caracterización más comúnmente utilizada en estos estudios, son: lepidocrocita, goetita, akaganeita y, magnetita/maghemita.

i. Magnetita/maghemita

La técnica XRD presenta una importante limitación cuando se trata de diferenciar ambas fases de herrumbre, ya que las dos muestran prácticamente idénticos difractogramas (estructuras cristalinas muy similares). La dificultad se acentúa aún más al tratarse de mezclas con otras fases, como ocurre en las capas de herrumbre formadas en atmósferas marinas. La utilización conjunta de varias técnicas sensibles a estos dos compuestos, p. ej. espectroscopía Raman y Mössbauer, de forma complementaria, resulta imprescindible para una mejor discriminación de ambas fases.

ii. Productos de corrosión amorfos

El problema de la discriminación de fases se exacerba al tratarse de fases menos cristalizadas (amorfos): feroxihita, ferrihidrita, etc. Existe escasa información publicada sobre la

caracterización de estas fases de gran reactividad electroquímica, así como sobre la cuantificación de su contenido en las capas de herrumbre formadas sobre el acero expuesto a la atmósfera. Esta investigación es imprescindible para profundizar en los mecanismos de la corrosión atmosférica.

iii. Akaganeita

Ha quedado bien establecido en esta Memoria la importancia de esta fase de herrumbre en la aceleración del proceso de corrosión atmosférica marina del acero al carbono. No existen dudas sobre el mecanismo de formación de la akaganeita, si, en cambio, sobre el proceso de su reducción electroquímica a óxidos amorfos de tipo espinela (magnetita/maghemita) en la etapa húmeda de los ciclos de humectación/ secado.

El fenómeno de exfoliación de las gruesas capas de herrumbre formadas en las atmósferas marinas con elevadas velocidades de depósito de cloruros.

La exposición del acero al carbono a atmósferas marinas muy severas conduce a la formación de capas de herrumbre muy gruesas que tienden a exfoliarse (desprenden) del sustrato de acero. La mayor singularidad de estas capas consiste en la existencia en su interior de subcapas de herrumbre compacta (ricas en maghemita) alternadas con subcapas de herrumbre de muy baja consistencia (ricas en akaganeita). En la Memoria se propone un mecanismo complejo de formación de estas gruesas capas de herrumbre, con una estructura tipo sándwich integrada por una o varias subcapas de herrumbre compacta, que llegado un punto se desprenden (exfolian) del sustrato de acero. Sin embargo convendría clarificar algunos interrogantes, para la total comprensión del fenómeno, tales como:

(a) La compacidad (volumen molar) de las distintas subcapas.
(b) El papel que pueden desempeñar en el proceso las propiedades mecánicas de estas subcapas: tensiones de compresión/ expansión, formación de vacíos etc.
(c) Las causas que motivan la aparición de una o varias subcapas de herrumbre compacta en el interior de estas gruesas capas de herrumbre. Sobre esta cuestión pensamos que el secado “extremo” de la capa de herrumbre, todavía no desprendida, puede contribuir de algún modo a la formación de una segunda capa de herrumbre compacta cuando se inicie una nueva etapa de humectación de la capa de herrumbre.

8. BIBLIOGRAFÍA

1. T.P. HOAR, «*Report of the Committee on Corrosion and Protection*», London, Dept. of Trade and Industry, 1971.

2. J. KRUGUER, «Cost of metallic corrosion», in *Uhlig's Corrosion Handbook*, R. Winston Revie (ed.), Hoboken, New Jersey, John Wiley and Sons, 2011, pp. 15-20.

3. H.R. AMBLER and A.A.J. BAIN, «Corrosion of metals on the tropics», *Journal of Applied Chemistry* 5 (1955) 437-527.

4. K. BARTON, «*Protection against atmospheric corrosion: theories and methods*», London, John Wiley and Sons, 1976.

5. T. NISHIMURA, H. KATAYAMA, K. NODA and T. KODAMA, «Electrochemical behavior of rust formed on carbon steel in a wet/dry environment containing chloride ions», *Corrosion* 56(9) (2000) 935-941.

6. T. NISHIMURA, K. TANAKA and Y. SHIMIZU, «Effect of NaCl on rusting of steel in wet and dry corrosion cycle», *Journal of The Iron Steel Institute of Japan* 81 (1995) 1079-1084.

7. EN ISO 9223, «*Corrosion of metals and alloys - Corrosivity of atmospheres - Classification, determination and estimation*», Brussels, European Committee for Standardization, 2012.

8. I.S. COLE, W.D. GANTHER, J.D. SINCLAIR, D. LAU and D.A. PATERSON, «A study of the wetting of metal surfaces in order to understand the process controlling atmospheric corrosion», *Journal of the Electrochemical Society* 151(12) (2004) B627-B635.

9. E. SCHINDELHOLZ and R.G. KELLY, «Wetting phenomena and time of wetness in atmospheric corrosion: a review», *Corrosion Reviews* 30(5/6) (2012) 135-170.

10. R. FERNÁNDEZ PATIER, «La contaminación atmósferica en España. Niveles que alcanzan algunos contaminantes atmosféricos con influencia en los fenómenos de corrosión», in *Mapas de España de Corrosividad Atmosférica*, M. Morcillo and S. Feliu (eds.), Madrid, CYTED, 1993, pp. 31-53.

11. EN ISO 8565, «*Metals and alloys - Atmospheric corrosion testing - General requirements*», Geneva, International Organization for Standardization, 2011.

12. EN ISO 9225, «*Corrosion of metals and alloys - Corrosivity of atmospheres - Measurement of environmental parameters affecting corrosivity of atmospheres*», Brussels, European Committee for Standardization, 2012.

13. I. DÍAZ, «*Corrosión atmosférica de aceros patinables de nueva generación*», Tesis Doctoral, Madrid, Universidad Complutense, 2012.

14. W. CALLISTER, «*Introducción a la Ciencia e Ingeniería de los Materiales*», Vol. 1, Barcelona, Reverte, 1996.

15. C.R. HUBBARD and R.L. SNYDER, «RIR-Measurement and use in quantitative XRD», *Powder Diffraction* 3 (1988) 74-77.

16. H.M. RIETVELD, «A profile refinement method for nuclear and magnetic structures», *Journal of Applied Crystallography* 2 (1969) 65-71.

17. D.L. BISH and S.A. HOWARD, «Quantitative phase analysis using the Rietveld method», *Journal of Applied Crystallography* 21 (1988) 86-91.

18. ASM INTERNATIONAL and MATERIAL PHASES DATA SYSTEM, «*Pearson's Crystal Structure - Database for inorganic compounds - Release 2015/16*», Ohio, ASM International, 2015.

19. A. RAMAN, B. KUBAN and A. RAZVAN, «The application of infrared spectroscopy to the study of atmospheric rust systems—I. Standard spectra and illustrative applications to identify rust phases in natural atmospheric corrosion products», *Corrosion Science* 32(12) (1991) 1295-1306.

20. A. RAMAN and B. KUBAN, «Infrared spectroscopic analysis of phase transformation processes in rust layers formed on weathering steels in bridge spans», *Corrosion* 44(7) (1988) 483-488.

21. A. RAMAN, A. RAZVAN, B. KUBAN, K.A. CLEMENT and W.E. GRAVES, «Characteristics of the Rust from Weathering Steels in Louisiana Bridge Spans», *Corrosion* 42(8) (1986) 447-456.

22. T. MISAWA, K. ASAMI, K. HASHIMOTO and S. SHIMODAIRA, «Mechanism of atmospheric rusting and protective amorphous rust on low-alloy steel», *Corrosion Science* 14(4) (1974) 279-289.

23. R.M. CORNELL and U. SCHWERTMANN, «*The iron oxides: structure, properties, reactions, occurrences and uses*», 2nd ed, Weinheim, Wiley-VCH Verlag GmbH, 2003.

24. S. AUREL, V. CHIOSA and C. MANDRAVEL, «The characterization of some steel corrosion products by FT-IR spectroscopy», *Chimie Bucharest* 59 (2008) 1266-1270.

25. F. PÉREZ, C. BARRERO MENESES, O. ARNACHE, L. SÁNCHEZ PACHECO, S. PEÑARANDA, K.E. GARCÍA and M. PÉREZ, «Caracterización de herrumbres en procesos de corrosión de aceros en inmersión total», *Revista Colombiana de Física* 39(1) (2007) 83-86.

26. Y. MA, Y. LI and F. WANG, «The effect of β-FeOOH on the corrosion behavior of low carbon steel exposed in tropic marine environment», *Materials Chemistry and Physics* 112 (2008) 844-852.

27. H. NAMDURI and S. NASRAZADANI, «Quantitative analysis of iron oxides using Fourier transform infrared spectrophotometry», *Corrosion Science* 50(9) (2008) 2493-2497.

28. J.A. JAÉN, O. ADAMES, J. IGLESIAS and C. HERNÁNDEZ, «Caracterización de la pátina protectora del acero patinable ASTM A709 HPS 70W del puente centenario», *Tecnociencia* 13(2) (2011) 81-99.

29. R. BALASUBRAMANIAN and A.V.R. KUMAR, «Characterization of Delhi iron pillar rust by X-ray diffraction, Fourier transform infrared spectroscopy and Mössbauer spectroscopy», *Corrosion Science* 42 (2000) 2085-2101.

30. E. MURAD and J.L. BISHOP, «The infrared spectrum of synthetic akaganéite, β-FeOOH», *American Mineralogist* 85(5-6) (2000) 716-721.

31. M. ISHII, M. NAKAHIRA and T. YAMANAKA, «*Infrared absorption spectra and cation distributions in (Mn, Fe)$_3$O$_4$*», Vol. 11, 1972.

32. R.A. ANTUNES, I. COSTA and D.L.A. DE FARIA, «Characterization of corrosion products formed on steels in the first months of atmospheric exposure*», Journal of Materials Research* 6 (2003) 403-408.

33. J.G. CASTAÑO, C.A. BOTERO, A.H. RESTREPO, E.A. AGUDELO, E. CORREA and F. ECHEVERRÍA, «Atmospheric corrosion of carbon steel in Colombia*», Corrosion Science* 52 (2010) 216-223.

34. K.K. SAGOE-CRENTSIL and F.P. GLASSER, «Constitution of green rust and its significance to the corrosion of steel in Portland cement*», Corrosion* 49 (1993) 457-463.

35. D. DE LA FUENTE, I. DIAZ, J. SIMANCAS, B. CHICO and M. MORCILLO, «Long-term atmospheric corrosion of mild steel*», Corrosion Science* 53(2) (2011) 604-617.

36. A. RAMAN, S. NASRAZADANI and L. SHARMA, «Morphology of rust phases formed on weathering steels in various laboratory corrosion test*», Metallography* 22 (1989) 79-96.

37. A. RAZVAN and A. RAMAN, «Morphology of rust phases formed on naturally weathered weathering steels in bridge spans*», Practical Metallography* 23(5) (1986) 223-236.

38. A. RAMAN, S. NASRAZADANI, L. SHARMA and A. RAZVAN, «Morphology of rust phases formed on weathering steels during outdoor atmospheric exposure in open, bold locations*», Practical Metallography* 24(12) (1987) 577-589.

39. A. RAMAN, S. NASRAZADANI, L. SHARMA and A. RAZVAN, «Morphology of rust phases formed on weathering steels during outdoor atmospheric exposure in sheltered locations under the bridges*», Practical Metallography* 24(11) (1987) 535-548.

40. S. CAMBIER, D. VERREAULT and G. FRANKEL, «Raman investigation of anodic undermining of coated steel during environmental exposure*», Corrosion* 70(12) (2014) 1219-1229.

41. T. OHTSUKA and S. TANAKA, «Monitoring the development of rust layers on weathering steel using in situ Raman spectroscopy under wet-and-dry cyclic conditions*», Journal of Solid State Electrochemistry* 19 (2015) 3559-3566.

42. R.J. THIBEAU, C.W. BROWN and R.H. HEIDERSBACH, «Raman spectra of possible corrosion products of iron*», Journal of Applied Spectroscopy* 32(6) (1978) 532-535.

43. D. THIERRY, D. PERSSON, C. LEYGRAF, D. DELICHERE, S. JOIRET, C. PALLOTTA and A. HUGOT -LE GOFF, «In-situ Raman spectroscopy combined with X-ray photoelectron spectroscopy and nuclear microanalysis for studies of anodic corrosion film formation on Fe-Cr single crystals*», Journal of the Electrochemical Society* 135(2) (1988) 305-310.

44. N. BOUCHERIT, P. DELICHERE, S. JOIRET and A. HUGOT LE GOFF, «Passivity of iron and iron alloys studied by voltammetry and Raman spectroscopy*», Materials Science Forum* 44-45 (1991) 51-62.

45. J. DÜNNWALD and A. OTTO, «An investigation of phase transitions in rust layers using Raman spectroscopy», *Corrosion Science* 29(9) (1989) 1167-1176.

46. T. OHTSUKA, «Raman spectra of passive films of iron in neutral borate solution», *Materials Transaction, JIM* 37(1) (1996) 67-69.

47. D.L.A. DE FARIA, S. VENÂNCIO SILVA and M.T. DE OLIVEIRA, «Raman microspectroscopy of some iron oxides and oxyhydroxides», *Journal of Raman Spectroscopy* 28 (1997) 873-878.

48. S.J. OH, D.C. COOK and H.E. TOWNSEND, «Characterization of iron oxides commonly formed as corrosion products on steel», *Hyperfine Interactions* 112(1) (1998) 59-66.

49. D. NEFF, L. BELLOT-GURLET, P. DILLMANN, S. REGUER and L. LEGRAND, «Raman imaging of ancient rust scales on archaeological iron artefacts for long-term atmospheric corrosion mechanisms study», *Journal of Raman Spectroscopy* 37 (2006) 1228-1237.

50. F. DUBOIS, C. MENDIBIDE, T. PAGNIER, F. PERRARD and C. DURET, «Raman mapping of corrosion products formed onto spring steels during salt spray experiments. A correlation between the scale composition and the corrosion resistance», *Corrosion Science* 50 (2008) 3401-3409.

51. A. DEMOULIN, C. TRIGANCE, D. NEFF, E. FOY, P. DILLMANN and V. L'HOSTIS, «The evolution of the corrosion of iron in hydraulic binders analysed from 46 and 260 year-old buildings», *Corrosion Science* 52(10) (2010) 3168-3179.

52. P. COLOMBAN, «Potential and drawbacks of Raman (micro)spectrometry for the understanding of iron and steel corrosion», in *New Trends and Developments in Automotive System Engineering*, P.M. Chiaberge (ed.), InTech, 2011, pp. 567-589.

53. S. LI and L. HIHARA, «*A micro-Raman spectroscopic study of marine atmospheric corrosion of carbon steel: the effect of akaganeite*», Vol. 162, 2015.

54. T. OHTSUKA, K. KUBO and N. SATO, «Raman spectroscopy of thin corrosion films on iron at 100 to 150 C in air», *Corrosion* 42(8) (1986) 476-481.

55. D. NEFF, S. REGUER, L. BELLOT-GURLET and P. DILLMANN, «Structural characterization of corrosion products on archaeological iron: an integrated analytical approach to establish corrosion forms», *Journal of Raman Spectroscopy* 35 (2004) 739-745.

56. D. NEFF, P. DILLMANN, L. BELLOT-GURLET and G. BERANGER, «Corrosion of iron archaeological artefacts in soil: characterisation of the corrosion system», *Corrosion Science* 47 (2005) 515-535.

57. S. RÉGUER, P. DILLMANN and F. MIRAMBET, «Buried iron archaeological artefacts: corrosion mechanism related to the presence of Cl-containing phases», *Corrosion Science* 49 (2007) 2726-2744.

58. S. HARA, T. KAMIMURA, H. MIYUKI and M. YAMASHITA, «Taxonomy for protective ability of rust layer using its composition formed on weathering steel bridge», *Corrosion Science* 49 (2007) 1131-1142.

59. A. RAMAN, «Atmospheric corrosion problems with weathering steels in Lousiana bridges», in *Degradation of Metals in the Atmosphere, ASTM STP 965*, S.W. Dean and T.S. Lee (eds.), Philadelphia, American Society for Testing and Materials, 1988, pp. 16-29.

60. N. BOWER, «*Principles of Instrumental Analysis*», 4th ed, Vol. 69, 1992.

61. R.A. NYQUIST and R.O. KAGEL, «Infrared spectra of inorganic compounds», in *Handbook of Infrared and Raman Spectra of Inorganic Compounds and Organic Salts*, San Diego, Academic Press, 1971, pp. 1-18.

62. J. ALCÁNTARA, D. DE LA FUENTE, B. CHICO, J. SIMANCAS, I. DÍAZ and M. MORCILLO, «Marine atmospheric corrosion of carbon steel: a review», *Materials* 10(4) (2017) 406.

63. E. MURAD and J.H. JOHNSTON, «Iron oxides and oxyhydroxides», in *Mössbauer Spectroscopy Applied to Inorganic Chemistry*, G.J. Long (ed.), New York, PlenumPress, 1987, pp. 507-582.

64. M. MORCILLO, J.M. GONZÁLEZ-CALBET, J.A. JIMÉNEZ, I. DÍAZ, J. ALCÁNTARA, B. CHICO, A. MAZARÍO-FERNÁNDEZ, A. GÓMEZ-HERRERO, I. LLORENTE and D. DE LA FUENTE, «Environmental conditions for akaganeite formation in marine atmosphere mild steel corrosion products and its characterisation», *Corrosion* 71(7) (2015) 872-886.

65. D. DE LA FUENTE, J. ALCÁNTARA, B. CHICO, I. DÍAZ, J.A. JIMÉNEZ and M. MORCILLO, «Characterisation of rust surfaces formed on mild steel exposed to marine atmospheres using XRD and SEM/micro-Raman techniques», *Corrosion Science* 110 (2016) 253-264.

66. M. MORCILLO, R. WOLTHUIS, J. ALCÁNTARA, B. CHICO, I. DÍAZ and D. DE LA FUENTE, «Scanning electron microscopy/microRaman: a very useful technique for characterizing the morphologies of rust phases formed on carbon steel in atmospheric exposures», *Corrosion* 72(8) (2016) 1044-1054.

67. M. MORCILLO, B. CHICO, J. ALCÁNTARA, I. DÍAZ, R. WOLTHUIS and D. DE LA FUENTE, «SEM/micro-Raman characterization of the morphologies of marine atmospheric corrosion products formed on mild steel», *Journal of the Electrochemical Society* 163 (2016) C426-C439.

68. J. ALCÁNTARA, B. CHICO, J. SIMANCAS, I. DÍAZ, D. DE LA FUENTE and M. MORCILLO, «An attempt to classify the morphologies presented by different rust phases formed during the exposure of carbon steel to marine atmospheres», *Materials Characterization* 118 (2016) 65-78.

69. M. MORCILLO, B. CHICO, J. ALCÁNTARA, I. DÍAZ, J. SIMANCAS and D. DE LA FUENTE, «Atmospheric corrosion of mild steel in chloride - rich environments. Questions to be answered», *Materials and Corrosion* 66(9) (2015) 882-892.

70. J.P. RILEY and R. CHESTER, «*Chemical Oceanography*», 2nd ed, Vol. 7, London, Academic Press Inc., 1978.

71. M.E.R. GUSTAFSSON and L.G. FRANZÉN, «Dry deposition and concentration of marine aerosols in a coastal area», *Atmospheric Environment* 30 (1996) 977-989.

72. S. FELIU, M. MORCILLO and B. CHICO, «Effect of distance from sea on atmospheric corrosion rate», *Corrosion* 55(9) (1999) 883-891.

73. R. OHBA, K. OKABAYASHI, M. YAMAMOTO and T. TSURU, «A method for predicting the content of sea salt particles in the atmosphere», *Atmospheric Environment* 24A(4) (1990) 925-935.

74. M.J. TEN HARKEL, «The effects of particle-size distribution and chloride depletion of sea-salt aerosols on estimating atmospheric deposition at a coastal site», *Atmospheric Environment* 31(3) (1997) 417-427.

75. W.A. MCKAY, J.A. GARLAND, D. LIVESLEY, C.M. HALLIWELL and M.I. WALKER, «The characteristics of the shore-line sea spray aerosol and the landward transfer of radionuclides discharged to coastal sea water», *Atmospheric Environment* 28(20) (1994) 3299-3309.

76. B. LE MÉHAUTÉ, «An introduction to hydrodynamics and water wares», Springer Study (ed.), New York, Springer-Verlag, 1976, pp. 197-272.

77. S. NESHYBA, «*Oceanography*», New York, Wiley, 1987.

78. D.C. BLANCHARD and A.H. WOODCOCK, «The production, concentration and vertical distribution of the sea-salt aerosol», *Annals of the New York Academy of Sciences* 338 (1980) 330-347.

79. J.W. FITZGERALD, «Marine aerosol: a review», *Atmospheric Environment* 25A (1991) 533-545.

80. J. ALCÁNTARA, B. CHICO, I. DÍAZ, D. DE LA FUENTE and M. MORCILLO, «Airborne chloride deposit and its effect on marine atmospheric corrosion of mild steel», *Corrosion Science* 97 (2015) 74-88.

81. G.R. MEIRA, C. ANDRADE, C. ALONSO, I.J. PADARATZ and J.C. BORBA JR, «Salinity of marine aerosols in a Brazilian coastal area - Influence of wind regime», *Atmospheric Environment* 41(38) (2007) 8431-8441.

82. J. WU, «Evidence of sea spray produced by bursting bubbles», *Science* 212 (1981) 324-326.

83. T.A. MCMAHON and P.J. DENISON, «Empirical atmospheric deposition parameters. A survey», *Atmospheric Environment* 13(5) (1979) 571-585.

84. M. MORCILLO, B. CHICO, E. OTERO and L. MARIACA, «Effect of marine aerosol on atmospheric corrosion», *Materials Performance* 38 (1999) 72-77.

85. L. ESPADA, A.M. GONZÁLEZ, A. SÁNCHEZ and P. MERINO, «Estudio de la velocidad de corrosión de aceros de bajo contenido de carbono en nieblas salinas de distinta concentración», *Revista Iberoamericana de Corrosión y Protección* XIX(4) (1988) 227-229.

86. M. KIMURA, T. MIZOGUCHI, H. KIHIRA and M. KANEKO, «Various scale analyses to create functioning corrosion products», in *Characterization of Corrosion*

Products on Steel Surfaces, Y. Waseda and S. Suzuki (eds.), Heildelberg, Advances in Materials Research, Springer, 2006, pp. 245-272.

87. H. KIHIRA, «Colloidal aspects of rusting of weathering steel », in *Electrical phenomena at interfaces, fundamentals, measurements and applications*, H. Ohshima and K. Furusawa (eds.), New York, Marcel Dekker, Inc., 1998, pp. 429-440.

88. J.P. JOLVIET, «*Metal Oxide Chemistry and Synthesis*», West Sussex, England, John Wiley & Sons Ltd., 2000.

89. T. ISHIKAWA, T. YOSHIDA, K. KANDORI, T. NAKAYAMA and S. HARA, «Assessment of protective function of steel rust layers by N_2 adsorption*», Corrosion Science* 49(3) (2007) 1468-1477.

90. P. LOPESINO, «Resultados sin publicar*»,* (2016).

91. T. ISHIKAWA, A. MAEDA, K. KANDORI and A. TAHARA, «Characterization of rust on Fe-Cr, Fe-Ni, and Fe-Cu binary alloys by Fourier transform infrared and N_2 adsorption*», Corrosion* 62(7) (2006) 559-567.

92. I. DÍAZ, H. CANO, D. DE LA FUENTE, B. CHICO, J.M. VEGA and M. MORCILLO, «Atmospheric corrosion of Ni-advanced weathering steels in marine atmospheres of moderate salinity*», Corrosion Science* 76 (2013) 348-360.

93. E. MURAD, «Mössbauer and X-ray data on β-FeOOH*», Clay Minerals* 14 (1979) 273-283.

94. D. REZEL and J.M.R. GENIN, «The substitution of chloride ions to OH^- - Ions in the akaganeite beta ferric oxyhydroxide studied by Mössbauer effect*», Hyperfine Interactions* 57 (1990) 2067-2075.

95. A. ASKEY, S.B. LYON, G.E. THOMPSON, J.B. JOHNSON, G.C. WOOD, M. COOKE and P. SAGE, «The corrosion of iron and zinc by atmospheric hydrogen chloride*», Corrosion Science* 34(2) (1993) 233-247.

96. G.T. BURSTEIN, «Passivity and localised corrosion*»*, in *Corrosion Metal/Environment Reactions*, L.L. Shreir, R.A. Jarman and G.T. Burstein (eds.), Oxford, Butterworth - Heinemann, 1994, pp. 118-150.

97. P. REFAIT and J.M.R. GENIN, «The mechanism of oxidation of ferrous hydroxychloride β-$Fe_2(OH)_3Cl$ in aqueous solution: the formation of akaganeite vs goethite*», Corrosion Science* 39 (1997) 539-553.

98. C. RÉMAZEILLES and P. REFAIT, «Formation, fast oxidation and thermodynamic data of Fe(II) hydroxychlorides*», Corrosion Science* 50(3) (2008) 856-864.

99. C. RÉMAZEILLES and P. REFAIT, «On the formation of β-FeOOH (akaganeite) in chloride-containing environments*», Corrosion Science* 49(2) (2007) 844-857.

100. P. REFAIT, M. ABDELMOULA and J.M.R. GÉNIN, «Mechanisms of formation and structure of green rust one in aqueous corrosion of iron in the presence of chloride ions*», Corrosion Science* 40(9) (1998) 1547-1560.

101. P. REFAIT and J.M.R. GÉNIN, «The oxidation of ferrous hydroxide in chloride-containing aqueous media and Pourbaix diagrams of green rust one», *Corrosion Science* 34(5) (1993) 797-819.

102. P.J. SEREDA, «Weather factors affecting corrosion of metals», in *Corrosion in Natural Environments, ASTM STP 558*, W.H. Ailor, S.W. Dean and F.H. Haynie (eds.), Philadelphia, PA, American Society for Testing and Materials, 1974, pp. 7-22.

103. J.J. SANTANA, F.J. SANTANA and J.E. GONZÁLEZ, «XRD and SEM studies of the layer of corrosion products for carbon steel in various different environments in the province of Las Palmas (The Canary Islands, Spain)», *Corrosion Science* 44 (2002) 2425-2438.

104. A.F. WELLS, «*Structural Inorganic Chemistry*», 4th ed, London, Oxford University Press, 1975.

105. E.J. FASISKA, «Structural aspects of the oxides and oxyhydrates of iron», *Corrosion Science* 7(12) (1967) 833-839.

106. H. SCHWARZ, «Über die wirkung des magnetits beim atmosphärischen rosten und beim unterrosten von anstrichen», *Werkstoffe und Korrosion* 23(8) (1972) 648-663.

107. A.K. SINGH, «Mössbauer and X-ray difracction phase analysis of rusts from atmospheric test sites with different environments in Sweden», *Corrosion Science* 25(10) (1985) 931-945.

108. T. ISHIKAWA, Y. KONDO, A. YASUKAWA and K. KANDORI, «Formation of magnetite in the presence of ferric oxyhydroxides», *Corrosion Science* 40(7) (1998) 1239-1251.

109. H. TANAKA, R. MISHIMA, N. HATANAKA, T. ISHIKAWA and T. NAKAYAMA, «Formation of magnetite rust particles by reacting iron powder with artificial α-, β- and γ-FeOOH in aqueous media», *Corrosion Science* 78(0) (2014) 384-387.

110. U.R. EVANS, «Mechanism of rusting», *Corrosion Science* 9 (1969) 813-821.

111. U.R. EVANS and C.A.J. TAYLOR, «Mechanism of atmospheric rusting», *Corrosion Science* 12(3) (1972) 227-246.

112. M. STRATMANN, K. BOHNENKAMP and T. RAMCHANDRAN, «The influence of copper upon the atmospheric corrosion of iron», *Corrosion Science* 27(9) (1987) 905-926.

113. M. STRATMANN and K. HOFFMANN, «In situ Mössbauer spectroscopic study of reactions within rust layers», *Corrosion Science* 29(11–12) (1989) 1329-1352.

114. J.E. HILLER, «Phasenumwandlungen im Rost», *Werkstoffe und Korrosion* 17 (1966) 943-951.

115. R.J. JEFFREY and R.E. MELCHERS. «*The changing composition of the corrosion products of mild steel in severe marine atmospheres*», in *Annual Conference of the Australasian Corrosion Association*, Melbourne, 2012.

116. C. HACES, F. CORVO and N.R. FURET. «*Mecanismo de la corrosión atmosférica del acero en una zona de alta salinidad*», in *Proceedings of the 3rd Iberoamerican Congress of Corrosion and Protection*, Río de Janeiro, ABRACO, 1989.

117. C. LEYGRAF, I. ODNEVALL WALLINDER, J. TIDBLAD and T. GRAEDEL, «*Atmospheric Corrosion*», 2nd ed, Hoboken, New Jersey, The Electrochemical Society Series, John Wiley and Sons, 2016.

118. H. CANO, «*Aceros patinables (Cu, Cr, Ni): Resistencia a la corrosión atmosférica y soldabilidad*», Tesis Doctoral, Madrid, Universidad Complutense, 2013.

119. C. ARROYAVE and M. MORCILLO, «Atmospheric corrosion products in iron and steels*», Trends in Corrosion Research* 2 (1997) 1-16.

120. J.B. HORTON, «*The composition, structure and growth of the atmospheric rust on various steels*», Tesis Doctoral, Bethlehem, Lehigh University, 1964.

121. H. OKADA, Y. HOSOI, K. YUKAWA and H. NAITO, «Structure of the protective and decirative rust formed on low-alloy steels in the atmosphere*», ASM-Trans* 62 (1969) 278-281.

122. I. SUZUKI, Y. HISAMATSU and N. MASUKO, «Nature of atmospheric rust on iron*», Journal of the Electrochemical Society* 127(10) (1980) 2210-2215.

123. M. MORCILLO, B. CHICO, I. DÍAZ, H. CANO and D. DE LA FUENTE, «Atmospheric corrosion data of weathering steels. A review*», Corrosion Science* 77 (2013) 6-24.

124. M. MORCILLO, D. DE LA FUENTE, I. DÍAZ and H. CANO, «Atmospheric corrosion of mild steel. A review*», Revista de Metalurgia de Madrid* 47 (2011) 426-444.

125. T. ISHIKAWA, R. KATOH, A. YASUKAWA, K. KANDORI, T. NAKAYAMA and F. YUSE, «Influences of metal ions on the formation of β-FeOOH particles*», Corrosion Science* 43 (2001) 1727-1738.

126. H. CANO, D. NEFF, M. MORCILLO, P. DILLMANN, I. DÍAZ and D. DE LA FUENTE, «Characterization of corrosion products formed on Ni 2,4 wt% – Cu 0,5 wt% – Cr 0,5 wt% weathering steel exposed in marine atmospheres*», Corrosion Science* 87 (2014) 438-451.

127. B. CHICO, J. ALCÁNTARA, E. PINO, I. DÍAZ, J. SIMANCAS, A. TORRES-PARDO, D. DE LA FUENTE, J.A. JIMÉNEZ, J.F. MARCO, J.M. GONZÁLEZ-CALBET and M. MORCILLO, «Rust exfoliation on carbon steels in chloride-rich atmospheres*», Corrosion Reviews* 33(5) (2015) 263-282.

128. M. MORCILLO, B. CHICO, D. DE LA FUENTE, J. ALCÁNTARA, I. ODNEVALL WALLINDER and C. LEYGRAF, «On the mechanism of rust exfoliation in marine environments*», Journal of the Electrochemical Society* 164(2) (2017) C8-C16.

129. I.L. ROZENFELD. «*Atmospheric corrosion of metals. Some questions of theory*», in *Proceedings of the 1st International Congress on Metallic Corrosion*, London, Butterworths, 10-15 April 1961.

130. N. MIKHAILOVSKII, «*Atmospheric Corrosion of Metals and Protection Methods*», Moscow, 1989.

131. P. KELLER, «Occurrence, formation and phase transformation of β-FeOOH in rust», *Werkstoffe und Korrosion* 20(2) (1969) 102-108.

132. T. ISHIKAWA, R. ISA, K. KANDORI, T. NAKAYAMA and T. TSUBOTA, «Influences of metal chlorides and sulfates on the formation of β-FeOOH particles by aerial oxidation», *Journal of the Electrochemical Society* 151 (2004) B586-B594.

133. D. DE LA FUENTE, I. DÍAZ, J. ALCÁNTARA, B. CHICO, J. SIMANCAS, I. LLORENTE, A. GARCÍA-DELGADO, J.A. JIMÉNEZ, P. ADEVA and M. MORCILLO, «Corrosion mechanisms of mild steel in chloride-rich atmospheres», *Materials and Corrosion* 67 (2015) 227-238.

134. A. SÁNCHEZ, «*Corrosión atmosférica y marina en las zonas costeras gallegas*», Tesis Doctoral, Vigo, Universidad de Santiago, 1987.

135. D.C. COOK, «Spectroscopic identification of protective and non-protective corrosion coatings on steel structures in marine environments», *Corrosion Science* 47(10) (2005) 2550-2570.

136. S. HARA, M. YAMASHITA, T. KAMIMURA and M. SATO, « Synchrotron XRD analysis of local positions in laminated heavy rust layer formed on weathering steel bridge», *Journal of the Japan Institute of Metals* 71(3) (2007) 346-353.

137. D.C. COOK and A.C. VAN ORDEN. «*The Luling bridge: an inside story*», in *Proceedings Corrosion*, NACE, 2000.

138. U. SCHWERTMANN and R.M. TAYLOR, «The transformation of lepidocrocite to goethite», *Clay Minerals* 20 (1972) 151-158.

139. E. PINO, J. ALCÁNTARA, B. CHICO, I. DÍAZ, J. SIMANCAS, D. DE LA FUENTE and M. MORCILLO, «Atmospheric corrosion of mild steel in marine atmospheres», *Corrosão e Protecção de Materiais* 34 (2015) 35-41.

140. M. STRATMANN, K. BOHNENKAMP and H.J. ENGELL, «An electrochemical study of phase-transitions in rust layers», *Corrosion Science* 23(9) (1983) 969-985.

141. V. LAIR, H. ANTONY, L. LEGRAND and A. CHAUSSÉ, «Electrochemical reduction of ferric corrosion products and evaluation of galvanic coupling with iron», *Corrosion Science* 48(8) (2006) 2050-2063.

142. E. MATSUBARA, S. SUZUKI and Y. WASEDA, «Corrosion mechanism of iron from an X-ray structural viewpoint», in *Characterization of Corrosion Products on Steel Surfaces*, Y. Waseda and S. Suzuki (eds.), Heidelberg, Advances in Materials Research, Springer, 2006, pp. 105-129.

9. ANEXOS (PUBLICACIONES)

ANEXO I

“Airborne chloride deposit and its effect on marine atmospheric corrosion of mild steel.”

Corrosion Science 97 (2015) 74–88

Contents lists available at ScienceDirect

Corrosion Science

journal homepage: www.elsevier.com/locate/corsci

Airborne chloride deposit and its effect on marine atmospheric corrosion of mild steel

J. Alcántara, B. Chico, I. Díaz, D. de la Fuente, M. Morcillo *

National Centre for Metallurgical Research (CENIM-CSIC), Avda. Gregorio del Amo, 8, 28040 Madrid, Spain

ARTICLE INFO

Article history:
Received 8 October 2014
Accepted 18 April 2015
Available online 28 April 2015

Keywords:
A. Mild steel
B. SEM
B. XRD
C. Atmospheric corrosion
C. Rust

ABSTRACT

Research has been carried out for one year in six pure marine atmospheres with annual average chloride deposition rates of 70–1906 mg Cl^-/m^2 day. A study of some environmental parameters and their influence in the airborne chloride deposit on the site has been accomplished. The paper also considers mild steel corrosion rate and the resulting corrosion products and layers, and its dependence of atmospheric salinity of the site. In addition to lepidocrocite and goethite, high akaganeite and magnetite contents were found in the corrosion products. Additional magnetite formation is possible due to the transformation of lepidocrocite.

1. Introduction

The atmospheric corrosion of metals is an electrochemical process which is the sum of the individual processes that take place when an electrolyte layer forms on the metal. This electrolyte can be either an extremely thin moisture film (just a few monolayers) or an aqueous film of hundreds of microns in thickness (when the metal is perceptibly wet). Aqueous precipitation (rain, fog, etc.) and humidity condensation due to temperature changes (dew) are the main promoters of metallic corrosion in the atmosphere.

Atmospheric salinity in coastal regions generates a notable increase in the atmospheric corrosion rate compared to a clean atmosphere, as marine chlorides dissolved in the moisture layer considerably raise the conductivity of the electrolyte film on the metal and tend to destroy any passivating films. The corrosion rate is a function of the Cl^- ion activity.

In 1973 Barton noted that the mechanism governing the effects of Cl^- ions in atmospheric corrosion had not been fully explained, and that the higher corrosion rate of steel in marine atmospheres could also be due to other causes [1]: (a) being hygroscopic, chloride species (NaCl, $CaCl_2$ or $MgCl_2$) promote the electrochemical corrosion process, favouring the formation of electrolytes at relatively low relative humidity (RH) values; and (b) the solubility of the corrosion products formed also plays an important role. Thus, in the case of iron, which does not form stable basic chlorides, the action of chlorides is more pronounced than with other metals (Zn, Cu, etc.) whose basic salts are only slightly soluble. Since then, there has been great progress in scientific knowledge of atmospheric corrosion in marine environments. A brief review of state of the art on the matter is subsequently presented.

In addition to the corrosion products commonly found in the atmospheric exposure of steel, namely lepidocrocite (γ-FeOOH) and goethite (α-FeOOH), in marine atmospheres the formation of akaganeite (β-FeOOH) and magnetite (Fe_3O_4) is particularly important. The formation mechanisms and the identification of these phases in corrosion layers have been and continue to be the cause of considerable controversy.

The research presented in this paper has a double aim. On the one side a study of some environmental parameters and their influence in the airborne chloride deposit on the site has been accomplished: spectral wave height in the nearby sea, the wind speed and the marine wind run. It is of interest to carry out studies in relation with this matter. A greater knowledge of this effect would enable us, for example, to make a rough estimate atmospheric salinities simply by analysing information about wave high in the nearby and wind characteristics already existing in the environmental databases of any country. The inclusion of salinity values in the numerous published damage functions between corrosion and environmental factors [2–4] would also make it possible to estimate atmospheric corrosion simply from environmental databases without having to carry out natural corrosion tests in a specific site, which involve long waiting times and considerable expenses. On the other hand the paper assesses the mild steel corrosion rate and analyses the resulting corrosion products and layers, and its dependence of atmospheric salinity of the site of exposure.

* Corresponding author. Tel.: +34 91 553 8900; fax: +34 91 534 7425.
E-mail address: morcillo@cenim.csic.es (M. Morcillo).

http://dx.doi.org/10.1016/j.corsci.2015.04.015
0010-938X/

The exceptional weather conditions experienced at the test site over the year in which the study was carried out (April 2013–March 2014) led to very high Cl^- ion deposition rates of up to 1906 mg Cl^-/m^2 day, not normally found in the scientific literature on marine atmospheric corrosion, which have given rise to high levels of akaganeite and magnetite/maghemite in the corrosion layers formed in the different testing stations.

1.1. Atmospheric corrosion of mild steel in marine atmospheres. A brief state of the art

Atmospheric salinity in coastal regions promotes a notable increase in the atmospheric corrosion rate of steel compared to a clean atmosphere. The corrosion rate is a function of Cl^- ion activity in the moisture film, under which the steel corrodes according to the anodic reaction:

$$Fe \rightarrow Fe^{2+} + 2e^- \quad (1)$$

where the cathodic process consists of the reduction of oxygen dissolved in the moisture film:

$$1/2O_2 + H_2O + 2e^- \rightarrow 2OH^- \quad (2)$$

The OH^- ions formed migrate towards the anodic zones forming $Fe(OH)_2$ as the initial rust product:

$$Fe^{2+} + 2OH^- \rightarrow Fe(OH)_2 \quad (3)$$

There is currently consensus that in pure atmospheres (free of pollutants) or atmospheres with low Cl^- deposition the main corrosion products formed on steel are lepidocrocite, goethite and magnetite. The oxidation by oxygen from the air of Fe^{2+} ions produced as a consequence of the dissolution of Fe in the thin aqueous films formed in periods of wetting of the metallic surface, lead to the precipitation and crystallisation of lepidocrocite in the drying stage via the prior formation of $Fe(OH)_2$; the atmospheric corrosion process starts with the formation of lepidocrocite [5].

Evans [6] was the first researcher to electrochemically postulate that the oxidation of iron was balanced by the reduction of rust in periods of high water content within the porous structure of the rust. Subsequently, Strattmann et al. [7], in an electrochemical study of phase transitions in already formed rust layers, proposed a three-stage rust formation mechanism (wetting, wet surface, and drying), demonstrating that the anodic reaction of iron dissolution in the first stage was not balanced by the cathodic reaction of reduction of the oxygen present in the moisture layer, but by the reduction of the pre-existing oxide, giving rise to a "reduced lepidocrocite" transition phase.

$$\gamma\text{-FeOOH (lepidocrocite)} + H^+ + e^- \rightarrow \gamma\text{-Fe}\cdot OH\cdot OH \text{ (reduced lepidocrocite)} \quad (4)$$

Once the reducible lepidocrocite is exhausted, importance is acquired by the cathodic reaction of reduction of the oxygen dissolved in the rust layer (2), whose slow diffusion in the electrolyte-filled pores in the rust layer means that the metallic dissolution rate is highly limited. During drying, oxygen diffusion is extremely high due to the thinning of the electrolyte film, giving rise to high corrosion rates, where (2) is the cathodic reaction, accompanied by the reoxidation of the previously formed reduced lepidocrocite to lepidocrocite.

$$2\gamma\text{-Fe}\cdot OH\cdot OH + 1/2O_2 \rightarrow 2\gamma\text{-FeOOH} + H_2O \quad (5)$$

In Cl^--rich atmospheres, Nishimura et al. note that more than the role played by lepidocrocite in the corrosion process of steel in chloride-free atmospheres, the formation of akaganeite is the cause that extremely accelerates the atmospheric corrosion process [8]. In a laboratory study these researchers saw that at low Cl^- concentrations the oxyhydroxide that formed was lepidocrocite, while high Cl^- concentrations led to the formation of akaganeite via the formation of green rust, $Fe(OH, Cl)_{2.55}$ (GR1), a process that required a certain time for the complete disappearance of GR1. They show that akaganeite can also be reduced electrochemically in the corrosion process, being consumed in the wetting period of the metallic surface. Subsequently, Antony et al. [9] and Lair et al. [10] also experimentally saw that lepidocrocite was not the only species of the different phases comprising the rust that was electrochemically reducible by Fe (galvanic couple), and that the order of reducing capacity was as follows:

ferrihydrite, GR > akaganeite and feroxyhyte > lepidocrocite

The reduction of goethite by iron was not favoured, and if it occurred it would only be at an extremely low reaction rate.

Nomura et al. [11], in a laboratory study in which Fe is made to react with a 3% NaCl solution, note that lepidocrocite forms on the rust surface that is easily accessible to oxygen dissolved in the aqueous layer, whereas the formation of akaganeite and magnetite takes place in the interior of the rust layer, specifically at the steel/rust interface, where the access of oxygen from the air is more limited. The formation of these phases takes place by the transformation, after a certain time, of basic iron complexes containing Cl^- and the slow oxidation of Fe, respectively. Thus the oxygen deficit and the presence of a high Cl^- content are fundamental factors for akaganeite formation.

Nowadays it is fully accepted that the iron oxychloride β-$Fe_2(OH)_3Cl$ is involved in the formation of akaganeite and that this requires a certain time to develop from the metastable precursors [$Fe(OH)_2$]. In research carried out by Remazeilles and Refait [12] it was seen that for low $R = [Cl^-]/[OH^-]$ ratios ($R < 1.16$) the formation of $Fe(OH)_2$ takes place, while for $R > 2.25$ only β-$Fe_2(OH)_3Cl$ forms and for intermediate R values ($1.40 < R < 2.25$) both form. These same researchers have also carried out very important laboratory studies that have enormously clarified the akaganeite formation mechanism, controlling the reaction of $FeCl_2{\cdot}4H_2O$ with NaOH by varying the $R = [Cl^-]/[OH^-]$ ratio [13]. For $R \geqslant 8$, i.e. in conditions of great excess of ferrous chloride, akaganeite formation only takes place via the formation of intermediate GR1 components, whereas at small excesses of $FeCl_2$ only lepidocrocite forms. When $R \leqslant 6$ the formation of goethite takes place, and when $6.5 \leqslant R \leqslant 8$ both goethite and akaganeite form. The akaganeite formation mechanism implies the presence of high Cl^- concentrations (at least 2–3 mol L^{-1}) and acid conditions (pH 4–6), by the hydrolysis of ferrous chloride ($FeCl_2$), conditions that occur in confined spaces where Cl^- ions accumulate: metal/corrosion products interface, crevice zones, etc.

With regard to the formation of magnetite, attention is drawn to the work of Ishikawa et al. [14]. These researchers saw that in oxygen-free aqueous solutions the reaction of the oxyhydroxides (goethite, akaganeite and lepidocrocite) with Fe^{2+} ions led to the formation of magnetite across a broad range of temperatures (25–100 °C) and pH (3–13), with a notable reduction in the oxyhydroxide content. The magnetite concentration depended on the $R = [Cl^-]/[OH^-]$ molar ratio of the suspension, showing a maximum for $R = 2$, and Fe_3O_4 is produced by the reaction of dissolved species of FeOOH with those $Fe(OH)_2$. The maximum Fe_3O_4 content was in the order:

akaganeite > lepidocrocite ≫ goethite

In a recent study of Tanaka et al. [15], in which the oxyhydroxides were made to react with iron powder, the amount of magnetite formed was greater with akaganeite than with lepidocrocite, not taking into account when the oxyhydroxide was goethite.

The high steel corrosion rates promoted by the presence of akaganeite give rise to an expansion of the rust volume which leads to

the formation of cracks, flakes and exfoliation [16]. Asami and Kikuchi [17,18], for their part, note that akaganeite is more porous than lepidocrocite and goethite, capturing more chlorides from the atmosphere and acting as a Cl^- ion reservoir. In this respect, attention is drawn to a study by Ishikawa et al. [19] on the protective characteristics of rust layers formed on steel exposed to the atmosphere by determination of the specific surface area (SA). They note that the SA of rusts decreases as the corrosion and atmospheric salinity increases, due to the growth of rust particles with the corrosion process, increasing the diameter of the pores and forming less and less compact rust layers with low protective properties.

2. Experimental

Research has been carried out in the pure marine atmosphere of Cabo Vilano wind farm (Camariñas, Spain) at six corrosion stations located at different distances from the shore (Table 1). The atmospheric SO_2 content was negligible (0.7–0.9 mg SO_2/m^2 day) [20]. Meteorological information of the site was supplied by the Spanish Meteorological Agency (AEMET) in a weather station located very close (25 m) to corrosion station 1. Likewise, information about the wave height in the sea in this area has been supplied by the Villano-Sisargas buoy belonging to the Spanish State Port Authority.

The corrosion stations (Fig. 1) were affixed using magnets to the north-facing side of different wind turbine towers, which according to historic records is the predominant wind direction at the exposure site. Each station consisted of a rack containing a device at the bottom to measure the atmospheric salinity (wet candle) [21] and the mild steel specimens, whose composition is shown in Table 2, at the top.

The exposure time of the test specimens was 12 months (April 2013–March 2014). One series of mild steel specimens and the wet candles for analysis of Cl^- ion deposition rate were withdrawn every 3 months, while mild steel specimens for mass loss calculations were withdrawn after 6 and 12 months of exposure.

The attack experienced by the steel as a consequence of its exposure to the atmosphere was determined in triplicate using the mass loss technique, in accordance with Annex A, designation C.3.5 of ISO 8407 standard [22].

The soluble chloride content of the rust has been determined. The procedure consisted of extraction from 100 mg of rust in 20 mL of distilled water in an ultrasonic bath for 2 h at room temperature. The solution was then filtered and made up to a constant volume, and the chlorides in solution were analysed by means of a selective electrode.

The study has taken into account the rust formed on both sides of the specimens: side A (skyward-facing) and side B (groundward-facing). A detailed description has been made of the rust formed, taking into account aspects such as: (a) colouring and texture, (b) formation of rust particles (grains) or flakes and (c) occurrence of exfoliation [23]. Grain size has been determined using the "tape method", consisting of adhering a 2×2 cm^2 piece of adhesive tape to the rust layer, pressing firmly and evenly on the surface, and lifting off to examine the size and density of rust particles [24].

The corrosion products formed have been characterised by XRD using a Bruker AXS X-ray diffractometer (model D8 Advance) equipped with a cobalt X-ray tube and a diffracted beam monochromator. The applied voltage was 40 kV and the filament current was 30 mA. Angular scanning was carried out from 10° to 80°, with a step width of 0.03° and a step acquisition time of 3 s. XRD analysis was carried out with the rust remaining on the sample after removing the exfoliation laminas, when this occurred. The rust was screened to obtain a particle size of less than 125 μm. Semi-quantitative analysis was performed using the I/I_C ratio, also known as the Relative Intensity Ratio (RIR) method from the Powder Diffraction Files (PDF) card [25].

Microscopic observation has been carried out using a Hitachi S4800 high resolution scanning electron microscope (SEM) (3 nm in high vacuum mode) equipped with secondary electron and backscattered electron detectors and an Oxford Inca energy dispersive microanalysis system (EDS). Microscopic analysis was carried out on cross sections, observing the structure of the rust layer, pit formation and Cl^- distribution in the rust, and on the rust surface, observing the morphology of the different rust phases.

Table 1
Location of test sites, distance between the testing stations and the shore in northerly direction and annual average salinity values.

Corrosion station	Location (coordinates)	Distance to the shore (m)	Annual average salinity (mg Cl^-/m^2 day)
1	43°9′9.80″N 9°12′16.71″W	332	1906[a]
2	43°9′4.54″N 9°12′13.38″W	420	665
3	43°8′58.12″N 9°12′0.13″W	590	272
4	43°8′46.83″N 9°12′1.40″W	945	206
5	43°8′37.85″N 9°11′54.18″W	1250	109
6	43°8′51.22″N 9°10′45.09″W	2400	70

[a] This value corresponds to the first 6 months of exposure.

3. Results

3.1. Meteorological characteristics of Cabo Vilano wind farm test site

Table 3 shows climate parameters characterising the environment in the study period of April 2013 to March 2014, taken from the Spanish Meteorological Agency (AEMET) database for Cabo Vilano weather station located just a few metres away from station 1. Table 3 also shows the significant spectral wave heights in the study period supplied by Villano-Sisargas buoy of the State Port Authority buoy network, close to Cabo Vilano.

The area is seen to present a high relative humidity (RH_{avg} 83.5%), mild temperature (T_{avg} 13 °C) and high precipitation (9908 l/m^2/year and >150 days of precipitation/year). These values indicate high times of wetness of the metallic surface which favour atmospheric corrosion processes. It is also noted that the test site is subjected to strong winds, mainly north-easterly, and the average wind speed is high (29.2 km/h), as is the number of days per year with gusts of more than 70 km/h (97 days). The preferential wind direction and the proximity of the stations to the shore indicate that the test stations have been subjected to strong marine winds with considerable entrainment of marine aerosol (atmospheric salinity) which has greatly boosted the metallic corrosion process.

The study period (April 2013–March 2014) has been atypical from a meteorological point of view. The atmospheric salinity values found during this period have been much higher than those determined in previous studies carried out in this area in earlier periods [20], as shown in Table 4. In fact, the salinity found in the study period has been 3–4 times higher. This is related with the higher wave heights observed in this marine region and the longer marine wind runs registered in the area, as will be seen later.

3.2. Atmospheric salinity

Fig. 2 sets out the three-monthly atmospheric salinity data obtained in the different test stations during the study year. Data

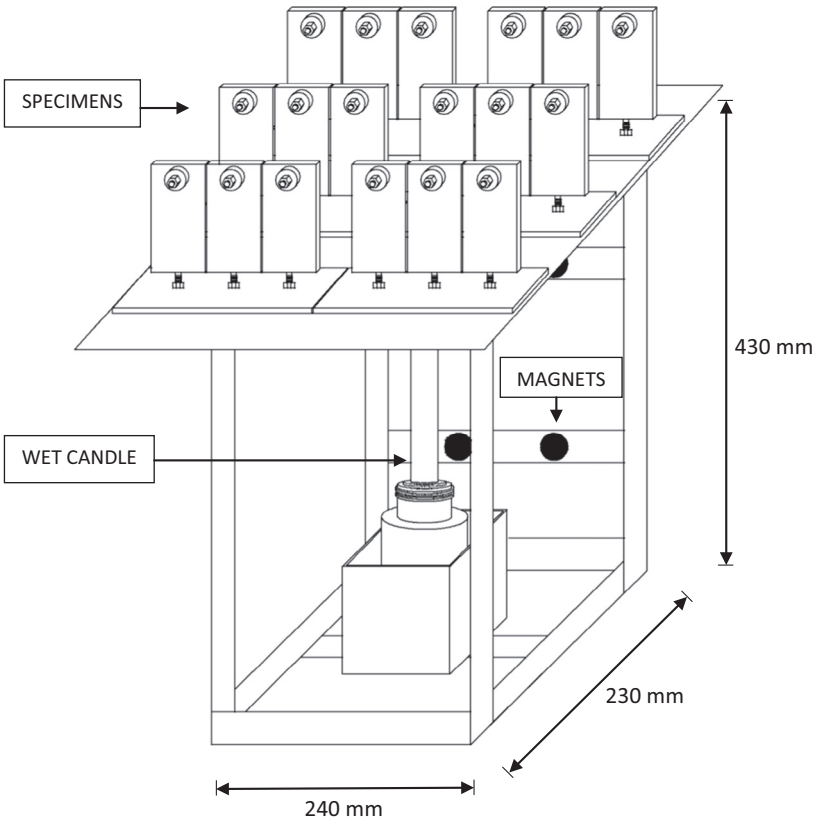

Fig. 1. Atmospheric corrosion testing station.

Table 2
Test specimen dimensions and chemical composition of the steel used.

Type of steel	Dimensions (mm)	Chemical composition (wt.%)							
		C	Si	Mn	P	S	Cr	Ni	Cu
Mild steel	100 × 50 × 1.0	0.13	0.09	0.55	0.02	0.018	0.12	0.02	0.02

Table 3
Meteorological characteristics of Cabo Vilano wind farm test site in the study year (April 2013–March 2014).

	T (°C)	HR (%)	Total precipitation (l/m^2)	Days of precipitation	Average wind speed (km/h)	Significant spectral wave height (m)	Number of days with maximum gusts ⩾70 km/h	Wind direction with frequencies ⩾20%
April'13	11.7	78.0	874	15	35	3.38	10[a]	NE, NNE
May'13	12.4	78.8	917	14	30	2.46	2[a]	NE
June'13	14.3	85.8	464	13	29	2.28	9[a]	NE
July'13	16.8	86.8	138[a]	>6	[b]	1.61	2[a]	[b]
August'13	17.6	85.0	202	9	29	1.52	9[a]	NE
September'13	[b]	[b]	74[a]	>7	21	1.84	2[a]	NE, NNE
October'13	14.9	85.8	634[a]	>4	29	2.42	18[a]	SSW, S
November'13	12.2	77.8	9814	17	32	3.24	13[a]	NE
December'13	[b]	[b]	1140[a]	>9	[b]	4.14	7[a]	[b]
January'14	9.7	88.0	1636[a]	>22	26	5.08[a]	8[a]	WSW
February'14	9.5	84.5	2242[a]	>20	36	4.97[a]	14[a]	WSW, SSW
March'14	10.9	84.0	606[a]	>14	25	3.22	8[a]	$WSW_{(15-20\%)}$, $N_{(15-20\%)}$
Annual average	13.0[a]	83.5[a]	9908[a]	>150	29.2[a]	3.01[a]	97[a]	

[a] Values obtained with available data.
[b] Data not available.

for station 1 in the 3rd and 4th periods is missing due to the detachment of the wet candles by the strong winds. As can be seen, the atmospheric salinities recorded at the area during the study year are high. Table 1 sets out the annual average salinity values for the different testing stations, which go from 70 to 1906 mg Cl^-/m^2 day. Attention is drawn to the very high salinity value at station 1, which is higher than the salinity values found normally in the literature.

Table 4
Average atmospheric salinity values for different time periods at stations 1, 3 and 6.

Corrosion station	Time period	Average salinity (mg Cl^-/m^2 day)
1	April 2010–September 2010	393.3
	April 2011–September 2011	606.0
	April 2013–September 2013	1905.5
3	March 2010–March 2011	73.9
	March 2011–March 2012	68.9
	April 2013–April 2014	266.3
6	March 2010–March 2011	29.1
	March 2011–March 2012	11.6
	April 2013–April 2014	69.4

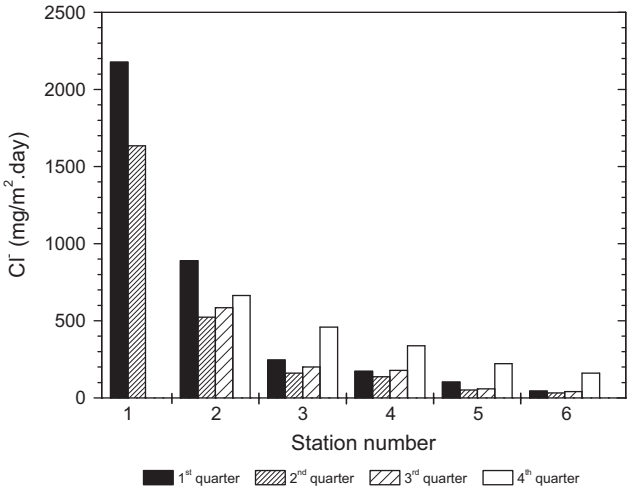

Fig. 2. Three-month atmospheric salinity data for the different testing stations over the study year. Data is not available for station 1 in the third and fourth period due to the detachment of the wet candles by the strong winds.

3.3. Corrosion losses

Table 5 sets out the corrosion rate data found for mild steel exposed for 6 and 12 months in the different testing stations. A drop in the corrosion rate is seen as the distance from the shore increases (decrease in atmospheric salinity) (Table 1). The corrosion rate decreases considerably as the exposure time goes on.

3.4. Characteristics of the rusts formed

3.4.1. Appearance

The colour of the rust varies with the corrosivity of the atmosphere, steel type, exposure time, etc. In the present research, lighter rust colours have been seen in the atmospheres with greater salinity (more corrosive) and darker rusts in the less aggressive atmospheres. Similarly, the rust colour becomes darker as the exposure time progresses. A difference is also seen between the appearance of rust on either side of the test specimens, with darker colourings on the skyward side (side A) and lighter colours on the groundward side (side B).

Table 5
Corrosion rates obtained for mild steel after 6 and 12 months of exposure at the corrosion stations.

Steel	Corrosion station	Corrosion rates (μm/year)	
		6 months	12 months
Mild steel	1	352.5	[a]
	2	289.6	240.5
	3	201.9	123.8
	4	149.0	78.2
	5	118.6	65.5
	6	114.4	50.1

[a] Data not available.

With regard to the texture of the rusts formed, this is seen to vary according to the atmospheric aggressivity. In general terms, a more heterogeneous surface appearance and coarser granulometry is found in the more aggressive stations (stations with very high salinity like stations 1 and 2) which becomes more accentuated with exposure time. In contrast, more homogenous textures and finer granulometries are seen in the atmospheres with lower salinity values, i.e. stations 5 and 6. Stations 3 and 4, with intermediate salinity values, present an intermediate appearance half-way between the other two.

As has been noted in Section 2, a tape test was used to determine the morphology of the outermost rust. The morphology of the outer rust can take the form of grains or particles, flakes, or exfoliations (layers or laminates) [23]. By way of example, Fig. 3 presents the granulometries of the rusts formed on mild steel after 6 and 12 months of atmospheric exposure in different testing stations. In the more aggressive atmospheres (stations 1–3) the formation of exfoliations and coarse flakes is seen, while in the less aggressive atmospheres (stations 4–6) exfoliations are not seen and flakes and grains are finer. The groundward side of the specimens (side B), which is subject to higher moisture retention and atmospheric salinity, generally presents larger flakes and particles than the skyward side (side A).

3.4.2. Nature of the corrosion products formed

3.4.2.1. Soluble chloride content of the rust. In general, as the salinity of the atmosphere decreases, so the soluble chloride content of the rust layer removed by vigorous brushing also decreases; a small iron-wire brush was used for that purpose. Rainwater rinses the rust layer, leaching soluble chlorides and giving rise to a lower chloride concentration on the skyward side of the specimens (Table 6) [26].

Following the removal of the outer rust layer by gentle brushing, the inner rust layer, removed by vigorous brushing, is seen to present a higher soluble chloride content (Table 7). The soluble chlorides present in the outer rust layer are more easily leached out by the action of rain water. This fact is often underlined in the literature [1]. As the exposure time increases, the soluble chloride content in the rust layer decreases notably [27].

3.4.2.2. Oxides and oxyhydroxides. The composition of the rust layer depends on the characteristics of the surface electrolyte layer that forms during the exposure of steel to the atmosphere and which gives rise to the atmospheric corrosion process; and therefore varies with the type of atmosphere [28].

As has been noted in Section 1 of this paper, the corrosion products most commonly found in rust formed on steel exposed at the atmosphere are lepidocrocite, goethite and magnetite/maghemite. Hiller [5] considers that lepidocrocite is the first crystalline corrosion product to form. In mild acid solutions lepidocrocite is transformed into goethite, which is the most stable of the different oxyhydroxides. Magnetite is also one of the main constituents of rust and is usually detected in the inner zone closest to the base steel, where the oxygen concentration is depleted. In marine atmospheres, where the surface electrolyte contains chloride, akaganeite also forms [29] and magnetite content is usually higher [5]. Other phases (feroxyhyte, ferrihydrite, maghemite, etc.) can also be formed.

The phases maghemite (γ-Fe_2O_3) and hematite (α-Fe_2O_3) have also been found in other studies on steel surfaces exposed to different types of atmospheres. The former is practically impossible to distinguish from magnetite by XRD as both have similar crystalline

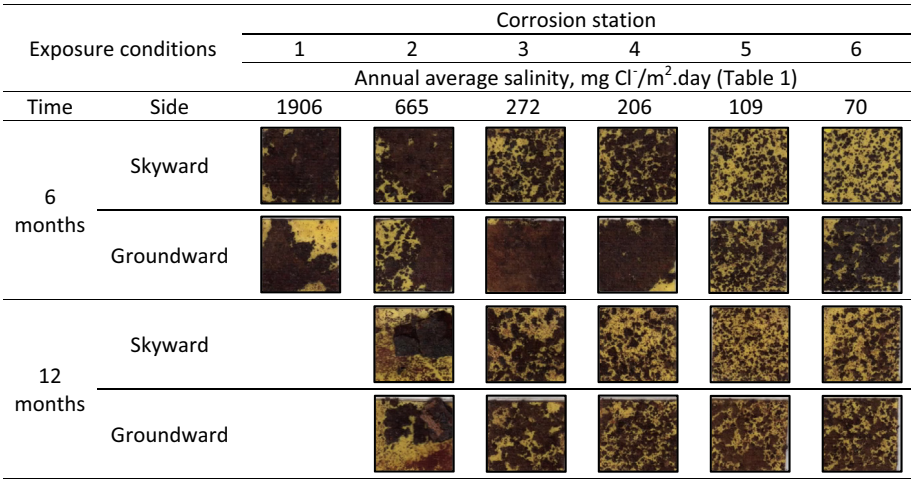

Fig. 3. Granulometries of outermost rusts formed on skyward and groundward-facing side of the specimens after 6 and 12 months of exposure at the different corrosion stations.

Table 6
Soluble chloride contents of the rusts formed on mild steel in three months of exposure at different corrosion stations. Rust removed by vigorous brushing of both sides of the exposed specimens.

Corrosion station	Salinity (mg Cl^-/m^2 day)	Side A (skyward-facing) (wt.%)	Side B (groundward-facing) (wt.%)
1	1906	1.32	1.84
6	70	0.46	1.51

structures (both phases are associated to the diffraction angle next to 35° [30]). The latter is frequently found in industrial atmospheres [30,31].

Fig. 4 by way of example presents the typical diffractogram found in this study. The same phases are always seen but in different proportions. Three iron oxyhydroxides have been identified, lepidocrocite, goethite and akaganeite, as well as the strongest diffraction peak of an iron oxide, magnetite and/or maghemite, which as noted above show practically identical diffractograms and whose identification by XRD is very complicated when mixed with large amounts of the other phases.

Table 8 shows a summary of results of semi-quantitative XRD analysis of the species found in the rust formed on mild steel in different exposure conditions. In all, the lepidocrocite phase is the major corrosion product in the rust, goethite and akaganeite are intermediate components, and magnetite/maghemite is present in a minor way. The high Cl^- ion deposits recorded over the year in the atmospheres of this study explain the formation of abundant akaganeite in the rusts. It is not common to find such high akaganeite contents in marine atmospheric corrosion studies, and in many cases this phase is not detected at all.

3.4.3. Microstructure of the rust layers formed

3.4.3.1. Cross section. SEM observations were made of cross sections of the rust layer formed on mild steel exposed for 3 months

Table 7
Soluble chloride contents of the rust formed on mild steel in three months of exposure at different corrosion stations. Outer rust and inner rust removed by gentle and vigorous brushing, respectively.

Corrosion station	Salinity (mg Cl^-/m^2 day)	Outer rust	Inner rust
3	272	1.40	3.35
5	109	0.27	0.56

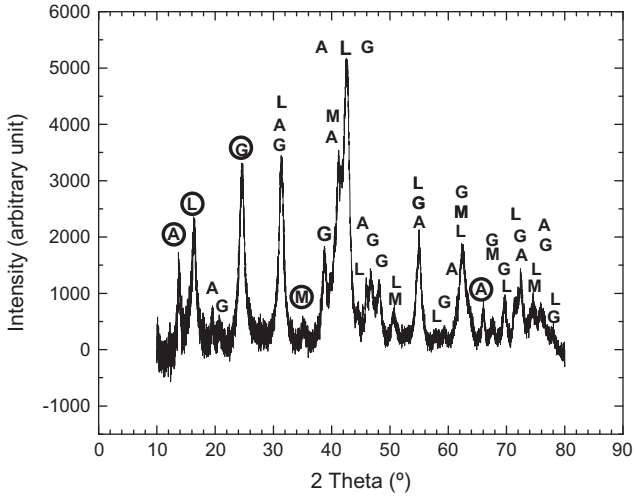

Fig. 4. Typical X-ray diffractogram of the rusts formed on the study steels, showing the presence of lepidocrocite (L), goethite (G), akaganeite (A) and magnetite/maghemite (M) phases. The circled letters mark the strongest diffraction peaks for each phase.

in all the testing stations, analysing by EDS the chemical composition in different areas of the rust layer. In Fig. 5 and Table 9 representative SEM microstructures observed and the corresponding EDS spectra are respectively shown.

3.4.3.2. Rust surface. The morphology of the different rust phases can vary considerably, depending on numerous factors: synthesis method used in the laboratory, formation conditions in the atmosphere, etc. The literature contains few rigorous studies of the surface morphologies of the different rust phases as a consequence of the exposure of carbon steels in different types of atmospheres. Mention may be made of the exhaustive work of Raman et al. [32–37] in which rust phases formed on weathering steels on bridges in Luisiana (United States) were identified by SEM by comparison with rusts synthesised in the laboratory and identified by infrared spectroscopy. In many papers other researchers have assigned morphologies to the different phases in their studies, often making claims of identification without presenting a rigorous analytical check.

Table 8
Results of semi-quantitative XRD analysis of the phases found in rusts formed on mild steel in different exposure conditions.

Corrosion station	Side of the sample	Exposure time (months)	Lepidocrocite	Goethite	Akaganeite	Magnetite/maghemite
1	Side A	3	47.1	24.3	21.7	7.0
	Side B	3	43.7	25.7	25.2	5.4
	Side A	9	29.3	24.2	21.8	24.7
2	Side A	3	44.5	21.8	27.8	5.9
	Side B	3	34.1	26.2	32.5	7.1
	Side A	12	35.8	27.0	12.5	24.7
4	Side A	3	60.1	18.4	17.7	3.8
	Side B	3	52.8	17.9	24.2	5.2
6	Side A	3	62.8	15.2	17.8	4.2
	Side B	3	56.9	16.7	21.2	5.1
	Side A	12	59.6	20.1	17.6	2.8

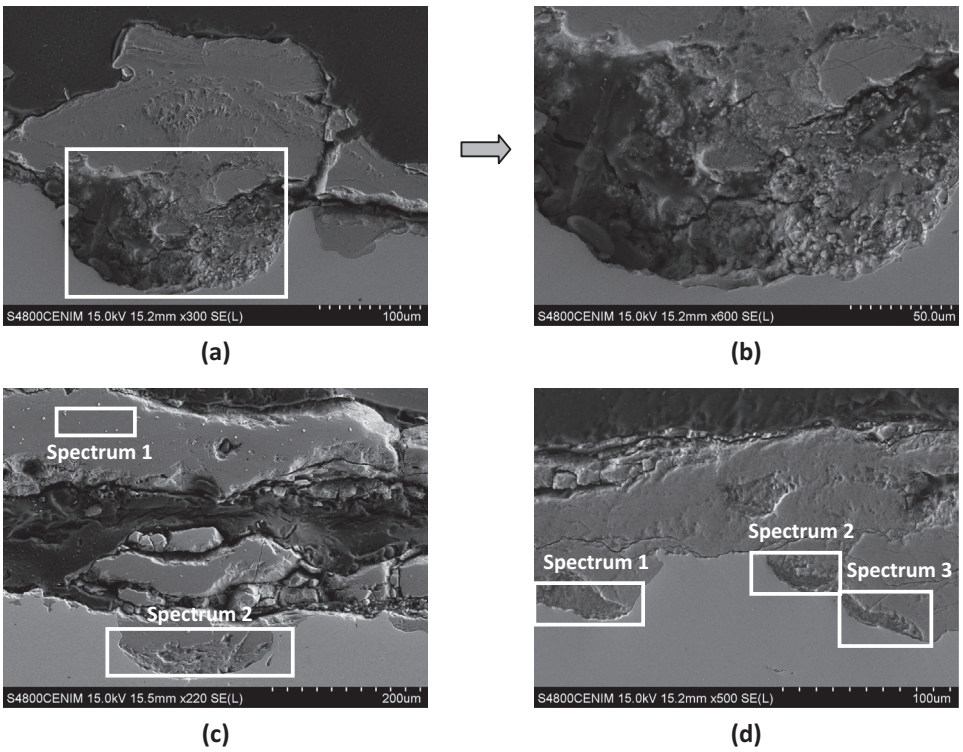

Fig. 5. Cross-section SEM observations of mild steel specimens exposed for 3 months at different corrosion stations. Results of EDS spectra are shown in Table 9. Side A of the sample in station 1 (a and b); side B of the sample in station 1 (c); side B of the sample in station 5 (d).

Table 9
Results of EDS spectra corresponding to different zones in the rust corrosion layers shown in Fig. 5.

Zone (Fig. 5)	Element (atomic%)					
	Fe	O	C	Cl	S	Na
Fig. 5a	16.11	33.00	49.93	0.96	–	–
Fig. 5c (Spectrum 1)	22.21	63.71	12.47	0.69	–	0.93
Fig. 5c (Spectrum 2)	23.11	47.79	27.06	2.04	–	–
Fig. 5d (Spectrum 1)	30.74	39.23	29.02	0.43	0.58	–
Fig. 5d (Spectrum 2)	26.34	39.20	33.95	0.51	–	–
Fig. 5d (Spectrum 3)	29.27	43.42	26.22	0.38	–	–

Based on the findings of Raman et al. [32–37], we tentatively propose the identification of the morphologies of the different phases in our rusts as presented in SEM micrographs in Fig. 6.

The following comments may be made concerning the different morphologies that appear in the rusts formed in the present study: a*morphous rust* does not present any specific crystallographic feature (Fig. 6a); f*eroxyhyte* shows open "rose-type flower" structure with bent and folded laminas (Fig. 6b); f*errihydrite* presents different morphologies: coarse laminas forming "compartments" (Fig. 6c) and laminas resembling tentacles, reminiscent of tree roots (Fig. 6d); g*oethite* presents many different morphologies: thin, straight, sharp laminas (Fig. 6e), whisker-type needles (Fig. 6f), rod-type morphology (Fig. 6g), etc; *lepidocrocite* shows coarse laminas resembling a "worm's nest" (Fig. 6h), whereas *maghemite* and *magnetite* present sandy crystal-like texture (Fig. 6i) and round discs resembling "doughnuts" (Fig. 6j), respectively. Normally the different phases are very close to one another.

Great effort has been dedicated to searching for akaganeite morphologies, bearing in mind the high content of this phase in the corrosion products formed in the atmospheres in the present study. However, the lack of references to rigorous studies in the literature on akaganeite morphologies formed on steel exposed to the atmosphere has prevented us from inequivocally assigning this phase in the SEM observations of our rusts. In a previous study the authors observed by micro-Raman spectroscopy the presence of akaganeite in both the outer and inner rust layers formed on steel

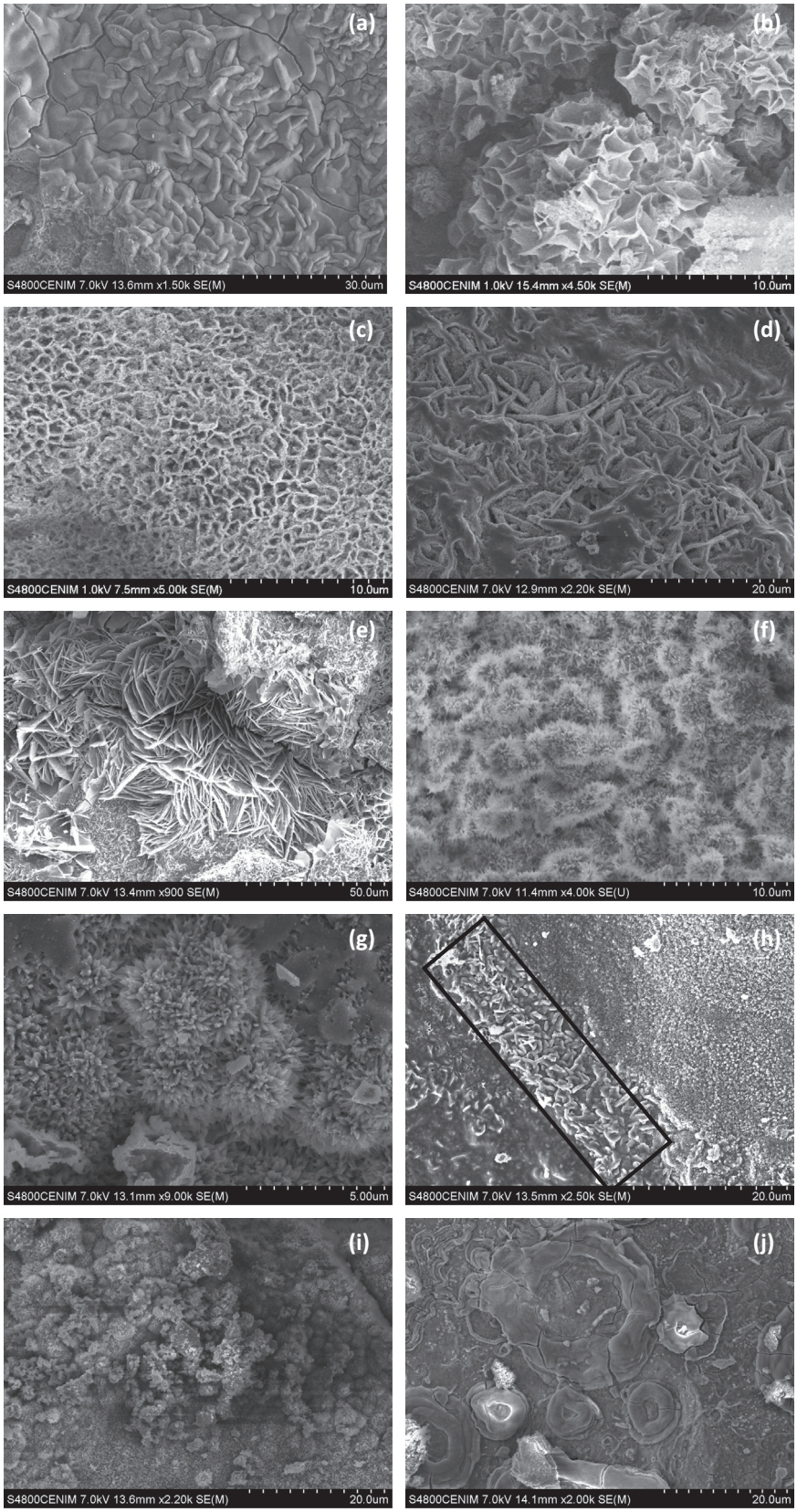

Fig. 6. SEM observations of the outermost surface of the rusts showing different morphologies for the phases formed on mild steel: amorphous rust (a), feroxyhyte (b), ferrihydrite (c and d), goethite (e–g), lepidocrocite (h), maghemite (i) and magnetite (j).

exposed to a marine atmosphere [38]. For this reason, we have used the SEM/Raman technique to identify this phase on the surface of our rusts. With great difficulty, in only one case has it been possible to assign a morphology to this oxyhydroxide (Fig. 7a) in the outer rust layer [39]. The instrumental technique used was a Renishaw structural chemical analyser (SCA), which combines

SEM and Raman spectroscopy. Fig. 7b shows the Raman spectrum obtained, indicating the peaks that correspond with typical characteristics peaks for akaganeite.

4. Discussion

As was pointed out in the introduction of the paper, the research work has been conducted with a double aim: (a) study of some environmental variables and their influence in the airborne chloride deposit on the site, and (b) to assess mild steel corrosion rate and corrosion products and layers and its dependence of atmospheric salinity of the site of exposure.

4.1. Marine aerosol. Its dependence of environmental parameters

4.1.1. Formation of marine aerosol

The wind, which stirs up and entrains sea water, is the force responsible for the salinity present in marine atmospheres. The waves whose breaking leads to the formation of marine aerosol originate in the so-called "generating zones", which are generally associated with the strong winds of storms. Wave height depends not only on the wind speed but also on the size of the generating zone across which the wind blows (fetch) and the number of hours the wind has been blowing (wind persistence). When waves propagate outside the generating zone, through an area of calm, a sea swell is originated. Finally, when the swell reaches the coast the waves become unstable and break [40]. On the high seas the breaking of waves depends on the speed of the wind blowing over them. In the coastal surf zone waves can break without the need for simultaneous wind action, and the amount of aerosol generated is largely dependent on the type of sea floor (uniformity, slope, etc.) and the width of the surf zone [41,42].

In a previous study carried out by Feliu et al. at Tarragona (Spain) a close relationship was seen between salinity and wave height [43], although the average salinity values found were not excessively high (112 mg Cl^-/m^2 day). It has been wished to check this relationship using higher salinity values. The graph in Fig. 8 shows the variation in atmospheric salinity at station 1 in relation to the average spectral wave height (H) supplied by the Villano-Sisargas buoy. This graph has been prepared considering data obtained in previous work carried out by our research group in the same test zone [44,45]. Despite the notable dispersion of the points in the graph, a clear relationship between the two parameters is seen. For salinity values below 800 mg Cl^-/m^2 day, the higher the wave height, the higher the atmospheric salinity. Due to the small amount of information available, the graph does not take into account salinities of more than 800 mg Cl^-/m^2 day, as is the case of station 1 in this study, which registered an unusual average salinity of 1906 mg Cl^-/m^2 day during the first six months of exposure. As can be seen in Fig. 8, the monthly average spectral wave height values (1.5–2.0 m) are sufficient to produce high monthly average salinity values (100–200 mg Cl^-/m^2 day).

4.1.2. Entrainment of marine aerosol inland

Aerosol particles can be entrained inland by marine winds, settling after a certain time and after travelling a certain distance. The wind regime directly influences aerosol production and transportation, and is significantly affected by geostrophic winds, large-scale atmospheric stability, and the difference between diurnally-averaged land and sea temperatures, which varies according to the season of the year. It is also dependent on the latitude, ruggedness of the coastline, and undulation of the land surface [41,42]. A reduction in the size and mass of aerosol particles due to drying of the droplets can considerably increase the entrainment distance.

The largest fraction (by mass) of aerosol particles have diameters of between 8 μm and 80 μm [41]. The largest aerosol particles (diameter >10 μm) remain in the atmosphere for short time periods; the larger the particle size the shorter the time. In contrast, particles of a diameter of <10 μm can travel hundreds of kilometres in the air without settling [46].

It is known that the main effect of marine atmospheres reaches just a few hundreds of metres from the shoreline and subsequently drops off further inland [46]. This initial decrease in the marine aerosol particle concentration (atmospheric salinity) is due mainly to a dry deposition process. Essentially two mechanisms are responsible for the dry deposition of aerosol [47]: (a) sedimentation due to the effect of gravity, and (b) removal by contact of the turbulent air mass with the land. This effect depends on the roughness and type of terrain (open land, presence of vegetation, etc.).

Thus, the possibility of aerosol particles reaching points that are more or less distant from the shoreline will depend on the balance between entrainment inland by the action of marine winds and deposition on the land by the aforementioned mechanisms. This matter was addressed in previous studies [48,49] by developing a simple exponential model of the variation in atmospheric salinity with distance from the shore.

In the present study an exponential relationship is also clearly seen between the atmospheric salinity values obtained in the three-monthly periods from April 2013 to June 2013 (1st quarter)

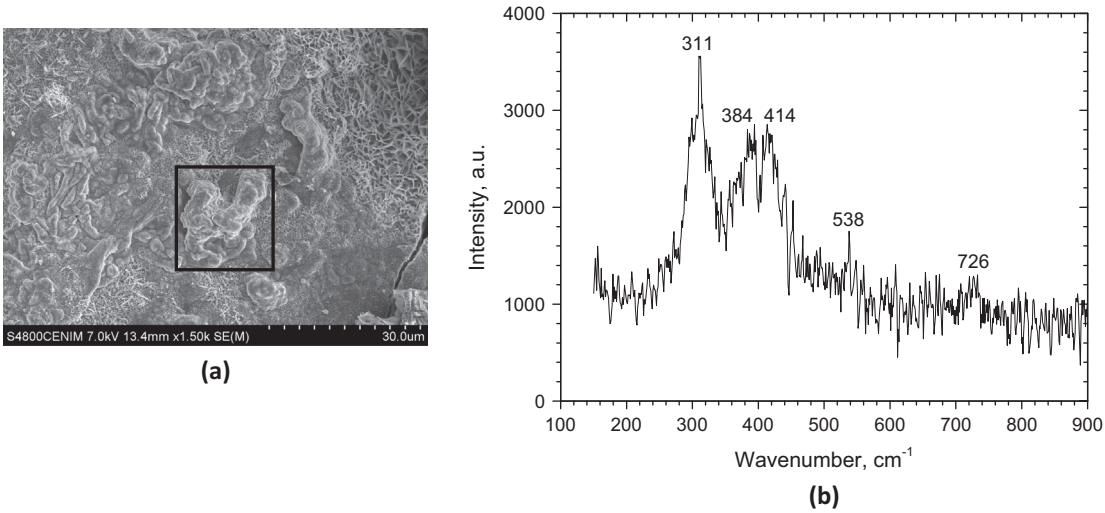

Fig. 7. Akaganeite aggregate (a) and characteristic Raman spectrum of this phase (b).

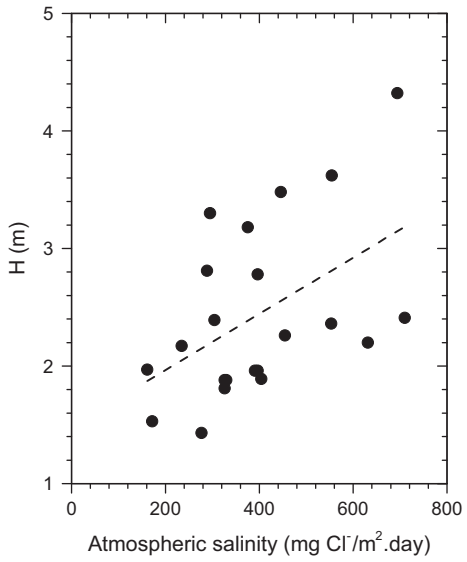

Fig. 8. Variation in monthly average salinity at station 1 with monthly average spectral wave height values (H). Period: April 2010–February 2012. The dashed line shows the general trend.

and July 2013 to September 2013 (2nd quarter) and the distance between stations 1 and 6 and the shoreline (Fig. 9). The corresponding exponential equations would be:

$$Y = 78288.23 \exp\left(\frac{-X}{91.34}\right) + 108.40 \quad (6)$$

$$Y = 163563.84 \exp\left(\frac{-X}{71.25}\right) + 83.03 \quad (7)$$

being Y the atmospheric salinity expressed as mg Cl^-/m^2 day and X the distance from the shore in meters (m).

Unfortunately, complete information is not available for periods 3 (October–December 2013) and 4 (January–March 2014) due to the fact that the strong winds experienced in the area detached the wet candles from station 1, as noted above.

Comparison of the atmospheric salinity at the exposure site (station 1) and the average wind speed fails to yield a clear relationship between both parameters. The calculation of the average wind speed takes into account the wind speeds recorded in all directions and not only the marine winds on the wind rose, which

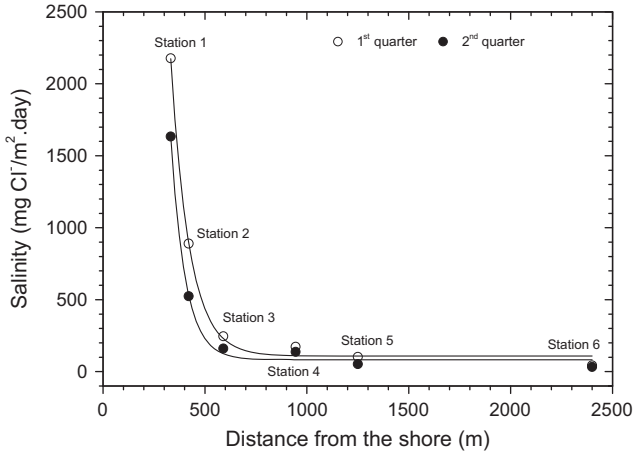

Fig. 9. Variation in atmospheric salinity with distance from the shore. Stations 1–6. April–June 2013 (○) and July–September 2013 (●).

are those that carry the salinity to the testing station. Thus it would be interesting to known whether the atmospheric salinity of the site is related with the run of marine winds, which is the sum of adding together the marine wind speed in each direction multiplied by the time it has been blowing [50]. Fig. 10 has been prepared accordingly and clearly explains the decrease in the salinity value obtained in the 2nd three-month period at station 1 by a decline in the run of all marine winds, especially the most frequent (north-easterly, NE). Therefore, more than the average wind speed in the study area, the total run of marine winds is the parameter that has the greatest influence on the atmospheric salinity of the test site.

4.2. Mild steel marine atmospheric corrosion and its dependence of atmospheric salinity

4.2.1. Corrosion rate versus atmospheric salinity

In studies of atmospheric corrosion in marine atmospheres, a direct relationship is generally established between corrosion and the saline content of the atmosphere. Ambler and Bain [46] were the first to demonstrate this relationship, which has subsequently been addressed in many other papers, such as the work of Morcillo et al. presenting abundant bibliographic information for atmospheric salinities of up to 600 mg Cl^-/m^2 day [48]. It is interesting to extend the atmospheric salinity range to values in excess of 600 mg Cl^-/m^2 day, which are very rarely found in the literature, and to know whether the aforementioned linear relationship between salinity and steel corrosion is maintained. The high salinity values recorded in the study area present a good opportunity in this respect.

Fig. 11 shows the variation in the mild steel corrosion rate with atmospheric salinity in a broader spectrum of airborne salt concentrations. The graph in Fig. 11 has been drawn up using information obtained in the present study and other data taken from the scientific literature [3,44,46,51–76] in an exhaustive bibliographic review (Table 10). Consideration has also been made of other data pertaining to studies currently under way and which will be published in coming papers.

The data (N = 329) was represented in a box-whisker type graph representing the statistical data as separate boxes with markings that indicate the 25, 50 and 75 percentiles. The lines that go from the box correspond to the values ±1.5 × IQR (Interquartile Range), considering values below and above these to be atypical.

There is obviously a great spread in the information collected in the review for a wide variety of reasons. This data dispersion is attributable to uncertainties inherent in the data and the probable influence of other variables with marked effects on corrosion that were not considered in the survey; the salinity of the atmosphere only partly explains the corrosion data. Salinity and corrosion data are sometimes of poor quality due to a number of factors: chloride pollution is sometimes measured by different methods using different units and conversions and equivalences are naturally prone to errors, imprecise corrosion data may be a result of deficient removal of corrosion products, metal attack by pickling baths, or differences in chemical composition, metallographic structure, etc. Corrosion data can also be influenced by the initial conditions, exposure time, specimen size, shape and orientation, and the number of replicates used in corrosion tests, etc. The lack of coincidence between the years when the metal was exposed and the years when the salinity data was recorded, and between the locations of the salinity and corrosion measuring sites, are other potential sources of errors in this context.

Nevertheless, the graph in Fig. 11 offers an important overview of the relationship between the mild steel corrosion rate and atmospheric salinity. For salinities of less than 600 mg Cl^-/m^2 day a linear relationship trend between both parameters can be deduced

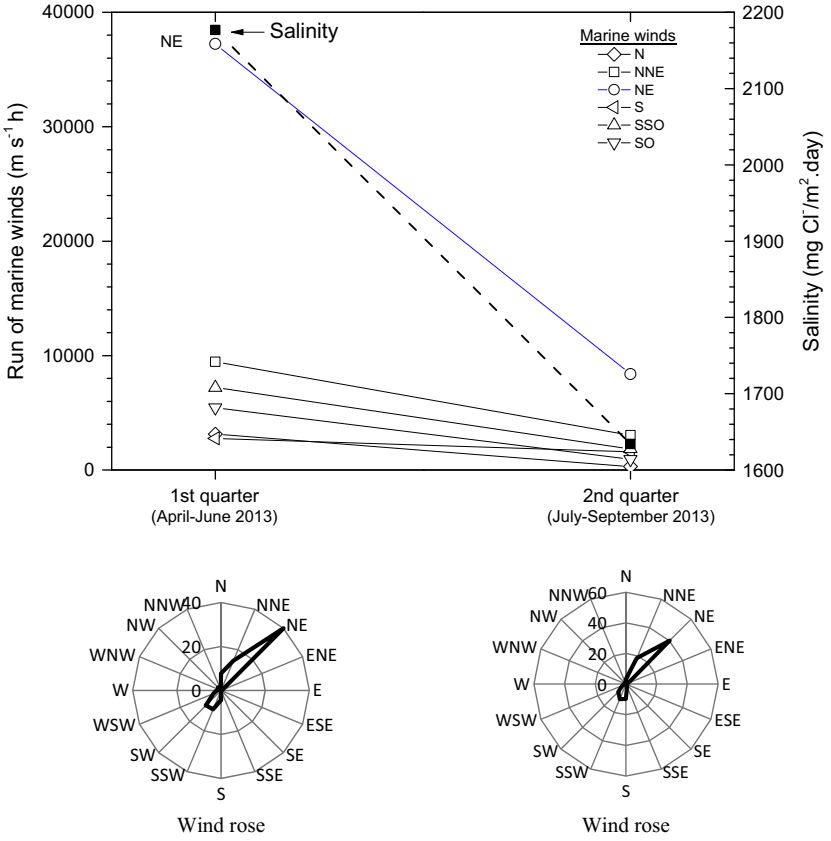

Fig. 10. Salinity data for station 1 and run of the different marine winds in the first two three-month periods of the study. Wind roses for two periods are also shown.

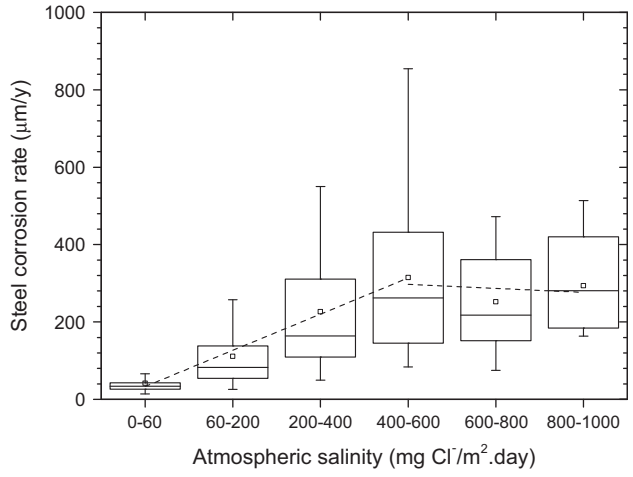

Fig. 11. Variation in the corrosion rate of mild steel with salinity over a broad spectrum of atmospheric salinities. The graph shows a trend (broken line). Information obtained in an exhaustive bibliographic search (Table 10).

Table 10
References used to obtain information on the corrosion rates of mild steel and chloride deposit values, and countries for which information was reported.

Country	Refs.
Argentina	[3]
Australia	[53]
Belgium	[54,55]
Brazil	[3,56]
Chile	[3]
China	[52]
Colombia	[3]
Costa Rica	[3]
Cuba	[3,57–63]
Ecuador	[3]
France	[64]
India	[65–67]
Japan	[64]
Mexico	[3,68]
New Zealand	[69]
Nigeria	[46]
Norway	[64]
Panama	[3]
Peru	[3]
Portugal	[3]
Russia	[70]
Saudi Arabia	[51]
Spain	[3,44,71,72]
Sweden	[64]
United Kingdom	[64,73]
Uruguay	[3]
USA	[64,74]
Venezuela	[3,75]
Vietnam	[76]

[48], in which the mild steel corrosion rate increases considerably with atmospheric salinity. For salinities above this value the corrosion rate seems to be stabilised.

4.2.2. Corrosion rate versus distance from the shore

Bearing in mind the aforementioned relationship between steel corrosion and atmospheric salinity, the variation in corrosion with the distance from the shore should be an exponential function similar to that observed in Fig. 9 between this variable and atmospheric salinity. In fact, Fig. 12, constructed with corrosion rate data obtained after 6 and 12 months of exposure in stations 1–6, shows the fulfilment of an exponential decay function in the corrosion rate with the distance from the shore, a fact that is also seen in

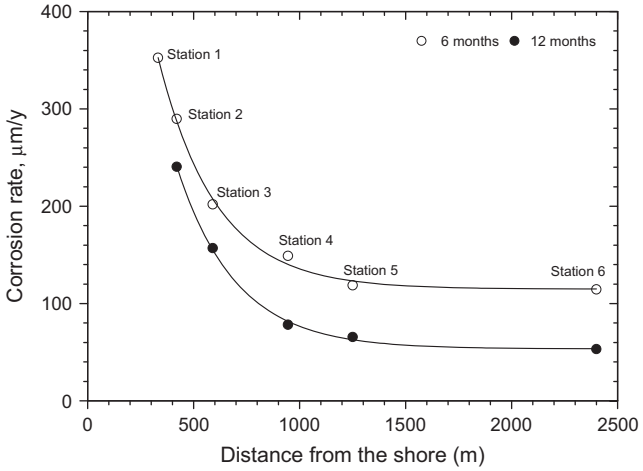

Fig. 12. Variation in the corrosion rate of mild steel with distance from the shore. Stations 1–6. Exposure time: 6 months (○) and 12 months (●). Corrosion data is not available for station 1 for 12 months of exposure due to the wind damage sustained.

other marine environments in different parts of the world, as noted in [49]. The corresponding exponential equations would be:

$$Y = 799.72 \exp\left(\frac{-X}{273.78}\right) + 114.88 \ (6 \text{ months}) \quad (8)$$

$$Y = 852.96 \exp\left(\frac{-X}{277.41}\right) + 53.44 \ (12 \text{ months}) \quad (9)$$

being Y the atmospheric salinity expressed as mg Cl^-/m^2 day and X the distance from the shore in meters (m).

4.2.3. Characteristics of rust layers formed

As can be observed in Fig. 3, the rust formed on mild steel in the stations with very high salinity, around 300 mg Cl^-/m^2 day or higher (stations 1–3), was strongly exfoliated, with rust layers detached in some areas, leaving the steel uncovered (Fig. 5a). This exfoliation phenomenon, widely reported in the literature [23,32,33,77–80], is typical in very severe marine atmospheres. In contrast, other areas presented remains of the rust layer or all the rust layer, albeit notably cracked (Fig. 5c). In the EDS spectra (Table 9) it is possible to observe a high Cl content on the surface of the rust (spectrum 1 in Fig. 5c) and in the pits in the base steel (spectrum in Fig. 5a and spectrum 2 in Fig. 5d), which correspond to chloride ion either from a NaCl deposit or from akaganeite formation. In this type of atmospheres the base steel undergoes strong pitting with deep pits that hold a considerable chlorine content, in correspondence with the high soluble chloride contents found in the corrosion products (Tables 6 and 7). The rust layer formed in stations with lower salinity (stations 4–6) was not exfoliated and presented less cracking (Fig. 5d). The pits in the base steel are less deep than in the atmospheres of high salinity (Fig. 5a). EDS spectra also show the presence of Cl in the bottom of the pits, albeit a lower content. A detailed study of the exfoliation phenomenon is beyond the scope of this work, and will be addressed in detail in a forthcoming publication by the authors.

4.2.4. Rust phases formed and its evolution with time of exposure

Table 8 shows a summary of the content of the different rust phases found in rust formed on mild steel in different exposure conditions. The high atmospheric salinities recorded throughout the year and high times of wetness have created suitable conditions for the formation of akaganeite throughout the entire exposure time in all corrosion stations. This has not been the case in many field studies reported in the literature that have failed to identify the akaganeite phase among the corrosion products formed, even in marine atmospheres with important Cl^- ion deposition rates [20,51,52,81,82], raising uncertainty as to what conditions are necessary for the formation of this oxyhydroxide. To elucidate this point the authors have been carrying out a bibliographic study to clarify the environmental conditions that lead to the formation of akaganeite, which will be the subject of a forthcoming publication.

With regard to the formation of magnetite/maghemite in the rusts generated in this study, it is seen that the content of this phase is higher when the rusts form in the atmosphere with the highest salinity (stations 1 and 2) (Table 8), confirming Hiller's finding [5] that the rust formed in atmospheres with a high Cl^- ion concentration contains more magnetite than the rust formed in Cl^- free atmospheres.

The formation of akaganeite and magnetite takes place preferentially in the interior of the rust layer, close to the steel substrate where the access of oxygen from the air is more limited, by the transformation after a certain time of basic Cl^--containing iron complexes and slow oxidation of Fe, respectively [11]. Therefore an oxygen deficit and the presence of high Cl^- contents are fundamental factors for the formation of magnetite and akaganeite. As it was mentioned in the Introduction of the paper the akaganeite formation mechanism implies the presence of high Cl^- concentrations and acid conditions (pH 4–6) due to the hydrolysis of ferrous chloride ($FeCl_2$), conditions that occur in confined spaces where Cl^- ions accumulate, such as the metal/corrosion product interface and crevice zones [12,13], which agrees with the high chloride levels found in pits formed on the steel exposed to the atmospheres with the highest chloride deposition rate (stations 1–3) (see Tables 7 and 9).

With regard to the presence of akaganeite on the two sides of the specimens, attention is again drawn to the important chloride rinsing effect of rainwater on the skyward side (side A) which leads to a lower chloride content in the electrolyte films and thus a reduction in akaganeite formation (Table 6).

Looking at Table 8 it is observed that in the atmospheres with greater salinity (stations 1 and 2) the akaganetite, goethite and magnetite/maghemite contents are higher than those recorded in atmospheres of lower salinity (stations 4 and 6). In contrast, the lepidocrocite content is notably lower. These results do not seem to obey the mechanism proposed by Ishikawa et al. [14,15], also suggested by Asami and Kikuchi [17], according to which magnetite may form at the expense of akaganeite. Our results are more in agreement with the findings of Tamaura et al. [77], who suggest that lepidocrocite is transformed into magnetite in the absence of oxygen according to the reaction:

$$2\gamma\text{-FeOOH} + Fe^{2+} \rightarrow Fe_3O_4 + 2H^+ \quad (10)$$

Fig. 13 shows the evolution with exposure time of the content of the different phases in the rusts formed on the skyward side in three atmospheres representative of the salinities found at the test site: station 1 (very high salinity), station 3 (high salinity) and station 6 (moderate salinity). It can be seen how in the most aggressive atmosphere (station 1) for exposure times of more than 6 months the magnetite/maghemite content rises at the expense of an important reduction in the lepidocrocite content.

The presence of akaganeite may perhaps be more abundant in the inner stratum of the rust layer, at the steel/rust interface, as suggested by some researchers [11–13]. For this reason, SEM/EDS microscopic observation was performed on one of the mild steel specimens exposed for 12 months in the atmosphere with the highest salinity (station 1), in an area where the rust layer had been detached due to exfoliation. Together with dark zones that

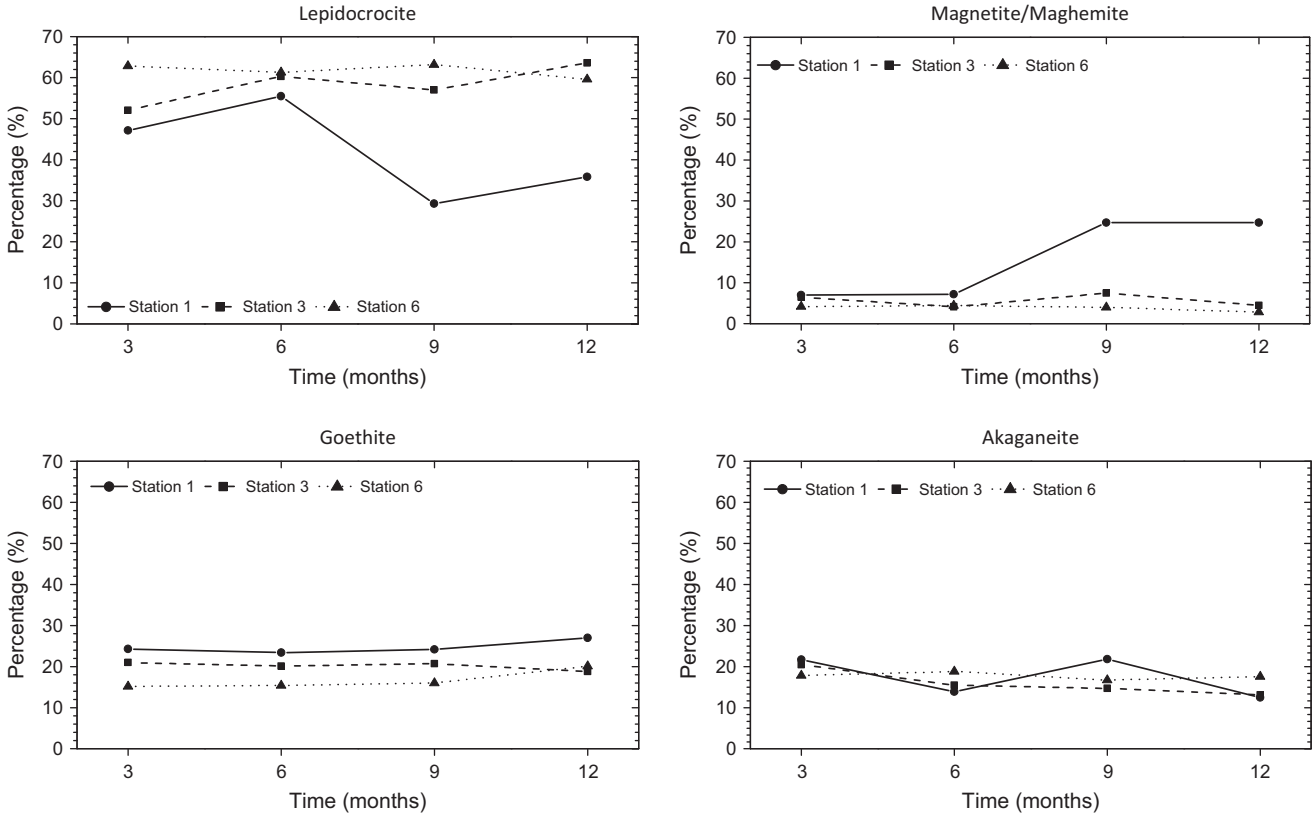

Fig. 13. Evolution with exposure time of the content of the different phases in the rusts formed on mild steel (side A) in the atmospheres with different levels of chloride deposit: very high salinity (station 1), high salinity (station 3) and moderate salinity (station 6).

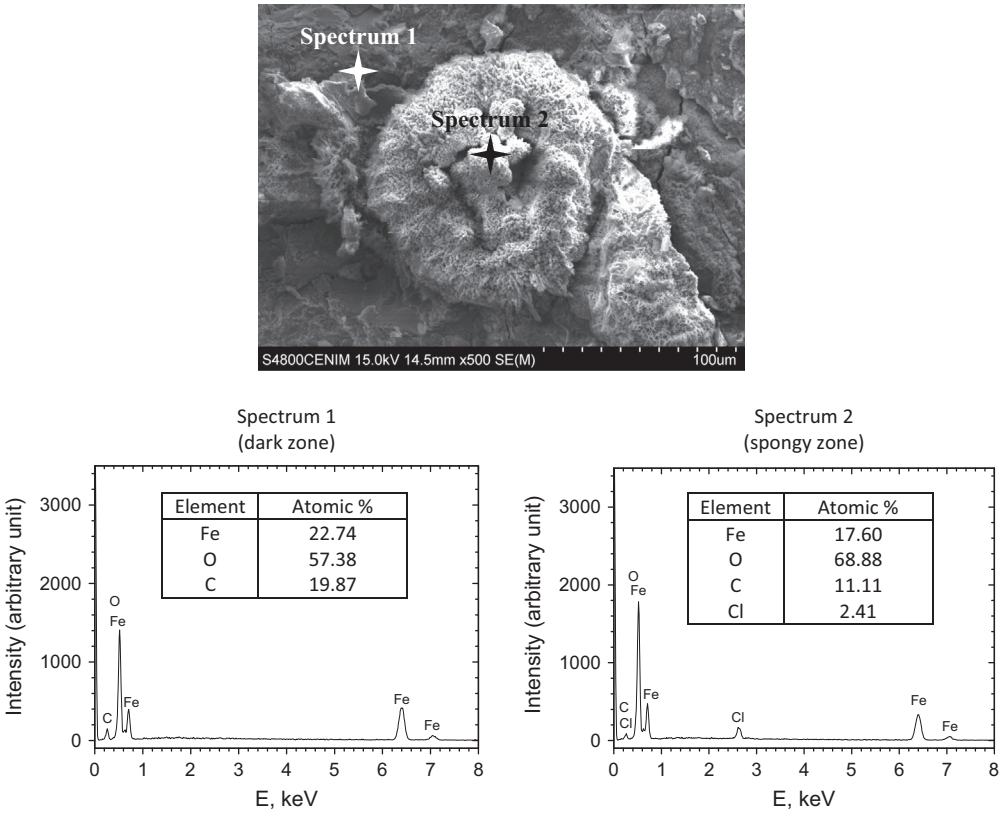

Fig. 14. SEM/EDS observations of dark (left) and spongy (right) zones on the underlying steel where the rust layer had been detached due to exfoliation.

could correspond to magnetite formations (spectrum 1 in Fig. 14) it was possible to observe the existence of very spongy formations with a high Cl content which could be attributed to the akaganeite phase (spectrum 2 in Fig. 14). These formations are very similar to those observed by Razvan and Raman [33], also on exfoliated steel, and which these researchers note as possibly due to magnetite and akaganeite respectively. In order to clarify this matter it would be important to carry out a rigorous study of these rust phases (magnetite and akaganeite), typical of marine atmospheres, using the most appropriate characterisation techniques. Our research group is currently in the process of carrying out studies with this aim.

5. Conclusions

The following are the most relevant conclusions of this work:

1. A clear relationship is seen between the wave height in the nearby sea, run of marine winds and the deposition of Cl^- ions in marine atmospheres. On one side, monthly average spectral wave height values (1.5–2.0 m) are sufficient to produce high monthly average salinity values (100–200 mg Cl^-/m^2 day). On other side, more than the average wind speed in the study area, the total run of marine winds is the parameter that has the greatest influence on the atmospheric salinity of the test site.
2. From an exhaustive bibliographic review it is seen that for atmospheric salinities below 600 mg Cl^-/m^2 day there seems to be a linear relationship between the mild steel corrosion rate and Cl^- ion deposition. For salinities above this value the corrosion rate seems to be stabilised.
3. Both atmospheric salinity and the steel corrosion rate obey an exponential decay function with the distance from the shore.
4. As the atmospheric salinity rises, the rusts formed exhibit increasingly coarse granulometries (coarser grains and flakes). The rust layers are less protective and more cracked and can become detached due to exfoliation (salinities around 300 mg Cl^-/m^2 day or higher) from the underlying steel. This experiences strong pitting and the pits contain considerable chlorine contents.
5. High akaganeite contents in the rust formed on mild steel has been found due to the high atmospheric salinities recorded in the area during the year of exposure. Important chloride rinsing effect of rainwater on the skyward side of the steel exposed in marine atmospheres, leads to a lower chloride content in the rust and thus to a reduction in akaganeite formation.
6. In the atmospheres richest in Cl^- there is additional magnetite formation possibly due by transformation of lepidocrocite.
7. SEM has allowed the identification of morphologies possibly associated with the akaganeite and magnetite phases; an aspect upon which the existing scientific literature is very scarce.

Acknowledgements

The authors would like to express their gratitude to the companies ENEL and GAS NATURAL for the facilities provided and for allowing the attachment of the corrosion stations to the towers of their wind turbines at Cabo Vilano wind farm (Camariñas, Spain), as well as for the provision of wind data obtained in their anemometers.

We would also like to thank the Spanish Meteorology Agency (AEMET) and the Spanish State Port Authority for the data provided on meteorological and wave height parameters, respectively, in the study area.

References

[1] K. Barton, Protection against Atmospheric Corrosion, John Wiley and Sons, New York, 1973.
[2] S. Feliu, M. Morcillo, S. Feliu Jr, The prediction of atmospheric corrosion from meteorological and pollution parameters. 1. Annual corrosion, Corros. Sci. 34 (1993) 403–414.
[3] M. Morcillo, E. Almeida, B. Rosales, J. Uruchurtu, M. Marrocos, Corrosion y Protección de Metales en las Atmósferas de Iberoamérica, Parte I – Mapas de Iberoamérica de Corrosividad Atmosférica (Proyecto MICAT, XV.1/CYTED), CYTED, Madrid, 1998.
[4] S.W. Dean, D. Knotkova, J.K. Kreislova, ISOCORRAG International Atmospheric Exposure Program: Summary of Results, ASTM Series 71, ASTM International, West Conshohocken, 2011.
[5] J.E. Hiller, Phasenumwandlungen im Rost, Werkst. Korros. 17 (1966) 943–951.
[6] U.R. Evans, Electrochemical mechanism of atmospheric rusting, Nature 206 (1965) 980–982.
[7] M. Stratmann, K. Bohnenkamp, H.J. Engell, An electrochemical study of phase-transitions in rust layers, Corros. Sci. 23 (1983) 969–985.
[8] T. Nishimura, H. Katayama, K. Noda, T. Kodama, Electrochemical behavior of rust formed on carbon steel in a wet/dry environment containing chloride ions, Corrosion 56 (2000) 935–941.
[9] H. Antony, L. Legrand, L. Maréchal, S. Perrin, P. Dillmann, A. Chaussé, Study of lepidocrocite γ-FeOOH electrochemical reduction in neutral and slightly alkaline solutions at 25 °C, Electrochim. Acta 51 (2005) 745–753.
[10] V. Lair, H. Antony, L. Legrand, A. Chaussé, Electrochemical reduction of ferric corrosion products and evaluation of galvanic coupling with iron, Corros. Sci. 48 (2006) 2050–2063.
[11] K. Nomura, M. Tasaka, Y. Ujihira, Conversion electron Mössbauer spectrometric study of corrosion products of iron immersed in sodium chloride solution, Corrosion 44 (1988) 131–135.
[12] C. Rémazeilles, P. Refait, On the formation of β-FeOOH (akaganéite) in chloride-containing environments, Corros. Sci. 49 (2007) 844–857.
[13] C. Rémazeilles, P. Refait, Formation, fast oxidation and thermodynamic data of Fe(II) hydroxychlorides, Corros. Sci. 50 (2008) 856–864.
[14] T. Ishikawa, Y. Kondo, A. Yasukawa, K. Kandori, Formation of magnetite in the presence of ferric oxyhydroxides, Corros. Sci. 40 (1998) 1239–1251.
[15] H. Tanaka, R. Mishima, N. Hatanaka, T. Ishikawa, T. Nakayama, Formation of magnetite rust particles by reacting iron powder with artificial α-, β- and γ-FeOOH in aqueous media, Corros. Sci. 78 (2014) 384–387.
[16] K. Ståhl, K. Nielsen, J. Jiang, B. Lebech, J.C. Hanson, P. Norby, J. van Lanschot, On the akaganéite crystal structure, phase transformations and possible role in post-excavational corrosion of iron artifacts, Corros. Sci. 45 (2003) 2563–2575.
[17] K. Asami, M. Kikuchi, In-depth distribution of rusts on a plain carbon steel and weathering steels exposed to coastal–industrial atmosphere for 17 years, Corros. Sci. 45 (2003) 2671–2688.
[18] K. Asami, M. Kikuchi, Characterization of rust layers on weathering steels air-exposed for a long period, Mater. Trans. 43 (2002) 2818–2825.
[19] T. Ishikawa, T. Yoshida, K. Kandori, T. Nakayama, S. Hara, Assessment of protective function of steel rust layers by N_2 adsorption, Corros. Sci. 49 (2007) 1468–1477.
[20] I. Díaz, H. Cano, D. de la Fuente, B. Chico, J.M. Vega, M. Morcillo, Atmospheric corrosion of Ni-advanced weathering steels in marine atmospheres of moderate salinity, Corros. Sci. 76 (2013) 348–360.
[21] EN ISO 9225, Corrosion of metals and alloys. Corrosivity of atmospheres. Measurement of environmental parameters affecting corrosivity of atmospheres, European Committee for Standardization, Brussels, 2012.
[22] ISO 8407, Corrosion of Metals and Alloys – Removal of Corrosion Products from Corrosion Test Specimens, International Standards Organization, Genève, 1991.
[23] A. Raman, Atmospheric corrosion problems with weathering steels in Lousiana bridges, in: S.W. Dean, T.S. Lee (Eds.), Degradation of Metals in the Atmosphere, ASTM STP 965, American Society for Testing and Materials, Philadelphia, 1988, pp. 16–29.
[24] S. Hara, T. Kamimura, H. Miyuki, M. Yamashita, Taxonomy for protective ability of rust layer using its composition formed on weathering steel bridge, Corros. Sci. 49 (2007) 1131–1142.
[25] C.R. Hubbard, R.L. Snyder, RIR-measurement and use in quantitative XRD, Powder Diffr. 3 (1988) 74–77.
[26] S. Flores, M. Morcillo, Anticipated levels of soluble salts remaining on rusty steel prior to painting, Surf. Coat. Int. 82 (1999) 19–25.
[27] F. Corvo, J. Minotas, J. Delgado, C. Arroyave, Changes in atmospheric corrosion rate caused by chloride ions depending on rain regime, Corros. Sci. 47 (2005) 883–892.
[28] M. Morcillo, D. De la Fuente, I. Díaz, H. Cano, Atmospheric corrosion of mild steel. A review, Rev. Metal. Madrid 47 (2011) 426–444.
[29] P. Keller, Occurrence, formation and phase transformation of β-FeOOH in rust, Werkst. Korros. 20 (1969) 102–108.
[30] R.A. Antunes, I. Costa, D.L.A. de Faria, Characterization of corrosion products formed on steels in the first months of atmospheric exposure, Mater. Res. 6 (2003) 403–408.
[31] D. de la Fuente, I. Diaz, J. Simancas, B. Chico, M. Morcillo, Long-term atmospheric corrosion of mild steel, Corros. Sci. 53 (2011) 604–617.
[32] A. Raman, A. Razvan, B. Kuban, K.A. Clement, W.E. Graves, Characteristics of the rust from weathering steels in Louisiana bridge spans, Corrosion 42 (1986) 447–456.

[33] A. Razvan, A. Raman, Morphology of rust phases formed on naturally weathered weathering steels in bridge spans, Pract. Met. 23 (1986) 223–236.
[34] A. Raman, S. Nasrazadani, L. Sharma, Morphology of rust phases formed on weathering steels in various laboratory corrosion test, Metallography 22 (1989) 79–96.
[35] A. Raman, S. Nasrazadani, L. Sharma, A. Razvan, Morphology of rust phases formed on weathering steels during outdoor atmospheric exposure in sheltered locations under the bridges, Pract. Met. 24 (1987) 535–548.
[36] A. Raman, S. Nasrazadani, L. Sharma, A. Razvan, Morphology of rust phases formed on weathering steels during outdoor atmospheric exposure in open, bold locations, Pract. Met. 24 (1987) 577–589.
[37] A. Raman, B. Kuban, Infrared spectroscopic analysis of phase transformation processes in rust layers formed on weathering steels in bridge spans, Corrosion 44 (1988) 483–488.
[38] H. Cano, D. Neff, M. Morcillo, P. Dillmann, I. Díaz, D. De la Fuente, Characterization of corrosion products formed on Ni 2.4 wt%–Cu 0.5 wt%–Cr 0.5 wt% weathering steel exposed in marine atmospheres, Corros. Sci. 87 (2014) 438–451.
[39] M. Morcillo, B. Chico, J. Alcántara, I. Díaz, J. Simancas, D. De la Fuente, Atmospheric corrosion of mild steel in chloride – rich environments. Questions to be answered, Mater. Corros. (2014), http://dx.doi.org/10.1002/maco.201407940.
[40] S. Neshyba, Oceanography, Wiley, New York, 1987.
[41] D.C. Blanchard, A.H. Woodcock, The production, concentration and vertical distribution of the sea-salt aerosol, Ann. NY Acad. Sci. 338 (1980) 330–347.
[42] J.W. Fitzgerald, Marine aerosol: a review, Atmos. Environ. 25A (1991) 533–545.
[43] S. Feliu, M. Morcillo, B. Chico, Effect of state of sea on atmospheric corrosion in coastal zones, Br. Corros. J. 36 (2001) 157–160.
[44] I. Díaz, Corrosión atmosférica de aceros patinables de nueva generación, Ph. Thesis, Complutense University, Madrid, 2012.
[45] H. Cano, Aceros patinables (Cu, Cr, Ni): Resistencia a la corrosión atmosférica y soldabilidad, Ph. Thesis, Complutense University, Madrid, 2013.
[46] H.R. Ambler, A.A.J. Bain, Corrosion of metals on the tropics, J. Appl. Chem. 5 (1955) 437–527.
[47] T.A. McMahon, P.J. Denison, Empirical atmospheric deposition parameters—a survey, Atmos. Environ. 13 (1979) 571–585.
[48] M. Morcillo, B. Chico, E. Otero, L. Mariaca, Effect of marine aerosol on atmospheric corrosion, Mater. Perform. 38 (1999) 72–77.
[49] S. Feliu, M. Morcillo, B. Chico, Effect of distance from sea on atmospheric corrosion rate, Corrosion 55 (1999) 883–891.
[50] M. Morcillo, B. Chico, L. Mariaca, E. Otero, Salinity in marine atmospheric corrosion: its dependence on the wind regime existing in the site, Corros. Sci. 42 (2000) 91–104.
[51] S. Syed, Atmospheric corrosion of hot and cold rolled carbon steel under field exposure in Saudi Arabia, Corros. Sci. 50 (2008) 1779–1784.
[52] Y. Ma, Y. Li, F. Wang, Corrosion of low carbon steel in atmospheric environments of different chloride content, Corros. Sci. 51 (2009) 997–1006.
[53] G.A. King, B. Carberry, Atmospheric Corrosivity of the Greater Newcastle Region, Technical Report TR 92/1, CSIRO, Australia, 1992.
[54] A.A. Bragard, H.E. Bonnarens, Prediction at long terms of the atmospheric corrosion of structural steels from short-term experimental data, in: S.W. Dean Jr., E.C. Rhea (Eds.), Atmospheric Corrosion of Metals, ASTM STP 767, American Society for Testing and Materials, 1982, pp. 339–358.
[55] A. Bragard, H. Bonnarens, Atmospheric Conditions and Durability of Weathering Steels, Report N. 57, Centre de Recherches Metallurgiques (C.R.M.), Liége, Belgium, December 1980.
[56] A.C. Dutra, R.d.O. Vianna, Atmospheric corrosion testing in Brazil, in: W.H. Ailor (Ed.), Atmospheric Corrosion, The Electrochemical Society, John Wiley and Sons, New York, 1982, pp. 755–774.
[57] F. Corvo, N. Betancourt, L. Muleshkova, C. Haces, Y. Leon, J. Pérez, E. Bricuyet, Primera variante del mapa de agresividad corrosiva de Cuba, in: 3rd Iberoamerican Corrosion Congress, Brazil, 1989, p. 405.
[58] F. Corvo, N. Betancourt, J.C. Díaz, C. Lariot, Y. Leon, J. Pérez, O. Rodríguez, E. Bricuyet, F. Catala, M. Castro, R. González, C. Echevarria, M. Lorente, M.E. Ladrón de Guevara, Segunda variante del mapa regional de agresividad corrosiva de la atmósfera de Cuba, in: Proc. Primer Taller Internaciónal de Corrosión, CONACYT-CINVESTAV, Merida, Yucatan, Mexico, 1992.
[59] F. Corvo, C. Haces, N. Betancourt, L. Maldonado, L. Veleva, M. Echeverría, O.T. de Rincón, A. Rincón, Atmospheric corrosivity in the Caribbean Area, Corros. Sci. 39 (1997) 823–833.
[60] F. Corvo, Atmospheric corrosion of steel in humid tropical climate. Influence of pollution, humidity, temperature, rainfall and sun radiation, Corrosion 40 (1984) 170–175.
[61] F. Corvo, N. Betancourt, A. Mendoza, The influence of airborne salinity on the atmospheric corrosion of steel, Corros. Sci. 37 (1995) 1889–1901.
[62] N. Betancourt, F. Corvo, M. Lorente, C. Proenza, J. Pérez, Y. Leon, Agresividad corrosiva de la atmósfera de una zona de la provincia Holquín, in: Proc. 1st International Symposium on Corrosion, Protection and Tropicalization, Quimindustria 90, La Habana, Cuba, 1990, pp. 47–52.
[63] F. Corvo, N. Betancourt, J.C. Díaz, L. Muleshkova, I. Leon, J. Pérez, E. Bricuyet, O. Rodríguez, M. Lorente, La salinidad de la atmósfera en Cuba y su influencia sobre la corrosión del acero, in: Proc. 1st International Symposium on Corrosion, Protection and Tropicalization, Quimindustria 90, La Habana, Cuba, 1990, pp. 167–170.
[64] D. Knotkova, K. Kreislova, S.W.J. Dean, ISOCORRAG: International Atmospheric Exposure Program: Summary of results, ASTM Data Series 71, ASTM International, West Conshohocken, 1990.
[65] D.K. Basu, D.K. Khan, A short communication on role of different variables on atmospheric corrosion in marine environment – effect of proximmity to sea, NML Tech. J. 14 (1972) 34–36.
[66] K.S. Rajagopalan, P.L. Annamalai, M. Sundaram, C. Rajagopal, Atmospheric corrosion of steel in some tropical locations in India, in: Proc. of the 3rd International Congress on Metallic Corrosion, vol. 4, MIR, 1969, Moscow, 1966, pp. 532–541.
[67] S. Chandrasekaran, R. Jayabalou, Y.V. Subrahmanyam, D. Raguraman, Effect of air pollution on corrosion of mild steel: preliminary field studies at three sites in Madras city, Key Eng. Mater. 20–28 (1988) 131–142.
[68] L. Mariaca, J. Genescá, J. Uruchurtu, L. Salvador, Corrosividad Atmosférica (MICAT-México), Plaza y Valdés, S.A., México, 1999.
[69] J.R. Duncan, J.A. Balance, Marine salts contribution to atmospheric corrosion, in: S.W. Dean, T.S. Lee (Eds.), Degradation of Metals in the Atmosphere, STP 965, American Society of Testing and Materials, West Conshohocken, PA, 1986, pp. 316–326.
[70] P.V. Strekalov, Y.M. Panchenko, The role of marine aerosols in atmospheric corrosion of metals, Prot. Met. 30 (1994) 254–263.
[71] M. Morcillo, S. Feliu, Mapas de España de Corrosividad Atmosférica, CYTED, Madrid, 1993.
[72] B. Chico, L. Mariaca, E. Otero, M. Morcillo, Evaluación de la corrosión atmosférica en ambientes marinos mediante probetas alambre sobre tornillo, Afinidad 54 (1997) 241–245.
[73] H.R. Ambler, Atmospheric salinity and metal corrosion at various places in Great Britain, J. Appl. Chem. 10 (1960) 213–225.
[74] E.A. Baker, Long-term corrosion behaviour of materials in the marine atmosphere, in: S.W. Dean, T.S. Lee (Eds.), Degradation of Metals in the Atmosphere, STP 965, American Society of Testing and Materials, West Conshohocken, PA, 1986, pp. 125–144.
[75] A. Rincón, O.T. De Rincón, C. Haces, N.R. Furet, F. Corvo, Evaluation of steel corrosion products in tropical climates, Corrosion 53 (1997) 835–841.
[76] V.D. Huy, Atmospheric Corrosion of Metals in Tropics, Nauka, Moscow, Russia, 1994.
[77] Y. Tamaura, K. Ito, T. Katsura, Transformation of γ-FeO(OH) to Fe_3O_4 by adsorption of iron(II) ion on γ-FeO(OH), J. Chem. Soc. Dalton Trans. (1983) 189–194.
[78] S. Hara, M. Yamashita, T. Kamimura, M. Sato, Synchrotron XRD analysis of local positions in laminated heavy rust layer formed on weathering steel bridge, J. Japan Inst. Metals 71 (2007) 346–353.
[79] S. Hara, A X-ray diffraction analysis on constituent distribution of heavy rust layer formed on weathering steel using synchrotron radiation, Corros. Eng. Japan 57 (2008) 70–75.
[80] D.C. Cook, Spectroscopic identification of protective and non-protective corrosion coatings on steel structures in marine environments, Corros. Sci. 47 (2005) 2550–2570.
[81] D.D.N. Singh, S. Yadav, J.K. Saha, Role of climatic conditions on corrosion characteristics of structural steels, Corros. Sci. 50 (2008) 93–110.
[82] Z. Wang, Study of the corrosion behaviour of weathering steels in atmospheric environments, Corros. Sci. 67 (2013) 1–10.

ANEXO II

“An attempt to classify the morphologies presented by different rust phases formed during the exposure of carbon steel to marine atmospheres.”

Materials Characterization 118 (2016) 65–78

Contents lists available at ScienceDirect

Materials Characterization

journal homepage: www.elsevier.com/locate/matchar

An attempt to classify the morphologies presented by different rust phases formed during the exposure of carbon steel to marine atmospheres

J. Alcántara, B. Chico, J. Simancas, I. Díaz, D. de la Fuente, M. Morcillo *

National Centre for Metallurgical Research (CENIM/CSIC), Avda. Gregorio del Amo 8, 28040 Madrid, Spain

ARTICLE INFO

Article history:
Received 1 March 2016
Received in revised form 8 April 2016
Accepted 30 April 2016
Available online 2 May 2016

Keywords:
Carbon steel
SEM
Morphology
Rust phases
Raman spectroscopy

ABSTRACT

The scientific literature contains very little knowledge on the morphology of the different rust phases formed upon exposure of carbon steel to the atmosphere. In recent years this topic has attracted the attention of many researchers working on atmospheric corrosion, but the various morphologies seen in microscopic observations and reported in many publications lack a rigorous characterisation and identification in terms of the rust phases that give rise to them.

The aim of this paper is to advance in this respect with a dual purpose: firstly to try to make a classification of the numerous different types of morphologies seen in the microscopic observation of rusts formed on carbon steel exposed to marine atmospheres, and secondly to identify some of these morphologies, perhaps the most common, using the powerful SEM/Micro-Raman spectroscopic technique.

This work distinguishes several main types of morphology: globular, acicular, laminar, tubular and toroidal, and the variants existing within each group. The rust phases most commonly found are the oxyhydroxides lepidocrocite, goethite and akaganeite and the iron oxide magnetite.

1. Introduction

Cornell and Schwertmann dedicated an entire chapter of their well-known and well referenced book "The iron oxides, structure, properties, occurrence and uses" to iron oxide crystal morphology and size, mainly concerned with synthetic iron oxides, and provided an overview of the common crystal habits of the various Fe(III) oxides [1], noting that the range of shapes and sizes reflects to a large extent the growth environment.

In an interesting paper published in this journal some years ago, Raman et al. stated that very little was known about the morphology of the different forms of rust [2]. Since that time, little progress has been made in this respect. In their studies, Raman et al. presented a collection of selected Scanning Electron Microscopy (SEM) micrographs corresponding to nearly a couple of hundred carbon steel specimens exposed for different times on bridges in the states of Louisiana and Texas [2–6], and attempted to indirectly identify the rust morphologies observed by SEM by comparison with the morphologies of standard rust phases grown in the laboratory and identified by X-ray diffraction (XRD) and particularly by Infrared Spectroscopy (IRS). Terms such as "sandy grains", "cotton balls", "nest-like", "honeycomb", "flowery", etc. were coined by these authors.

It should however be noted that the morphologies of synthetic iron oxides produced in laboratory conditions may be very different to those obtained during the corrosion of carbon steel in the atmosphere, as pointed out by Waseda and Suzuki in the preface to an interesting book on "Characterisation of corrosion products on steel surfaces" [7]. As they note, the morphology of atmospheric corrosion products is often not describable in terms of typical iron oxides structures but is much more complicated; the component phases in rust formed on steel in outdoor exposure show imperfections in their structures and real component structures appear to diverge from an ideal crystallographic structure of typical iron oxides.

Table 1 presents the main habits (morphologies) of iron oxides according to Cornell and Schwertmann [1] and Raman et al. [2–6].

In recent years the research teams working on atmospheric corrosion, including ourselves [8–13], have generally attributed rust phases to the morphologies obtained by SEM simply on the basis of Raman et al. publications without carrying out a rigorous analytical characterisation of the components formed, which has often given rise to speculation and unreliable results.

The aim of this paper is to advance in this respect with a dual purpose: firstly to try to make a classification of the different types of morphologies observed in the corrosion products that form on steel when

* Corresponding author.
E-mail address: morcillo@cenim.csic.es (M. Morcillo).

http://dx.doi.org/10.1016/j.matchar.2016.04.027
1044-5803/

Table 1
Principal habits (morphologies) of iron oxides according to Cornell and Schwertmann [1] and Raman et al. [2–6].

Iron oxide	Cornell and Schwertmann [1]	Raman et al. [2–6]
Lepidocrocite (γ-FeOOH)	Laths	Fine powdery (sandy) grains Thick plates (bent and wiggled) appearing like a pack of worms
Goethite (α-FeOOH)	Acicular	Needles (whiskers) crystals Tiny rods Crystals forming structures such as: honey-comb, nest-like, feathery (or brush-like or broken glass) patterns, cotton balls, thorny (sponge-type) plates with sharp edges, etc.
Akaganeite (β-FeOOH)	Rods, somatoids	–
Feroxyhyte (δ-FeOOH)	Plates	Thin, flat and sharp plates (bend and fold) forming a diversity of flowery crystalline patterns
Magnetite (Fe_3O_4)	Octohedra	Flat dark layers Circular grains with bulging at the periphery with doughnut-like appearance
Maghemite (γ-Fe_2O_3)	Laths or cubes	Powdery sandy grains
Hematite (α-Fe_2O_3)	Hexagonal plates, rhombohedra	–
Ferrihydrite ($Fe_5HO_8 \cdot 4H_2O$)	Spheres	Unevenly thick plates or cylindrical tubes with the appearance of compartments, tentacles or cooked spaghetti

exposed to marine atmospheres, and secondly to try to analytically identify some of them, perhaps the most common, by using the powerful SEM/Micro-Raman spectroscopy technique. For this purpose we have selected the SEM views most commonly seen on 36 carbon steel specimens exposed for different times to various marine atmospheres in an ample research programme carried out in the marine atmospheric environment of Cabo Vilano in Spain, as reported in previous papers [13–19].

Table 2
Wavelength shift ranges (cm^{-1}) in which the main Raman peaks of the rust phase compounds are often located in different bibliographic sources [20–36].

Compound	Refs.	Wavelength shifts (cm^{-1})
Lepidocrocite (γ-FeOOH)	[20,22–27, 30,32–36]	(248–252)[a], (378–380), (528–530), (650–655), (1300 − 1310)
Goethite (α-FeOOH)	[20–22,24–29, 32–35]	(241–250), (298–301), (385–390)[a], (478–483), (549–552), (680–685), (1000 − 1120)[M]
Akaganeite (β-FeOOH)	[23,25,27, 31–33,35,36]	(310–314)[a], (385–390)[a], (497–499), (538–541), (720–723)
Feroxyhyte (δ-FeOOH)	[23,25–27,30,35]	(385–392), 400, (655–680)[a]
Magnetite (Fe_3O_4)	[20–22,24–28, 32,33,35,36]	(298–302), (540–550), (636–670)[a]
Maghemite (γ-Fe_2O_3)	[21–23,25–27, 30,32,33,35]	350, (500–506)[a], (700–720)[a], (1400–1440)[M]
Hematite (α-Fe_2O_3)	[20–22,25–28, 32,33,35]	(220–228)[a], (240–247), (289–299)[a], (400–415)[a], (497–502), (609–615), (1320 − 1330)[M]
Ferrihydrite ($Fe_5HO_8 \cdot 4H_2O$)	[1,30,33,35]	370, 510, 710[a], (1380–1600)

Underlined: The next strongest peak.
[M]: Magnon peak.
[a] The strongest peak.

2. Experimental

Research has been carried out in the pure marine atmospheres of Cabo Vilano wind farm (Coruña, Spain) in corrosion stations affixed to several wind turbine towers. Information on the experimental details has been published elsewhere [13–19].

350 panels of plain carbon steel were exposed on open-air racks and withdrawn from the marine atmospheric station (annual average chloride deposition rates from 55 to 652 $mg/m^2 \cdot day$) after different exposure times (3, 6 and 12 months). After their withdrawal from the testing stations, representative $1 \times 1\ cm^2$ fragments of 36 selected specimens were subjected to a laboratory characterisation of the rust formed by means of microscopic observation using a Hitachi S4800 high resolution scanning electron microscope (SEM) (3 nm in high vacuum mode) equipped with secondary electron and backscattered electron detectors.

Two samples from the 36 selected specimens were considered to be most representative of the typical morphologies exhibited by the different rust phases formed during exposure of the carbon steel to the marine atmosphere. Analytical characterisation of rust phases was carried out using the SEM/Micro-Raman technique. This study was performed by the authors in the laboratories of Hybriscan Technologies B.V. in Arnhem (The Netherlands). One of the samples was a carbon steel specimen that had been exposed for six months to a marine atmosphere with an average chloride deposition rate of 130 $mg/m^2 \cdot day$. It has a red-brown rust layer adhered to the steel substrate. The other one was a carbon steel specimen that had been exposed for twelve months to a marine atmosphere with an average chloride deposition rate of 390 $mg/m^2 \cdot day$. It showed a very thick rust layer that was easily lifted off (exfoliated) using a utility knife.

Raman spectra (spectral images) were measured with a Hybriscan Technologies HSCMM-21 Raman module attached to a JEOL JSM-6610LV SEM equipped with EDX and a backscatter detector. The Raman module was a fully integrated confocal Raman microscopy module that included an optical video microscope and a high resolution XY stage placed on top of the SEM main stage. The module integrated fully with the SEM in such a way that the optical path and the electron beam path did not interfere with each other. The excitation source was a 785 nm laser with an adjustable power of between 0 and 30 mW delivered on the sample.

After preliminary tests Raman spectroscopy measurements were adjusted to the conditions of 75 μW laser power and a total acquisition time of 60 s, conditions that were successful in most cases. The spectral range of the spectrometer was 220 to 2580 cm^{-1} with a resolution of better than 5 cm^{-1} and a dispersion of between 1.6 and 2.6 cm^{-1} per pixel. Raman imaging was obtained by scanning the sample point by point with the high resolution XY stage mounted on top of the JEOL main stage. Correlation between the SEM images and Raman images was achieved by overlaying the video and SEM image of the sample

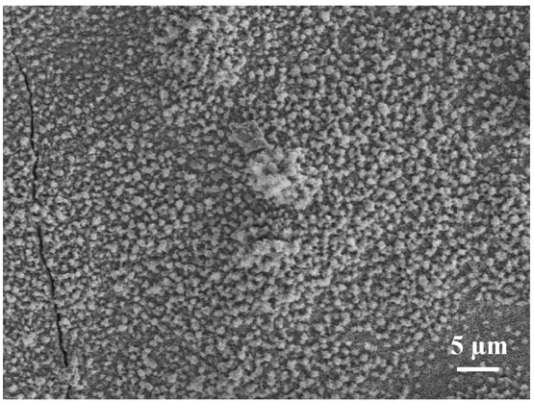

Fig. 1. Globular "sandy grain" type lepidocrocite formations.

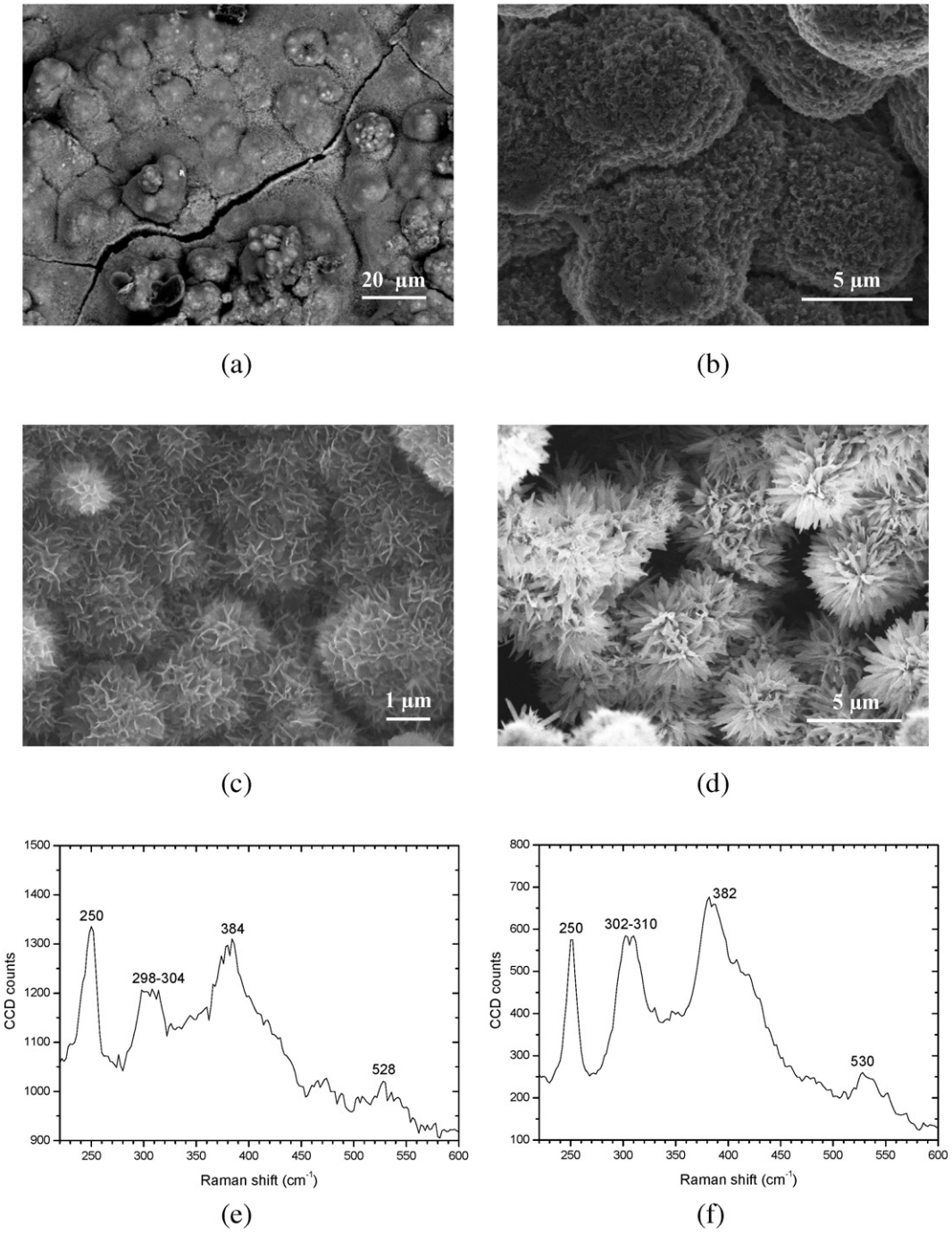

Fig. 2. (a–d): Different globular type lepidocrocite formations. (e–f): Raman spectra corresponding to morphologies (a) and (d), respectively.

itself. Once such an overlay was obtained, the region of interest for Raman imaging could be selected based on the SEM image.

The procedure followed in this work consisted of raising the SEM resolution until it was possible to clearly observe the formations corresponding to the different morphologies present in the rust, selecting the point or area of the morphological feature (e.g. lamina, globule, needle, etc.) where the Raman spectra would subsequently be performed.

A certain dispersion was seen in the wavelength shifts (cm^{-1}) of the characteristic peaks for the different iron oxides forming part of atmospheric corrosion product layers and reported by different researchers. The Raman frequencies of the peaks did not always match perfectly, though in general they agreed to within a few cm^{-1}. This variability of results may be due to multiple causes, such as: the source of the reference compound, differences in reference sample preparation, surface morphology, degree of sample crystallinity, laser power, focal position of laser light illumination, resolution of spectrometer setting, and uncertainty in instrument wavelength calibration. For this reason, in order for easier interpretation of the Raman spectra in this work it has been preferred to use an interval where the characteristic peaks reported by the different researchers are most frequently found [1,20–36], rather than specific wavelength shifts. Table 2, prepared following this criterion, may be useful when it comes to assigning a given corrosion product from the corresponding Raman spectrum obtained.

3. Results and discussion

The diversity of rust morphologies formed on carbon steel exposed to marine atmospheres is enormous, with a great variety of shapes

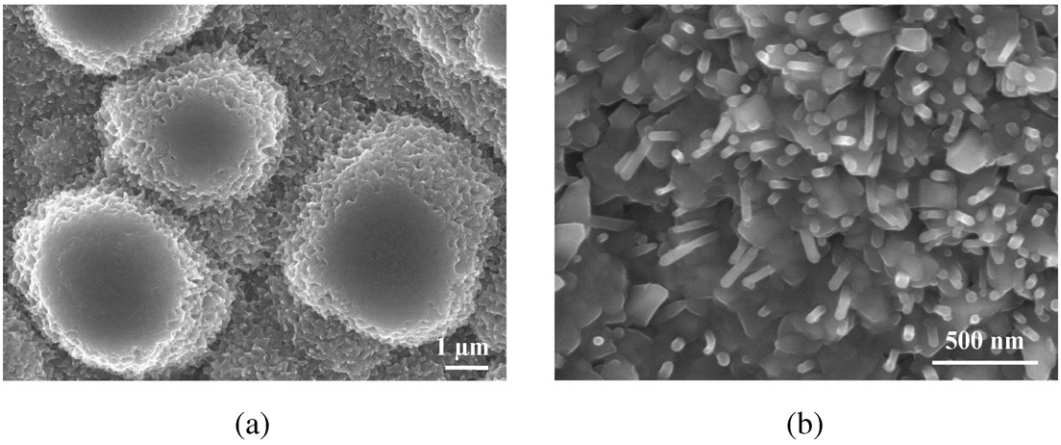

Fig. 3. Globular formations composed of successive layers of amorphous agglomerates upon which rod-type akaganeite crystals seem to form.

and sizes of the crystalline aggregates that reflect to a large extent the different growth conditions: chemical characteristics of the aqueous layers formed by humidity condensation, rainfall, etc., temperature, wet/dry cycle characteristics, etc. Atmospheric rusting is not a homogenous process and different phases form at the same time. The rust that forms during exposure to the atmosphere is usually a complex mixture of several phases.

Without seeking to be exhaustive, there follows below a tentative classification of the different types of morphology observed.

3.1. Globular

These are hemispheric shaped aggregated formations like small mounds. When the surface of the outermost rust layer is observed at low magnification a fine powdery grain type morphology is often seen (Fig. 1) which Raman et al. termed as "sandy grains" [2–6]. However, observation at greater magnification shows a very different morphology in which the existence of globular formations of a very different type can be seen (Fig. 2a–d). Thus, the type of morphology of a given rust phase is obviously dependent on the magnification at which the SEM observation is made.

In Fig. 2a we can see globular formations in which the globules present a very smooth surface without the presence of any crystalline substructure. These may correspond to amorphous lepidocrocite aggregates [2–6]. The Raman spectrum performed on one of the globules (Fig. 2e) shows the presence of a strongest peak at 250 cm^{-1}, a second strong peak at 384 cm^{-1}, and a weaker peak at 528 cm^{-1}, indicating that this phase corresponds to lepidocrocite (see Table 2). A weak peak at 298–304 cm^{-1} is also present, referring to lepidocrocite according to other researchers [30,34].

In Fig. 2b–d we can see the existence of a crystalline substructure in the interior of the globules. The substructure is coarse in Fig. 2b, presents very thin laminas with a thorny appearance in Fig. 2c, and in Fig. 2d it is even possible to see the existence of needles (whiskers) typical of goethite [2,37] around the periphery of the globules. The Raman spectrum performed in this latter case (Fig. 2f) shows the presence of one strongest peak at 382 cm^{-1}, two second strongest peaks at 250 cm^{-1} and 302–310 cm^{-1}, and a fourth weaker peak at 528 cm^{-1}, which could well correspond to a mixture of lepidocrocite and goethite. The existence of the strongest peak at 382 cm^{-1} and the peak at 302–310 cm^{-1}, characteristic of goethite, would represent the contribution to the spectrum of the needles around the periphery of the globules, while the weaker peak (528 cm^{-1}) would correspond to lepidocrocite in the interior of the globules. The peak at 250 cm^{-1} is characteristic of both compounds.

In general it is usual to find large proportions of both phases in the outermost surface of the rust layer formed on carbon steel in marine environments. Both compounds form very close to each other, which is logical considering the well-known transformation of lepidocrocite to goethite [38,39], and their characteristic Raman peaks present a certain similarity, which at times makes it difficult to unequivocally identify them. An aid in their differentiation is the location of the strongest peak in the Raman spectrum; in the case of lepidocrocite the strongest peak is located close to 250 cm^{-1}, while for goethite the strongest peak is located close to 380 cm^{-1}.

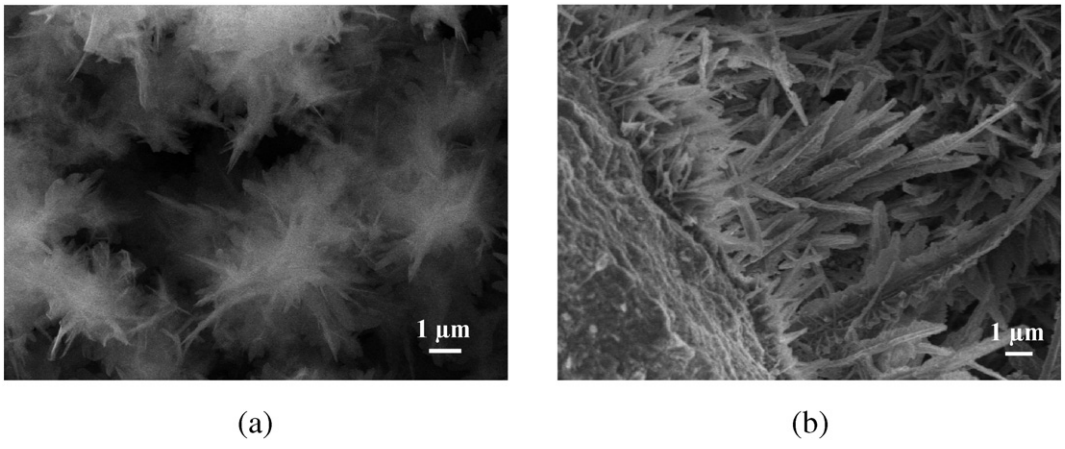

Fig. 4. Acicular goethite formations: star-like (a) and filiform (b).

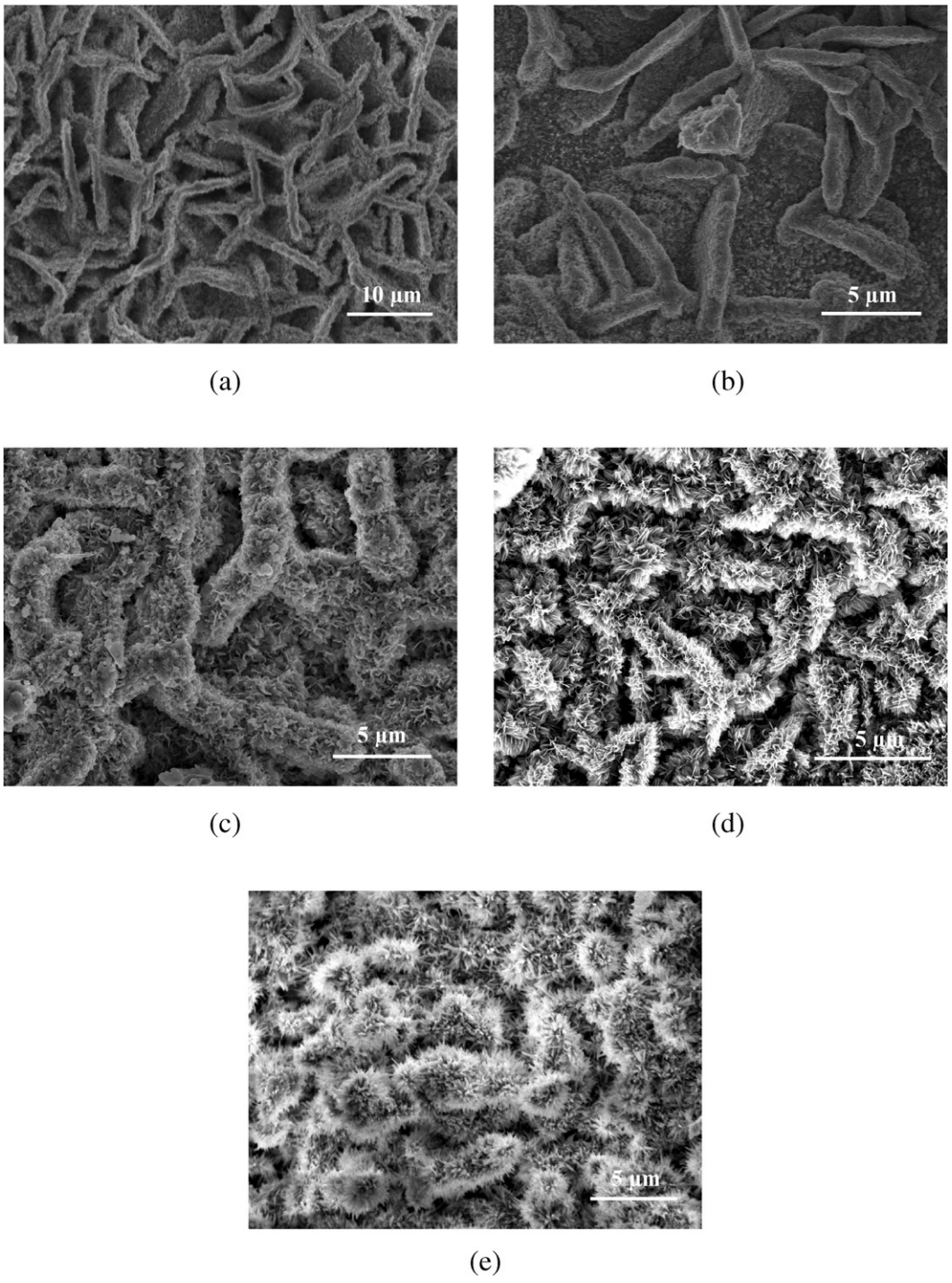

Fig. 5. Different types of laminar (bar type) lepidocrocite formations.

Other globular type formations appear at the steel/rust interface when the carbon steel is exposed to atmospheric conditions with high chloride ion deposition rates where the formation of akaganeite takes place [15]. Fig. 3a shows a new type of globular formations which are very different to those shown in Fig. 2 and are composed of successive layers of amorphous agglomerates. As they form in the vicinity of porous whitish akaganeite zones, it may be speculated that these could be ferrous hydroxychloride (β-$Fe_2(OH)_3Cl$) formations or intermediate oxidation products such as green rust 1 (Cl^-), whose simplified formula is $Fe_4(OH)_8Cl$, considered to be the precursor of akaganeite [40]. Observation of one of the globules in Fig. 3b at much higher magnification indicates the formation of prismatic crystallites (cigar-shaped) typical of akaganeite [15,17] on the amorphous granules that constitute the globules shown in Fig. 3a.

3.2. Acicular morphologies

These are crystalline aggregates with a similar appearance to needles, hairs or threads and are referred to by researchers using terms such as needle-like, needle-shaped, filiform, whiskers, etc. These formations correspond to the goethite phase [1,2,37], as has previously been noted. Fig. 4 shows two SEM micrographs illustrating this type of crystalline growth, in one case with a star-like shape (Fig. 4a) and in the other case with a filiform appearance (Fig. 4b).

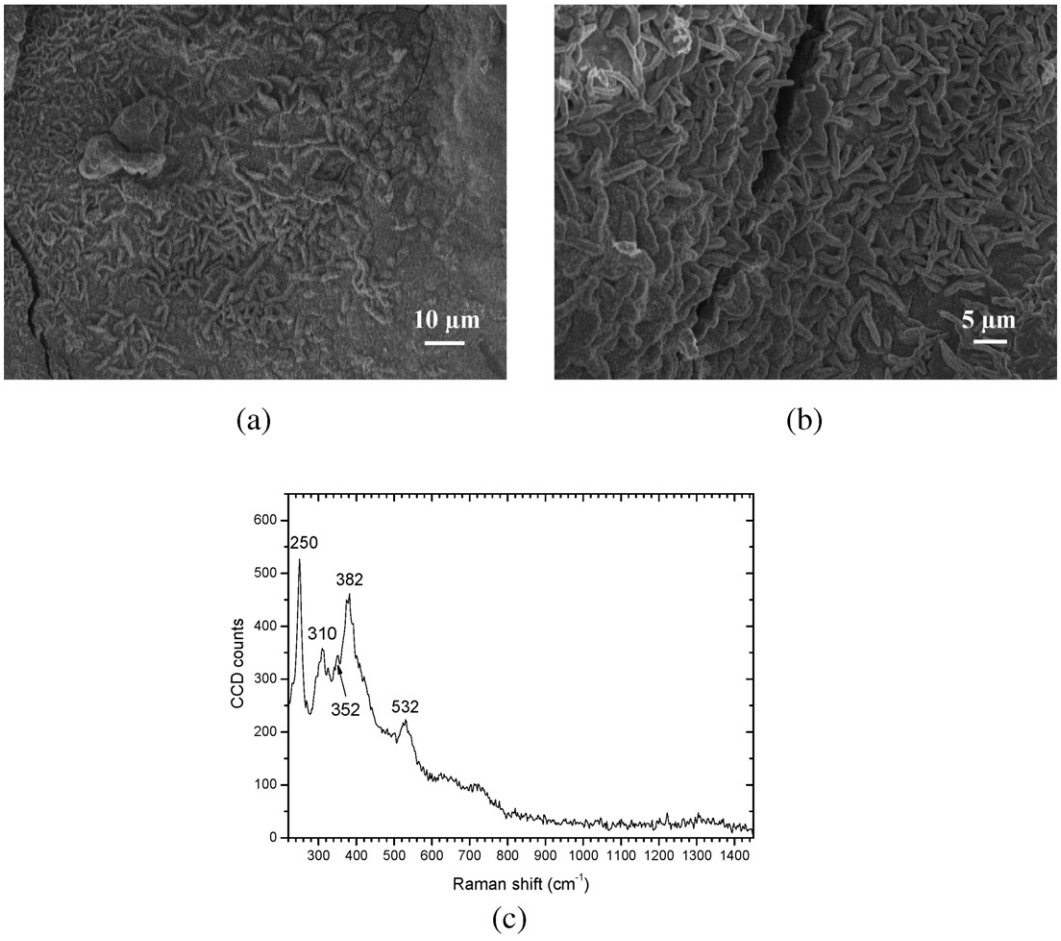

Fig. 6. Laminar (worm nest type) lepidocrocite formations (a–b) and Raman spectrum.

3.3. Laminar morphologies

These laminar morphologies can appear in a wide range of different formations (Fig. 5 to Fig. 11) in which the laminas grow perpendicularly to the surface. There follows a presentation of the different types or appearances observed.

3.3.1. Bar-shaped

These formations are similar to the "bacillus" type morphology that can be observed in bacteria. As in the case of the globular lepidocrocite formations (see Fig. 2), under this heading it is possible to distinguish different types of morphologies that go from a flat surface apparently without any crystalline substructure, which may correspond to amorphous lepidocrocite aggregates (Fig. 5a–b), to others in which a crystalline substructure can be seen in the form of very thin thorny type laminas (Fig. 5c–d), it even being possible to see the formation of typical goethite needles around the periphery of the bars (Fig. 5e), as occurs with the globular morphologies (see Fig. 2d).

3.3.2. Worm nest shape

This morphology, which also corresponds to the lepidocrocite phase and is commonly referred to by other researchers in atmospheric corrosion studies [2–5,8,13], is shown in Fig. 6a–b. Its appearance is something similar to that described in the preceding point.

The Raman spectrum corresponding to Fig. 6a is shown in Fig. 6c. The spectrum signals two strongest peaks at 250 and 382 cm^{-1}, the first being the stronger, and a weaker peak at 532 cm^{-1}. These three peaks are characteristic of the lepidocrocite phase (see Table 2). In addition to this, a shoulder peak is seen at 310 cm^{-1}, between the two strongest peaks, also refers to lepidocrocite according to other researchers [27,33].

3.3.3. Bird's nest shape

Fig. 7 shows this type of morphology, which has also commonly been referred to by other researchers [2–5,8,13]. The Raman spectrum corresponding to one of the laminas (Fig. 7c) presents the characteristic peaks of lepidocrocite at 248, 378 and 524 cm^{-1} (see Table 2). In addition to this, a shoulder peak is also seen between the two strongest peaks, situated at 312 cm^{-1}, also referring to lepidocrocite, as in the preceding case.

As mentioned before, the rust formed during exposure of carbon steel to the atmosphere is usually a complex mixture of several phases, formed close to each other, each rust phase acquiring a wide variety of morphologies and crystal sizes due to differences in their growth conditions. Fig. 8, by way of example, shows lepidocrocite formations with different morphologies (worm nest and bird's nest) very close to each other.

3.3.4. Flower petal shape

Fig. 9 shows SEM views corresponding to this type of morphology. The petals (laminas) that comprise the flowery structures can be of different types, in some cases taking the form of very thin laminas (Fig. 9a) and in others having a hexagonal appearance with more or less rounded (Fig. 9b) or serrated edges (Fig. 9c).

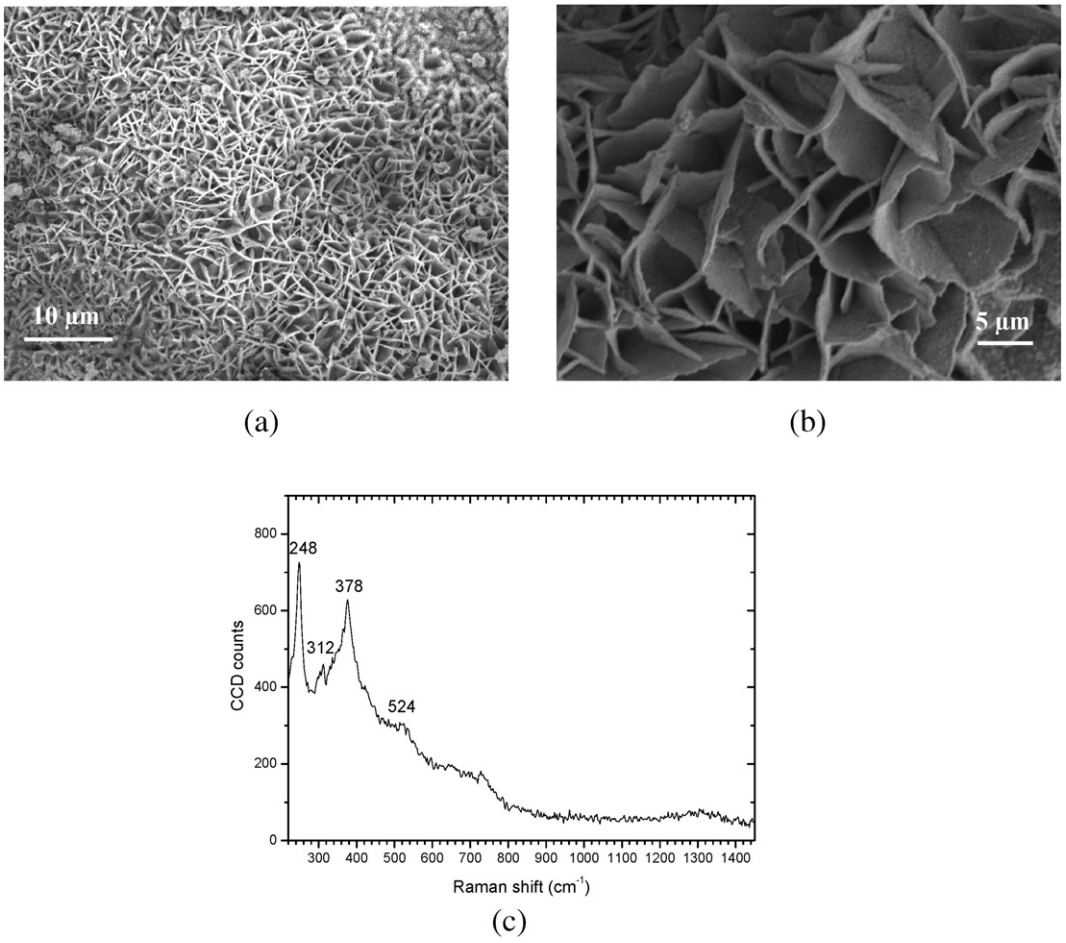

Fig. 7. Laminar (bird's nest type) lepidocrocite formations. SEM view at different magnification (a–b) and the corresponding Raman spectrum (c).

3.3.5. Feather shape

Fig. 10a presents this type of morphology, which is somewhat different to the preceding ones. Its appearance is reminiscent of fragments of a feather or broken glass, terms coined by Raman et al. [2–5].

The corresponding Raman spectrum (Fig. 10b) indicates the following peaks: 250, 380, 530, 642 and 1300 cm^{-1}, typical of the lepidocrocite phase (see Table 2). A shoulder peak is also observed at 304 cm^{-1} that could correspond to goethite phase although according to other researchers also refers to lepidocrocite [30,34].

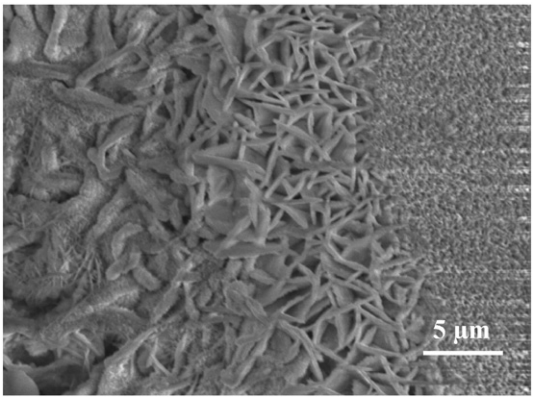

Fig. 8. Laminar lepidocrocite formations in the form of a bird's nest (right) and worm nest (left) formed close to each other.

3.3.6. Miscellaneous

Fig. 11 depicts a number of laminar morphologies with different features to those described above, namely: clumps of grass (Fig. 11a) or weeds (Fig. 11b); hanks of string or threads (Fig. 11c–d); cooked spaghetti (Fig. 11e), as termed by Raman et al. [2]; laminas forming compartments (Fig. 11f); and laminas in the form of tentacles or tree roots that are reminiscent of the arms of a starfish (Fig. 11g–h).

3.4. Tubular morphologies

These are formations in which the crystalline aggregates are constituted by prisms, tubes or rods, etc. Fig. 12 presents different morphologies with these characteristics.

The prismatic formations shown in Fig. 12a–b correspond to goethite crystals, as noted by Raman et al. [2–5] and Cornell and Schwertmann [1] in their publications and at time form twin crystals as can be seen in Fig. 12b.

The tubular formations that are shown in Fig. 12c are constituted by a lattice of elongated cylinder- , tube- or cigar-shaped crystals typical of the "rod-type" morphology exhibited by akaganeite [15,17]. The Raman spectrum obtained for these crystals (Fig. 12e) shows the strong peaks at wavelengths of 308 and 386 cm^{-1} and other weaker peaks at 496 and 722 cm^{-1}, indicating that they do indeed correspond to the akaganeite phase.

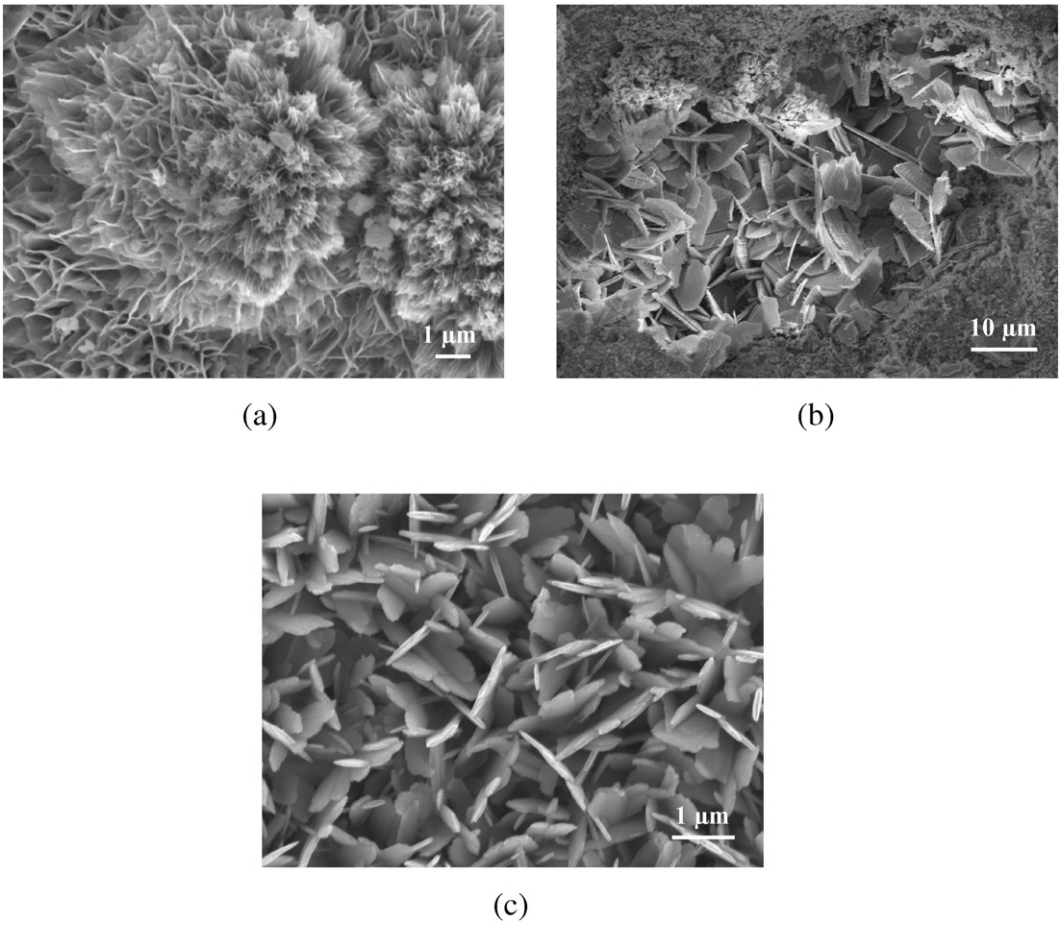

Fig. 9. Laminar formations with a flowery appearance, where the petals show different morphologies.

3.5. Toroidal morphologies

Fig. 13 shows a number of toroidal formations observed sporadically by SEM in the rust formed in marine atmospheres. The micrograph in Fig. 13a corresponds to the outermost surface of a rust formed on carbon steel that had been exposed for 12 months in a marine atmosphere at a certain distance from the shoreline with lower chloride deposition rate (245 mg/m^2·day), while the micrographs in Fig. 13b–c and d correspond to rusts formed during 3 and 12 months in very severe marine atmospheres (very close to the shoreline) with higher chloride deposition rates, 1634 and 390 mg/m^2·day respectively. Specifically, the observed surface corresponding to the latter micrographs was the remaining steel after detachment of the thick rust layers formed in these conditions with the assistance of a utility knife.

The internal substructure of the ring in Fig. 13a is very similar to the substructures shown previously for the globular (Fig. 2c) or laminar

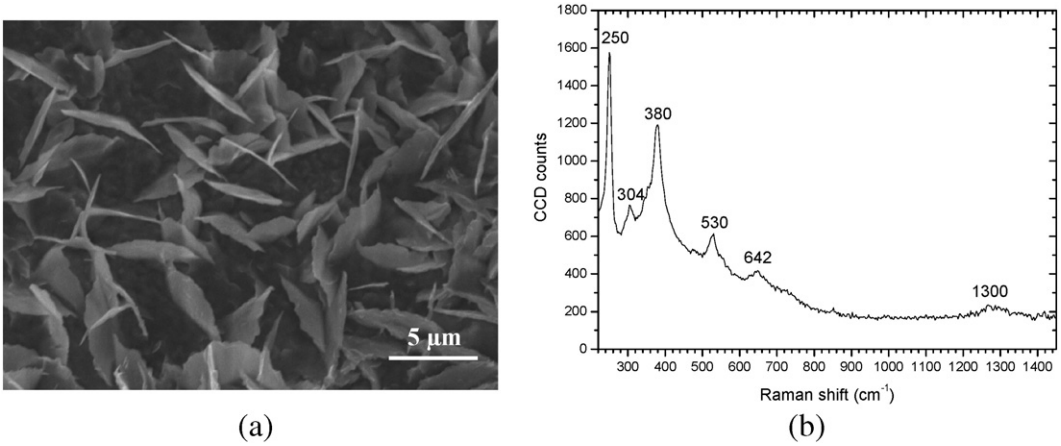

Fig. 10. Lamina formations with a feather-like appearance. SEM view (a) and the corresponding Raman spectrum (b).

formations (Fig. 5c), in the form of very thin laminas with a thorny appearance, and therefore it may be speculated that these rings are of lepidocrocite.

In contrast, the toroidal formations in Fig. 13b–d present a highly different morphology in the form of blackish circular rings, which according to Raman et al. [2] correspond to magnetite. These researchers infer

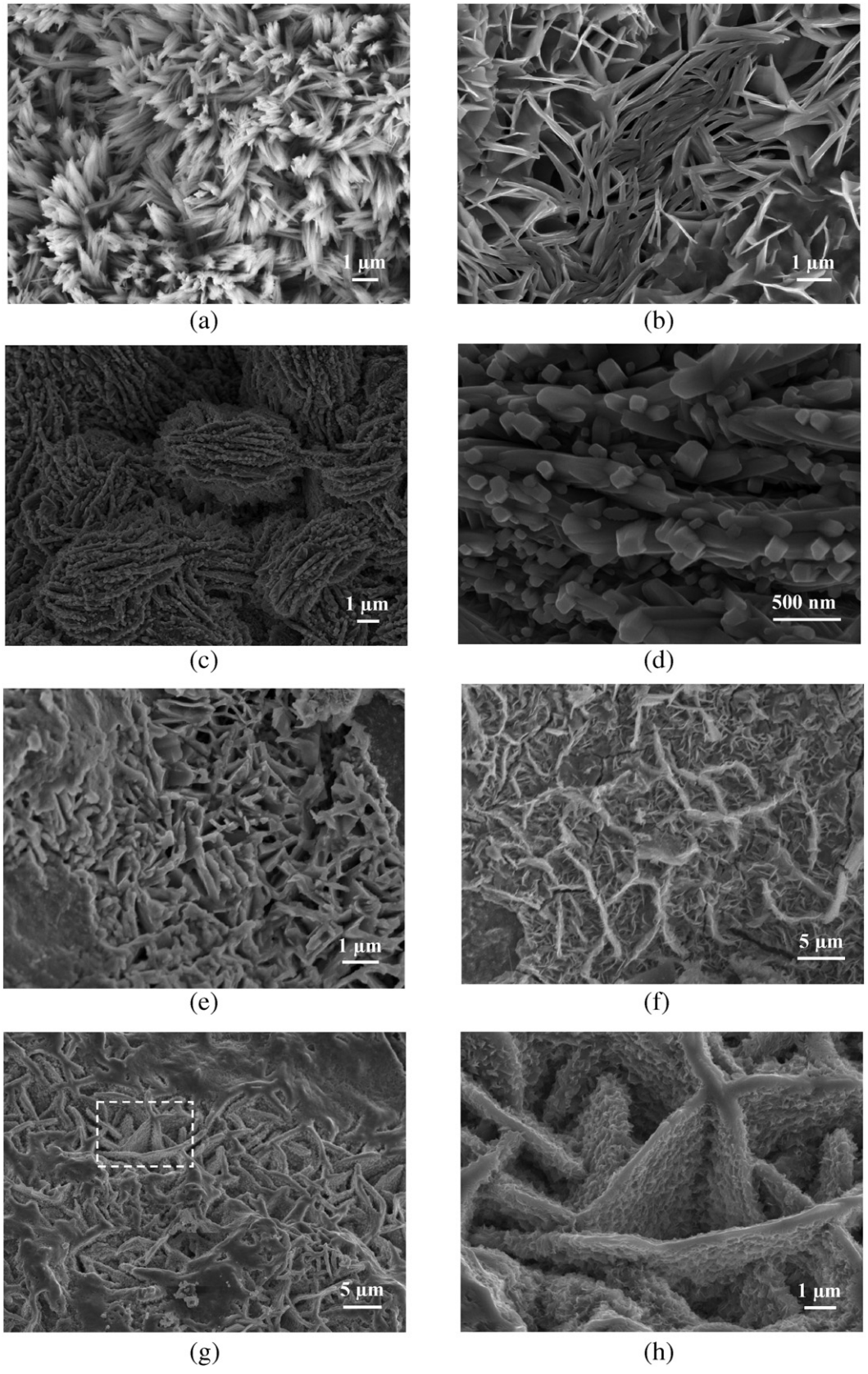

Fig. 11. Miscellaneous other laminar morphologies.

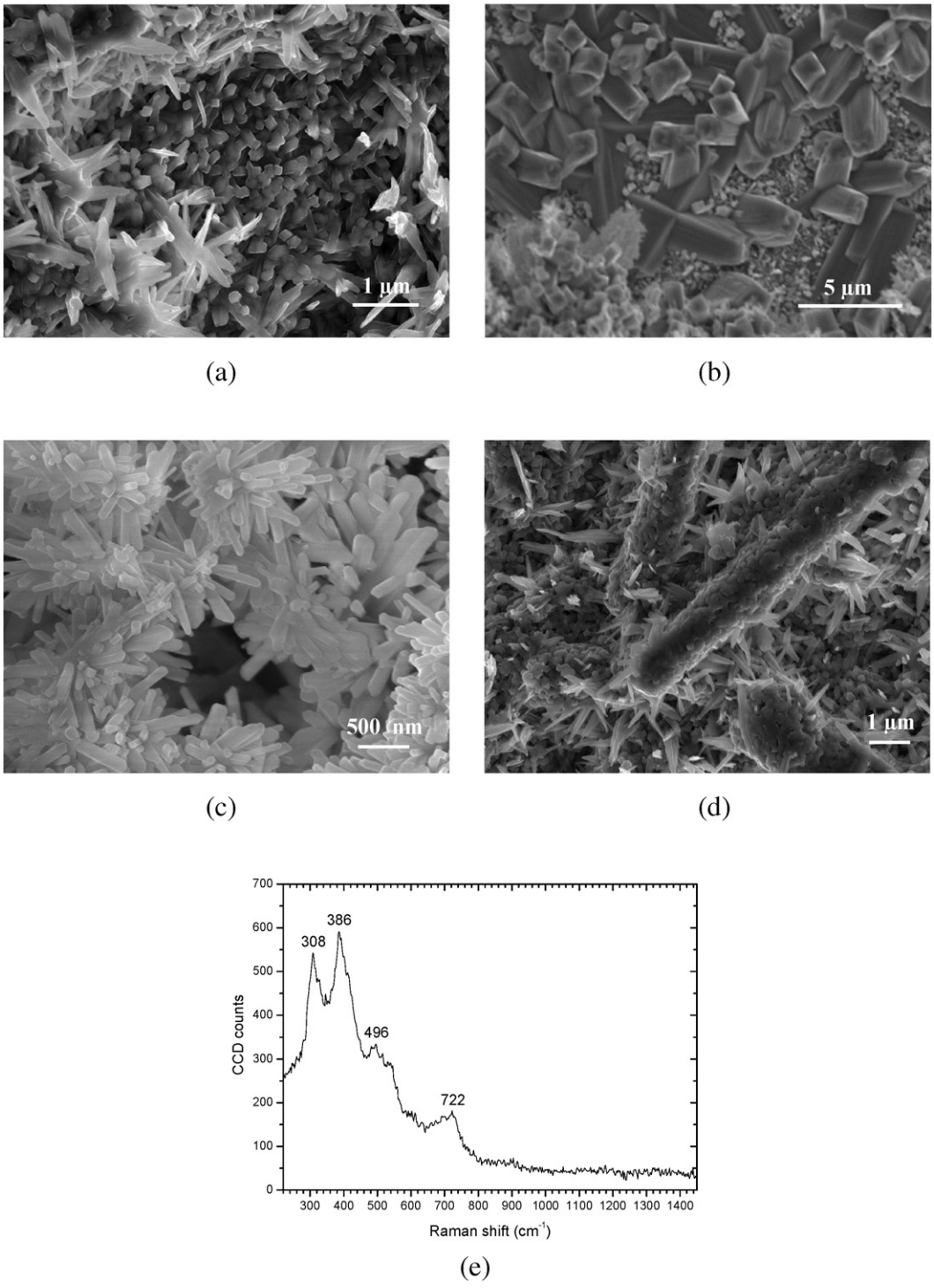

Fig. 12. Tubular formations with different morphologies: prismatic type (a–b) and rod type (c–d). The Raman spectrum (e) corresponds to the SEM view of the formation shown in (c).

that the bulging of these rings, which they term as "doughnuts", must be due to structural transformations taking place along the outer edges of the magnetite in "flat black patch" type formations of this component such as that shown in Fig. 14. The blackish "doughnut" type rings sometimes appear piled one on top of the other, as can be seen in Fig. 13c, similar formations to those observed by Raman et al. [2].

The Raman spectrum prepared by the authors on the surface of the doughnuts is shown in Fig. 13e. Despite containing abundant noise, a very weak Raman signal is observed at 667 cm^{-1}, indicating that this was magnetite (see Table 2). It was not easy to obtain the Raman spectrum on the doughnut-type blackish formations, a difficulty also encountered by other researchers [26,32]. In many attempts no Raman response was obtained due to the fact that magnetite is highly sensitive to laser irradiation [30], causing it to decompose and be transformed into a more stable phase such as hematite [26,30,32].

The fact that we have initially observed this type of black doughnut-like morphology on the remaining steel after exfoliation of the thick rust layer that covered it, in other words at the steel/rust interface, is logical

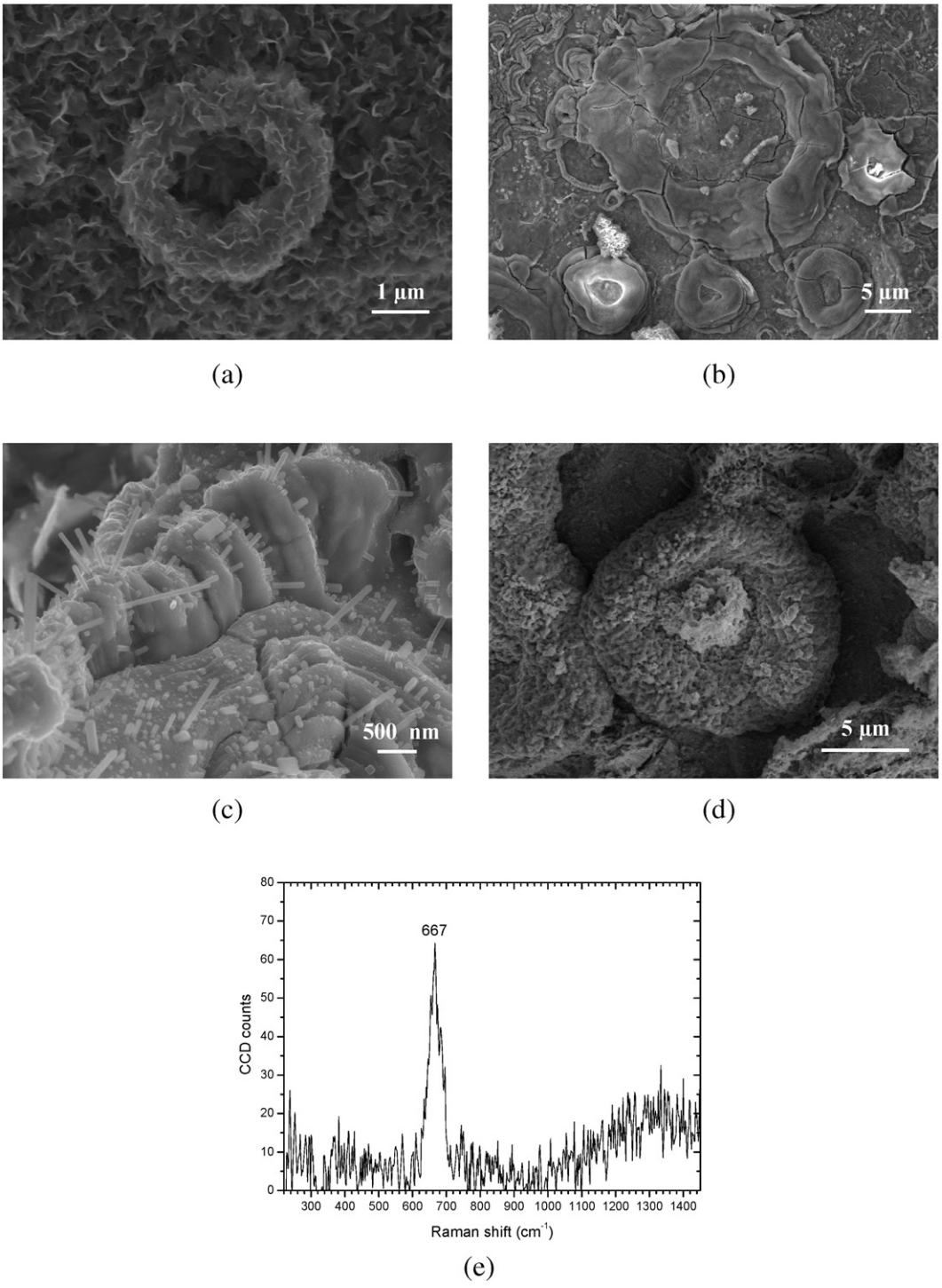

Fig. 13. Toroidal formations of different natures, possibly lepidocrocite (a) and magnetite (b–d). The Raman spectrum of magnetite (e) corresponds to the SEM view shown in (b).

considering that this rust phase is known to form on areas where the oxygen concentration is depleted [14,16–18,40].

3.6. Geode type morphology

This unusual and singular oolitic or globular morphology is constituted by fish-egg-like spherical formations (Fig. 15a). When these formations are split open (Fig. 15b) it is possible to see the crystalline aggregates that comprise their interior, which is reminiscent of the crystalline growth that occurs inside mineral geodes.

On the outer surface of one of these formations (Fig. 15c) a Raman spectrum was performed (Fig. 15d) showing the following peaks: three strongest peaks at 248, 306 and 380 cm^{-1} (in increasing order of strength) and two weaker peaks at 522 and 608 cm^{-1}. The peaks at 248 and 522 cm^{-1} may correspond to lepidocrocite, while those defined at 306, 380 and 608 cm^{-1} may correspond to akaganeite. It may therefore be speculated that this is a mixture of lepidocrocite and

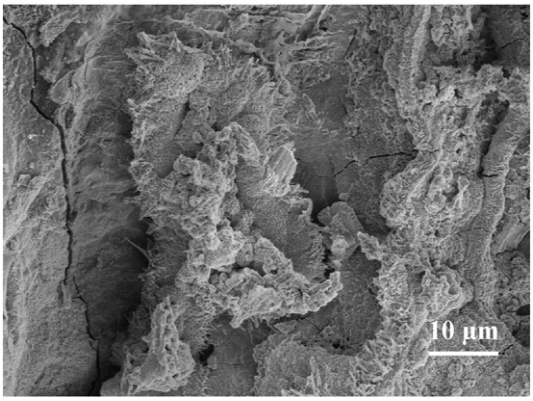

Fig. 14. Black flat patch magnetite formations.

akaganeite phases. The location of these formations at the steel/rust interface, as in the case of magnetite in the preceding point, would lend credibility to this interpretation as it is the place where the akaganeite phase is preferentially formed [14,15,17].

3.7. Deposits

We cannot end this classification without mentioning that during the SEM study of the outermost rust layer, it was common to observe structures that have nothing to do with rust phases but rather with deposits of bacteria, spores, particulate matter, etc. from the atmosphere or the terrain around the corrosion stations where the study was carried out, all of which has frequently led to errors and misinterpretations. Fig. 16a–d show several examples of the deposits obtained in our studies. Such deposits should obviously not yield a Raman response, as is confirmed in the spectrum shown in Fig. 16e which was carried out on the spherical formation in Fig. 16d.

4. Conclusions

The following most relevant conclusions of this study may be drawn:

–Five main rust phases morphological types are distinguished: globular, acicular, laminar, tubular and toroidal.

–The lepidocrocite rust phase, which is the most abundant when observing the outermost surface of the rust layer, tends to form globular morphologies and laminar morphologies of different types, in the form of bars, worm nests, bird's nests, feather-like, etc.

–The goethite rust phase presents two very different types of morphology: acicular morphologies in the form of needles and hairs and tubular morphologies in the form of prisms.

–The akaganeite rust phase can present different globular morphologies or tubular morphologies in the form of tubes or rods comprising cigar-shaped crystals.

–The magnetite rust phase basically presents two types of morphologies: flat black patches and black toroidal formations in the form of doughnut-like circular rings.

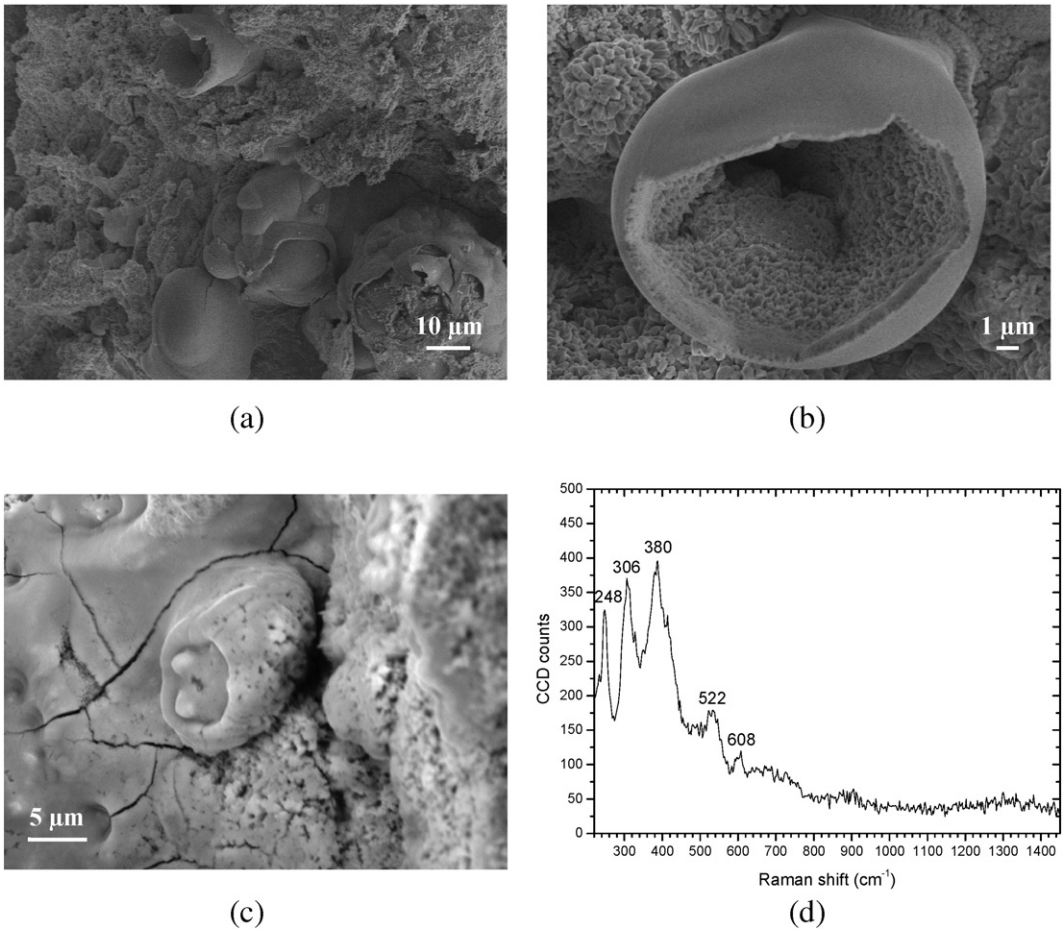

Fig. 15. Geode type formations (a–c). The Raman spectrum (d) corresponds to the SEM view shown in (c).

–The SEM/Micro-Raman technique has proven to be extremely useful for characterising the different morphologies shown by the various rust phases.

Acknowledgements

The authors gratefully acknowledge the financial support for this study from the Ministry of Science and Innovation of Spain (CICYT-MAT2008-06649). The authors would like to express their gratitude to the companies ENEL and GAS NATURAL-FENOSA for the facilities provided and for allowing the location of the corrosion stations at Cabo Vilano wind farm (Camariñas, Spain). A special acknowledgement must be done to R. Wolthuis, L. van Kollenburg and C. Otto from Hybriscan Technologies (Arnhem, The Netherlands) and to F. Agulló-Rueda from ICMM-CSIC (Madrid, Spain) for SEM/MicroRaman measurements and analysis. I. Díaz also acknowledge the PhD scholarship financed by CSIC JAE Programme.

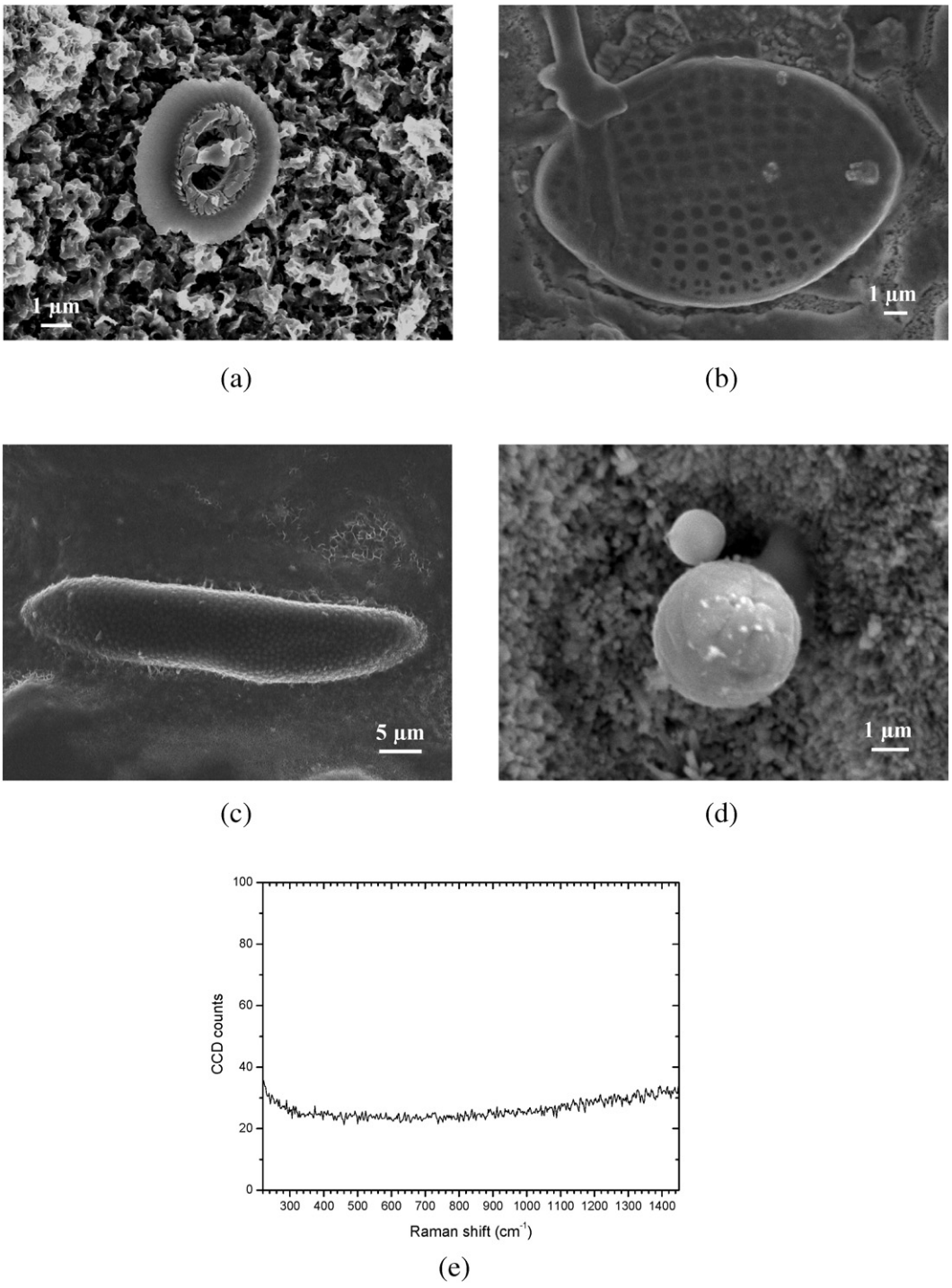

Fig. 16. Deposits coming from the atmosphere or the terrain around the corrosion stations where the study was carried out (a–d). The Raman spectrum (e) corresponds to the SEM view of deposit shown in (d).

References

[1] R.M. Cornell, U. Schwertmann, The Iron Oxides, Structure, Properties, Occurrences and Uses, VCH, Weinheim, 1996.
[2] A. Raman, S. Nasrazadani, L. Sharma, Morphology of rust phases formed on weathering steels in various laboratory corrosion test, Metallography 22 (1989) 79–96.
[3] A. Raman, S. Nasrazadani, L. Sharma, A. Razvan, Morphology of rust phases formed on weathering steels during outdoor atmospheric exposure in open, bold locations, Prakt. Metallogr. 24 (1987) 577–589.
[4] A. Razvan, A. Raman, Morphology of rust phases formed on naturally weathered weathering steels in bridge spans, Prakt. Metallogr. 23 (1986) 223–236.
[5] A. Raman, S. Nasrazadani, L. Sharma, A. Razvan, Morphology of rust phases formed on weathering steels during outdoor atmospheric exposure in sheltered locations under the bridges, Prakt. Metallogr. 24 (1987) 535–548.
[6] A. Raman, A. Razvan, B. Kuban, K.A. Clement, W.E. Graves, Characteristics of the rust from weathering steels in Louisiana bridge spans, Corrosion 42 (8) (1986) 447–456.
[7] Y. Waseda, S. Suzuki, Characterization of Corrosion Products on Steel Surfaces, Springer, Berlin, 2006.
[8] R.A. Antunes, I. Costa, D.L.A. de Faria, Characterization of corrosion products formed on steels in the first months of atmospheric exposure, Mater. Res. 6 (2003) 403–408.
[9] R.A. Antunes, R.U. Ichikawa, L.G. Martinez, I. Costa, Characterization of corrosion products on carbon steel exposed to natural weathering and to accelerated corrosion tests, Int. J. Corros. 2014 (2014) 1–9, ID 419570.
[10] J.G. Castaño, C.A. Botero, A.H. Restrepo, E.A. Agudelo, E. Correa, F. Echeverría, Atmospheric corrosion of carbon steel in Colombia, Corros. Sci. 52 (2010) 216–223.
[11] Y. Ma, Y. Li, F. Wang, The effect of B-FeOOH on the corrosion behavior of low carbon steel exposed in tropic marine environment, Mater. Chem. Phys. 112 (2008) 844–852.
[12] D. de la Fuente, I. Diaz, J. Simancas, B. Chico, M. Morcillo, Long-term atmospheric corrosion of mild steel, Corros. Sci. 53 (2011) 604–617.
[13] J. Alcántara, B. Chico, I. Díaz, D. de la Fuente, M. Morcillo, Airborne chloride deposit and its effect on marine atmospheric corrosion of mild steel, Corros. Sci. 97 (2015) 74–88.
[14] M. Morcillo, B. Chico, J. Alcántara, I. Díaz, J. Simancas, D. de la Fuente, Atmospheric corrosion of mild steel in chloride - rich environments. Questions to be answered, Mater. Corros. 66 (2015) 882–892.
[15] M. Morcillo, J.M. González-Calbet, J.A. Jiménez, I. Díaz, J. Alcántara, B. Chico, A. Mazarío-Fernández, A. Gómez-Herrero, I. Llorente, D. de la Fuente, Environmental conditions for akaganeite formation in marine atmosphere mild steel corrosion products and its characterisation, Corrosion 71 (2015) 872–886.
[16] B. Chico, J. Alcántara, E. Pino, I. Díaz, J. Simancas, A. Torres-Pardo, D. de la Fuente, J.A. Jiménez, J.F. Marco, J.M. González-Calbet, M. Morcillo, Rust exfoliation on carbon steels in chloride-rich atmospheres, Corros. Rev. 33 (2015) 263–282.
[17] D. de la Fuente, I. Díaz, J. Alcántara, B. Chico, J. Simancas, I. Llorente, A. García-Delgado, J.A. Jiménez, P. Adeva, M. Morcillo, Corrosion mechanisms of mild steel in chloride-rich atmospheres, Mater. Corros. 67 (2016) 227–238.
[18] M. Morcillo, J. Alcántara, I. Díaz, B. Chico, J. Simancas, D. de la Fuente, Marine atmospheric corrosion of carbon steels, Rev. Metal. 51 (2) (2015), e045.
[19] E. Pino, J. Alcántara, B. Chico, I. Díaz, J. Simancas, D. de la Fuente, M. Morcillo, Atmospheric corrosion of mild steel in marine atmospheres, Corros. Prot. de Mater 34 (2) (2015) 35–41.
[20] J. Thibeau Richard, W. Brown Chris, H. Heidersbach Robert, Raman spectra of possible corrosion products of iron, Appl. Spectrosc. 32 (6) (1978) 532–535.
[21] T. Ohtsuka, K. Kubo, N. Sato, Raman spectroscopy of thin corrosion films on iron at 100 to 150 °C in air, Corrosion 42 (1986) 476–481.
[22] D. Thierry, D. Persson, C. Leygraf, D. Delichere, S. Joiret, C. Palotta, A. Hugot-Le Goff, In-situ Raman spectroscopy combined with X-ray photoelectron spectroscopy and nuclear microanalysis for studies of anodic corrosion film formation on Fe-Cr single crystals, J. Electrochem. Soc. 135 (1988) 305–310.
[23] N. Boucherit, D. Delichere, S. Joiret, A. Hugot-Le Goff, Passivity of iron and iron alloys studied by voltammetry and Raman spectroscopy, Mater. Sci. Forum 44-45 (1989) 51–62.
[24] J. Dünnwald, A. Otto, An investigation of phase transitions in rust layers using Raman spectroscopy, Corros. Sci. 29 (1989) 1167–1176.
[25] T. Ohtsuka, Raman spectra of passive films of iron in neutral borate solution, Mater. Trans. JIM 37 (1996) 67–69.
[26] D.L.A. de Faria, S. Venâncio Silva, M.T. de Oliveira, Raman microspectroscopy of some iron oxides and oxyhydroxides, J. Raman Spectrosc. 28 (1997) 873–878.
[27] S.J. Oh, D.C. Cook, H.E. Townsend, Characterization of iron oxides commonly formed as corrosion products on steel, Hyperfine Interact 112 (1998) 59–65.
[28] D. Neff, P. Dillmann, L. Bellot-Gurlet, G. Beranger, Corrosion of iron archaeological artefacts in soil: Characterisation of the corrosion system, Corros. Sci. 47 (2005) 515–535.
[29] D. Neff, S. Reguer, L. Bellot-Gurlet, P. Dillmann, R. Bertholon, Structural characterization of corrosion products on archaeological iron: An integrated analytical approach to establish corrosion forms, J. Raman Spectrosc. 35 (2004) 739–745.
[30] D. Neff, L. Bellot-Gurlet, P. Dillmann, S. Réguer, L. Legrand, Raman imaging of ancient rust scales on archaeological iron artefacts for long-term atmospheric corrosion mechanisms study, J. Raman Spectrosc. 37 (2006) 1228–1237.
[31] S. Réguer, P. Dillmann, F. Mirambet, Buried iron archaeological artefacts: Corrosion mechanisms related to the presence of Cl-containing phases, Corros. Sci. 49 (2007) 2726–2744.
[32] F. Dubois, C. Mendibide, T. Pagnier, F. Perrard, C. Duret, Raman mapping of corrosion products formed onto spring steels during salt spray experiments. A correlation between the scale composition and the corrosion resistance, Corros. Sci. 50 (2008) 3401–3409.
[33] A. Demoulin, C. Trigance, D. Neff, E. Foy, P. Dillmann, V. L'Hostis, The evolution of the corrosion of iron in hydraulic binders analysed from 46- and 260-year-old buildings, Corros. Sci. 52 (2010) 3168–3179.
[34] S. Li, L.H. Hihara, A micro-Raman spectroscopic study of marine atmospheric corrosion of carbon steel: the effect of akaganeite, J. Electrochem. Soc. 162 (2015) C495–C502.
[35] P. Colomban, Potential and drawbacks of Raman (micro) spectrometry for the understanding of iron and steel corrosion, in: M. Chiaberge (Ed.), New Trends and Developments in Automotive Systems Engineering, INTECH, Rijeka, 2011.
[36] T. Ohtsuka, S. Tanaka, Monitoring the development of rust layers on weathering steel using in situ Raman spectroscopy under wet-and-dry cyclic conditions, J. Solid State Electrochem. 19 (2015) 3559–3566.
[37] K.J. Gallagher, D.N. Phillips, Proton transfer studies in the ferric oxy-hydroxides. Part 1. Hydrogen exchange between α-FeOOH and water, Trans. Faraday Soc. 64 (3) (1968) 785–795.
[38] I. Díaz, H. Cano, D. de la Fuente, B. Chico, J.M. Vega, M. Morcillo, Atmospheric corrosion of Ni-advanced weathering steels in marine atmospheres of moderate salinity, Corros. Sci. 76 (2013) 348–360.
[39] M. Morcillo, I. Díaz, B. Chico, H. Cano, D. de la Fuente, Weathering steels: From empirical development to scientific design. A review, Corros. Sci. 83 (2014) 6–31.
[40] P. Refait, J.M.R. Genin, The mechanism of oxidation of ferrous hydroxychloride B-$Fe_2(OH)_3Cl$ in aqueous solution: The formation of akaganeite vs goethite, Corros. Sci. 39 (1997) 539–553.

ANEXO III

“Environmental conditions for akaganeite formation in marine atmosphere mild steel corrosion products and its characterization.”

Environmental Conditions for Akaganeite Formation in Marine Atmosphere Mild Steel Corrosion Products and Its Characterization

M. Morcillo,[‡,] J.M. González-Calbet,[**] J.A. Jiménez,[*] I. Díaz,[*] J. Alcántara,[*] B. Chico,[*] A. Mazarío-Fernández,[**] A. Gómez-Herrero,[**] I. Llorente,[*] and D. de la Fuente[*]*

ABSTRACT

The corrosion of mild steel in chloride-rich atmospheres is a highly topical issue. The formation of the oxyhydroxide akaganeite (β-FeOOH) in this type of atmosphere leads to a notable acceleration of the steel corrosion process. The scientific literature contains many references to outdoor marine atmospheric tests, but so far has failed to clarify two basic matters in relation to akaganeite: the environmental conditions necessary for its formation, and its morphological characterization. Research has been performed at three atmospheric corrosion stations located at Cabo Vilano wind farm (Camariñas, Spain) at different distances from the shoreline (332, 590, and 2,400 m), with chloride deposition rates of 390, 74, and 29 mg/m^2/day, respectively, with the exposure of mild steel specimens for 1 year. This paper reports the environmental conditions that generally led to the formation of akaganeite: an annual average relative humidity of around 80% or higher, and simultaneously, an annual average chloride deposition rate of approximately 60 mg/m^2/day or higher. Rigorous characterization of akaganeite was performed by x-ray diffraction, scanning electron microscopy/energy dispersive spectroscopy, and transmission electron microscopy/selected area electron diffraction.

KEY WORDS: atmospheric corrosion, mild steel, rust, scanning electron microscopy, transmission electron microscopy, x-ray diffraction

Submitted for publication: February 17, 2015. Revised and accepted: April 16, 2015. Preprint available online: April 17, 2015, http://dx.doi.org/10.5006/1672.

‡ Corresponding author. E-mail: morcillo@cenim.csic.es.

* National Centre for Metallurgical Research (CENIM-CSIC), Avda. Gregorio del Amo, 8, 28040-Madrid, Spain.

** Dpto. Q. Inorgánica I, Facultad CC. Químicas, Universidad Complutense de Madrid, 28040-Madrid, Spain.

INTRODUCTION

Atmospheric salinity in coastal regions notably increases the atmospheric corrosion rate of steel in comparison with a clean atmosphere, as marine chlorides dissolved in the moisture layer considerably raise the conductivity of the electrolyte film on the metal and tend to destroy any passivating films. The corrosion rate is a function of the chloride deposition rate.[1-3]

The higher corrosion rate of steel in marine atmospheres may also be a result of other causes: (a) being hygroscopic, chloride species (sodium chloride, magnesium chloride, etc.) promote the electrochemical corrosion process, favoring the formation of electrolytes at relative humidity (RH) values lower than 100%, and (b) the solubility of the corrosion products formed also plays an important role. Thus, in the case of iron, which does not form stable basic chlorides, the action of chlorides is more pronounced than with other metals (zinc, copper, etc.) whose basic salts are only slightly soluble.[4]

The rust layer composition depends on the characteristics of the surface electrolyte layer that forms during exposure of the steel to the atmosphere and which originates the atmospheric corrosion process, and thus varies according to the type of atmosphere.[5] Lepidocrocite (γ-FeOOH) and goethite (α-FeOOH) are the major products most commonly found. Magnetite (Fe_3O_4) is another important though minor rust constituent, which is usually detected in the inner part of the rust layer, close to the bare steel where the oxygen concentration is depleted. In marine atmospheres,

ISSN 0010-9312 (print), 1938-159X (online)
15/000143/$5.00+$0.50/0

ANEXO IV

“Rust exfoliation on carbon steels in chloride-rich atmospheres.”

Original article

Belen Chico, Jenifer Alcántara, Elizabeth Pino, Iván Díaz, Joaquín Simancas, Almudena Torres-Pardo, Daniel de la Fuente, José Antonio Jiménez, José F. Marco, José María González-Calbet and Manuel Morcillo*

Rust exfoliation on carbon steels in chloride-rich atmospheres

DOI 10.1515/corrrev-2015-0025
Received April 17, 2015; accepted July 15, 2015; previously published online August 21, 2015

Abstract: The exposure of carbon steel in marine atmospheres can lead in certain circumstances to the formation of thick rust layers (containing a number of compact laminas) that are easily detached (exfoliated) from the steel substrate, leaving it unprotected and considerably accelerating the corrosion process. This deterioration phenomenon is of particular concern in steel infrastructures located close to the sea (civil constructions, bridges, etc.), whose service lifetime can be extraordinarily limited. High times of wetness of the metallic surface and high chloride ion deposition rates play a decisive role in the formation of this type of rust. Research has been carried out for 1 year in eight pure marine atmospheres with annual average chloride deposition rates of 70–1906 mg Cl^-/m^2 day. The studied carbon steels consisted of one mild steel, one conventional weathering steel (Corten A), and one high nickel (~3 wt.%) advanced weathering steel (AWS). The paper describes the environmental conditions that lead to the formation of these thick multilaminar rust layers and presents a characterisation study of this singular type of rust using a variety of analysis techniques: scanning electron microscopy/energy-dispersive X-ray spectroscopy, X-ray diffraction, Mössbauer spectroscopy, and transmission electron microscopy/electron diffraction. The Ni-AWS shows greater resistance to the occurrence of rust exfoliation.

Keywords: carbon steel; Mössbauer spectroscopy; SEM; TEM; XRD.

***Corresponding author: Manuel Morcillo,** National Centre for Metallurgical Research (CENIM-CSIC), Avda. Gregorio del Amo, 8, 28040 Madrid, Spain, e-mail: morcillo@cenim.csic.es
Belen Chico, Jenifer Alcántara, Elizabeth Pino, Iván Díaz, Joaquín Simancas, Daniel de la Fuente and José Antonio Jiménez: National Centre for Metallurgical Research (CENIM-CSIC), Avda. Gregorio del Amo, 8, 28040 Madrid, Spain.
http://orcid.org/0000-0001-8697-6298 (Belen Chico)
Almudena Torres-Pardo and José María González-Calbet: Department of Inorganic Chemistry, Complutense University of Madrid, 28040 Madrid, Spain
José F. Marco: Institute of Physical Chemistry "Rocasolano" (CSIC), C/Serrano, 119, 28006 Madrid, Spain

1 Introduction

The exposure of carbon steel in marine atmospheres can lead in certain circumstances to the formation of thick rust layers containing a number of compact laminas. High times of wetness of the metallic surface and an atmosphere with a high chloride deposition rate play a decisive role in the formation of this type of rust. These thick rust layers tend to become detached from the steel substrate, leaving it uncovered and without protection and thus accelerating the metallic corrosion process.

This type of deterioration is of particular concern in relation to the durability of steel infrastructures located close to the sea, especially bridges, where the tendency has been to use weathering steels without any paint coating to achieve target service lifetimes of 100 years (Hara, 2008). In Japan and the United States, widespread corrosion reviews are currently under way to evaluate old and new steel bridges for corrosion problems that may shorten their serviceable life (Cook, 2005b).

This particular kind of damage is not only limited to marine atmospheres with high chloride ion deposition rates. Although typically associated with marine environments, chlorides are actually also prevalent in the environment from the use of road deicing salts. As Cook (2005b) pointed out, heavy use of deicing salts, as much as 20 tons/lane-mile/year, is common throughout the regions of the snow belt in the northern states of America.

ANEXO V

“Corrosion mechanisms of mild steel in chloride-rich atmospheres.”

 DOI: 10.1002/maco.201508488

Corrosion mechanisms of mild steel in chloride-rich atmospheres

D. de la Fuente, I. Díaz, J. Alcántara, B. Chico, J. Simancas, I. Llorente, A. García-Delgado, J. A. Jiménez, P. Adeva and M. Morcillo*

This work analyses the corrosion mechanisms of carbon steel when exposed to marine atmospheres with very different chloride ion deposition rates. Two extreme situations are described, characterized by a "consolidated rust layer" (at relatively low atmospheric salinities), formed by a diffusion-controlled corrosion mechanism in which the reduction of dissolved oxygen in the aqueous film deposited on the metal is the predominant cathodic reaction, and an "exfoliated rust layer" (at high atmospheric salinities), where the cathodic reaction of hydrogen evolution becomes important, notably accelerating the corrosion process. The research has employed a range of near-surface and bulk sensitive analytical techniques (SEM/EDS, μXRD, and SEM/μRaman) to characterize the corrosion products and rust layers formed.

1 Introduction

Atmospheric salinity in coastal regions causes a notable increase in the atmospheric corrosion rate compared to clean atmospheres. At first, several causes were proposed: (a) marine chlorides dissolved in the moisture layer considerably raise the conductivity of the electrolyte film on the metal and tend to destroy any passivating films; the corrosion rate is a function of the chloride ion activity, (b) being hygroscopic, chloride species (sodium chloride, magnesium chloride, etc.) promote the electrochemical corrosion process, favoring the formation of electrolytes at relative humidity (RH) values below 100% [1], and (c) the solubility of the corrosion products formed in the case of iron is more pronounced than with other metals (zinc, copper, etc.) whose basic salts are only slightly soluble [2]. In the last 15 years, there has been great progress in scientific knowledge of atmospheric corrosion in this type of atmospheres.

The rust layer composition depends on the characteristics of the surface electrolyte layer that forms during exposure of the steel to the atmosphere and which originates the atmospheric corrosion process and thus varies according to the type of atmosphere. Lepidocrocite and goethite are the major corrosion products most commonly found. Magnetite is another important though minor rust constituent which is usually detected in the inner part of the rust layer, close to the bare steel where the oxygen concentration is depleted. In marine atmospheres, where the surface electrolyte contains chlorides, another ferric oxyhydroxide, akaganeite may also form, and the magnetite content is usually higher [3].

In a previous article, the authors described the peculiarities of carbon steel corrosion in very severe marine atmospheres and pointed out a number of uncertainties that still needed to be explained, among them, the fundamental mechanisms of rust formation in chloride-rich marine atmospheres [4]. *Nishimura* et al. also point out that research on this aspect has been rather scarce [5]. Thus, it is important to analyze in greater depth the carbon steel corrosion mechanisms that operate in this type of atmospheres, where the variable with the greatest influence is the chloride ion deposition rate (atmospheric salinity) at the exposure site.

The present work considers three marine atmospheres with very different salinity levels with the aim of shedding light on the various mechanisms involved in the corrosion of mild steel in this type of atmospheres. The research has employed a range of near-surface and bulk sensitive analytical techniques: Scanning electron microscopy (SEM)/energy dispersive spectrometry (EDS), X-ray microdiffraction (μXRD), and micro-Raman spectroscopy (μRaman).

2 Experimental procedure

Research has been carried out in the pure marine atmosphere at Cabo Vilano wind farm (Camariñas, Spain) using two corrosion stations located at different distances from the shoreline. Table 1 shows the environmental characteristics and corrosivity categories of the atmospheres where the study was carried out. Meteorological data was supplied by a weather station belonging to the Spanish Meteorological Agency (AEMET), situated very close (25 m) to corrosion station 1. The atmospheric corrosion stations

D. de la Fuente, I. Díaz, J. Alcántara, B. Chico, J. Simancas, I. Llorente, A. García-Delgado, J. A. Jiménez, P. Adeva, M. Morcillo
National Centre for Metallurgical Research (CENIM-CSIC), Avda. Gregorio del Amo, 8, 28040 Madrid (Spain)
E-mail: morcillo@cenim.csic.es

Table 1. Atmospheric corrosion stations. Distance from shore, environmental characteristics, and corrosivity categories

Corrosion station	Distance to the shore (m)	T (ºC)	RH (%)	Annual average chloride deposition rate (mg m^{-2} day^{-1})	1st year corrosion	
					Attack penetration (μm)	Corrosivity category [6]
Cabo Vilano (station 1)	332	13.0	83.5	1906[a)]	177[a)]	CX
Cabo Vilano (station 2)	2400	13.0	83.5	70	50	C3-C4
Ponto Do Porto (background station) [7,8]	7000	12.0	79.0	3.6	29	C3

[a)]Values corresponding to the first 6 months of exposure.

were equipped with the necessary instrumentation to measure atmospheric pollution in terms of the chloride deposition rate [9]. The atmospheric sulfur dioxide content was negligible (1.0 mg sulfur dioxide/$m^2 \cdot$ day) [10].

In order to know the background corrosivity of the testing area, measured at a point sufficiently far away from the shoreline for the atmospheric salinity to be practically negligible, Table 1 includes as a control information from the Ponte Do Porto corrosion station (background station belonging to other researchers) [7,8] and located some 7 km from Cabo Vilano with very similar climatic characteristics, where the reported salinity is a very low 3.6 mg chloride/$m^2 \cdot$ day.

Panels of mild steel (whose composition is shown in Table 2) measuring $100 \times 50 \times 1$ mm^3 were exposed in quadruplicate for one year on open-air racks at an angle of 45 ° from the horizontal plane [11]. After exposure, the specimens were withdrawn from the testing stations in order to obtain data on mass loss due to corrosion (in triplicate) and a fourth specimen was employed for characterization of the corrosion products formed.

The total exposure time of the test specimens was 12 months (April 2013–March 2014). One series of mild steel specimens (for characterization of corrosion products and rust layers) and the wet candles for analysis of the chloride ion deposition rate were withdrawn every 3 months, while steel specimens for mass loss calculations were withdrawn after 6 and 12 months. Unfortunately, annual salinity data and annual steel corrosion data is not available for station 1 due to wind damage sustained in the third quarter of the test year.

2.1 Determination of corrosion rate

The corrosion rate of the steels during atmospheric exposure was determined gravimetrically by mass loss using a solution of hydrochloric acid and hexamethylenetetramine (corrosion inhibitor) according to ISO 8407, Annex A, designation C.3.5. [11]. In all cases, a Mettler AT261 DeltaRange microbalance to the nearest 10^{-4} g was used.

Table 2. Composition of the mild steel (wt%)

C	Si	Mn	P	S	Ca
0.050	<0.050	0.17	<0.010	≤0.010	<0.005

2.2 XRD measurements

XRD analysis was carried out on powdered rust samples obtained by grinding in an agate mortar the corrosion product layer formed on the skyward surface of the steel specimens and screening the rust to obtain a particle size of less than 125 μm. The powdered rust was removed by vigorous brushing with a small nylon brush.

XRD measurements were performed with a Bruker AXS D8 diffractometer equipped with a cobalt X-ray tube, Goebel mirror optics and a LynxEye linear position sensitive detector for ultra-fast XRD measurements. This type of radiation is especially suitable for iron-rich samples to avoid the strong fluorescence resulting from copper radiation and to produce high resolution data. A current of 30 mA and a voltage of 40 kV were employed as tube settings. Operating conditions were selected to obtain XRD profiles of sufficient quality, namely optimal counting statistics, narrow peaks, and detection of small diffraction peaks of minor phases. The XRD data was collected over a 2θ range of 10–80 ° with a step size of 0.02 °. The qualitative identification of crystalline phases present in the rust formed on steels was performed from XRD patterns using the JCPDS database and DIFFRACplus EVA software by Bruker AXS.

In the case of the exfoliated rust samples formed at station 1, X-ray microdiffraction measurements were also performed in order to know the composition of the rust throughout the thickness of the exfoliated layer. XRD microdiffraction measurements were collected with a Bruker AXS D8 diffractometer equipped with a cobalt X ray-tube, a primary-beam collimator, a laser that focused on the point of the surface to be analyzed (500 μm in diameter), and a LynxEye linear detector. The generator settings were 40 kV and 30 mA. XRD data was collected over a 2θ range of 10–100 ° with a step width of 0.03 ° and a counting time of 3 s/step.

2.3 SEM/EDS study

High resolution SEM was carried out with a Hitachi S4800 working at an acceleration voltage of 2 kV at different magnifications. SEM equipment was equipped with secondary electron and backscattered electron detectors. Energy-dispersive X-ray spectroscopy (EDS) was conducted with an Oxford Inca analyzer system attached to the SEM working at an acceleration voltage of 15 kV to minimize the matrix effect.

2.4 SEM/μRaman study

An integrated Raman-SEM microscope consisting of a SEM JEOL 6610LV and a Hybriscan HSCMM21 confocal Raman was used. The lateral and axial resolutions of this microscope are approximately 0.5 and 5 μm, respectively. The Raman module is equipped with a 785 nm laser as the excitation source. The laser power was adjusted so that approximately 50–100 μW of light was delivered on the sample with exposure times of 15 s or more and averaging over multiple spectra. SEM images were obtained with 650× magnification and 5 kV acceleration voltage with the backscatter detector.

3 Results

3.1 Attack penetration

Table 1 shows the annual corrosion (attack penetration) of mild steel at the three corrosion stations with very different chloride deposition rates of 3.6, 70.0, and 1906.0 mg chloride/$m^2 \cdot$ day. Enormous differences can be seen between the attack penetration values found and leads us to think that very different steel corrosion mechanisms may act depending on the atmospheric salinity of the exposure site.

In a previous study, the authors saw that the rust layers formed at atmospheric salinities of less than 100 mg chloride/$m^2 \cdot$ day were fairly well consolidated, relatively compact, and presented little cracking. However, when the chloride deposition rate of the atmosphere exceeded that value, the rust layers showed greater cracking and at atmospheric salinities of around 300 mg chloride/$m^2 \cdot$ day and above even became detached from the steel substrate [12]. The SEM micrographs in Fig. 1, carried out on cross sections of the specimens exposed for 3 months at stations 1 and 2, clearly show the enormous difference in the intensity of the attack that has taken place. Attention is drawn to the exfoliation and almost complete detachment of the corrosion product layer at station 1, leaving the underlying steel exposed (with some remains of rust) and showing considerable pitting. The EDS spectrum (Fig. 1a) indicates the existence of abundant chlorine among the remains of rust. In contrast, the rust layer formed on the mild steel exposed at station 2 is seen to be fairly compact and unaffected by exfoliation. The chlorine signal in the EDS spectrum is weaker (Fig. 1b), as is the pitting of the underlying steel.

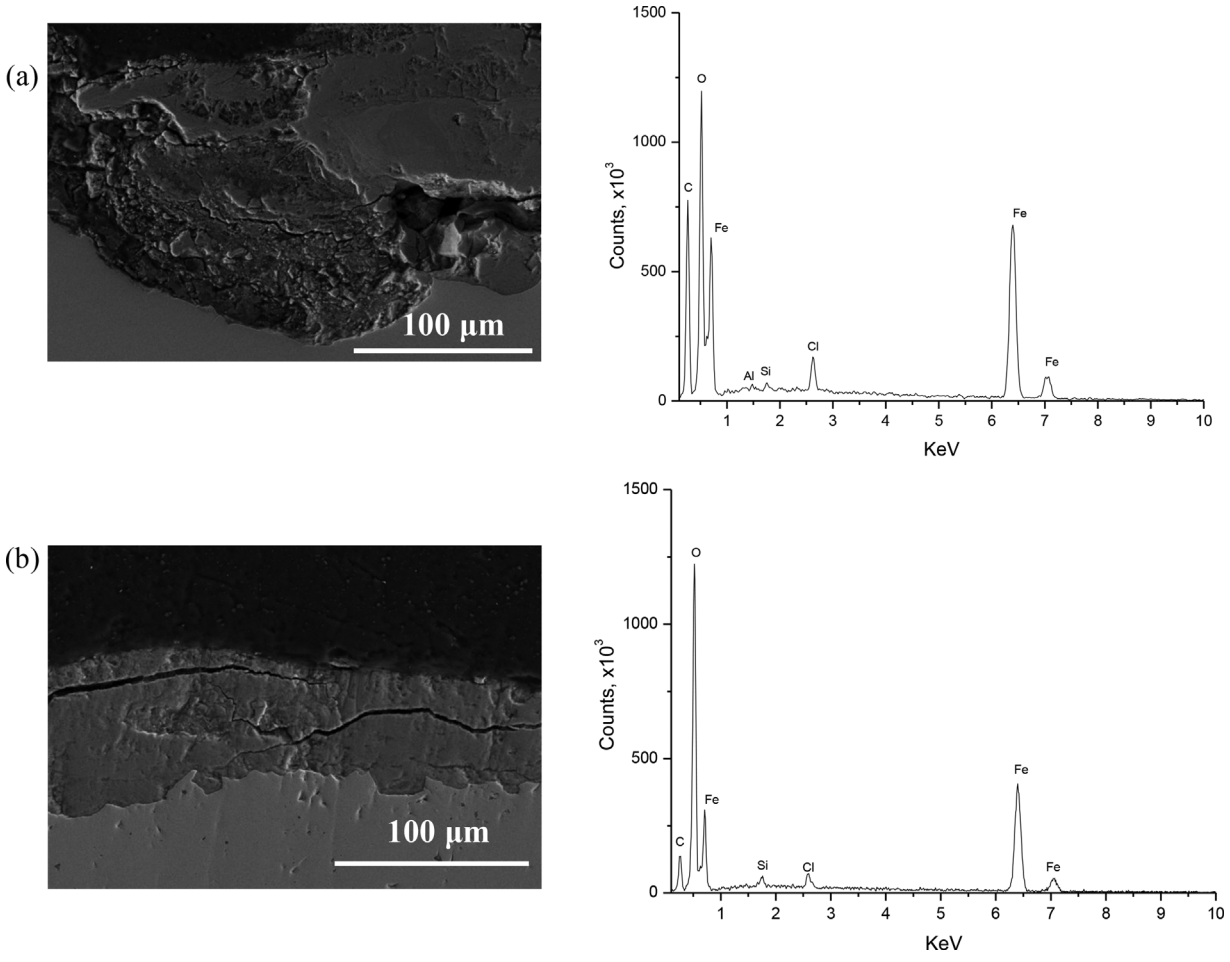

Figure 1. Cross-section SEM observations of mild steel specimens exposed for 3 months at corrosion station 1 (a) and 2 (b). Results of EDS spectra are also shown.

3.2 Rust phases

When semi-quantitative XRD information about the content of the different phases in the rust is required, the quickest way to carry out XRD analysis is to use the reference intensity ratio (RIR) method. Semi-quantitative analysis was thus performed using the I/I_c ratio from each phase (where I is the intensity of the strongest peak of the phase and I_c is the intensity of the strongest corundum reflection in a 50/50 weight fraction mixture) taken from the powder diffraction files (PDF) card [13]. The I/I_c values for the phases considered and corresponding positions for the reflections with the highest intensity are given in Table 3. An example of peak fitting analysis of individual peaks used for the RIR method is shown in Fig. 2a.

However, the RIR method is subject to high inaccuracy, in this case due to systematic peak overlap of the different phases present, especially with minor phases. This problem can be overcome by using Rietveld analysis. As this method fits the whole diffraction pattern, all reflections, overlapping or not, are used in the fitting process, and the complex severely overlapped patterns of our samples can, in principle, be analyzed. For this reason, the Rietveld method has been widely reported as one of the most suitable techniques for quantifying crystalline phases in multi-phase systems from the XRD pattern [14,15]. As shown in the Rietveld refinement of Fig. 2b, in phase mixtures containing akaganeite, magnetite/maghemite, lepidocrocite, and goethite, the most intense spinel peak (113) at ~41.4 °, and lepidocrocite peak (210), at ~31.5 °, overlap with several reflections of the other phases, producing a high relative error in the determination of phase fractions using the RIR fitting method.

Besides, the Rietveld refinement explicitly includes other parameters like the lattice parameter, crystal structure, micro-strain, crystallite size, etc., which are very useful in micro-structure characterization [16]. In this work, version 4.2 of the TOPAS Rietveld analysis program (Bruker AXS) was used for XRD data refinement. For the application of Rietveld refinement, instrument functions were empirically parameterized from profile shape analysis of a corundum sample measured in the same conditions. The refinement protocol also included major parameters like background, zero displacement, scale factors, peak breadth, and unit cell parameter. The quality and reliability of the Rietveld analysis was quantified by the corresponding figures of merit: the weighted sum of residuals of the least squares fit, R_{wp}, the statistically expected least squares fit, R_{exp}, the profile residual, R_p, and the goodness of fit (sometimes referred as chi-squared), G_oF [17]. As $G_oF = R_{wp}/R_{exp}$, a $G_oF = 1.0$ means a perfect fitting.

Table 3. I/I_c values for the phases used and corresponding peak positions for cobalt radiation

Phase	JCPDS card	Reflection (hkl)	Peak position (2θ)	I/I_c
Lepidocrocite	044–1415	(210)	31.513	1.20
Goethite	081–0463	(110)	24.668	2.79
Magnetite/Maghemite	019–0629	(113)	41.375	4.90
Akaganeite	042–1315	(10–1)(101)	13.758	1.32

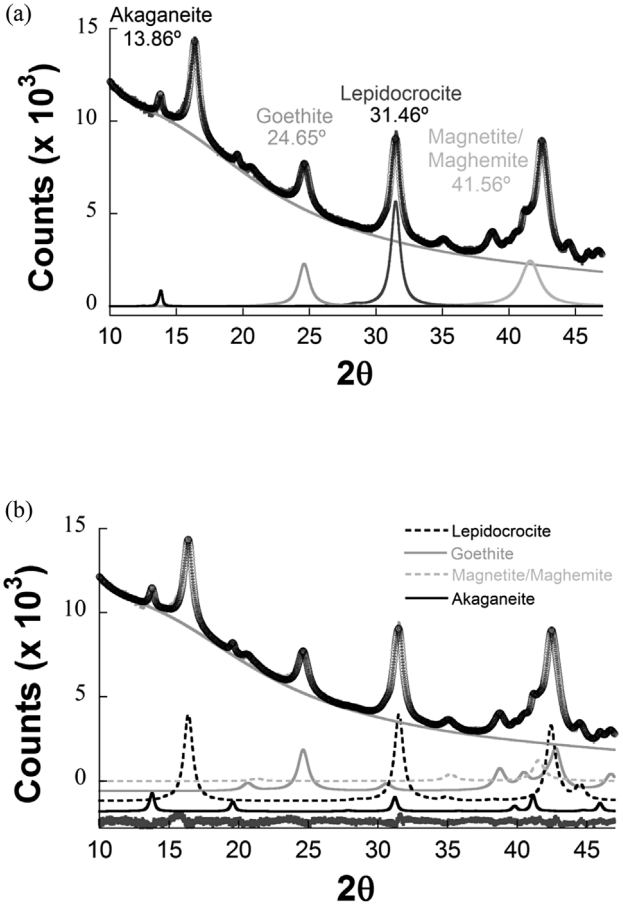

Figure 2. Details of peak fitting analysis of individual peaks used for the RIR method (a) and Rietveld analysis (b) of an experimental diffractogram obtained for the rust formed on mild steel exposed during 9 months in station 2.

Figure 3 displays X-ray diffractograms obtained for the rust samples formed in one year at corrosion stations 1 (Fig. 3a) and 2 (Fig. 3b) after fitting by the Rietveld method. The diffractograms show the presence of lepidocrocite, goethite, and akaganeite phases along with the strongest diffraction peak corresponding to a cubic iron oxide, magnetite, and/or maghemite. Because both oxide compounds crystallize in a spinel crystal structure and their lattice parameters are very similar, their diffractograms are practically identical. Both phases are associated to the diffraction angle next to 35 ° [18]. As it is very complicated to discriminate between magnetite and maghemite, all cubic iron oxides have been referred to in this paper as "spinel." It is noted that in the background corrosion station of Ponte Do Porto, located in an atmosphere with a practically negligible chloride deposition rate (see Table 1), the researchers who carried out the study only report the presence of lepidocrocite (not ruling out a small contribution of the goethite phase) in the corrosion products formed on steel after one year of atmospheric exposure [7,8].

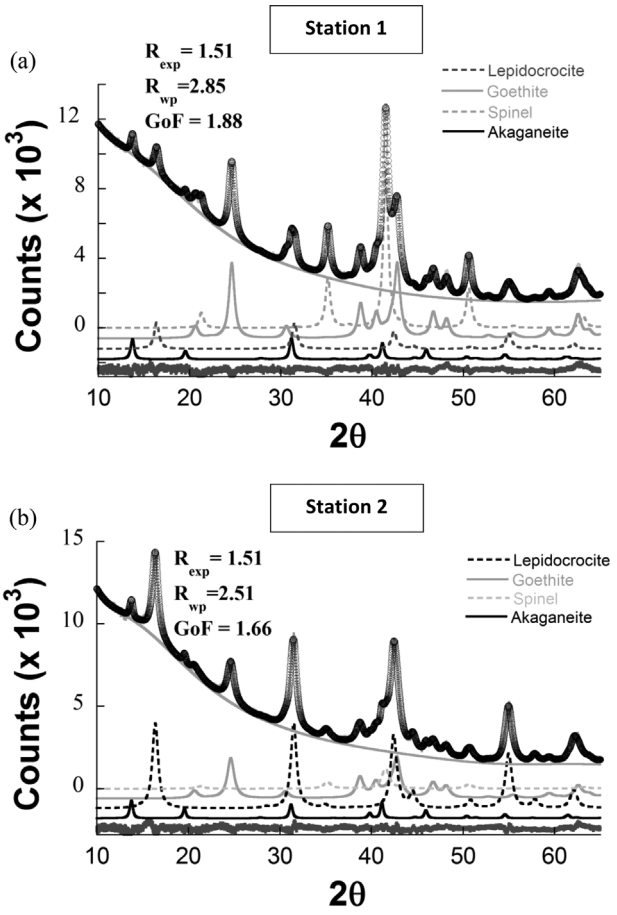

Figure 3. X-ray diffractograms (Rietveld) of the rusts formed on mild steel exposed during one year at corrosion stations 1 (a) and 2 (b).

Table 4 sets out the results obtained by XRD using the Rietveld fitting method for rust phases present in the corrosion product layers formed on mild steel exposed for 3, 6, 9, and 12 months at the corrosion stations 1 and 2. From observation of Table 4, a higher spinel content is inferred in the rust formed in the marine atmosphere of highest salinity (station 1). It is also seen that the spinel content increases even more after 6 months of exposure. In contrast, the lepidocrocite content is notably lower.

4 Discussion

The rust layer composition depends on the characteristics of the surface electrolyte layer that forms during exposure of the steel to the atmosphere and which originates the atmospheric corrosion process, and therefore varies according to the type of atmosphere. There is currently consensus that in pure atmospheres (free of pollutants) or atmospheres with very low chloride deposition the main corrosion products formed on steel are lepidocrocite and goethite. Magnetite can be also formed as one of the main constituents of the rust although with a minor content and is usually detected in the inner part of rust adhering to the steel surface of specimens that have been subjected to prolonged exposure, where oxygen depletion may occur [19,20]. In marine atmospheres, where the surface electrolyte contains chlorides, akaganeite is also found [21]. As shown by *Keller* [22], rust can contain up to 6 wt% chloride and be formed at an early corrosion stage in chloride-containing solutions by hydrolysis of iron (II) chloride in the presence of iron.

In view of the information obtained in the three marine atmospheres with different levels of chloride ion deposition (Table 1), there seem to be two notably different situations with regard to the mild steel atmospheric corrosion mechanisms involved: (a) establishment of a consolidated, adherent and continuous rust layer (stations 2 and Ponte Do Porto), and (b) formation of an exfoliated rust layer that is easily detached from the base steel leaving large areas of this uncovered (station 1).

4.1 Consolidated rust layer

When a consolidated layer of corrosion products remains on the steel surface, the conditions are right for a diffusion-controlled corrosion mechanism to act, in which the aggressive species from the atmosphere (oxygen, water, and chloride) pass through the rust layer to interact with the underlying steel. This situation seems to occur in relatively low chloride-containing atmospheres (stations 2 and Ponte Do Porto). The steel corrodes according to the anodic reaction:

$$Fe \rightarrow Fe^{2+} + 2e^{-} \quad (1)$$

Table 4. XRD quantification (Rietveld) of rust phases formed on mild steel exposed in the corrosion stations

Corrosion station	Cl^- deposition rate (mg/m^2 day)	Time (months)	wt%			
			Lepidocrocite	Goethite	Akaganeite	Spinel
1	1906	3	26.0	53.5	9.2	11.2
		6	31.7	41.9	6.3	12.9
		9	8.6	42.5	6.5	42.4
		12	13.1	44.4	0.5	42.0
2	70	3	47.4	40.6	7.2	4.8
		6	43.8	36.8	10.9	8.6
		9	48.0	36.4	5.6	10.0
		12	51.6	35.9	4.3	8.2

where the cathodic process consists of the reduction of oxygen dissolved in the moisture film:

$$\frac{1}{2}O_2 + H_2O + 2e^- \rightarrow 2OH^- \quad (2)$$

The hydroxide ions formed migrate toward the anodic zones forming iron (II) hydroxide as the initial rust product:

$$Fe^{2+} + 2OH^- \rightarrow Fe(OH)_2 \quad (3)$$

The oxidation by oxygen from the air of iron (II) ions produced as a consequence of the dissolution of iron in the thin aqueous films formed in periods of wetting of the metallic surface, leads to the precipitation and crystallization of lepidocrocite in the drying stage via the prior formation of iron (II) hydroxide. *Hiller* considers lepidocrocite to be the primary crystalline corrosion product [3]. In mildly acidic solutions, lepidocrocite is transformed into goethite being this phase the most stable of the ferric oxyhydroxides.

Stratmann et al. [23], in an electrochemical study of phase transitions in already formed rust layers, proposed a three-stage rust formation mechanism (wetting, wet surface, and drying), demonstrating that the anodic reaction of iron dissolution in the first stage was not balanced by the cathodic reaction of reduction of the oxygen present in the moisture layer, but by the reduction of the pre-existing oxide (lepidocrocite), giving rise to a "reduced lepidocrocite" transition phase.

$$\gamma\text{-FeOOH (lepidocrocite)} + H^+ + e^- \rightarrow \gamma\text{-Fe.OH.OH (reduced lepidocrocite)} \quad (4)$$

Once the reducible lepidocrocite is exhausted, importance is acquired by the cathodic reaction of reduction of the oxygen dissolved in the rust layer (2), whose slow diffusion in the electrolyte-filled pores in the rust layer means that the metallic dissolution rate is highly limited. During drying, oxygen diffusion is extremely high due to the thinning of the electrolyte film, giving rise to high corrosion rates, where (2) is the cathodic reaction, accompanied by the reoxidation of the previously formed reduced lepidocrocite to lepidocrocite.

$$2\,\gamma\text{-Fe.OH.OH} + \frac{1}{2}O_2 \rightarrow 2\,\gamma\text{-FeOOH} + H_2O \quad (5)$$

Under this basic mechanism, the steel corrosion rate will be influenced by the concentration of ionizable substances in the moisture film, as is the case of the chlorides present in marine atmospheres. In general, there is a direct relationship between steel corrosion and the saline content of the atmosphere, as has been experimentally shown by numerous researchers [12]. This explains the notable increase in the steel corrosion rate at station 2 compared to the Ponte Do Porto background station (Table 1), as the chloride deposition rate rises from 3.6 mg chloride/$m^2 \cdot$ day at Ponte Do Porto to 70 mg chloride/$m^2 \cdot$ day at Cabo Vilano station 2.

According to *Nishimura* et al., in chloride-rich atmospheres, more than the role played by lepidocrocite in the corrosion process of steel, as noted above for chloride-free atmospheres, the formation of akaganeite is the cause that extremely accelerates the atmospheric corrosion process [5]. In a laboratory study, these researchers saw that at low chloride concentrations, the oxyhydroxide that formed was lepidocrocite, while high chloride concentrations led to the formation of akaganeite via the formation of green rust (GR1). They show that akaganeite can also be reduced electrochemically in the corrosion process, being consumed in the wetting period of the metallic surface. Subsequently, *Lair* et al. [24] also experimentally saw that lepidocrocite was not the only species of the different phases comprising rust that was electrochemically reducible by iron (galvanic couple), and that the order of reducing capacity was as follows: akaganeite > lepidocrocite >> goethite. The reduction of goethite by iron was not favored, and if it occurred it would only be at an extremely low reaction rate.

The consumption of akaganeite by its electrochemical reduction in the rust layer would explain the gradual decrease in its content as exposure time progresses as was found in our research (see Table 4). *Remazeilles* and *Refait* [25], *Nishimura* et al. [5], and *Lair* et al. [24] observed that the electrochemical reduction of oxyhydroxides drive to magnetite.

4.2 Exfoliated rust layer

However, the corrosion mechanisms that act on steel exposed to a very severe marine atmosphere (station 1) can differ notably to that based on the existence of a consolidated layer of corrosion products (station 2). In this new situation, there is a notable acceleration of the corrosion process and the rust layers formed present heavy cracking and tend to exfoliate and become partly or completely detached from the base steel, which in turn presents heavy pitting with very deep pits. The high chloride concentration in the aqueous layer deposited on the metal and the high moisture retention in very deteriorated areas of the rust give rise to the formation of ferrous chloride, which hydrolyses the water:

$$FeCl_2 + H_2O \rightarrow FeO + 2HCl \quad (6)$$

notably raising the acidity of the electrolyte. In this situation the cathodic reaction of discharge of hydrogen ions:

$$2H^+ + 2e \rightarrow H_2 \quad (7)$$

becomes important, accelerating the corrosion process; the anolyte on the steel surface and in the pits that have formed becomes saturated (or close to saturation) with the highly acidic ferrous chloride solution. Both the metallic cations and the hydrogen ions require neutralisation, which occurs by the entry of chloride ions, but this leads to an increase in the chloride concentration which intensifies the metal dissolution, giving rise in turn to the entry of more chloride which further intensifies the corrosion process. This attack mechanism is fed by the corrosion products themselves (feedback mechanism) and is sometimes referred to as "autocatalytic" [26].

On the remained rusted steel surface in the sample exposed during one year at station 1, which as a result of exfoliation had lost the rust layer formed, pH-indicator strips (Merck

MColorpHast™) were used to measure a pH of 5, which dropped to 4 when the residual rust layer was removed by gentle brushing to expose the highly pitted surface of the base steel. This indicates the acidification of the steel/rust interface area on the specimens exposed to the chloride richest atmosphere of station 1.

At the interface steel/corrosion products, where chloride ions can accumulate, large chloride concentrations and acidic conditions give rise to akaganeite formation previous precipitation of ferrous hydroxychloride due to the large excess of ferrous chloride. As *Remazeilles* and *Refait* point out large dissolved iron (II) species and large chloride concentrations are both necessary for akaganeite formation [25]. In a recent study involving a marine atmospheric corrosion test, the authors of this work have seen that the formation of akaganeite requires an annual average relative humidity of around 80% or higher, and simultaneously an average annual chloride ion deposition rate of around 60 mg chloride/m^2day or higher [10], confirming the conditions indicated by *Remazeilles* and *Refait* [25] based on laboratory tests. These authors in an interesting laboratory study controlling the reaction of iron (II) chloride tetrahydrate with sodium hydroxide by varying the R = [chloride]/[hydroxide] ratio, observed that for $R \geq 8$, i.e., in conditions of a high excess of iron (II) chloride, only akaganeite forms via the formation of intermediate GR1 compounds, whereas with small excesses of iron (II) chloride, only lepidocrocite forms. When $R \leq 6$, goethite forms, and when $6.5 \leq R \leq 8$, goethite and akaganeite form. The akaganeite formation mechanism implies the presence of high chloride concentrations and acid conditions (pH 4–6) due to the hydrolysis of iron (II) chloride, conditions that occur in confined spaces where chloride ions accumulate, such as the metal/corrosion product interface, crevice zones, etc. This explains how the different situations that can be found at the steel/rust interface, depending on the R ratio value, can give rise to the formation of the three iron oxyhydroxides lepidocrocite, goethite, and akaganeite, as has happened on the mild steel specimens exposed in the atmosphere at station 1 of high chloride deposition rate.

Spinel-type iron oxides are also formed in chloride-rich atmospheres. *Evans* and *Taylor* [27] and *Stratmann* et al. [23] have reported that the magnetite rust formed by the reaction of iron oxyhydroxide rust with the steel surface at a wet condition as follows:

$$Fe \rightarrow Fe^{2+} + 2e^- \quad (1)$$

$$3FeOOH + H^+ + e^- \rightarrow Fe_3O_4 + 2H_2O \quad (8)$$

$$2FeOOH + Fe^{2+} \rightarrow Fe_3O_4 + 2H^+ \quad (9)$$

The formation of magnetite rust can be represented as the following reaction:

$$Fe^{2+} + 8FeOOH + 2e^- \rightarrow Fe_3O_4 + 4H_2O \quad (10)$$

In a recent article, *Shibata* [28] noted that in an oxygen-depleted environment, as occurs in the interior of the rust layer close to the steel substrate, water works as an oxidizing agent to oxidize iron to produce magnetite with the evolution of hydrogen gas:

$$3Fe + 4H_2O \rightarrow Fe_3O_4 + 4H_2 \quad (11)$$

Studies of *Ishikawa* et al. [29] and *Tanaka* et al. [30] found that the formation of magnetite particles was caused by the reaction of dissolved ferric species of oxyhydroxides with ferrous species in the solution, also in the following order: akaganeite > lepidocrocite >> goethite.

Therefore an oxygen deficit, acidic conditions, and the presence of high chloride contents, as occurs at the steel/rust interface formed on steel exposed to chloride rich atmospheres, are fundamental factors for the formation of akaganeite and magnetite, both compounds performing a key role in mild steel corrosion in chloride containing environments.

Thus, it is important to gain a more in-depth knowledge of the steel/rust interface formed on mild steel exposed at marine atmospheres with very high chloride contents (station 1) and that has experienced an exfoliation process, considering both the residual rusted steel surface, following the detachment of the thick exfoliated rust layer, and the inner rust of the exfoliated rust layer.

4.2.1 The residual rusted steel surface

A SEM/EDS and SEM/μRaman study was carried out on the residual base steel from which the thick exfoliated rust layer was easily detached, placing special emphasis on the formation of the akaganeite and magnetite phases.

4.2.1.1 SEM/EDS study: In addition to the appearance of numerous flat dark patches characteristic of the formation of magnetite on the steel surface, it was also possible to see frequently the typical "doughnut" formations related with this compound in the form of circular discs with bulging around their periphery (Fig. 4a). According to *Raman* et al. this bulging is inferred to be due to structural transformations occurring along the outer edges of the magnetite [31]. Around the magnetite discs, the formation of a very porous and voluminous corrosion product takes place. Secondary electron images (Fig. 4c and d) show two different morphological aspects. In Fig. 4c, the SEM observation was conducted at 7 keV and the depth of field of the image reveals the porous morphology of that voluminous corrosion product. SEM micrograph of Fig. 4d, conducted at 2 keV, shows with higher resolution the microstructure inside the doughnut which is composed of numerous lamellas.

EDS element analysis (Fig. 4b) in different areas of Fig. 4a indicates the low chlorine contents, both in the hole (spectrum 1) and on the surface of the doughnut (spectrum 2). These low chlorine signals obtained can be assigned to the contribution of other areas close to that analyzed; the volume of X-ray excitation is larger than that corresponding to the analyzed area. In contrast, the voluminous mass of corrosion products surrounding the doughnut presents a very high chlorine signal, both at the crown around the doughnut (spectrum 3) and in a wider more outer area (spectrum 4). SEM micrographs (Fig. 5) of the latter area at 20 000 and 50 000 magnification show the formation of agglomerates of elongated cylinder- or tube-type crystals typical of akaganeite [10].

In Fig. 6, which shows another area of the specimen, it is possible to see the two morphologies presented by magnetite formations: a flat-type morphology upon which spectrum 1 has

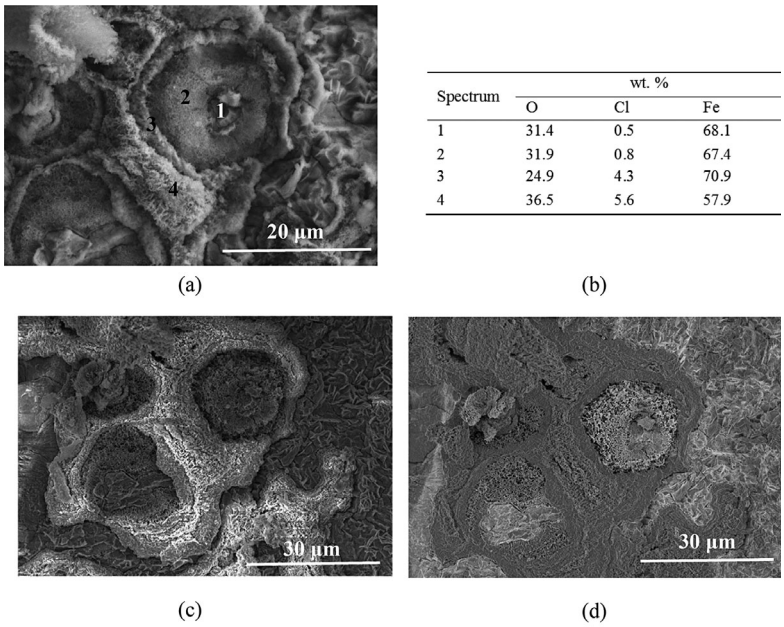

Spectrum	wt. %		
	O	Cl	Fe
1	31.4	0.5	68.1
2	31.9	0.8	67.4
3	24.9	4.3	70.9
4	36.5	5.6	57.9

Figure 4. SEM views of a typical "doughnut" of magnetite formed on mild steel exposed to a very rich chloride atmosphere. The EDS analysis in different zones in (a) is shown (b).

been prepared (note the absence of a chlorine signal) and the doughnut-type morphology upon which spectra 2 and 3 have been prepared, this morphology being similar to that presented in Fig. 4 with the difference that there is a large number of akaganeite crystals in the hole and on the surface of the doughnut, in agreement with the high chlorine signals found. All of this seems to indicate that the state seen here is posterior to that corresponding to Fig. 4. The sequence may be as follows: Firstly, magnetite discs or doughnuts form on the base steel. Subsequently, akaganeite crystals would form in areas not occupied by magnetite, in the hole in the disc and outlying areas around it (Fig. 4). After a certain time akaganeite crystals would also appear on the surface of the disc, after having crossed the bulge of the doughnut and the mesh of lamellas that comprise it (Fig. 6).

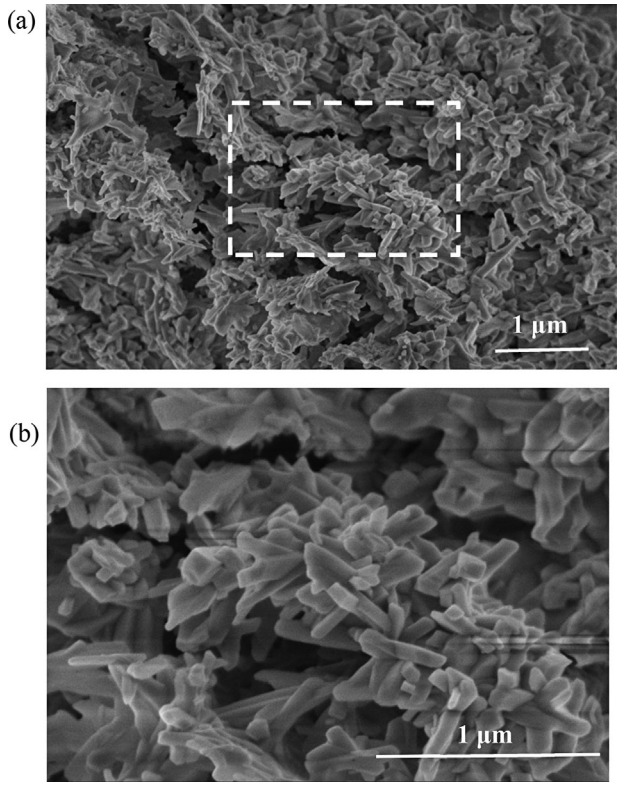

Figure 5. (a) SEM micrograph corresponding to aggregates of akaganeite nanocrystals. (b) Enlargement of the marked area of the previous micrograph.

These formations of magnetite, which precede in time the formation of akaganeite, must therefore, be of a different origin to the magnetite formed by electrochemical reduction of akaganeite, as has previously been reported. It should not be forgotten that the formation of magnetite also takes place in the absence of chloride ions, in the inner part of the rust, close to the steel surface where oxygen depletion occurs, as has also been previously reported. There are at least two ways that can give rise to magnetite phase:

(a) Oxidation of iron in the moisture film, being water working as oxidizing agent [28], reaction (11).
(b) Electrochemical reduction of lepidocrocite, as verified by *Evans* and *Taylor* [27] and *Stratmann* et al. [23], reaction (10).

4.2.1.2 SEM/Raman study: A SEM/µRaman study was also carried out on the residual steel surface from which the thick exfoliated rust layer had become detached. Figure 7 illustrates the study area where the Raman spectra were performed. As can be seen, this area is quite similar to that shown in Fig. 6, which was used to carry out the previous SEM/EDS study.

The SEM micrograph in Fig. 7 shows two areas, A and B, which correspond to two magnetite doughnuts of different

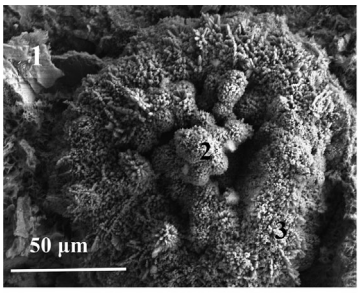

(a)

Spectrum	wt. %		
	O	Cl	Fe
1	42.0	0.0	58.0
2	50.8	3.9	45.3
3	48.8	3.8	47.4

(b)

Figure 6. (a) SEM view of a "doughnut" of magnetite invaded by akaganeite crystals. (b) Results of EDS analysis performed at different zones in (a): Flat formation of magnetite (spectrum 1); akaganeite formation at the doughnuts hole (spectrum 2); akaganeite crystals invading the doughnuts surface (spectrum 3).

sizes. Observation of the doughnut in area B at greater magnification reveals a similar morphology to that seen in Fig. 6, with akaganeite crystal formations in the hole and on the surface of the doughnut. The Raman spectra performed on these two areas of Fig. 7 show characteristic peaks for magnetite (A) and akaganeite (B). With regard to the identification of magnetite by Raman spectroscopy, it must be pointed out its difficulty because the Raman cross section is very small and requires long integration times, and the contribution to the Raman spectra is relatively weak [32]. As *Dubois* et al. note [33], it is difficult to detect magnetite as long as this oxide is not present as a pure compound in the analyzed corrosion scale (shadowing effect) due to the mix of rust phases. This explains why a Raman signal is often not obtained

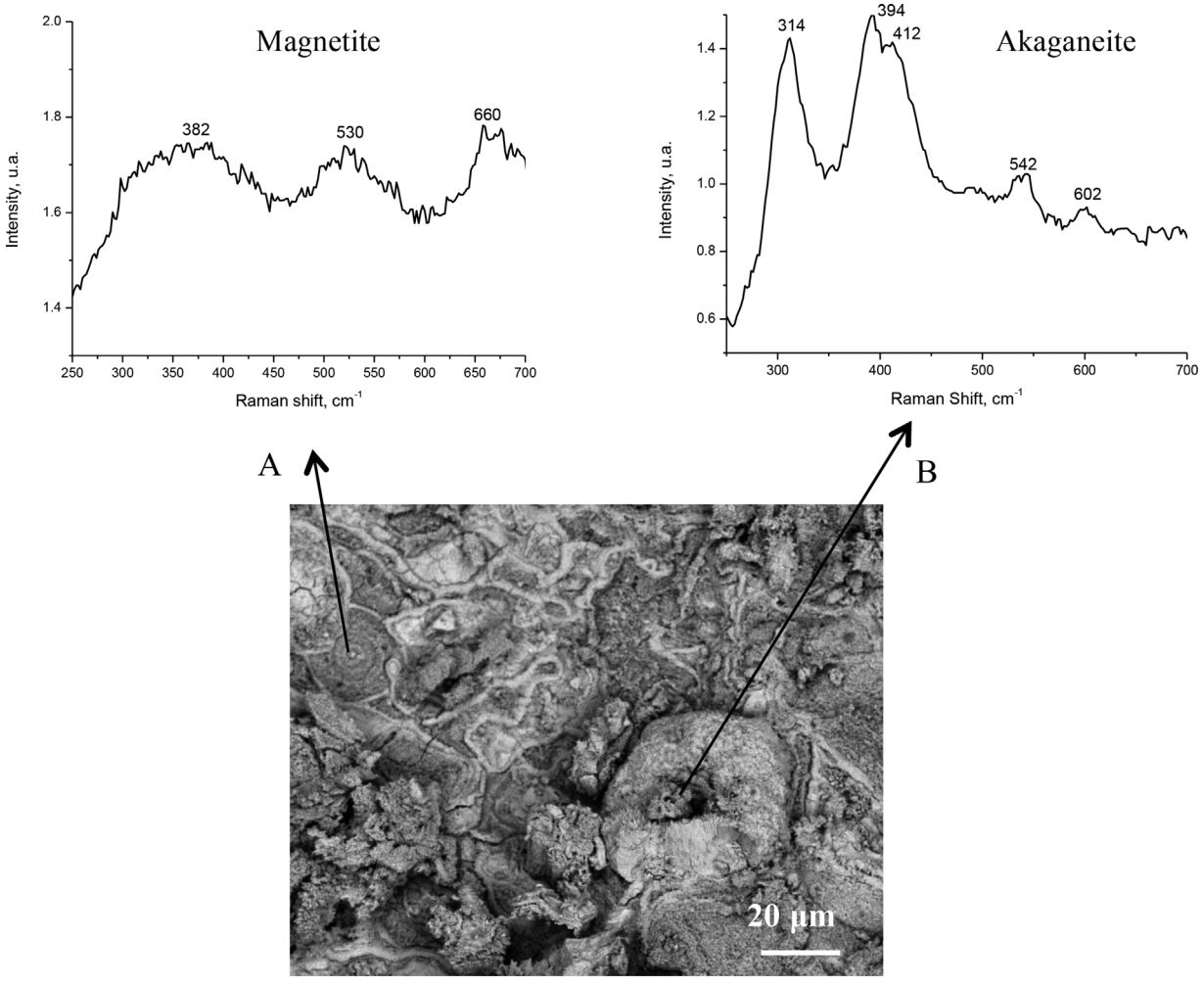

Figure 7. Doughnuts formation observed on the residual rusted steel surface after detachment of the thick exfoliated rust layer. The Raman spectra show the presence of magnetite (A) and akaganeite (B).

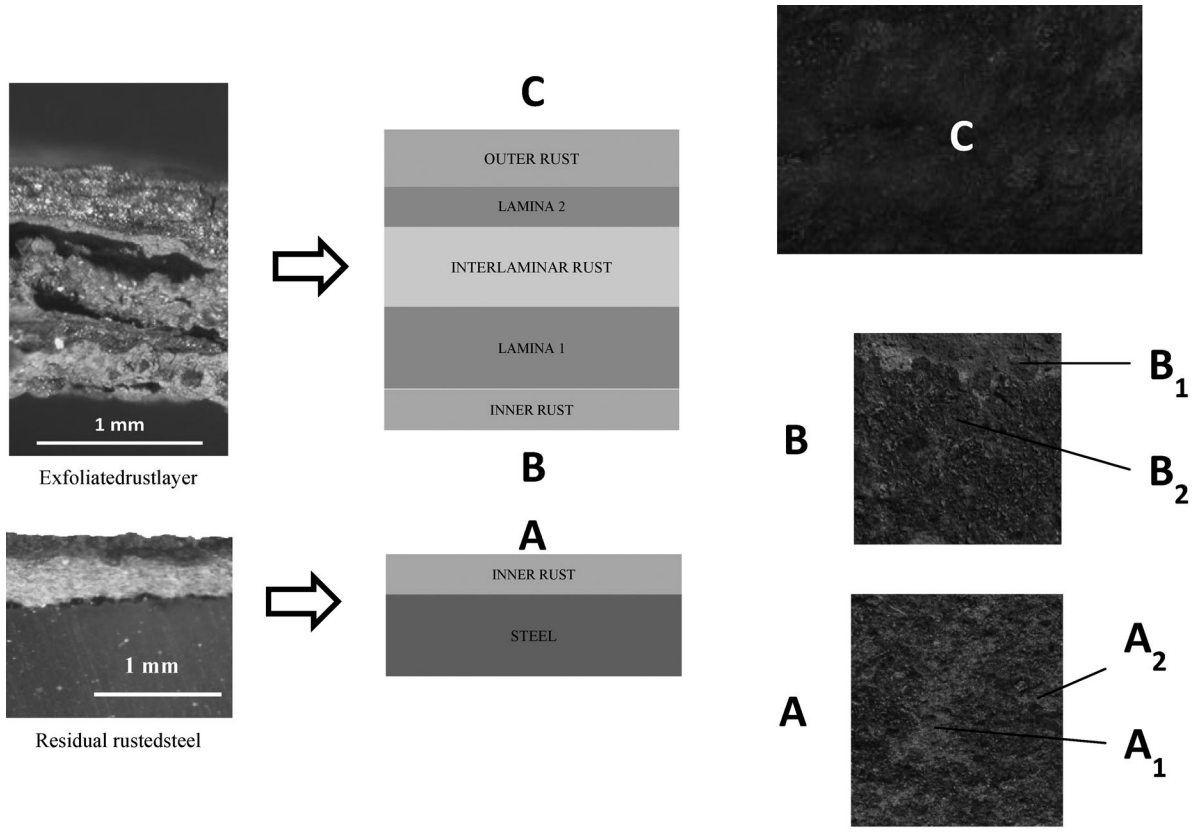

Figure 8. Optical microscopy view of a cross-section of the exfoliated rust layer. Different rust strata and surfaces (A–C) where the μXRD study has been carried out are shown in the diagram.

when the laser beam strikes on the surface of the doughnut, as occurred in our research a number of times.

4.2.2 The inner rust of the exfoliated rust layer

In previous work, a study was made of the environmental conditions that lead to the exfoliation of thick rust layers formed on mild steel exposed to highly chloride-rich atmospheres [34]. Figure 8 shows a cross section of an exfoliated rust layer formed on mild steel exposed for one year at station 1 (Table 2). The scheme in Fig. 8 presents the two fracture surfaces of the steel/rust interface, A and B, that appear when the thick rust layer is detached: surface A corresponding to the residual base steel and surface B corresponding to the more internal area (inner rust) of the exfoliated rust layer. Both present patterns of an orange color together with brown-colored areas. The appearance of the outermost surface (C) of the exfoliated layer is also shown.

The cross section in Fig. 8 shows the different rust strata present in the interior of the exfoliated rust layer, in which highly consistent and compact laminas, with a grayish coloring and a metallic shine, alternate with rust layers that show abundant internal porosity and little consistency (interlaminar rust). Table 5 displays the rust-phase composition obtained by μXRD (Rietveld) of the various rust surfaces and strata shown in Fig. 8. It is clearly seen that the outer rust layer is lepidocrocite-rich (56 wt%) while the inner rust layer is akaganeite-rich (orange patches) (78 wt%) and spinel-rich (brown patches) (51 wt%). The interior of the laminas is highly spinel-rich (63 wt%), unlike the interlaminar rust, where the highest percentages correspond to akaganeite (34 wt%) and goethite (41 wt%).

It is also worth commenting on the composition of the interior of the compact laminas. As has already been mentioned, XRD does not allow the differentiation of the two iron oxides, magnetite and maghemite, whose diffractograms are practically identical. In order to discern what compound is present in the interior of the compact laminas, be it magnetite, maghemite or both, a previous study made use of Mössbauer spectroscopy, a technique that allows the differentiation of these two phases. The results obtained were conclusive: the Mössbauer parameters

Table 5. μXRD quantification (Rietveld) of rust phases in different zones shown in Fig. 8

	wt%			
Zones (Fig. 8)	Lepidocrocite	Goethite	Akaganeite	Spinel
Outer rust	56	34	10	0
Laminas	5	32	0	63
Interlaminar rust	15	41	34	10
Inner rust				
Orange patch (A1, B1)	0	22	78	0
Brown patch (A2, B2)	9	34	6	51

obtained are characteristic of the maghemite phase and the presence of magnetite is ruled out. The increased formation of maghemite deeper into the interior of the lamina is in turn linked with a drop in the lepidocrocite and akaganeite contents compared to the interlaminar rust (see Table 5). The maghemite phase could be formed by the dry state transformation of the magnetite phase according to the following reaction [35]:

$$Fe_3O_4 + O_2 \rightarrow 6\gamma - Fe_2O_3 \quad (12)$$

5 Conclusions

1. The chloride deposition rate at the exposure site (atmospheric salinity) plays a decisive influence on the marine atmospheric corrosion of carbon steel. Depending on the atmospheric salinity level, the structure of the corrosion product layers formed on the steel surface presents two extreme situations, which go from the formation of a "consolidated rust layer" (at relatively low salinities) to the formation of highly imperfect and cracked thick "exfoliated rust layers" (at very high salinities) which are easily detached from the residual base steel.
2. The atmospheric corrosion mechanisms in these two situations are completely different. In the case of a "consolidated rust layer," a diffusion-controlled corrosion mechanism takes place, in which the aggressive species from the atmosphere (oxygen, water, and chloride) pass through the rust layer to interact with the underlying steel. The predominant cathodic reaction is the reduction of oxygen dissolved in the aqueous film
   The corrosion rate is dependent on the chloride ion concentration in the atmosphere. These ions become incorporated in the condensed moisture films or aqueous films deposited on the steel surface and accelerate the atmospheric corrosion process. The corrosion products formed are composed mainly of lepidocrocite and goethite, and to a lesser extent magnetite and akaganeite.
3. In the case of an "exfoliated rust layer," the high chloride concentration in the aqueous layer deposited on the steel surface gives rise to the formation of ferrous chloride, which hydrolyses the water, notably raising the acidity of the electrolyte. In this situation, the cathodic reaction of hydrogen evolution becomes important, accelerating the corrosion process. The high chloride concentration, acidic conditions and oxygen depletion at the steel/rust interface lead to the formation of high akaganeite and magnetite contents in the rust layer.

   3.1. Flat compact dark patches and dark discs (doughnut-like) are the typical morphologies found for magnetite. Akaganeite presents porous and voluminous formations (sponge-type morphology) comprised by aggregates of elongated cylinder- or tube-type nanocrystals.
   3.2. The exfoliated rust layer is composed of different strata, alternating between highly consistent and compact rust layers (laminas) and very porous rust layers of little consistency (interlaminar rust). The interior of the laminas is highly maghemite-rich, whereas the interlaminar rust presents major goethite and akaganeite contents.

4. SEM/EDS, μXRD, and SEM/μRaman have been in this work very useful experimental techniques to characterize the corrosion products and layers formed on mild steel exposed to chloride-rich atmospheres.

Acknowledgements: The authors gratefully acknowledge the financial support for this study from the Ministry of Science and Innovation of Spain (CICYT-MAT2008-06649). The authors would like to express their gratitude to the companies ENEL and GAS NATURAL-FENOSA for the facilities provided and for allowing the location of the corrosion stations at Cabo Vilano wind farm (Camariñas, Spain). They would also like to thank the Spanish Meteorology Agency (AEMET) for the data provided on meteorological parameters in the study area. A special acknowledgement must be done to Hybriscan Technologies (Arnhem, The Netherlands) for SEM/MicroRaman measurements. *I. Díaz* also acknowledge the PhD scholarship financed by CSIC JAE Programme.

6 References

[1] R. Ericsson, *Werkst. Korros.* **1978**, *29*, 400.
[2] K. Barton, *Protection Against Atmospheric Corrosion*, John Wiley and Sons, New York **1973**.
[3] J. E. Hiller, *Werkst. Korros.* **1966**, *17*, 943.
[4] M. Morcillo, B. Chico, J. Alcántara, I. Díaz, J. Simancas, D. de la Fuente, *Mater. Corros.* **2015**, *66*, 882.
[5] T. Nishimura, H. Katayama, K. Noda, T. Kodama, *Corrosion* **2000**, *56*, 935.
[6] EN ISO 9223, *Corrosion of Metals and Alloys - Corrosivity of Atmospheres - Classification, Determination and Estimation*, European Committee for Standardization, Brussels **2012**.
[7] M. Morcillo, S. Feliu, *Mapas de España de Corrosividad Atmosférica*, CYTED, Madrid, **1993**.
[8] A. Sánchez, *PhD. Thesis*, Universidad de Santiago, Vigo, **1987**.
[9] *EN ISO 9225, Corrosion of Metals and Alloys - Corrosivity of Atmospheres - Measurement of Environmental Parameters Affecting Corrosivity of Atmospheres*, European Committee for Standardization, Brussels 2012.
[10] M. Morcillo, J. M. González-Calbet, J. A. Jiménez, I. Díaz, J. Alcántara, B. Chico, A. Mazarío-Fernández, A. Gómez-Herrero, I. Llorente, D. de la Fuente, *Corrosion* **2015**, *71*, 872.
[11] *ISO 8407, Corrosion of Metals and Alloys - Removal of Corrosion Products From Corrosion Test Specimens*, International Organization for Standardization, Genève, **1991**.
[12] J. Alcántara, B. Chico, I. Díaz, D. de la Fuente, M. Morcillo, *Corros. Sci.* **2015**, *97*, 74.
[13] C. R. Hubbard, R. L. Snyder, *Powder Diffr.* **1988**, *3*, 74.
[14] H. M. Rietveld, *J. Appl. Crystallogr.* **1969**, *2*, 65.
[15] D. L. Bish, S. A. Howard, *J. Appl. Crystallogr.* **1988**, *21*, 86.
[16] L. Lutterotti, P. Scardi, *J. Appl. Crystallogr.* **1990**, *23*, 246.
[17] E. Jansen, W. Schäfer, G. Will, *J. Appl. Crystallogr.* **1994**, *27*, 492.

[18] R. A. Antunes, I. Costa, D. L. A. de Faria, *Mater. Res.* **2003**, *6*, 403.
[19] R. A. Francis, Presented at *10th International Congress on Metallic Corrosion*, Oxford and IBH Publishing Co., Madras, India **1987**, pp. 121–130.
[20] T. Misawa, K. Hashimoto, S. Shimodaira, *Corros. Sci.* **1974**, *14*, 131.
[21] E. Almeida, M. Morcillo, B. Rosales, *Mater. Corros.* **2000**, *51*, 865.
[22] P. Keller, *Werkst. Korros.* **1969**, *20*, 102.
[23] M. Stratmann, K. Bohnenkamp, H. J. Engell. *Corros. Sci.* **1983**, *23*, 969.
[24] V. Lair, H. Antony, L. Legrand, A. Chaussé, *Corros. Sci.* **2006**, *48*, 2050.
[25] C. Rémazeilles, P. Refait, *Corros. Sci.* **2007**, *49*, 844.
[26] L. L. Shreir, R. A. Jarman, G. T. Burstein, *Corrosion*, Butterworth-Heinemann, Oxford **1993**, pp. 1.146.
[27] U. R. Evans, C. A. J. Taylor, *Corros. Sci.* **1972**, *12*, 227.
[28] T. Shibata, Presented at *19th International Corrosion Congress*, The Corrosion Science Society of Korea, Jeju, Korea **2014**.
[29] T. Ishikawa, Y. Kondo, A. Yasukawa, K. Kandori, *Corros. Sci.* **1998**, *40*, 1239.
[30] H. Tanaka, R. Mishima, N. Hatanaka, T. Ishikawa, T. Nakayama, *Corros. Sci.* **2014**, *78*, 384.
[31] A. Raman, S. Nasrazadani, L. Sharma, *Metallography* **1989**, *22*, 79.
[32] D. L. A. de Faria, S. Venâncio Silva, M. T. de Oliveira, *J. Raman Spectrosc.* **1997**, *28*, 873.
[33] F. Dubois, C. Mendibide, T. Pagnier, F. Perrard, C. Duret, *Corros. Sci.* **2008**, *50*, 3401.
[34] B. Chico, J. Alcántara, E. Pino, I. Díaz, J. Simancas, A. Torres-Pardo, D. de la Fuente, J. A. Jiménez, J. F. Marco, J. M. González-Calbet, M. Morcillo, *Corros. Rev.* **2015**, *33*, 263.
[35] R. M. Cornell, U. Schwertmann, *The Iron Oxides: Structure, Properties, Reactions, Occurrences and Uses*, Wiley-VCH Verlag GmbH, Weinheim **2003**.

(Received: June 8, 2015) W8488
(Accepted: July 7, 2015)

ANEXO VI

“Marine atmospheric corrosion of carbon steel: a review.”

materials

MDPI

Review

Marine Atmospheric Corrosion of Carbon Steel: A Review

Jenifer Alcántara, Daniel de la Fuente, Belén Chico, Joaquín Simancas, Iván Díaz and Manuel Morcillo *

National Centre for Metallurgical Research (CENIM/CSIC), Avda. Gregorio del Amo n° 8, 28040 Madrid, Spain; j.alcantara@cenim.csic.es (J.A.); delafuente@cenim.csic.es (D.d.l.F.); bchico@cenim.csic.es (B.C.); jsimancas@cenim.csic.es (J.S.); ivan.diaz@cenim.csic.es (I.D.)

* Correspondence: morcillo@cenim.csic.es; Tel.: +34-915-538-900

Academic Editor: Yong-Cheng Lin

Received: 9 March 2017; Accepted: 7 April 2017; Published: 13 April 2017

Abstract: The atmospheric corrosion of carbon steel is an extensive topic that has been studied over the years by many researchers. However, until relatively recently, surprisingly little attention has been paid to the action of marine chlorides. Corrosion in coastal regions is a particularly relevant issue due the latter's great importance to human society. About half of the world's population lives in coastal regions and the industrialisation of developing countries tends to concentrate production plants close to the sea. Until the start of the 21st century, research on the basic mechanisms of rust formation in Cl^--rich atmospheres was limited to just a small number of studies. However, in recent years, scientific understanding of marine atmospheric corrosion has advanced greatly, and in the authors' opinion a sufficient body of knowledge has been built up in published scientific papers to warrant an up-to-date review of the current state-of-the-art and to assess what issues still need to be addressed. That is the purpose of the present review. After a preliminary section devoted to basic concepts on atmospheric corrosion, the marine atmosphere, and experimentation on marine atmospheric corrosion, the paper addresses key aspects such as the most significant corrosion products, the characteristics of the rust layers formed, and the mechanisms of steel corrosion in marine atmospheres. Special attention is then paid to important matters such as coastal-industrial atmospheres and long-term behaviour of carbon steel exposed to marine atmospheres. The work ends with a section dedicated to issues pending, noting a series of questions in relation with which greater research efforts would seem to be necessary.

Keywords: atmospheric corrosion; marine environment; carbon steel

1. Introduction

Steel is the most commonly employed metallic material in open-air structures, being used to make a wide range of equipment and metallic structures due to its low cost and good mechanical strength. Much of the steel that is manufactured is exposed to outdoor conditions, often in highly polluted atmospheres where corrosion is much more severe than in clean rural environments.

The atmospheric corrosion (AC) of carbon steel (CS) is an extensive topic that has been studied by many researchers. Useful books and chapters have been published by a number of authors [1–8].

Since the 1920's much time and effort has been devoted to studying the corrosion of metals in natural atmospheres. As a result, the importance of various meteorological and pollution parameters on metallic corrosion in now fairly well known. The effect of sulfur dioxide (SO_2) on AC has been widely studied, but until relatively recently researchers have paid surprisingly little attention to the action of marine chlorides in AC, despite it being well known that airborne salt in coastal regions promotes a marked increase in AC rates compared to clean atmospheres.

The issue of corrosion in coastal regions is particularly relevant in view of the latter's great importance to human society. About half of the world's population lives in coastal regions and the industrialisation of developing countries tends to concentrate production plants close to the sea.

The first rigorous study on the salinity of marine atmospheres and its effect on metallic corrosion was carried out in Nigeria by Ambler and Bain [9] and dates from 1955. For many years it was simply accepted that marine chlorides dissolved in the aqueous adlayer considerably raised the conductivity of the electrolyte on the metal surface and tended to destroy any passivating films. In 1973 Barton noted that the mechanism governing the effects of chloride ions (Cl^-) in AC had not been completely explained, and that the higher corrosion rate of steel in marine atmospheres could also be due to other causes, such as: (a) the hygroscopic nature of Cl^- species (sodium chloride (NaCl), calcium chloride ($CaCl_2$), magnesium chloride ($MgCl_2$)), which promotes the electrochemical corrosion process by favouring the formation of electrolytes at relatively low relative humidity (RH); and (b) the solubility of the corrosion products. Thus, in the case of iron, which does not form stable basic chlorides, the action of chlorides is more pronounced than with other metals (zinc, copper, etc.) whose basic salts are only slightly soluble [4].

In the year 2000, Nishimura et al. noted that with the exception of a few studies, research on the basic mechanisms of rust formation in Cl^--rich marine atmospheres had been rather scarce [10]. Since then, scientific knowledge of marine atmospheric corrosion (MAC) has advanced greatly, perhaps as a result of the need to develop new weathering steels (WS) with greater MAC resistance than conventional WS, whose main limitation is precisely their low corrosion resistance in this type of environment [11]. This hypothesis seems to be confirmed by the high proportion of MAC studies that consider this type of materials.

Therefore, this is a relatively young scientific field and there continue to be great gaps in its comprehension [12]. Nevertheless, in the authors' opinion a considerable body of knowledge has been built up in a large number of published scientific papers, and it is now time to make an up-to-date review of the current state-of-the-art and to assess what issues still need to be addressed. That is the purpose of the present review.

2. Basic Concepts

The AC of metals is an electrochemical process which is the sum of individual processes that take place when an aqueous adlayer forms on the metal. This electrolyte can be either an extremely thin moisture layer (just a few monolayers) or an aqueous film of hundreds of microns in thickness (when the metal is perceptibly wet). Aqueous precipitation (rain, fog, etc.) and humidity condensation due to temperature changes (dew), capillary condensation when the surfaces are covered with corrosion products or with deposits of solid particles, and chemical condensation due to the hygroscopic properties of certain polluting substances deposited on the metallic surface, are the main promoters of metallic corrosion in the atmosphere [2]. Recent studies on the wetting of metal surfaces in order to understand the process controlling AC, as well as the effect of RH on steel corrosion in the presence of sea salt aerosols (NaCl and $MgCl_2$) can be found in references [13–16].

The magnitude of AC is basically controlled by the length of time that the surface is wet, though it ultimately depends on a series of factors such as RH, temperature, exposure conditions, atmospheric pollution, metal composition, rust properties, etc. [5,17]. The AC process involves simultaneous oxidation and reduction reactions which can be accompanied by other chemical reactions in which the corrosion products may take part.

The anodic reaction, consisting of the oxidation of the metal, can be given as:

$$Fe \rightarrow Fe^{2+} + 2e^-, \quad (1)$$

Oxygen (O_2), which is highly soluble in the aqueous layer, is a possible electron acceptor. Oxygen reduction in neutral or basic media takes place according to the reaction:

$$O_2 + 2H_2O + 4e^- \rightarrow 4OH^-, \quad (2)$$

The hydroxide ions migrate to anodic areas, forming ferrous hydroxide [$Fe(OH)_2$] as the initial corrosion product.

Oxygen diffusion through the aqueous adlayer is usually a corrosion rate-controlling factor. The corrosion rate reaches a maximum value for intermediate thicknesses of the aqueous adlayer on the metal surface. The joining up of individual droplets to form relatively thick electrolyte layers somewhat reduces the rate of attack, as it hampers the arrival of oxygen. On the other hand, an excessive decrease in the moisture layer thickness halts the corrosion process, due to the high ohmic resistance of very thin layers where the ionisation and dissolution reactions of the metal are obstructed. Fast drying and repeated wetting of the surface leads to stronger corrosion effects. During drying periods, the convective currents caused by evaporation of the electrolyte lead to a decrease in the effective thickness of the diffusion layer, with the consequent rise in the transportation rate of cathodic depolariser, thus making the corrosion rate a cathodically controlled process. The electrolyte is self-stirring during evaporation [3,18].

Another factor that substantially determines the intensity of the corrosive phenomenon is the chemical composition of the atmosphere (air pollution by gases, acid vapours or seawater aerosols). SO_2 and NaCl are the most common corrosive agents in the atmosphere. Nitrogen oxides (NO_x) are another important source of atmospheric pollution.

2.1. Sulfur Dioxide

The effect of SO_2 on AC has been studied by many authors [7]. SO_2 is often found in the atmosphere in concentrations that vary considerably depending on the type of industries in the region, the presence of power plants, time of year, etc. SO_2 is much more aggressive to steel when its concentration exceeds 0.1 $mg \cdot m^{-3}$, a level that is easily reached in many towns, especially in winter. Fortunately, the SO_2 concentration in urban air has decreased greatly in recent years due to efforts to reduce pollution [19].

Rozenfeld [3] has shown that SO_2 is also an active cathodic depolarising agent due to its susceptibility to be reduced on metals. SO_2 is some 2600 times more soluble in water than oxygen, so even if the SO_2 gas content in the atmosphere is very small, its concentration in the electrolyte and its effect can be similar to that of oxygen, which is the depolarising agent par excellence. Thus, above a certain acidity level in polluted atmospheres, SO_2 can act as an oxidising agent and greatly accelerate the cathodic process.

Rainwater can absorb SO_2 from the atmosphere as it falls, giving rise to what is known as acid rain. For this reason the pH of rainwater collected downwind of highly industrialised regions of Europe sometimes presents clearly acid values, as in Norway [20], where average daily and monthly measurements of down to pH 2.9 have been recorded. In such situations, the cathodic reaction of hydrogen evolution can be relevant.

$$2H^+ + 2e^- \rightarrow H_2, \quad (3)$$

Kucera [21] distinguishes between the rinsing effect of rainwater, which tends to wash away pollutants that accumulate on the metallic surface, and the harmful effect of acid precipitation. In terms of corrosion, Kucera suggests a predominance of the rinsing effect in appreciably polluted areas, whereas in rural areas rainwater with a circumstantially low pH may worsen the situation.

SO_2 gives rise to the formation and propagation of sulfate "nests", according to reactions (4,5), which start to appear at isolated points on the surface but whose number increases until all the surface is coated with a rust film (Figure 1a) [22].

$$SO_2 + H_2O + \frac{1}{2}O_2 \rightarrow H_2SO_4, \quad (4)$$

$$2H_2SO_4 + 2Fe + O_2 \rightarrow 2H_2O + 2FeSO_4, \quad (5)$$

Hydrolysis of the ferrous sulfate formed in these nests controls their propagation (reactions 6,7).

$$6FeSO_4 + H_2O + 3/2O_2 \rightarrow 2Fe_2(SO_4)_3 + 2FeOOH, \quad (6)$$

$$Fe_2(SO_4)_3 + 4H_2O \rightarrow 2FeOOH + 3H_2SO_4, \quad (7)$$

Osmotic pressure may cause the nests to burst, thus raising the corrosion rate [22].

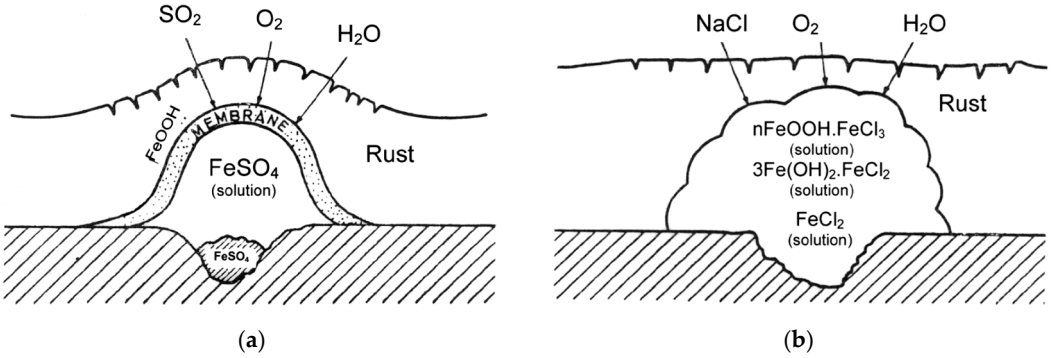

Figure 1. Schematic representation of a sulphate nest (**a**) and a chloride agglomeration (**b**) [22].

2.2. Saltwater Aerosols

The deposition of salt particles on a metallic surface accelerates its corrosion, especially, as in the case of chlorides, if they can give rise to soluble corrosion products rather than the only slightly soluble products formed in pure water.

Cl^- ions are abundant in marine atmospheres, where the fundamental source of mineralisation consists of saltwater particles that are carried along by air masses as they pass over seas, oceans and salt lakes [3]. According to Ambler and Bain [9], only salt particles and droplets of more than 10 μm cause corrosion when deposited on a metallic surface. Given that such particles remain in the atmosphere for a short time, usually corrosion completely loses its marine character just a few kilometres inland.

For salt to accelerate corrosion the metallic surface needs to be wet. The RH level that marks the point at which salt starts to absorb water from the atmosphere (hygroscopicity) seems to be critical from the point of view of corrosion.

As has been noted above, the effect of Cl^- ions on CS corrosion mechanisms has been much less widely studied than the effect of SO_2. A high Cl^- concentration in the aqueous adlayer on the metal and high moisture retention in very deteriorated areas of the rust give rise to the formation of ferrous chloride ($FeCl_2$), which hydrolyses the water:

$$FeCl_2 + H_2O \rightarrow FeO + 2HCl, \quad (8)$$

Notably raising the acidity of the electrolyte. In this situation the cathodic reaction (3) becomes important, accelerating the corrosion process. The anolyte on the steel surface and in the pits that have formed becomes saturated (or close to saturation) with the highly acidic $FeCl_2$ solution. Both the metallic cations and hydrogen ions require neutralisation, which occurs by the entry of Cl^- ions, but this leads to an increase in the Cl^- concentration which intensifies metal dissolution, giving rise in turn to the entry of more Cl^-, which further intensifies the corrosion process. This attack mechanism is fed by the corrosion products themselves (feedback mechanism), and it is sometimes referred to as "autocatalytic" [23].

Unlike SO_2 pollution, Cl^- pollution does not cause the formation of nests but Cl^- agglomerates. The literature also sometimes mentions the formation of "chloride nests" [24], but the osmotic pressure

of $FeCl_2$ or NaCl does not influence corrosive activity, which instead is determined by other causes such as the ability of ferrous and ferric chlorides to form complexes ($nFeOOH{\cdot}FeCl_3$) or a solution of $FeCl_3$ in FeOOH in the form of a gel. No amorphous oxide/hydroxide membrane is originated (Figure 1b) [22].

2.3. Hydrogen Chloride Vapours

Askey et al. [25] published an interesting study of iron corrosion by atmospheric hydrogen chloride (HCl), in which they suggest a direct reaction between CS and HCl. HCl reacts directly with the metal to produce soluble $FeCl_2$, which is then oxidised to FeOOH, releasing HCl.

$$Fe + 2HCl + \frac{1}{2}O_2 \rightleftharpoons FeCl_2 + H_2O, \quad (9)$$

$$2FeCl_2 + 3H_2O + \frac{1}{2}O_2 \rightleftharpoons 2FeOOH + 4HCl, \quad (10)$$

It should be noted that this is a reaction cycle in which rereleased HCl reacts with iron to form fresh $FeCl_2$. Once started, therefore, the cycle is independent of incoming HCl. Corrosion continues until the Cl^- ions are removed (possibly by washing away of $FeCl_2$) after which fresh incoming HCl reacts with the metal surface and reinitiates the cycle. The cycle proposed above is analogous to the acid regeneration cycle proposed by Schikorr [26] for the action of SO_2 on iron.

3. Experimentation on Marine Atmospheric Corrosion

Most studies of MAC have involved the performance of field exposure tests. Specimens of appropriate dimensions are mounted on racks using porcelain or plastic insulating clips. The exposure angle is generally 45° to the horizontal in Europe or 30° to the horizontal in the United States. It is general practice to have the panel racks facing south in the northern hemisphere or north in the southern hemisphere. However, when panels are mounted in coastal locations it is desirable to have the racks facing the shore. Further to these general requirements it is advised to follow the appropriate specific standards that have been published [27,28].

Atmospheric exposure tests usually involve the use of flat specimens of metals and alloys, although wire specimens are sometimes also used, such as in the ISOCORRAG International Atmospheric Exposure Program [29]. It is increasingly common to use both flat and wire specimens to evaluate the aggressivity (corrosivity) of atmospheres [30]. It is also interesting to note the quick response and high sensitivity of the wire-on-bolt technique, using specimens originally devised by Bell Telephone Laboratories [31] and subsequently developed by the Canadian company Alcan International [32]. This technique consists of the atmospheric exposure for just three months of metallic wires wound firmly around bolts of another metal. The functioning of the galvanic couple depends among other factors on the atmosphere where it is exposed. Doyle and Godard report that aluminium wire wound around an iron bolt is highly sensitive to the marine atmosphere [33].

The specimens are exposed to the atmosphere for a given time and subsequently analysed in the laboratory by gravimetric techniques to determine the corrosion losses experienced. Mass-loss data allows structural integrity to be estimated after a given number of years of service. Structural engineers typically use mass-loss data to overbuild a structure, allowing for a given mass loss over the predicted lifetime.

Over the course of time different accelerated tests have been developed to simulate AC in the laboratory. The disadvantage of accelerated corrosion tests is that the results obtained do not always coincide with those found in real atmospheric exposure tests. For instance, the laboratory simulation of marine atmosphere exposure has long been carried out by constant exposure to salt fog. However, the classic salt fog test has a bad reputation and is unanimously considered to offer poor reproducibility and correlation with atmospheric exposure. The application of intermittent salt spray, on the other hand, is a much better approximation to marine and coastal conditions [34], and

the cyclic salt fog test, along with the use of alternative saline solutions to NaCl, provides much better correlations [35].

As has been noted above, the existence and duration of wetting and drying stages play an important role in AC mechanisms. The need for wet/dry cycles to simulate AC is now well established and any accelerated laboratory test for this purpose needs to take this aspect into account. Today's standard accelerated tests for the simulation of atmospheric exposure are all based on wet/dry cycles. Although some standards set out conditions for the performance of such tests [36], they tend to be carried out in many different ways, and the results of one researcher are not always comparable to those of another. Despite this difficulty, analysis of the data obtained by researchers throughout the world in the most varied of experimental conditions has led to great advances in the knowledge of MAC. As will be mentioned below, it would nevertheless be desirable to standardise a universal wet/dry cyclic test that could be followed by all researchers so that the results obtained would be comparable.

Considerable efforts have been made to obtain reliable estimates of AC without the limitations of gravimetric tests, especially in terms of their enormous duration. Very good results have been obtained with electrochemical cells [37]. Electrochemical techniques, and in particular impedance measurements, have been widely used by many researchers in numerous studies related with AC.

In particular, attention is drawn to the important atmospheric rusting cycle mechanism proposed by Stratmann [38]. In an electrochemical study of phase transitions in rust layers, Stratmann showed that when a pre-rusted iron sample was wetted, iron dissolution was not immediately balanced by a reaction with oxygen, but rather by the reduction of the preexisting rust (lepidocrocite) with later reoxidation of the reduced species. Thus, Stratmann [38] proposed dividing the AC mechanism of pure iron into the following three stages (Figure 2): (a) wetting of the dry surface; (b) wet surface; and (c) drying-out of the surface.

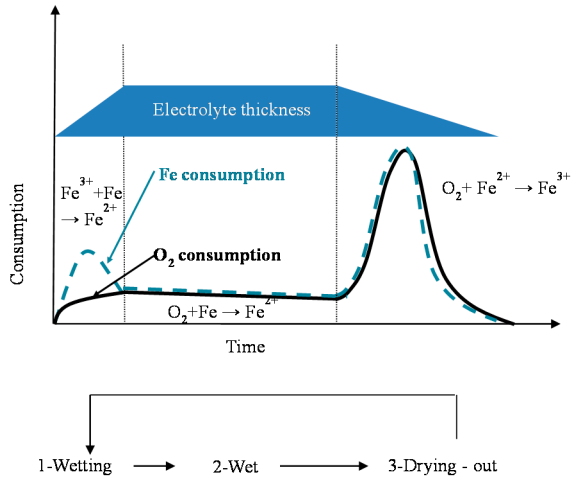

Figure 2. Schematic representation according to Stratmann [38] of atmospheric rusting cyclic mechanism.

Nishimura et al. [10,39] carried out a laboratory study of the electrochemical behaviour of rust formed on CS in wet/dry cycles in solutions containing Cl^- ions, simulating exposure in marine atmospheres. They observed that akaganeite formation was the cause which enormously accelerated the AC process in this type of atmosphere, being electrochemically reduced and consumed during the wetting of the metallic surface, in contrast to the important role played by lepidocrocite in steel corrosion in Cl^--free atmospheres [38].

Over the last decade, great advances have been made in the understanding of AC mechanisms. Many of these advances have been due to the research groups of Legrand [40] and Dillmann [41]. Basic research carried out in this field has been related with a greater knowledge of the electrochemical

reactivity of the ferric phases that constitute atmospheric rust and the coupling or decoupling of anodic and cathodic reactions.

A fine characterisation of corrosion product layers identifying the oxide phases on a metal surface yields valuable information on the evolution of the corrosion process in a given atmosphere. Not only is it important to identify the different oxides but also to ascertain the fraction of each corrosion product and its distribution in the rust layer in order to gain a better understanding of the corrosion process. The distribution of the phases can drastically influence local corrosion mechanisms. Elemental composition can be determined by energy dispersive X-ray (EDX) analysis and electron probe microanalysis (EPMA), and several macroscopic techniques such as X-ray diffraction (XRD), infrared spectroscopy (IRS) and Mössbauer spectroscopy (MS) are commonly used for corrosion products characterisation. However, it may be very important to obtain a fine and local determination of the structure of corrosion products in order to understand corrosion mechanisms. In such cases the local structure of the corrosion layers must be characterised with the help of microprobes: Raman microspectroscopy (μRS), X-ray microdiffraction (μXRD), X-ray absorption spectroscopy (XAS), etc. The specificities of each analysis method strongly influence the type of phase identified [11].

XRD is one of the most commonly used techniques for identifying the rust composition and the structure of different components in corrosion products. One of the limitations of XRD is the separate identification of magnetite and maghemite. Both oxides have a cubic structure and nearly identical lattice parameters at room temperature, making them nearly indistinguishable by XRD. However, their magnetic and electric properties are quite different, thereby allowing MS to identify each. According to Cook [42], corrosion research is one area in which MS has become a required analytical technique. This is in part due to the need to identify and quantify the nanophase iron oxides that are nearly transparent to most other spectroscopic techniques.

Rust composition studies using μRS usually demand a high laser power for the excitation of spectra because some of the most common iron oxides and oxyhydroxides are poor light scatterers. Sample degradation frequently occurs under intense sample illumination and may lead to the misinterpretation of spectra. Low laser power minimises the risks of spectral changes due to sample degradation [43]. Moreover, in some cases, particularly when the phases are less crystallised, it is difficult to discriminate one phase from another only by μRS because the Raman shift is very close.

According to Monnier et al., the use of complementary analytical techniques (μXRD, XAS and MS) is needed to obtain accurate Raman phase characterisation. Each technique provides complementary information. μXRD is more sensitive to crystallised phases while μRS presents a higher spatial resolution and allows the detection and location of crystallised phases (goethite, lepidocrocite, maghemite, akaganeite) from less crystallised ones (feroxyhyte, ferrihydrite). Discrimination of maghemite, feroxyhyte and ferrihydrite could be partially solved by the use of XAS [44].

Knowledge of the rust layer structure is another aspect widely studied by researchers. The techniques traditionally used are optical microscopy (OM), polarised light microscopy, scanning electron microscopy (SEM) and transmission electron microscopy (TEM)/electron diffraction (ED). In order to characterise corrosion product structures in various scales, Kimura et al. [45] use several analytical approaches that are sensitive to three structural-correlation lengths: long-range order (LRO) (>50 nm), middle-range order (MRO) (~1–50 nm), and short-range order (SRO) (<1 nm) and Konishi et al. employ X-ray absorption fine structure analysis (XAFS) methods, including extended XAFS and X-ray absorption near-edge structure (XANES), for characterisation of rust layers formed on Fe, Fe-Ni and Fe-Cr alloys exposed to Cl^--rich environments [46].

Complementary analyses on the porosity of rust layers have also been conducted by several researchers. Dillmann et al. use various techniques such as small-angle X-ray scattering (SAXS), Brunauer-Emmett-Teller (BET) and mercury intrusion porosimetry (MIP) [47]. Attention is also drawn to the studies of Ishikawa et al., where the specific surface area of the pores was calculated by fitting the BET equation to N_2 adsorption isotherms [48].

Over the past few decades, the new analytical techniques developed to study properties of solid surfaces, such as chemical composition, oxidation state, morphology, structure, etc. have continued to increase and improve in terms of resolution and sensitivity. The more recent analytical techniques are both surface-sensitive and able to provide information under in-situ conditions. According to Leygraf et al. [8], it is anticipated that the number and variety of in-situ techniques for probing surfaces will continue to increase.

4. The Marine Atmosphere

From the point of view of MAC, the marine atmosphere is characterised by the presence of marine aerosol. Cl^- ions are abundant in marine atmospheres, where the fundamental source of mineralisation consists of saltwater particles that are carried along by air masses as they pass over seas, oceans, and salt lakes. Marine salts are mainly NaCl, but quite appreciable amounts of potassium, magnesium and calcium ions are also found in rainfall.

4.1. Atmospheric Salinity

Atmospheric salinity is a parameter related with the amount of marine aerosol present in the atmosphere at a certain geographic point. Marine aerosols, consisting of wet aerosols, partially wet aerosols and non-equilibrium aerosols depending on the atmospheric humidity, are carried along by the wind and can come into contact with metallic structures and greatly accelerate the corrosion process. The sizes of the three types of aerosols and the resultant dry aerosols were estimated by Cole et al. [49].

Salinity in marine atmospheres varies within very broad limits (<5 to >300 mg $Cl^-/m^2 \cdot d$) [50]. While extremely high values have been recorded close to surf, salinity at other points on the shoreline near calmer waters is no more than moderate. The concentration of marine aerosol decreases with altitude [51,52]. Meira et al. find that this relationship can be represented by an exponential decrease function which is influenced by the wind regime [52].

An increase in wind speed, even on the same coast, does not always lead to an increase in salinity, as the final result is dependent on the wind direction. In fact, an increase in wind speed can even reduce the degree of pollution by purifying the exposure site of pollutant. This will naturally depend on the situation of the exposure site in relation with the sea, and on the direction and type of winds blowing at a given time.

Marine aerosol is comprised of fine particles suspended in the air (jet drops, film drops, brine drops and sea-salt particles), solid or liquid, whose sizes vary from a few angstroms to several hundred microns in diameter [53]. Marine aerosol particles are usually classified by size into two classes: coarse particles, with an equivalent aerodynamic diameter of >2 μm; and small particles, with a diameter of <2 μm. Fine particles are in turn subdivided into Aitken nuclei (<0.05 μm) and particles formed by accumulation (with diameters of between 0.05 and 2 μm). In coastal locations (<2 km from the seashore) the most common aerosols deposited are in the coarse size range: 2–100 μm in diameter [54,55].

Large marine aerosol particles (diameter >10 μm) remain for only a short time in the atmosphere; the larger the particle size, the shorter the time. On the other hand, particles of a diameter of <10 μm may travel hundreds of kilometres in the air without sedimenting [9,56].

Li and Hihara [55] in a study of natural salt particle deposition on CS for only 30 min in a severe marine site in Hawaii, found that most airborne salt particles had diameters ranging from approximately 2–10 μm, and varied in composition ranging from almost pure NaCl or KCl to mixtures of NaCl, KCl, $CaCl_2$ and $MgCl_2$. These differences in composition may depend on whether the seawater droplets dehydrate, crystallise and fragment while airborne, or if they are deposited as liquid droplets before crystallising.

4.2. Production of Marine Aerosol

Cole et al. described marine aerosol formation, chemistry, reaction with atmospheric gases, transport, deposition onto surfaces, and reaction with surface oxides [57].

The wind, which stirs up and carries along seawater particles, is the force responsible for the salinity present in marine atmospheres. Oceanic air is rich in marine aerosols resulting from the evaporation of drops of seawater, mechanically transported by the wind. The origin, concentration and vertical distribution of marine aerosol over the surface of the sea has been studied by Blanchard and Woodcock [51].

The first step in the production of aerosol particles is the breaking of waves [51,58,59]. The turbulence that accompanies this phenomenon introduces air bubbles into the water which subsequently burst and launch sea salt particles into the atmosphere. On the high seas the breaking of waves depends on the speed of the wind blowing over them. In the coastal surf zone, waves can break without the need for simultaneous wind action, and the amount of aerosol generated is largely dependent on the type of sea floor (uniformity, slope, etc.) and the width of the surf zone.

Aerosol levels at the seashore depend both on the aerosol that is generated out at sea, which is carried to the coast by marine winds, and that which is generated in the surf zone close to the shoreline [60–62]. Of the two, the latter seems to be the main contributor to the Cl^- levels measured in the lower layers of the atmosphere in coastal areas [61,63].

A relationship has been seen between salinity and wave height [64]. The graph in Figure 3 shows the variation of atmospheric salinity with the average spectral wave height. As can be seen in the figure, monthly average spectral wave height values of 1.5–2.0 m are sufficient to produce high monthly average salinity values of 100–200 mg $Cl^-/m^2 \cdot d$.

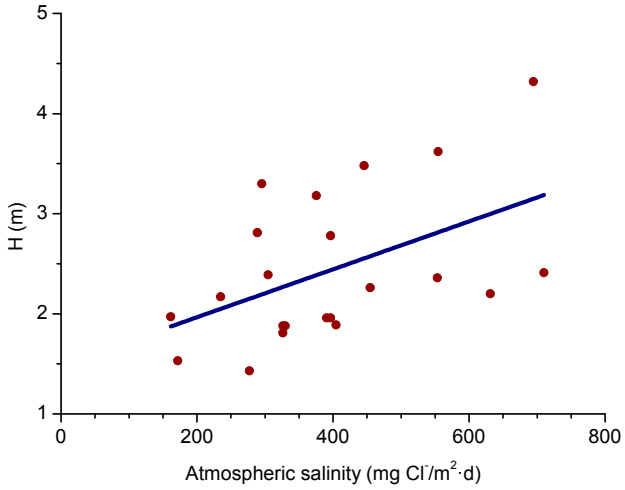

Figure 3. Variation of monthly average salinity with monthly average spectral wave height values (H). The regression line shows the general trend [64].

Several studies in the literature have attempted to relate aerosol levels measured at high sea and on the coast with wind speed. Potential and exponential type functions express the considerable effect of this variable on marine aerosol production (especially when the wind speed exceeds some 3–5 m/s) [51,65–67]. In Figure 4, Morcillo et al. note that the wind only needs to blow short time at speeds above 3 m/s in directions with high entrainment of marine aerosol (they call them "saline winds") for atmospheric salinity to reach important values [66].

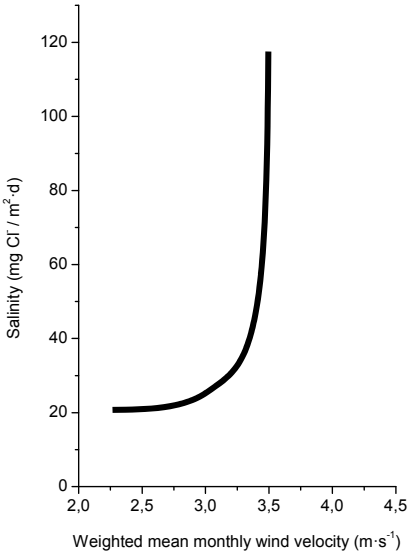

Figure 4. Relation between atmosphere salinity and weighted mean monthly wind velocity for marine winds [66].

4.3. Entrainment of Marine Aerosol Inland

Aerosol particles can be entrained inland by marine winds (winds proceeding from the sea), settling after a certain time and after travelling a certain distance. The wind regime directly influences aerosol production and transportation, and is significantly affected by geostrophic winds, large-scale atmospheric stability, and the difference between diurnal land and sea temperatures, which varies according to the season of the year. It is also dependent on the latitude, ruggedness of the coastline, and undulation of the land surface [51,58]. A reduction in the size and mass of aerosol particles due to drying of the droplets can considerably increase the entrainment distance.

In a recent study by Alcántara et al. [64], it was seen that the variation in salinity with the distance from the shoreline (Figure 5) clearly showed an exponential relationship.

$$Y = 78288.23 \exp(-X/91.34) + 108.40, \quad (11)$$

Being Y the atmospheric salinity expressed as mg $Cl^-/m^2 \cdot d$ and X the distance from the shore in meters (m).

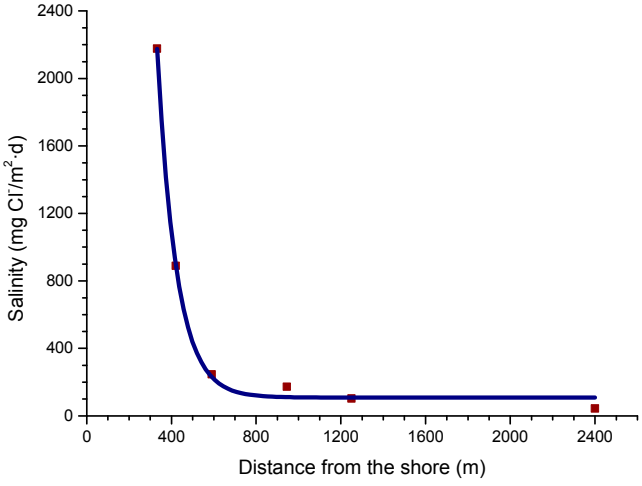

Figure 5. Variation in atmospheric salinity with distance from the shore [64].

Comparison of the atmospheric salinity at an exposure site and the average wind speed often fails to yield a clear relationship between both parameters. Calculation of the average wind speed takes into account the speeds recorded in all wind directions, and not only marine winds, which it would be reasonable to suppose are those that govern the presence of marine aerosol masses in coastal regions. In this sense it would be interesting to know whether the atmospheric salinity at the site is related with the run of marine winds, which is the sum of adding together the marine wind speed in each direction multiplied by the time it has been blowing [64]. Figure 6 has been prepared accordingly and clearly explains the decrease in the salinity value obtained in the second three-month period by a decline in the run of all marine winds, especially the most frequent (north-easterly, NE). Therefore, more than the average wind speed in the study area, the total run of marine winds is the parameter that has the greatest influence on the atmospheric salinity of the test site.

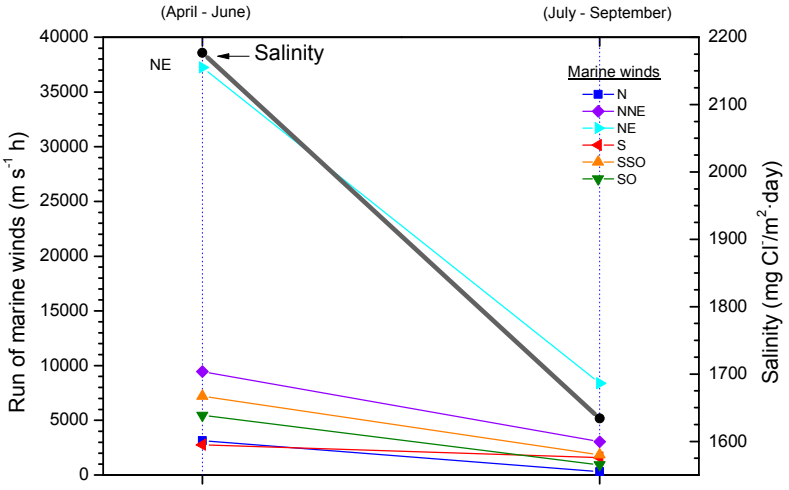

Figure 6. Salinity data and run of different marine winds in two three-month periods [64].

Nevertheless, the topography of the land and the general wind regime of the zone can also lead continental winds to influence salinity values. This has been shown in a study by the Academy of Sciences in Russia [65,68] involving long-term studies at Murmansk and Vladivostok, which concluded that chloride entrainment in both areas was dependent on both the average speed of total winds (marine + continental) and the product of the wind speed by its duration (wind power).

Further studies on this effect would be of great interest as a fuller knowledge would allow, for instance, the estimation of atmospheric salinities simply by analysing information on winds available in existing meteorological databases. The inclusion of salinity values in the numerous published damage functions between corrosion and environmental factors would also make it possible to estimate MAC at a specific site from meteorological data without the need to carry out lengthy and expensive natural corrosion tests.

4.4. Effect of Salinity on Steel Corrosion

For salt to accelerate corrosion the metallic surface must be wet. Preston and Sanyal [69] showed that corrosion of an iron surface under a deposit of NaCl particles starts to be seen at 70% RH, and is notably accelerated at higher RH. However, Evans and Taylor also note that sea salt particles cause corrosion at a lower RH than NaCl particles, due to the fact that sea salt contains very hygroscopic magnesium salts [70].

4.4.1. Steel Corrosion versus Salinity

In studies of MAC a direct relationship is generally established between corrosion and the saline content of the atmosphere. Ambler and Bain were the first to demonstrate this relationship [9].

In Figure 7, corresponding to the studies of Ambler and Bain [9], it is clearly seen how steel corrosion already experiences a notable acceleration at low atmospheric salinities, increasing from 10 to 100 mg $Cl^-/m^2 \cdot d$, as has also been reported by many other researchers. This effect has subsequently been addressed in other papers [64,71]. Figure 8 shows the variation in the CS corrosion rate with atmospheric salinity over a broad spectrum of airborne salt concentrations [64].

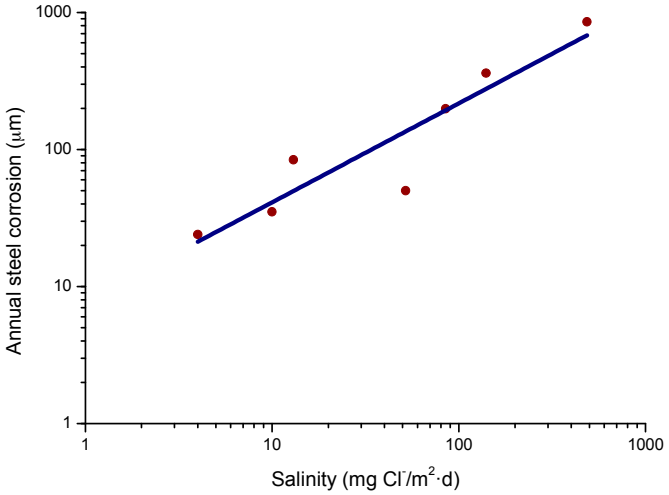

Figure 7. Annual steel corrosion versus salinity according to Ambler and Bain [9].

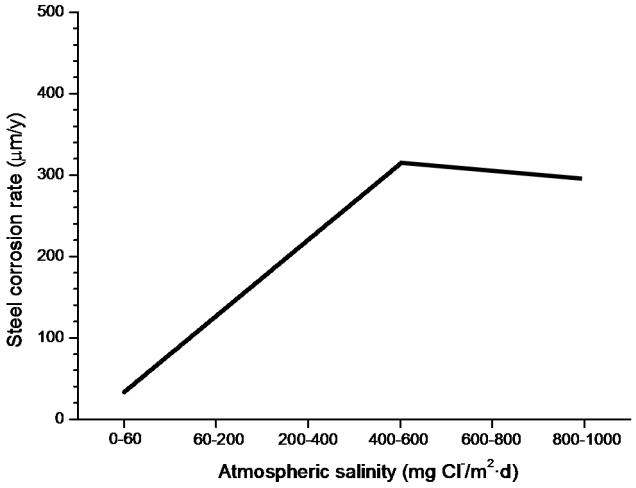

Figure 8. Variation in the corrosion rate of mild steel with salinity over a broad spectrum of atmospheric salinities. The graph shows a trend. Information obtained in an exhaustive bibliographic search [64].

For salinities of less than 600 mg $Cl^-/m^2 \cdot d$, a linear relationship trend between both parameters can be deduced, with the CS corrosion rate increasing considerably as the atmospheric salinity rises. For salinities above this value the corrosion rate seems to be stabilised.

Only a small number of MAC studies have been carried out at sites with very high atmospheric salinities. Morcillo et al. observed less steel corrosion at sites with a high Cl^- deposition rate (1905 mg/$m^2 \cdot d$) than at other very nearest site with lower atmospheric salinity values (824 mg/$m^2 \cdot d$) [12]. The explanation of this fact lies in the lower oxygen solubility in the aqueous layer on the metallic surface at a very high Cl^- concentration. Oxygen is a fundamental element for the cathodic process of metallic corrosion. This finding is not an isolated occurrence. Pascual Marqui [72] explains this effect in terms of competitive adsorption: at high Cl^- concentrations the adsorbed O_2 concentration on the metal surface is lower, in contrast to the adsorption of Cl^- ions. Espada et al. [73] also observed this

effect with salt fogs at high NaCl concentrations. In another study by Hache [74] it was experimentally seen in immersion tests that both steel corrosion and dissolved oxygen decreased when the saline solution concentration exceeded a threshold of 10 g NaCl/L.

The literature contains very little steel corrosion data corresponding to salinities above 600 mg $Cl^-/m^2 \cdot d$. It would be important to have more information from very severe marine atmospheres in order to rigorously confirm these observations.

4.4.2. Steel Corrosion versus Distance from the Shore

The influence of the distance from the sea is one of the most important aspects of MAC in coastal areas. Empirically, it is known that the effect of marine atmospheres basically runs to a few hundred metres from the shoreline and decays rapidly further inland.

The complexity of the phenomena associated with MAC makes it difficult to devise a model that can cover all possible scenarios. However, for areas closest to the shoreline (~400 to 600 m), published data shows that the decrease in the corrosion rate with the distance from the sea is fairly well represented by a simple exponential relationship [60].

$$C = C_0 \exp(-\beta X) + A, \quad (12)$$

where C is the corrosion rate, C_0 is the corrosion rate at the shoreline; β is a constant; X is the distance inland from the shoreline; and A is the corrosion rate at zero salinity.

Bearing in mind the aforementioned relationship between steel corrosion and atmospheric salinity, the variation in corrosion with the distance from the shore (Figure 9) should be an exponential function similar to that observed in Figure 5 between this variable and atmospheric salinity.

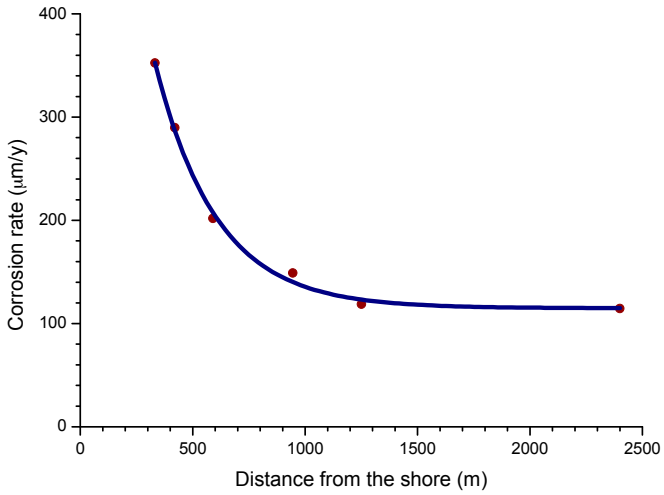

Figure 9. Variation in the corrosion rate of mild steel with distance from the shore [64].

4.5. Measurement of Atmospheric Salinity

Airborne salinity is the amount of marine aerosol present in a given marine atmosphere, and a value that is commonly measured in corrosion studies. Strekalov carried out an important review of this matter [75].

In MAC studies chlorides are usually captured by the wet candle method [9] or the dry cloth (or gauze) method [76,77], both of which are set out in ISO standard 9225 [78]. The dry cloth method was developed in the former Soviet Union and is also widely used in Asia. Both methods offer great benefits from the point of view of corrosion studies as they are suitable for long-term measurements (usually one month in duration) and the fact that their data refers to the amount of salt deposited per unit of surface area (generally expressed as mg $Cl^-/m^2 \cdot d$), which is a more relevant indicator

for the corrosion process than the saline content per unit of air volume. Foran et al. [79] suggest the possibility of measuring atmospheric salinity simply by determining the amount of chlorides dissolved in the rainwater collected in pluviometers.

As is noted in ISO 9223 standard [30], the results obtained by applying these various methods are not always directly comparable or convertible. In fact, ISO 9225 standard [78] provides a number of conversion factors. Corvo et al. [80] find that the following relationship:

$$[Cl^-]_{wc}\ (mg/m^2{\cdot}d) = -54.5 + 1.6\ [Cl^-]_{dc}\ (mg/m^2{\cdot}d), \quad (13)$$

where:
$[Cl^-]_{wc}$ = salinity determined by the wet candle method
$[Cl^-]_{dc}$ = salinity determined by the dry cloth method
Is only valid for salinity values of a considerable magnitude.

Figure 10 shows the relationship between the Cl^- deposition rates measured using both methods at two sites in Japan [81]. It is seen that the wet candle method is more sensitive to the presence of NaCl, capturing a greater amount of aerosol than the gauze method for NaCl levels of more than 5 $mg/m^2{\cdot}d$.

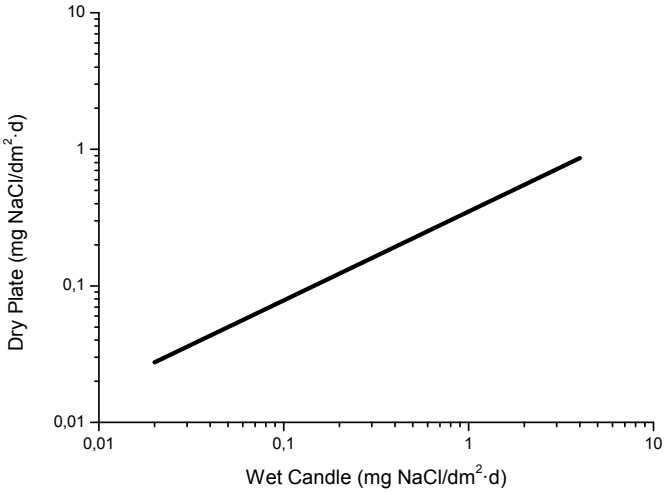

Figure 10. Relationship between salinity values reported by wet candle and dry plate methods [81].

In Australia, the INGALV Corrosion Mapping System [82] appears to calculate the Cl^- deposition rate at any location primarily on the basis of its proximity to the coast. However, it may be misleading to rely on simple subjective appreciations in the hope of correlating environment and pollution. For instance, points relatively close to the shoreline may in fact have lower Cl^- levels that a simple glance at the area and its surroundings might seem to suggest.

Finally, the Civil Research Institute (CRI) of the Ministry of Construction in Japan developed the CRI method in order to allow the absorption of a larger amount of salt than the relatively limited gauze method (Japanese standard JIS-Z-2381 [83]). This method uses a large capacity salt collector [84].

4.6. Salt Lake Atmospheres

Very little research work has focused on steel corrosion in salt lake environments, though several papers have recently been published in relation with Qinghai salt lake in north-west China [85,86]. Qinghai salt lake possesses an extremely high Cl^- ion concentration, with an average of 34 wt % Cl^- ions in the salt lake water, ten times that of seawater. It is important to note that the Mg content in the salt water of this lake is very high, much higher than other cations in the salt lake water and in seawater, and must be taken into account that the critical RH for $MgCl_2$ is 35%, much lower than the 75% corresponding to NaCl.

According to the authors, as the steel surface went though wet/dry cycles the alien magnesium cations got a good chance to participate in the corrosion reactions by replacing the ferrous ions and forming Mg-containing intermediates.

4.7. Deicing Salts

Although typically associated with marine environments, NaCl is actually more prevalent in the environment from the use of road deicing salt. Extensive use of deicing salts for snow removal, generally NaCl with small amounts of $CaCl_2$ and $MgCl_2$, began in the early 1960s. Heavy use of deicing salt, as much as 20 tons per lane mile per year, is common throughout regions of the snow belt in the northern states of the US. The widespread use of salt has been associated with a significant amount of damage to the environment and highway structures. Road spray, dirt and salts are carried by the air blast created by heavy traffic and quickly contaminate horizontal specimens. The prolonged wet period caused by deposits, chlorides and sulfates in close contact with the steel tends to accelerate poultice corrosion [42,87].

It is well known that deicing salts often cause corrosion problems and produce thick and flaky rust on steel bridges. This kind of rust is strongly dependent upon the local environment and topography around the bridges, where the RH is usually high, the air circulation is poor, and the steels are exposed to wetness for long times. In addition, chlorides accumulate in the rusts on girders that receive less washing from rainfall. Cook et al. [42] have evaluated several WS bridges in the USA exposed to road deicing salt and showing signs of significant corrosion and exfoliated rust. Rust samples have been collected from steel girders directly above roadways that are regularly deiced during winter. In these locations total thickness losses of about 1.5 mm have been measured on the girders over a period of 20 years.

Takebe et al. [88] estimated the amount of Cl^- from deicing salts on WS used for bridges and developed a method to evaluate the amount of salt present on bridge girders due to deicing salts. The sampling method is described in [89].

In a review of publications on this matter in the USA and Japan, Hara et al. [90] reported that Cl^- concentrations exceeding approximately 0.2–0.3 wt % in the rusts accelerated the increase in rust thickness and led to the development of extremely thick rust layers. A countermeasure to this problem is to periodically wash adhered salts from the girders. According to Hara et al. [90], periodic washing with pressurised tap water, delivering 2–4 MPa (high pressure washing) at the outlet nozzle, effectively suppresses the growth of rust particles by Cl^- ions and the development of thick rust layers, and may be useful as a suppression technology for deicing salts.

5. Atmospheric Corrosion Products

Atmospheric corrosion products of iron, referred to as rust, comprise various types of oxides, hydroxides, oxyhydroxides and miscellaneous crystalline and amorphous substances (chlorides, sulfates, nitrates, carbonates, etc.) that form as a result of the reaction between iron and the atmosphere [91] (Table 1).

In marine environments other rust products not listed in Table 1 may also appear, in some cases quite significantly. These include ferrous and ferric chlorides ($FeCl_2$ and $FeCl_3$), ferrous-ferric chloride [$Fe_4Cl_2(OH)_7$], etc., which are highly stable and therefore easily leachable from the corrosion product layers during atmospheric exposure. Table 2 shows the iron corrosion species that contain chlorine in their composition. Gilberg and Seeley [92] have investigated the context in which Cl^- ions can be found within iron corrosion products. Thus, they note that $FeCl_3$ and FeOCl are unstable to hydrolysis, being converted to akaganeite.

After short-term atmospheric exposure, oxyhydroxides (lepidocrocite, goethite, and akaganeite) and oxides (magnetite and maghemite) are the main crystalline products comprising the rust layers. The composition of the rust layer depends on the conditions in the aqueous adlayer and thus varies according to the type of atmosphere.

Table 1. Iron corrosion species according Cornell and Schwertmann [91].

Type	Name	Formula
Oxides	Magnetite	Fe_3O_4
	Maghemite	γ-Fe_20_3
	Hematite	α-Fe_20_3
Hydroxides	-	$Fe(OH)_2$
	Bernalite	$Fe(OH)_3$
	Green rusts	$Fe_x^{III}\ Fe_y^{II}\ (OH)_{3x+2y-z}\ (A^-)_z$ where $A^- = Cl^-$; $\frac{1}{2}SO_4^{2-}$
	Ferrydrite	$Fe_5O_8H{\cdot}H_2O$
Oxyhydroxides	Goethite	α-FeOOH
	Lepidocrocite	γ-FeOOH
	Akaganeite	β-FeOOH
	Feroxyhite	δ-FeOOH
	Schwertmannite	$Fe_{16}O_{16}(OH)_y(SO_4)_z{\cdot}nH_2O$

Table 2. Iron corrosion species containing chloride [92].

Name	Formula
Ferrous chloride (lawrencite)	$FeCl_2$
Ferric chloride (molysite)	$FeCl_3$
Ferric oxychloride	FeOCl
Ferrous hydroxychloride	β-$Fe_2(OH)_3Cl$
Green rusts	GR1 (GR Cl)
β-oxihydroxide (akaganeite)	β-FeOOH

One matter that has not yet been completely clarified is the content and composition of the amorphous phase of rust. Authors often try to study the structure of the corrosion products by quantitative powder XRD. The amorphous phase represents the difference between the sum of all the crystallised phase portions and 100%. According to Dillmann et al. [47], because powder XRD quantitative measurements are not very precise (about 10–20 relative percent error), measurements of the amorphous part of rust provided by this method need to be considered with great caution. If the techniques normally used to identify the different crystalline phases of rust (XRD, Fourier transform infrared (FTIR), MS, Raman spectroscopy (RS)) often have difficulty discriminating one phase from another, in the case of less crystallised (amorphous) rust phases such as feroxyhyte (δ-FeOOH), ferrihydrite, etc. this difficulty is further exacerbated. Monnier et al. [93] and Neff et al. [94] suggest combining the use of different complementary techniques in order to obtain improved characterisation, e.g., using μXRD, X-ray absorption under synchrotron radiation, μRS, etc.

It is unanimously accepted that lepidocrocite (γ-FeOOH) is the primary crystalline corrosion product formed in the atmosphere. In marine atmospheres, where the surface electrolyte contains chlorides, akaganeite (β-FeOOH) is also formed. As the exposure time increases and the rust layer becomes thicker, the active lepidocrocite is partially transformed into goethite (α-FeOOH) and spinel (magnetite (Fe_3O_4)/maghemite (γ-Fe_2O_3)). An increase in the airborne Cl^- deposition rate is accompanied by a drop in the lepidocrocite content of the rust and a rise in the goethite, akaganeite and spinel contents [95], as will be seen later.

Bernal et al. [96] in 1959 identified the conditions for the formation of the different iron oxides and hydroxides, noting the importance of the physicochemical conditions of the aqueous adlayer on the oxidation products of $Fe(OH)_2$: goethite, feroxyhyte, green rusts, spinels, etc. They also noted that the common feature of the group of iron oxides and hydroxides was that they were composed of different stackings of close-packed oxygen/hydroxyl sheets, with various arrangements of the iron ions in the octahedral or tetrahedral interstices.

5.1. Most Significant Corrosion Products in Steel Corrosion in Marine Atmospheres

The following section focuses on the most significant corrosion products of steel when exposed in Cl^--rich atmospheres, describing their formation mechanisms, structure, etc.

5.1.1. Green Rust 1 (GR1 or GR(Cl^-))

Green rusts (GR) are unstable intermediate products, very often amorphous, which occasionally emerge in the presence of anions such as Cl^-, SO_4^{2-}, etc., and replace OH^- ions in processes involving the ferrous-ferric transformation of hydroxides, oxides and oxyhydroxides in poorly aerated environments. Their name is derived from their bluish-green colour [97]. Two broad groups of GR have been distinguished. One contains primarily monovalent anions such as OH^- and Cl^- and is designated GR1, while the other contains mainly divalent ions such as SO_4^{2-} and is designated GR2 [98].

Green rusts rarely exhibit a well-defined stoichiometry and their composition depends on the particular environmental conditions. The formula of GR1 sometimes reported in the literature is $[3Fe(OH)_2 \cdot Fe(OH)_2Cl \cdot nH_2O]$, containing an equal number of Cl^- and Fe^{3+} ions, while GR2 conforms to the formula $[2Fe(OH)_3 \cdot 4Fe(OH)_2 \cdot FeSO_4 \cdot nH_2O]$ [99].

The crystal structures of GRs are assumed to be similar to that of the mineral pyroaurite [100], $Mg_6^{II}Fe_2^{III}(OH)_{16}CO_3 \cdot 4H_2O$. According to Refait et al. [99] a structural model derived from the pyroaurite structure can be reasonably proposed for GR1. The Fe atoms of the hydroxide layers are randomly distributed among the octahedral positions. The interlayers are mainly composed of Cl^- ions and O_2 atoms belonging to the water molecules connecting two OH^- ions of adjacent hydroxide layers.

GR1 is usually prepared by aerial oxidation of $Fe(OH)_2$ suspensions in the presence of a slight excess of dissolved $FeCl_2$. Thus, in slightly basic and Cl^--containing aqueous media, GR1 should be obtained as a corrosion product of iron and steels either by oxidation of an initial $Fe(OH)_2$ layer or by direct precipitation in the simultaneous presence of Fe^{2+} and Fe^{3+} dissolved species.

$$7Fe(OH)_2 + Fe^{2+} + 2Cl^- + \frac{1}{2}O_2 + (2n+1)H_2O \rightarrow 2[3Fe(OH)_2 \cdot Fe(OH)_2Cl \cdot nH_2O], \quad (14)$$

GR1 found in Cl^--containing aqueous media occurs during the corrosion of steels before the formation of the end products such as lepidocrocite, goethite, akaganeite and magnetite, as its formation is more favoured [99].

5.1.2. Akaganeite ((β-FeOOH) or β-FeO(OH,Cl^-))

Akaganeite is the rust phase of capital importance in the MAC process of steel, and thus is discussed here in the greatest detail. Akaganeite is one of the polymorphs of ferric oxyhydroxides (-FeOOH). Its formation requires halogen ions to stabilise its crystalline structure. Since it always contains Cl^- ions, this compound is not strictly speaking an oxyhydroxide. Stahl et al. have determined its chemical formula as $FeO_{0.833}(OH)_{1.167}Cl_{0.167}$ [101].

Watson et al. [102] observed that the crystal possessed a regular porous structure and suggested that the subcrystals might not be solid rods but tubes which, though externally still square prisms, contained a circular central channel or tunnel running the whole length of the subcrystal. The tunnels in the akaganeite structure, with a diameter of 0.21–0.24 nm, are stabilised by Cl^- ions, and Cl^- levels ranging from 2 to 7 mol % have been reported. A minimum amount of Cl^-, 0.25–0.50 mmol/mol seems essential to stabilise the crystalline structure of akaganeite [91]. According to Keller [103], akaganeite has been shown to contain up to 5 wt % Cl^- ions in marine atmospheres. At ambient temperature these tunnels are full of water and Cl^- [91]. The impossibility of leaching the Cl^- by washing confirms that at least part of the Cl^- ions are found in the crystalline lattice, as noted by Rezel et al. [104] and Ståhl et al. [101].

Gallagher [105] describes akaganeite as a fascinating substance that precipitates as unusual cigar-shaped crystals with a tetragonal unit cell, although this has given rise to much controversy.

The structural refinement by XRD (Rietveld) carried out by Post and Buchwald confirms that the unit cell is monoclinic, having eight formula units per unit cell [106]. The Fe^{3+} ions were each surrounded octahedrally by six OH^- ions.

The crystals are very small and the crystallographic structure is isostructural with hollandite ($BaMn_8O_{16}$) characterised by the presence of tunnels parallel to the C-axis of the lattice. The size distribution of the crystals is fairly narrow and their length is only exceptionally greater than 500 nm. Due to its special structure (presence of tunnels) akaganeite is less dense than other oxyhydroxides like lepidocrocite or goethite [107,108]. In this respect, Shiotani et al. note that akaganeite has a relatively larger volume in relation to the initial iron [109].

Akaganeite displays two basic morphologies: somatoids (spindle-shaped crystals) and rods (cigar-shaped crystals). The former type is the usual morphology of akaganeite when it forms in laboratory conditions by hydrolysis of acid $FeCl_3$ solutions at 25–100 °C [107,108]. The latter type, according to the authors' experience, is the usual morphology of the akaganeite crystals that form in atmospheric conditions. Researchers have assigned SEM morphologies to akaganeite without an unequivocal characterisation of this oxyhydroxide. Morcillo et al. were able to do this using the SEM/μRS technique [110,111], observing aggregates of akaganeite crystals, a sponge-type morphology, constituted by a lattice of elongated cylinder- or tube-shaped crystals typical of the rod morphology (cigar-shaped crystals) of this oxyhydroxide.

With regard to akaganeite formation mechanisms when steel is exposed to a Cl^--rich marine atmosphere, the following may be noted. The formation of akaganeite is preceded by the accumulation of Cl^- ions in the aqueous adlayer giving rise to the formation of $FeCl_2$, which hydrolyses water according to:

$$FeCl_2 + 2H_2O \rightarrow Fe(OH)_2 + 2HCl, \quad (15)$$

At the steel/corrosion products interface, where Cl^- ions accumulate, high Cl^- concentrations and acidic conditions with pH values between 4 and 6 give rise to the formation of ferrous hydroxychloride (β-$Fe_2(OH)_3Cl$), a very slow process requiring the transformation of metastable precursors [112,113]. Remazeilles and Refait concluded that large amounts of dissolved Fe(II) species and high Cl^- concentrations are both necessary for akaganeite formation [114]. The oxidation process of β-$Fe_2(OH)_3Cl$ which leads to akaganeite formation passes through different steps via the formation of intermediate GR1 ($Fe_3^{II}Fe^{III}(OH)_8Cl^- nH_2O$) [99,113,115]. In all, the whole oxidation process leading to akaganeite can be summarised as follows [99,112–115]:

$$FeCl_2 \rightarrow \beta\text{-}Fe_2(OH)_3Cl \rightarrow GR1\ (Cl^-) \rightarrow \beta\text{-}FeOOH, \quad (16)$$

Thus requiring a relatively long time.

5.1.3. Magnetite (Fe_3O_4)/Maghemite (γ-Fe_2O_3)

The structure of magnetite is that of an inverse spinel. Magnetite has a face-centred cubic unit cell based on thirty-two O^{2-} ions which are regularly cubic close packed. There are eight formula units per unit cell [91]. Magnetite differs from most other iron oxides in that it contains both divalent and trivalent iron. Its formula is written as $Y[XY]O_4$, where X = Fe^{II}, Y = Fe^{III} and the brackets denote octahedral sites. Eight tetrahedral sites are distributed between Fe^{II} and Fe^{III}, i.e., the trivalent ions occupy both tetrahedral and octahedral sites. The structure consists of octahedral and mixed tetrahedral/octahedral layers [91]. However, magnetite, if it were the normal spinel structure, would have eight tetrahedral sites occupied by eight Fe^{2+} ions and sixteen octahedral sites occupied by sixteen Fe^{3+} ions [116].

In stoichiometric magnetite $Fe^{II}/Fe^{III} = 0.5$, however, magnetite is frequently non-stoichiometric, in which case it has a cation-deficient Fe^{III} sub-lattice. Magnetite is also said to have a defect structure with a narrow composition range, the Fe:O ratio of which varies from 0.750 to 0.744 [117]. Thus, magnetite usually presents vacancies, preferably on octahedral sites, which form to maintain the

electroneutrality of the crystal when H_2O or OH^- molecules enter the network, as well as ferrous and ferric ions sharing their valence electrons.

Maghemite has a similar structure to magnetite, but differs in that all or most Fe is in the trivalent state. Cation vacancies compensate for the oxidation of Fe^{II}. Maghemite also has a cubic unit cell, each cell contains thirty-two O^{2-} ions, twenty-one and one-third Fe^{III} ions and two and a third vacancies. Eight cations occupy tetrahedral sites and the remaining cations are randomly distributed over the octahedral sites. The vacancies are confined to the octahedral sites [91]. Maghemite is also a defect structure with the Fe:O ratio in the range of 0.67–0.72 [117].

XRD presents an important limitation when it comes to differentiating the magnetite phase from the maghemite phase, as both show practically identical diffractograms (similar crystalline structures) and are very hard to differentiate when mixed with large amounts of other phases (lepidocrocite, goethite and akaganeite), as occurs in the corrosion products formed on steel when exposed to marine atmospheres. Both phases are associated to the diffraction angle at 35° [118]. Both phases are usually detected in the inner part of the rust adhering to the steel surface, where oxygen depletion can occur [119,120].

Spinel phase (magnetite and/or maghemite) may form by oxidation of $Fe(OH)_2$ or intermediate ferrous-ferric species such as green rust [119]. It may also be formed by lepidocrocite reduction in the presence of a limited oxygen supply [120] according to:

$$2\gamma\text{-FeOOH} + Fe^{2+} \rightarrow Fe_3O_4 + 2H^+, \quad (17)$$

With a broader view, Ishikawa et al. [121] and Tanaka et al. [122] found that the formation of magnetite particles was caused by the reaction of dissolved ferric species of oxyhydroxides with ferrous species in the solution, in the following order: akaganeite > lepidocrocite >> goethite. The formation of magnetite can be represented as the following reaction:

$$Fe^{2+} + 8\text{FeOOH} + 2e^- \rightarrow 3Fe_3O_4 + 4H_2O, \quad (18)$$

Remazeilles and Refait [114], Nishimura et al. [10] and Lair et al. [40] all observe that the electrochemical reduction of oxyhydroxides leads to spinel phase formation.

As Hiller noted some time ago, the rust formed in marine atmospheres contains more magnetite than that formed in Cl^--free atmospheres [123]. In severe marine atmospheres the spinel phase can be the main rust constituent, as was found by Jeffrey and Melchers [124] and by Haces et al. [125].

There is often uncertainty as to which of the two phases, magnetite or maghemite, is present in AC products, and indeed both species could be present depending on the local formation conditions and the corrosion mechanisms involved in the process. This lack of definition may also be intimately related with the analytical techniques used for their determination. Many researchers have reported the presence of magnetite in AC products on the basis of XRD data, but much of this data is suspect since the XRD patterns of magnetite and maghemite are very similar. The same happens when the ED method is used [126]. However, Graham and Cohen [127] do show convincing evidence on the basis of MS that magnetite is a component of corrosion products on several samples. However, Leidheiser and Music [128] and Chico et al. [129], also using this technique, found no evidence of magnetite. Likewise, Oh et al. [130], using MS and RS, find a high magnetic maghemite content in the exposure of CS at 250 m from the seashore. In contrast, Nishimura et al. [10], using X-ray photoelectron spectroscopy (XPS) and TEM, find high magnetite contents.

Antony et al. [131] reported that FTIR is also not very appropriate to precisely identify magnetite, and Monnier et al. [93] also note that MS has difficulty in discriminating phases of the same oxidation state that have similar local environments, particularly in the case of complex mixes, as is the case of magnetite and maghemite. Thus, it seems that the specific nature of each analysis method strongly influences the type of phase identified.

The identification of rust amorphous phases as well as the classification of the type of spinel formed (magnetite or maghemite) are two issues where more research effort is needed.

5.2. Other Characteristics of the Steel Atmospheric Corrosion Products

5.2.1. Towards a Greater Knowledge of the Structure of Iron Oxides

As Bernal et al. [96] suggested in 1959, the common feature of the group of iron oxides and hydroxides is that they are composed of different stackings of close-packed oxygen/hydroxyl sheets, with various arrangements of the iron ions in the octahedral or tetrahedral interstices, and their mutual transformations are topotactic by rearrangement of the atoms. These authors interpreted in a rational crystallochemical way the transformations involving the compounds $Fe(OH)_2$, δ-FeOOH, FeO, γ-Fe_2O_3, α-FeOOH, α-Fe_2O_3 and Fe_3O_4. Only some of these transformations were not topotactic and seemed to have dissimilar structures, with renucleation being necessary for the transformation process. This is the case, for instance, with β-FeOOH→α-Fe_2O_3 [96].

According to Matsubara et al. [132], it is important to know the fundamental structures of the components of iron corrosion products in order to understand the characteristic features of various types of corrosion products. The ideal crystallographic structures of three ferric oxyhydroxides—lepidocrocite, goethite and akaganeite—are described using FeO_6 octahedral units (Figure 11). Furthermore, the structure of a $Fe(OH)_2$ is composed of layers of FeO_6 octahedra intercalated with hydroxyl OH^-. There are also several kinds of GR containing ferric and ferrous ions which have a layered structure as $Fe(OH)_2$. In the structure of GR, the fractions of ferric and ferrous ions in layers of FeO_6 octahedra are variable and different anions and water molecules are intercalated between the layers. Although there are other iron oxide structures including hydroxides, they are fundamentally described in a similar way.

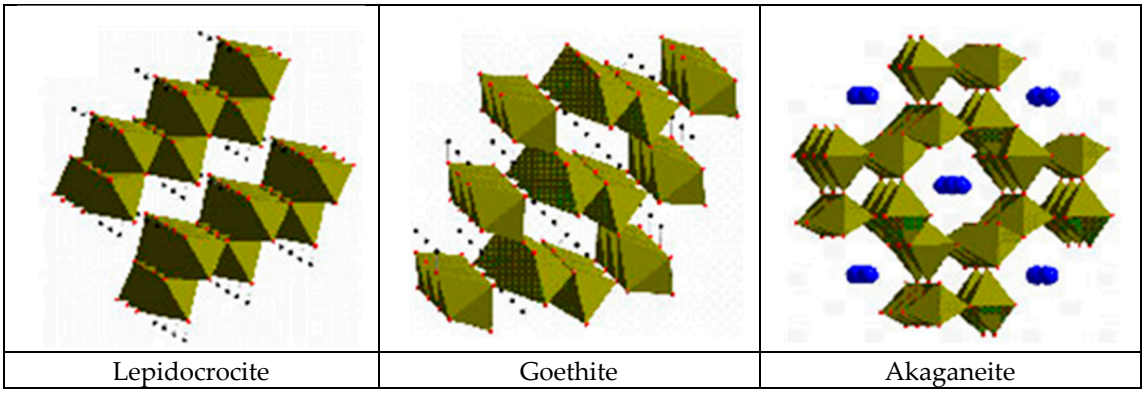

Figure 11. Ideal crystallographic structures of lepidocrocite (γ-FeOOH), goethite (α-FeOOH) and akaganeite (β-FeOOH). The structures are described using FeO_6 octahedral units. Small circles: hydrogen, medium circles: chlorine [132,133].

MS has been used to identify components in corrosion products and to analyse their fine structures. Other analytical methods, such as EPMA, TEM, FTIR and RS are often used for analysing corrosion products formed on the surface of steel. The results obtained by these methods provide information on the composition, morphology and structure of corrosion products. However, structural information on corrosion products obtained by these methods is limited [132].

As was seen in Section 3, in order to characterise corrosion product structures in various scales, Kimura et al. [45] have used several analytical approaches that are sensitive to three structural-correlation lengths (LRO, MRO and SRO). Thus, conventional XRD techniques can detect detailed structural information in terms of LRO. However, this technique yields broad peaks when the grain size is smaller than ~50 nm, as is often found in corrosion products. Contrarily, XFAS is useful for in-situ observation of SRO. In XAFS, oscillatory modulation near an X-ray absorption

edge of a specific element of a specimen provides information in terms of the local structure around an atom (Fe, Cl, etc.) in the rust layer or determines the distance between the centred atom and the neighbouring ligands, the number of ligands, and the stereographic arrangement of ligands. However, some reservations should be made regarding information about linkage of the FeO_6 octahedral unit structure, because XAFS data is obtained only from near neighbour atomic arrangements. This strongly suggests the great importance of middle-range ordering (MRO) for characterising corrosion products. This has been achieved by a combination of X-ray scattering (AXS) and reverse Monte Carlo simulation (RMC), which visualises the atomic configurations [45].

5.2.2. Morphology

The rust formed on steel when exposed to the atmosphere is usually a complex mixture of several phases. Moreover, each of these phases can take on a wide variety of morphologies depending on their growth conditions. Thus, the diversity of rust morphologies formed on CS exposed to marine atmospheres is enormous, with a great variety of shapes and sizes of the crystalline aggregates that reflect to a large extent the different growth conditions: chemical characteristics of the aqueous adlayers formed by humidity condensation, rainfall, etc., temperature, wet/dry cycle characteristics, etc.

Cornell and Schwertmann dedicated an entire chapter of their well known and well referenced book "The iron oxides, structure, properties, occurrence and uses" to iron oxide crystal morphology and size, mainly concerned with synthetic iron oxides. Table 3 shows the principal habits (morphologies) of iron oxides according to Cornell and Schwertmann [91].

Table 3. Principal habits (morphologies) of iron oxides according to Cornell and Schwertmann [91].

Iron Oxide	Morphology
Lepidocrocite (γ-FeOOH)	Laths
Goethite (α-FeOOH)	Acicular
Akaganeite (β-FeOOH)	Rods, somatoids
Feroxyhyte (δ-FeOOH)	Plates
Magnetite (Fe_3O_4)	Octohedra
Maghemite (γ-Fe_2O_3)	Laths or cubes
Hematite (α-Fe_2O_3)	Hexagonal plates, rhombohedra
Ferrihydrite ($Fe_5HO_8{\cdot}4H_2O$)	Spheres

It should however be noted that the morphologies of synthetic iron oxides produced in laboratory conditions may be very different to those obtained during CS corrosion in the atmosphere, as pointed out by Waseda and Suzuki in the preface to an interesting book on "Characterisation of corrosion products on steel surfaces" [134]. As they note, the morphology of AC products is often not describable in terms of typical iron oxide structures but is much more complicated; the component phases in rust formed on steel in outdoor exposure show imperfections in their structures and real component structures appear to diverge from an ideal crystallographic structure of typical iron oxides.

For some time now, articles published on AC studies usually include SEM views of rust formations and in some cases even attribute certain morphologies to specific rust phases without an analytical characterisation. An exception can be seen in the pioneering work of Raman et al. [135]. These researchers attempted to indirectly identify the morphologies observed by SEM by comparison with the morphologies of standard rust phases grown in the laboratory and identified by XRD and IRS.

Very recently, the research group of Morcillo et al. has progressed in this field using the powerful SEM/μRS spectroscopic technique to perform a more direct and rigorous characterisation of the different morphologies that can be displayed by the main rust phases (lepidocrocite, goethite, akaganeite and magnetite) formed on CS specimens exposed to marine atmospheres for a certain time [110,111,136,137].

Without seeking to be exhaustive, there follows a tentative classification of the different types of morphology observed by the authors in the rust formed on steel exposed to marine atmospheres [137]:

(a) Globular: hemispheric-shaped aggregated formations like small mounds.
(b) Acicular: aggregates with a similar appearance to needles, hairs, or threads.
(c) Laminar: this can appear in a wide range of different formations in which laminas grow perpendicularly to the surface: bar shape, worm nest shape, bird's nest shape, flower petal shape, feather shape, etc.
(d) Tubular: formations in which the crystalline aggregates are constituted by prisms, tubes, or rods, etc.
(e) Toroidal
(f) Geode-type: unusual or singular oolitic or globular morphology constituted by fish-egg-like spherical formations.

Figure 12 presents typical characteristic morphologies of the four rust phases normally present among the corrosion products formed in marine atmospheres: lepidocrocite, goethite, akaganeite and magnetite.

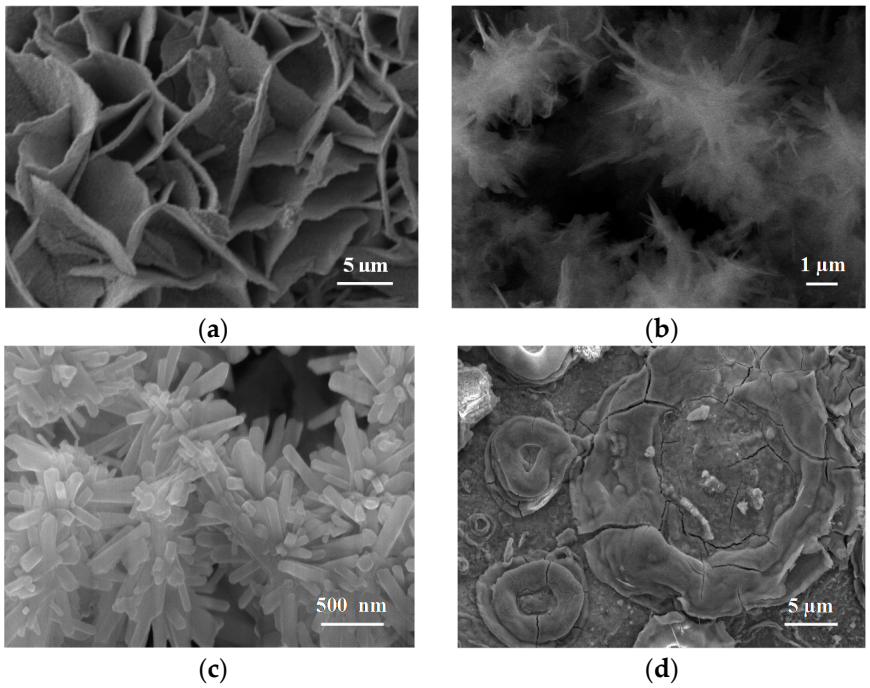

Figure 12. SEM view of laminar lepidocrocite (**a**); acicular goethite (**b**); tubular akaganeite (**c**) and toroidal magnetite (**d**) formations [137].

5.2.3. Grain Size (Granulometry)

As shown in Figure 13, from Kimura et al. [45], which shows a schematic illustration of corrosion on an iron surface in the atmosphere, the formation process of solid particles can be visualised by three steps: (a) nucleation; (b) growth; and (c) ageing [138].

(a) Nucleation corresponds to the first step of precursor condensation and solid formation. On an atomic scale, iron forms cations that are coordinated by six water molecules $[Fe(H_2O)_6]^{2+}$ [139]. In a neutral solution, metal cations react with OH^-, O_2, and H_2O resulting in the formation of hydroxo cations $[Fe(OH)_X(H_2O)_{6-X}]^{(3-X)+}$.
(b) Then the growth process follows, where $Fe(O,OH)_6$ octahedra units as cations or smaller sized growing nuclei accumulate to form larger particles. On a colloidal scale, polymerisation of

these $Fe(O,OH)_6$ octahedra leads to the formation of fine particles of hydroxides, oxyhydroxides or oxides.

(c) These particles grow into grains or layers through a long period of ageing processes affected by repeated wet and dry cycles. Reaction conditions (concentration, acidity, temperature, nature of anions, etc.) have a strong influence on the structural or morphological changes of poly-octahedra during corrosion. Coagulation and adhesion processes ensue to generate corrosion products, which undergo ageing processes leading the system to stability. During ageing the particles may undergo modifications such as increases in size, changes in crystal type, changes in morphology, etc. [140]. Thus, according to Ishikawa et al. [141], steel rusts can be regarded as agglomerates of colloidal nanoparticles of ferric oxyhydroxides (goethite, akaganeite and lepidocrocite), spinels (magnetite/maghemite), and poorly recrystallised iron oxides (amorphous substances). Voids of different sizes form between the fine particles in the rust layer.

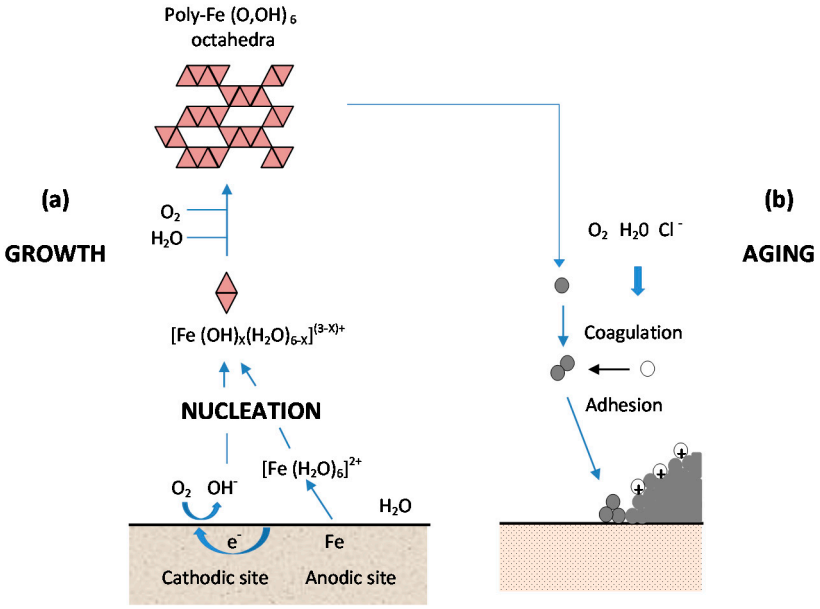

Figure 13. Scheme of iron corrosion in the atmosphere according Kimura et al. [45]: (**a**) reactions in the initial wet cycle; (**b**) reactions during repetition of wet/dry cycles for a long period. Triangle pairs represent $Fe(O,OH)_6$ octahedra.

Resulting from these complicated processes, corrosion products are generally classified as coarse or fine grains, both of which are composed of crystallites and inter-crystallites. The structure in the former are similar to those of ideal crystals, while in the latter the linkage of $Fe(O,OH)_6$ octahedra is disordered, due to the existence of defects and/or different sizes of $Fe(O,OH)_6$.

A practical laboratory method for determining the grain size of rusts formed on steel during atmospheric exposure, known as the "tape method" [142], consists of adhering a 2×2 cm^2 piece of adhesive tape to the outermost surface of the rust layer, pressing firmly and evenly on the surface, and lifting off to examine the size and density of rust particles. The morphology takes the form of grains or particles, agglomerates of grains, flakes, and even exfoliations (layers or laminates) [143] (Figure 14). The texture of rust is seen to vary according to the atmospheric aggressivity (Figure 15). A more heterogeneous surface appearance and coarser granulometry is found in more aggressive atmospheres (industrial and marine) [144]. In marine atmospheres, the granulometries are coarser and become more accentuated with airborne salinity and exposure time (Figure 16). In the marine atmosphere with the highest Cl^- deposition rate (665 mg/m^2·d) the formation of coarse flakes and exfoliations is seen [64]. These results confirm the observations of Ishikawa et al. [144,145].

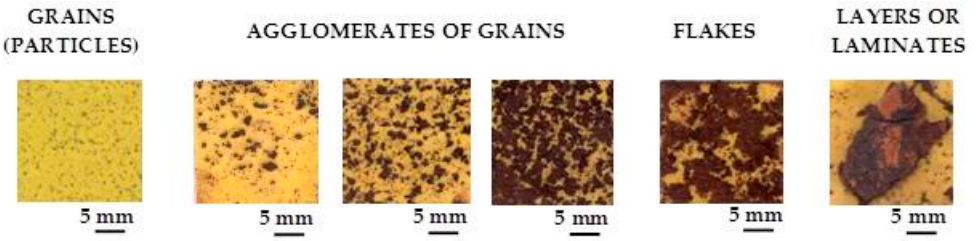

Figure 14. Type of rust morphologies formed on carbon steel exposed to marine atmospheres [143].

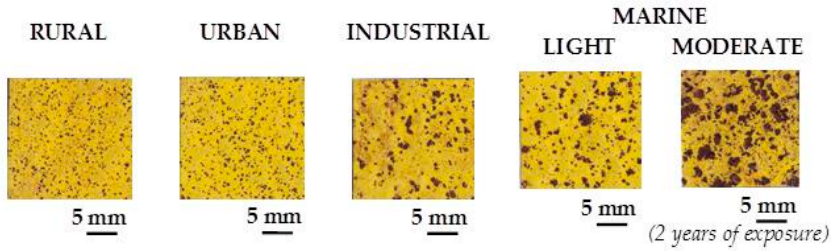

Figure 15. Granulometries of outermost rusts formed on skyward- facing side of carbon steel exposed for 5 years at different type of atmospheres.

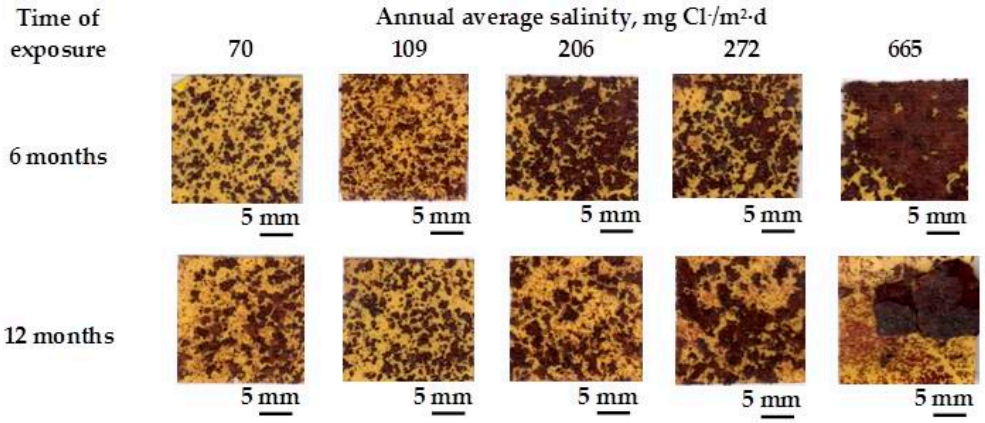

Figure 16. Granulometries of outermost rusts formed on skyward- facing side of carbon steel exposed for 6 and 12 months at marine atmospheres of different aggressivity [64].

The compactness of the rust layers depends on the morphology of the rust particles; smaller particles form more compact and less permeable layers. However, as Ishikawa et al. note [144], particle size analysis of rust is not easy because of the heterogeneous morphology and strong aggregation of rust particles. Ishikawa et al. [146] use the N_2 adsorption method to estimate the particle size of rust formed on steel exposed to various situations. It was revealed that the specific surface area (SSA) obtained by N_2 adsorption decreased with increasing airborne salinity (Figure 17). This finding shows that rust particles grow with an increase in airborne salinity, and that less compact rust layers with low corrosion resistance are formed in Cl^- environments such as coastal areas. In contrast, in a low salinity environment fine rust particles assemble to form densely packed rust layers with high corrosion resistance. Ishikawa et al. attribute the high SSA obtained by H_2O adsorption on the rusts generated on the coast to the tunnels of akaganeite crystals, accessible to H_2O but not to N_2 [146].

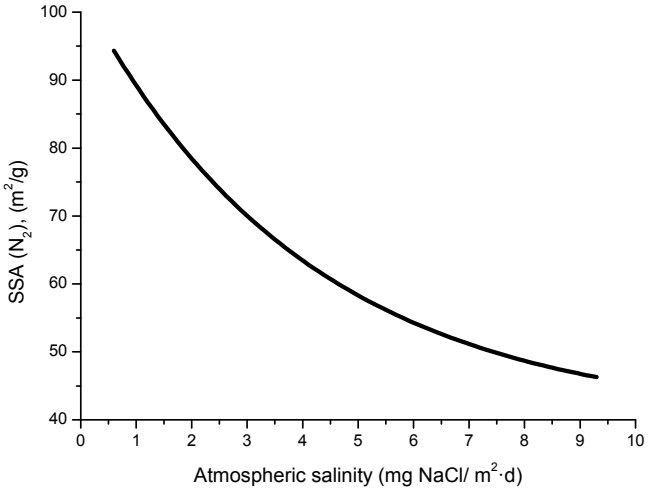

Figure 17. Relationships (trend curve) between SSA(N2) of rusted carbon steel and atmospheric NaCl contents [146].

Ishikawa et al., examining the texture of rusts, note that the rusts formed at coastal sites were aggomlerates of large particles and had larger pores than rusts formed at rural and urban sites. This finding suggests that NaCl promotes rust particle growth, resulting in the formation of larger pores as voids between larger particles in the rust layer and facilitating further corrosion.

6. The Rust Layer

When the thin layer of corrosion products has grown to cover the whole surface, further growth requires reactive species from the aqueous adlayer to be transported inwards through the rust layer while metal ions are transported outwards. In addition to this, electrons must be transported from anodic to cathodic sites on the surface, so that those produced in the anodic reaction can be consumed in the cathodic reaction. As long as the metal substrate is covered only by a thin oxide film, electron transportation through the film is generally not a rate-limiting step. However, when the corrosion products grow in thickness, electron transportation may become rate-limiting [8].

This section considers the different physical and chemical properties of corrosion product layers. It starts by addressing the organoleptical properties of rust layers, such as their colour and texture, before going on to consider other properties more related with their protective capacity: stratification, stabilisation, adhesion, thickness, and porosity and their evaluation using different indices.

6.1. Organoleptical Properties

6.1.1. Colour

CS exposed to the atmosphere develops ochre-coloured rust which becomes dull brown as the exposure time increases. Lighter rust colours are seen in atmospheres with greater salinity (more corrosive) and darker rusts in less aggressive atmospheres [64]. In marine atmospheres, the colour of rust varies not only with the salinity of the atmosphere, but also according to the steel type, exposure time, etc.

Some time ago, LaQue [147] exposed different steels for 6 months to the marine atmosphere of Kure Beach (250 m from the shoreline) and found that the colouring of 84% of the tested steels was within the range seen in Figure 18, which shows the relationship between the rust colour ratings as developed early in the test and the corrosion resistance of the steels after long-term exposure.

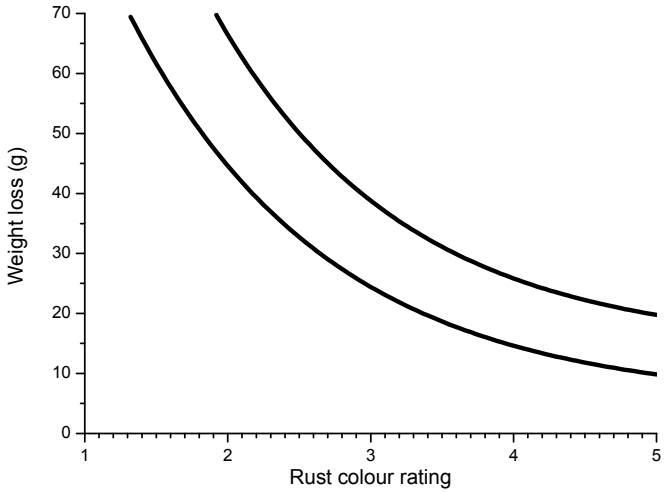

Figure 18. Band showing the relationships between rust colour rating after 6 months of exposure and corrosion of steels (4 × 6 in. specimens) after 7.5 years of exposure in marine atmosphere at Kure beach [147].Rust color rating: 1 (lightest)–5(darkest).

6.1.2. Texture

In Section 5.2.3 reference was made to the granulometry of corrosion products. In part, this property is closely related with the texture of the outer surface of the rust layer. Sense of touch is used to determine aspects of texture such as smoothness, unevenness and roughness. Ph. Doctoral Thesis of I. Díaz [148] and H. Cano [149] reported one to three-year exposure of a variety of CS in different types of atmospheres, where differences in texture were observed in the rust layers formed. Patinas with smoother textures (more homogenous appearance and finer granulometry) were found in rural and urban atmospheres, while rougher textures with a more heterogeneous appearance and a coarser granulometry were observed in industrial and marine atmospheres, all the more so the higher the corrosivity of the atmosphere (higher Cl^- deposition rate) and the longer the exposure time.

6.2. Properties More Related with the Protective Capacity of Rust Layers

6.2.1. Stratification of Rust Layers

There is controversy about the stratification of the rust layer in different sublayers on unalloyed CS [97]. According to Díaz et al. [150] rust is always stratified irrespective of the steel composition, be it WS or plain CS. In their investigations these authors have found the presence of two sublayers in all rust films: an uncoloured (dark grey) inner layer and an orangey-brown-coloured outer layer (Figure 19). Thus, the dual nature of the rust layer is not an exclusive characteristic of WS since plain CS with less AC resistance also generates a stratified rust.

According to Suzuki [151], rust layers usually present considerable porosity, spallation, and cracking. Cracked and non-protective oxide layers allow corrosive species easy access to the metallic substrate, and is the typical situation in atmospheres of high aggressivity. However, compact oxide layers formed in atmospheres of low aggressivity favour the protection of the metallic substrate. The higher the Cl^- deposition rate in marine atmospheres, the greater the degree of flaking observed, with loosely adherent flaky rust favouring rust film breakdown (detachment, spalling) and the initiation of fresh attack. As time elapses, the number and size of defects may decrease due to compaction, agglomeration, etc. of the rust layer, thereby lowering the corrosion rate [152,153].

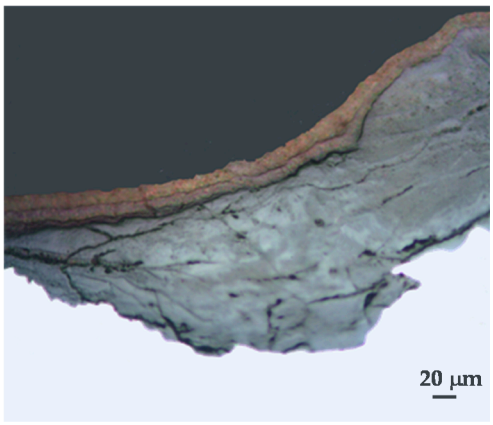

Figure 19. Dual structure of a consolidated rust layer formed during one year on carbon steel exposed al unsheltered conditions in a marine atmosphere with low chloride deposit (21 mg $Cl^{-}/m^2 \cdot d$). Optical micrograph obtained by polarized light. The outer orange-coloured layer is mainly lepidocrocite while the inner greyish layer is mainly goethite and magnetite [150].

6.2.2. Stabilisation of Rust Layers and Steady-State Corrosion Rate

Bibliographic information on this aspect is highly erratic and variable. The gradual development of a corrosion layer takes several years before steady-state conditions are obtained, though the exact time taken to reach a steady state of AC will obviously depend on the environmental conditions of the atmosphere where the steel is exposed.

Morcillo et al. have determined the stabilisation times of rust layers formed on WS [87], considering the steady state corrosion rate to be the rate corresponding to the year from which corrosion slows by $\leq$10%. Previously it was confirmed that the corrosion rate (y) plotted against the exposure time (x) fitted an exponential decrease equation:

$$y = A_1 \exp(-x/t_1) + y_0, \quad (19)$$

where

y = corrosion rate, μm/y
x = time, years
$1/t_1$ = decrease constant
y_0 = steady state corrosion rate, μm/y
$A_1 + y_0$ = corrosion rate at x = 0, μm/y

The rust layer stabilisation time decreases as the corrosivity category (ISO 9223) [30] of the atmosphere rises. The stabilisation time depends, among other factors, on the exposure time, the existence of wet/dry cycles, the corrosivity of the atmosphere, and in short on the volume of corrosion products formed. However, a shorter stabilisation time does not imply a greater protective capability of the rust. In this respect, stabilisation of the rust layer occurs faster in marine atmospheres, due to their greater corrosivity, but the protective value of this rust is lower than that of rusts formed in less aggressive atmospheres (rural, urban, etc.) where stabilisation times are longer. The steady-state corrosion rate increases in line with the corrosivity of the atmosphere in both rural, urban, industrial, and marine atmospheres (Figure 20) [87].

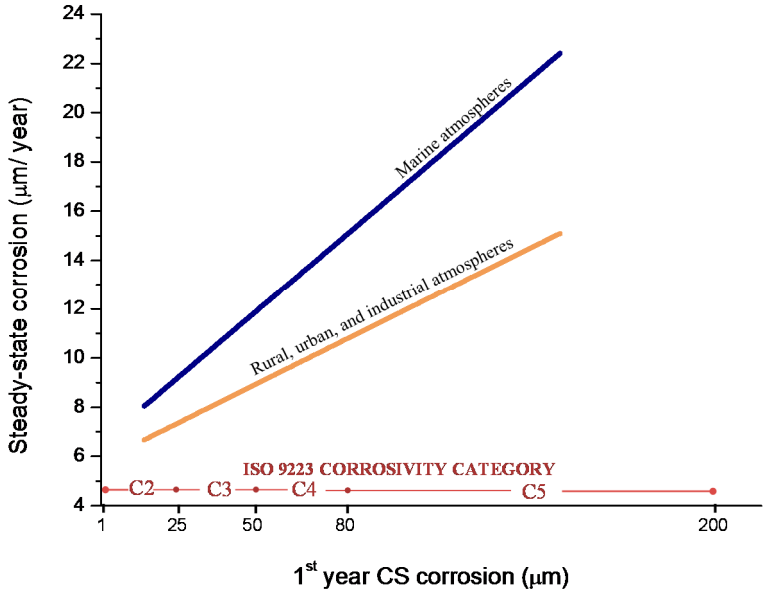

Figure 20. Relationship between steady-state corrosion rate of carbon steel and atmospheric corrosivity category according ISO 9223 for different type of atmospheres [87].

6.2.3. Adhesion

According to Honzak [154] it is possible to differentiate three layers in rust: surface rust that is easily removable (e.g., by light scraping), an intermediate rust layer that can be "burst off" by bending the specimen, and a very adherent layer on the metal surface which cannot be removed by scraping but is removable by abrasive cleaning or chemical methods (e.g., pickling).

Not all steel corrosion products become incorporated in the rust layer. Some examples [124] include:

(a) Brown stains as a consequence of run-off processes
(b) Leaching of soluble components of the rust layer (iron chlorides in marine atmosphere) by rainwater, and
(c) Rust lost through abrasion and erosion, the latter particularly in high wind areas.

It has long been known that not all the corroded metal becomes part of the measurable rust product [155], but there have been very few attempts to quantify this part. One exception is the work of García et al. [156–158], who classified adherent rust as: (i) removable by scraping the steel surface with a metallic brush; and (ii) removable by hitting the steel with a hammer. According to these authors, the protective properties of rust on CS in a given corrosive environment depends on the characteristics of the adherent rust, i.e., that which is bonded to the metal surface, but a full overview of the corrosion process also requires the characterisation of non-adherent rust, i.e., that which is loosely bound to the metal surface, and that which is lost during the corrosion process. The authors found that the amount of corroded iron that is converted into adherent rust on steels exposed to Cl^- in wet/dry cycles ranged from 0.55 to 0.90, the amount of corrode iron converted into non-adherent rust ranged between 0.3 and 0.18, and the amount of iron that is lost ranged between 0.2 and 0.38.

6.2.4. Thickness and Internal Structure

The thickness of the rust layer increases with time of exposure and the aggressivity of the atmosphere. A direct (linear) relationship is found between the rust layer thickness and the substrate corrosion rate [159] (Figure 21).

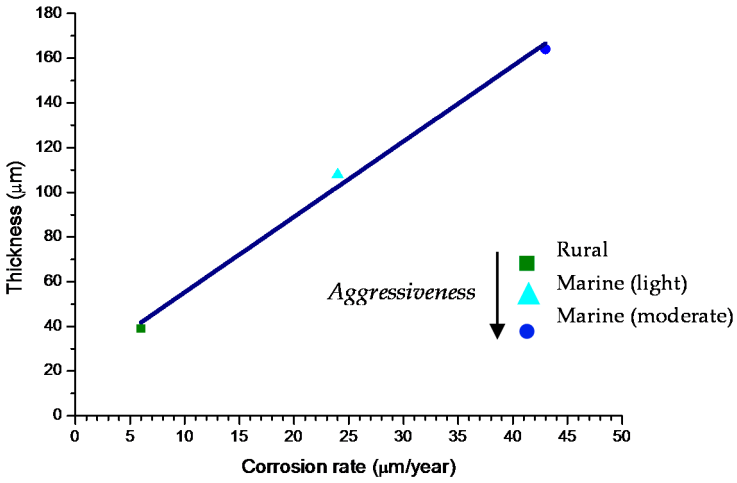

Figure 21. Corrosion rate versus rust thickness for low carbon steel exposed during two years in atmospheres of different aggressivity [159].

The thickness of the rust layer formed in marine atmospheres is not usually uniform, being thicker in some areas than in others, and the attack profile of the underlying steel generally shows the abundant formation of pits of variable depths [64]. Asami and Kikuchi [160] published an interesting study on in-depth distribution of rust components (determined by TEM/ED) on steel exposed to the atmosphere for 17 years under a bridge in a coastal-industrial region of Japan. They saw the aforementioned thick and thin areas within the rust layers and found that akaganeite was preferentially located in the thick areas and was scarce in the thin areas of the rust layers. The existence of akaganeite inside the pits formed on CS exposed for three months in a marine atmosphere with a high Cl^- deposition rate (1136 mg/m^2·d) has been confirmed by RS in unpublished results obtained by the authors of this work (Figure 22).

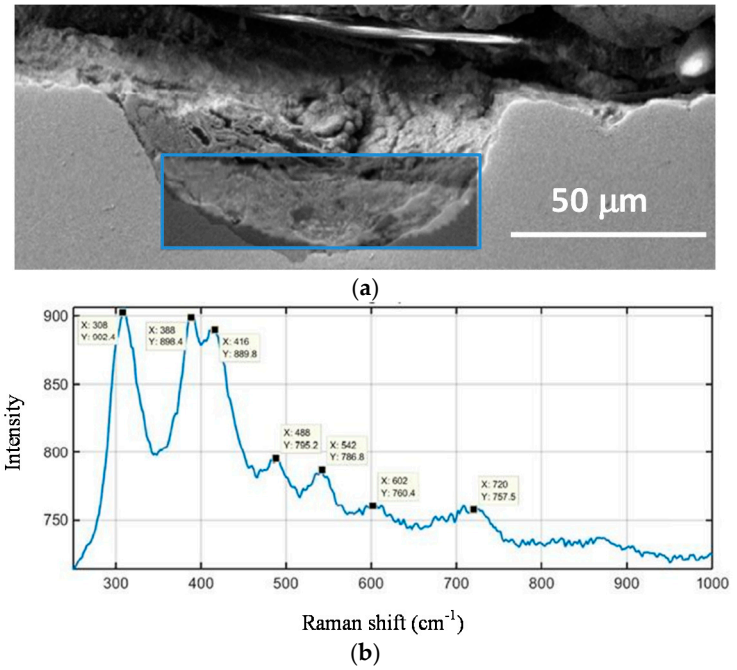

Figure 22. The rust present inside the pits formed on carbon steel substrates when exposed to severe marine atmospheres is almost entirely composed of akaganeite: (**a**) cross section affecting a deep pit; (**b**) Raman spectrum of rust inside the pit.

In not highly aggressive marine atmospheres, consistent (consolidated), adherent, and continuous rust layers present a two-sublayer organisation, as has been seen above (Figure 19). However, the exposure of CS in very aggressive marine atmospheres can in certain circumstances lead to the formation of heterogeneous and anomalous thick rust layers. High times of wetness of the metallic surface and an atmosphere with a high Cl^- deposition rate lead to the formation of this type of rust. These thick rust layers tend to become detached from the steel substrate (exfoliated), leaving it uncovered and without protection and thus accelerating the metallic corrosion process [129]. The rust exfoliation phenomenon can only take place if such anomalous thick rust layers are formed, as has also been observed in studies carried out by other researchers [42,161]. In studies by the authors on CS corrosion in Cl^--rich atmospheres, the average Cl^- deposition rate needed to exceed a critical threshold of close to 300 mg/m^2·d for exfoliation to take place; the annual steel corrosion at that atmospheric salinity was higher than 100 µm [129].

The exfoliated rust layers are composed of multiple rust strata, this can clearly be seen in the cross section of Figures 23 and 24. Observation by optical microscopy shows that in general the thick rust layer contains one or more strata of compact rust, exhibiting a greyish colouring and a metallic shine, whose number varied according to the area of the rust layer observed. With regard to the rust exfoliation mechanism, it is recommended to consult recent publications by the authors [129,153,162].

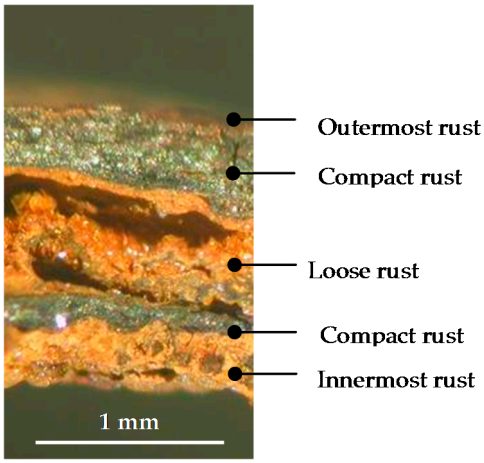

Figure 23. Optical micrograph of exfoliated (multilayered) rust formed on mild steel after one year in a very aggressive marine atmosphere (390 mg Cl^-/m^2·d) [129]. The characteristic of the different rust sublayer within the rust multilayer are described in Figure 24 [162].

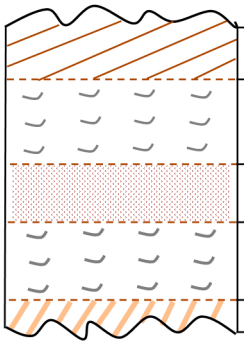

DENOMINATION	CHARACTERISTICS
Outermost rust	Red-brown coloured. Its surface appearance, texture and chemical composition are all typical of the outermost rust formed on mild steel in marine atmospheric
Compact rust	Fragile compact rust layer exhibiting a grayish colouring and a metallic shine. Its internal structure is highly porous with abundant fine linearly arrayed voids
Loose rust interlayer	Orange-red coloured. Highly porous loose rust layer
Compact rust	
Innermost rust	Heterogeneous pattern with orange and brown patches

Figure 24. Schematic illustration of different rust sublayers in exfoliated rust (Figure 23). The denomination and characteristic of each rust layer is given [162].

6.2.5. Porosity

Voids of different sizes are formed among the rust particles in the corrosion layer, whose compactness depends on the rust particle size.

Important parameters for the protective ability of rust layers include their thickness, porosity and Specific Surface Area (SSA). According to Dillmann et al. [47] these parameters directly influence the amount of oxyhydroxides that will be in contact with the electrolyte and will be reduced. Thus, these characteristics of the rust layer directly influence the AC mechanisms.

The pore structure of the rust layer is clearly related with steel corrosion because various molecules and ions such as O_2, H_2O, and Cl^- diffuse through the rust layer in the corrosion process [146,163]. Despite this fact, few studies of rust pore structures have been reported. The pore size of atmospheric rust is in the range of up to 15 nm, and the highest peak always appears below 5 nm [151].

Dillmann et al. [47] characterised the overall porosity, pore diameter and SSA of pores in rust layers using different complementary methods: MIP, BET and SAXS. However, as the authors note, these methods do not provide quantitative data on the three-dimensional distribution of pores in the rust layer, their tortuosity or their connectivity; three other parameters about which information is desirable for AC modelling [41].

Ishikawa et al. [48,141,146] have published abundant information on this subject, using the adsorption method to obtain more complete information than the aforementioned techniques on a wide range of rust layers. The SSA of rust layers is evaluated by fitting the BET equation [164] to the adsorption isotherms of nitrogen (S_N) and water molecules (S_W) and using the cross-sectional area of nitrogen and water molecules (0.162 and 0.108 nm^2, respectively) [165]. Among the results obtained using this technique, attention is drawn to the following which are considered particularly relevant:

(a) Estimation of rust particle size [141]

Ishikawa et al. apply adsorption of nitrogen molecules to estimate the rust particle size, successfully demonstrating that the SSA of the rust layer is a valid means of assessing its protective nature. They saw that the pores formed between larger particles were more accessible to O_2, H_2O and SO_4^{2-} and Cl^- ions, which are important substances in the AC of steel.

Compact rust layers with a high S_N or a small particle size exhibit high corrosion resistance (Figure 25). The corrosion resistance of rust layers is a result of pore filling by the adsorption and capillary condensation of water [141], according to the proposed scheme shown in Figure 26.

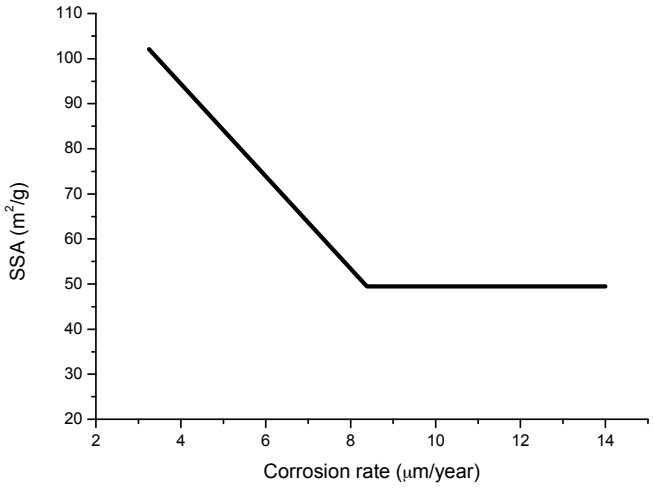

Figure 25. Trend plot of specific surface area (SSA) against corrosion rate for the rusts formed by exposing carbon steels at different bridges in Japan for 17 years [141].

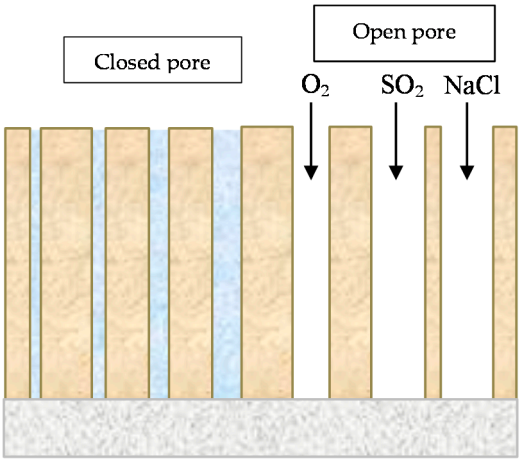

Figure 26. Schematic representation of pore filling by adsorption and capillary condensation of water, according to Ishikawa et al. [141].

(b) Pore size distribution of rusts formed on exposed steels [146]

Figure 27 depicts the pore size distribution trend curve of rusts formed on steels, as calculated by the Dollimore-Heal (D-H) method [165] from N_2 adsorption isotherms. The curve rises steeply at pore diameters (D) of <~5 nm and still increases at D = ~2 nm, suggesting that these rusts contained micropores with a D < 2 nm.

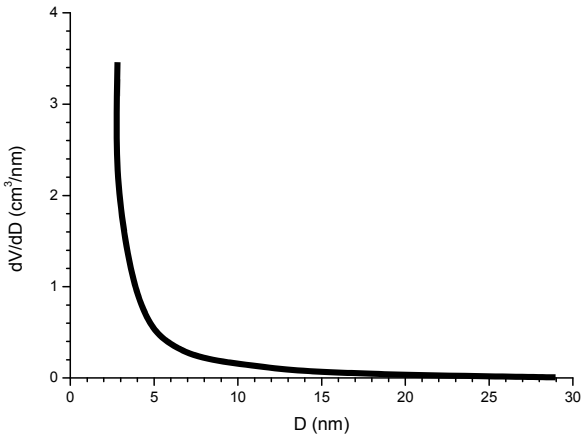

Figure 27. Trend plot of pore size distributions of the rust formed on steels exposed to coastal conditions [48]. V: adsorbed amount of N_2; D: pore diameter.

(c) Influence of particle size and pore size distribution on rusts formed in marine atmospheres

Rusts formed in saline environments, such as marine or coastal regions or districts where deicing salts are used, show larger particle sizes than rusts formed in rural and urban areas, resulting in the formation of larger pores which act as voids between larger particles in the rust layer and facilitate further corrosion.

The Cl^- ion promotes the growth of rust particles to yield less compact rust layers composed of larger particles, which leads to a high corrosion rate of steels in the saline environment [48,146].

(i) Effect of chloride deposition rate on rust particle size [146]

Figure 28 shows the adsorption isotherms of nitrogen (S_N) and water (S_W) molecules on rusts obtained on CS exposed to atmospheres with different Cl^- deposition rates and times of wetness (TOW). S_N and S_W depend strongly on the Cl^- deposition rate and the TOW duration.

Thus, the formation and growth of rust particles is influenced by both parameters. These results confirm that the development of rust particles in aqueous solutions and the particle growth of rusts is promoted by Cl^- ions.

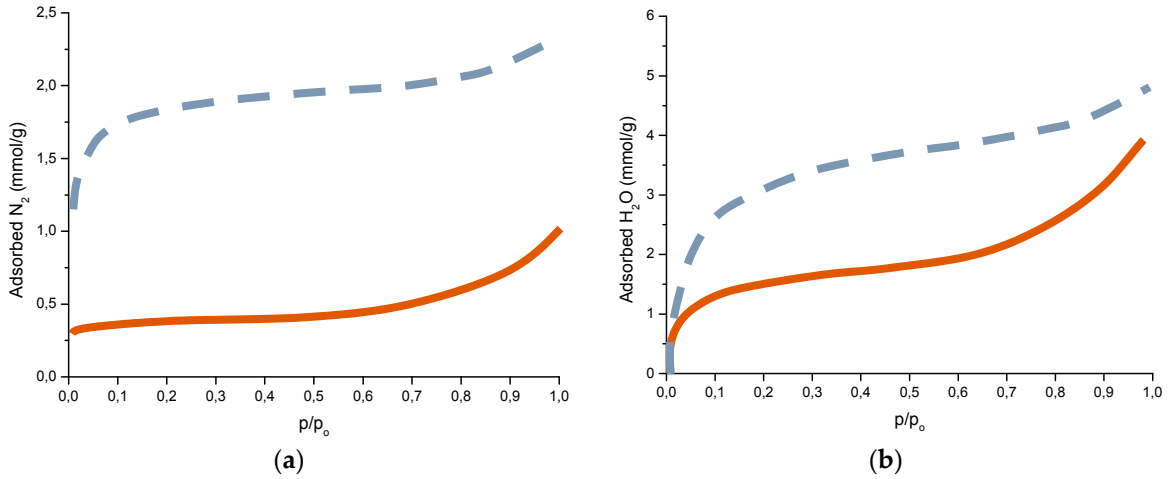

Figure 28. Adsorption isotherms of nitrogen (**a**) and water (**b**) on the rusts generated by exposing a carbon steel for 3 months at two atmospheres with different NaCl deposition rates [146]. 5.6 mg NaCl/m^2; wet period: 56%; 10.7 mg NaCl /m^2; wet period: 82%; p/p_o is the relative pressure of water or relative humidity (RH).

(ii) Effect of chloride deposition rate on rust pore size [146]

The SSA (determined by N_2 adsorption) (Figure 17) decreases as the NaCl content of the atmosphere increases (the micropores volume (MPV) shows a similar tendency), indicating that the rusts formed at coastal sites are agglomerates of large particles which give rise to large pores, consistent with the fast corrosion rate at the coast. This finding again suggests that NaCl promotes rust particle growth.

6.2.6. Indices to Evaluate the Protective Capacity of Rust Layers

Yashamita and Misawa [166] found that the mass ratio of goethite to lepidocrocite contents (α/γ) in the rust layer formed on WS exposed in industrial and rural environments, determined by XRD, is a function of the exposure time, as is shown in Figure 29a. The α/γ ratio increases proportionally with exposure time due to the long-term phase transformation. The relationship between α/γ and the corrosion rate is shown in Figure 29b. It can be said that the corrosion rate decreases as the α/γ increases, and that $\alpha/\gamma > 2$ is a necessary condition for the final protective rust layer. α/γ can be considered a useful index to evaluate the protective ability of the rust layer.

Kamimura et al. [167] and Hara et al. [142] later noted that this tendency for the α/γ mass ratio to increase with exposure time was not seen in marine atmospheres where the corrosion species akaganeite (β) and magnetite (M) also form on steel. In contrast, they saw that the relationship between goethite and the total mass of lepidocrocite, akaganeite and magnetite (α/γ^*) was related to the corrosion rate, even in coastal environments with more than 0.2 mg/dm^2·d of airborne sea salt particles. When the α/γ^* ratio exceeded a certain critical threshold, steel corrosion was less than 10 μm/year.

Despite the fact that magnetite is a conducting phase, Dillmann et al. [47] consider it to be protective because of its relatively good stability, suggesting a new protective ability index (α^*/γ^*):

$$\alpha^*/\gamma^* = (\alpha + M)/(\gamma + \beta), \quad (20)$$

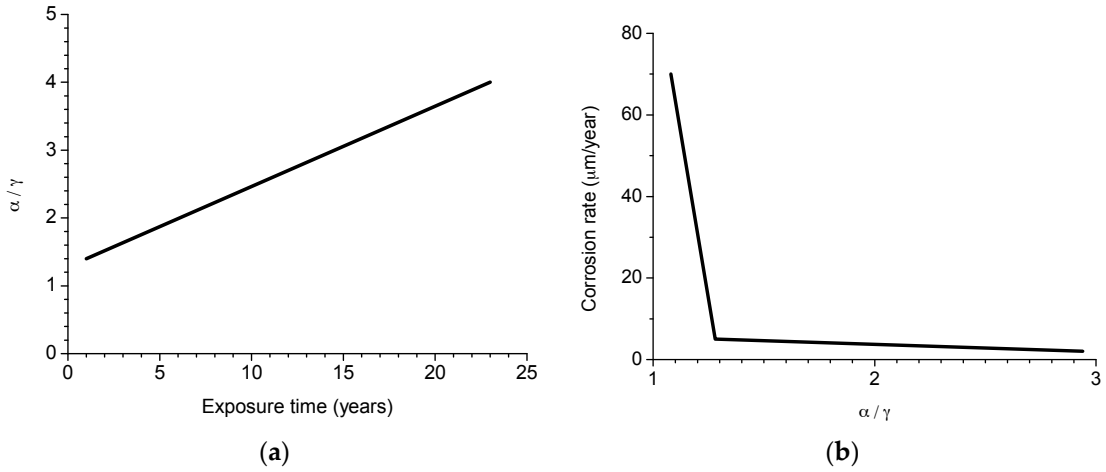

Figure 29. Relation between α/γ of the rust layer formed on weathering steel and exposure time (**a**) and corrosion rate (**b**). According to Yamashita and Misawa [166].

7. Mechanisms of Steel in MAC

7.1. First Researches

As has been noted in the introduction to this review, it is rather surprising that despite the great practical importance of this issue it has only recently that it has started to attract the interest of corrosion scientists.

It is well known that the presence of atmospheric pollutants (natural or anthropogenic) notably accelerates the AC process of CS. The two most common pollutants, which have drawn the majority of research efforts, are SO_2 and marine chlorides. In principle most of the attention has been focused on SO_2, and considerable progress has been made in this respect [4]. However, as Nishimura et al. [10,39] point out, it was not until the final decade of the 20th century that major research started to be carried out on the fundamental mechanisms of rust formation in Cl^--rich marine atmospheres. Until then very little research was undertaken in this field, the most notable being the work of Keller [103], Feitknecht [24], Henriksen [168] and Misawa [169–171].

Keller in 1948 [103] reported three basic chlorides obtained by partial precipitation from $FeCl_2$ solution in various concentrations, noting that these three basic chlorides were presumably the precursors of GR1. Feitknecht [24] reported the existence of chloride accumulations (nests) containing $FeCl_2$ in the rust layers formed on steel exposed in coastal areas and their role in stimulating AC. Henriksen [168], using autoradiography, noted that the AC of CS in marine atmospheres starts at weak spots in the oxide film. Na^+ and Cl^- in the aqueous adlayer migrate to these weak spots and once Cl^- has been adsorbed and corrosion has begun, Na^+ migrates to the cathodic areas. Misawa et al. [169–171], who had carried out important basic research on the formation mechanisms of the different AC products of iron, noted in their work the formation of an intermediate compound, GR1, in marine atmospheres, also in accordance with Keller [103].

At around the same time, Barton [4], in his important book on AC, pointed out three causes which explained the high corrosion rates of steel exposed to marine atmospheres: (a) the increase in the ionic conductivity of the aqueous adlayer due to the presence of ionising substances (chlorides); (b) the hygroscopic nature of the Cl^--containing corrosion products formed; and (c) the solubility of the latter, unlike the stable basic chlorides that form in the case of other metals (Cu, Zn, etc.), indicating that the mechanism which governs the effects of Cl^- ions in AC had not been completely explained.

In addition to the above, two other causes of enormous importance should be mentioned: (a) he strong cathodic depolarising role of Cl^- ions, accelerating the cathodic process by tens and hundreds of times, as formulated in 1961 by Rozenfeld [18]; and (b) the catalytic role of

chlorides [23,172]. With regard to the latter effect, it is noted that the anodic reaction generates cations by dissolution and H^+ by hydrolysis of the dissolved cations. Both Fe^{2+} and H^+ require neutralisation, which is accomplished by the ingress of chlorides. The locally higher Cl^- concentration enhances local metal dissolution, then draws more Cl^- and enhances dissolution even further [23]. Migration of Cl^- to the corroding substrate is facilitated by its high permeability in the rust layer. As noted in [23], this is a feedback mechanism, sometimes referred to as autocatalytic. The high concentrations of Cl^- in the inner rust layer will facilitate the formation of akaganeite, as was also previously noted by Keller [103] and Misawa [169].

According to Misawa et al. [169], when the aqueous adlayer on the metal surface is neutral or slightly acidic, $Fe(OH)_2$ cannot be formed, but various Fe(II) hydroxo-complexes may be formed, depending on the existing anion in the aqueous solution. Fe(II) hydroxo-complexes thus formed are oxidised by dissolved oxygen, resulting in lepidocrocite through an intermediate GR.

$$\text{Fe(II) hydroxo-complexes} \rightarrow \text{GR} \rightarrow \gamma\text{-FeOOH}, \tag{21}$$

In marine atmospheres, the intermediate generally has a GR1 structure that forms in the presence of Cl^- ion [96,107,108]. GR1 is converted to black magnetite by slow oxidation in solution and this reaction is considered to correspond to the formation of magnetite in the underlying rust layer where the oxygen supply is limited. Also, akaganeite can be obtained by the dry oxidation of solid β-$Fe_2(OH)_3Cl$ precipitated from the slightly acidic solution in the presence of Cl^- ions.

$$\text{Fe(II) hydroxo-complexes} \rightarrow \text{GR1} \rightarrow \beta\text{-}Fe_2(OH)_3Cl \rightarrow \beta\text{-FeOOH}, \tag{22}$$

Worch et al. reported in 1983 [173] that GR1 is often seen on iron and steel exposed to marine environments and that chloride may also be involved catalytically in the formation of akaganeite. Akaganeite is produced only in the presence of sufficient concentrations of Cl^- [107,108].

Askey et al. [25] suggest a cyclical rust formation process, similar to the acid regeneration cycle proposed by Schikorr [26,174] for the action of SO_2 in iron, by which the accumulation of Cl^- ions in the underlying steel gives rise to the formation of $FeCl_2$, which hydrolyses water according to

$$2FeCl_2 + 3H_2O + \frac{1}{2}O_2 \rightarrow 2FeO(OH) + 4HCl, \tag{10}$$

Releasing HCl. It should be noted that this represents a reaction cycle in which rereleased HCl will react with iron to form fresh $FeCl_2$. Once started, therefore, the cycle will be independent of incoming HCl. Corrosion will continue until the Cl^- ions are removed (possibly by the washing away of $FeCl_2$).

7.2. The Fundamental Role of Akaganeite in the Atmospheric Corrosion Process of Steel in Marine Atmospheres

A fundamental advance in relation with the role played by akaganeite in the AC process of steel in marine atmospheres was made by Nishimura et al. in studies carried out in the last decade of the 20th century [10,39]. Nishimura et al. in 1995 used a wet and dry corrosion test to study the relationship between steel corrosion resistance and NaCl concentration, analysing the corrosion products by in-situ XRD [39]. The steel corrosion rate increased as the NaCl concentration rose, and a very strong increase in the akaganeite/lepidocrocite weight ratio was observed from a NaCl concentration of 0.05 wt % (Figure 30).

Akaganeite was reduced to an amorphous intermediate oxide during the wet stage of the cycle and reproduced in the dry stage, giving rise to the proposal of the following rusting model of iron in wet and dry corrosion in the presence of NaCl (Figure 31).

Later, in the year 2000, continuing with the in-situ XRD technique but here in combination with alternating current impedance, Nishimura et al. observed the transition of akaganeite from GR1 in the dry process; the amount of GR1 also depended on the Cl^- ion concentration [10]. After dripping a Cl^- solution (3% Cl^-) on the steel surface, the dry process progressed with the formation of akaganeite

at a high corrosion rate. When a low Cl^- concentration was used (0%–0.3% Cl^-), lepidocrocite was formed from $Fe(OH)_2$ instead of akaganeite and the corrosion rate was low.

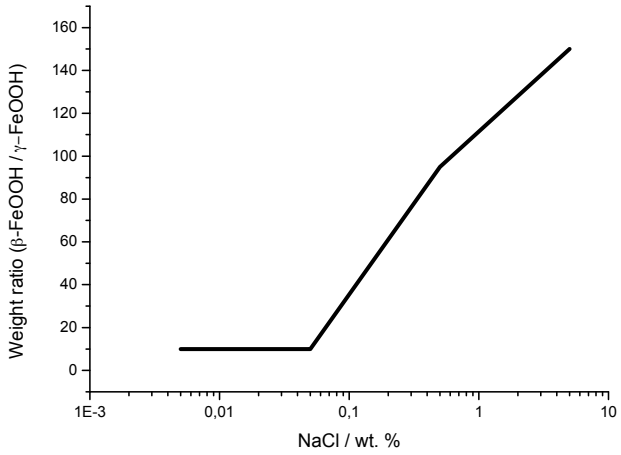

Figure 30. Weight ratio of β-FeOOH to γ-FeOOH as a function of NaCl concentration [39].

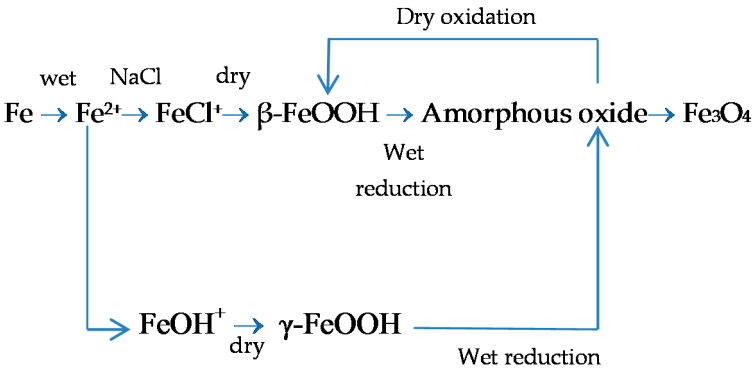

Figure 31. Rusting model of iron in wet and dry corrosion condition containing NaCl [39].

The integral intensity of akaganeite decreased after dripping a Cl^- solution, which implied that akaganeite was consumed in the wet process. After 60 min in the dry process of the cycle the presence of GR1 was detected. GR1 could still be detected after 180 min (Figure 32), but disappeared after 12 h of testing, indicating that the transformation to akaganeite was complete.

Quantitative analysis of the identified phases was carried out using an XRD standard method. Akaganeite was the most abundant crystalline phase in the iron rust, and its proportion grew considerably as the Cl^- concentration increased, as was previously seen [39]. The other large phase was goethite. In contrast, the amounts of lepidocrocite and magnetite were low. These two phases were not affected by the Cl^- concentration. Nishimura et al. concluded that in a Cl^--rich environment the corrosion process was dominated by the formation of akaganeite, rather than lepidocrocite, which acts as the oxidation agent that accelerates corrosion in Cl^--free environments [38].

The authors carried out XPS and TEM observations on those portions of iron rust that could not be detected by XRD. It was determined that they contained large amounts of spinel oxide (magnetite structure) with bivalent/trivalent iron. This spinel oxide may have been formed by reduction of akaganeite during the wet process of the cycle.

These findings mark a turning point in the knowledge of the MAC mechanisms of steel, determining that steel corrosion progresses by the formation of akaganeite from GR1 (dry stage or "drying-out stage" following the terminology of Stratmann [38]) and its reduction (wet stage).

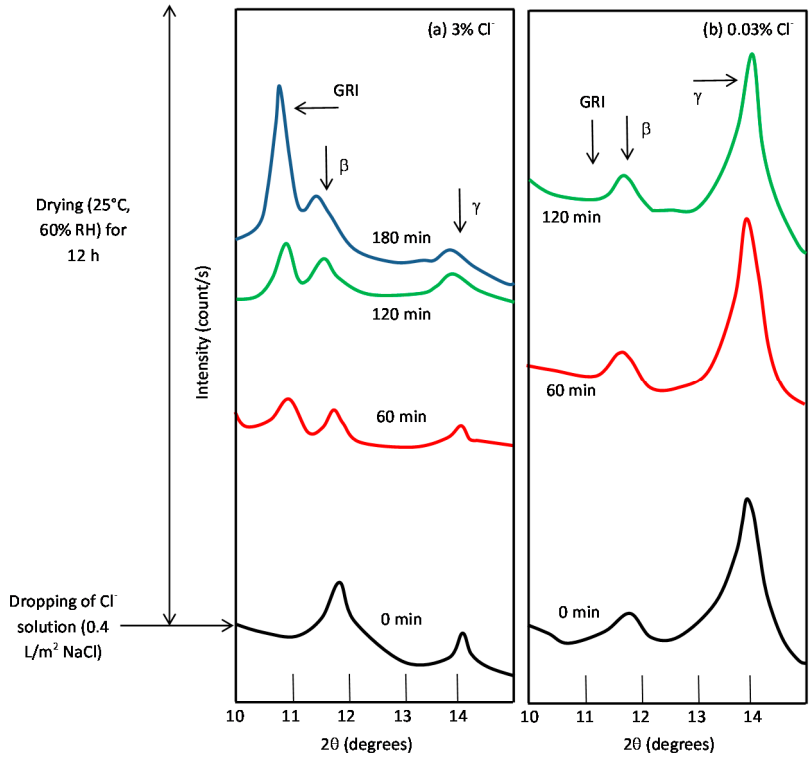

Figure 32. In-situ X-ray diffraction (XRD) results in wet and dry corrosion test using (**a**) 3% Cl^- and (**b**) 0.03% Cl^- solution [10].

7.3. Initial Stages of MAC

In marine atmospheres, corrosion is generally driven by the deposition of hygroscopic sea salt aerosols that absorb moisture from the environment and form salt droplets. These aerosols range from a few angstroms to several hundred microns in diameter. Lan et al. [175] point out that coarse sea salt particles are those that contribute most to CS corrosion in marine atmospheres. In coastal marine locations (<2 km from the shoreline) the most common aerosols deposited are in the "coarse mode" size range: 1–100 μm in diameter [57].

Li and Hihara [55] studied salt particle deposition and the initial stage of MAC at severe marine test sites. They found both: (a) small sea-salt particles (D < 5 μm) and sea-salt clusters (D < 10 μm) formed by dehydration on the steel substrate that did not corrode under relatively small seawater droplets (D < 30 μm); and (b) sea-salt clusters integrated with iron corrosion products formed on the steel substrate that did corrode from larger seawater droplets (D > 30 μm). The corrosion that occurred under larger seawater droplets (D > 30 μm) showed the typical characteristics of droplet corrosion, with Cl^- and Na^+ ions migrated to the central anode and peripheral cathode, respectively. The corrosion products were identified as lepidocrocite.

These same researchers [176,177], in a laboratory study in which they manually deposited NaCl droplets of different diameters on CS steel, used RS to analyse the very initial stage of NaCl particle-induced corrosion. They found that corrosion did not initiate under NaCl droplets with diameters of less than 45 μm after 6 h (at 80% RH). At larger NaCl droplet diameters, corrosion initiated quickly under the droplets in the form of pitting. In-situ and ex-situ Raman spectra show the formation of GR in regions close to the anodic sites and the precipitation of lepidocrocite clusters over cathodic sites surrounding the GR region. Magnetite was detected mostly in the rust clusters formed in the transitional region from GR to lepidocrocite. Upon exposure to ambient air, GR transformed to the more stable lepidocrocite due to oxidation. Li and Hihara underline the need for more research effort in droplet electrochemistry [178].

Risteen et al. [179] recently used a new methodology to study corrosion under NaCl solution droplets ranging in diameter from 20 to 1000 μm. They also observed the dependence of the occurrence of corrosion on drop size, noting that this behaviour appears to be strongly dependent on the microstructure and surface finish: corrosion initiation on 1010 steel was dominated by manganese sulfide inclusions when a mirror surface finish was maintained. In contrast, for high purity iron, initiation was dominated by surface roughness.

Ohtsuka and Tanaka have recently used RS to carry out a study of changes in rust composition on CS over six days of cyclic exposure: 4 h wet (90% RH)/4 h dry (10% RH) in the presence of NaCl droplets (0.93 and 0.11 mg/cm^2) [180]. The NaCl solution was first dripped and immediately dried in a vacuum desiccator. A Raman spectrum was recorded every 15 min.

The Raman spectra of the rust surface in the presence of 0.93 mg/cm^2 NaCl deposits corresponded to lepidocrocite and magnetite in the initial 12 h of exposure. After 12 h of exposure, akaganeite started to form, and its molar ratio on the rust surface increased to 90% at 30 h of exposure (Figure 33). They assume that in order for akaganeite to form, a lepidocrocite + magnetite rust layer of some thickness is required. The Raman spectra further changed after 30 h of exposure, when lepidocrocite again emerged. The reappearance of lepidocrocite is assumed to be caused by the capture of Cl^- ions in the akaganeite, resulting in a decrease in the free Cl^- ions in the aqueous adlayer.

When the amount of NaCl deposit is decreased to 0.11 mg/cm^2, the steel surface does not reach high enough concentrations to form akaganeite. Only after repeated wet/dry cycles may a spot with a high concentration of NaCl emerge on the surface and akaganeite form on that spot.

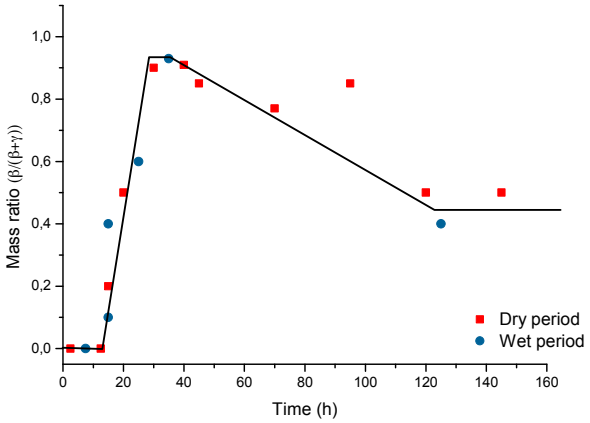

Figure 33. Change of mass ratio of (β-FeOOH /(β-FeOOH + γ-FeOOH)) of rust on weathering steel during the exposure of dry and wet periods in the presence of NaCl deposition at 0.93 mg/cm^2 [180].

7.4. Formation and Growth of the Corrosion Layer

Once the corrosion process has started on the steel surface it will be necessary to consider the possible mechanisms that take place in the formation and growth of the rust layer, where, as is known, the corrosion products transform from one compound to a more stable form and may involve any of a number of processes including hydrolysis, nucleation, crystallisation, precipitation, dehydration, thermal transformation, dehydroxylation, etc. [91]. Temperature, time and pH are the main factors governing such transformations [97].

In 1965, Evans [181] formulated the first electrochemical method for atmospheric rusting, in which the oxidation of iron (wet periods)

$$Fe \rightarrow Fe^{2+} + 2e^-, \quad (1)$$

Is balanced by the reduction of ferric rust to magnetite

$$Fe^{2+} + 2\ FeOOH \rightarrow Fe_3O_4 + 2H^+, \quad (23)$$

Later, after partial drying of the pore structure of the rust (dry period), magnetite is reoxidised by oxygen that now has free access through the pores due to gas diffusion

$$Fe_3O_4 + 3/2\ O_2 + H_2O \rightarrow 3\ \gamma\text{-FeOOH}, \quad (24)$$

The autocatalytic cycle responsible for the fact that rust promotes further rusting involves alternate reduction and reoxidation of the preexisting rust.

Subsequently, Stratmann et al. [182], in an electrochemical study of phase transitions in rust layers, experimentally showed that the oxidation of magnetite to lepidocrocite, as proposed by Evans, was not possible. Stratmann et al. used a combination of magnetic and volumetric measurements to show that when a prerusted iron sample is wetted, iron dissolution is not immediately balanced by a reaction with oxygen, but rather by reduction of the preexisting rust

$$\gamma\text{-FeOOH (lepidocrocite)} + H^+ + e^- \rightarrow \gamma\text{-Fe.OH.OH (reduced lepidocrocite)}, \quad (25)$$

With later reoxidation of the reduced species

$$2\ \gamma\text{-Fe.OH.OH} + 1/2\ O_2 \rightarrow 2\ \gamma\text{-FeOOH} + H_2O, \quad (26)$$

Thus, Stratmann [38] proposed dividing the AC mechanism of pure iron into the following three stages: wetting of the dry surface, wet surface, and drying-out of the surface (see Figure 2).

Misawa [170] notes the following mechanism for the rusting process (Figure 34):

(a) In the first stage of rusting the aerial oxidation of ferrous ions, dissolved from the steel into a slightly acidic thin water layer formed by rain on the steel surface, leads to the precipitation of lepidocrocite. Fine weather accelerates the precipitation and crystallisation of lepidocrocite by drying.

(b) The lepidocrocite is formed on the steel surface and transformed to amorphous ferric oxyhydroxide and goethite during the atmospheric rusting process. The amorphous ferric oxyhydroxide transforms to goethite by deprotonation using hydroxyl ions provided by the rainwater.

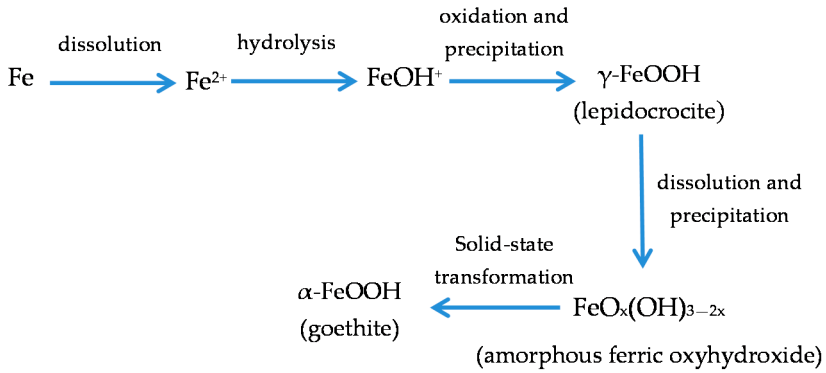

Figure 34. Mechanism for the rusting process according to Misawa [170].

Another important aspect to consider is how the rust layer grows. Horton [183] in 1964 observed that rust layers grow by several mechanisms: (i) by iron ions diffusing outward through the rust to form fresh rust at the air-rust interface; (ii) at the steel-rust surface; and (iii) within the rust layer to fill pores and cracks. It was the first time that this observation was reported in scientific literature. Years later, Burger et al. [184] using an ingenious technique known as the "gold marker method", addressed the following two aspects:

(a) the location at which precipitation of corrosion products occurs within the corrosion system (steel/rust/atmosphere), and

(b) the structural evolution of the corrosion product layer during wet/dry cycles.

With regard to (a), they observed a significant contribution of inward diffusion of oxidant through the corrosion product layer. With regard to (b) they note that the continuous decrease in the reactivity of the corrosion product layer seems to be related with a two-step process in the corrosion mechanisms: the preliminary formation of ferrihydrite (a highly reactive hydrated iron oxide) close to the metal/rust interface, followed by its progressive transformation into goethite, a more stable oxyhydroxide. This progressive transformation may be the consequence of incremented cyclic reduction/reoxidation reactions which are not completely reversible. As these cyclic electrochemical reactions require electrical contact between the reactive phase and the metallic substrate, and given the complex morphology of the corrosion patterns, an important outlook is to take into account the connectivity and conductivity of the different phases constituting the corrosion product layer and their influence on its structural evolution. Due to the expansive nature of the corrosion products, mechanical stresses may develop in these materials, thus inducing two opposing effects: pore blocking and formation of cracks/spalling in the rust layer.

In the last decade great advances have been made in the understanding of AC mechanisms. As has been mentioned above, many of these advances have been due to the French research groups of Professors Legrand and Dillmann [40,41,44,47,93,131,185,186]. Both groups have made important advances in: (a) the electrochemical reactivity of the ferric phases that constitute rust; (b) the localisation of oxygen reduction sites; (c) the decoupling of anodic and cathodic reactions; (d) in-situ characterisation of reduction and reoxidation processes, etc.

With a view to the development of a model of the AC process that can predict the long term AC behaviour of iron, they note the need to consider several important parameters in order to describe rust layer: average lepidocrocite fraction, thickness, average porosity, tortuosity and specific area, connectivity of the phases inside the rust layer, etc. [41,47]. As these researchers note, there is still a long way to go before long-term AC mechanisms are fully clarified.

As has been mentioned several times in this paper, considerable advances have been made in the knowledge of AC mechanisms in atmospheres polluted with SO_2 (e.g., urban and industrial atmospheres) while less progress has been made on corrosion mechanisms in marine atmospheres. In addition to the proposals of Nishimura et al. [10,39] referred to in 7.2., other authors have made contributions relating to the subject of MAC which will be enumerated below, and more are sure to appear in the forthcoming years, considering the growing interest of researchers in this field of knowledge.

In 1988 Nomura et al. [187] applied conversion electron MS to study the formation of akaganeite on iron in a NaCl (3 wt %) solution. On the basis of the study on early stages of $Fe(OH)_2$ formation, the reaction that takes place on the iron surface in a Cl^- solution can be expressed as follows:

$$O_2 + 2H_2O + 4e^- \rightarrow 4OH^-, \quad (2)$$

$$Fe \rightarrow Fe(OH)^+ \rightarrow Fe(OH)_2{}^+, \quad (27)$$

In conditions of high dissolved oxygen (initial stages)

$$Fe(OH)_2{}^+ + 2OH^- \rightarrow Fe^{3+}(OH)_4{}^-, \quad (28)$$

$$2Fe(OH)_4{}^- \rightarrow 2FeOOH + 2H_2O + 2OH^-, \quad (29)$$

Poorly crystalline FeOOH is considered to deposit on the iron surface by the initial corrosion reaction listed above.

However, in conditions of low dissolved oxygen, when a first rust layer is formed, the supply of OH^- (Equation (28)) is suppressed, and Cl^- ions begin to have a relatively strong affinity to the iron(III) ion, thus iron(III) oxyhydroxide complexes containing Cl^- may be formed.

$$Fe(OH)_2{}^+ + (2 - X)OH^- + XCl^- \rightarrow Fe[OH_{4-X}Cl_X]^-, \quad (30)$$

Before the start of the polymerisation process to form rust according to the following equation:

$$2Fe[OH_{4-X}Cl_X]^- \text{ (polymerisation)} \rightarrow 2\beta\text{-FeOOH } (Cl_X^-) + H_2O + 2_{(1-X)}OH^-, \quad (31)$$

In short, when unstable oxyhydroxide is first formed on iron, lepidocrocite is formed on the surface where dissolved oxygen has easy access, and then akaganeite and magnetite start to be produced by the transformation of the $Fe(OH)_2$ complex containing Cl^- at the intermediate surface between the lepidocrocite layer and the iron substrate and by the slow oxidation of iron, respectively, because the supply of dissolved oxygen to the intermediate layers is restricted by the top lepidocrocite layer.

It is relevant to note at this point the important laboratory studies carried out by Refait and Genin [113,115] and subsequently by Remazeilles and Refait [112,114] on the formation conditions of Fe(II) hydroxychlorides, GR1 and akaganeite previously mentioned in Section 5.

More recently, Ma et al. [188,189], using XRD and IRS, detected the formation of akaganeite in the inner rust layer accompanied by an acceleration of the corrosion rate on steel exposed to very severe marine atmospheres. After six months of exposure the akaganeite content and the corrosion rate decrease and akaganeite is gradually transformed into maghemite until it completely disappears. The authors speculate on the need to exceed a critical chloride threshold in order for akaganeite to form.

In atmospheres with less Cl^- pollution akaganeite was not formed, though the Cl^- content facilitated the transformation of lepidocrocite into goethite (Figure 35). The wet/dry cycle accelerates these transformation processes, and especially in the dry cycle HCl is released into the environment.

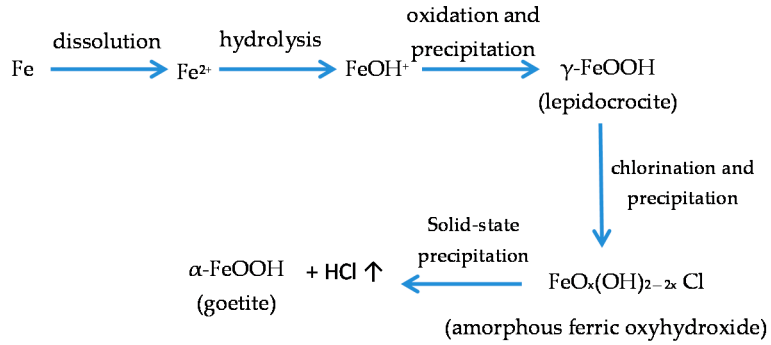

Figure 35. In marine atmospheres with low chloride deposition rates, Cl^- content facilitates the transformation of lepidocrocite into goethite [188,189].

7.5. Proposal of an Overall Mechanism for the MAC Process of Steel

The composition of the rust layer depends on the conditions in the aqueous adlayer and thus varies according to the type of atmosphere. It is unanimously accepted that lepidocrocite is the primary crystalline corrosion product formed in the atmosphere. As the exposure time increases and the rust layer becomes thicker, the active lepidocrocite is partially transformed into goethite and magnetite.

In mildly acidic solutions lepidocrocite is transformed into goethite. Schwertmann and Taylor established that the transformation occurs in solution through different steps: dissolution of lepidocrocite, formation of goethite nuclei, and nuclei growth [190].

Magnetite may be formed by oxidation of $Fe(OH)_2$ or intermediate ferrous-ferric species such as GR [119], but also by lepidocrocite reduction in the presence of a limited oxygen supply [119,120]:

$$2\gamma\text{-FeOOH} + Fe^{2+} \rightarrow Fe_3O_4 + 2H^+, \quad (17)$$

Thus it is not surprising that magnetite is usually detected in the inner part of rust adhering to the steel surface, where oxygen depletion may occur.

With a broader view, Ishikawa et al. [121] and Tanaka et al. [122] found that the formation of magnetite particles was caused by the reaction of dissolved ferric species of oxyhydroxides with

ferrous species in the solution. The formation of magnetite rust can be represented by the following cathodic reaction:

$$Fe^{2+} + 8FeOOH + 2e^{-} \rightarrow 3Fe_3O_4 + 4H_2O, \quad (18)$$

In marine atmospheres, where the surface electrolyte contains chlorides, akaganeite is also formed. How does akaganeite form? The high Cl^- concentration in the aqueous adlayer on the steel surface gives rise to the formation of $FeCl_2$, which hydrolyses the water [25]:

$$2FeCl_2 + 3H_2O + \frac{1}{2}O_2 \rightarrow 2FeOOH + 4HCl, \quad (10)$$

Notably raising the acidity of the electrolyte. At the steel/corrosion products interface, where Cl^- ions can accumulate, large Cl^- concentrations and acidic conditions give rise to akaganeite formation after the precipitation of ferrous hydroxychloride (β-$Fe_2(OH)_3Cl$), a very slow process requiring the transformation of metastable precursors [112,113].

As Remazeilles and Refait point out, large amounts of dissolved Fe(II) species and high Cl^- concentrations are both necessary for akaganeite formation [114]. The oxidation process of ferrous hydroxychloride which leads to akaganeite formation passes through different steps via the formation of GR1 intermediate compounds. The whole oxidation process can be summarised as follows [99,112–115]:

$$FeCl_2 \rightarrow \beta\text{-}Fe_2(OH)_3Cl \rightarrow GR1 \rightarrow \beta\text{-}FeOOH, \quad (16)$$

Thus requiring a relatively long time. This time will depend on the environmental conditions: temperature, Fe^{2+}, Cl^- and OH^- conditions, O_2 flow, etc. The acid environment at the steel/rust interface also leads to an acceleration of corrosion of the underlying steel and pitting [23,191], where the dominant cathodic reaction is hydrogen evolution.

$$2H^+ + 2e^- \rightarrow H_2, \quad (3)$$

There has been much speculation about the need to exceed a critical atmospheric salinity threshold for akaganeite formation to take place. Morcillo et al. provide a general indication of the environmental conditions in the atmosphere which lead to akaganeite formation: annual average RH around 80% or higher and simultaneously an annual average Cl^- deposition rate of around 60 mg/m^2·d or higher [192] (Figure 36). This confirms the laboratory experiments carried out by Remazeilles and Refait [114], which indicate that a high Cl^- concentration is not the only condition for akaganeite formation. The medium must also be characterised by large dissolved Fe^{2+} concentrations, as occur during the high TOW of the metallic surface in high RH atmospheres.

With regard to the corrosion products that form on CS in this type of atmospheres, Table 4 has been prepared using field data obtained by the authors in different studies carried out at various sites in Spain [64,150,193] and allows the following facts to be deduced: (a) in marine atmospheres with extremely low Cl^- deposition rates (Ponte do Porto) only lepidocrocite and goethite phases form, the latter in a practically insignificant proportion; (b) above a certain atmospheric salinity, akaganeite and spinel (magnetite/maghemite) phases appear; (c) the akaganeite and spinel contents increase notably as the atmospheric salinity rises (Cabo Vilano-2 and Cabo Vilano-3); and (d) it can clearly be seen how an increase in the Cl^- deposition rate is accompanied by a drop in the lepidocrocite phase content of the rust and a rise in the goethite, akaganeite and spinel contents. This fact is well seen in Figure 37, which shows rusts formed after 3 months exposure of CS in marine atmospheres with different salinities [95].

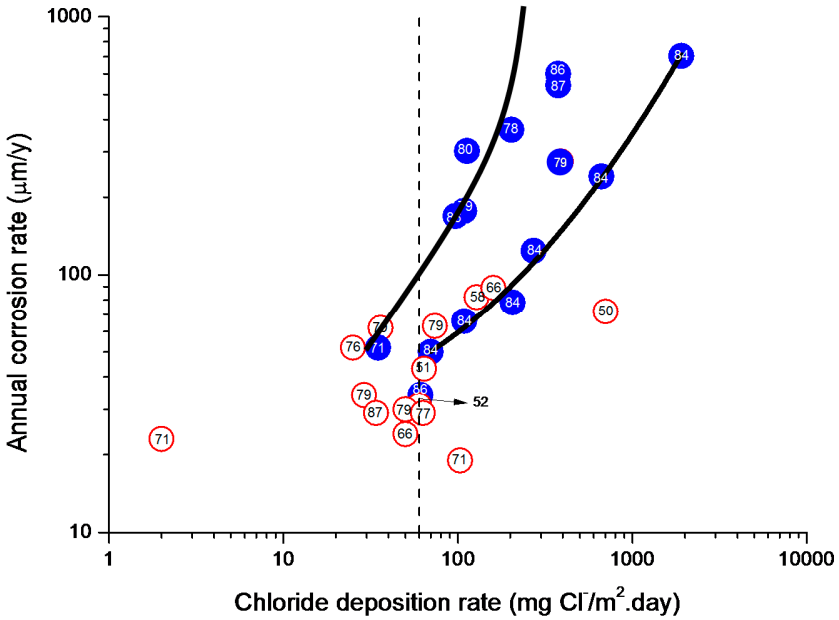

Figure 36. Corrosion rate of mild steel during the first year of atmospheric exposure as a function of the annual average chloride deposition rate at the exposure site. The points of the graph, represented by circles, include an indication of the annual average RH at exposure site. Blue circle represent test site where akaganeite had been identified, and white circle represent test sites where it had not been possible to identify it by XRD [192].

Table 4. Variation of rust phases content on mild steel exposed during one year in test sites with different chloride deposition rate [64,150,193].

Test Site	Annual Average Chloride Deposition Rate, mg/m²·d	wt %			
		Lepidocrocite	Goethite	Akaganeite	Spinel
Ponte do Porto	4	100	*	0	0
Cabo Vilano-1	30	80.0	16.0	0	4.0
Cabo Vilano-2	70	59.6	20.0	17.6	2.7
Cabo Vilano-3	665	35.8	27.0	12.5	24.7

* The authors not ruling out a small contribution of this phase.

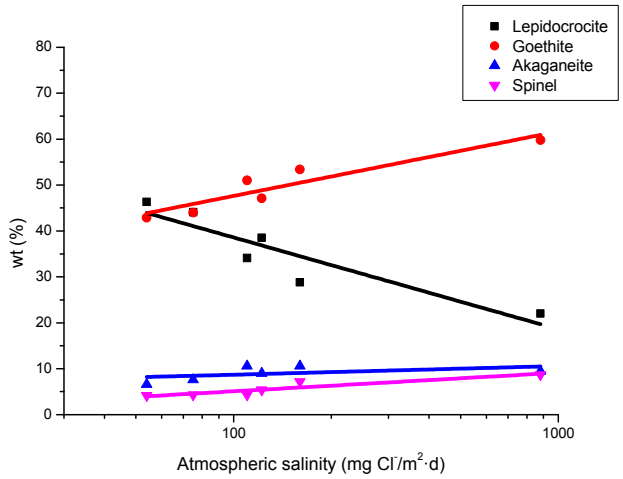

Figure 37. Variation of rust phases content in rusts formed on mild steel exposed during 3 months in marine atmospheres with different levels of salinity [95].

Akaganeite could be reduced electrochemically in the corrosion process, being consumed in the wetting of the metallic surface [10]. Lair et al. [40] experimentally saw the high reducing capacity of akaganeite in comparison with other oxyhydroxides, reporting the following order: akaganeite > lepidocrocite >> goethite.

This explains the high magnetite contents found in the rust formed on steel exposed to atmospheres with heavy Cl^- ion pollution. As Hiller noted some time ago, the rust formed in atmospheres with high Cl^- deposition rates contains more magnetite than that formed in Cl^- free atmospheres [123].

Rust layers present considerable porosity and cracking. Ishikawa et al., examining the textures of rusts, note that the rusts formed at coastal sites are agglomerates of large particles and have larger pores than rusts formed at rural and urban sites. NaCl promotes rust particle growth, resulting in the formation of larger pores and voids between larger particles in the rust layer and facilitating further corrosion [145,163]. The SSA of rusts decreases as salinity increases, enlarging the diameter of the pores and forming less and less compact rust layers with low protective properties.

Thus the compactness of the corrosion product layers formed is dependent on the salinity of the atmosphere at the exposure site. At low Cl^- deposition rates, even when the time of wetness (TOW) of the metallic surface is high, relatively consistent (less porous) layers, whose thickness does not usually exceed 100 µm, are formed. However, high Cl^- deposition rates lead to the formation of very porous rust layers showing cracks and even flaking and exfoliation [129].

In Figure 38 it is possible to see the variation in the structure of the rust layer as the atmospheric salinity rises. While at relatively low atmospheric salinities (44 and 110 mg $Cl^-/m^2 \cdot d$) the rust layers are fairly compact (though they can show the presence of longitudinal cracks), at higher atmospheric salinities (173 and 245 mg $Cl^-/m^2 \cdot d$) the rust layers present abundant cracking which facilitates their subsequent detachment (exfoliation), as can clearly be seen at the highest atmospheric salinities (889 and 1136 mg $Cl^-/m^2 \cdot d$) [64].

Figure 38 also indicates how the content of the different phases in the rust layers varies as the atmospheric salinity rises. The lepidocrocite phase decreases while the goethite and akaganeite phase contents increase [64].

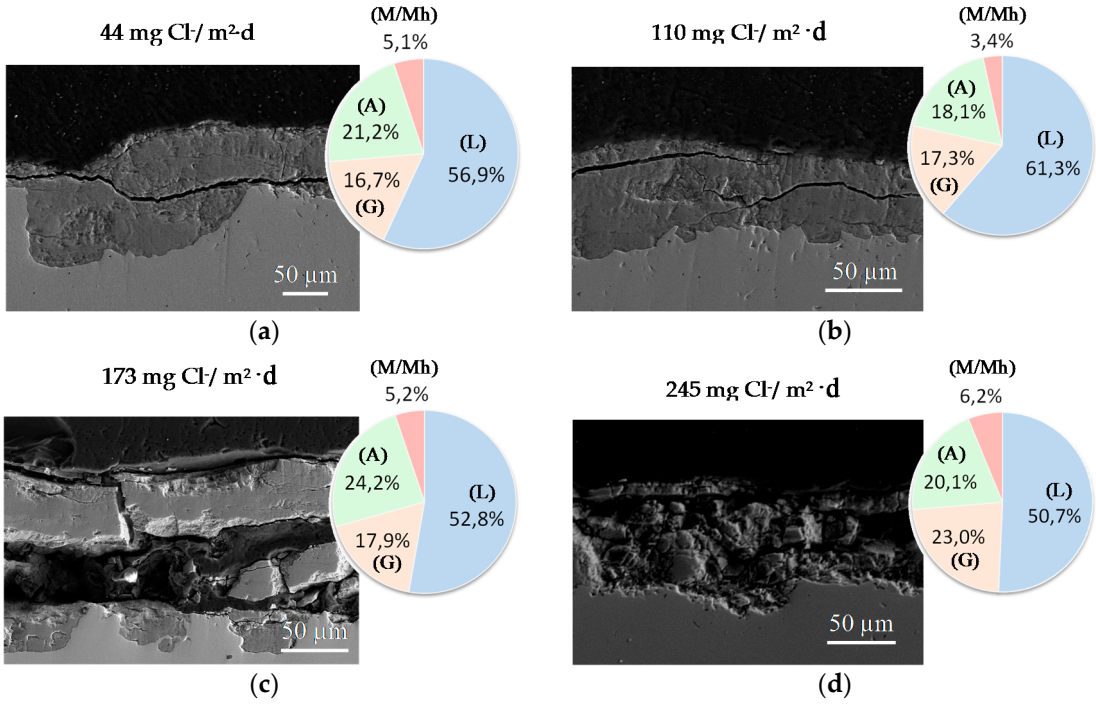

Figure 38. *Cont.*

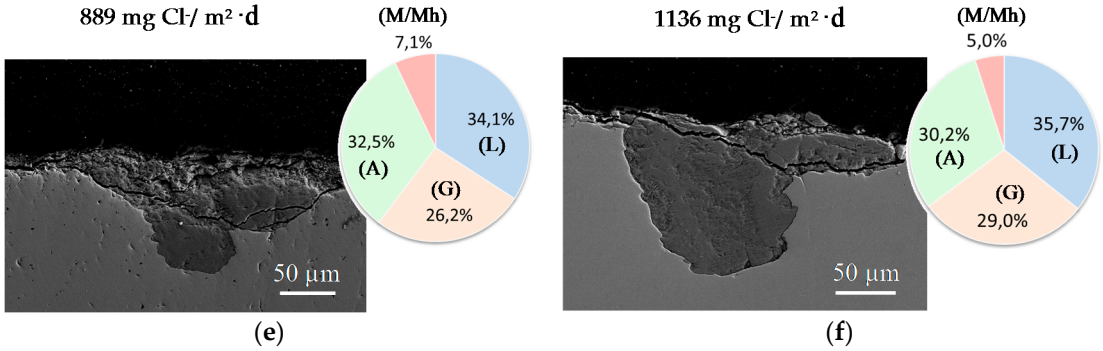

Figure 38. Variation in rust layer structure with atmospheric salinity: 44 mg $Cl^-/m^2 \cdot d$ (**a**); 110 mg $Cl^-/m^2 \cdot d$ (**b**); 173 mg $Cl^-/m^2 \cdot d$ (**c**); 245 mg $Cl^-/m^2 \cdot d$ (**d**); 889 mg $Cl^-/m^2 \cdot d$ (**e**); 1136 mg $Cl^-/m^2 \cdot d$ (**f**). Carbon steel specimens were exposed for three months in different marine atmospheres. The circles indicate the content of different phases in the rust, information obtained by XRD (RIR) of powdered rust [64]. L: lepidocrocite; G: goethite; A: akaganeite; M: magnetite and Mh: maghemite.

The base steel shows the formation of pits when exposed to marine atmospheres. As the atmospheric salinity rises, pitting becomes more significant and the Cl signal obtained by EDS inside the pits also rises (Figure 39) [64]. As has been seen in Section 6 (Figure 22), there is a strong presence of akaganeite in the interior of the pits formed on the base steel in severe marine environments.

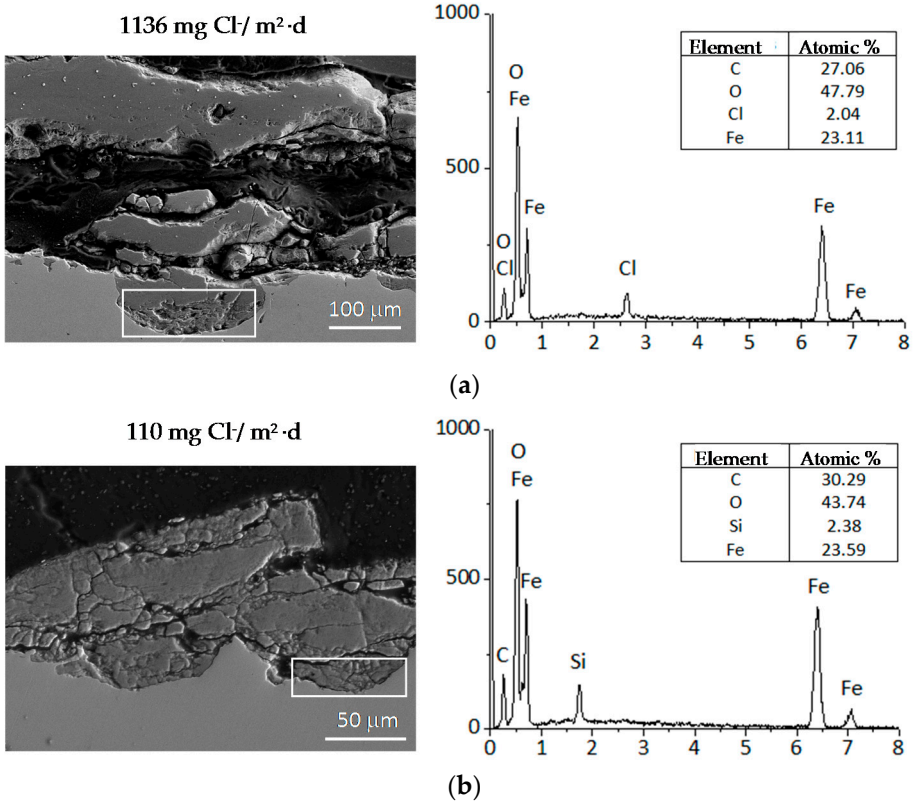

Figure 39. Formation of pits in steel substrate exposed to two atmospheres of different salinities. The EDS signal for Cl is more intense in the atmosphere of higher salinity [64].

Thus there seem to be two notably different situations with regard to the mechanisms involved in the MAC of CS: (a) establishment of a consistent (consolidated), adherent and continuous rust layer

(at low Cl^- deposition rates); and (b) formation of a thick rust layer that is easily detached (exfoliated) from the base steel, leaving large areas uncovered (at high Cl^- deposition rates) [193].

When a consolidated layer of corrosion products remains on the steel surface, the conditions are right for a diffusion-controlled corrosion mechanism to act, in which the aggressive species from the atmosphere (O_2, H_2O and Cl^-) pass through the rust layer to interact with the underlying steel (Figure 38a). This situation seems to occur in relatively low Cl^--containing atmospheres. The steel corrosion process consists of the following reactions:

Steel starts to corrode according to the anodic reaction:

$$Fe \rightarrow Fe^{2+} + 2e^-, \quad (1)$$

where the cathodic process consists of reduction of oxygen dissolved in the aqueous adlayer:

$$O_2 + 2H_2O + 4e^- \rightarrow 4OH^-, \quad (2)$$

The OH^- ions formed migrate towards the anodic zones forming $Fe(OH)_2$ as the initial rust product:

$$Fe^{2+} + 2OH^- \rightarrow Fe(OH)_2, \quad (32)$$

Under this basic mechanism, the steel corrosion rate will be highly influenced by the concentration of ionisable substances in the aqueous adlayer, as in the case of chlorides present in marine atmospheres. This explains the notable increase in the steel corrosion rate at station Cabo Vilano-2 compared to the Ponte Do Porto background station (Table 4), as the Cl^- deposition rate rises from 3.6 mg $Cl^-/m^2 \cdot d$ at Ponte Do Porto to 70 mg $Cl^-/m^2 \cdot d$ at Cabo Vilano-2.

In contrast, the exposure of CS to severe marine atmospheres can lead in certain circumstances to the formation of thick rust layers. High times of wetness of the metallic surface and an atmosphere with a high Cl^- deposition rate lead to the formation of this type of rust. These thick rust layers tend to become detached from the steel substrate, leaving it uncovered and without protection and thus accelerating the metallic corrosion process. The formation of anomalous thick rust layers and the accompanying exfoliation phenomenon has also been observed in studies carried out by the authors and other researchers [42,129,153,161].

In studies by Chico et al. on CS in Cl^--rich atmospheres, the average Cl^- deposition rate needed to exceed a critical threshold of close to 300 mg $Cl^-/m^2 \cdot d$ for exfoliation to take place. The annual steel corrosion at that atmospheric salinity was higher than 100 μm [129].

Exfoliated rust layers are composed of multiple rust strata, as can clearly be seen in the cross-section of Figure 23. The characteristics of the different rust sublayers within the rust multilayer are described in Figure 24: the outermost rust layer (OR) (rich in lepidocrocite and goethite), and a succession of alternating strata of fragile compact rust (CR) and loose interlayer rust (LIR) layers [12,129,153,162].

The CRs present high goethite and maghemite contents, low lepidocrocite contents and the practical absence of akaganeite. The mechanism that is proposed for the formation of CRs consists of two stages: (i) the formation of magnetite by electrochemical reduction of lepidocrocite and akaganeite phases (wet stage); and (ii) the solid-state transformation of magnetite into maghemite (dry stage). The LIR presents high goethite and akaganeite contents along with low lepidocrocite and spinel contents. It is proposed that the akaganeite and lepidocrocite phases will be electrochemically reduced to magnetite (maghemite at a later stage) and the formation of the CR layer takes place by consumption of the akaganeite and lepidocrocite phases leading to the complete disappearance of the interlayer rust stratum. An extremely dry period may cause the corrosion process to end without fully exhausting the interlayer rust stratum.

Subsequently, once the extremely dry period has come to an end and a new wet period starts, the formation of a second CR layer would begin, and so on, giving rise to the formation of a sandwich-type

structure constituted by alternate CR and LIR layers. A scheme of a feasible multilayered rust formation and rust exfoliation mechanism for CS exposed to severe marine atmospheres is shown in Figure 40 [129,153].

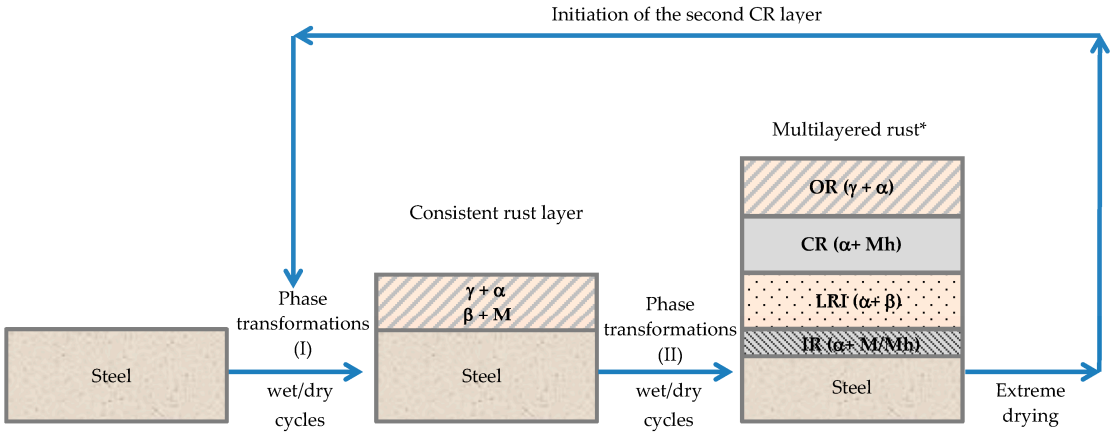

*Only the phases with higher content are indicated

Abreviations: Outermost rust layer (**OR**); Compact rust layer (**CR**); Loose rust interlayer (**LRI**), Innermost rust layer (**IR**)

Rust phases: lepidocrocite (γ); goethite (α); akaganeite (β); magnetite (**M**); maghemite (**Mh**).

Phase transformations: **I**: γ → α; γ → M; γ, β → M; **II**: γ, β → M; M → Mh (Solid state)

Figure 40. Scheme of a feasible multilayered rust formation mechanism of carbon steel exposed to severe marine atmospheres [129,153].

The detachment (exfoliation) of multilayered rust from the steel substrate takes place after complete drying of the whole rust layer, creating expansion stresses that exceed the adhesion forces which keep the multilayered rust joined to the steel substrate.

The difference in density between the sublayers involved (CR and LIR) suggests that compactness combined with mechanical properties may play an important role in the triggering of rust exfoliation. A closer look at the molar volume of the rust phases, i.e., the ratio between the molar mass and the density of each phase expressed in cm^3/mol, indeed shows great variations [162]. Table 5 displays a factor of 5 when going from the most compact rust phases involved (goethite, lepidocrocite; molar volume around 20 cm^3/mol), over medium compact phases (magnetite, maghemite; around 40 cm^3/mol), to the least compact phase (akaganeite; around 100 cm^3/mol) [194]. The much lower compactness of akaganeite is due to the presence of tunnels of the akaganeite lattice into which the Cl^- ions can enter and become integrated, resulting in a much less dense structure than the other rust phases [162].

Table 5. Molar volume of different rust phases. Data from Crystallographic and Crystallochemical Database for Minerals and their Structural Analogues, WWW-MINCRYST. Institute of Experimental Mineralogy, Russian Academy of Sciences [194].

Phase	Molar Volume (cm^3/mol)
Goethite (α-FeOOH)	20.84
Lepidocrocite (γ-FeOOH)	22.40
Maghemite (γ-Fe_2O_3)	43.71
Magnetite (Fe_3O_4)	44.56
Akaganeite (β-FeOOH)	101.62

Taking this difference in molar volume into consideration, it is possible to anticipate a great volume contraction and consequent void formation when the least compact phase akaganeite is structurally transformed into the much more compact spinel phase during primarily wet periods. Similarly, great volume expansion and stress introduction is induced when lepidocrocite is transformed into spinel. Hence, considering the molar volume data, it is not surprising that the compact rust sublayer contains the rust phases with the lowest molar volume (goethite and spinel) while the loose rust interlayer is dominated by akaganeite with a higher molar volume than the main phases in the solid rust sublayer [162].

Thus it is suggested that rust exfoliation is the result of frequent phase transformations, together with great variations in compactness between the rust phases involved. At some critical point the changes in compactness, compressive stresses and void formation become too large and the whole rust sublayer collapses mechanically and results in a fracture along the innermost rust layer [162].

8. Coastal-Industrial Atmospheres

The atmosphere of many coastal cities in developing countries is polluted with SO_2 due to the growth of industry, and in many cases formerly pure marine atmospheres can now be categorised as marine-industrial. The effect of SO_2 on the corrosion behaviour of steel in atmospheres containing Cl^- has not been widely studied. The first information on this subject was published by Copson [195] in 1945, who reported that a combined influence of Cl^- deposited on the surface and SO_2 in the atmosphere was considered to cause extensive corrosion. The first laboratory research was carried out by Ericsson [196], who observed a synergic effect of the combined influence of SO_2 (1 mg $SO_2/cm^2 \cdot h$) and NaCl (8 mg $NaCl/cm^2$) at 90% RH which was not seen at 70% RH.

The small amount of research that has been performed on this matter has been carried out in field tests by Corvo [80], Allam [197], Almeida et al. [198], Feliu and Morcillo [5], Liang et al. [199] and Wang et al. [200].

Corvo [80], after 6 months of atmospheric exposure of steel at marine testing stations in Cuba, found the following damage function:

$$C(g/m^2) = 64.9 + 6.9\,[Cl^-] + 0.15\,[SO_2]^2 - 0.17\,[Cl^-]\,[SO_2]^2, \quad (33)$$

From which a very significant influence of Cl^- is deduced, according to the coefficient obtained. SO_2 also influences weight loss with a lower coefficient, but in a quadratic form. However, the combined influence of SO_2 and Cl^- has a negative sign, indicating a decrease in corrosion. The results corresponding to multilinear stepwise regression and correlation for annual data are however different, where coefficients affecting SO_2 alone or combined with Cl^- are not significant.

$$C(g/m^2) = 243.7 + 6.7\,[Cl^-], \quad (34)$$

Allam [197], on the basis of results obtained in a study carried out at the shoreline on the western coast of the Arabian Gulf, with the presence of SO_2 (10 ppb) and H_2S (70 ppb) in the atmosphere, formulated the following mechanism for tests from 10 h to 12 months in duration, in which advanced surface analysis was used to characterise the corrosion products.

During the initial stage, the formation of iron sulfate ($FeSO_4$) takes place concurrently with the formation of iron chlorides. The negatively charged sulfate ions may compete with Cl^- ions for the ferrous ions (Fe^{2+}) produced by anodic reaction. This competitive effect has been reported in different papers [70,201,202].

$$Fe^{2+} + 2Cl^- \rightarrow FeCl_2, \quad (35)$$

$$Fe^{2+} + {SO_4}^{2-} \rightarrow FeSO_4, \quad (36)$$

Iron chlorides, as a major constituent in the initially formed blister covers, indicate that Cl^- ions are more aggressive than sulfate ions during the initial stages of AC. During the formation of $FeSO_4$ at anodic sites, sodium ions (Na^+) in the electrolyte are expected to migrate to the cathodic sites at the periphery of the anodic sites (blister site) to form sodium sulfate (Na_2SO_4). As blisters grow to form a thick continuous corrosion product layer, the formation of iron chlorides will eventually decrease compared to that seen during the initial stages. In contrast, further formation of iron sulfates takes place at the metal/rust interface during prolonged exposure times.

Feliu and Morcillo [5] in mixed atmospheres with SO_2 and NaCl contents ranging from 0.2–1.6 mg $SO_2/dm^2 \cdot d$ and 0.5–3.8 mg $NaCl/dm^2 \cdot d$, respectively, observe an additivity of effects as both pollutants act together.

Almeida et al. [198] carried out a study involving a large number of atmospheres in the Ibero-American region in which both pollutants were found: Cl^- ranging from 4.4 to 203.0 mg $Cl^-/m^2 \cdot d$ and SO_2 ranging from 16.7 to 65.2 mg $SO_2/m^2 \cdot d$. Figure 41 shows the evolution of CS corrosion with the atmospheric concentration of both pollutants, in which it is possible to see the significantly more corrosive action of Cl^- compared to SO_2. At low Cl^- contents the presence of SO_2 shows a beneficial effect on the corrosion of the base steel, as SO_2 favours the transformation of lepidocrocite into goethite. As the Cl^- concentration rises, the attack is intensifies with the SO_2 content (perhaps a synergic effect) and among the corrosion products it is possible to see the presence of akaganeite together with the lepidocrocite and goethite phases. After passing a certain threshold in the concentration of both pollutants, the attack of the steel seems to decrease, but this observation will need to be confirmed in a greater number of atmospheres with very high concentrations of both pollutants.

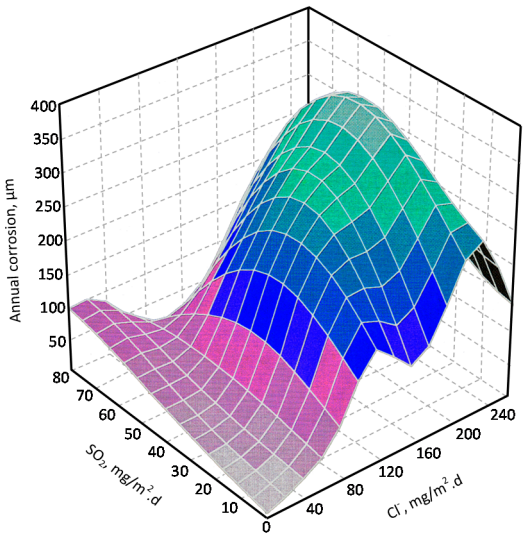

Figure 41. 3D representation of annual steel corrosion rate as a function of SO_2 and Cl^- contents in the atmosphere [198].

Liang et al. [199] carried out a sixteen-year AC exposure study of steels and found that SO_2 only had an obvious deteriorating effect in the initial stages of atmospheric exposure. Wang et al. [200] also confirm this effect, indicating that Cl^- is the ion that plays the main role in later stages, contrarily to the findings of Allam [197].

Some laboratory studies have also been carried out on the joint effect of both pollutants acting in combination. Attention is drawn to the contributions of Knotková et al. [203], Bastidas [204] and Chen et al. [205].

Knotková et al. [203] studied the joint action of both pollutants by alternate exposure of steel in cabinets containing SO_2 and sprayed NaCl solution (100–200 mg $NaCl/m^2.d$ or equivalent Cl^- contents in artificial seawater), respectively. They also studied the effect of SO_2 using Na_2SO_4 solutions.

They saw that (a) the corrosion products formed exhibited sulfate nests and akaganeite, the latter in smaller quantities than when the Cl^- pollutant acted individually. From the morphological point of view, the influence of Cl^- was predominant; and (b) a synergic effect on steel corrosion which would disappear by the end of the test, and their effect would only be additive.

These researchers conclude that the steel corrosion process when the two pollutants act together is a complex process involving two fundamental factors: the activity of H^+ in the aqueous adlayer formed on the metal

$$SO_2 + H_2O + \frac{1}{2}O_2 \rightarrow H_2SO_4, \quad (37)$$

Which acquires an acid pH, and the ion capturing capacity of the corrosion products that are formed. In this respect they note that when SO_4^{2-} is introduced in the form of sodium sulfate (Na_2SO_4) solution there is an increase in the pH value, an opposing effect to the situation noted above, as a consequence of the formation of a very stable NaOH solution:

$$Na_2SO_4 \rightarrow 2Na^+ + SO_4^{2-}, \quad (38)$$

$$Fe + SO_4^{2-} \rightarrow FeSO_4 + 2e^-, \quad (39)$$

$$\frac{1}{2}O_2 + H_2O + 2e^- \rightarrow 2OH^-, \quad (40)$$

Bastidas [204], in alternate exposure to NaCl (20, 50 and 100 $mg/m^2 \cdot d$) and iron sulfate at the same concentrations, observe that Cl^- is more harmful than an identical concentration of SO_2, and that the presence of one pollutant increases the attack caused by the other; the higher the concentration, the greater the combined effect (Figure 42). They find an additivity of effects when both pollutants act together.

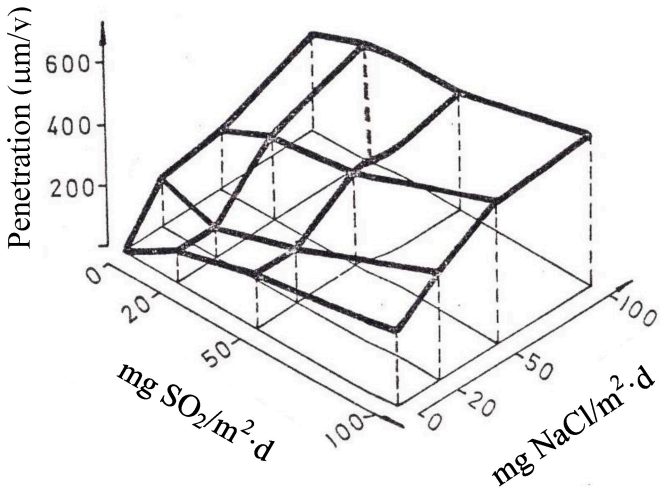

Figure 42. Effect of chlorides, SO_2 and the combination of both pollutants on iron corrosion kinetics. Electrochemical testing in conditions of 100% RH and 30 °C temperature [204].

Finally, Chen et al. [205] have recently carried out a wet/dry cyclic corrosion test using electrolytes prepared by adding different amounts of Na_2SO_3 (from 25.6 to 256 $mg/m^2 \cdot d$) into a NaCl solution (710 $mg/m^2 \cdot d$). They note that in the co-presence of Cl^- and SO_2, the steel corrosion mass gain increases as the SO_2 content rises up to a certain level, and beyond this level the steel shows a slower mass gain. From the kinetic point of view this finding is not in accordance with the commonly held idea [30] that a higher SO_2 content in the atmosphere should lead to a higher steel corrosion rate. Cl^- dominates the corrosion process in the initial stage and the effect of SO_2 comes later, accelerating the corrosion process as Allam reported [197].

Thus, this is a topic of great practical importance where, as has been seen, there is still considerable controversy on the effect of SO_2 in relation with the effect of Cl^- in the initial stages of the AC process and the total magnitude of the corrosive attack with exposure time. Accordingly, greater research efforts are needed on both aspects.

9. Long-Term Behaviour of Carbon Steel Exposed to Marine Atmospheres

For socio-economically advanced societies with heavy infrastructure investments in coastal regions, steel corrosion may be a considerable problem. Thus it is fundamental for engineers and political policy-makers to be able to predict AC well into the future (25, 50, 100 years). It must be considered that in some highly developed countries efforts are now being made to design civil structures such as bridges and other load-bearing structures for 50–100 years of service without any maintenance. Data mining and modelling tools can help to improve AC forecasts and anti-corrosive designs, but despite great progress in the development of damage functions (dose-response) in wide-scale international cooperative research programmes there is still a way to go for such long-term modelling of AC processes.

9.1. Nature of Corrosion Products

The nature of the rust constituents is barely affected by the exposure time; in fact, the same species are usually detected at a given site however long the exposure. The time factor only alters the proportions of the constituents, or at most determines the appearance or disappearance of intermediate or minor compounds [97]. Thus, lepidocrocite, goethite, akaganeite and spinel phase (magnetite/maghemite) are usually the main corrosion products found on steel after long-term marine atmospheric exposure. Akaganeite is a typical component of rust developed in marine atmospheres. On contacting the steel surface, akaganeite is gradually transformed into magnetite [121,122], in such a way that in severe marine atmospheres this substance can become the main component of the corrosion layer [124].

9.2. First Year Steel Corrosion

There are numerous published damage functions on CS corrosion and environmental parameters, both meteorological (air temperature, RH, rainfall, TOW, etc.) and atmospheric-pollution-related (mainly SO_2 and airborne salinity). In this respect, attention is drawn to the efforts made by ISO with regard to atmospheric corrosivity classification (ISO 9223 [30]) and the international cooperative programmes on AC: ISOCORRAG [29], ICP Materials [206], and MICAT [207].

In Section 4 it was seen that the annual corrosion of steel accelerates as the saline content in the atmosphere rises (Figure 7); the magnitude of the attack in marine atmospheres normally exceeds that found in other types of atmospheres.

9.3. Long-Term Steel Corrosion

For long-term AC, most of the experimental data has been found to adhere to the following kinetic relationship:

$$C = At^n, \tag{41}$$

where C is the corrosion after time t, and A and n are constants.

Thus, corrosion penetration data is usually fitted to a power function involving logarithmic transformation of the exposure time and corrosion penetration:

$$\log C = \log A + n \log t, \tag{42}$$

This power function (also called the bilograrithmic law) is widely used to predict the AC behaviour of metallic materials even after long exposure times, and its accuracy and reliability have been

demonstrated by a great number of authors. Figure 43, obtained from CS corrosion data after different exposure times in marine atmospheres at different test sites [87], confirms the verification of the power function (Equation (41)).

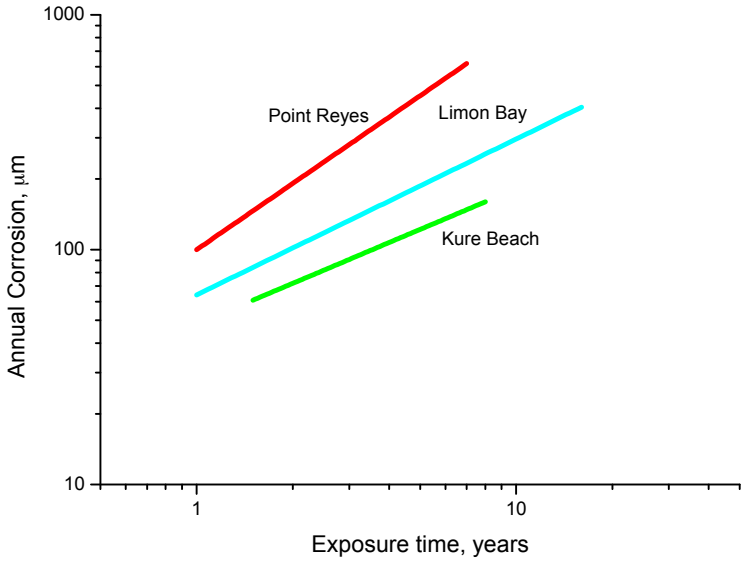

Figure 43. Typical log-log plots for carbon steel corrosion versus exposure time at different marine sites: Kure Beach (USA), Limon Bay (Panamá) and Point Reyes (USA). Data obtained from the reference [87].

According to Benarie and Lipfert [208], Equation (41) is a mass-balance equation, showing that the diffusion process is rate-determining, and this rate depends on the diffusive properties of the layer separating the reactants. The exponential law with n close to 0.5, can result from an ideal diffusion-controlled mechanism when all the corrosion products remain on the metal surface. This situation seems to occur in slightly polluted inland atmospheres. On the other hand, n values of more than 0.5 arise due to acceleration of the diffusion process (e.g., as a result of rust detachment by erosion, dissolution, flaking, cracking, etc.). This situation is typical of marine atmospheres, even those with low Cl^- contents. Conversely, n values of less than 0.5 result from a decrease in the diffusion coefficient with time through recrystallisation, agglomeration, compaction, etc. of the rust layer. Therefore, the exponent n value can be used as an indicator of the physico-chemical behaviour of the corrosion product layer and thus of its interaction with the local atmosphere, exposure conditions, nature of wetting/drying cycles, etc.

According to Benarie and Lipfert [208], as a rule $n < 1$ and there is no physical sense for $n > 1$, as $n = 1$ is the limit for unimpeded diffusion (high permeable corrosion products or no layer at all). Thus, values of $n > 1$, very frequent in severe marine atmospheres, have been dismissed in many MAC studies as being due to outliers or errors in mass loss determinations.

However, many of these may be real values and not be due to error in mass loss determinations. The reason for this behaviour lies in the fact that in highly severe marine atmospheres, Equation (41), based on diffusion mechanisms, can sometimes not be applicable. When applied, it is common to find exponent n values of close to 1 due to the existence of highly permeable (and barely protective) corrosion layers or the absence of corrosion layers because of their detachment by delamination (exfoliation), or even values of $n > 1$ due to acceleration of the corrosive attack as a result of an "autocatalytic" mechanism [23], in contrast to the diffusion mechanism upon which Equation (41) is based. Figure 44 shows the evolution of steel corrosion with exposure time in marine atmospheres with high deposited Cl^- ion contents. The acceleration of the attack as exposure time advances is evident [12].

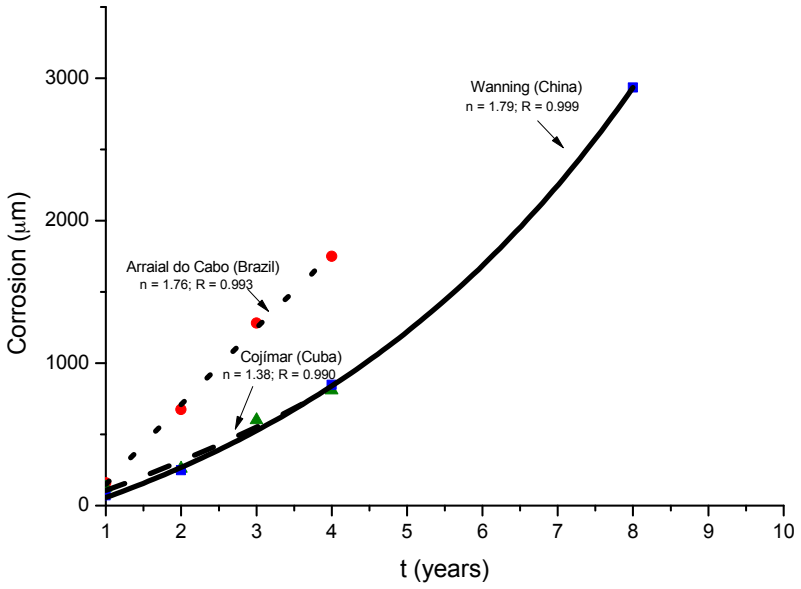

Figure 44. Evolution of mild steel corrosion with exposure time in severe marine atmospheres: Wanning, China, Arraial do Cabo, Brazil and Cojímar, Cuba. Values of exponent n and correlation coefficient (R) have been obtained from log C vs. log t plots for each site [12].

In an attempt to relate the exponent *n* value with atmospheric salinity, Figure 45, prepared using data obtained in the ISOCORRAG [29] and MICAT [207] programmes, for marine atmospheres with low SO_2 levels (<35 mg $SO_2/m^2 \cdot d$), shows the tendency for the exponent *n* value to increase with atmospheric salinity and how *n* can acquire values of more than unity. It would be important to have a greater volume of data for $n > 1$ in order to perfect Figure 45 [12].

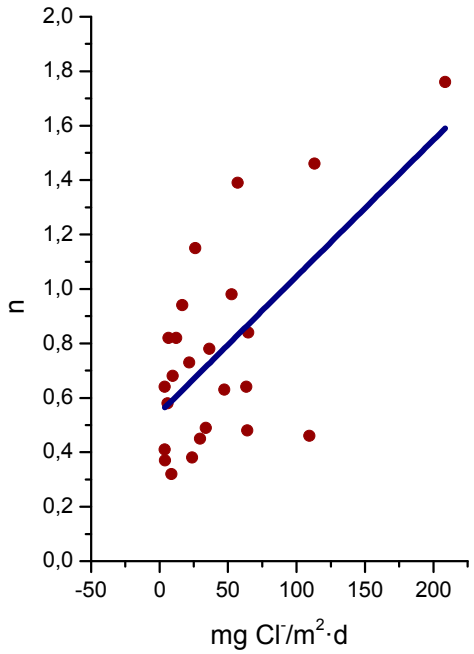

Figure 45. Variation in exponent n with atmospheric salinity at marine test sites in the MICAT [207] and ISOCORRAG [29] programmes.

Highly permeable corrosion layers or the absence of thick corrosion layers at all because of their detachment by delamination (exfoliation) (see Figure 38) must be constituted by macropores ($2 < D < 10$ nm) or perhaps even mesopores (D ~10–30 nm), instead of micropores ($D < 2$ nm), as occurs in consolidated rust layers formed in marine atmospheres of less aggressivity. According to Ishikawa et al. [146], macropores are considered to be too large to govern diffusion of molecules and ions through the rust layers.

9.4. Modelling of the Long-Term Atmospheric Corrosion Process

Data on the corrosion resistance of metals over long periods of time is important for determining the service life of metal structures and for developing the methods and means for their protection and preservation. Reliable estimates of corrosion resistance can be provided by corrosion tests under natural conditions. Such tests are time-consuming and expensive. In view of this, researchers pay great attention to the development of models that allow long-term forecasts without requiring testing under natural conditions.

It has been seen that the power function (Equation (41)) is widely used in long-term forecasts of the AC of metals. Table 6 sets out average values of exponent *n* for plain CS in different types of atmospheres, and Figure 46 shows the corresponding box-whisker plots of *n* values. It is possible to see a clear tendency towards higher *n* values in marine atmospheres.

Table 6. Average values of exponent n in bi-logarithmic plots of the power function ($C = At^n$) for plain carbon steel in non-marine (rural-urban-industrial) and marine atmospheres [87].

Non-Marine (Rural-Urban-Industrial) Atmospheres		**Marine Atmospheres**	
Av. n	Range of *n* in Equation (41)	*Av. n*	Range of *n* in Equation (41)
0.49	0.26–0.76	0.73	0.37–0.98

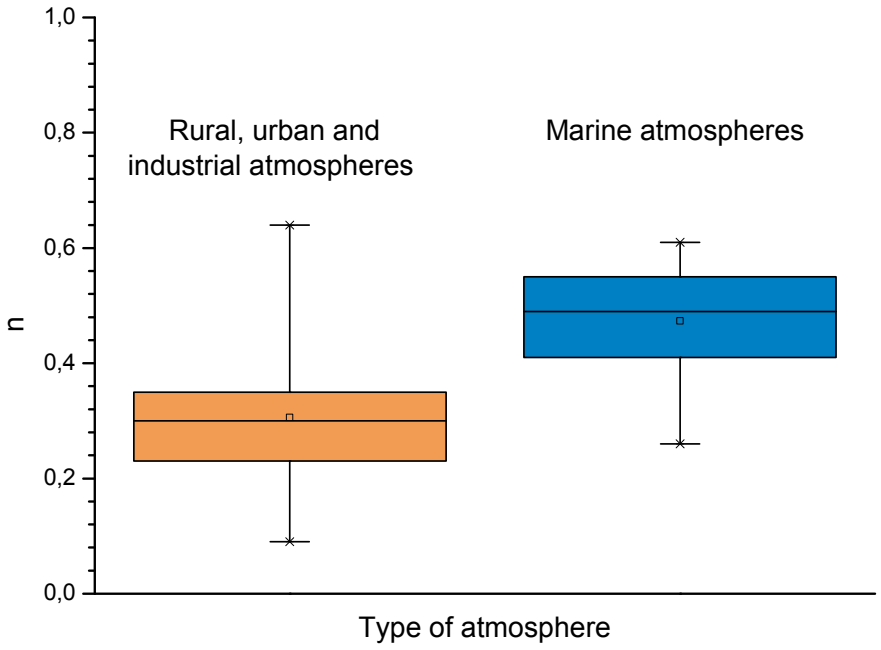

Figure 46. Box-whisker plots of n values in power function ($C = At^n$) for carbon steel in different types of atmospheres [87].

Panchenko et al. [209] propose a modification of the model for the long-term forecasting of corrosion losses of metals in any type of atmosphere after the establishment of the steady state. They find a stochastic relationship between exponent *n* of the power function (Equation (41)) and

corrosion losses over the first year, and make a forecast of corrosion losses based on a power function using the n values calculated from the identified stochastic relationships.

McCuen and Albrecht [210] proposed improving the power model by replacing it with two different approaches: numerical model and power-linear model, the latter consisting of a power function at the initial stage (Equation (41)) and a linear function:

$$C_t = C_0 + \alpha_t, \tag{43}$$

at the steady-state stage.

As to whether this law provides a better prediction of the AC of WS for exposure times of at least 20 years, McCuen et al. compared both models (the power model and the power-linear model) using AC data reported for WS in the United States and concluded that the experimental data fitted the power-linear model better than the power model and thus provided more accurate predictions of long-term AC [210].

Panchenko et al. [211] propose methods for the calculation of n and α (Equation (43)) and make a comparative estimate of long-term predictions using the power-linear function and ISOCORRAG standard, obtaining comparable results in atmospheric corrosivity categories C1–C3 [30].

Albrecht and Hall [212], by refinement of the power-linear model, have proposed a new bi-linear model based on ISO 9224 [213], called modified ISO 9224, as well as an adjustment of this new bi-linear model that accounts for a modified corrosion rate during the first year of exposure and a steady state in subsequent years.

Finally, Melchers [214,215] suggests a bi-modal model for long-term forecasts of the corrosion loss of WS and grey cast iron in marine atmospheres. The model consists of a number of sequential corrosion phases, each representing the corrosion process that is dominant at that time and which controls the instantaneous corrosion rate. The phases are summarised in Figure 47. The important difference from conventional models is that the bi-modal model has longer-term corrosion governed by microbial activity. Melchers has successfully applied this model to different sets of data points for long-term exposures at different test sites.

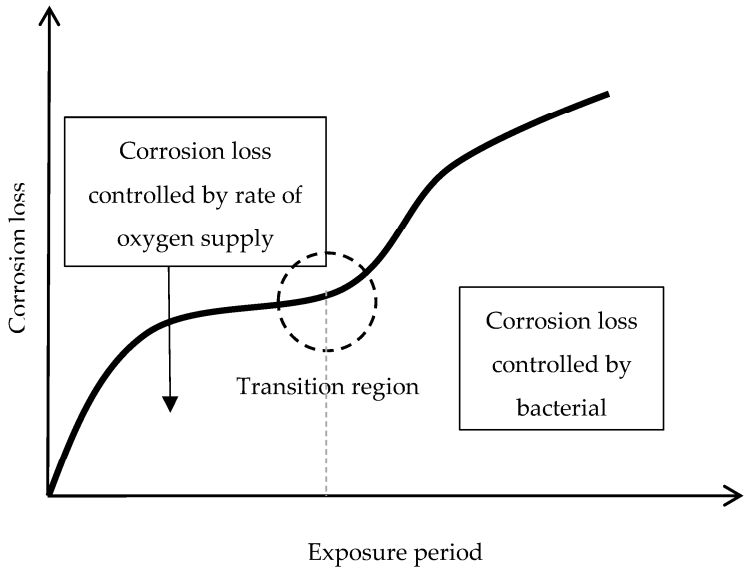

Figure 47. Bi-modal model for corrosion loss showing the changing behavior of corrosion process, according to Melchers [214,215].

9.5. Towards an Estimation of the Marine Atmospheric Corrosion of Steel Based on Existing Environmental Parameters

Following the philosophy of ancient ISO 9223 [216], an estimation of the atmospheric corrosivity of a particular coastal region could be made from the knowledge of three fundamental parameters: TOW of the metallic surface, SO_2 concentration in the atmosphere, and Cl^- deposition rate due to airborne sea-salt particles.

Nowadays most countries have ample meteorological databases covering their entire territories which would allow estimations of TOW. Furthermore, information on atmospheric SO_2 concentrations is increasingly available. However, there tends to be very little information available on atmospheric salinity in different coastal areas, and reliable databases on this subject do not generally exist. It would be desirable to include this data in the numerous published damage functions between steel corrosion and environmental factors. This would make it possible to estimate AC simply from environmental data, without having to carry out natural corrosion tests at a specific site, which involve long waiting times and considerable expense.

9.5.1. Time of Wetness

TOW can generally be defined as the amount of time a metal surface remains wet during atmospheric exposure. The most commonly used practical definition of TOW is that given by ISO 9223 [30], which defines it as the total time when the RH of the ambient environment is equal to or greater than 80% at temperatures above 0 °C.

A number of limitations of the ISO definition have been pointed out in the literature and even in the ISO 9223 standard itself: (a) One major issue is that by definition precipitation and dewing events are excluded in ISO 9223. With regard to the latter, temperature differences between the ambient air and the surface can cause quite large deviations between the RH of the surface and the surrounding air; and (b) many atmospheric pollutants deliquesce at humidity levels far below 80%. A study by Cole et al. [13] clearly shows wetness measured on resistance-type sensors occurring well below the 80% threshold. Wetting phenomena associated with AC along with TOW definitions and determination methods were overviewed by Schindelholz and Kelly [14–16].

According to Cole et al. [13], in the case of salt deposits on the metallic surface, as occurs in marine atmospheres, it is necessary to take into account the simple principle that a metal surface is wetted when the surface RH exceeds the deliquescent RH (DRH) of any salts on the surface, as the ambient RH increasingly exceeds the DRH. They note the need for a more flexible method for predicting not only TOW but also the cycles of moisture accumulation and depletion. Given the established role of hygroscopic salts in promoting wetting in particulates, whether airborne or on surfaces, a model of surface wetting should address the role of deposited salts. The basic principle of the model is that the TOW of metal surfaces fully exposed to the environment can be approximated by the time of condensation (TCD) plus rain periods, i.e.,

$$\text{TOW} = \text{TCD} + \text{rain period}, \tag{44}$$

Thus, these researchers propose a method for estimating the wetting of a surface based on a comparison of surface RH and the deliquescence of salts that may pollute the surface, deriving relatively simple rules for wetting based on the DRH model and ISO classifications. These rules predict the total TOW to a high degree of accuracy.

9.5.2. Chloride Deposition Rate

Studies have shown that the two main sources of salt aerosol carried by the wind are ocean waves and breaking surf [60,66,217–219]. The magnitude of atmospheric salinity (Cl^- deposition rate) at any given place depends on numerous factors. To mention just a few (see Section 4): wave height at high sea and at the coast; presence or absence of a surf zone on the coast; direction, speed and persistence of

marine winds; height above sea level; distance from the shore; topographical effects; etc. Thus it has been seen in Section 4 that for instance wave height values of 1.5–2.0 m are sufficient to produce high monthly average salinity values, or that the wind blowing for a relatively short time at speeds above 3 m/s in a direction with great influence on the entrainment of marine aerosol is sufficient for atmospheric salinity to acquire important values.

There is abundant literature on this topic. Perhaps a less studied aspect has been the degree of shielding or sheltering on wind speed. In relation with this matter, Nakajima [220] has developed a mapping method based on grids with topographic factors to assess the influence of several factors on average wind speed at locations near a sea coast. The concept integrates the geographical texture of the environment in all directions with its effect on airflow. The most significant factor affecting sea wind is the degree of shielding.

Similarly, Klassen and Roberge [221] have measured and modelled by CLIMAT units [222] the influence of wind effects on local atmospheric corrosivity considering various degrees of wind sheltering. They found a 34-fold difference between the average mass loss of the most wind-protected and the least wind-protected points.

As noted by Roberge et al. [223], the dispersion of airborne salinity is highly dependent upon the local geography and wind patterns and is therefore rather difficult to model with simplistic functions. In this respect, Cole et al. [218] developed an aerosol penetration model applying the principles of aerosol transport using fluid dynamics principles. Salt aerosol sinks, such as gravity, rain and trees (obstacles), were accounted for. The study also noted that a high surface RH and a lower cloud height led to decreased penetration inland, and further reductions occurred in areas of high rainfall. It was also noted that structures in the airflow, such as forests and urban environments, reduced the Cl^- concentration. This work illustrated that complex variables such as airspeed, ground roughness (vegetation), surface air RH, cloud height and rainfall could be incorporated into a model. A good correlation was reported to exist between the model and empirical results from a limited data set.

Despite the high number of factors involved, it is hoped that the growing flow of knowledge on this subject will soon lead to the desirable goal of being able to make a rough estimate of atmospheric salinity in a given geographic area without the need for measurements involving marine aerosol capturing techniques.

The prediction of atmospheric corrosivity at a given site is even more complex, as it is necessary to take into account an even greater number of variables. Thus, Roberge et al. paint a pessimistic view when they note that a single transferable and comprehensive environmental corrosivity prediction model still has to be published and may not be possible due to the complexity of the issues [223].

10. Issues Pending

AC has been extensively researched over the last one hundred years, and as a result the effects of meteorological and pollution variables on AC are now well known. Even so, our knowledge on this issue still holds many gaps, such as how to accurately estimate the total TOW of metallic structures, and the effects of climate change and acid rain, etc.

The issue of steel corrosion in coastal regions is particularly relevant in view of the latter's great importance to human society, considering that about half of the world's population lives in coastal regions. Thus it is surprising that marine atmospheric corrosion (MAC) has until recently received relatively little attention by corrosion scientists. This is therefore a relatively young scientific field, where there continue to be great gaps in knowledge.

In this review, we have noted a number of aspects in relation with which greater research efforts would seem to be necessary. To mention just a few:

1. Experimentation in this field is carried out at atmospheric corrosion testing stations and in the laboratory by means of wet/dry cyclic tests. A great amount of research is under way using both methods, but there are two issues of enormous importance that are not being paid sufficient attention: (a) experimentation in marine atmospheres with high Cl^- ion deposition

rates (>500 mg/m^2·d), where very little information is available; and (b) the standardisation of wet/dry laboratory cyclic tests by means of more specific codes in order to make research results more comparable.

It would also be necessary to undertake more research in the case of marine-industrial atmospheres, where there are great discrepancies among researchers. This is a particularly important issue in developing countries where factories are often located in coastal regions.

2. One currently unresolved question is concerned with the presence of the amorphous phase in the rust layer and the evolution of its amount with exposure time. With regard to the role played in corrosion mechanisms by the less crystalline phases of rust (ferrihydrite, feroxyhyte, etc.), despite the enormous research effort that has been carried out in recent years by a number of research teams using highly sophisticated analytical techniques, there are still numerous gaps in knowledge.

   Another matter that generates a great deal of uncertainty is the differentiation of magnetite and maghemite phases, both of which are very similar in many of their characteristics, but which can play a different role in the MAC process.

3. In the rust layers formed, aspects such as decoupling of the anodic and cathodic corrosion reactions, localisation, connectivity and reactivity of the different rust phases inside the corrosion layers, as well as characteristics such as porosity, tortuosity, etc., are also of primary importance in the determination of corrosion mechanisms.

   At high Cl^- ion deposition rates, rust layers can exfoliate and become detached from the steel substrate. Although great advances have recently been made in this field, there are still a number of basic aspects that remain to be clarified in order for a complete comprehension of rust exfoliation phenomena.

4. Finally, a matter of enormous technical importance for engineers and political policy-makers is to be able to predict steel corrosion rate well into the future (20, 50, 100 years). Data mining and modelling tools can help to improve forecasts and anti-corrosive designs, but despite great progress in the development of damage functions (dose-response) in wide-scale international cooperative research programmes, there is still a long way to go for such long-term modelling of atmospheric corrosion processes.

   In this sense, better scientific knowledge is needed towards the desirable goal of being able to estimate atmospheric salinity in a given geographic area without the need for measurements involving marine aerosol capturing techniques.

Conflicts of Interest: The authors declare no conflict of interest.

References

1. Evans, U.R. *The Corrosion and Oxidation of Metals: Scientific Principles and Practical Applications*; Edward Arnold Ltd.: London, UK, 1960.
2. Tomashov, N.D. *Theory of Corrosion and Protection of Metals. The Science of Corrosion*; The MacMillan Co.: New York, NY, USA, 1966.
3. Rozenfeld, I.L. *Atmospheric Corrosion of Metals*; NACE: Houston, TX, USA, 1972.
4. Barton, K. *Protection against Atmospheric Corrosion*; John Wiley and Sons: New York, NY, USA, 1976.
5. Feliu, S.; Morcillo, M. *Corrosión y Protección de los Metales en la Atmósfera*; Bellaterra: Barcelona, Spain, 1982.
6. Graedel, T.E.; Mc Gill, R. Degradation of materials in the atmosphere. *Environ. Sci. Technol.* **1986**, *20*, 1093–1100. [CrossRef]
7. Kucera, V.; Mattsson, E. Atmospheric corrosion. In *Corrosion Mechanisms*; Mansfeld, F., Ed.; Marcel Dekker: New York, NY, USA, 1987; pp. 211–284.
8. Leygraf, C.; Odnevall Wallinder, I.; Tidblad, J.; Graedel, T. *Atmospheric Corrosion*, 2nd ed.; The Electrochemical Society Series; John Wiley and Sons: Hoboken, NJ, USA, 2016.
9. Ambler, H.R.; Bain, A.A.J. Corrosion of metals on the tropics. *J. Appl. Chem.* **1955**, *5*, 437–527. [CrossRef]

10. Nishimura, T.; Katayama, H.; Noda, K.; Kodama, T. Electrochemical behavior of rust formed on carbon steel in a wet/dry environment containing chloride ions. *Corrosion* **2000**, *56*, 935–941. [CrossRef]
11. Morcillo, M.; Díaz, I.; Chico, B.; Cano, H.; de la Fuente, D. Wethearing steels: From empirical development to scientific desing. A review. *Corros. Sci.* **2014**, *83*, 6–31. [CrossRef]
12. Morcillo, M.; Chico, B.; Alcántara, J.; Díaz, I.; Simancas, J.; de la Fuente, D. Atmospheric corrosion of mild steel in chloride—Rich environments. Questions to be answered. *Mater. Corros.* **2015**, *66*, 882–892.
13. Cole, I.S.; Ganther, W.D.; Sinclair, J.D.; Lau, D.; Paterson, D.A. A study of the wetting of metal surfaces in order to understand the process controlling atmospheric corrosion. *J. Electrochem. Soc.* **2004**, *151*, B627–B635. [CrossRef]
14. Schindelholz, E.; Risteen, B.E.; Kelly, R.G. Effect of relative humidity on corrosion of steel under sea salt aerosol proxies: I. NaCl. *J. Electrochem. Soc.* **2014**, *161*, C450–C459. [CrossRef]
15. Schindelholz, E.; Risteen, B.E.; Kelly, R.G. Effect of relative humidity on corrosion of steel under sea salt aerosol proxies: II. $MgCl_2$, artificial seawater. *J. Electrochem. Soc.* **2014**, *161*, C460–C470. [CrossRef]
16. Schindelholz, E.; Kelly, R.G. Wetting phenomena and time of wetness in atmospheric corrosion: A review. *Corros. Rev.* **2012**, *30*, 135–170. [CrossRef]
17. Costa, J.M.; Morcillo, M.; Feliu, S. Effect of environmental parameters on atmospheric corrosion of metals. In *Encyclopedia of Environmental Control Technology: Air Pollution Control*; Cheremisinoff, P.N., Ed.; Gulf Publishing Company: Houston, TX, USA, 1989; Volume 2, pp. 197–238.
18. Rozenfeld, I.L. Atmospheric corrosion of metals. Some questions of theory. In Proceedings of the 1st International Congress on Metallic Corrosion, London, UK, 10–15 April 1961; pp. 243–253.
19. Tidblad, J.; Kucera, V.; Ferm, M.; Kreislova, K.; Brüggerhoff, S.; Doytchinov, S.; Screpanti, A.; Grøntoft, T.; Yates, T.; de la Fuente, D.; et al. Effects of air pollution on materials and cultural heritage: ICP materials celebrates 25 years of research. *Int. J. Corros.* **2012**, *2012*. [CrossRef]
20. Haagenrud, S.; Ottar, B. Long range transport of air pollutants and corrosion effects. In Proceedings of the 7th Scandinavian Corrosion Congress, Trondheim, Norway, May 1975; p. 102.
21. Kucera, V. Effects of sulphur dioxide and acid precipitation on metals and anti-rust painted steel. *Ambio* **1976**, *5*, 243–248.
22. Feliu, S.; Morcillo, M. Corrosión atmosférica. In *Corrosión y Protección metáLicas*; Andrade, M.C., Feliu, S., Eds.; CSIC (Colección Nuevas Tendencias): Madrid, Spain, 1991; Volume II.
23. Burstein, G.T. Passivity and localised corrosion. In *Corrosion. Metal/Environment Reactions*, 3rd ed.; Shreir, L.L., Jarman, R.A., Burstein, G.T., Eds.; Butterworth-Heinemann: Oxford, UK, 1994; Volume 1, p. 1:146.
24. Feitknecht, W. The breakdown of oxide films on metal surfaces in acidic vapors and the mechanism of atmospheric corrosion. *Chimia* **1952**, *6*, 3–13.
25. Askey, A.; Lyon, S.B.; Thompson, G.E.; Johnson, J.B.; Wood, G.C.; Cooke, M.; Sage, P. The corrosion of iron and zinc by atmospheric hydrogen chloride. *Corros. Sci.* **1993**, *34*, 233–247. [CrossRef]
26. Schikorr, G. On the mechanism of atmospheric corrosion of iron. *Werkst. Korros.* **1963**, *14*, 63–80.
27. International Organization for Standardization. *ISO 8565, Metals and Alloys—Atmospheric Corrosion Testing—General Requirements*; International Organization for Standardization: Geneva, Switzerland, 2011.
28. American Society for Testing and Materials. *ASTM G50, Conducting Atmospheric Corrosion Tests on Metals*; American Society for Testing and Materials: Philadelphia, PA, USA, 1991.
29. Knotkova, D.; Kreislova, K.; Dean, S.W.J. *ISOCORRAG. International Atmospheric Exposure Program: Summary of Results*; ASTM: West Conshohocken, PA, USA, 2010.
30. European Committee for Standardization. *EN ISO 9223, Corrosion of Metals and Alloys—Corrosivity of Atmospheres—Classification, Determination and Estimation*; European Committee for Standardization: Brussels, Belgium, 2012.
31. Compton, K.G.; Mendizza, A.; Bradley, W.W. Atmospheric galvanic couple corrosion. *Corrosion* **1955**, *11*, 35–44. [CrossRef]
32. Doyle, D.P.; Godard, H.P. Rapid determination of corrosivity of an atmosphere to aluminium. In *Proceedings of the 3rd International Congress on Metallic Corrosion*; MIR Publishers: Moscow, Russia, 1969; Volume IV, pp. 429–437.
33. Doyle, D.P.; Godard, H.P. A rapid method for determining the corrosivity of the atmosphere at any location. *Nature* **1963**, *200*, 1167–1168. [CrossRef]

34. Haynes, G. Cabinet. In *Corrosion Tests and Standards. Application and Interpretation*; Baboian, R., Ed.; American Society for Testing and Materials: Philadelphia, PA, USA, 1995; pp. 91–97.
35. American Society for Testing and Materials. *ASTM B117, Test Method of Salt Spray (Fog) Testing*; American Society for Testing and Materials: Philadelphia, PA, USA, 2011.
36. International Organization for Standardization. *ISO 11130, Corrosion of Metals and Alloys—Alternate Immersion Test in Salt Solution*; International Organization for Standardization: Geneve, Switzerland, 1999.
37. González, J.A. *Control de la Corrosión. Estudio y Medida por téCnicas Electroquímicas*; CSIC: Madrid, Spain, 1989.
38. Stratmann, M. The atmospheric corrosion of iron steel. *Metal Odlew* **1990**, *16*, 46–52.
39. Nishimura, T.; Tanaka, K.; Shimizu, Y. Effect of NaCl on rusting of steel in wet and dry corrosion cycle. *J. Iron Steel Inst. Jpn.* **1995**, *81*, 1079–1084.
40. Lair, V.; Antony, H.; Legrand, L.; Chaussé, A. Electrochemical reduction of ferric corrosion products and evaluation of galvanic coupling with iron. *Corros. Sci.* **2006**, *48*, 2050–2063. [CrossRef]
41. Hœrlé, S.; Mazaudier, F.; Dillmann, P.; Santarini, G. Advances in understanding atmospheric corrosion of iron. II. Mechanistic modelling of wet–dry cycles. *Corros. Sci.* **2004**, *46*, 1431–1465.
42. Cook, D.C. Spectroscopic identification of protective and non-protective corrosion coatings on steel structures in marine environments. *Corros. Sci.* **2005**, *47*, 2550–2570. [CrossRef]
43. De Faria, D.L.A.; Venâncio Silva, S.; de Oliveira, M.T. Raman microspectroscopy of some iron oxides and oxyhydroxides. *J. Raman Spectrosc.* **1997**, *28*, 873–878. [CrossRef]
44. Monnier, J.; Réguer, S.; Foy, E.; Testemale, D.; Mirambet, F.; Saheb, M.; Dillmann, P.; Guillot, I. XAS and XRD in situ characterisation of reduction and reoxidation processes of iron corrosion products involved in atmospheric corrosion. *Corros. Sci.* **2014**, *78*, 293–303. [CrossRef]
45. Kimura, M.; Mizoguchi, T.; Kihira, H.; Kaneko, M. Various scale analyses to create functioning corrosion products. In *Characterization of Corrosion Products on Steel Surfaces*; Waseda, Y., Suzuki, S., Eds.; Advances in Materials Research; Springer: Heildelberg, Germany, 2006; pp. 245–272.
46. Konishi, H.; Yamashita, M.; Uchida, H.; Mizuki, J. Characterization of rust layer formed on Fe, Fe-Ni and Fe-Cr alloys exposed to Cl-rich environment by Cl and Fe k-edge XANES measurements. *Mater. Trans.* **2005**, *46*, 329–336. [CrossRef]
47. Dillmann, P.; Mazaudier, F.; Hoerlé, S. Advances in understanding atmospheric corrosion of iron. I. Rust characterization of ancient ferrous artefacts exposed to indoor atmospheric corrosion. *Corros. Sci.* **2004**, *46*, 1401–1429.
48. Ishikawa, T. Asessment of rust layers formed on WS in saline environment by gas adsorption. *Mater. Corros.* **2015**, *66*, 1460–1466. [CrossRef]
49. Cole, I.S.; Lau, D.; Paterson, D.A. Holistic model for atmospheric corrosion part 6—From wet aerosol to salt deposit. *Corros. Eng. Sci. Technol.* **2004**, *39*, 209–218. [CrossRef]
50. Johnson, E.; Stanners, J.F. *The Characterisation of Corrosion Test Sites in the Community*; Commission of the European Communities: Luxembourg, 1981.
51. Blanchard, D.C.; Woodcock, A.H. The production, concentration and vertical distribution of the sea-salt aerosol. *Ann. N. Y. Acad. Sci.* **1980**, *338*, 330–347. [CrossRef]
52. Meira, G.R.; Pinto, W.T.A.; Lima, E.E.P.; Andrade, C. Vertical distribution of marine aerosol salinity in a brazilian coastal area—The influence of wind speed and the impact on chloride accumulation into concrete. *Constr. Build. Mater.* **2017**, *135*, 287–296. [CrossRef]
53. Zezza, F.; Macrì, F. Marine aerosol and stone decay. *Sci. Total Environ.* **1995**, *167*, 123–143. [CrossRef]
54. Whitby, K.T. The physical characteristics of sulfate aerosols. *Atmos. Environ.* **1978**, *12*, 135–159. [CrossRef]
55. Li, S.; Hihara, L.H. Aerosol salt particle deposition of metals exposed to marine environments: A study related to marine atmospheric corrosion. *J. Electrochem. Soc* **2014**, *161*, C268–C275. [CrossRef]
56. Gustafsson, M.E.R.; Franzén, L.G. Dry deposition and concentration of marine aerosols in a coastal area. *Atmos. Environ.* **1996**, *30*, 977–989. [CrossRef]
57. Cole, I.S.; Azmat, N.S.; Kanta, A.; Venkatraman, M. What really controls the atmospheric corrosion of zinc? Effect of marine aerosols on atmospheric corrosion of zinc. *Int. Mater. Rev.* **2009**, *54*, 117–133.
58. Fitzgerald, J.W. Marine aerosol: A review. *Atmos. Environ.* **1991**, *25A*, 533–545. [CrossRef]
59. Wu, J. Evidence of sea spray produced by bursting bubbles. *Science* **1981**, *212*, 324–326. [CrossRef] [PubMed]
60. Feliu, S.; Morcillo, M.; Chico, B. Effect of distance from sea on atmospheric corrosion rate. *Corrosion* **1999**, *55*, 883–891. [CrossRef]

61. Ohba, R.; Okabayashi, K.; Yamamoto, M.; Tsuru, T. A method for predicting the content of sea salt particles in the atmosphere. *Atmos. Environ.* **1990**, *24A*, 925–935. [CrossRef]
62. Ten Harkel, M.J. The effects of particle-size distribution and chloride depletion of sea-salt aerosols on estimating atmospheric deposition at a coastal site. *Atmos. Environ.* **1997**, *31*, 417–427. [CrossRef]
63. McKay, W.A.; Garland, J.A.; Livesley, D.; Halliwell, C.M.; Walker, M.I. The characteristics of the shore-line sea spray aerosol and the landward transfer of radionuclides discharged to coastal sea water. *Atmos. Environ.* **1994**, *28*, 3299–3309. [CrossRef]
64. Alcántara, J.; Chico, B.; Díaz, I.; de la Fuente, D.; Morcillo, M. Airborne chloride deposit and its effect on marine atmospheric corrosion of mild steel. *Corros. Sci.* **2015**, *97*, 74–88. [CrossRef]
65. Strekalov, P.V.; Panchenko, Y.M. The role of marine aerosols in atmospheric corrosion of metals. *Prot. Met.* **1994**, *30*, 254–263.
66. Morcillo, M.; Chico, B.; Mariaca, L.; Otero, E. Salinity in marine atmospheric corrosion: Its dependence on the wind regime existing in the site. *Corros. Sci.* **2000**, *42*, 91–104. [CrossRef]
67. Meira, G.R.; Andrade, C.; Alonso, C.; Padaratz, I.J.; Borba, J.C., Jr. Salinity of marine aerosols in a brazilian coastal area—Influence of wind regime. *Atmos. Environ.* **2007**, *41*, 8431–8441. [CrossRef]
68. Strekalov, P.V. Wind regimes, chloride aerosol particle sedimentation and atmospheric corrosion of steel and copper. *Prot. Met.* **1988**, *24*, 630–641.
69. Preston, R.S.J.; Sanyal, B. Atmospheric corrosion by nuclei. *J. Appl. Chem.* **1956**, *6*, 26–44. [CrossRef]
70. Evans, U.R.; Taylor, C.A.J. Mechanism of atmospheric rusting. *Corros. Sci.* **1972**, *12*, 227–246. [CrossRef]
71. Morcillo, M.; Chico, B.; Otero, E.; Mariaca, L. Effect of marine aerosol on atmospheric corrosion. *Mater. Perform.* **1999**, *38*, 72–77.
72. Pascual Marqui, R.D. Influencia de la concentración de ion cloruro sobre la corrosión atmosférica de un acero al carbono bajo capa de fase de humedad. *Rev. Corros. Prot.* **1980**, *XI*, 37–40.
73. Espada, L.; González, A.M.; Sánchez, A.; Merino, P. Estudio de la velocidad de corrosión de aceros de bajo contenido de carbono en nieblas salinas de distinta concentración. *Rev. Iberoam. Corros. Prot.* **1988**, *19*, 227–229.
74. Hache, A. Contribution à l'étude de la corrosion de l'acier en solutions salines. *Rev. Metall.* **1956**, *53*, 76–80. [CrossRef]
75. Strekalov, P.V. Estimation of atmospheric salinity from analysis of dry and wet chloride precipitates. *Prot. Met.* **1994**, *30*, 59–64.
76. State System for Standardization of Russian Federation. *GOST 9.039–74, Unified System of Corrosion and Ageing Protection. Corrosive Aggressiveness of atMosphere*; State System for Standardization of Russian Federation: Moscow, Russia, 1974.
77. Beruksitis, G.K.; Klark, G.B. *Corrosion Fatigue of Metals and Metals Coatings under Atmospheric Conditions*; Nauka: Moscow, Russia, 1971.
78. European Committee for Standardization. *EN ISO 9225, Corrosion of Metals and Alloys—Corrosivity of Atmospheres—Measurement of Environmental Parameters Affecting Corrosivity of Atmospheres*; European Committee for Standardization: Brussels, Belgium, 2012.
79. Foran, M.R.; Gibbons, E.V.; Wellington, J.R. The measurement of atmospheric sulfur dioxide and chlorides. *Chem. Can.* **1958**, *10*, 33–41.
80. Corvo, F. Atmospheric corrosion of steel in humid tropical climate. Influence of pollution, humidity, temperature, rainfall and sun radiation. *Corrosion* **1984**, *40*, 170–175.
81. Dean, S.W. Atmospheric. In *Corrosion Tests and Standards. Application and Interpretation*; Baboian, R., Ed.; ASTM: Philadelphia, PA, USA, 1995; pp. 116–125.
82. Industrial Galvanizers (INGALV). Corrosion Mapping System. Available online: http://www.valmontcoatings.com/locations/asia-pacific (accessed on 12 April 2017).
83. Japan Industrial Standard. *JIS-Z-2381, Recommended Practice for Weathering Test*; Japan Industrial Standard: Tokyo, Japan, 1987.
84. Hujioara, M.; Danakka, O. Weathering due to the chloride of ferro-concrete structure. *Concr. Eng.* **1987**, *25*, 44–47.
85. Li, Q.X.; Wang, Z.Y.; Han, W.; Han, E.H. Characterization of the rust formed on weathering steel exposed to Qinghai salt lake atmosphere. *Corros. Sci.* **2008**, *50*, 365–371. [CrossRef]

86. Wang, J.; Wang, Z.Y.; Ke, W. A study of the evolution of rust on weathering steel submitted to the Qinghai salt lake atmospheric corrosion. *Mater. Chem. Phys.* **2013**, *139*, 225–232. [CrossRef]
87. Morcillo, M.; Chico, B.; Díaz, I.; Cano, H.; de la Fuente, D. Atmospheric corrosion data of weathering steels. A review. *Corros. Sci.* **2013**, *77*, 6–24. [CrossRef]
88. Takebe, M.; Ohya, M.; Ajiki, S.; Furukawa, T.; Adachi, R.; Gan-ei, R.; Kitagawa, N.; Ota, J.; Matsuzaki, Y.; Aso, T. Estimation of quantity of Cl^- from deicing salts on weathering steel used for bridges. *Int. J. Steel Struct.* **2008**, *8*, 73–81.
89. Takebe, M.; Matsuzaki, Y.; Ohya, M.; Ajiki, S.; Furukawa, T.; Aso, T. Study of corrosion level and composition of accumulating salt on weathering bridges. *J. JSCE* **2007**, *63*, 172–180. [CrossRef]
90. Hara, S.; Miura, M.; Uchiumi, Y.; Fujiwara, T.; Yamamoto, M. Suppression of deicing salt corrosion of weathering steel bridges by washing. *Corros. Sci.* **2005**, *47*, 2419–2430. [CrossRef]
91. Cornell, R.M.; Schwertmann, U. *The Iron Oxides: Structure, Properties, Reactions, Occurrences and Uses*, 2nd ed.; Wiley-VCH Verlag GmbH: Weinheim, Germany, 2003.
92. Gilberg, M.R.; Seeley, N.J. The identity of compounds containing chloride ions in marine iron corrosion products: A critical review. *Stud. Conserv.* **1981**, *26*, 50–56. [CrossRef]
93. Monnier, J.; Neff, D.; Réguer, S.; Dillmann, P.; Bellot-Gurlet, L.; Leroy, E.; Foy, E.; Legrand, L. A corrosion study of the ferrous medieval reinforcement of the amiens cathedral. Phase characterisation and localisation by various microprobes techniques. *Corros. Sci.* **2010**, *52*, 695–710. [CrossRef]
94. Neff, D.; Reguer, S.; Bellot-Gurlet, L.; Dillmann, P. Structural characterization of corrosion products on archaeological iron: An integrated analytical approach to establish corrosion forms. *J. Raman Spectrosc.* **2004**, *35*, 739–745. [CrossRef]
95. Pino, E.; Alcántara, J.; Chico, B.; Díaz, I.; Simancas, J.; de la Fuente, D.; Morcillo, M. Atmospheric corrosion of mild steel in marine atmospheres. *Corros. Prot. Mater.* **2015**, *34*, 35–41.
96. Bernal, J.D.; Dasgupta, D.R.; Mackay, A.L. The oxides and hydroxides of iron and their structural inter-relationships. *Clay Miner. Bull.* **1959**, *4*, 15–30. [CrossRef]
97. Arroyave, C.; Morcillo, M. Atmospheric corrosion products in iron and steels. *Trends Corros.* **1997**, *2*, 1–16.
98. Butler, G.; Beynon, J.G. The corrosion of mild steel in boiling salt solutions. *Corros. Sci.* **1967**, *7*, 385–404. [CrossRef]
99. Refait, P.; Abdelmoula, M.; Génin, J.M.R. Mechanisms of formation and structure of green rust one in aqueous corrosion of iron in the presence of chloride ions. *Corros. Sci.* **1998**, *40*, 1547–1560. [CrossRef]
100. Stampfl, P.P. Ein basisches eisen-II-III-karbonat in rost. *Corros. Sci.* **1969**, *9*, 185–187. [CrossRef]
101. Ståhl, K.; Nielsen, K.; Jiang, J.; Lebech, B.; Hanson, J.C.; Norby, P.; van Lanschot, J. On the akaganéite crystal structure, phase transformations and possible role in post-excavational corrosion of iron artifacts. *Corros. Sci.* **2003**, *45*, 2563–2575. [CrossRef]
102. Watson, J.H.L.; Cardell, R.R.; Heller, W. The internal structure of colloidal crystals of β-Feooh and remarks on their assemblies in schiller layers. *J. Phys. Chem.* **1962**, *66*, 1757–1763. [CrossRef]
103. Keller, P. Occurrence, formation and phase transformation of β-Feooh in rust. *Werkst. Korros.* **1969**, *20*, 102–108. [CrossRef]
104. Rezel, D.; Genin, J.M.R. The substitution of chloride ions to OH^--ions in the akaganeite beta ferric oxyhydroxide studied by Mössbauer effect. *Hyperfine Interact.* **1990**, *57*, 2067–2075. [CrossRef]
105. Gallagher, K.J. The atomic structure of tubular subcrystals of β-iron (III) oxide hydroxide. *Nature* **1970**, *226*, 1225–1228. [CrossRef] [PubMed]
106. Post, J.E.; Buchwald, V.F. Crystal-structure refinement of akaganeite. *Am. Mineral.* **1991**, *76*, 272–277.
107. Mackay, A.L. β-ferric oxyhydroxide. *Mineral. Mag.* **1960**, *32*, 545–557. [CrossRef]
108. Mackay, A.L. β-ferric oxyhydroxide—Akaganeite. *Mineral. Mag.* **1962**, *33*, 270–280. [CrossRef]
109. Shiotani, K.; Tanimoto, W.; Maeda, C.; Kawabata, F.; Amano, K. Structural analysis of the rust layer on a bare weathering steel bridge exposed in a coastal industrial zone for 27 years. *Corros. Eng.* **2000**, *49*, 99–109. [CrossRef]
110. Morcillo, M.; Chico, B.; Alcántara, J.; Díaz, I.; Wolthuis, R.; de la Fuente, D. SEM/micro-Raman characterization of the morphologies of marine atmospheric corrosion products formed on mild steel. *J. Electrochem. Soc.* **2016**, *163*, C426–C439. [CrossRef]

111. De la Fuente, D.; Alcántara, J.; Chico, B.; Díaz, I.; Jiménez, J.A.; Morcillo, M. Characterisation of rust surfaces formed on mild steel exposed to marine atmospheres using XRD and SEM/micro-Raman techniques. *Corros. Sci.* **2016**, *110*, 253–264. [CrossRef]
112. Rémazeilles, C.; Refait, P. Formation, fast oxidation and thermodynamic data of Fe(II) hydroxychlorides. *Corros. Sci.* **2008**, *50*, 856–864. [CrossRef]
113. Refait, P.; Genin, J.M.R. The mechanism of oxidation of ferrous hydroxychloride β-$Fe_2(OH)_3Cl$ in aqueous solution: The formation of akaganeite vs goethite. *Corros. Sci.* **1997**, *39*, 539–553. [CrossRef]
114. Rémazeilles, C.; Refait, P. On the formation of β-FeOOH (akaganéite) in chloride-containing environments. *Corros. Sci.* **2007**, *49*, 844–857. [CrossRef]
115. Refait, P.; Génin, J.M.R. The oxidation of ferrous hydroxide in chloride-containing aqueous media and Pourbaix diagrams of green rust one. *Corros. Sci.* **1993**, *34*, 797–819. [CrossRef]
116. Wells, A.F. *Structural Inorganic Chemistry*, 4th ed.; Oxford University Press: London, UK, 1975.
117. Fasiska, E.J. Structural aspects of the oxides and oxyhydrates of iron. *Corros. Sci.* **1967**, *7*, 833–839. [CrossRef]
118. Antunes, R.A.; Costa, I.; de Faria, D.L.A. Characterization of corrosion products formed on steels in the first months of atmospheric exposure. *Mater. Res.* **2003**, *6*, 403–408. [CrossRef]
119. Schwarz, H. Über die Wirkung des magnetits beim atmosphärischen Rosten und beim Unterrosten von Anstrichen. *Werkst. Korros.* **1972**, *23*, 648–663. [CrossRef]
120. Singh, A.K. Mössbauer and X-ray diffraction phase analysis of rusts from atmospheric test sites with different environments in Sweden. *Corros. Sci.* **1985**, *25*, 931–945. [CrossRef]
121. Ishikawa, T.; Kondo, Y.; Yasukawa, A.; Kandori, K. Formation of magnetite in the presence of ferric oxyhydroxides. *Corros. Sci.* **1998**, *40*, 1239–1251. [CrossRef]
122. Tanaka, H.; Mishima, R.; Hatanaka, N.; Ishikawa, T.; Nakayama, T. Formation of magnetite rust particles by reacting iron powder with artificial α-, β- and γ-FeOOH in aqueous media. *Corros. Sci.* **2014**, *78*, 384–387. [CrossRef]
123. Hiller, J.E. Phasenumwandlungen im rost. *Werkst. Korros.* **1966**, *17*, 943–951. [CrossRef]
124. Jeffrey, R.J.; Melchers, R.E. The changing composition of the corrosion products of mild steel in severe marine atmospheres. In Proceedings of the Annual Conference of the Australasian Corrosion Association, Melbourne, Australia, 11–14 November 2012.
125. Haces, C.; Corvo, F.; Furet, N.R. Mecanismo de la corrosión atmosférica del acero en una zona de alta salinidad. In Proceedings of the 3rd Iberoamerican Congress of Corrosion and Protection, ABRACO, Río de Janeiro, Brazil, 26–30 June 1989; Volume 1, pp. 415–419.
126. Asami, K. Characterization of rust layers on a plain-carbon steel and weathering steels exposed to industrial and coastal atmosphere for years. In *Characterization of Corrosion Products on Steel Surfaces*; Waseda, Y., Suzuki, S., Eds.; Advances in Materials Research; Springer: Heidelberg, Germany, 2006; pp. 159–197.
127. Graham, M.J.; Cohen, M. Analysis of iron corrosion products using Mössbauer spectroscopy. *Corrosion* **1976**, *32*, 432–438. [CrossRef]
128. Leidheiser, H., Jr.; Musíc, S. The atmospheric corrosion of iron as studied by Mössbauer spectroscopy. *Corros. Sci.* **1982**, *22*, 1089–1096. [CrossRef]
129. Chico, B.; Alcántara, J.; Pino, E.; Díaz, I.; Simancas, J.; Torres-Pardo, A.; de la Fuente, D.; Jiménez, J.A.; Marco, J.F.; González-Calbet, J.M.; et al. Rust exfoliation on carbon steels in chloride-rich atmopsheres. *Corros. Rev.* **2015**, *33*, 263–282. [CrossRef]
130. Oh, S.J.; Cook, D.C.; Townsend, H.E. Atmospheric corrosion of different steels in marine, rural and industrial environments. *Corros. Sci.* **1999**, *41*, 1687–1702. [CrossRef]
131. Antony, H.; Perrin, S.; Dillmann, P.; Legrand, L.; Chaussé, A. Electrochemical study of indoor atmospheric corrosion layers formed on ancient iron artefacts. *Electrochim. Acta* **2007**, *52*, 7754–7759. [CrossRef]
132. Matsubara, E.; Suzuki, S.; Waseda, Y. Corrosion mechanism of iron from an X-ray structural viewpoint. In *Characterization of Corrosion Products on Steel Surfaces*; Waseda, Y., Suzuki, S., Eds.; Advances in Materials Research; Springer: Heidelberg, Germany, 2006; pp. 105–129.
133. Environmental Geochemistry of Ferric Polymers in Aqueous Solutions and Precipitates. Available online: http://geoweb.princeton.edu/research/geochemistry/research/aqueous-polymers.html (accessed on 11 April 2017).

134. Waseda, Y.; Suzuki, S.; Saito, M. Structural characterization for a complex system by obtaining middle-range ordering. In *Characterization of Corrosion Products on Steel Surfaces*; Waseda, Y., Suzuki, S., Eds.; Advances in Materials Research; Springer: Heidelberg, Germany, 2006; pp. 77–104.
135. Raman, A.; Nasrazadani, S.; Sharma, L. Morphology of rust phases formed on weathering steels in various laboratory corrosion test. *Metallography* **1989**, *22*, 79–96. [CrossRef]
136. Morcillo, M.; Wolthuis, R.; Alcántara, J.; Chico, B.; Díaz, I.; de la Fuente, D. Scanning Electron Microscopy/microRaman: A very useful technique for characterizing the morphologies of rust phases formed on carbon steel in atmospheric exposures. *Corrosion* **2016**, *72*, 1044–1054.
137. Alcántara, J.; Chico, B.; Simancas, J.; Díaz, I.; de la Fuente, D.; Morcillo, M. An attempt to classify the morphologies presented by different rust phases formed during the exposure of carbon steel to marine atmospheres. *Mater. Charact.* **2016**, *118*, 65–78. [CrossRef]
138. Kihira, H. Colloidal aspects of rusting of weathering steel. In *Electrical Phenomena at Interfaces, Fundamentals, Measurements and Applications*, 2nd ed.; Ohshima, H., Furusawa, K., Eds.; Marcel Dekker, Inc.: New York, NY, USA, 1998.
139. Licheri, G.; Pinna, G. EXAFS and X-ray diffraction in solutions. In *EXAFS and Near Edge Structure*; Springer: Frascati, Italy, 13–17 September 1982; pp. 240–247.
140. Jolviet, J.P. *Metal Oxide Chemistry and Synthesis*; John Wiley & Sons Ltd.: West Sussex, UK, 2000.
141. Ishikawa, T.; Yoshida, T.; Kandori, K.; Nakayama, T.; Hara, S. Assessment of protective function of steel rust layers by N_2 adsorption. *Corros. Sci.* **2007**, *49*, 1468–1477. [CrossRef]
142. Hara, S.; Kamimura, T.; Miyuki, H.; Yamashita, M. Taxonomy for protective ability of rust layer using its composition formed on weathering steel bridge. *Corros. Sci.* **2007**, *49*, 1131–1142. [CrossRef]
143. Calero, J.; Alcántara, J.; Chico, B.; Díaz, I.; Simancas, J.; de la Fuente, D.; Morcillo, M. Wet/dry accelerated laboratory test to simulate the formation of multilayered rust on carbon steel in marine atmospheres. *Corros. Eng. Sci. Technol.* **2017**. [CrossRef]
144. Ishikawa, T.; Maeda, A.; Kandori, K.; Tahara, A. Characterization of rust on Fe-Cr, Fe-Ni, and Fe-Cu binary alloys by Fourier Transform Infrared and N_2 adsorption. *Corrosion* **2006**, *62*, 559–567. [CrossRef]
145. Ishikawa, T.; Katoh, R.; Yasukawa, A.; Kandori, K.; Nakayama, T.; Yuse, F. Influences of metal ions on the formation of β-FeOOH particles. *Corros. Sci.* **2001**, *43*, 1727–1738. [CrossRef]
146. Ishikawa, T.; Kumagai, M.; Yasukawa, A.; Kandori, K. Characterization of rust on weathering steel by gas adsoption. *Corrosion* **2001**, *57*, 346–352. [CrossRef]
147. LaQue, F.L. Corrosion testing. *Proc. ASTM* **1951**, *51*, 495–582.
148. Díaz, I. Corrosión Atmosférica de Aceros Patinables de Nueva Generación. Ph.D. Thesis, Complutense University, Madrid, Spain, October 2012.
149. Cano, H. Aceros Patinables (Cu, Cr, Ni): Resistencia a la Corrosión Atmosférica y Soldabilidad. Ph.D. Thesis, Complutense University, Madrid, Spain, December 2013.
150. Díaz, I.; Cano, H.; de la Fuente, D.; Chico, B.; Vega, J.M.; Morcillo, M. Atmospheric corrosion of Ni-advanced weathering steels in marine atmospheres of moderate salinity. *Corros. Sci.* **2013**, *76*, 348–360. [CrossRef]
151. Suzuki, I.; Hisamatsu, Y.; Masuko, N. Nature of atmospheric rust on iron. *J. Electrochem. Soc.* **1980**, *127*, 2210–2215. [CrossRef]
152. De la Fuente, D.; Diaz, I.; Simancas, J.; Chico, B.; Morcillo, M. Long-term atmospheric corrosion of mild steel. *Corros. Sci.* **2011**, *53*, 604–617. [CrossRef]
153. Morcillo, M.; Alcántara, J.; Díaz, I.; Chico, B.; Simancas, J.; de la Fuente, D. Marine atmospheric corrosion of carbon steels. *Rev. Metal. Madrid* **2015**, *51*, e045. [CrossRef]
154. Honzák, J. *Schutz von Stahlkonstruktion Gegen Atmospharische Korrosion (Protection of Steel Structures againts Atmospheric Corrosion)*; 57 Veranstaltung EFK: Prague, Czech Republic, 1971.
155. Copson, H.R. Atmospheric corrosion of low alloy steels. *Proc. ASTM* **1952**, *52*, 1005–1026.
156. García, K.E.; Morales, A.L.; Barrero, C.A.; Greneche, J.M. On the rusts products formed on weathering and carbon steels exposed to chloride in dry/wet cyclical processes. *Hyperfine Interact.* **2005**, *161*, 127–137. [CrossRef]
157. García, K.E.; Barrero, C.A.; Morales, A.L.; Greneche, J.M. Lost iron and iron converted into rust in steels submitted to dry–wet corrosion process. *Corros. Sci.* **2008**, *50*, 763–772. [CrossRef]
158. Barrero, C.A.; García, K.E.; Morales, A.L.; Greneche, J.M. A proposal to evaluate the amount of corroded iron converted into adherent rust in steels exposed to corrosion. *Corros. Sci.* **2011**, *53*, 769–775. [CrossRef]

159. Cano, H.; Neff, D.; Morcillo, M.; Dillmann, P.; Díaz, I.; de la Fuente, D. Characterization of corrosion products formed on Ni 2.4 wt%–Cu 0.5 wt%–Cr 0.5 wt% weathering steel exposed in marine atmospheres. *Corros. Sci.* **2014**, *87*, 438–451. [CrossRef]
160. Asami, K.; Kikuchi, M. In-depth distribution of rusts on a plain carbon steel and weathering steels exposed to coastal–industrial atmosphere for 17 years. *Corros. Sci.* **2003**, *45*, 2671–2688. [CrossRef]
161. Hara, S. A X-ray diffraction analysis on constituent distribution of heavy rust layer formed on weathering steel using synchrotron radiation. *Corros. Eng. Jpn.* **2008**, *57*, 70–75. [CrossRef]
162. Morcillo, M.; Chico, B.; de la Fuente, D.; Alcántara, J.; Odnevall Wallinder, I.; Leygraf, C. On the mechanism of rust exfoliation in marine environments. *J. Electrochem. Soc.* **2017**, *164*, C8–C16. [CrossRef]
163. Ishikawa, T.; Isa, R.; Kandori, K.; Nakayama, T.; Tsubota, T. Influences of metal chlorides and sulfates on the formation of β-FeOOH particles by aerial oxidation. *J. Electrochem. Soc* **2004**, *151*, B586–B594. [CrossRef]
164. Brunauer, S.; Emmett, P.H.; Teller, E. Adsorption of gases in multimolecular layers. *J. Am. Chem. Soc.* **1938**, *60*, 309–319. [CrossRef]
165. Rouguerol, F.; Rouguerol, J.; Sing, K. *Adsorption by Powders and Porous Solids*; Academic Press: London, UK, 1999.
166. Yamashita, M.; Misawa, T. Recent progress in the study of protective rust-layer formation on weathering steel. In Proceedings of the Corrosion' 98, San Diego, CA, USA, 22–27 March 1998; Technical Publication; NACE International: Houston, TX, USA, 31 December 1998; p. 357.
167. Kamimura, T.; Hara, S.; Miyuki, H.; Yamashita, M.; Uchida, H. Composition and protective ability of rust layer formed on weathering steel exposed to various environments. *Corros. Sci.* **2006**, *48*, 2799–2812. [CrossRef]
168. Henriksen, J.F. Distribution of NaCl on Fe during atmospheric corrosion. *Corros. Sci.* **1969**, *9*, 573–577. [CrossRef]
169. Misawa, T.; Kyuno, Y.; Suëtaka, W.; Shimodaira, S. The mechanism of atmospheric rusting and the effect of Cu and P on the rust formation of low-alloy steels. *Corros. Sci.* **1971**, *11*, 35–48. [CrossRef]
170. Misawa, T.; Hashimoto, K.; Shimodaira, S. The mechanism of formation of iron oxide and oxyhydroxides in aqueous solutions at room temperature. *Corros. Sci.* **1974**, *14*, 131–149. [CrossRef]
171. Misawa, T.; Asami, K.; Hashimoto, K.; Shimodaira, S. Mechanism of atmospheric rusting and protective amorphous rust on low-alloy steel. *Corros. Sci.* **1974**, *14*, 279–289. [CrossRef]
172. Mikhailovskii, N. *Atmospheric Corrosion of Metals and Protection Methods*; Metallurgiia: Moscow, Russia, 1989.
173. Worch, H.; Forker, W.; Rahner, D. Rust formation on iron. A model. *Werkst. Korros.* **1983**, *34*, 402–410. [CrossRef]
174. Schikorr, G. Korrosionsverhalten von zink und zinküberzügen and der atmosphäre. *Werkst. Korros.* **1964**, *15*, 537–543. [CrossRef]
175. Lau, T.T.N.; Thoa, N.T.P.; Nishimura, R.; Tsujino, Y.; Yokoi, M.; Maeda, Y. Atmospheric corrosion of carbon steel under field exposure in the southern part of Vietnam. *Corros. Sci.* **2006**, *48*, 179–192.
176. Li, S.; Hihara, L.H. In situ Raman spectroscopy study of NaCl particle-induced marine atmospheric corrosion of carbon steel. *J. Electrochem. Soc.* **2012**, *159*, C147–C154. [CrossRef]
177. Li, S.; Hihara, L.H. Atmospheric corrosion initiation on steel from predeposited NaCl salt particles in high humidity atmospheres. *Corros. Eng. Sci. Technol.* **2010**, *45*, 49–56. [CrossRef]
178. Li, S.; Hihara, L.H. Atmospheric corrosion electrochemistry of NaCl droplets on carbon steel. *J. Electrochem. Soc.* **2012**, *159*, C461–C468. [CrossRef]
179. Risteen, B.E.; Schindelholz, E.; Kelly, R.G. Marine aerosol drop size effects on the corrosion behavior of low carbon steel and high purity iron. *J. Electrochem. Soc.* **2014**, *161*, C580–C586. [CrossRef]
180. Ohtsuka, T.; Tanaka, S. Monitoring the development of rust layers on weathering steel using in situ Raman spectroscopy under wet-and-dry cyclic conditions. *J. Solid State Electrochem.* **2015**, *19*, 3559–3566. [CrossRef]
181. Evans, U.R. Electrochemical mechanism of atmospheric rusting. *Nature* **1965**, *206*, 980–982. [CrossRef]
182. Stratmann, M.; Bohnenkamp, K.; Engell, H.J. An electrochemical study of phase-transitions in rust layers. *Corros. Sci.* **1983**, *23*, 969–985. [CrossRef]
183. Horton, J.B. The Composition, Structure and Growth of the Atmospheric Rust on Various Steels. Ph.D. Thesis, Lehigh University, Bethlehem, PA, USA, May 1964.
184. Burger, E.; Fenart, M.; Perrin, S.; Neff, D.; Dillmann, P. Use of the gold markers method to predict the mechanisms of iron atmospheric corrosion. *Corros. Sci.* **2011**, *53*, 2122–2130. [CrossRef]

185. Antony, H.; Legrand, L.; Maréchal, L.; Perrin, S.; Dillmann, P.; Chaussé, A. Study of lepidocrocite γ-FeOOH electrochemical reduction in neutral and slightly alkaline solutions at 25 °C. *Electrochim. Acta* **2005**, *51*, 745–753. [CrossRef]
186. Monnier, J.; Burger, E.; Berger, P.; Neff, D.; Guillot, I.; Dillmann, P. Localisation of oxygen reduction sites in the case of iron long term atmospheric corrosion. *Corros. Sci.* **2011**, *53*, 2468–2473. [CrossRef]
187. Nomura, K.; Tasaka, M.; Ujihira, Y. Conversion electron Mössbauer spectrometric study of corrosion products of iron immersed in sodium chloride solution. *Corrosion* **1988**, *44*, 131–135. [CrossRef]
188. Ma, Y.; Li, Y.; Wang, F. The effect of β-FeOOH on the corrosion behavior of low carbon steel exposed in tropic marine environment. *Mater. Chem. Phys.* **2008**, *112*, 844–852. [CrossRef]
189. Ma, Y.; Li, Y.; Wang, F. Corrosion of low carbon steel in atmospheric environments of different chloride content. *Corros. Sci.* **2009**, *51*, 997–1006. [CrossRef]
190. Schwertmann, V.; Taylor, R.M. The transformation of lepidocrocite to goethite. *Clays Clay Miner.* **1972**, *20*, 151–158. [CrossRef]
191. Saha, J.K. *Corrosion of Constructional Steels in Marine and Industrial Environment*; Springer: New Delhi, India, 2013.
192. Morcillo, M.; González-Calbet, J.M.; Jiménez, J.A.; Díaz, I.; Alcántara, J.; Chico, B.; Mazarío-Fernández, A.; Gómez-Herrero, A.; Llorente, I.; de la Fuente, D. Environmental conditions for akaganeite formation in marine atmosphere mild steel corrosion products and its characterisation. *Corrosion* **2015**, *71*, 872–886. [CrossRef]
193. De la Fuente, D.; Díaz, I.; Alcántara, J.; Chico, B.; Simancas, J.; Llorente, I.; García-Delgado, A.; Jiménez, J.A.; Adeva, P.; Morcillo, M. Corrosion mechanisms of mild steel in chloride-rich atmospheres. *Mater. Corros.* **2015**, *67*, 227–238. [CrossRef]
194. Institute of Experimental Mineralogy. *Crystallographic and Crystallochemical Database for Minerals and Their Structural Analogues*; www.Mincryst; Institute of Experimental Mineralogy, Russian Academy of Sciences: Chernogolovka, Russia, 2016; Available online: http://database.iem.ac.ru/mincryst/index.php (accessed on 11 April 2017).
195. Copson, H.R. A theory of the mechanism of rusting of low-alloy steels in the atmosphere. *Proc. ASTM* **1945**, *45*, 554–580.
196. Ericsson, R. Influence of sodium-chloride on atmospheric corrosion of steel. *Werkst. Korros.* **1978**, *29*, 400–403. [CrossRef]
197. Allam, I.M.; Arlow, J.S.; Saricimen, H. Initial stages of atmospheric corrosion of steel in the arabian gulf. *Corros. Sci.* **1991**, *32*, 417–432. [CrossRef]
198. Almeida, E.; Morcillo, M.; Rosales, B. Atmospheric corrosion of mild steel part II—Marine atmospheres. *Mater. Corros.* **2000**, *51*, 865–874. [CrossRef]
199. Liang, C.; Hou, W. Sixteen year atmospheric corrosion exposure study of steels. *J. Chin. Soc. Corros. Prot.* **2005**, *25*, 1–6.
200. Wang, Z. Study of the corrosion behaviour of weathering steels in atmospheric environments. *Corros. Sci.* **2013**, *67*, 1–10. [CrossRef]
201. Scully, J.C. *The Fundamentals of Corrosion*, 3rd ed.; Pergamon Press: Oxford, UK, 1990; p. 106.
202. Brown, P.W.; Masters, L.W. Factors affecting the corrosion of metals in the atmosphere. In *Atmospheric Corrosion*; Ailor, W.H., Ed.; Wiley: New York, NY, USA, 1982; pp. 34–49.
203. Knotkova, D.; Barton, K.; van Tu, B. Atmospheric corrosion in maritime industrial atmospheres: Laboratory research. In *Degradation of Metals in the Atmosphere*; ASTM STP 965; Dean, S.W., Lee, T.S., Eds.; American Society for Testing and Materials: Philadelphia, PA, USA, 1987; pp. 290–305.
204. Bastidas, J.M. Corrosión del Al, Cu, Fe y Zn en atmóSferas Controladas. Ph.D. Thesis, Complutense University, Madrid, Spain, 1981.
205. Chen, W.; Hao, L.; Dong, J.; Ke, W. Effect of sulphur dioxide on the corrosion of a low alloy steel in simulated coastal industrial atmosphere. *Corros. Sci.* **2014**, *83*, 155–163. [CrossRef]
206. *UNECE International Cooperative Programme on Effects on Materials Including Historic and Cultural Monuments, Report No. 01: Technical Manual*; Swedish Corrosion Institute: Stockholm, Sweden, 1988.
207. Morcillo, M.; Almeida, E.; Rosales, B.; Uruchurtu, J.; Marrocos, M. *Corrosion y Protección de Metales en las Atmósferas de Iberoamérica. Parte I—Mapas de Iberoamérica de Corrosividad Atmosférica (Proyecto MICAT, XV.1/CYTED)*; CYTED: Madrid, Spain, 1998.

208. Benarie, M.; Lipfert, F.L. A general corrosion function in terms of atmospheric pollutant concentrations and rain pH. *Atmos. Environ.* **1986**, *20*, 1947–1958. [CrossRef]
209. Panchenko, Y.M.; Marshakov, A.I.; Igonin, T.N.; Kovtanyuk, V.V.; Nikolaeva, L.A. Long-term forecast of corrosion mass losses of technically important metals in various world regions using a power function. *Corros. Sci.* **2014**, *88*, 306–316. [CrossRef]
210. McCuen, R.H.; Albrecht, P.; Cheng, J.G. A new approach to power-model regression of corrosion penetration data. In *Corrosion Forms and Control for Infrastructure*; Chaker, V., Ed.; ASTM STP 1137; American Society for Testing and Materials: Philadelphia, PA, USA, 1992; Volume 1137, pp. 46–76.
211. Panchenko, Y.M.; Marshakov, A.I. Long-term prediction of metal corrosion losses in atmosphere using a power-linear function. *Corros. Sci.* **2016**, *109*, 217–229. [CrossRef]
212. Albrecht, P.; Hall, T.T. Atmospheric corrosion resistance of structural steels. *J. Mater. Civ. Eng.* **2003**, *15*, 2–24. [CrossRef]
213. European Committee for Standardization. *EN ISO 9224, Corrosion of Metals and Alloys—Corrosivity of Atmospheres—Guiding Values for the Corrosivity Categories*; European Committee for Standardization: Brussels, Belgium, 2012.
214. Melchers, R.E. A new interpretation of the corrosion loss processes for weathering steels in marine atmospheres. *Corros. Sci.* **2008**, *50*, 3446–3454. [CrossRef]
215. Melchers, R.E. Long-term corrosion of cast irons and steel in marine and atmospheric environments. *Corros. Sci.* **2013**, *68*, 186–194. [CrossRef]
216. International Organization for Standardization. *ISO 9223 1st Edition, Corrosion of Metals and alloys—Corrosivity of Atmospheres—Classification*; International Organization for Standardization: Geneve, Switzerland, 1992.
217. Cole, I.S.; Neufeld, A.K.; Kao, P.; Ganther, W.D.; Chotimongkol, L.; Bharmornsut, C.; Hue, N.V.; Bernardo, S.; Purwadaria, S. Development of performance verification methods for the durability of metallic components in tropical countries. In Proceedings of the 11th Asia-Pacific Corrosion Control Conference, Ho Chi Minh City, Vietnam, 1–5 November 1999; Volume 2, pp. 555–570.
218. Cole, I.S.; Furman, S.A.; Neufeld, A.K.; Ganther, W.D.; King, G.A. A holistic approach to modelling in atmospheric corrosion. In Procededings of the 14th International Corrosion Congress, Cape Town, South Africa, 26 September–1 October 1999.
219. Cole, I.S.; King, G.A.; Trinidad, G.S.; Chan, W.Y.; Paterson, A. An Australia-wide map of corrosivity: A gis approach. In Proceedings of the 8th International Conference on Durability of Building Materials and Components, Vancouver, BC, Canada, 30 May–3 June 1999.
220. Nakajima, M. Mapping method for salt attack hazzard using topographic effects analysis. In Proceedings of the 1st Asia/Pacific Conference on Harmonisation of Durability Standards and Performance Tests for Components in the Building Industry, Bangkok, Thailand, 8–10 September 1999.
221. Klassen, R.D.; Roberge, P.R. The effects of wind on local atmospheric corrosivity. In *Corrosion 2001*; NACE International: Houston, TX, USA, 2001.
222. Doyle, D.P.; Wright, T.E. Rapid method for determining atmospheric corrosivity and corrosion resistance. In *Atmospheric Corrosion*; Ailor, W.H., Ed.; Wiley: New York, NY, USA, 1982; pp. 227–243.
223. Roberge, P.R.; Klassen, R.D.; Haberecht, P.W. Atmospheric corrosivity modeling—A review. *Mater. Des.* **2002**, *23*, 321–330. [CrossRef]

“Siempre parece imposible hasta

que se hace.”

Nelson Mandela


VNIVERSITAS COMPLVTENSIS
MATRITENSIS


CENIM
Centro Nacional de Investigaciones Metalúrgicas


CSIC
Consejo Superior de Investigaciones Científicas